

FINITE ELEMENT ANALYSES ON COHESIVE SOIL BEHAVIOR DUE TO  
ADVANCED SHIELD TUNNELING

by

Takeshi Shirasuna

Dissertation submitted to the Faculty of the  
Virginia Polytechnic Institute and State University  
in partial fulfillment of the requirements for the degree of

DOCTOR OF PHILOSOPHY

in

Civil Engineering

APPROVED:

---

G. W. Clough, Chairman

---

J. M. Duncan

---

T. Kuppusamy

---

R. M. Barker

---

R. M. Jones

November, 1985

Blacksburg, Virginia

FINITE ELEMENT ANALYSES ON COHESIVE SOIL BEHAVIOR DUE TO  
ADVANCED SHIELD TUNNELING

BY

Takeshi Shirasuna

Committee Chairman: G. Wayne Clough  
Civil Engineering

(ABSTRACT)

Soil tunnels are usually constructed using a shield with an open face. However, in the past decade, innovations in shield tunneling technology have brought closed-faced shields that provide continuous support to the face and permit tunneling through even the most difficult conditions of soft ground. These new machines are typically operated in such a way that during tunneling the soil at the face is actually heaved away from the shield. This operating procedure has been said to allow greater control of the ground movements around and above the shield, and to minimize detrimental settlements. However, there is little hard evidence to this effect and there is no rational basis to judge the actual influence of the soil heave.

Building on former researchers' efforts, this thesis is directed towards developing a suitable finite element method (FEM) approach to the advanced shield problem. The FEM program developed includes the Prevost elasto-plastic soil model, allows for analysis of development and dissipation of excess pore pressure, large deformation, and simulation of the construction procedure of advanced shield tunneling.

This is the first time that the Prevost model was applied to a soft clay. Modifications were made, in particular for the parameter determination, to make the model applicable for the soft clay of San Francisco Bay Mud. Examination of two other soil models for the tunnel analysis, non-linear pseudo-elastic and Cam Clay models, showed the Prevost model to be preferable. Loading procedures were also examined to accurately simulate the heaving and tail void closure effects.

The finite element simulation of the N-2 sewer project, which is the first advanced shield project in the United States, demonstrated that the prediction agreed consistently well with the observations in the field. Further analyses indicated that heave at the face of the shield increases long-term consolidation settlements while it decreases immediate settlements and thus the final settlement may be reduced. The tail void simply increases settlements.

The results suggest that strict control of heaving and elimination of tail void with proper and prompt grouting are crucial for mitigating ground movements with advanced shield tunneling.

## ACKNOWLEDGEMENTS

I would like to express gratitude to my advisor, Professor G. Wayne Clough, for his guidance and continuous encouragement during the course of the thesis work. His patient review and criticism of the manuscript was of the greatest assistance in the preparation of the dissertation. I have learned so much from his acute analytical ability in solving problems in the past four years.

I would like to thank every member of my advisory committee for his careful review of the manuscript. Discussions with Professors T. Kuppusamy and Z. Mroz were very valuable in providing insight into the numerical analysis. I also would like to thank Dr. Donald W. Mckeon, my international student advisor, for his kind guidance and encouragement.

Special appreciation is due to my Stanford friends; \_\_\_\_\_, \_\_\_\_\_, \_\_\_\_\_, and \_\_\_\_\_. They kindly encouraged a new student from Japan who was then linguistically disabled. It was a special opportunity for me to share work on a project with \_\_\_\_\_.

Appreciation is also due to my friends at VA TECH; \_\_\_\_\_ who gave me the honor of being the first fisherman to open the trout season in Virginia, \_\_\_\_\_ who was an organizer of a wonderful picnic at Duck Pond, \_\_\_\_\_ who was a founder of our regular Greek Restraunt meetings after seminar, Jotaro Iwabuchi who, together with Professor Clough, was instrumental in helping me improve my golf. They know the right

approach to school life, and they taught me well.

I am indebted to Messrs. S. Yokoyama, J. Saito, I. Naramura, Y. Goto, S. Kurosawa, Y. Yokoyama, Y. Kumoi, and other individuals in Ohbayashi Corporation, Tokyo, Japan who supplied understanding and support over the duration of the thesis work. Special thanks are due to Mr. K. Tonoda who helped me to keep study.

Funding for the work was provided by Ohbayashi Corporation and Virginia TECH. Their assistance is greatly appreciated.

The work could not have been accomplished without the love and support of my wife, , who typed the manuscript four times. Even my three little daughters cheered me on. It is to my wife's and my parents, who constantly sacrificed for their children's well-being, that this thesis is dedicated.

## CONTENTS

ABSTRACT . . . . .	ii
ACKNOWLEDGEMENT . . . . .	iv
List of Figures . . . . .	xii
List of Tables . . . . .	xxii
List of Symbols . . . . .	xxiv

Chapter	Page
1. INTRODUCTION . . . . .	1
2. SHIELD TUNNELING METHOD AND ASSOCIATED GROUND MOVEMENT STUDIES	8
2.1 Introduction . . . . .	8
2.2 Shield Tunneling Techniques . . . . .	8
2.2.1 Conventional Open-faced Shields . . . . .	10
2.2.2 Advanced Shields . . . . .	11
2.2.3 Variations of Advanced Shields . . . . .	13
2.2.4 Summary . . . . .	14
2.3 Surface Settlement Induced by Shield Tunneling . . . . .	15
2.3.1 Surface Settlement Profile . . . . .	15
2.3.2 Causes of Settlement . . . . .	16
2.3.3 Prediction of Surface Settlement . . . . .	20
2.4 Measured Ground Movements Induced by Advanced Shields . . . . .	22
2.4.1 Measured Ground Movements and Pore Pressure . . . . .	23
Development	
2.4.2 Ground Movements of the N-2 Tunnel Case . . . . .	24
2.5 Analytical Procedures for Shield Tunneling . . . . .	27
2.5.1 Closed Form Solutions . . . . .	27
2.5.2 Finite Element Solutions . . . . .	27
2.5.3 Solutions of Limit Analysis and Boundary Element . . . . .	29
Method	
2.5.4 Requirements for Modeling Tunneling Procedure . . . . .	30
2.6 Summary . . . . .	31

3.	THEORETICAL DEVELOPMENT OF PREVOST MODEL IN SOIL PLASTICITY . . . . .	45
3.1	Introduction . . . . .	45
3.1.1	Historical Development of Soil Model in Soil Plasticity . . . . .	46
3.1.2	Multisurface Models . . . . .	48
3.1.3	Prevost Model . . . . .	50
3.2	Elasto-plastic Formulation -- Prevost Pressure-Sensitive Model . . . . .	51
3.2.1	Elastic Stress-Strain Relation . . . . .	51
3.2.2	Yield Function . . . . .	52
3.2.3	Flow Rule . . . . .	53
3.2.4	Consistency Condition . . . . .	54
3.2.5	Combined Hardening Rule . . . . .	55
3.2.6	Plastic Strain Increment . . . . .	57
3.2.7	Elasto-plastic Modulus . . . . .	58
3.3	Hydrostatic Axis and Deviatoric Subspace . . . . .	59
3.3.1	Decomposed Formulation . . . . .	60
3.3.2	Decomposed Constitutive Equations . . . . .	62
3.4	Nested Yield Surfaces . . . . .	63
3.4.1	Yield Function of Nested Yield Surfaces . . . . .	63
3.4.2	Contacting Surfaces . . . . .	64
3.4.3	Translation Rule . . . . .	65
3.4.4	Plastic Modulus . . . . .	67
3.4.5	Nonassociativity and Plastic Potential . . . . .	71
3.5	Bounding Surface . . . . .	72
3.5.1	Role of Bounding Surface . . . . .	72
3.5.2	The Critical State . . . . .	73
3.5.3	Plastic Modulus . . . . .	75
3.6	Summary . . . . .	77
4.	IMPLEMENTATION OF PREVOST MODEL . . . . .	85
4.1	Introduction . . . . .	85
4.2	Rotationally Symmetric Stress Condition . . . . .	87
4.3	Consideration of Model Bulk Response . . . . .	90
4.3.1	Volumetric Response to Mean Stress . . . . .	90
4.3.2	Pore Pressure Response to Shear Stress . . . . .	93
	-- A Special Case	
4.3.3	Effects of Bulk Shear Interaction . . . . .	97
4.4	Conventional Parameter Determination Procedure . . . . .	99
4.4.1	Interpretation of the Conventional Parameter Evaluation Procedure . . . . .	99
4.4.2	Consistency Conditions . . . . .	101

4.4.3	Kinematic Conditions . . . . .	102
4.4.4	Slope Condition . . . . .	104
4.4.5	Evaluation of Parameters . . . . .	104
4.4.6	Flow Chart . . . . .	105
4.5	Discussion on Problems with Model Parameters . . . . .	107
4.5.1	Justification of Model Parameters . . . . .	107
4.5.2	Defective Aspect of the Model . . . . .	109
4.5.3	Examination of Slope Condition . . . . .	114
4.6	Improved Evaluation of Model Parameters . . . . .	119
4.6.1	Consideration of Loading History . . . . .	119
4.6.2	Bulk Modulus Constraint . . . . .	121
4.6.3	Transition Zone at Low Stress Levels . . . . .	124
4.6.4	Model Prediction with New Model Parameters . . . . .	127
4.7	Summary and Conclusions . . . . .	128
5.	APPLICABILITY OF PREVOST MODEL TO SAN FRANCISCO BAY MUD . . . . .	154
5.1	Introduction . . . . .	154
5.2	Description of San Francisco Bay Mud . . . . .	154
5.3	Prevost Model Representation . . . . .	156
5.3.1	Interpretation of Undrained Triaxial Test Results . . . . .	157
5.3.2	Calculation of Prevost Model Predictions for Simple Loadings . . . . .	158
5.4	Undrained Behavior in Triaxial Test . . . . .	159
5.5	Drained Behavior on Oedometer Test . . . . .	161
5.6	Undrained Behavior in Plane Strain Shear Test . . . . .	162
5.7	Model Response to Multicubical Test . . . . .	163
5.7.1	Cubical Shear on Isotropically Consolidated Bay Mud . . . . .	164
5.7.2	Cubical Shear on Anisotropically Consolidated Bay Mud . . . . .	165
5.8	Summary and Conclusions . . . . .	166
6.	DEVELOPMENT OF FINITE ELEMENT CODE FOR USE IN SHIELD TUNNELING SIMULATION . . . . .	189
6.1	Introduction . . . . .	189
6.2	Finite Element Formulation . . . . .	189
6.2.1	Elasto-plastic and Nonlinear Elastic Constitutive Equations . . . . .	190
6.2.2	Integration Formulation . . . . .	191
6.2.3	Finite Element Approximation . . . . .	192
6.3	Pore Fluid Flow and Consolidation . . . . .	193
6.3.1	Consolidation Theory . . . . .	193
6.3.2	Governing Equations and Integral Formulation . . . . .	194

6.3.3	Finite Element Approximation . . . . .	196
6.3.4	Time Integration . . . . .	197
6.3.5	Hydrostatic Pressure and Seepage . . . . .	198
6.3.6	One-Dimensional Consolidation . . . . .	199
6.3.7	Two-Dimensional Consolidation . . . . .	201
6.3.8	Pseudo-Three Dimensional Consolidation . . . . .	202
6.3.9	Summary . . . . .	204
6.4	Large Deformations . . . . .	204
6.4.1	Reference Frame . . . . .	204
6.4.2	Large Deformation Form of Constitutive Equation . . . . .	205
6.4.3	Stress Corrections . . . . .	206
6.4.4	Large Deformation Analysis of One-Dimensional Consolidation . . . . .	208
6.4.5	Summary . . . . .	208
6.5	Incorporation of Elasto-plastic Constitutive Law . . . . .	209
6.5.1	Deviatoric Yielding under Plane Strain Condition . . . . .	209
6.5.2	Volumetric Yielding under Plane Strain Condition . . . . .	213
6.5.3	Bearing Capacity of Flooring . . . . .	214
6.5.4	Partially Drained Plane Strain Test . . . . .	215
6.5.5	Consolidation of Clay Layer between Sand Strata . . . . .	218
6.5.6	Summary . . . . .	220
6.6	Summary and Conclusions . . . . .	220
7.	FINITE ELEMENT ANALYSES OF THE N-2 PROJECT . . . . .	250
7.1	Introduction . . . . .	250
7.2	Finite Element Idealization of the N-2 Tunnel . . . . .	250
7.2.1	Soil Properties and Idealization of the N-2 Tunnel, Line 4 . . . . .	251
7.2.2	Analytical Procedure Simulating Tunnel Construction . . . . .	253
7.3	Ground Response at Instrument Line 4 . . . . .	256
7.3.1	Heaving Process . . . . .	256
7.3.2	Tail Void Closure . . . . .	257
7.3.3	Surface and Deep Ground Movements . . . . .	257
7.3.4	Predicted Excess Pore Pressures and Stress Levels . . . . .	258
7.4	Comparisons of Ground Response for Instrument Lines 2, 3 and 4 . . . . .	260
7.4.1	Lateral Displacements and Settlements . . . . .	260
7.4.2	Earth Pressures and Liner Stresses . . . . .	263
7.4.3	Changes in Tunnel Diameter . . . . .	265
7.4.4	Predicted Excess Pore Pressures and Stress Levels . . . . .	266
7.4.5	Soil Volume Balance about Shield . . . . .	267
7.5	Summary and Conclusions . . . . .	269

8.	PARAMETRIC STUDIES OF EPB SHIELD TUNNELING . . . . .	308
8.1	Introduction . . . . .	308
8.1.1	Objectives . . . . .	308
8.1.2	Analytical Procedures . . . . .	309
8.2	Effects of Heaving Pressure Level . . . . .	311
8.2.1	Completion of Heaving and Tail Void Closure . . .	311
8.2.2	Development of Ground Surface Settlements . . . .	313
8.2.3	Pore Pressure Development and Stress Level . . .	314
	Mobilized	
8.2.4	Relative Surface Settlement between Construction Stages	315
8.2.5	Discussion of Results . . . . .	318
8.3	Effects of Volume Loss upon Tail Void Closure . . . . .	319
8.3.1	Tail Void Closure and Volume Loss . . . . .	319
8.3.2	Development of Ground Surface Settlement . . . .	321
8.3.3	Immediate Settlement and Consolidation Settlement	322
8.3.4	Discussion of Results . . . . .	323
8.4	Summary and Conclusions . . . . .	324
9.	EFFECTS OF DIFFERENT PROCEDURE FOR MODELING ADVANCED SHIELD TUNNELING	343
9.1	Introduction . . . . .	343
9.2	Loading Models for Heaving and Tail Void Closure Stages	343
9.3	Predicted Ground Responses Obtained from Different . . .	345
	Procedures	
9.3.1	Lateral Displacement Profile . . . . .	345
9.3.2	Surface Movements . . . . .	346
9.4	Summary and Conclusions . . . . .	347
10.	COMPARISON OF RESULTS PREDICTED WITH DIFFERENT TYPES OF SOIL . MODEL	353
10.1	Introduction . . . . .	353
10.2	Brief Description of Soil Models . . . . .	355
10.2.1	Nonlinear Anisotropic Pseudo-elastic Model . . .	355
10.2.2	Cam Clay Model . . . . .	359
10.3	Conditions in Tunnel Analysis . . . . .	361
10.4	Comparison of Predicted Ground Response . . . . .	362
10.4.1	Lateral Displacements . . . . .	362
10.4.2	Ground Surface Movements . . . . .	364
10.4.3	Variation of Pore Pressure and Stress Levels . .	366
10.4.4	Stress Paths . . . . .	368
10.5	Summary and Conclusions . . . . .	370
11.	CONCLUSIONS . . . . .	389

BIBLIOGRAPHY . . . . .	395
------------------------	-----

Appendix

A. MATHEMATICAL EXPRESSION OF PREVOST MODEL . . . . .	412
A.1 Inversion Procedure of Constitutive Equation . . . . .	412
A.2 Translation Rule for Nested Yield Surface . . . . .	413
A.3 Translation and Expansion Rule for the Bounding Yield Surface . . . . .	416
B. USER'S MANUAL OF PROGRAM PRVCNST . . . . .	419
B.1 General Description of Program PRVCNST . . . . .	419
B.2 Input Data . . . . .	422
B.2.1 Control Cards . . . . .	422
B.2.2 Material Cards . . . . .	425
B.2.3 Loading Cards . . . . .	428
B.3 Output Listing . . . . .	429
B.3.1 Model Parameters Used . . . . .	430
B.3.2 Results . . . . .	430
B.3.3 Yielding Information . . . . .	431
B.4 Sample Input and Output . . . . .	434
C. USER'S MANUAL OF PROGRAM JFSEST . . . . .	438
C.1 Introduction . . . . .	438
C.2 Program Capabilities . . . . .	438
C.3 Program Overview . . . . .	440
C.3.1 Structure and Storage Allocation System . . . . .	440
C.3.2 Element Library . . . . .	442
C.3.3 Material Library (MAT) . . . . .	443
C.4 Input Data Assembly . . . . .	449
C.4.1 Control Block (CNT) . . . . .	450
C.4.2 Mesh Block (MSH) . . . . .	459
C.4.3 Initial Stress Block (INT) . . . . .	465
C.4.4 Load Block (LOA) . . . . .	469
C.5 Restart File and External Memories . . . . .	477
C.5.1 DD Statement in JCL Cards . . . . .	477
C.5.2 Print out of Restart File . . . . .	478
C.5.3 Plotting Functions . . . . .	479
C.5 Sample Input . . . . .	480
VITA . . . . .	488

## List of Figures

Figure	Title	Page
1. 1	Soil Movements at Face and Tail of Open-faced Conventional Shield and Closed-faced Advanced Shield	7
2. 1	Cycle of Shield Tunneling (after Lo and Rowe 1982)	36
2. 2	Typical Types of Shield Machines	37
2. 3	Error Function Curve Approximating Surface Settlement Trough	38
2. 4	Time Dependent Surface Movement with Relative Position of Shield	38
2. 5	Relationship between Surface Settlement and Gap	39
2. 6	Relation between Settlement and Dimensionless Depth	39
2. 7	Relation between Width of Settlement Trough and Dimensionless Tunnel Depth for Various Shield Tunneling Methods	40
2. 8	Liner Relation between Width of Settlement Trough and Depth of Tunnel in Clay and Sand	40
2. 9	Relationship between Overload Factor and Ground Loss (Clough and Schmidt 1977)	41
2.10	Generalized Subsurface Profile of N-2 Project Site (Clough, et al. 1982a)	42
2.11	Summary of Soil Data at Line 2, 3 and 4 of N-2 Project (Clough, et al. 1982a)	42
2.12	Displacements ahead of Shield Face at Line 4, N-2 Project (Clough, et al. 1982a)	43
2.13	Lateral Displacements during and after Shield Construction at Line 4, N-2 Project (Clough, et al. 1982a)	43
2.14	Long Term Lateral Displacements at Lines 1 through 4, N-2 Project (Clough, et al. 1982a)	44
2.15	Surface Movement above Tunnel Centerline during and well after Shield Passage at Line 4, N-2 Project (Clough, et al. 1982a)	44

3. 1	Isotropic Hardening Response with Ellipsoidal Yield Surface of Modified Cam Clay Soil Model	80
3. 2	Pressure Sensitive Multisurface Model with Critical State Concept to which Prevost Model Belongs	81
3. 3	Stress Strain Relation in Elasto-plastic Formulation	81
3. 4	Consistency Condition and Nonassociative Flow Rule	82
3. 5	Translation Rule and Contacting Yield Surfaces	83
3. 6	Bounding Yield Surface and Critical State Line	84
4. 1	Volumetric Strain vs Mean Pressure Relation of Consolidation Test (Data Modified after Duncan 1962)	133
4. 2	Relation between Volumetric Strain and Logarithm of Mean Pressure of Consolidation Test (Data Modified after Duncan 1962)	134
4. 3	Relation between Volumetric Strain and Logarithm of Mean Pressure with Different Moduli for Unloading and Reloading Processes	135
4. 4	Stress Paths and Yield Surfaces for a Hypothetical Undrained Behavior on Triaxial Test	136
4. 5	Stress Strain Curve and Excess Pore Pressure Development for Triaxial Test	137
4. 6	Comparison of Stress Strain Curves Predicted by Pressure Sensitive and Pressure Nonsensitive Models Simulating Undrain Triaxial Tests	138
4. 7	Comparison of Excess Pore Pressure Development Predicted by Pressure Sensitive and Pressure Nonsensitive Models Simulating Undrained Triaxial Tests	139
4. 8	Comparison of Conventional Stress Paths for Pressure Sensitive and Pressure Nonsensitive Models Simulating Undrained Triaxial Tests	140
4. 9	Predicted Shearing Deformation and Dilatating of Sand on Drained Triaxial Test with Model Parameters Referred to Hughes (1979)	141
4.10	Model Parameter Evaluation Procedure on Distorted Triaxial Plane associated with Stress Strain Curve	142

4.11	Comparison of Predicted Stress Strain Curves and Stress Paths with Calibration Data	143
4.12	Position of Stress Points on $f_m$ in Relation to Nonassociative Flow Rule	144
4.13	Overlapping of Yield Surfaces	144
4.14	Unrealistic Distribution of Plastic Moduli	145
4.15	Effect of Routing of Stress Path with regard to Yield Surface Configuration	146
4.16	Shear Moduli Evaluation of Pressure Nonsensitive Model after Prevost (1977)	147
4.17	Various Stress Paths associated with Slope Condition	148
4.18	Expansion of Yield Surface due to Delayed Compression after Consolidation	149
4.19	Bulk Modulus Constraint along Consolidation Paths	150
4.20	Interpolation of Bulk Modulus along Consolidation Paths	150
4.21	Description of Transition Zone reflecting Initial Soil Anisotropy	151
4.22	Yield Surface Configuration for San Francisco Bay Mud Obtained by Modified Parameter Evaluation Procedure	152
4.23	Predicted Response of San Francisco Bay Mud on Triaxial Tests	153
5. 1	Various Stress Paths to be examined for San Francisco Bay Mud	169
5. 2	Stress Strain Relation in Triaxial Compression (CTC) and Extension (RTE) Tests of Bay Mud ( $K_0 = 0.7$ )	170
5. 3	Effective Stress Paths in Triaxial Compression (CTC) and Extension (RTE) Tests on Bay Mud ( $K_0 = 0.7$ )	171
5. 4	Predicted Stress Strain Curve in Triaxial Test with Loading Reversals	172
5. 5	Predicted Effective Stress Path in Triaxial Test with Loading Reversals	173

5. 6	Predicted and Experimental Consolidation Curves of Oedometer Test (after Denby 1977)	174
5. 7	Ratio of Horizontal to Vertical Stresses in Oedometer Test	175
5. 8	$K_0$ Values in Overconsolidated Range of Oedometer Test	175
5. 9	Stress Strain Relation in Plane Strain Test of Bay Mud ( $K_0 = 0.5$ )	176
5.10	Excess Pore Pressure Development in Plane Strain Test of Bay Mud ( $K_0 = 0.5$ )	177
5.11	Explanation of Stress State associated with Pressuremeter and Multicubical Tests	178
5.12	Multicubical Test for Isotropically, Normally Consolidated (INC) Bay Mud	179
5.13	Preparation of Prevost Model for INC Bay Mud	180
5.14	Stress Strain Curve and Pore Pressure Changes in Multicubical Test, INC Bay Mud	181
5.15	Variation of Effective Loading Face Stress and Effective Stress Path in Multicubical Test, INC Bay Mud	182
5.16	Variation of Effective Vertical Stress in Multicubical Test, INC Bay Mud	183
5.17	Multicubical Test for Anisotropically, Normally Consolidated (ANC) Bay Mud	184
5.18	Preparation of Prevost Model for ANC Bay Mud	185
5.19	Stress Strain Curve and Mean Pressure Changes in Multicubical Test, ANC Bay Mud	186
5.20	Variation of Effective Loading Face Stress and Effective Stress Path in Multicubical Test, ANC Bay Mud	187
5.21	Variation of Effective Vertical Stress in Multicubical Test, ANC Bay Mud	188
6. 1	Steady State of Pore Pressure, Hydrostatic Pressure and Seepage	223
6. 2	Steady State of Pore Pressure, Radial Flow	224

6. 3	Excess Pore Pressure Distributions for One Dimensional Consolidation	225
6. 4	Degree of Consolidation for one Dimensional Condolidation	225
6. 5	Excess Pore Pressure Distribution for Nonlinear One Dimensional Consolidation	226
6. 6	Time Dependent Variation of Excess Pore Pressure for Nonlinear One Dimensional Consolidation	227
6. 7	Finite Element Idealization of a Strip Load on Ground Surface	228
6. 8	Dimensionless Excess Pore Pressure Changes under a Strip Loading	229
6. 9	Acceleration of Consolidation due to Out of Plane Drainage	230
6.10	Stress Correction due to Rigid Rotation	231
6.11	Various Stress Corrections in Simple Shear Stress State	232
6.12	Comparison of One Dimensional Consolidation between Small and Large Deformation Analyses	233
6.13	Yield Surfaces of Various Yield Criteria on Octahedral Stress plane	234
6.14	Analysis of Strain Controlled Undrained Plane Strain Test with Isotropic Hardening	235
6.15	Comparison of Stress Paths in Plane Strain Test between Isotropic and Kinematic Hardening	236
6.16	Stress Strain Curves and Stress Paths in Drained Plane Strain Test with Different Loading Increment	237
6.17	Footing Settlement Curves	238
6.18	Corrected Footing Settlement Curves	239
6.19	Development of Yielded Zone of Footing Bearing Problem	240
6.20	Velocity Field in Footing Bearing Problem	241
6.21	Undrained and Drained Stress Paths of Plane Strain Test on Bay Mud	242

6.22	Plane Strain Test with Free Surface Drainage	243
6.23	Stress Paths Predicted for Various Locations of Plane Strain Test with Free Surface Drainage	244
6.24	Variation of Excess Pore Pressure with Loading Rate in Plane Strain Test with Free Surface Drainage	245
6.25	Stress Paths Predicted for Different Loading Rates in Plane Strain Test with Free Surface Drainage	246
6.26	Stress Strain Curves Predicted for Different Loading Rates in Plane Strain Test with Free Surface Drainage	247
6.27	One Dimensional Consolidation Problem of Mixed Ground Profile with Drained and Hardly Drained Subsoils	248
6.28	Ground Settlement Curves of Consolidation of Mixed Ground Profile with Drained and Hardly Drained Subsoils	249
7. 1	Finite Element Mesh for N-2 Tunnel Simulation, Line 4	272
7. 2	Analytical Procedure Modeling Tunnel Construction Stages	273
7. 3	Pressure Distribution applied along Tunnel Periphery for Modeling of Heaving and Tail Void Closure, Line 4	274
7. 4	Predicted and Observed Lateral Displacements after Heaving, Line 4	275
7. 5	Predicted Displacement Field after Heaving, Line 4	276
7. 6	Predicted and observed Lateral Displacement Degradation with Distance from Tunnel at Springline and Invert, Line 4	277
7. 7	Predicted and Observed Lateral Displacements after Tail Void Closure, Line 4	278
7. 8	Predicted Displacement Field at Liner Installation, Line 4	279
7. 9	Predicted and Observed Variation of Centerline Surface Movement with Time, Line 4	280
7.10	Predicted and Observed Shape of Surface Settlement Trough, Line 4	281
7.11	Predicted Displacement Field after Consolidation, Line 4	282

7.12	Predicted and Observed Displacement Vectors after Consolidation, Line 4	283
7.13	Variation of Pore Pressure Development Predicted for Different Loading Stages, Line 4	284
7.14	Variation of Stress Level Distributions Predicted for Different Loading Stages, Line 4	285
7.15	Comparison of Lateral Displacements after Heaving between Lines 2, 3 and 4	286
7.16	Comparison of Lateral Displacements after Tail Void Closure between Lines 2, 3 and 4	287
7.17	Variation of Centerline Surface Settlement for Lines 2, 3 and 4	288
7.18	Predicted and Observed Displacement Vector after Consolidation, Line 2	289
7.19	Predicted and Observed Displacement Vector after Consolidation, Line 3	290
7.20	Vectors of Predicted Displacements after Consolidation Relative to Heaving Stage, Lines 2, 3 and 4	291
7.21	Predicted Displacement Fields after Heaving and Consolidation, Line 2	292
7.22	Predicted Displacement Fields after Heaving and Consolidation, Line 3	293
7.23	Predicted Pressure Distributions Normal to Shield Periphery after Heaving, Lines 2, 3 and 4	294
7.24	Predicted Pressure Distributions Normal to Tunnel Liner at Tail Void Closure, Lines 2, 3 and 4	295
7.25	Predicted Stress Distributions Induced in Tunnel Liner after Liner Installation, Line 4	296
7.26	Comparisons of Predicted Axial and Bending Stress Distributions after Liner Installation for Lines 2, 3 and 4	297
7.27	Changes in Predicted Axial and Bending Stress Distributions during Consolidation of Ground, Line 4	298
7.28	Predicted and Observed Liner Diameter Changes, Line 2	299

7.29	Predicted and Observed Liner Diameter Changes, Line 3	300
7.30	Predicted and Observed Liner Diameter Changes, Line 4	301
7.31	Contour of Stress Levels after Heaving, Lines 2, 3 and 4	302
7.32	Contour of Stress Levels after Liner Installation, Lines 2, 3 and 4	303
7.33	Excess Pore Pressure Development after Liner Installation, Liner 2, 3 and 4 (psf)	304
7.34	Soil Volume Balance around Shield, Line 4	305
7.35	Soil Volume Balance around Shield, Lines 2 and 3	306
7.36	Relation between Surface Movements and Reference Soil Volume about Shield	307
8. 1	Volume Consideration of Soil Movement around Shield due to Heaving and Tail Void Closure	326
8. 2	Normalized Heaving Volume Varying with Normalized Average Heaving Pressure	327
8. 3	Displacements of Soils around Shield at Heaving and Liner Installation Stages for Three Levels of Heaving Pressure	328
8. 4	Settlement Curves at Ground Surface for Different Heaving Pressures	329
8. 5	Widths of Settlement Bowl at Ground Surface as Posi- tions of Inflection Points	330
8. 6	Centerline Surface Movements Varying with Time Needed for Construction Stages for Different Heaving Pressure	331
8. 7	Nondimensional Excess Pore Pressure Development upon Liner Installation for Different Heaving Pressures ( $V_{\ell}/V_{TV} = 0.4$ )	332
8. 8	Stress Level Distributions in Subsoil upon Liner In- stallation for Different Heaving Pressures ( $V_{\ell}/V_{TV} = 0.4$ )	333
8. 9	Surface Movement Profile at Heaving, Tail Void Closure and Final Stages	334

8.10	Maximum Surface Settlements at Tail Void Closure and End of Consolidation Stages Relative to Surface Heave for Different Heaving Pressures	335
8.11	Variation of Ratio of Volume Loss due to Surface Settlement to That Occurred upon Tail Void Closure with Heaving Pressure	336
8.12	Net Heaving Volume and Volume Loss at Shield Tail after Tail Void Closure for Average Releasing Pressure	337
8.13	Settlement Curves at Ground Surface for Different Tail Void Volume Losses upon Closure	338
8.14	Centerline Surface Movements Varying with Time Needed for Consolidation Stages for Different Tail Void Volume Losses at Closure	339
8.15	Nondimensional excess Pore Pressure Development at Liner Installation Stage for Different Tail Void Volume Losses upon Closure ( $\bar{p}_H/p_V = 0.222$ )	340
8.16	Normalized Maximum Surface Settlements for Different Tail Void Volume Losses upon Closure	341
8.17	Variation of Ratio of Volume Loss due to Surface Settlement to That occurred upon Tail Void Closure	342
9. 1	Different Types of Pressure Distribution Simulating Heaving and Tail Void Closure	348
9. 2	Comparison of Lateral Displacements after Heaving between Proposed and Other Loading Methods, Line 4	349
9. 3	Comparison of Lateral Displacements after Tail Void Closure between Proposed and Other Loading Methods, Line 4	350
9. 4	Comparison of Centerline Surface Movements between Proposed and Other Loading Method, Line 4	351
9. 5	Comparison of Shapes of Surface Settlement Trough between Proposed and Other Loading Methods, Line 4	352
10. 1	Hyperbolic Stress Strain Approximation for Compression and Extension Tests for Nonlinear Pseudo-elastic Model	375

10. 2	Yield Surface of Cam Clay Model in Triaxial Stress Plane	376
10. 3	Comparison of Lateral Displacements after Heaving for Different Soil Models, Line 4	377
10. 4	Comparison of Lateral Displacement Degradation at Springline and Invert for Difference Soil Model, Line 4	378
10. 5	Comparison of Lateral Displacements after Tail Void Closure for Different Soil Models, Line 4	379
10. 6	Comparison of Movements of Soil Close to Tunnel after Heaving and Tail Void Closure Predicted by Different Soil Models, Line 4	380
10. 7	Comparison of Variation of Centerline Movements with Time Predicted by Different Soil Models, Line 4	381
10. 8	Comparison of Shape of Surface Settlement Trough Predicted by Different Soil Models, Line 4	382
10. 9	Comparison of Stress Level Distributions after Heaving Predicted by Different Soil Models, Line 4	383
10.10	Comparison of Variation of Pore Pressure Developments Predicted by Different Soil Models, Line 4 (psf)	384
10.11	Comparison of Stress Levels after Tail Void Closure Predicted by Different Soil Models, Line 4	385
10.12	Comparison of Stress Level Distribution after Consolidation Predicted by Prevost and Cam Clay Models, Line 4	386
10.13	Comparison of Effective Stress Paths Predicted by Prevost and Cam Clay Models, Line 4	387
10.14	Comparison of Total Stress Paths Predicted by Prevost and Nonlinear Elastic Models	388
C. 1	Program JFSEST Overview	481
C. 2	Memory Utilization Design for Restoration Procedure	481
C. 3	Element Library with Prevost Soil Model	482
C. 4	Description of Stress Vector VST for Prevost Type Material	483

## List of Tables

Table	Title	Page
2.1	Comparison of Construction Feature for Different Types of Shield (Naito 1984)	32
2.2	Relationship between Soil Conditions and Surface Settlements (Hanya 1977)	33
2.3	Components of Ground Loss (Hanya 1977)	33
2.4	Settlement Predicted by Palabolic Interpretation of Trough Width (Attewell 1981)	34
2.5	Settlement Predicted by Linear Interpretation of Trough Width (O'Reilly and New 1982)	34
2.6	Various Analytical Approaches to Shield Tunneling	35
3.1	Historical Development of Elasto-plastic Soil Modeling	79
4.1	Prevost Model Parameters Identified from a Special Case of Triaxial Test	130
4.2	Sign Selection Rule in Model Parameter Evaluation Procedure	131
4.3	Prevost Model Parameters for San Francisco Bay Mud ( $K_0 = 0.5$ )	132
5.1	Prevost Model Parameters for San Francisco Bay Mud ( $K_0 = 0.7$ )	168
6.1	Comparison of Strains due to Final Settlements in 1-D Consolidation Predicted by means of Large Deformation Theory	222
7.1	Material Parameters of Nonlinear Pseudo-elastic for Fill and Colluvium	271
7.2	Relation between Average Heaving Pressure and Shield Thrusting Pressure	271
10.1	Material Parameters of Nonlinear Pseudo-elastic Model accounting for Anisotropy of Recent Bay Mud	372

10.2	Material Parameters of Cam Clay Model for Recent Bay Mud (Finno 1983)	372
10.3	Material Parameters of Nonlinear Pseudo-elastic Model for Fill and Colluvium	373
10.4	Loading Conditions regarding to Tunnel Construction Stages for Different Types of Soil Model	374
C.1	Material Type Numbers	443
C.2	Parameters for Material Type 1, Elastic	444
C.3	Parameters for Material Type 8, Nonlinear Elastic	445
C.4	Common Parameters for Material Type 9, Prevost Elasto-plastic	446
C.5	Material State Parameters for Non-Prevost Material	447
C.6	Output Selection Code IXPRT	449

List of Symbols (English Letters)

$A_E$	Parameter for anisotropic modulus variation of clay
$A_f$	Pore pressure parameter at failure
$A_m$	Nonassociativity related to yield surface $f_m$
$A_s$	Parameter for anisotropic strength variation of clay
$a_{ij}$	Direction of bounding yield surface translation due to expansion
$B$	Pore pressure dissipation function in Terzaghi's 1-D consolidation theory
$B$	Elastic bulk modulus
$B$	Width of footing
$B'$	Plastic bulk modulus
$B_{ep}$	Elasto-plastic bulk modulus
$B_s$	Parameter for anisotropic strength variation of clay
$C$	A point on stress path of conventional triaxial compression (CTC) test
$c$	Cohesion of soil
$c$	Yield surface axis ratio
$\bar{c}$	Coefficient of consolidation based on soil's elastic shear modulus
$C_c$	Compression index
$C_{ijkl}$	Constitutive tensor
$C_r$	Recompression index
CSL	Critical state line
CTC	Conventional triaxial compression test or associated loading condition
$C_v$	Coefficient of consolidation
$D, D_s$	Outer diameter of shield machine
$D_T$	Outer diameter of tunnel lining
$d_i$	Displacement tensor

J	Second invariant of deviatoric stress
K	Modulus multiplier ( $E/s_u$ )
K	Modulus number in Duncan-Chang model
K	A parameter in $i/R$ vs $Z/2R$ relation of settlement trough
k	Size of yield surface
[K]	Stiffness matrix in FEM formulation
$K_E$	Anisotropic modulus ratio of clay
$K_f$	Failure line in conventional stress path plane
$k_{ij}$	Permeability tensor
$k_H$	Horizontal permeability
$K_S$	Anisotropic strength ratio of clay
$k_V$	Vertical permeability
$K_0$	Coefficient of lateral earth pressure at rest, anisotropic consolidation
[ $K_\sigma$ ]	Initial stress stiffness matrix in FEM large displacement formulation
L	Plastic loading function
[L]	Coupling matrix of soil skeleton with pore pressure in FEM consolidation formulation
$l_{eq}$	Equivalent length of out-of-plane drainage
$l_{inf}$	Width of surface settlement trough caused by tunneling
M	Slope of critical state line projected on $p$ - $q$ plane
m	Modulus multiplier ( $G/s_u$ )
$m_v$	Constraint volumetric compressibility
n	Bulk or modulus exponent for modulus pressure sensitivity
n	A parameter in $i/R$ vs $Z/2R$ relation of settlement trough
$N_d$	Shape function for displacements
$n_i$	Outward normal of yield or boundary surfaces

$N_u$	Shape function for pore pressure
$E$	Elastic young's modulus
$E$	A point on stress path of reduced triaxial extension (RTE) test
$e$	Void ratio
$e_{cs}$	Critical void ratio for unit pressure
$E_i$	Initial tangent modulus in hyperbolic stress strain representation
$e_{ij}$	Deviatoric strain tensor $\epsilon_{ij} - \frac{1}{3} \epsilon_v \delta_{ij}$
$E_t$	Tangent modulus in hyperbolic stress strain representation
$e_q$	Vertical component of deviatoric strain tensor $e_{yy}$
$e_y$	Engineering strain deviator in triaxial stress state $\epsilon_{yy} - \epsilon_{xx}$
$f$	Yield surface, yield function
$f_m$	m-th yield surface of nested yield surfaces
$f_p$	Bounding yield surface of nested yield surfaces
$f_t$	Transition yield surface of nested yield surfaces
$\{f\}$	Nodal load vector in FEM formulation
$f_i$	Body force in FEM formulation
$G$	Elastic shear modulus
$g$	Plastic potential
$GAP$	Theoretical maximum tail void of shield, $D_T - D_S$
$H$	Cover of tunnel
$H$	Depth of clay layer
$h$	Water head of ground water
$H'_m$	Hardening modulus associated with $f_m$
$h'_m$	Plastic shear modulus associated with $f_m$
$h_m$	Scaled plastic shear modulus of $f_m$ with respect to $2G$
$H_p$	Plastic modulus mobilized with volumetric hardening of $f_p$

i	Distance from center to inflection point of error function curve
$I_1$	First invariant of stress
0	Center of yield surface with coordinate $\xi_{ij}$ in stress space
OCR	Overconsolidation ratio
OF	Overload factor
P	Concentrated force loaded on a structure
p	Pressure, mean effective pressure of soil element, hydrostatic axis
$P''$	Projection of $P_{ij}$ along hydrostatic axis, $\frac{1}{3} \cdot \partial g / \partial p$
$p_a$	Atmospheric pressure in Duncan-Chang model
$p_a$	Neumatic pressure applied in tunnel
$\bar{p}_H$	Average heaving pressure
PI	Plastic index
$P_{ij}$	Gradient of plastic potential, $\partial g / \partial \sigma_{ij}$
$P'_{ij}$	Projection of $P_{ij}$ onto deviatoric stress subspace, $\partial g / \partial s_{ij}$
$\bar{p}_{rs}$	Average releasing pressure modeling unloading process of tail void closure
$p_v$	Overburden pressure at level of tunnel springline
q	Bearing pressure of footing
q	Equivalent deviatoric stress, stress deviator in triaxial stress state
$Q''$	Projection of $Q_{ij}$ along hydrostatic axis, $\frac{1}{3} \cdot \partial f / \partial p$
$\bar{q}$	Maximum shear stress
{q}	Nodal value of pore pressure
$Q_{ij}$	Gradient of yield surface, $\partial f / \partial \sigma_{ij}$
$Q'_{ij}$	Projection of $Q_{ij}$ onto deviatoric stress subspace, $\partial f / \partial s_{ij}$
$q_{ult}$	Ultimate bearing capacity of footing
R	Radius of tunnel, a half of $D_T$

$R_f$	Failure ratio
RTE	Reduced triaxial extension test, or associated loading condition
$S_E$	Boundary surface with prescribed essential boundary conditions in FEM formulation
$s_{ij}$	Deviatoric stress tensor
$S_N$	Boundary surface with prescribed natural boundary condition in FEM formulation
$s_u$	Undrained shear strength of clay
T	Nondimensional time factor $(k_y/\gamma_w m_v)$
t	Time
$T_i$	Surface traction in FEM formulation
U	Degree of consolidation
u	Pore pressure or excess pore pressure
$V_E$	Shield face volume for unit length of advancement
$V_G$	Grouting volume
$V_H$	Heaving volume
$v_i$	Superficial velocity of pore fluid
$V_\ell$	Volume loss created during tail void closure
$V^S$	Soil volume of surface settlement trough
$V_{TV}$	Theoretical tail void volume for unit length of shield advancement
x	Physical, horizontal coordinate, in-plane lateral axis in plane strain condition
$x_i$	Cartesian coordinate system
y	Physical vertical coordinate
Z	Depth of tunnel
z	Physical, horizontal coordinate, out-of-plane axis in plane strain condition, vertical axis in cylindrical condition

## List of Symbols (Greek Letters)

$\alpha$	A constant relating soil movements at crown and ground surface
$\alpha$	Deviatoric coordinate of yield surface position in triaxial stress plane
$\alpha_{ij}$	Projection of yield surface position $\xi_{ij}$ onto deviatoric stress subspace
$\beta$	Projection of yield surface position $\xi_{ij}$ along hydrostatic axis
$\beta$	Principal stress rotation angle accounting for clay's anisotropy in Hansen model
$\beta$	Time integration parameter
$\gamma$	Engineering shear strain
$\gamma$	Slope of stress path in triaxial plane, $\dot{p}/\dot{q}$
$\gamma$	Interpolation constant for elasto-plastic bulk modulus
$\gamma'$	Submerged unit weight of soil
$\gamma_t$	Total unit weight of soil
$\gamma_R$	Maximum shear strain upon incidence of loading reversal
$\gamma_w$	Unit weight of pore fluid
$\Delta$	Difference in slope of deviatoric stress strain curves of slope condition
$\delta$	Settlement
$\delta^S$	Ground surface settlement due to tunneling
$\{\delta\}$	Nodal displacement vector in FEM formulation
$\delta^C$	Soil movement close to tunnel crown
$\delta d_i$	Virtual displacements in variational expression
$\delta \epsilon_{ij}$	Virtual strains in variational expression
$\delta_{ij}$	Kronecker delta
$\delta u$	Virtual pore pressure in variational expression

$\Delta\sigma$	Surcharge to cause consolidation
$\delta\mu$	Scalar factor in Mroz's translation rule
$\epsilon_e^p$	Equivalent plastic deviatoric strain
$\epsilon_{ij}$	Strain tensor, Lagrangian strain
$\tilde{\epsilon}_{ij}$	Eulerian strain in large deformation approach
$\epsilon_v$	Volumetric strain
$\eta_c$	Stress level defined for Cam Clay model
$\eta_H$	Stress level defined for Hansen model
$\eta_p$	Stress level defined for Prevost model
$\theta$	Angle between stress point and hydrostatic semiaxis of yield surface in distorted triaxial plane q-cp
$\kappa$	Slope of swelling line in e-log p plane of isotropic consolidation test
$\lambda$	Slope of normally isotropic consolidation line in e-log p plane
$\lambda$	Scalar coefficient in flow rule
$\bar{\mu}$	Scalar function of kinematic hardening due to plastic deviatoric strain
$\mu''$	Projection of $\mu_{ij}$ along hydrostatic axis, $\frac{1}{3} \cdot \partial\mu_{ij}\delta_{ij}$
$\mu_{ij}$	Direction of line segment linking conjugate points of adjoining yield surfaces
$\mu'_{ij}$	Projection of $\mu_{ij}$ onto deviatoric stress subspace
$\nu$	Poisson ratio
$\nu_f$	Poisson ratio at failure in Duncan-Chang model
$\xi_{ij}$	Position of yield surface center in stress space
$\sigma_a$	Axial consolidation pressure in triaxial test
$\sigma_l$	Lateral consolidation pressure in triaxial test

$\sigma_{ij}$	Stress; tensor stress expression denotes effective stress without a prime on it. Engineering expression of primed directional stress also designates effective stress. Engineering stress expression with superscript of T means total stress. Lagrangian nominal stress or Cauchy stress in Eulerian reference frame.
$\sigma_n$	Soil pressure acting normal to tunnel liner
$\sigma'_v$	Effective overburden pressure
$(\sigma_1 - \sigma_3)_f$	Principal stress difference at failure
$(\sigma_1 - \sigma_3)_{ult}$	Maximum principal stress difference predicted by hyperbolic stress strain relationship
$\tau$	Engineering shear stress
$\tau_{ij}$	Kirchoff stress tensor
$\phi, \phi'$	Effective internal friction angle
$\phi$	Angle between stress point and hydrostatic semiaxis of yield surface in triaxial plane
$[\phi]$	Coefficient matrix controlling pore pressure dissipation in FEM formulation
$\omega$	Loading rate, $d\epsilon_y/dT$
$\omega_{ij}$	Skew tensor

### List of Symbols (Superscripts)

C	Stress point on CTC stress path
E	Stress point on RTE stress path
e	Elastic
e-p	Elasto-plastic
(m)	Associating with m-th nested yield surface
p	Plastic
(p)	Associating with bounding yield surface
T	Total stress in engineering expression
(t)	Associating with transition yield surface
.	Dot. incremental quantity, material derivative in Eulerian expression
'	Prime, effective stress in engineering expression
*	Asterisk, Jaumann derivative of stress

### List of Symbols (Subscripts)

i,j, etc.	Indices in tensor expression
m	Associating with m-th nested yield surface
p	Associating with bounding yield surface
v	Volumetric component
t	Associating with transition yield surface
r,θ,z	Physical, cylindrical coordinate system
x,y,z	Physical, Cartesian coordinate system
0	Initial or reference value; no principal stress rotation in vertical compression
90	90 degree principal stress rotation in extension condition
~	Tilde, tensor indicator

## Chapter 1

### INTRODUCTION

Tunneling in soft soil is normally carried out through the use of a shield. The conventional shield is an open circular steel element which is pushed through the soil by means of propulsion jacks which generate a force by reacting against in-place liner segments. Inside the shield, tunnelers can excavate soil at the face and erect a liner ring inside the tail, or rear portion of the shield. As a natural consequence of the shield construction technique, ground movements take place. These are generated by the movement of the soil towards the liner after the shield advances, and in soft or granular soil, by displacements towards the open face of the shield as shown in Figure 1.1(a). The soil movements at and near the ground surface, causing problems with utilities and overlying structures. Older techniques to control the shield induced movements are expensive and time-consuming. Recently, the advanced shield was introduced as a means of addressing the problem.

The advanced shield utilizes a rotating cutterhead at the face to excavate the soil, allowing close control on soil movements into the shield, shown in Figure 1.1(b). Details of advanced shield methods have been discussed by many authors, for example, Naito (1984), Civil Engineering (1980), Clough (1980) and Miki (1977). The shield is operated such that there is an approximate balance between the shield thrusting pressure and the earth pressure in front of the shield face. There are a number of different types of advanced shields, including slurry, earth pressure

balance (EPB), water pressure balance, and mud shields. These types of machines have found frequent application for more than ten years mainly in Japan and Europe. Accumulated experiences have demonstrated that use of advanced shields leads to smaller surface settlements (Fujita 1981) and lower costs than the conventional shield in poor ground conditions (Naito 1984).

While there have been a number of cases of surface settlement measurements made during the process of advanced shield tunneling, relatively little has been done to define the general ground response. Thus, it is not clear exactly how the advanced shield limits movements relative to conventional shields. This thesis is directed towards developing a suitable finite element method (FEM) approach to the advanced shield problem. The FEM is chosen as the basis of the model because it is able to incorporate many of the complexities associated with the advanced shield tunneling. The model allows careful analytical study of the ground deformation processes during tunneling, assuming it is properly calibrated.

The ideal way to calibrate the model is via testing the predicted results against observed behavior. Fortunately, a relatively complete set of ground movement data are available from the first application of the advanced shield technology in the United States, the N-2 contract of the San Francisco Clean Water Project in San Francisco, California. A 12-foot diameter 3000-foot long tunnel was excavated by means of EPB shield within very soft clayey deposits. The field instrumentation data for the project were published by Clough and his colleagues (1982a). The results suggested that the surface settlements were small relative to that expected

for a conventional shield. Three unique aspects of the ground behavior were noted: (1) The soil in front of the shield was heaved away from the shield, (2) high pore water pressure developed in the clays in front of the shield, and (3) the settlements were time dependent with movements occurring up to 150 days after shield passage.

The N-2 tunnel experience suggests that the FEM program must be able to follow a complex loading situation and allow explicitly in pore water pressure development and the dissipation of the pore pressures with time. As this thesis was being done, Finno (1983) developed an FEM program for the analysis of advanced shield problems, and the N-2 project in particular. His approach utilized a Cam Clay soil model and made certain assumptions relative to the closure of the soil into the gap, or tail void, left by the shield. The FEM work of this thesis builds on Finno's effort, implementing a more sophisticated soil model and more accurately simulating the closure problem. These developments allow a more complete analysis of the N-2 project and other parametric problems than was possible before. For example, because of an instability encountered with the Cam Clay soil model, Finno (1983) was unable to analyze the N-2 instrumented section where large initial heaves occurred during shield passage. The approach taken herein circumvented these problems and allowed all situations to be considered.

In contrast to the Cam Clay model, the Prevost model (Prevost 1978b) used herein allows for kinematic hardening and allows consideration of more general stress conditions. Interestingly, however, the tunnel problem in soft soil was found to extend the Prevost model beyond previous appli-

cations of this technique, particularly in the "pressure sensitive" version, which was needed in this work. In the work of this thesis, the pressure sensitive model was extended to represent soft, normally consolidated clays. Also, a special program was written for calculation of the Prevost model parameters for these circumstances.

The new finite element program is entitled JFSEST to recognize all of the contributing authors; Johnston (1981), who wrote the first version, Finno (1983), who made the original version more efficient, and the present author, who added the Prevost model to the program.

It is demonstrated that the new program, JFSEST, is capable of predicting soil behavior in response to tunneling because the predictions for the N-2 tunnel case agreed consistently well with the results for all the three instrumentation lines observed in the field. It is shown that the initial heaving upon shield passage interacts the succeeding tail void closure to form the final settlement. Without separating the two opposing types of movements, an incorrect picture can be obtained for the overall behavior.

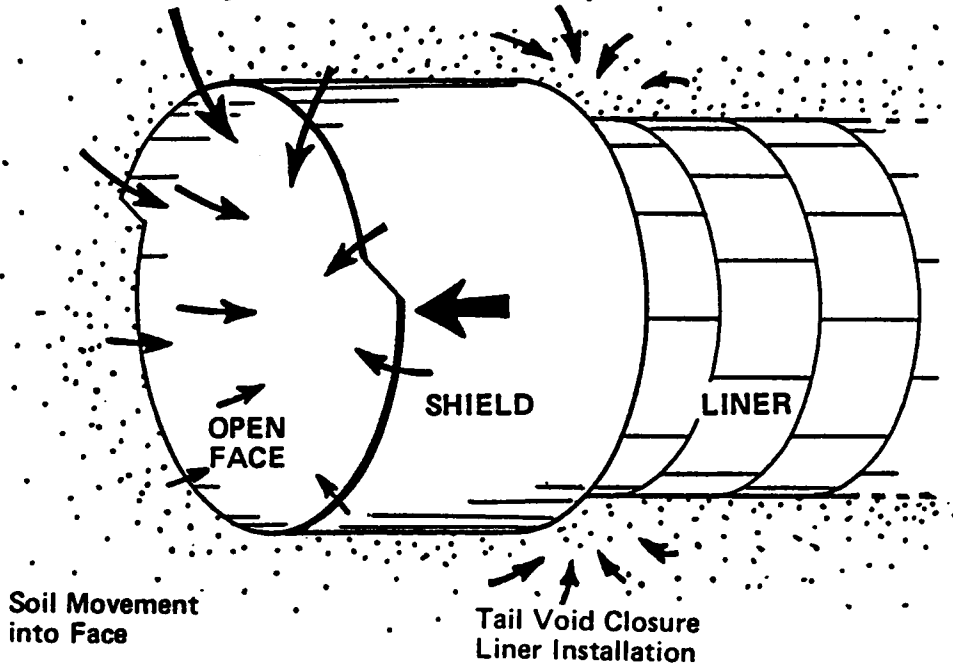
Further parametric analyses are conducted in order to make clear how the heaving effect and the tail void gap are responsible for the ground settlement. It is found that an insufficient backfill of the tail void adversely increases soil disturbance and settlement while a small amount of the initial heaving is favorable to control ground movements.

This dissertation consists of eleven chapters. The following chapter gives the background to the problems in shield tunneling, particularly

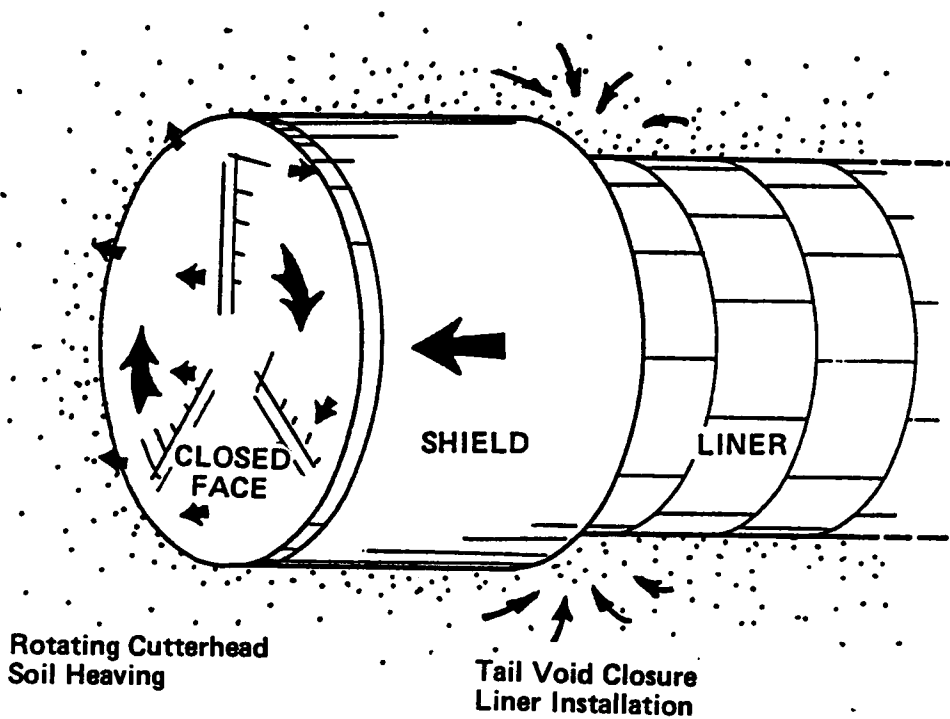
that of advanced shield tunneling, and reviews field measurement results and analytical efforts in modeling shield tunneling. Chapter 3 provides the theoretical development of the Prevost model. Its implementation is discussed in Chapter 4 where several problems in model parameter definition are discussed; suggestions are made to solve them for tunnel analyses. As proof of the modification, the Prevost model version is tested against the results of laboratory tests carried out on the San Francisco Recent Bay Mud using a variety of stress paths. Chapter 6 presents the entire scope of the finite element program JFSEST with capabilities for analyzing a time-dependent consolidation, large deformations and an elasto-plastic soil response. The case history study of advanced shield tunneling, the N-2 tunnel project, is introduced to be carried out with an FEM simulation. The results are presented in Chapter 7. The three subsequent chapters provide results of parametric studies. The effect of initial heaving at the shield face and volume loss due to insufficient backfill grouting of the tail void are discussed in Chapter 8. Chapter 9 presents differences in procedures to model the effects of the heaving and stress relief at the tail void to find which procedure is reasonable. Chapter 10 gives predictions for the N-2 tunnel using different soil models -- the nonlinear elastic model, the Cam Clay model, and the Prevost model. Conclusions from all the work are summarized in Chapter 12.

Three appendices follow. Appendix A concerns detailed mathematical derivations of the Prevost model. In particular the translation rules for finite stress increments are explained. Appendix B gives the user's manual of the program PRVCNST, which calculates stress-strain relation

with respect to the Prevost model. And the final section, Appendix C, is prepared to provide the user's manual of the FEM program JFSEST for possible users.



(a) Open-faced Conventional Shield



(b) Closed-Faced Advanced Shield

Figure 1.1 Soil Movements at Face and Tail of Open-faced Conventional Shield and Closed-faced Advanced Shield

## Chapter 2

### SHIELD TUNNELING METHOD AND ASSOCIATED GROUND MOVEMENT STUDIES

#### 2.1 Introduction

Control of ground movements during shield tunneling depends not only on the skillful operation of the shield but also on the utilization of knowledge of previous research and the instrumentation studies. Shield tunneling is reviewed from various angles in this chapter. Basic operations for conventional open-faced shield and advanced closed-faced shield techniques are summarized. Data on surface settlements are reviewed as are developments of analytical approaches to shield tunneling.

#### 2.2 Shield Tunneling Techniques

Shield tunneling is about 150 years old, having been first used by Brunel for a tunnel under the river Thames. The original procedure simply allowed for the construction of a tunnel in soft ground without much interest in reducing soil disturbance and movements during construction.

The cycle of operation of conventional shield tunneling is illustrated in three stages in Figure 2.1. During stage (a), as soil is excavated at the face, the shield machine is shoved forward by means of shield jacks against the previously erected liner. The shield jacks are fully expanded at stage (b); then the shield jacks are released one after another for the erection of new liner segments while active jacks ensure that sufficient forces will keep the face stabilizing measure. This is stage (c),

which is ready for the next cycle of shield operation. The basic operations illustrated in the figure are the same regardless of which shield tunneling method is used.

Recently concerns with settlements in the surrounding ground around a shield have lead to the development of new procedures. Open-faced shields with only a limited capability of stabilizing the tunnel face are being replaced by closed-faced shields that are capable of maintaining face stability even in poor ground. In fact, in Japan where shield tunnels are very frequently used because of the soft soil deposits, advanced shields have been used more than conventional ones since 1979 (Fujita 1981).

Shield tunneling is a system which is made up of a combination of stages such as excavation at the face, face stabilizing measures, muck transportation, advancement of the shield machine, liner erection, and backfill grouting behind the liner. The mechanism of advanced shields in this regard are summarized by many writers, for example, Miki, et al. (1977), Clough (1980), Kurosawa (1981), and Naito (1984).

A classification of shields is helpful to describe their characteristics. Advanced shields are equipped with a mechanical excavation method at the shield face and may also use automated muck transportation methods, e.g., a slurry shield.

Configurations of various types of shield machines are shown in Figure 2.2. Open-faced shields and blind shields are described as conventional and slurry shield and EPB shield are depicted as advanced. Naito (1984) compared performance between EPB shield, slurry shield and open-faced

shield methods in a tabulated form shown in Table 2.1. Advantages and disadvantages of these methods are indicated in the table.

### 2.2.1 Conventional Open-faced Shields

A typical open-faced shield consists of three parts: the face, the main body, and the tail, as explained in Figure 2.1. The face in the front is accessed by excavation equipment and temporary supports if needed. Both hand digging and mechanical excavation are commonly used. The main body provides structural rigidity and houses shield thrusting jacks which advance the shield by jacking against previously erected liners. The tail provides the space to assemble liner segments in place.

Since the outer diameter of tunnel lining  $D_T$  is smaller than that of the shield machine,  $D_S$ , a gap, or tail void, is created when the shield advances. The gap is equal to a sum of the thickness of the shield shell and the clearance which allows tolerance for the liner erection. The tail void is common to all shields, and is filled with pea gravel or grout if possible before the soil moves into the gaps. A tail seal is used in order to prevent the grouting material from flowing into the shield chamber through the space between the shield shell and the erected liner.

Figure 2.2(a) shows an ordinary open shield, and Figure 2.2(b) depicts a blind shield with a reduced face opening so that it may control the excavation rate to some extent. The blind shield is considered a variation of open-faced shield and is positioned somewhere between the conventional

shield and the advanced shield. This shield method is applicable only to limited ground conditions like homogeneous soft clay and does not offer strict ground control if sands and silts under the water table are encountered.

### 2.2.2 Advanced Shields

In contrast with the open-faced shield, an advanced shield has a bulkhead which separates soil spoils retaining area from the remainder of the shield. The bulkhead helps the soil to provide resistance against earth pressure of the ground at the face. In addition, the rotating cutterhead also partially supports the face. Therefore, face stability is provided without use of supplementary measures such as compressed air, dewatering, grouting or ground freezing. This advantage of the advanced shield is greatest when the tunnel is shoved through very soft, saturated cohesive soils and/or loose pervious soils below the ground water table.

The advanced shield uses the rotating cutterhead for mechanical excavation. As shield jacks advance the shield, the cutterhead brings soils into the soil spoil retaining area, and the spoil is continuously removed through the bulkhead at a controlled rate.

The slurry shield and the EPB shield are the most common types of advanced shields, though many variations have been developed. These two types are different mainly in the spoil removal method. As illustrated in Figure 2.2(c), the slurry shield uses a hydraulic soil transportation method. Pressurized bentonite-water slurry is introduced into the retain-

ing area through a pipe which runs from the surface slurry storage plant down through the tunnel. The slurry mixes with soils in the retaining area and then is pumped out through a return pipe to the surface for treatment and soil disposal. Control of slurry pressure inside of the bulkhead is crucial to maintain face stability and prevent ground water inflow. The slurry pressure is determined primarily by experience in view of the ground water pressure at the face.

One major advantage of the slurry shield is its applicability to a variety of subsurface conditions. Mixed soil profiles at the face are not a problem for the slurry shield. Its other advantage is a rapid advancement rate of tunneling. This is needed in view of the high cost of a slurry machine and the slurry circulation facilities and expenses associated with slurry disposal.

In contrast with the slurry shield, the EPB shield uses only a screw conveyor to remove soils from the spoil area out of the bulkhead, as shown in Figure 2.2(d). Although the cutterhead provides a partial support for the face, the face stability is established mainly due to the pressure applied to the soils in the spoil area. Ideally, the screw conveyor and the muck discharge equipment placed at the rear of the screw conveyor are adjusted so that the spoils are removed from the bulkhead at the same rate as the volume of soil occupied by the shield advancement. This volumetric equilibrium eliminates soil movement in front of the face, and provides an earth pressure balance.

Although the EPB shield was originally developed only for limited

soil conditions, accumulated experiences are improving its applicability to a wider range of soils. Fujiwara, et al.(1981) discussed conditions suitable for the EPB shield and provided guidelines for EPB shield applicability. Saito, et al.(1980) also discussed the EPB shield capability and problems associated with practical operations. Problem soils are well graded materials like a clay and sand mixture which can block the screw conveyer entrance and prevent soil discharge. Also, soils with low water content are easily compacted within the spoil area resulting in a blockage of soil discharge. Finally, very plastic cohesive soils tend to adhere to the wall of the spoil area so that a smooth soil discharge is not obtained. These types of discharge problems may be eliminated by means of improving consistency of soil in the spoil area by adding water or other plasticizer agents to the spoil.

### 2.2.3 Variations of Advanced Shields

Many variations of advanced shields exist which use a modification of the more common types of advanced shields. Some of the more popular types are explained in this section. The basic EPB shield is not suited for ground water control in pervious soils because of limited water tightness through the auger screw conveyer. In such cases, localized air pressure can be applied in the spoil area to balance the ground water pressure (Saito, et al. 1984). An alternative version uses pressurized water to compensate for the ground water pressure at the exit gate (Ishihara 1978).

Soil blockage occasionally occurs at the screw conveyer entrance and causes a soil discharge problem. A counter-measure to cope with this is

to improve the consistency of the excavated soil. A slime shield (Naito 1985) and a mud balance shield (Sasaki 1981) are designed to mix excavated soils with slurry in order to become very plastic so that an effective EPB shield operation may be maintained even in adverse soil conditions. Disposal of the final muck in these cases requires special attention from an environmental standpoint. In order to overcome this disadvantage, an entrained foam is injected into the spoil area as a plasticizer agent. Soils mixed with bubbles show improved fluidity without disposal problems of sludge-like soil-slurry mixture (Fujiwara, et al. 1981). Once the muck becomes plastic enough to handle like remolded soft clay in the slime and mud balance shields, it may be continuously pumped through pipes out of the tunnel (Saito, et al. 1983).

Another problem with the conventional EPB shield is in ground with gravel, cobbles or boulders. Lumps larger than the critical size of the auger capacity can not be removed from the spoil area. A special version of the EPB shield (Tsukada and Niwa 1981) and slurry shield (Miyamoto, et al. 1984) can be equipped with a crusher to break the cobbles for removal. Alternatively, a helical auger can be used which can pass boulders through the auger.

To the author's knowledge, the largest EPB shield had a 28.3 feet (8.6 m) diameter (Minowa 1981). The largest slurry shield presently being used is 37.4 feet (11.4 m) in diameter (Osaka City 1985).

#### 2.2.4 Summary

Conventional and advanced shield tunneling techniques are described

in this section. The major difference between the conventional and the advanced shields lies in the use of a pressurized face to minimize soil and water movement into the shield. There is no need for compressed air in the tunnel, special dewatering techniques, or other auxiliary measures in case of advanced shield tunneling. The conventional open-faced shield still has the advantage over the advanced shield in bouldery or cobbly ground since boulders can easily be removed. However, new techniques are being rapidly developed to extend the applicability of the advanced shield to a wider variety of soil conditions.

### 2.3 Surface Settlement Induced by Shield Tunneling

The problems of surface settlements due to tunneling are discussed by Peck (1969), Cording and Hansmire (1975), Clough and Schmidt (1977), and Ward and Pender (1981). These reports and other sources in the literature are summarized in this section.

#### 2.3.1 Surface Settlement Profile

Based on field measurements Peck (1969) showed that the settlement profile above tunnels constructed by a conventional shield could be described by an error function. The equation of the settlement trough is

$$\delta = \delta_{\max} \exp(-x^2/2i^2) \quad (2.1)$$

where  $\delta$  a settlement at  $x$  from the tunnel centerline,  $\delta_{\max}$  the maximum settlement over the tunnel centerline, and  $i$  distance from the centerline to the point of inflection. The pertinent properties of the

error function and its relationship to the dimension of the tunnel are shown in Figure 2.3. Hanya (1977) examined a limited set of case histories with advanced shields and showed that the Peck's error function may also be representative of the settlement trough caused by the advanced shield tunneling. More recently, O'Reilly and New (1982) showed that the error function is not as accurate for tunnels driven by conventional shields in sandy or granular soils versus clayey soils.

A useful parameter which can be derived from the error function is the volume of the surface settlement trough per unit length along tunnel alignment,  $V^S$ . Integration of equation 2.1 with respect to  $x$  yields

$$V^S = \sqrt{2\pi} i \delta_{max} \quad (2.2)$$

This parameter is especially functional since ultimately the factors which cause settlements are related to volumes.

### 2.3.2 Causes of Settlement

The time sequence of the development of surface movement of a point above a shield tunnel is shown in Figure 2.4. As the shield approaches, the ground may initially heave. In the case of a conventional shield, this is followed by immediate settlement at the position of the shield face due to movements into the face. In an advanced shield, heaving effects are usually much larger than for a conventional machine and depend upon the rate at which muck is removed from the shield. In both cases settlement occurs after shield passage. This is caused as the soil moves toward the tunnel to close the tail void and usually a large portion of

this settlement is immediate. Secondary or long term settlement may continue for a long period of time, with this effect typically being larger where more ground disturbance has occurred during tunneling.

Face stability is important in movement control. The overload factor, OF, provides an index as to the face stability (Broms and Bennermark 1967), and it is defined as

$$OF = \frac{p_v - p_a}{s_u} \quad (2.3)$$

where  $p_v$  total overburden pressure at the tunnel springline,  $p_a$  pressure of compressed air in tunnel or pressure at the face of the shield, for a closed-faced shield, and  $s_u$  undrained shear strength of clay.

Broms and Bennermark (1967) conducted extrusion tests to check for critical values of OF and concluded that a vertical unsupported face would be unstable at OF greater than 6. Davis, et al. (1980) gave the lower bound of OF for the face stability as a function of ratios of cover to diameter. They showed that for a tunnel with a small cover to diameter with an OF of 6 may be unsafe due to yielding at the face of an open shield. Tunneling with an open shield is possible at higher OF values, although movements may be large. Cording and Hansmire (1975) suggested that 30 to 50 percent of the ground movements for conventional shields when  $OF > 6$  may be attributed to movements into the shield face. Fortunately, face stability is not a significant problem for the advanced shield if it is operated properly, since the face is continuously supported. This helps the advanced shield reduce ground movements.

The tail void is left at the end of the shield as the shield advances. It may be immediately filled with squeezing clay if the overload factor is high and if one accounts for settlements at the ground surface. If there is no face loss, the volume of the tail void,  $V_{TV}$ , is equal to the total ground loss. For moderate OF's above about 4, the void closure will occur before the shield advances by one liner ring cycle (Clough and Schmidt 1977). Grouting through the liner can be done to reduce, or even eliminate, the ground loss, if it can be done before the void closes. Under pressure, the grout may also push the soils outward, but this is a small effect since the soil mass offers so much resistance. For small OF values, or a very stable condition, the void behind the tail may stand unsupported for a sufficient time so that the grout fills the space.

The tail void can be increased if overcutting at the face of the shield is done. The most common cause of overcutting is due to steering problems with the shield causing it to be driven. A deviation from the design alignment also has the effect of increasing the tail void. In particular, the shield easily goes into an excessive pitch during operation. Then the soil immediately above the shield will settle along the shield crown going down with its pitching grade. Hansmire (1975) estimated the ground loss due to the shield pitch as an excess of volume occupied by the top half of the shield in pitching over that for the design grade.

A long term settlement may develop in certain soils after shield passage. In stiff clays like overconsolidated clays, ground movements are almost elastic and few subsequent settlements are observed (Eden and Bozozuk 1969). On the other hand, long term settlements in soft clay can

be a significant portion of the final settlement. These are caused by consolidation of soil due to excessive pore pressure dissipation or drainage into the tunnel.

The amount of the consolidation settlements has been shown to depend upon the degree of disturbance induced by the tunneling operation. A tunneling practice causing less disturbance leads to improved performance. As mentioned earlier, the EPB shield can be operated such that an initial heaving is created. In one sense this helps to trade off the inward soil movement into the tail void. However a large heaving would likely be detrimental since it would disturb and remold soils adjacent to the tunnel. This effect was observed for a blind shield in Chicago clay where large long term settlements resulted from a significant initial heave (Terzaghi 1942).

A final aspect of ground movements is related to leakage through a liner. If ground water flows through the liner into the tunnel, the water content of soils near the tunnel is reduced, and consolidation results within the area of soils losing water. Eden and Bozozuk (1969) predicted that the tunnel acts as a drain even after the concrete lining is placed. In such circumstance consolidation likely occurs.

In summary, the causes of settlement may be divided into the immediate and long term causes. The former results from volume loss at the tunnel face, shield deviation out of the design alignment, and closure of the overcutting space and the tail void. The latter develops as a result of consolidation.

### 2.3.3 Prediction of Surface Settlement

Rowe and Kack (1983b) present relations between ratio of maximum settlement to gap and dimensionless depth, which is shown in Figure 2.5. Larger settlements are observed for shallower tunnels in soft grounds. For reference, the data for the N-2 EPB shield project (Clough, et al. 1982a) are also plotted in the figure. Settlements for the N-2 project are on the lower end of the typical values. Similar to linear relations representing clays and sands in Figure 2.5, Atkinson and Potts (1977b) relate maximum surface settlements  $\delta^S$  to soil movements close to the tunnel crown  $\delta^C$  in an expression

$$\delta^S/\delta^C = 1 - \alpha(H/D) \quad (2.4)$$

where  $\alpha$  is a constant with a value of 0.40 for sands and 0.13 for clays.

Clough and Schmidt (1977) also developed a parabolic relation with an equation

$$\delta^S/\delta^C = (Z/2R)^{0.8} \quad (2.5)$$

In spite of the simplicity of the equations for predicting maximum settlement, the field data upon which the methods are based are widely scattered, and therefore limitations exist in regard to accuracy and reliability.

Hanya (1977) tabulated maximum settlements for different subsoil conditions in Table 2.2. Maximum settlement is expected to be from 30 mm to 100 mm for shield tunnels in alluvial soft cohesive soils. Fujita (1981) arranged data of various projects in such a way that maximum settle-

ments are classified according to different shield tunneling methods (Figure 2.6). Although advanced shields are frequently employed under more difficult subsurface conditions, such as alluvial soft ground, most of the maximum settlements are under three inches, a smaller value than that for the conventional shield (Fujita 1981). Maximum settlements for advanced shields shown in Figure 2.6 fall in the lower range of settlements in an alluvial soft ground shown in Table 2.2.

Fujita (1981) also found the relationship between the settlement trough shape and that shown by Peck (1969) to be typical for conventional tunnels. Peck (1969) used the inflection point  $i$  as a representative of width of the settlement trough, and then presented relations between width radius ratio  $i/R$  and depth diameter ratio  $Z/2R$  for different soil conditions as shown in Figure 2.7. In Figure 2.7 data observed for various advanced shields are presented by Fujita (1981), who concluded that Peck's criteria on the settlement trough width is valid even for the advanced shields.

Attewell (1981) developed a parabolic relationship between  $i/R$  and  $Z/2R$  for conventional shield in the expression

$$i/R = K(Z/2R)^n \quad (2.6)$$

where  $K$  and  $n$  are parameters given in Table 2.4.

In contrast to the method proposed by Peck (1969), he gave ground loss relative to the design excavation volume so that the maximum settlement may be evaluated by means of equation 2.2. Clough and Schmidt (1977) give values of 1 and 0.8 to  $K$  and  $n$ , respectively, in equation 2.6

for clays (Figure 2.7).

In contrast to the nonlinear relation of equation 2.6, the value of the unity of the exponent  $n$  results in a linear relation between  $i$  and  $Z$ . O'Reilly and New (1982) draw a linear variation of  $i$  with  $Z$  as shown in Figure 2.8. They developed a new expression

$$i = K Z \quad (2.7)$$

where  $K$  is a parameter with values given in Table 2.5. Ground losses are also given in the table to evaluate the maximum settlement.

When the magnitude of settlements is calculated by means of equation 2.2, it can not be established without accurate knowledge of the ground loss. Hanya (1977) showed various sources of ground loss in Table 2.3 for a conventional shield tunneling in clay. He indicated that ground losses due to relatively instantaneous settlement and consolidation settlement are about the same amount. Tables 2.4 and 2.5 give reference values of the ground loss for roughly classified soil conditions. Clays exhibit large ground loss which result from the consolidation. Clough and Schmidt (1977) presented relationship between the overload factor and ground loss with theoretical and observation data (Figure 2.9). This figure provides an idea of the magnitude of ground loss in the evaluation of surface settlement, even though the data fall in a wide range.

#### 2.4 Measured Ground Movements Induced by Advanced Shields

Field observations are essential to define how shield tunneling influences the surrounding ground and nearby structures. Terzaghi (1942)

presented one of the first well-documented cases of ground movements as a case where a blind shield was driven through Chicago clay. Since then, many field observations have been carried out and the accumulated results have considerably disclosed the ground behavior due to shield tunnel construction. The results are summarized in many state-of-the-art reports and recent specialization conferences (Lo 1984, Miki 1984).

#### 2.4.1 Measured Ground Movements and Pore Pressure Development

As advanced shields are employed more popularly than before, mainly in Japan, field measurements of ground movements due to advanced shield tunneling are frequently performed. Most of the early measurements consisted only of surface survey data. Yamazaki (1976) first described observed surface heaving as a slurry shield passed. Kitamura, et al. (1981) also monitored surface heaves due to an EPB shield tunneling. Sasaki and Tanaka (1981), Hashimoto (1984), Matsumoto, et al. (1981) and others have presented similar ground response due to advanced shield tunneling. Hirata and Aritome (1983) presented some detailed deep ground displacements by means of heavy instrumentation for an EPB shield tunneling. The results indicated that during an initial heave in front of the shield face, almost all the soils were pushed forwards with the shield advancement, but a limited amount of soil located near the tunnel crown moved into the shield.

The heaving effect of the advanced shield is in contrast with that of the conventional shield. Cording and Hansmire (1975) presented a detailed consideration of ground losses with the conventional shield and

found that especially in soft ground a significant loss occurs into the tunnel face.

In contrast with the ground movements into the shield face in the case of the conventional shield, a major advantage of the advanced shield is to control ground movements at the shield face by means of producing an initial heave. The heaving effect, which may be equivalently noted as a negative ground loss, is relatively difficult to measure in the field because of the complexity of the ground behavior (Hirata and Aritome 1983). Kobayashi (1984) suggested that the optimum level of heaving falls within 0 to 5 percent of the tunnel volume so that a minimum surface settlement results.

Pore pressure measurements are important to the understanding of the ground disturbance and long term consolidation behavior. Few such measurements have been made. One of the best documented cases was reported by Palmer and Belshaw (1980), who measured the pore pressure development associated with a conventional shield tunneling. They observed that the pore pressures increased when the shield approached within one meter of the instrument point. Hirata (1983) showed that the EPB shield increased the pore pressure by 10 to 20 percent at the springline at the location 0.5 meters from the shield. Higher pore pressure may have been induced in soils closer to the shield.

#### 2.4.2 Ground Movements of the N-2 Tunnel Case

Clough, et al.(1982a) provided documentation for the ground movements

of the N-2 tunnel project in San Francisco, the first EPB shield application in the United States. Their results obtained from the instrumentation program are briefly reviewed here because this case history is used as a means of calibrating the finite element program developed in this thesis.

The project involved a 3000 feet (915 m) long, 12.1 feet (3.7 m) diameter tunnel, driven through about 30 feet (9.1 m) deep bay sediment called Recent Bay Mud. This soft soil lies between a 20 feet (6.1 m) deep rubble fill and a colluvial sandy stratum as shown in Figure 2.10.

As illustrated in Figure 2.11, the Recent Bay Mud is a soft, normally consolidated silty clay with a shear strength of about 600 psf ( $29.2 \text{ kN/m}^2$ ) at the depth of the tunnel springline. Along the alignment four instrumentation lines were established, and three of them were intensively monitored to measure ground movements during and after the shield passage.

Five casings were set with approximate spacing of 10 feet (3 m) perpendicular to the tunnel alignment. Lateral and vertical subsurface soil movements were measured in front of and adjacent to the tunnel. Figures 2.12 and 2.13 indicate lateral displacements of ground at the time of different relative positions of the shield. As observed in the Japanese projects, a prominent heaving developed ahead of, and to the side of, the shield, concentrated in the Recent Bay Mud. Local excess pore pressure developed since water was expelled or rose in the casings during the shield passage. However, as the shield tail passed the line, reductions in heaving deflection were observed to occur in response to closure of the tail

void. Note that the closure occurred in spite of tail void grouting.

Figure 2.14 compares the lateral displacements for the four lines measured about one month after the shield passage. Lines 1 and 2 show net inward movements while Lines 3 and 4 show net outward movements. The differences in the lateral movements correlated well with the measured earth pressure inside the EPB shield bulkhead. Higher measured earth pressures led to net outward movements.

Figure 2.15 shows the variation of the vertical movements above the tunnel centerline at Line 4 with time for a period of 150 days. Frequent readings as the shield approached show that the ground surface initially heaved 0.25 in. (0.63 cm). After the shield passage, the ground began to settle and continued to do so for about 40 days and the final settlement of 1.2 in. (3.0 cm) was reached.

The results of field instrumentation program for the N-2 project disclosed a unique ground behavior induced by the EPB shield. They are summarized as follows:

1. Soils initially heaved away from the approaching shield.
2. The soil movements were confined within the Recent Bay Mud.
3. High excess pore pressure were locally induced.
4. The level of lateral deflections were different for the instrument lines, relating the earth pressure measured at the EPB shield bulkhead.
5. The tail void closure caused immediate inward soil movements, in spite of the backfill grouting.
6. Time dependent ground movements were observed after the shield passage.

The N-2 data are compared with other available data associated with shield tunneling in Figures 2.5 through 2.9. They generally illustrate

that the N-2 project showed a smaller settlement relative to that expected with the conventional shield and is typical of advanced shield performances.

## 2.5 Analytical Procedures for Shield Tunneling

Analytical procedures that can be used to study tunneling induced movements are reviewed in this section. Various analytical procedures are summarized in Table 2.6. The review will help to explain the needs for development of a new FEM program in this research.

### 2.5.1 Closed Form Solutions

Peck (1969) discussed the deformation of and pressure distribution on perfectly rigid and perfectly flexible tunnel lining under the initial ground stresses. This triggered the theoretical consideration of tunneling problems.

An earlier work by Mindlin (1939) gave an elastic closed form solution for a shallow tunnel which is influenced by the presence of a free surface. References are available based on the theory of elasticity. Recently, Carter and Booker (1982) extended the solution to take the consolidation effect into account. However, these approaches are effective only for every simple boundary conditions but are not applicable to practical problems.

### 2.5.2 Finite Element Solutions

The finite element method has been often used to analyze tunneling

problems. Linear elastic FEM analyses on a lined tunnel were reported by Peck (1972), and later Kasali (1981) conducted a three-dimensional linear elastic FEM analysis to predict ground movements into the shield face. Linear elastic idealization is a useful method for stiff soils and has contributed to the analysis of tunnel-ground interaction. However, it does not apply well to the behavior in soft ground.

Elastic-perfectly plastic FEM analysis has been widely used in tunnel analyses since Hoyaux and Ladanyi (1970) first employed that method. This approach is limited in its application to soils since it is well known that soil behavior is more complicated than assumed in this model.

The nonlinear pseudo-elastic FEM analysis is another popular approach which has been used for tunnel analyses. This method most commonly employs a hyperbolic idealization of the stress-strain relation for soil proposed by Duncan and Chang (1970). Using this method, Kawamoto and Okuzono (1977) calculated the surface settlement profile of a tunnel driven in sands and gravels. Tan and Clough (1980) considered the time-dependent effect of chemically grouted soil around a tunnel in addition to the nonlinear elastic soil modeling. Other variations of this analysis method are: accounting an anisotropy of clay (Hansen and Clough 1980), three-dimensional analysis (Katzenback and Breth 1981), and hybrid formulation to consider effects of pore pressure (Osaimi and Clough 1979).

The nonlinear elastic analysis has been demonstrated to give a significantly better prediction of settlements than the linear elastic analysis. It also provides useful data on the zones of yielded soil around the

tunnel. However, it does not account for coupling between shearing and bulk response, nor can excess pore pressure development be evaluated correctly.

The Cam Clay model (Roscoe and Burland 1968) was developed to provide a realistic plasticity-based mathematical model for the behavior of cohesive soils. Orr, et al.(1978), Mair, et al.(1981) and Adachi, et al. (1979) used this model in tunnel analyses. Johnston (1981) combined a pore fluid flow equation with the Cam Clay soil model so that excess pore pressure development and dissipation causing consolidation could be calculated in conjunction with the tunnel construction procedure. Consequently it became possible to theoretically consider both immediate and long term ground movements about the tunnel.

Finno (1983) extended Johnston's approach to deal with practical conditions of advanced shield tunneling, and carried out an analysis of the N-2 tunnel behavior. His results showed good agreement with much of the field data. However, the predicted ground movements due to the tail void closure and the surface settlement profile showed relatively poor agreement with the observed data. The reason for that is due in part to the fact that the Cam Clay model is not able to represent the unloading situation well because an elastic response is assumed upon unloading.

### 2.5.3 Solutions of Limit Analysis and Boundary Element Method

Several application examples of the limit analysis and the boundary element analysis (BEM) to tunneling problems are shown in Table 2.6. The

limit analysis and the BEM analysis has certain strong points over other types of numerical methods. However, difficulties lie with those methods to cope with sophisticated geotechnical conditions where shield tunneling is applied. Furthermore complexity in the boundary conditions, the sequence of the tunnel construction procedure, the effects of pore pressure changes, and the time dependent response of soil are difficult aspects to be accounted for in the BEM approach. The FEM is the only approach which can account for such difficulties currently.

#### 2.5.4 Requirements for Modeling Tunneling Procedure

When advanced shield tunneling is to be simulated by means of the finite element method, it must follow a complex process of tunneling in practice. The following features are desirable in an analytical procedure:

1. Consideration of ground movements associated with the initial heave and the tail void closure.
2. Consideration of stress transfer to lining after its installation and the tail void closure.
3. Consideration of excess pore pressure development and possible dissipation effects that cause consolidation.
4. A soil model capable of predicting soil behavior under the action of load reversals and large deformation.

Ground movements associated with advanced shield tunneling are not two-dimensional (2-D), and thus a three-dimensional (3-D) analysis may be more realistic. However, a 2-D analysis requires less computational effort and provides reasonable results.

## 2.6 Summary

Conventional and advanced shield tunnel methods are described along with the sources of ground movements in the two cases. Most importantly, it is observed that the advanced shield, with its closed face type of advance, can, and often does, lead to heaving of the soil away from the face of the shield during its advance. This contrasts with the conventional shield where the soil invariably moves towards the face of the shield, and ultimately this action contributes to the settlements and lateral movements which occur above the shield.

Trends from the observed data for field cases where conventional and advanced shield tunneling have been used lead to the following conclusions:

1. Surface settlements above the advanced shield are generally less than those for the conventional shield.
2. The shape of the settlement trough above the advanced shield tunnel is similar to that of the conventional shield.
3. A common problem in the case of both the advanced and conventional shield is closure of the tail void.
4. A long-term settlement is observed after the shield passage in the case of both advanced and conventional shields.

Because of the difficulties between the ground response to the advanced and conventional shields, the usual methods for predicting ground movements are not applicable to the advanced shield without modification. For this reason, additional studies are needed. A review of available techniques suggests that the finite element method is best adapted for this purpose. However, work with the technique to date has been limited by inadequate soil modeling and simulation of the tunneling process.

Table 2.1 Comparison of Construction Features for Different Types of Shield (Naito 1984)

Conditions	EPB Shield	Slurry Shield	Open-Face Shield
Geology and underground water	<ul style="list-style-type: none"> <li>• Applicable to a variety of soils due to many specially adapted types</li> <li>• Careful consideration is essential in the shield design phase if gravels and cobbles are expected</li> <li>• When silt or clay content is small in uniformly graded sandy ground or when water pressure is high, slime injection is preferred</li> </ul>	<ul style="list-style-type: none"> <li>• Applicable to various types of soils; careful consideration is essential in the shield design phase if gravel and cobbles are expected</li> <li>• In highly pervious ground, it's necessary to prevent the slurry from running out</li> <li>• Especially appropriate for aquifer ground, transocean, and river tunneling</li> </ul>	<ul style="list-style-type: none"> <li>• Tunnel face is unstable in very soft ground</li> <li>• Compressed air or chemical stabilization is necessary in aquifer</li> <li>• High compressed air is not desirable</li> </ul>
Access and construction	<ul style="list-style-type: none"> <li>• Almost the same as an open-face shield</li> <li>• When slime is used environmental protection against contaminated muck disposal is necessary</li> </ul>	<ul style="list-style-type: none"> <li>• Area for slurry screening and conditioning plant is essential</li> <li>• Environmental protection against contaminated muck and slurry disposal is necessary</li> <li>• Slurry disposal after chemical treatment should satisfy waste water requirements</li> </ul>	<ul style="list-style-type: none"> <li>• Area for muck disposal and materials handling is necessary near the access shaft</li> <li>• Compressed-air cannot be used when wells exist nearby</li> </ul>
Obstructions at the face	<ul style="list-style-type: none"> <li>• Removal from ground surface beforehand</li> <li>• Removal from inside of the tunnel after face is stabilized</li> <li>• Wooden piles can be cut and chopped with specially designed cutting bits</li> </ul>	<ul style="list-style-type: none"> <li>• Almost the same as an EPB shield for removal from above or inside</li> <li>• Wood fragments or cobbles sometimes clog the pressure chamber or discharge line</li> </ul>	<ul style="list-style-type: none"> <li>• Easy to handle boulders and piles encountered at tunnel face</li> </ul>
Curved tunneling	<ul style="list-style-type: none"> <li>• Difficulty same as with a conventional mechanical shield</li> </ul>	<ul style="list-style-type: none"> <li>• Almost the same as a conventional mechanical shield</li> <li>• Running out of slurry behind assembled lining sometimes disturbs the ground; curved tunneling experiences deterioration of reaction force support</li> </ul>	<ul style="list-style-type: none"> <li>• Relatively easy</li> <li>• Ground should be stabilized with steep curving due to large overcutting</li> </ul>
Tunneling productivity	<ul style="list-style-type: none"> <li>• With optimum tunneling control tunnel progress is excellent</li> </ul>	<ul style="list-style-type: none"> <li>• High level of tunnel progress</li> <li>• When silt or clay content is large, the progress is affected by slurry screening and conditioning capacity</li> </ul>	<ul style="list-style-type: none"> <li>• Very slow due to hand digging</li> <li>• Few mechanical troubles allow constant progress to be achieved</li> </ul>

Table 2.2 Relationship between Soil Conditions and Surface Settlements (Hanya 1977)

Soil layer at tunnel face		Soil layer above tunnel	Settlement (mm)
Alluvial layer	Soft cohesive soil	Alluvial layer	30 ~ 100
Diluvial layer	Cohesionless soil	diluvial layer with a thickness less than tunnel diameter	50 ~ 80
		Diluvial layer with a thickness layer than tunnel diameter	10 ~ 30
	Cohesive soil	Diluvial or alluvial layer	~ 30

Table 2.3 Components of Ground Loss (Hanya 1977)

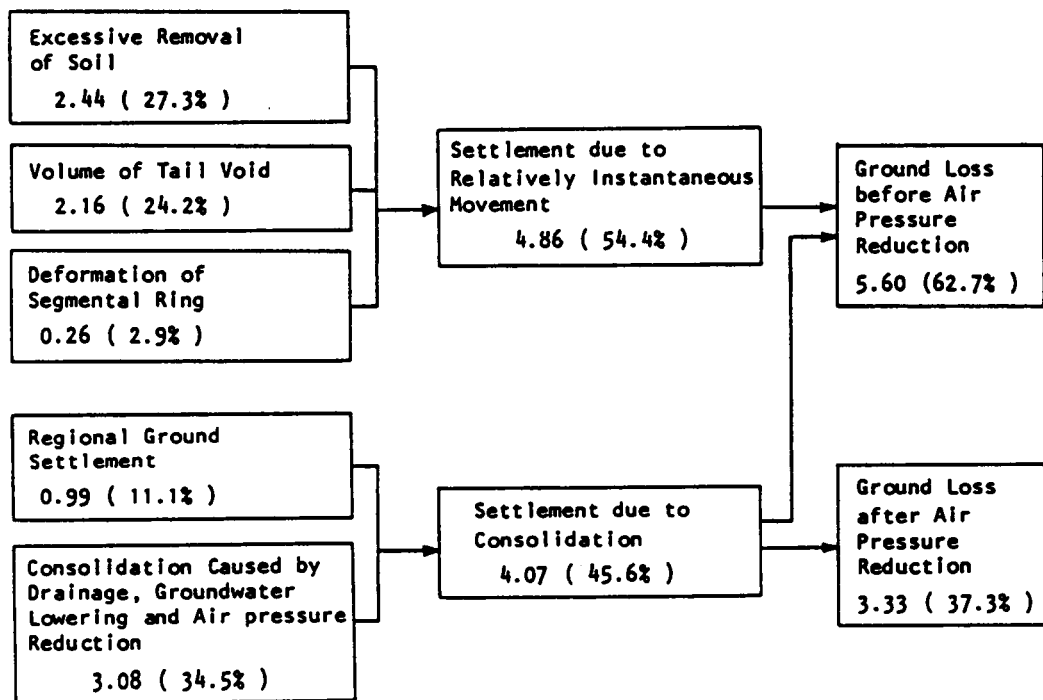


Table 2.4 Settlement Predicted by Parabolic Interpretation of Trough Width (Attewell 1981)

Ground condition	Ground Loss $V^S / V_E$ ( % )	Parameters		Remarks
		K	n	
Clay	1.3 - 2.5	1	1	
Sand	0.15 - 13	0.82	0.36	5 for prediction purpose Above water table
		0.74	0.90	Below water table
		0.63	0.97	Neglecting effects of water table

$$i/R = K ( Z/2R )^n$$

Table 2.5 Settlement Predicted by Linear Interpretation of Trough Width (O'Reilly and New 1982)

Ground conditions	Ground support method in tunnel	K	$V^S/V_E$ ( % )	Remarks
Stiff fissured clay	Shield or none	0.4-0.5	½-3	Considerable data available; losses normally 1-2%
Clacial deposits	Shield in free air	0.5-0.6	2-2½	
	Shield in compressed air		1-1½	Compressed air used to control ground Failure or near-failure conditions usual Some partial face values included
Recent silty clay deposits ( $C_u = 10-40 \text{ kN/m}^2$ )	Shield in free air	0.6-0.7	30-45	
	Shield in compressed air		5-20	

$$i = K \cdot Z , \quad \delta_{\max} = V^S / \sqrt{2\pi} \cdot i$$

Table 2.6 Various Analytical Approaches to Shield Tunneling

[Authors]	[Method of Analysis]	[Objectives]
<u>Closed Form Solution</u>		
1. Peck (1969)	Stress consideration	Earth pressure distribution and lining deformation for perfectly rigid and perfectly flexible tunnel
2. Mindlin (1939)	Elastic theory	Elastic half space with gravity effect, presence of free surface not important for the circumferential stress for an unlined tunnel of $H/D < 0.25$
3. Carter and Booker (1982)	Elastic theory	Consolidation effect around a tunnel
<u>FEM (Elastic)</u>		
4. Peck (1972)	Plain strain elastic FEM analysis	Lined shallow tunnel for $H/D < 2$ , stresses not changed very much with depth
5. Kasali (1981)	3-D elastic FEM	Three dimensional ground movements into the shield face
<u>FEM (Elastic-perfectly plastic)</u>		
6. Hoyaux and Ladanyi (1970)	Elastic-perfectly plastic FEM analysis	Simulating unlined tunnel in clay failed zone completely encompassing the tunnel
7. Saito, et al. (1973)	Elastic-perfectly plastic FEM analysis	Ground movements and failed zone developments around the tunnel in soft clay
8. Fujiwara and Yamashita (1983)	Elastic-perfectly plastic-viscous analysis	Rock tunnel analysis accounting for construction procedure and creep movement of rocks
<u>FEM (Nonlinear elastic: Duncan-Chang soil model)</u>		
9. Kawamoto and Okuzono (1977)	Nonlinear pseudo-elastic FEM analysis (Duncan-Chang soil model)	Analysis on a tunnel driven through sands and gravel fiving surface settlement profile
10. Sakurai (1981)	Nonlinear pseudo-elastic FEM analysis (Duncan-Chang soil model)	Simplified analysis of inward movements of rock tunnel
11. Katzenback and Breth (1981)	3-D nonlinear pseudo-elastic FEM analysis (Variation of Duncan-Chang soil model)	Analysis of a tunnel in clay supported with sprayed concrete
<u>Limit Analysis</u>		
12. Tan and Clough (1980)	Nonlinear pseudo-elastic rheological FEM analysis (Duncan-Chang soil model)	Effects of time dependent nature of chemically grouted soil around shield tunnel
13. Hansen and Clough (1980)	Nonlinear anisotropic pseudo-elastic FEM analysis (Modified Duncan-Chang soil model)	Effects of stress and strength anisotropy of clay for excavation loading of braced excavation (This method will be employed in Chapter 10)
<u>FEM (Elasto-plastic: Cam Clay soil model)</u>		
14. Orr, et al. (1978)	Elasto-plastic FEM analysis	Analysis of soil movements of a model tunnel in clay obtained from centrifugal tests
15. Haif, et al. (1981)	Elasto-plastic FEM analysis (Variation of Cam Clay model)	Analysis of a deep tunnel in heavily overconsolidated tuff for drained and undrained behavior
16. Adachi, et al. (1979)	Elasto-plastic FEM analysis (Variation of Cam Clay model)	Analysis of shield tunnel in soft clay accounting for pore pressure development and dissipation to cause condolidation settlement
17. Johnston (1981)	Elasto-plastic FEM analysis coupled with pore fluid flow (Cam Clay soil model)	Analysis of closed-faced advanced shield tunneling method, accounting for initial heaving effect
18. Finno (1983)	Same as above	Evaluation of breasting pressure to stabilize the face of open shield in granular soil
<u>Limit Analysis</u>		
19. Murayama and Matsuoka (1969)	Limit design method	Stability of lined or unlined tunnel in clay giving by overload factor
20. David, et al. (1980)	Upper and lower limit theorem	Stress and strains in plastic equilibrium about the tunnel
21. Atkinson and Potts (1977)	Method of associated field	Deformation of rock tunnel
<u>BEM (Boundary Element Method)</u>		
22. Shimizu and Sakurai (1983)	BEM analysis	Time dependent rock deformation properties for a rock tunnel
23. Ito and Hisatake (1981)	BEM and viscous analysis	Stress concentration in lining at the intersection of underground opening
24. Dendrou (1981)	BEM analysis	Simulating yielding or rock around a tunnel
25. Venturini and Brebbia (1981)	BEM analysis with material nonlinearly	

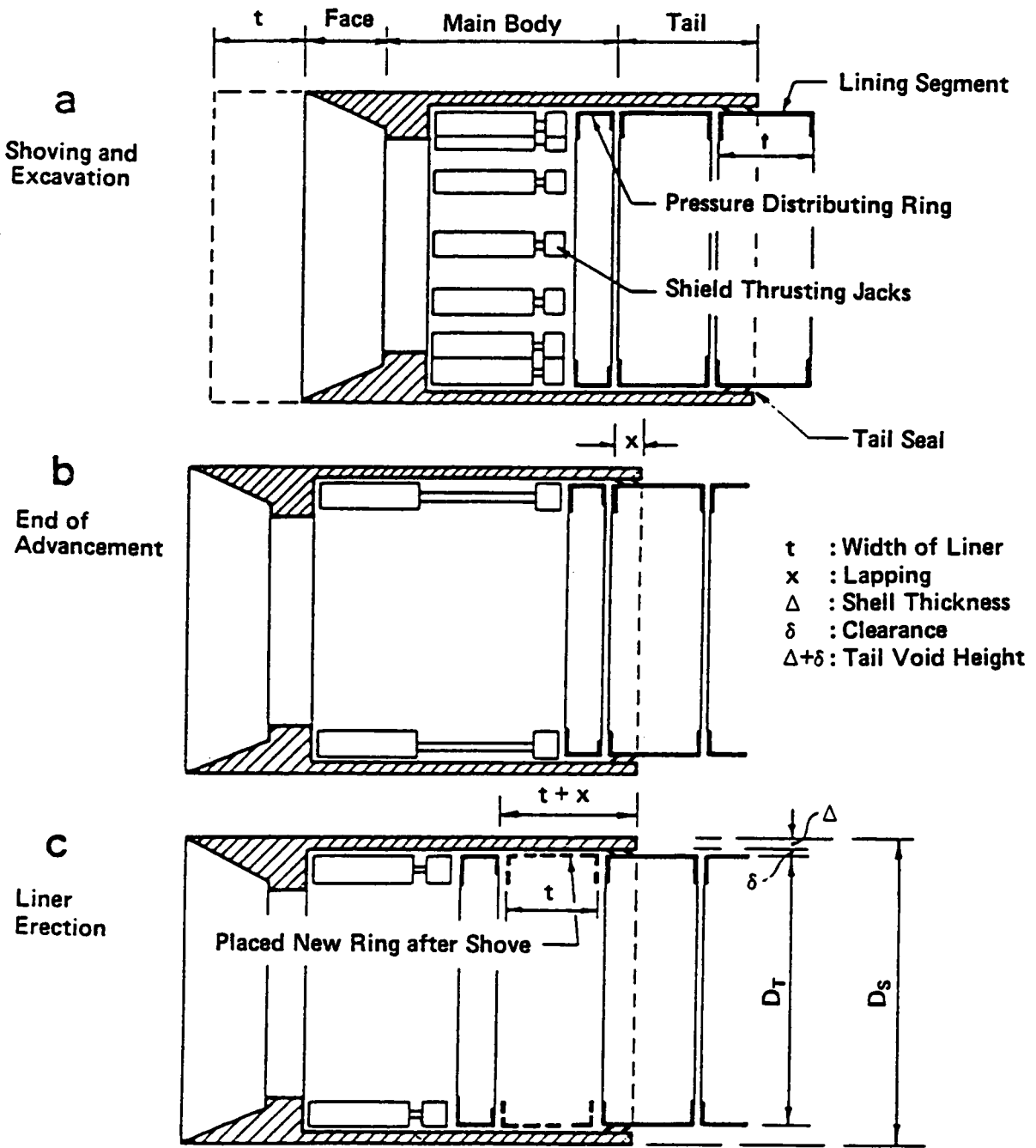
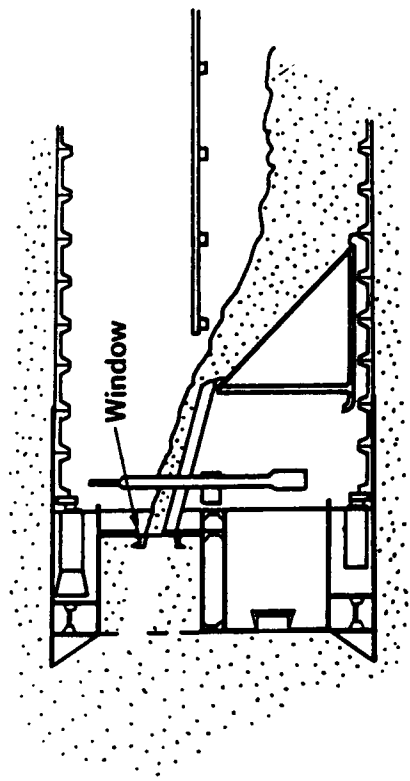
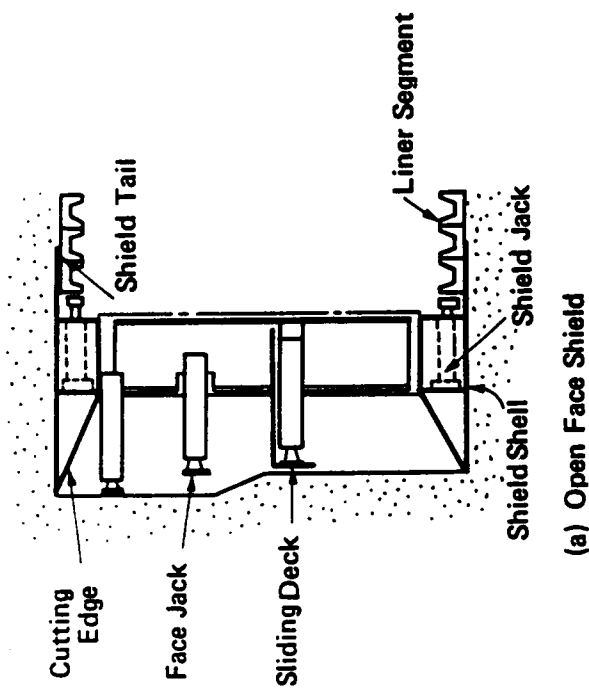
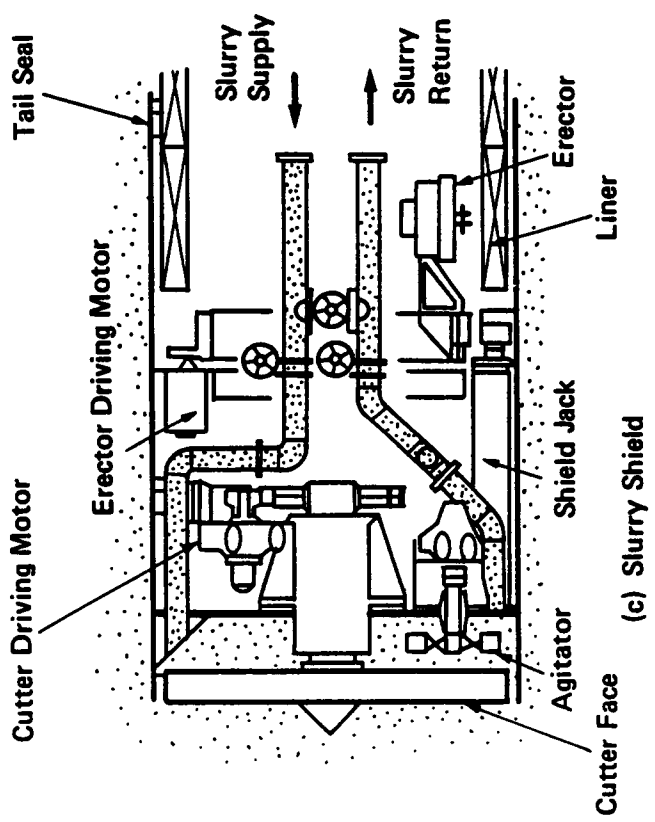


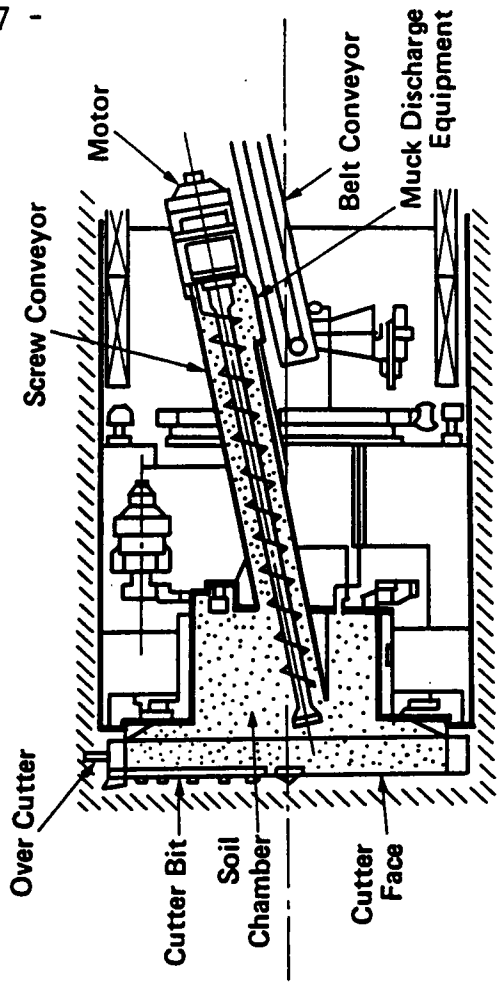
Figure 2.1 Cycle of Shield Tunneling ( after Lo and Rowe 1982 )



(b) Blind Shield



(c) Slurry Shield



(d) Earth Pressure Balance Shield

Figure 2.2 Typical Types of Shield Machines

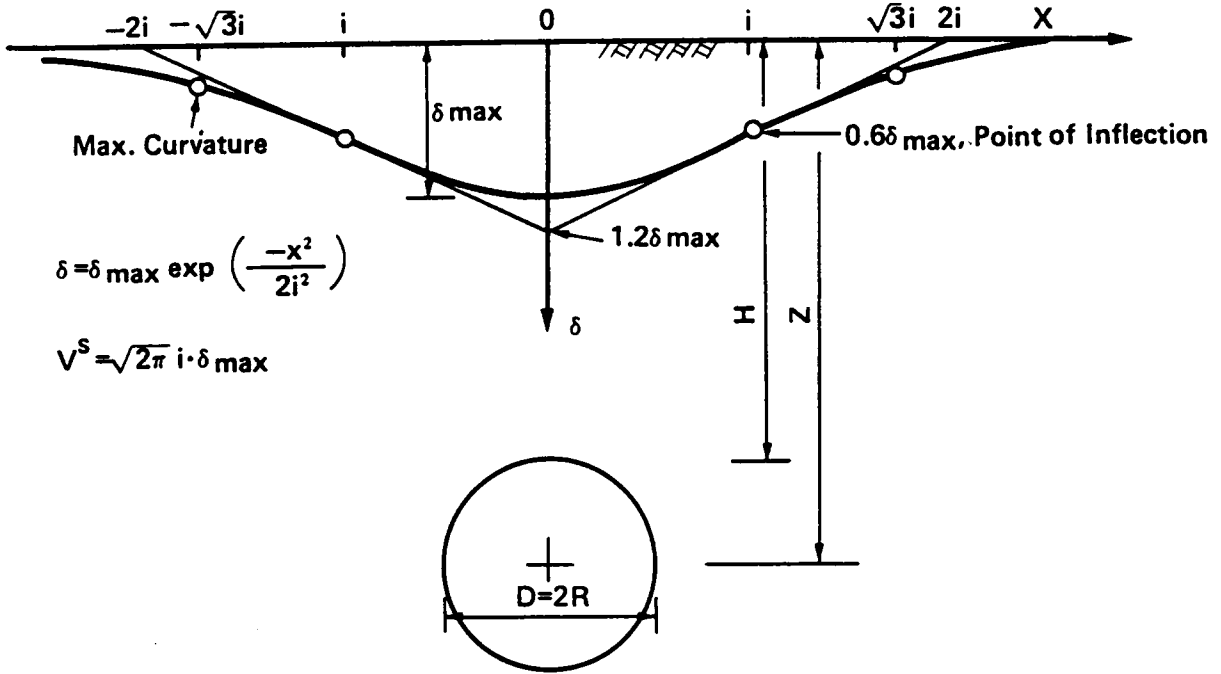


Figure 2.3 Error Function Curve Approximating Surface Settlement Trough

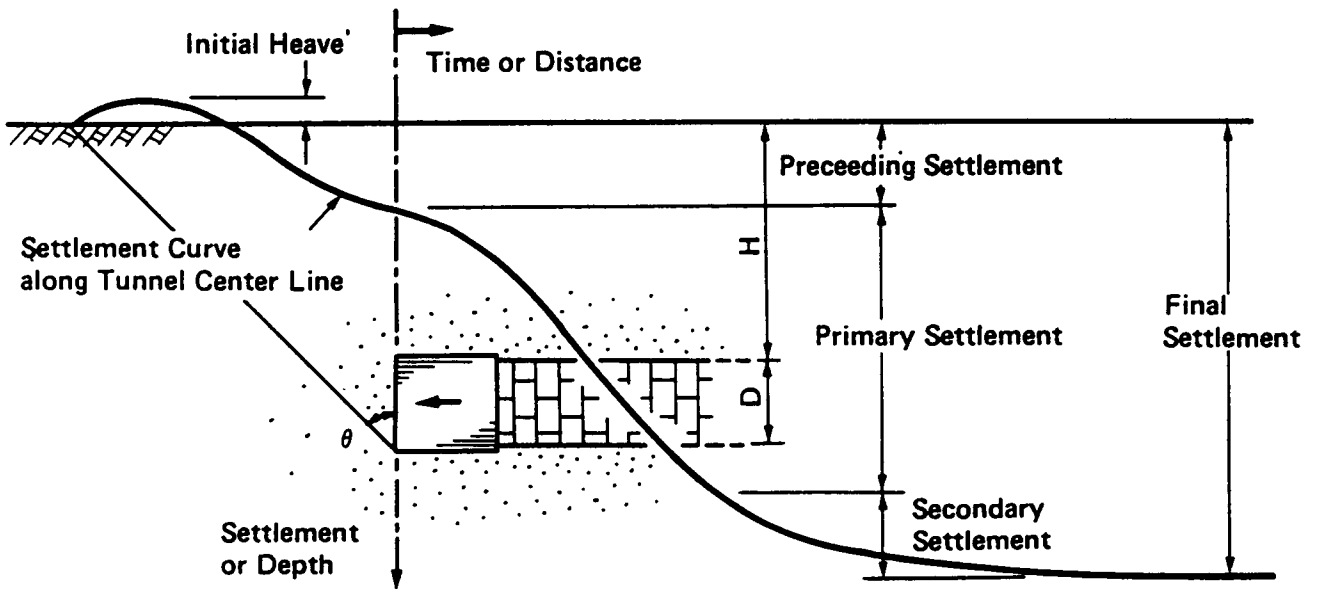


Figure 2.4 Time Dependent Surface Movement with Relative Position of Shield

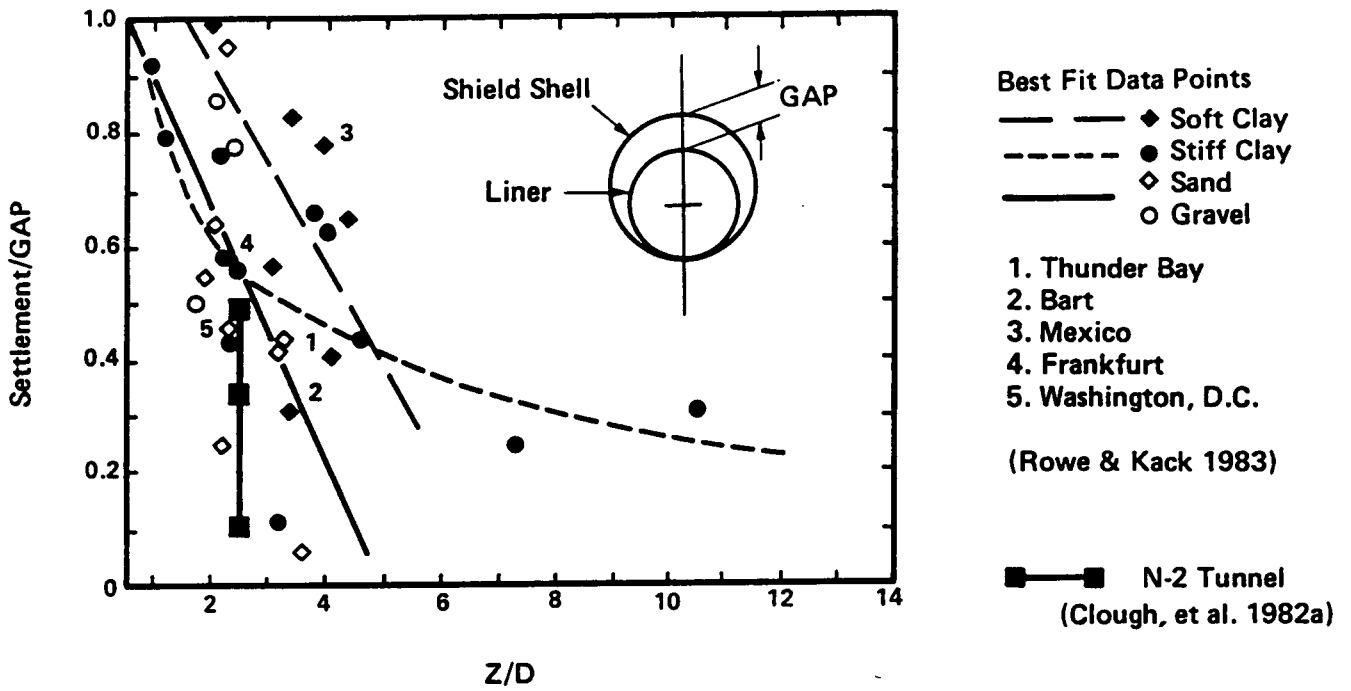


Figure 2.5 Relationship between Surface Settlement and Gap

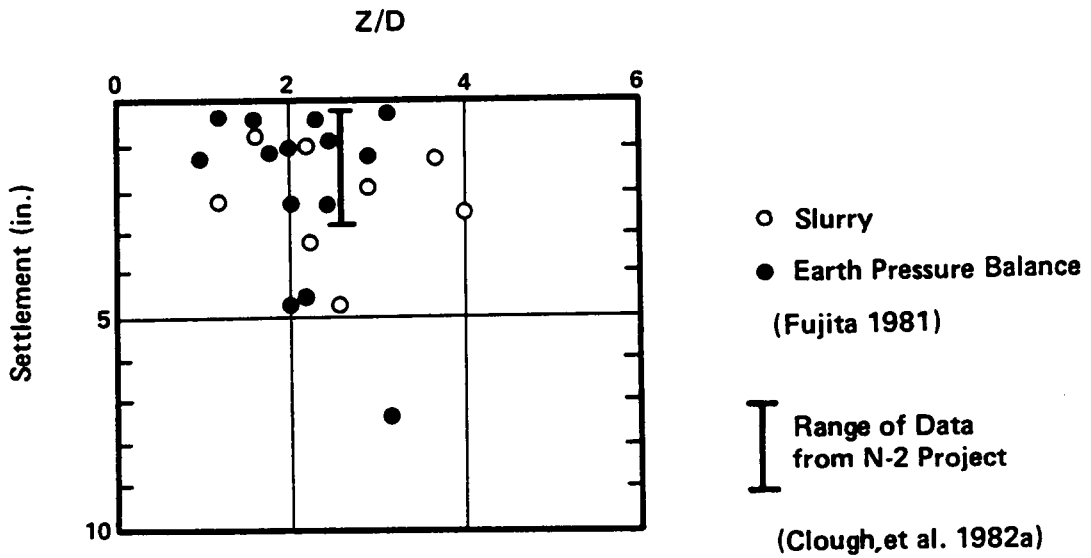


Figure 2.6 Relation between Settlement and Dimensionless Depth

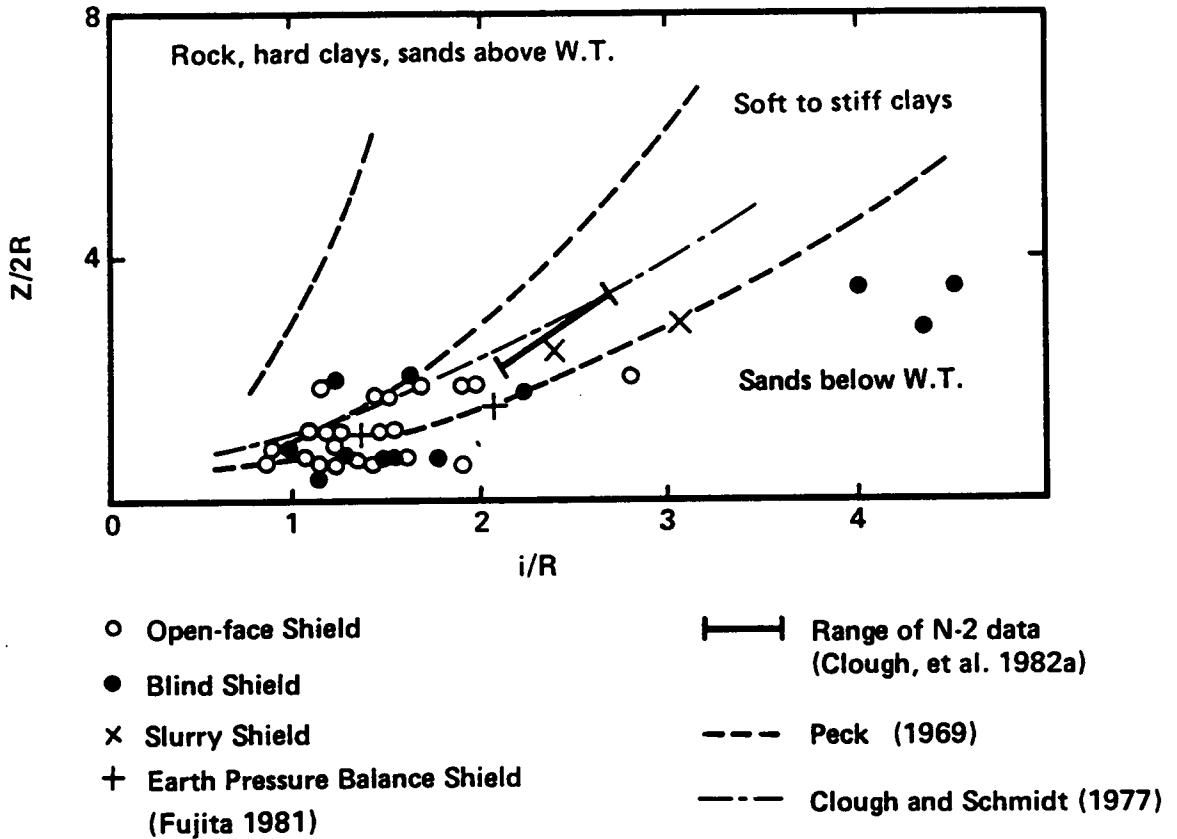


Figure 2.7 Relation between Width of Settlement Trough and Dimensionless Tunnel Depth for Various Shield Tunneling Methods

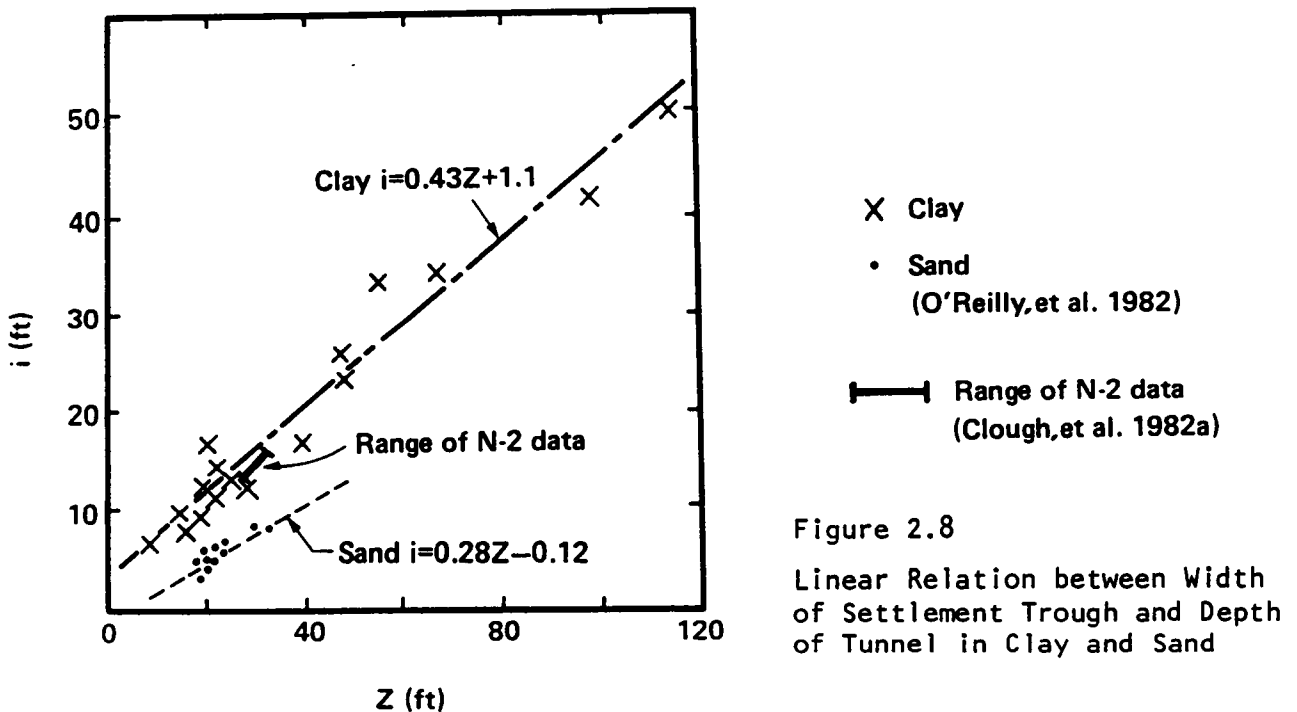


Figure 2.8 Linear Relation between Width of Settlement Trough and Depth of Tunnel in Clay and Sand

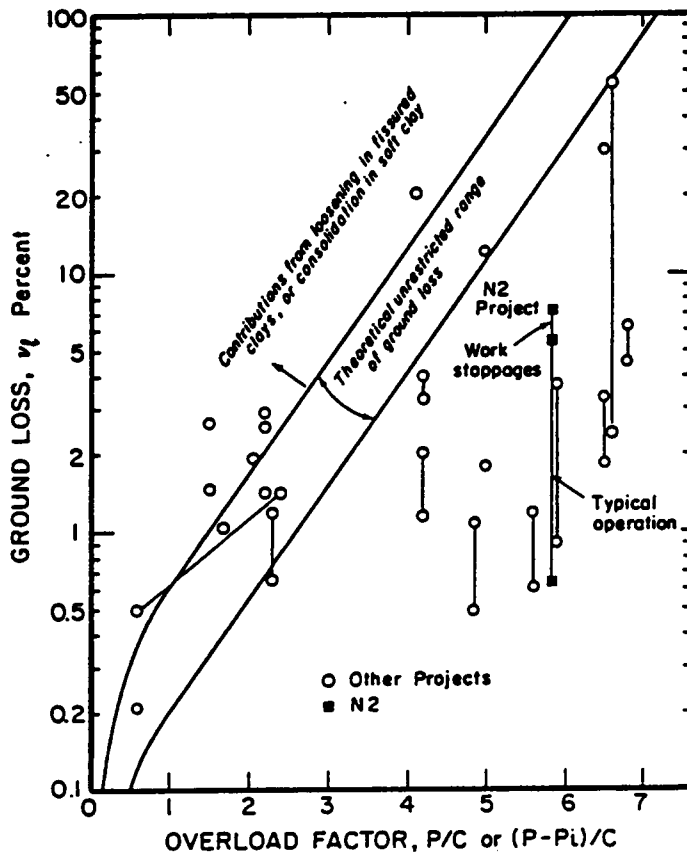


Figure 2.9 Relationship between Overload Factor and Ground Loss (Clough and Schmidt 1977)

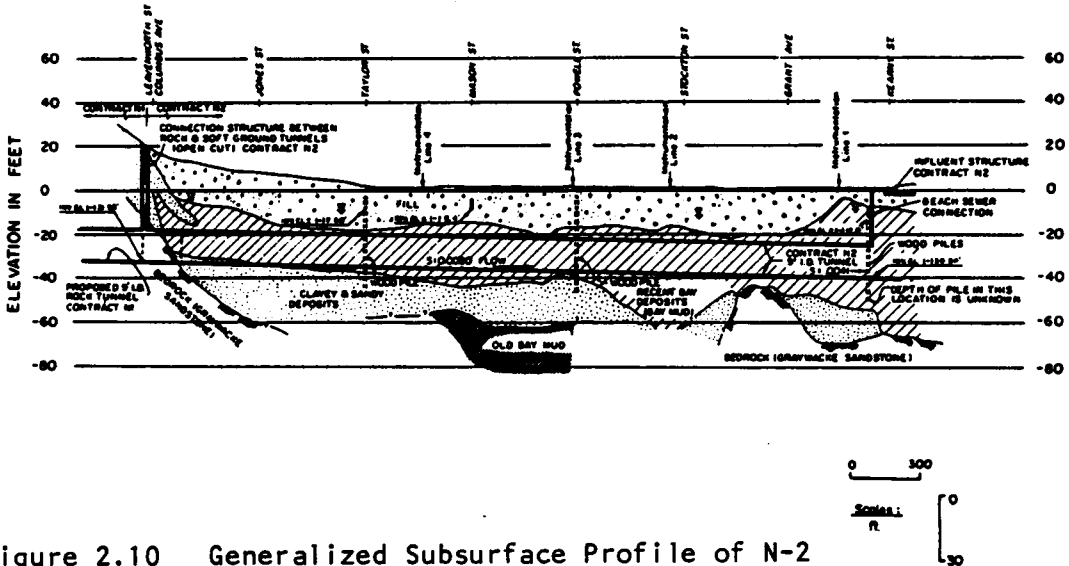


Figure 2.10 Generalized Subsurface Profile of N-2 Project Site (Clough, et al. 1982a)

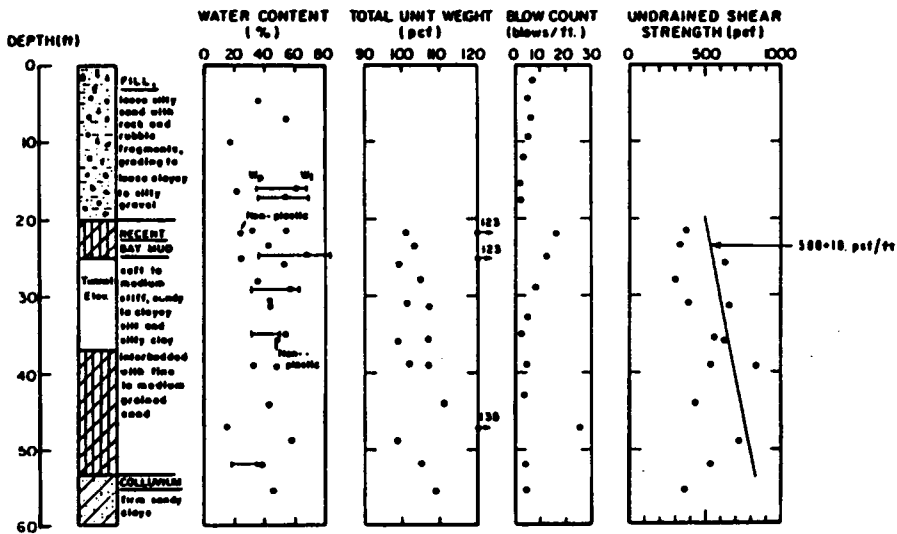


Figure 2.11 Summary of Soil Data at Lines 2, 3 and 4 of N-2 Project (Clough, et al. 1982a)

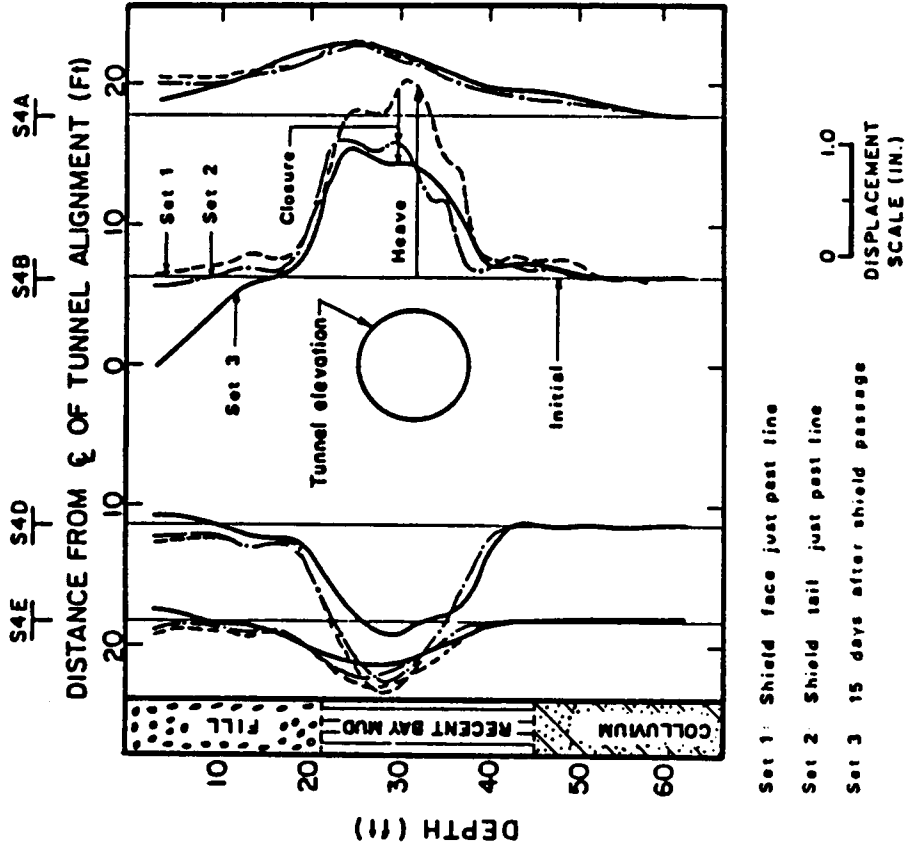


Figure 2.12 Displacements ahead of Shield Face at Line 4, N-2 Project (Clough, et al. 1982a)

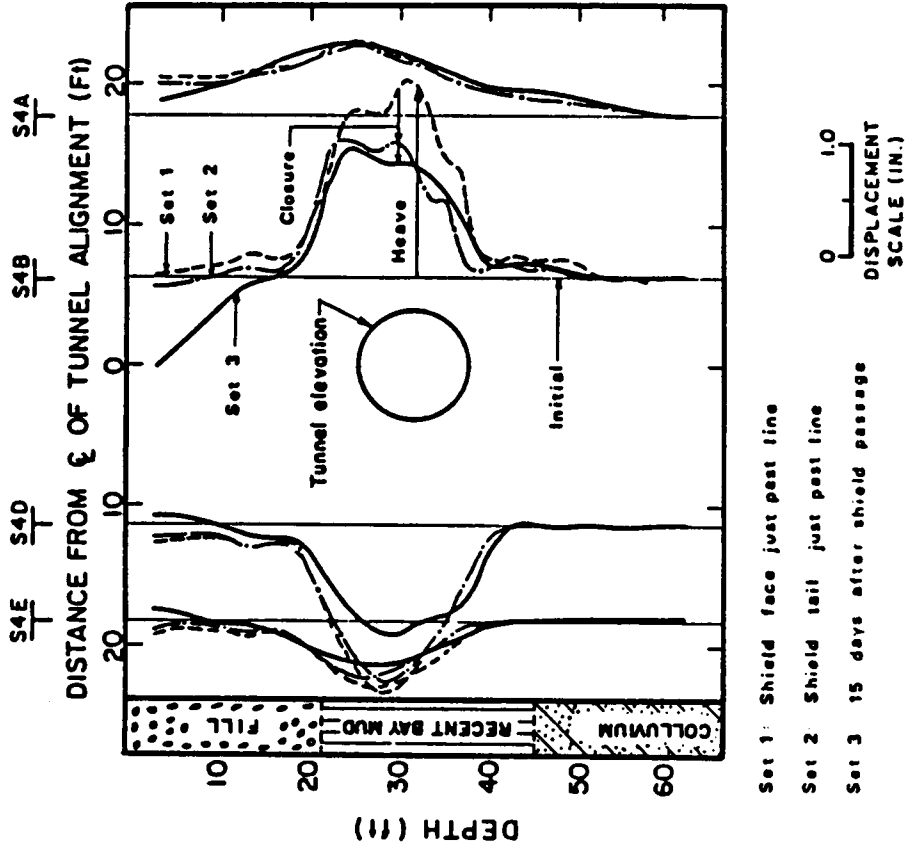


Figure 2.13 Lateral Displacements during and after Shield Construction at Line 4, N-2 Project (Clough, et al. 1982a)

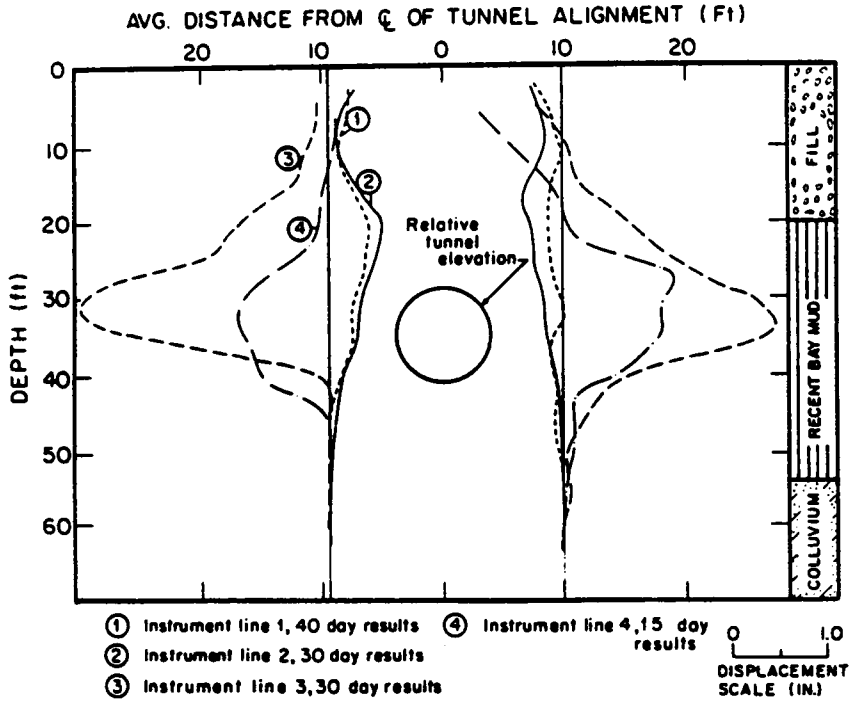


Figure 2.14 Long Term Lateral Displacements at Lines 1 through 4 (Clough, et al. 1982a)

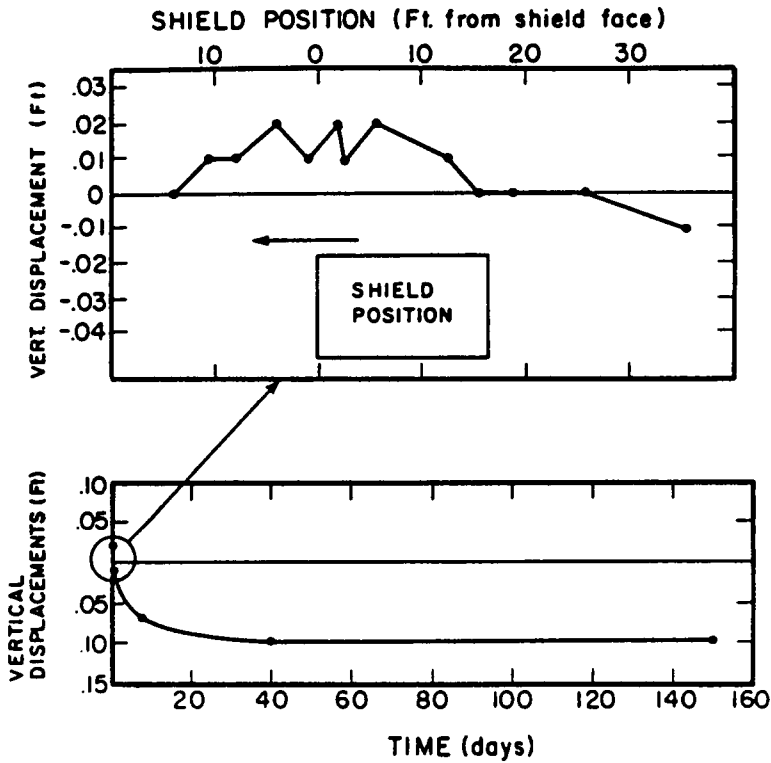


Figure 2.15 Surface Movement above Tunnel Centerline during and well after Shield Passage at Line 4 (Clough, et al. 1982a)

## Chapter 3

### THEORETICAL DEVELOPMENT OF PREVOST MODEL IN SOIL PLASTICITY

#### 3.1 Introduction

Mathematical modeling of soil is required in the numerical analysis of geotechnical problems. Modeling of soil should follow realistic response patterns which are typical of the problem under consideration. Many different types of soil models have been used in analyses of tunnel problems in the past: linear elastic, non-linear elastic, elasto-plastic, and many others. However, the advanced shield problem presents a particular complex behavior which can not be simulated using conventional approaches. As was noted in Chapter 2, when the complex loading process applied to the soil is involved, excessive pore pressure development occurs, and long-term dissipation of pore pressure results. Finno (1983) recently used the Cam Clay model for the advanced shield analysis. While this model was able to treat some of the aspects needed, it was noted to have shortcomings. Because of this, a different approach was attempted in this work with a new generation technique. The model implemented was developed by Prevost (1979). The basic theory was provided by Prevost (1978b), but it was found in the implementation work in this thesis that a number of details had to be solved to actually use the model, in particular for a soft clay. To help explain the implementation problems, the background and theory of the model are reviewed in detail.

### 3.1.1 Historical Development of Soil Model in Soil Plasticity

A brief historical development of soil plasticity is given in Table 2.1.

Every soil plasticity model is founded by means of a loading function, a yield criterion, a flow rule, a hardening rule, and a model parameter identification procedure. Soil plasticity is distinguished from the classical theory of the metal plasticity in such a way that volumetric yielding of soil and its failure at the critical state are accounted for in the formulation.

The yielding of a soil below the failure state is accommodated through the use of yield surfaces. In Cam Clay (Roscoe, et al. 1963) the yield surface is bullet-shaped and follows an isotropic hardening approach. The yield surface moves outward, or expands, with a loading vector, but its position is fixed if unloading occurs (Figure 3.1). Burland (1965) later proposed that the yield surface be elliptical for mathematical convenience. Further modifications were suggested by Roscoe and Burland (1968), but the simple elliptical yield concept is probably the most widely used.

The conventional Cam Clay model uses an associated flow rule. Poorooshasb, et al. (1966) introduced a nonassociative flow rule for sands. Since then the yielding of sands has been represented by means of the nonassociated flow rule to date. Pender (1978) and Benerjee and Stipho (1978) also discussed the nonassociative flow for clays.

Yielding of sands or overconsolidated clays are caused by shear follow-

ing the Mohr-Coulomb yield criterion, drawing a surface in stress space known as the Hvorslev surface (Atkinson and Bransby 1978). In addition to the shear yielding, volumetric yielding occurs on the state boundary, and this yield surface is often called "a cap." Although the Cam Clay model uses a simple yield surface to cover both the shear and volumetric yielding, more than one yield surface is used to handle shear and volumetric yielding in some other soil models, such as the Cap model (Dimaggio and Sandler 1971), the Lade model (Lade and Duncan 1974), the two conical surface models (Prevost and Höeg 1975), and so on.

As for the Cam Clay model, the plastic void ratio  $e^P$  or its counterpart, the plastic volumetric strain  $\epsilon_V^P$ , is taken as a state parameter which controls volumetric hardening. A general expression of this model was given by Mroz, et al. (1978). In contrast to the single state parameter approach, models with two state parameters were proposed. Mroz and Norris (1982) used deviatoric hardening in addition to the volumetric hardening.

The models described to this point can be successfully applied for any monotonic loading processes because they are based on an isotropic hardening rule (Hill 1950). However, for reversal loadings, or in particular, for cyclic loading when the hysteretic response of the soil is of importance, isotropic hardening must be replaced by anisotropic hardening (Prager 1955, Mroz 1967). Approaches using anisotropic hardening were introduced into soil modeling in the late 1970's.

### 3.1.2 Multisurface Models

Isotropic hardening models make the basis assumption that if a loading reversal occurs so that the local path is directed inside the yield surface, the soil behavior is assumed to be elastic. However, it is a fact that plastic strains develop inside the yield surface. This is indicative of what is termed anisotropic yielding, and it is theoretically expressed in terms of multi-yield surfaces. The multisurface model uses a combined concept of the kinematic hardening and the field of plastic moduli so that a smooth transition of the yielding may be accommodated.

Since soil exhibits plastic strains from the beginning of a loading reversal, the loading surface is not necessary identical to the yield surface (Phillips and Sierakowski 1965). The yield surface may enclose a small region within which soil behaves elastic-like, or the elastic region may shrink to a point as its extreme (Dafalias 1982). Therefore, the stress point reaches the yield surface in an early stage, and consecutive yielding is followed by ductile behavior of the soil. Consequently, accumulated hardening results, and is expressed in terms of different yield surfaces. The group of yield surfaces which characterize the multisurface model is termed "nested." A typical configuration of nested yield surfaces is shown in Figure 3.2. Each yield surface defines a respective yielding condition in particular plastic moduli (Mroz 1967). No surfaces intersect but they engage tangentially and move consecutively together as the stress point moves. The outmost surface on which the stress point lies is the active yield surface, and it defines the current plastic state until the next outer surface is reached. This suggests a linear segment of the stress-

strain curve for a loading with the stress point keeping steady on the active yield surface. Accordingly, when a loading is applied such that the stress point moves over the nested yield surfaces, the resulting stress-strain curve will be piecewise linear, as pointed out by Mroz (1969).

Among the nested yield surfaces, the outermost yield surface is often referred to as a bounding surface since the stress point never goes outside of it. Models which use the bounding surface concept were proposed independently by Dafalias and Popov (1975, 1977) and Krieg (1975). The plastic state for those models is defined by means of the relative configuration of the two surfaces, and they do not have a large memory requirement. However, they need a predefined analytical function to approximate the hardening properties, and presently these are not general enough to describe realistic soil behavior (Prevost 1982b).

In contrast to the two-surface model, a model which has an infinite number of yield surfaces, referred to as the INS model, was proposed by Pietruszczak and Mroz (1983, 1984). Every passive yield surface located inside of the active yield surface must be tangent to the active yield surface at the stress point. Therefore, once a new location of the active yield surface is found for a specified loading increment, then the configuration of all the passive yield surfaces can be established so that a loading reversal which may occur can be analyzed consistent with the characteristics of the multisurface model. This idea requires only a small amount of information to be kept in memory. The two-surface model and the INS model are limiting versions of the multisurface model family (Mroz 1982).

### 3.1.3 Prevost Model

The Prevost model is a member of the multisurface family. Prevost (1977) first applied it to describe undrained behavior of clay, following closely the work by Mroz (1967, 1969) in metal plasticity. Yield surfaces of the model are circular cylinders about the hydrostatic pressure axis, an assumption which is not applicable for other than undrained conditions.

Following this initial development, Prevost showed how to use his model for monotonic and cyclic loadings (Prevost 1977, Prevost and Hoeg 1977, Prevost 1978a). Subsequently the model was applied to boundary value problems, including stress localization into a shear band, a classical bearing capacity problem (Prevost and Hughes 1981), and a gravity offshore structure founded on clayey soil subjected to a cyclic loading (Prevost et al. 1980, 1981a). All of these applications were for undrained response clay and used the simple, nonpressure sensitive model.

Prevost (1978b) modified his model in consideration of pressure sensitivity, nonassociativity, a combined hardening rule, and the critical state concept. The yield surfaces of the new model were ellipsoidal in shape (Figure 3.2). This revised model is the one of principal interests of this thesis.

The new Prevost model was used to simulate the drained behavior of sand and yielded good agreement with the experimental results, especially for volumetric expansion under shear (Prevost 1979). Prevost (1980) also tested the model for a variety of undrained stress paths and was able to predict pore pressure changes. More recently, Mould (1983) reported some

difficulties with the model in applying it to multicubical test results on sand.

Applications of the pressure-sensitive Prevost model to situations with nonuniform stress conditions have been very limited. Use of this model to predict pore pressures in undrained or partially drained situations is also rare. The work in this thesis is apparently one of the first practical applications of the approach. As it turns out, it was particularly difficult to obtain the model parameters for the real soil considered herein since very little guidance has been provided for this task.

### 3.2 Elasto-plastic Formulation -- Prevost Pressure-Sensitive Model

The development of the pressure-sensitive Prevost model is presented in detail herein because it is felt that it is important to the development of an understanding for the parameters needed to define it. Also, the author has added his own modifications to the model and these can be documented in the exposition of the theory.

#### 3.2.1 Elastic Stress-Strain Relation

In the presence of plasticity, strain  $\epsilon_{ij}$  is decomposed into an elastic strain  $\epsilon_{ij}^e$  and a plastic strain  $\epsilon_{ij}^p$ . The former is recoverable, but the latter is not.

$$\epsilon_{ij} = \epsilon_{ij}^e + \epsilon_{ij}^p \quad (3.1a)$$

Or in incremental form,

$$\dot{\epsilon}_{ij} = \dot{\epsilon}_{ij}^e + \dot{\epsilon}_{ij}^p \quad (3.1b)$$

The incremental elastic strain  $\dot{\epsilon}_{ij}^e$  is simply related to the incremental stress  $\dot{\sigma}_{ij}$  with the generalized Hooke's law as shown in Figure 3.3. The Prevost model assumes an isotropic elastic response and thus only two independent parameters appear in the elastic modulus tensor as is well known.

$$\dot{\sigma}_{ij} = C_{ijkl}^e \dot{\epsilon}_{ij}^e \quad (3.2)$$

Eliminating  $\dot{\epsilon}_{ij}^e$ ,

$$\dot{\sigma}_{ij} = C_{ijkl}^e (\dot{\epsilon}_{ij} - \dot{\epsilon}_{ij}^p) \quad (3.3)$$

### 3.2.2 Yield Function

The yield function is a mathematical expression of the yield surface on which plastic flow occurs in a material. It is customarily defined as a function of the stress state and plastic state parameters. The Prevost model uses the size  $k$  and the position  $\xi_{ij}$  of the yield surface to describe the plastic state of the material.

$$f(\sigma_{ij}, k, \xi_{ij}) = 0 \quad (3.4)$$

Since the Prevost model is based on the volumetric hardening in conformity with the critical state concept, the  $k$ 's and  $\xi_{ij}$ 's are functions of plastic volumetric strain  $\epsilon_v^p$ .

Ellipsoidal yield surfaces of the Prevost model as shown in Figure 3.2 are expressed in terms of a set of second-order homogeneous functions.

$$f = (\sigma_{ij} - \xi_{ij})(\sigma_{ij} - \xi_{ij}) - k^2 = 0 \quad (3.5)$$

This can be modified in a hydrostatic and deviatoric decomposed form

$$f = \frac{3}{2} (s_{ij} - \alpha_{ij})(s_{ij} - \alpha_{ij}) + c^2 (p - \beta)^2 - k^2 = 0 \quad (3.6)$$

where  $s_{ij}$  and  $\alpha_{ij}$  are deviatoric components of, and also  $p$  and  $\beta$  are hydrostatic part of  $\sigma_{ij}$  and  $\xi_{ij}$ , respectively. Axes of  $p = \beta$  and  $s_{ij} = \alpha_{ij}$  are called the deviatoric and the hydrostatic semiaxes of the ellipsoidal yield surface, as illustrated in Figure 3.4(b). Variable  $c$  in the above equation defines a ratio of the hydrostatic and the deviatoric semiaxes of the ellipsoid, termed the axis ratio. When  $c$  is  $3/\sqrt{2}$ , equation 3.6 is identical to equation 3.5.

### 3.2.3 Flow Rule

The flow rule regulates the direction of the incremental plastic strain vector  $\dot{\epsilon}_{ij}^p$  in the strain space. In case of associative plasticity, the normality rule gives the  $\dot{\epsilon}_{ij}^p$  on an external normal to the yield surface at the stress point  $\sigma_{ij}$ . For a nonassociative flow rule, the normality rule is applied for the plastic potential surface  $g$  which is not identical to the yield surface  $f$ .

$$\dot{\epsilon}_{ij}^p = \lambda \frac{\partial g}{\partial \sigma_{ij}} \quad (3.7)$$

where  $\frac{\partial g}{\partial \sigma_{ij}}$  is the outward normal of the plastic potential.

Definition of the plastic potential is essential to evaluate the direction of the plastic flow. A nonassociative flow rule is often used in soil plasticity since volumetric response of plastic flow does not follow

the associative normality. The Prevost model uses a nonassociative flow rule for the spherical stresses and strains and an associative flow rule for the deviatoric stresses and strains as shown in Figure 3.4(b).

### 3.2.4 Consistency Condition

A stress increment applied to a material element creates a new plastic state which may be represented with updated yielding parameters. Such a transition must be smoothly achieved so that the stress point stays on the same yield surface even after loading (Figure 3.4(a)). As a stress increment  $\dot{\sigma}_{ij}$  is added to the current stress  $\sigma_{ij}$  at M, the stress point moves to N and the yield surface  $f$  also moves to  $f'$ . The translation of the yield surface  $\dot{\xi}_{ij}$  and the change in its size  $\dot{k}$  must satisfy the consistency condition (Prager 1949).

Since the stress point N satisfies a vector equation  $OM + MN = OO' + O'N$ , the proportionality gives

$$\dot{\sigma}_{ij} - \dot{\xi}_{ij} = \frac{\dot{k}}{k} (\sigma_{ij} - \xi_{ij}) \quad (3.8)$$

A smooth transition of the yield surface  $f$  allows for the differentiation of the yield function of equation 1.6, and leads to

$$\frac{\partial f}{\partial \sigma_{ij}} \dot{\sigma}_{ij} + \frac{\partial f}{\partial \xi_{ij}} \dot{\xi}_{ij} - 2k\dot{k} = 0 \quad (3.9)$$

Combining the above equations 3.8 and 3.9, the consistency condition is expressed as

$$\frac{\partial f}{\partial \sigma_{ij}} (\dot{\sigma}_{ij} - \dot{\xi}_{ij}) = 2k\dot{k} = \frac{\partial f}{\partial \sigma_{ij}} \frac{\dot{k}}{k} (\sigma_{ij} - \xi_{ij}) \quad (3.10)$$

A vector equation for the radius of the yield surface  $f$ ,  $OM$ , is

$$\sigma_{ij} - \xi_{ij} = k \frac{\frac{\partial f}{\partial \sigma_{ij}}}{\left( \frac{\partial f}{\partial \sigma_{kl}} \frac{\partial f}{\partial \sigma_{kl}} \right)^{1/2}} \quad (3.11)$$

So, another expression of the consistency condition is obtained,

$$\dot{\xi}_{ij} = \dot{\sigma}_{ij} - 2k\dot{k} \frac{\frac{\partial f}{\partial \sigma_{ij}}}{\frac{\partial f}{\partial \sigma_{kl}} \frac{\partial f}{\partial \sigma_{kl}}} \quad (3.12)$$

Equation 3.12 is useful to calculate the translation of the yield surface in case of kinematic hardening.

### 3.2.5 Combined Hardening Rule

Two basic concepts of hardening are isotropic hardening (Hill 1950) and kinematic hardening (Prager 1955). A yield surface may change its position to translate in the stress space for kinematic hardening while changing its size by expanding for isotropic hardening. The Prevost model uses a combination of the two principles.

The isotropic hardening rule applied to the Prevost model is equivalent to that for the Cam Clay model. Plastic volumetric strain  $\epsilon_v^p$  is selected as a hardening parameter which controls the expansion of the yield surface in accordance with  $e^p$ - $p$  curve of the isotropic consolidation test. As expansion of the yield surface takes place with respect to the origin of the stress space, its position as well as its size is changed. In fact the pure isotropic hardening rule is applied for the outermost yield surface of the Prevost model. This results in a model which is sim-

ilar to the Cam Clay model for a virgin stress state.

The size of yield surface  $k$  and the hardening modulus  $H'$  are functions of the plastic strain history. They are taken as functions of invariant measures of the amount of either or both plastic volumetric strain and plastic shear distortions (Prevost 1978b, 1979, 1981). However, only the plastic volumetric strain  $\epsilon_V^P$  is taken as a hardening parameter in this thesis since the model is intended to apply only to clay.

The kinematic hardening rule controls the hardening associated with the nested yield surfaces. This makes it possible to accurately predict the plastic deformation of soil at an early stage of loading reversals, similar to the Bauschinger effect. When the kinematic hardening rule is to be applied, both the direction of the yield surface translation and the updated size are determined. To do this, an additional condition must be introduced. Prager (1949) applied a rule such that the yield surface translates in the direction of a local normal  $n_M$  (Figure 3.5(a)). Ziegler (1959) specified translation along the radius of the yield surface  $OM$  in the figure. Phillips and Sierakowski (1965) simply stated that the translation occurs in the same direction of applied stress increment  $\dot{\sigma}$ . Translation that includes a rigid rotation of yield surface in general was considered by Pietruszczak and Mroz (1983). All of these kinematic rules define the direction of the translation without considering the coupling manner of nested surfaces, and so intersection of adjacent surfaces may occur such that a unique solution will be no more obtained. Fortunately, Mroz (1967) described a translation rule which dealt with this problem. In his own work, Prevost (1978b) proposed using a translation rule for his

model which applied the Mroz rule to the deviatoric part and the Prager rule to the spherical part. However, the author does not prefer to use such a combined rule because it does not seem to be general enough to deal with soft clays. Instead, the Mroz translation rule is used in the further development of the Prevost model, as will be discussed in Section 3.4.3.

### 3.2.6 Plastic Strain Increment

The plastic strain increment is assumed to be proportional to the projection of stress increment onto the normal of yield surface.

$$\dot{\epsilon}_{ij}^p \propto \frac{\partial f}{\partial \sigma_{ij}} \dot{\sigma}_{ij} \quad (3.13)$$

Equation 3.13 is combined with the flow rule of equation 3.7 and yields

$$\dot{\epsilon}_{ij}^p \propto \frac{\partial f}{\partial \sigma_{kl}} \dot{\sigma}_{kl} \frac{\partial g}{\partial \sigma_{ij}} \quad (3.14)$$

Introducing a proportionality term  $H'$  and normalizing with respect to the length of the normal of yield surface, we obtain

$$\dot{\epsilon}_{ij}^p = \frac{1}{H'} \frac{\frac{\partial f}{\partial \sigma_{kl}} \dot{\sigma}_{kl}}{\frac{\partial f}{\partial \sigma_{mn}} \frac{\partial f}{\partial \sigma_{mn}}} \frac{\partial g}{\partial \sigma_{ij}} \quad (3.15)$$

For a simple notation, gradients of  $f$  and  $g$  are expressed by  $Q_{ij}$  and  $P_{ij}$ , respectively.

$$Q_{ij} = \frac{\partial f}{\partial \sigma_{ij}} \quad (3.16a)$$

$$P_{ij} = \frac{\partial g}{\partial \sigma_{ij}} \quad (3.16b)$$

Then equation 3.15 is written as

$$\dot{\epsilon}_{ij}^p = \frac{1}{H'} \frac{Q_{kl} \dot{\sigma}_{kl}}{|Q_{mn}|^2} P_{ij} = \frac{L}{|Q_{mn}|^2} P_{ij} \quad (3.17)$$

where

$$L = \frac{1}{H'} Q_{ij} \dot{\sigma}_{ij} \quad (3.18)$$

is called a plastic loading function which has a value only when

$Q_{ij} \dot{\sigma}_{ij} \geq 0$  ; otherwise  $L$  is set equal to zero.

### 3.2.7 Elasto-plastic Modulus

The expression  $\dot{\epsilon}_{ij}^p$  in equation 3.17 may be substituted into equation 3.3. The result will be obtained in the form

$$\dot{\sigma}_{ij} = C_{ijkl}^{e-p} \dot{\epsilon}_{kl} \quad (3.19)$$

after the equation is inverted for stress increment, where  $C_{ijkl}^{e-p}$  is the elasto-plastic modulus tensor.

$$C_{ijkl}^{e-p} = C_{ijkl}^e - \frac{C_{ijmn}^e P_{mn} Q_{pr} C_{prkl}^e}{H' + Q_{mn} C_{mnp}^e P_{pr}} \quad (3.20)$$

Suppose  $C_{ijkl}^{e-p}$  satisfies a scalar equation,

$$D_{ij} C_{ijkl}^{e-p} D_{kl} = 0 \quad (3.21)$$

where  $D_{ij}$  is a nonzero, symmetric second-order tensor then,  $C_{ijkl}^{e-p}$  is said to be singular. Now taking  $D_{ij} = Q_{ij}$  and substituting equation 3.20 into equation 3.21,

$$\begin{aligned}
 Q_{ij} C_{ijkl}^{e-p} Q_{kl} &= Q_{ij} C_{ijkl}^e Q_{kl} - Q_{ij} \frac{C_{ijmn}^e P_{mn} Q_{pr} C_{prkl}^e}{H' + Q_{mn} C_{mnpr}^e P_{pr}} Q_{kl} \\
 &= H' \frac{Q_{ij} C_{ijkl}^e Q_{kl}}{H' + Q_{mn} C_{mnpr}^e P_{pr}} = 0
 \end{aligned} \tag{3.22}$$

Therefore  $C_{ijkl}^{e-p}$  is singular if  $H' = 0$ . When the material stiffness is singular, equation 3.21 yields

$$C_{ijkl}^{e-p} \dot{\epsilon}_{kl} = C_{ijkl}^{e-p} Q_{ij} = \underline{0} \tag{3.23}$$

where  $\underline{0}$  is zero second-order tensor, and the incremental strain is found to be parallel to the outward normal of the yield surface.

For rigid perfectly plastic associative material, the yield point is identical to the failure point and then the material stiffness becomes singular. On the other hand, for an elastic-perfectly plastic associative material,  $\dot{\epsilon}_{kl}$  comes extremely close to being parallel to  $Q_{ij}$  but never does because an elastic component  $\dot{\epsilon}_{kl}^p$  exists. For the multisurface model based on the volumetric yielding formulation like the Prevost model, the material stiffness will be singular when stresses reach the critical state. This characteristic of the elasto-plastic modulus will be used in Section 6.5.1 in order to verify how the constitutive law works in the FEM program.

### 3.3 Hydrostatic Axis and Deviatoric Subspace

The general form of the elasto-plastic modulus tensor derived in the last section is ready to use in calculation once the hardening properties are specified. However, it is convenient to express the Prevost model

formulation in a decomposed form in terms of spherical and deviatoric components since the yield function, the plastic potential, and the hardening modulus of the Prevost model are given in decomposed forms.

### 3.3.1 Decomposed Formulation

Stress space is broken down into a hydrostatic stress axis and a deviatoric stress subspace:

$$\sigma_{ij} = s_{ij} + p\delta_{ij} \quad (3.24)$$

in which  $s_{ij}$  denotes the deviatoric stress,  $p = \sigma_{kk}/3$  the effective mean stress, and  $\delta_{ij}$  the Kronecker delta. Since  $s_{ij} p \delta_{ij} = 0$ , the hydrostatic axis is normal to the deviatoric stress subspace.

In the similar manner, the position of the yield surface may be written as

$$\xi_{ij} = \sigma_{ij} + \beta\delta_{ij} \quad (3.25)$$

The normal of yield surface  $Q_{ij}$ , equation 3.16a, and the normal of plastic potential  $P_{ij}$ , equation 3.16b, are also expressed as

$$Q_{ij} = \frac{\partial f}{\partial \sigma_{ij}} = Q'_{ij} + Q''\delta_{ij} \quad (3.26a)$$

$$P_{ij} = \frac{\partial g}{\partial \sigma_{ij}} = P'_{ij} + P''\delta_{ij} \quad (3.26b)$$

$Q'_{ij}$  and  $Q''$  denotes projections of  $Q_{ij}$  onto the deviatoric stress subspace and along the hydrostatic axis, respectively; similarly,  $P'_{ij}$  and  $P''$  are those of  $P_{ij}$ .

$$3Q'' = \delta_{ij} Q_{ij} = \frac{\partial f}{\partial \sigma_{ij}} = \frac{\partial f}{\partial p} \quad (3.27)$$

$Q'_{ij} = 0$  at points C and D on the deviatoric semiaxis of  $f$  and  $Q'' = 0$  at points A and B on the hydrostatic semiaxis as their locations are shown in Figure 3.4(b). By using these notations the expression of the plastic strain increment, equation 3.17, is also decomposed into the two parts.

$$\dot{\epsilon}_V^p = \dot{\epsilon}_{ij}^p \delta_{ij} = \frac{1}{H'} \frac{Q'_{mn} \dot{s}_{mn} + 3Q'' \dot{p}}{|Q'_{kl}|^2 + 3|Q''|^2} 3P'' \quad (3.28a)$$

$$\dot{\epsilon}_{ij}^p = \dot{\epsilon}_{ij}^p - \frac{1}{3} \dot{\epsilon}_V^p \delta_{ij} = \frac{1}{H'} \frac{Q'_{mn} \dot{s}'_{mn} + 3Q'' \dot{p}}{|Q'_{kl}|^2 + 3|Q''|^2} P'_{ij} \quad (3.28b)$$

The elastic strain is also decomposed in a similar way,

$$\dot{\epsilon}_V^e = \frac{1}{B} \dot{p} \quad (3.29a)$$

$$\dot{\epsilon}_{ij}^e = \frac{1}{2G} \dot{s}_{ij} \quad (3.29b)$$

where  $B$  and  $G$  are an elastic bulk modulus and an elastic shear modulus, respectively.

The yield function  $f$  has been given in equation 3.6. Thus the normals of  $f$  are obtained.

$$Q'_{ij} = 3(s_{ij} - \alpha_{ij}) \quad (3.30a)$$

$$Q''_{ij} = \frac{2}{3} c^2 (p - \beta) \quad (3.30b)$$

$$|Q_{ij}|^2 = |Q'_{ij}|^2 + 3|Q''|^2 = 6k^2 + 6c^2 \left(\frac{2}{9}c^2 - 1\right) (p - \beta)^2 \quad (3.31)$$

Moduli  $H'$ ,  $B$  and  $G$  in equations 3.28 and 3.29 are assumed to follow the power law (Janbu 1963). Their values increase with the mean

stress when the bulk exponent  $n$  has a value.

$$B = B_0 \left( \frac{p}{p_0} \right)^n \quad (3.32a)$$

$$G = G_0 \left( \frac{p}{p_0} \right)^n \quad (3.32b)$$

$$H' = H'_0 \left( \frac{p}{p_0} \right)^n \quad (3.32c)$$

where  $B_0$ ,  $G_0$  and  $H'_0$  are specific values of moduli at a reference pressure  $p_0$ .

### 3.3.2 Decomposed Constitutive Equations

Strain increments are the sum of elastic and plastic strain increments in equations 3.28 and 3.29, respectively, and are represented in a decomposed form by,

$$\dot{\epsilon}_v = \frac{\dot{p}}{B} + \frac{1}{H'} 3P'' \frac{Q'_{mn} \dot{s}_{mn} + 3Q'' \dot{p}}{|Q_{kl}|^2 + 3|Q''|^2} \quad (3.33a)$$

$$\dot{s}_{ij} = \frac{\dot{s}_{ij}}{2G} + \frac{1}{H'} Q'_{ij} \frac{Q'_{mn} \dot{s}_{mn} + 3Q'' \dot{p}}{|Q_{kl}|^2 + 3|Q''|^2} \quad (3.33b)$$

The above equations may be inverted for stresses  $\dot{s}_{ij}$  and  $\dot{p}$

$$\dot{p} = B \dot{\epsilon}_v - 2G \frac{B}{H'} 3P'' X \quad (3.34a)$$

$$\dot{s}_{ij} = 2G \dot{\epsilon}_{ij} - \frac{4G^2}{H'} Q'_{ij} X \quad (3.34b)$$

in which

$$\begin{aligned} X &= \frac{1}{2G} \frac{Q_{mn} \dot{\sigma}_{mn}}{|Q_{kl}|^2} \\ &= \frac{Q'_{mn} \dot{\epsilon}_{mn} + \left( \frac{B}{2G} \right) 3Q'' \dot{\epsilon}_v}{\left( 1 + \frac{2G}{H'} \right) |Q'_{kl}|^2 + 3Q''^2 + 9 \left( \frac{B}{H'} \right) P'' Q''} \end{aligned} \quad (3.35)$$

The inversion procedure is described in Appendix A.1. Combining equations 3.34a and 3.34b, the final form of the constitutive equation is obtained as an alternative of equation 3.19:

$$\dot{\sigma}_{ij} = \left( B - \frac{2}{3} G \right) \dot{\epsilon}_v \delta_{ij} + 2G \dot{\epsilon}_{ij} - \frac{4G^2}{H'} \left[ Q'_{ij} + \left( \frac{B}{2G} \right) 3P'' \delta_{ij} \right] X \quad (3.36)$$

### 3.4 Nested Yield Surfaces

The collection of nested yield surfaces is used in the Prevost model. This approach allows the model to adjust the hardening rule to any kind of experimental behavior obtained from a laboratory testing program. The elasto-plastic formulation developed in the preceding sections is effective for the nested yield surfaces by replacing the yield function  $f$  by  $f_m$ , the plastic potential  $g$  by  $g_m$ , and the hardening modulus  $H'$  by  $H'_m$ .

In the following sections the geometric constraints of translations of yield surfaces, a field of plastic moduli, and nonassociativity of the Prevost model will be discussed.

#### 3.4.1 Yield Function of Nested Yield Surfaces

A yield function has been shown in equation 3.6, which represents each of the nested surfaces. For the  $m$ -th yield surface,

$$f_m = \frac{3}{2} (s_{ij} - \sigma_{ij}^{(m)}) (s_{ij} - \sigma_{ij}^{(m)}) + c^2 (p - \beta^{(m)})^2 - k_m^2 = 0 \quad (3.37)$$

It is assumed for simplicity that all the yield surfaces are similar and thus the yield surface axis ratio  $c$  has a unique value regardless of

yield surface number  $m$ . Variables  $s_{ij}$  and  $p$  represent the stress state,  $\alpha_{ij}^{(m)}$  and  $\beta^{(m)}$  the position of  $f_m$ , and  $k_m$  the size of  $f_m$ . Increments of these values denote changes in the stress state, modification of position, and size of  $f_m$ , respectively.

The current position and sizes of the yield surfaces reflect the past stress-strain history of the material. Such loading information with regard to material experience are considered as the material memory.  $\alpha_{ij}^{(m)}$  are not necessarily equal to zero because the material may become anisotropic as a result of deviatoric plastic flow. Therefore, initial positions and sizes of yield surfaces refer to the inherent anisotropy of the material and subsequent modification of the nested surface configuration corresponds to a stress-induced anisotropy.

### 3.4.2 Contacting Surfaces

As the stress point moves in stress space, the current active yield surface translates with changes in size so as to keep the stress point on itself. When the stress point reaches the yield surface  $f_m$ , all the surfaces  $f_1, f_2, \dots, f_m$  are tangential to each other at the contact point  $P$ , as shown in Figure 3.5(b) in order to avoid the intersection of the yield surfaces. Moreover,

$$\frac{\sigma_{ij} - \xi_{ij}^{(1)}}{k_1} = \frac{\sigma_{ij} - \xi_{ij}^{(2)}}{k_2} = \dots = \frac{\sigma_{ij} - \xi_{ij}^{(m)}}{k_m} \quad (3.38)$$

The radius of the yield surface  $f_m$ ,  $O_m P$ , is coaxial with other contacting surfaces  $f_1, f_2, \dots, f_{m-1}$ . The centers of these yield sur-

faces stay on the line  $O_m P$  in the stress space. The projection of the center points onto any stress plane, e.g., on the triaxial plane, conserves their linearity.

### 3.4.3 Translation Rule

The nested yield surfaces are controlled in translation by the Mroz translation rule.

When a stress increment  $\dot{\sigma}_{ij}$  is applied such that  $\dot{\sigma}_{ij}$  points in an outward direction of the yield surface  $f_m$ , that is,  $Q_{ij}\dot{\sigma}_{ij} > 0$  in loading condition, the yield surface  $f_m$  approaches  $f_{m+1}$ .

In order to avoid overlapping of the nested surfaces, the surfaces,  $f_m$  and  $f_{m+1}$ , are in contact at the conjugate points where the outward normals of the yield surfaces have the same direction. In Figure 3.5(a) M is the stress point,  $\sigma_{ij}^M = \sigma_{ij}$ , and R is the conjugate point to M. The position of conjugate point is defined from the proportionality equation

$$\sigma_{ij}^R - \xi_{ij}^{(m+1)} = \frac{k_{m+1}}{k_m} (\sigma_{ij} - \xi_{ij}^{(m)}) \quad (3.39)$$

Then the translation of  $f_m$  and  $f_{m+1}$  occurs along MR :

$$\mu_{ij} = MR = \frac{k_{m+1}}{k_m} (\sigma_{ij} - \xi_{ij}^{(m)}) - (\sigma_{ij} - \xi_{ij}^{(m+1)}) \quad (3.40)$$

Assuming that both surfaces  $f_m$  and  $f_{m+1}$  are allowed to translate and expand or contract, the consistency condition requires

$$\sigma_{ij} - \xi_{ij}^{(m)} = \frac{\dot{k}_m}{k_m} (\sigma_{ij} - \xi_{ij}^{(m)}) \quad (3.41a)$$

$$\dot{\sigma}_{ij}^R - \dot{\xi}_{ij}^{(m+1)} = \frac{\dot{k}_{m+1}}{k_{m+1}} (\sigma_{ij}^R - \xi_{ij}^{(m+1)}) \quad (3.41b)$$

If the relative motion of the current stress point  $M$  with respect to  $R$  occurs along  $MR$ , then simply

$$\dot{\sigma}_{ij} - \dot{\sigma}_{ij}^R = \delta\mu \mu_{ij} \quad (3.42)$$

where  $\delta\mu$  is a scalar factor. Combining equations 3.41a, 3.41b and 3.42, the coupling translation rule is expressed as

$$\dot{\xi}_{ij}^{(m)} = \dot{\xi}_{ij}^{(m+1)} + \delta\mu \mu_{ij} + \frac{\dot{k}_{m+1} - \dot{k}_m}{k_m} (\sigma_{ij}^{(m)} - \xi_{ij}^{(m)}) \quad (3.43)$$

However, when the surface  $f_{m+1}$  does not translate, that is,  $\dot{\xi}_{ij}^{(m+1)} = 0$  before  $f_m$  makes contact with  $f_{m+1}$ , equation 3.43 simplifies to

$$\dot{\xi}_{ij}^{(m)} = \delta\mu \mu_{ij} + \frac{\dot{k}_{m+1} + \dot{k}_m}{k_m} (\sigma_{ij} - \xi_{ij}^{(m)}) \quad (3.44)$$

The first term in this equation corresponds to the translation of the yield surface. The second term is due to the changes in size of the yield surfaces. The second term is small relative to the first and can be neglected in many cases (Mroz, et al. 1978). Then, equation 3.44 yields

$$\dot{\xi}_{ij} = \delta\mu \mu_{ij} \quad (3.45)$$

The scalar factor  $\delta\mu$  can be determined from the consistency condition of equation 3.12 and obtained as

$$\delta\mu = \frac{Q_{mn} \dot{\sigma}_{mn} - 2k_m \dot{k}_m}{Q_{kl} \mu_{kl}} \quad (3.46)$$

Now the translation rule has been established. Note that the above formulation is derived from consideration of infinitesimal stress increments

and infinitesimal translation of the yield surface in which the second order of quantities are neglected in the consistency condition. The finite incremental approach with equation 3.45 is described in Appendix A.2, which has been incorporated into the computer code.

### 3.4.4 Plastic Modulus

A plastic modulus  $H'_m$  is associated with each nested surface, and its value may vary along the yield surface  $f_m$  with the position of the stress point.

When the stress point stays on the hydrostatic semiaxis of  $f_m$  at a point C or D in Figure 3.4(b),  $Q_{ij} = 0$ , equation 3.28a of plastic strain is modified as

$$H'_m = \frac{3p''^{(m)}}{Q''^{(m)}} \frac{\dot{p}}{\dot{\epsilon}_V^p} \quad (3.47)$$

The plastic modulus  $H'_m$  plays the role of a plastic bulk modulus in this case, and such stress points can be thought of as a consolidation point because only volumetric response is involved.

On the other hand, when the stress point is located at the apex of deviatoric semiaxis at a point A or B in Figure 3.4(b), that is,  $Q_{ij}^{(m)} = 0$ , the deviatoric strain is related to the deviatoric stress from equation 3.28b and,

$$H'_m = \frac{|p'_{ij}|}{|Q'_{kl}|^2} \frac{Q'_{st} \dot{s}_{st}}{(\dot{\epsilon}_{mn}^p \dot{\epsilon}_{mn}^p)^{1/2}} \quad (3.48)$$

The plastic modulus  $H'_m$  acts as a plastic shear modulus in this case.

These limiting cases of the role of plastic modulus  $H'_m$  as a plastic bulk modulus and a plastic shear modulus suggest that the plastic modulus  $H'_m$  may be a function of the plastic volumetric strain  $\epsilon_V^P$  and the equivalent plastic deviatoric strain  $\epsilon_e^P = \left[ \frac{2}{3} \epsilon_{ij}^P \epsilon_{ij}^P \right]^{\frac{1}{2}}$ . It is assumed that the isotropic part of hardening is dependent on the plastic volumetric strain  $\epsilon_V^P$  and the kinematic part of hardening on the equivalent plastic deviatoric strain  $\epsilon_e^P$ .

The size of yield surface  $k_m$  is taken as a function of  $\epsilon_V^P$  alone and

$$k_m = k_{0m} \exp(\lambda \epsilon_V^P) \quad (3.49)$$

where  $k_0$  is a reference value and  $\lambda$  is a material constant. This is similar to the logarithmic relationship between the void ratio and effective confining pressure in the isotropic consolidation test.

The incremental form of equation 3.49 is simply

$$\dot{k}_m = \lambda k_m \dot{\epsilon}_V^P \quad (3.50)$$

From the consistency condition, equation 3.9, we have

$$Q_{ij}^{(m)} \dot{\sigma}_{ij} - Q_{ij}^{(m)} \dot{\xi}_{ij}^{(m)} - 2\lambda k_m \dot{\epsilon}_V^P = 0 \quad (3.51)$$

Substituting equation 3.50 and using the equation of incremental plastic volumetric strain, equation 3.28a, we obtain

$$H_m = - \frac{2\lambda k_m^2 p''^{(m)} Q_{ij}^{(m)} \dot{\sigma}_{ij}}{Q_{mn}^{(m)} \dot{\sigma}_{mn} - Q_{mn}^{(m)} \dot{\xi}_{mn}} \frac{1}{|Q_{kl}^{(m)}|^2} \quad (3.52)$$

The plastic modulus  $H_m$  varies not only with  $\epsilon_v^p$  and  $\epsilon_e^p$  but also with the direction of the stress increment and the translation and expansion of the yield surface.

The translation of a yield surface occurs in a direction so that the conjugate points of yield surfaces will be engaged. From equation 3.45, we have

$$\dot{\xi}_{ij}^{(m)} = \delta\mu \mu_{ij}^{(m)} \quad (3.53)$$

Due to the assumption that kinematic hardening stems from plastic deviatoric strain, the scalar factor  $\delta\mu$  in equation 3.53 may be a function of deviatoric strain increment  $\epsilon_e^p$ . For instance,  $\delta\mu$  is written in the form

$$\delta\mu = \bar{\mu}(\sigma_{ij}, \xi_{ij}^{(m)}, \epsilon_{ij}^p) \dot{\epsilon}_e^p \quad (3.54)$$

Substituting equations 3.52 and 3.53 into equation 3.54, we get

$$H_m = \bar{\mu} \frac{Q_{ij}^{(m)} \mu_{ij}^{(m)}}{|Q_{kl}^{(m)}|^2} \left( \frac{3}{2} p'_{mn}^{(m)} p'_{mn}^{(m)} \right)^{1/2} + 2\lambda k_m^2 \frac{3p''^{(m)}}{|Q_{kl}^{(m)}|^2} \quad (3.55)$$

The plastic modulus  $H_m$  is nicely separated into two parts, contributions of yield surface translation and of its expansion.

Equation 3.55 is simplified to apply in the Prevost model. The plastic modulus  $H_m$  with reduced complexity but remaining similar is assumed to be

$$H'_m = h'_m + \frac{\sqrt{3}Q''}{|O_{kl}|} B'_m \quad (3.56)$$

where  $h'_m$  and  $B'_m$  are assumed as material constants associated with the yield surface  $f_m$ .  $\sqrt{3}$  in the second term is a normalizing constant. Although the distribution of  $H'_m$  along the surface  $f_m$  is now simple, the characteristic of the plastic modulus acting as a plastic bulk modulus or plastic shear modulus on the semiaxes is still maintained since the distribution of  $H'_m$  is coaxial with the semiaxes of the yield surface  $f_m$ . And  $h'_m$  and  $h'_m \pm B'_m$  correspond to the plastic shear and bulk moduli, respectively. In view of equation 3.55, the two terms are related to the projection of the plastic strain increment onto the deviatoric subspace and the hydrostatic axis, respectively. They are assumed to change their values according to the power law analogous to equation 3.32.

$$h'_m = h'_{m0} \left(\frac{p}{p_0}\right)^n \quad (3.57a)$$

$$B'_m = B'_{m0} \left(\frac{p}{p_0}\right)^n \quad (3.57b)$$

Since  $h'_m$  varies from infinity for an elastic state to zero at failure, it is convenient to scale  $h'_m$  into a smaller range:

$$h_m = \frac{2Gh'_m}{2G + h'_m} \quad (3.58)$$

The scaled plastic shear modulus  $h_m$  varies from  $2G$  for an elastic state to zero at failure.

The simple form of  $H'_m$  given in equation 3.56 violates the consistency condition because  $H'_m$  is not affected by the relative configuration

of yield surfaces, but rather is related to the current active yield surface  $f_m$ . Such a simplified description of the plastic modulus  $H'_m$  makes it possible to calculate the two independent parameters  $h'_m$  and  $B'_m$  from experimental stress-strain relations of two selected loading paths which are usually selected as triaxial compression and extension tests.

### 3.4.5 Nonassociativity and Plastic Potential

For nested yield surfaces, a nonassociative flow rule is used. The plastic potential is selected such that the plastic deviatoric strain increment remains normal to the projection of the yield surface onto the deviatoric stress subspace. However, its projection onto the hydrostatic axis departs from the normal of the yield surface. In the Prevost model, this deviation is assumed to be proportional to the magnitude of the normal of the yield surface projected onto the deviatoric stress subspace, as shown in Figure 3.4(b). With a proportionality constant  $A_m$ , referred to as the nonassociativity constant, the plastic potential is written in terms of gradients such as

$$\frac{\partial g}{\partial s_{ij}} = P'_{ij} = Q'_{ij} \quad (3.59a)$$

$$\frac{\partial g}{\partial p} = 3P'' = 3Q'' + \frac{Q''}{|Q''|} A_m |Q'_{ij}| \quad (3.59b)$$

The nonassociativity term serves to reduce volumetric strain due to hydrostatic pressure, since volumetric strain is often overestimated using associative plasticity with ellipsoidal yield surfaces (Banerjee and Stipho 1978).

Note that the plastic potential surface  $g$  of the Prevost model has a discontinuity on the deviatoric plane  $p = \beta$  at points A and B, as shown in Figure 3.4(b). This may not be important if the advantage of potential function, equation 3.59, is recognized. The modification of plastic volumetric strain is valid for both the normally consolidated side ( $p > \beta$ ) and the overconsolidated side ( $p < \beta$ ). Mould (1983) modified the overconsolidated side of  $P''$  as being antisymmetric with respect to a deviatoric surface AB so that the discontinuity of the plastic potential surface was removed. Moreover the parameter evaluation procedure becomes simple in this case.

Effects of nonassociativity become important when the bulk response to shear stress is concerned. This will be discussed further in the next chapter.

### 3.5 Bounding Surface

The bounding surface is the outermost yield surface of the nested surfaces, and bounds a field in the stress space corresponding to the largest stress history experienced by the material. A stress point never goes outside of the bounding surface since it defines the final condition of the soil for both shearing and volumetric yielding.

#### 3.5.1 Role of Bounding Surface

An important aspect of this surface is to keep track of the critical state so that the material can behave with volumetric hardening when the

stress point is on this surface. Therefore the bounding surface plays a role very similar to the yield surface of the Cam Clay model. In fact, the formulation for the bounding surface is adopted to introduce useful concepts of the Cam Clay model such as the isotropic hardening, the associative volumetric yielding flow, and the critical state concept. This approach differs somewhat from the latest Prevost model formulation which has been implemented in the finite element programs DIRTII (Hughes and Prevost 1979) and DYNAFLOW (Prevost 1981) to evaluate a hardening modulus. The hardening modulus is defined in terms of the consistency condition under the volumetric yielding as is for the Cam Clay model, but does not depend on the simplified representation like the moduli  $h'_m$  and  $B'_m$  developed in the last section for the nested yield surfaces.

### 3.5.2 The Critical State

The bounding surface  $f_p$  is the outermost yield surface outside of which the stress point and the inner nested surfaces are not allowed to go (Figure 3.6). It plays the role of a failure surface for shearing and of a volumetric yielding surface for consolidation. The hardening rule associated with this yield surface is characterized by means of the critical state concept (Roscoe and Burland 1968), and so the hardening modulus is defined in a different manner from that of the nested surfaces, although a similar yield function is used for the bounding surface.

On the bounding surface, an associative flow rule is used to calculate plastic strain increment. For the associative flow  $p_{ij}^{(p)} = q_{ij}^{(p)}$  and the nonassociativity constant  $A_p$  is equal to zero. The following

assumptions are introduced: first, the yield function  $f_p$  is a function only of the plastic volumetric strain as a state parameter similar to the Cam Clay model. Second, the translation and expansion of the yield surface occur such that the failure point on the yield surface is always kept on the critical state line, as shown in point C and E in Figure 3.6.

The critical state line is defined in  $p - q - e$  space as an intersection of the Roscoe surface and the Hvorslev surface (Atkinson and Bransby 1978). Its projection onto the triaxial plane is composed of two straight lines with the slope of  $M^C$  and  $M^E$  for axial compression and extension test, respectively.  $M^C$  and  $M^E$  are related to the effective friction angle of soil  $\phi'$  based on the Mohr-Coulomb failure criteria.

$$M^C = \frac{6 \sin \phi'}{3 - \sin \phi'} \quad (3.60a)$$

$$M^E = \frac{6 \sin \phi'}{3 + \sin \phi'} \quad (3.60b)$$

The projection of the critical state line on a deviatoric plane gives a different shape from a circle, which is the case for the yield function used here. In order to approximate the critical state, stress points on the critical state lines with the same density corresponding to axial compression and extension tests are used as calibration points of the yield function  $f_p$ . These calibration points must stay on and move along the critical state lines when the yield surface  $f_p$  expands or contracts according to changes in the plastic volumetric strain. Therefore the size of the yield surface is always in proportion to its position in the stress space.

$$\xi_{ij}^{(p)} = a_{ij} k_p \quad (3.61)$$

where  $a_{ij}$  is a material constant defined by the friction angle  $\phi'$  and shown in Figure 3.6. Since the critical state draws a straight line on  $e - \log p$  plane with the same slope of  $\lambda$  as of the normal isotropic consolidation line, we can write, analogous to equation 3.49,

$$k_p = k_{0p} \exp(\lambda \epsilon_V^p) \quad (3.62)$$

where  $k_{0p}$  is a reference value.

The expansion rule for  $f_p$  along the critical state line is formulated for finite stress increments and shown in Appendix A.3.

### 3.5.3 Plastic Modulus

In contrast to the nested surface, the position of the bounding yield surface  $\xi_{ij}^{(p)}$  is not an independent parameter but a function of the plastic volumetric strain. Then the consistency condition can be written as

$$\frac{\partial f_p}{\partial \sigma_{ij}} \dot{\sigma}_{ij} + \frac{\partial f_p}{\partial \epsilon_V^p} \dot{\epsilon}_V^p = 0 \quad (3.63)$$

The second term reflects the contribution of the expansion or contraction of the yield surface  $f_p$  according to equation 3.61 and 3.62, and can be modified by the substitution of equation 3.12 and 3.61

$$\begin{aligned} \frac{\partial f_p}{\partial \epsilon_V^p} &= \frac{\partial f_p}{\partial \xi_{ij}} \frac{\partial \xi_{ij}}{\partial k} \frac{\partial k}{\partial \epsilon_V^p} + \frac{\partial f_p}{\partial k} \frac{\partial k}{\partial \epsilon_V^p} \\ &= \left( -Q_{ij}^{(p)} \frac{\xi_{ij}^{(p)}}{k_p} - 2k_p \right) \frac{\partial k}{\partial \epsilon_V^p} \end{aligned}$$

$$= \frac{1}{k_p} Q_{ij}^{(p)} \sigma_{ij} \frac{\partial k}{\partial \epsilon_v^p} \quad (3.64)$$

The equation of plastic volumetric strain increment is

$$\dot{\epsilon}_v^p = \frac{1}{H'_p} \frac{Q_{mn}^{(p)} \sigma_{mn}}{|Q_{kl}^{(p)}|^2} \frac{\partial f_p}{\partial p} \quad (3.65)$$

Substituting above two equations into 3.63, we have

$$H_p = \frac{\partial f_p}{\partial p} \frac{\partial k_p}{\partial \epsilon_v^p} \frac{1}{|Q_{kl}^{(p)}|^2} \frac{Q_{ij}^{(p)} \sigma_{ij}}{k_p} \quad (3.66)$$

In view of equation 3.66, the plastic modulus  $H_p$  varies along the bounding yield surface  $f_p$  with the value of  $\partial f_p / \partial p$ .  $\partial k_p / \partial \epsilon_v^p$  describes the expansion or contraction of the yield surface and is always positive although the sign of  $\dot{k}_p$  may change with the sign of  $\dot{\epsilon}_v^p$ . For a consolidation process, this term is expressed in terms of equation 3.62. Since  $\partial k_p / \partial \epsilon_v^p$  is positive, and  $Q_{ij}^{(p)} \sigma_{ij}$  is positive because of the convexity of  $f_p$  with respect to the origin of stress space,  $H_p$  has the same sign as  $\partial f_p / \partial p$ . When  $H_p > 0$  as soil reduces its volume as loaded resulting in consolidation. When  $H_p < 0$ , the soil dilates. A critical condition exists for which  $H_p = 0$ . For the Prevost model,

$$\frac{\partial f_p}{\partial p} = 3Q''(p) = 2c^2(p - \beta^{(p)}) \quad (3.67)$$

and the apex of the deviatoric semiaxis of  $f_p$  represents the critical state. This is shown at points C and E in Figure 3.6. When the stress point is on  $f_p$  and  $H_p > 0$ , the material behavior is stable. If the stress increment is applied to the material such that the stress increment

points are out of  $f_p$ , plastic deformation causes the yield surface  $f_p$  to expand and move outward with the stress point according to equations 3.61 and 3.62. On the other hand, when  $H_p < 0$  the material behavior is unstable. The stress increment is directed toward the inside of  $f_p$ , and plastic deformation causes the yield surface  $f_p$  to contract and to move inwards with the stress point corresponding to the materials softening. However this type of softening effect is not considered for soft clays.

When equations 3.62 and 3.67 are substituted into equation 3.66, it follows

$$H_p = 2c^2 \lambda (p - \beta^{(p)}) \frac{Q_{mn}^{(p)} \sigma_{mn}}{|Q_{kl}|^2} \quad (3.68)$$

In case of  $c = 3/\sqrt{2}$ , which leads  $|Q_{kl}|^2 = \sqrt{6} k_p^2$ ;  $H_p$  becomes

$$H_p = \frac{3}{2} \lambda (p - \beta^{(p)}) \frac{Q_{mn}^{(p)} \sigma_{mn}}{k_p^2} \quad (3.69)$$

When the stress point is on the hydrostatic semiaxis of  $f_p$ , where  $Q_{ij}^i = 0$ ,  $H_p$  of the above equation can be expressed in the simplest form as

$$H_p = 3\lambda p \quad (3.70)$$

### 3.6 Summary

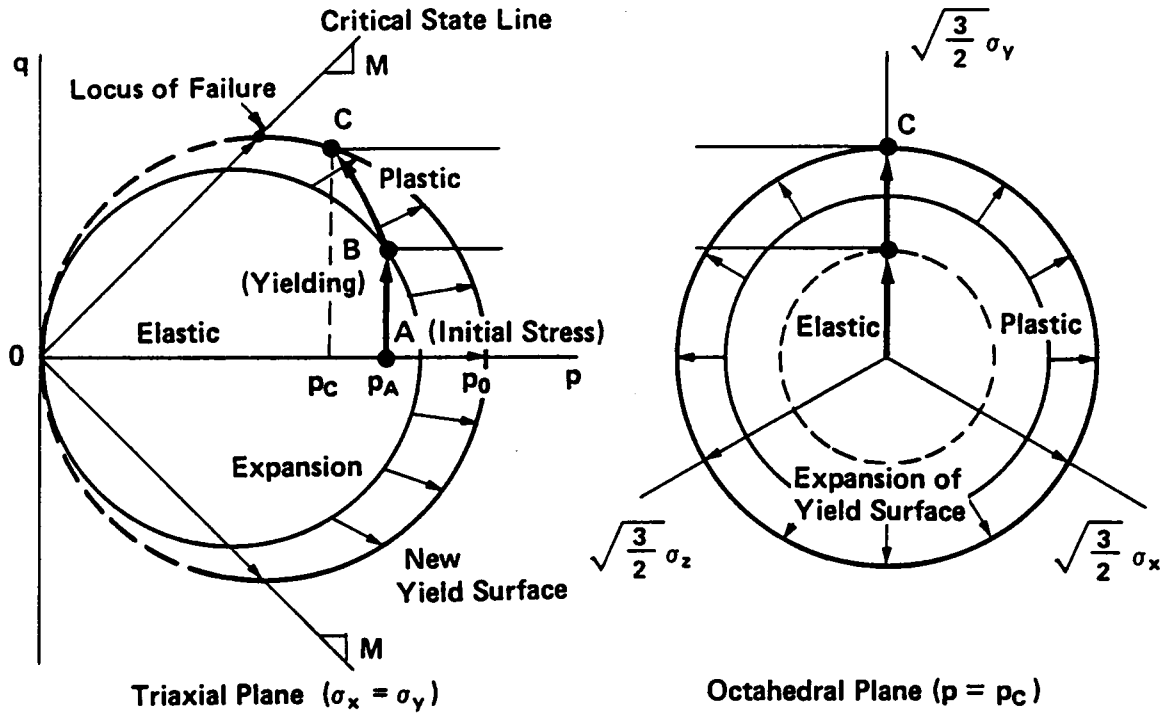
The theoretical development of the Prevost model and the modifications used herein are described. The Prevost model is a multisurface elasto-plastic soil model which exhibits versatility in simulating the inelastic behavior of soil.

The largest advantage in using the Prevost model is that it can deal with anisotropic yielding of soil. To take maximum advantage of the model, the aspects considered include: hydrostatic, deviatoric decomposed formulation, the combination of the kinematic and isotropic hardening rules, the translation rule of nested yield surfaces, the critical state concept associated with the bounding surface, the interpretation of plastic moduli, and the nonassociative plastic potential.

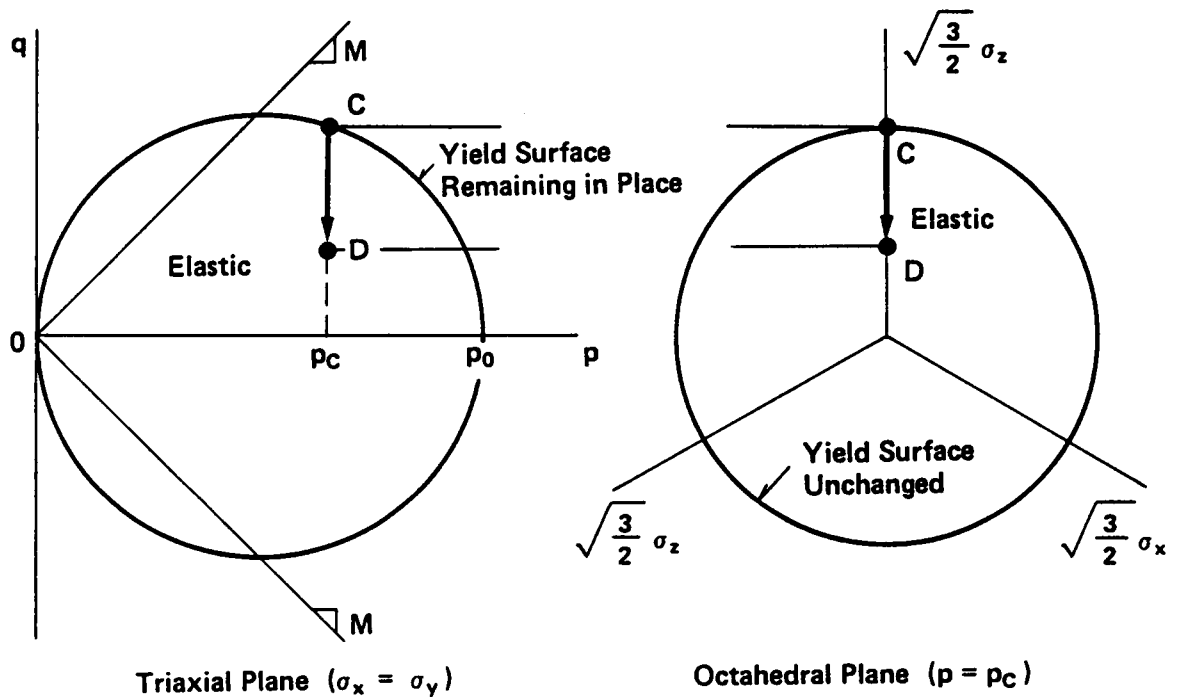
Procedures to identify the parameters as well as calibration of the model will be discussed in the next chapter.

Table 3.1 Historical Development of Elasto-plastic Soil Modeling

<u>Early Development of Plasticity</u>	<u>Combined Surface Model</u>
Haigh (1920); Westergaard (1920)	Two conical yield surfaces combined
von Mises (1928)	Cap model combining Drucker-Prager surface with an elliptical cap
Prager (1949)	A conical yield surface and a spherical cap
Hill (1950)	
Drucker, Prager (1952)	
Prager (1955); Ziegler (1959); Phillips, Sierakowski (1965); Mroz (1967)	Monassociative flow rule for sands
Green (1956); Truesdell (1955)	Nonassociative flow rule for overconsolidated clays
<u>Cam Clay Model</u>	Nonassociative flow rule for a soft clay
Hvorslev (1937, 1960)	
Drucker, Gibson, Menkel (1957)	Concept of loading surface not necessarily identical to yield surface
Henke (1960)	No elastic region enclosed by yield surface
Roscoe, Schofield, Thuraiajah (1963)	Nested yield surfaces with anisotropic hardening, concept of field of plastic moduli
Schofield, Wroth (1968); Atkinson, Bransby (1978)	Overlay model accounting cumulative hardening
Burland (1965)	Two surface model, concept of bounding surface
Roscoe, Burland (1968)	Application of Mroz (1969) model to soil mechanics
Mroz, Morris, Zienkiewicz (1978)	Further developments and applications of multisurface model, in particular for cyclic loading
Mroz, Morris (1982)	A proposal of New multisurface model
	Model with infinite number of yield surfaces



(a) Loading with Expanding Yield Surface (A → B → C)



(b) Unloading while Yield Surface Unchanged (C → D)

Figure 3.1 Isotropic Hardening Response with Ellipsoidal Yield Surface of Modified Cam Clay Soil Model

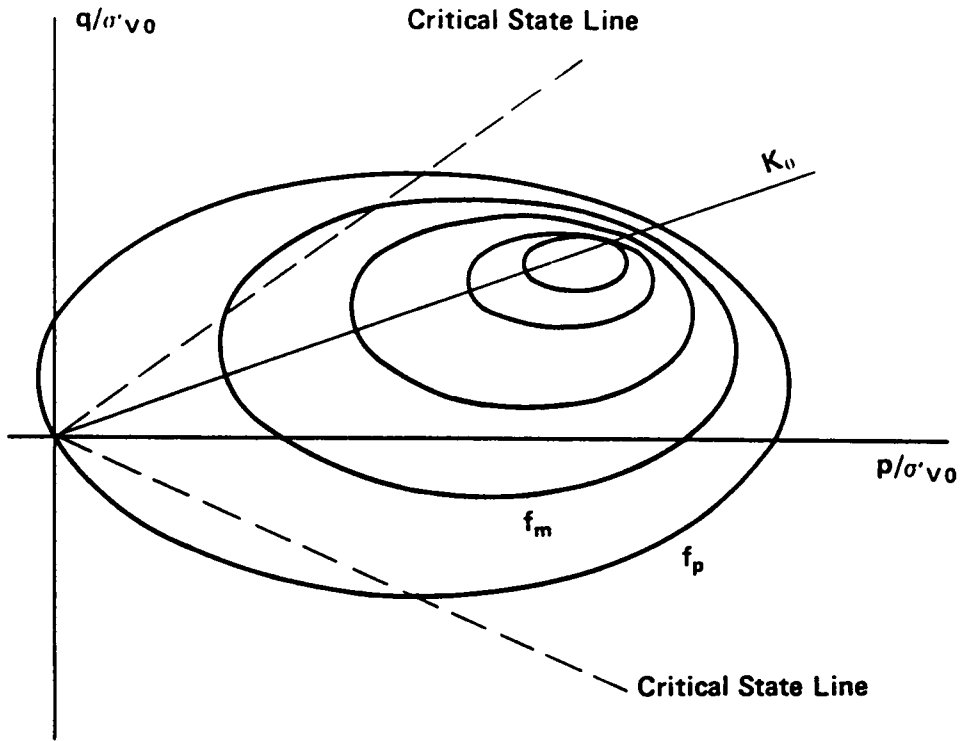


Figure 3.2 Pressure-Sensitive Multisurface Model with Critical State Concept to which Prevost Model Belongs

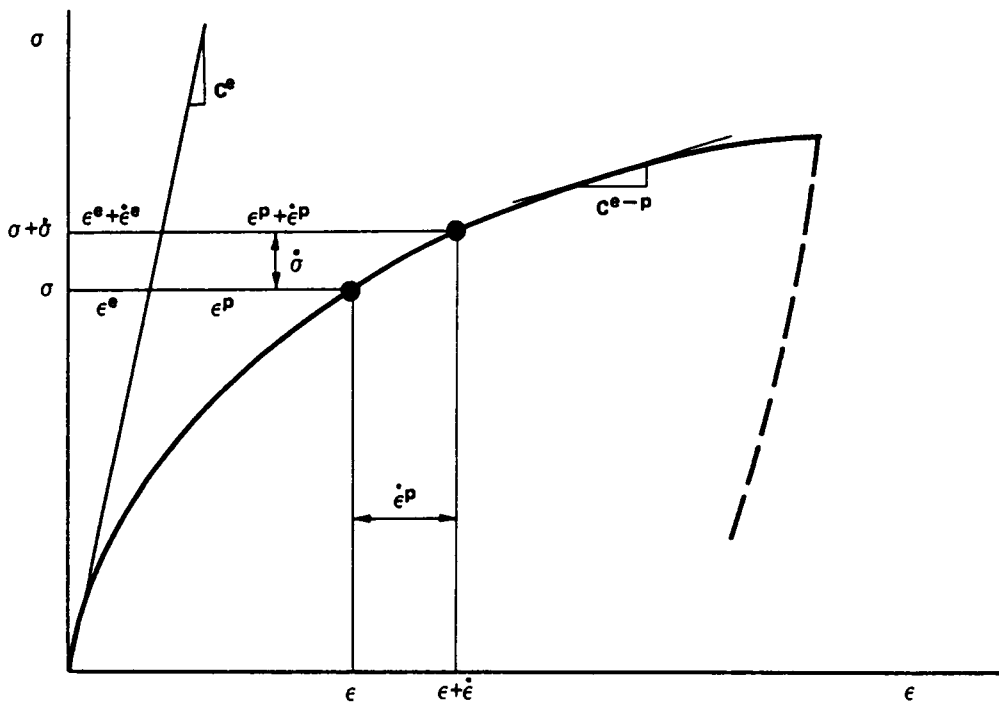
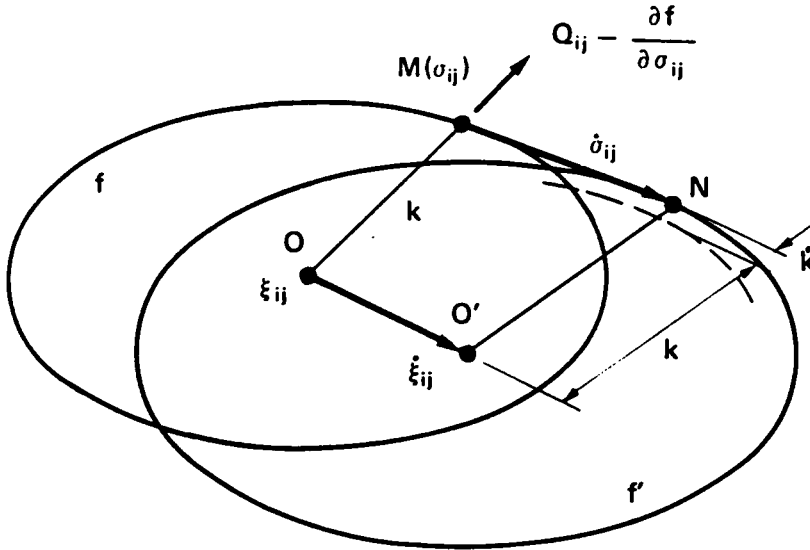
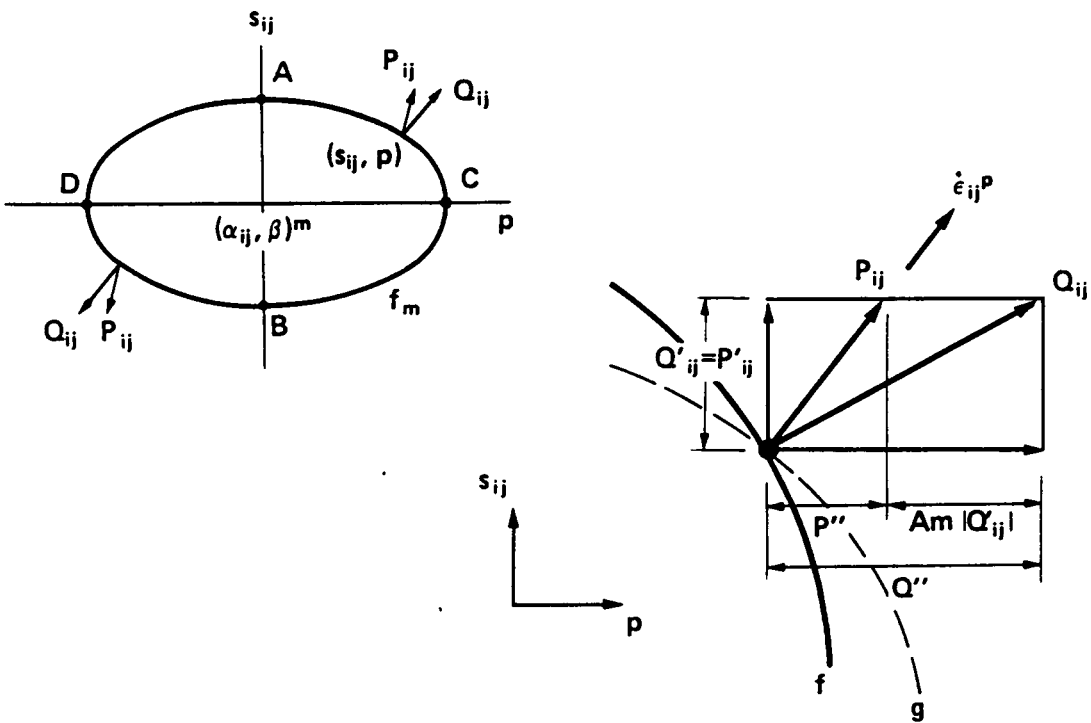


Figure 3.3 Stress-Strain Relation in Elasto-plastic Formulation

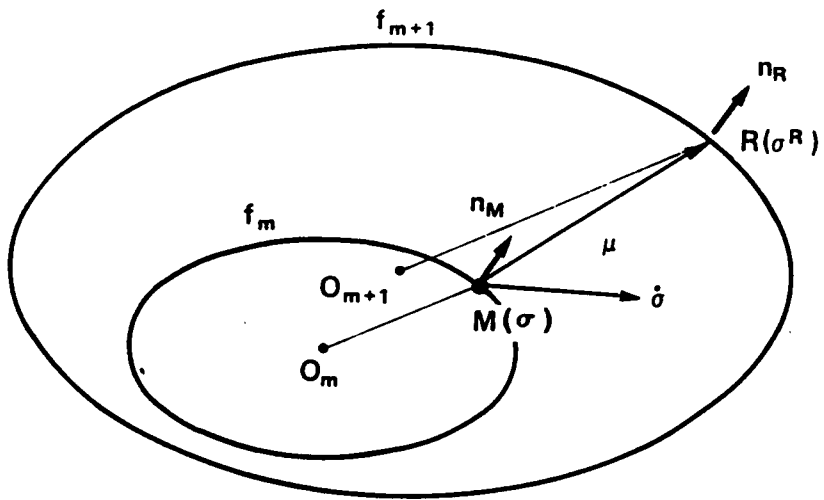


(a) Consistency Condition of Yield Surface  $f$  in conformity with Stress Increment  $\dot{\sigma}_{ij}$

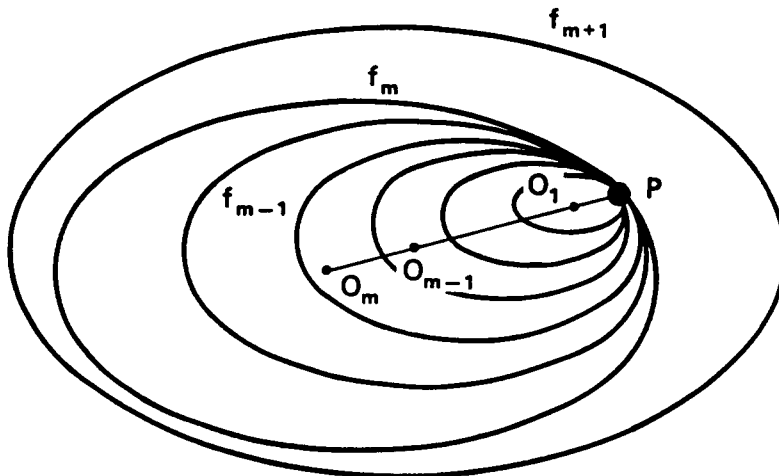


(b) Relation between Normality and Flow Rule with Nonassociativity Parameter  $A_m$

Figure 3.4 Consistency Condition and Nonassociative Flow Rule



(a) Mroz's Translation Rule



(b) Relative Positions of Inactive Yield Surfaces

Figure 3.5 Translation Rule and Contacting Yield Surfaces

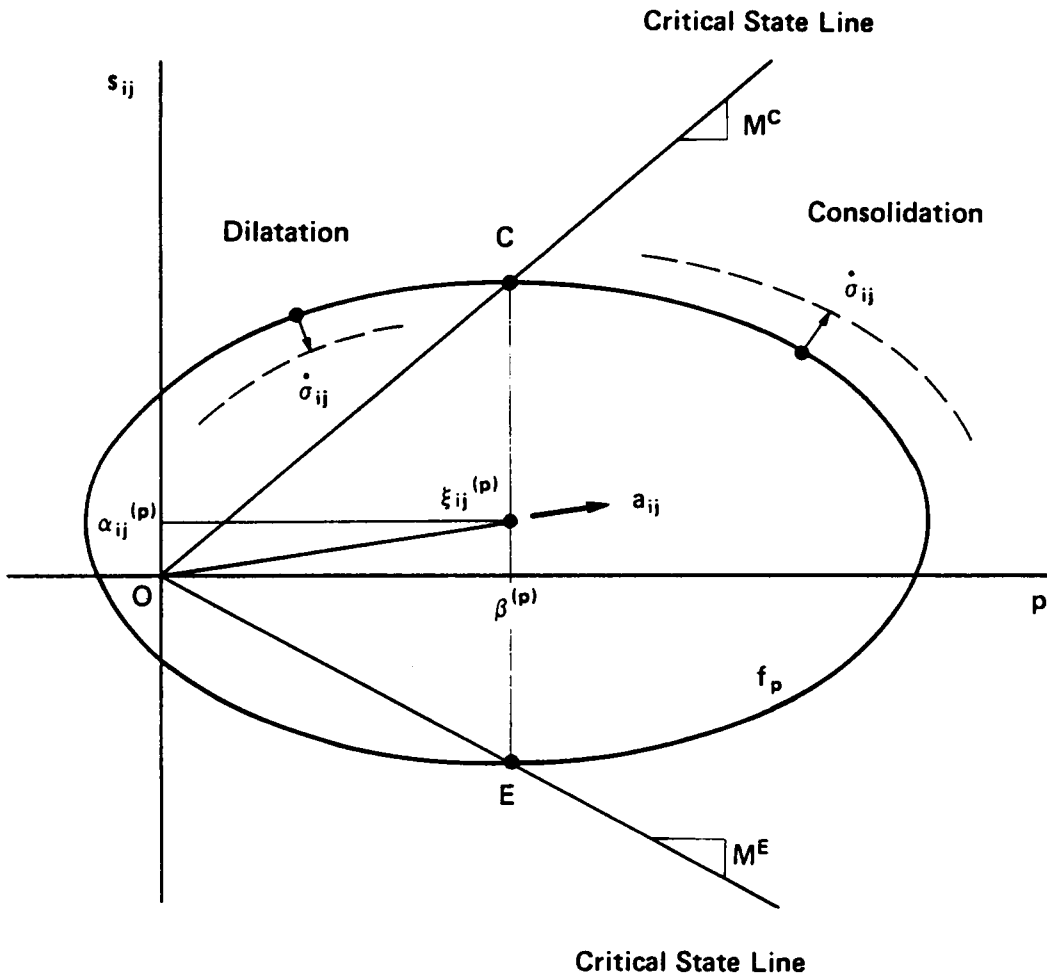


Figure 3.6 Bounding Yield Surface and Critical State Line

## Chapter 4

### IMPLEMENTATION OF PREVOST MODEL

#### 4.1 Introduction

The model parameter identification and implementation procedures are described in this chapter. Problems encountered during parameter determination by means of the parameter evaluation procedure (Prevost 1980) are discussed with a focus on the undrained behavior of soft clays. The conventional procedure is modified to cope with the problems. Examples of the model prediction are demonstrated, but are limited only for loading conditions with which the model parameters have been determined.

In spite of the relatively large amount of basic discussions of the Prevost model, information supporting it is limited. To the author's knowledge, the pressure-sensitive version has only been applied to sand (Prevost 1979), and the undrained behavior of laboratory prepared kaolin clay (Prevost 1980). In the latter case the clay was overconsolidated with low water content and showed effective stress paths of the triaxial test analogous to those in a drained triaxial test. There have been no model applications to normally consolidated soft clays. It is interesting to note that even when the model was used to simulate a consolidation process in consideration of coupling between effective stress and pore pressure dissipation, sand, but not clay, was used (Prevost 1981). This thesis has applied the Prevost model to soft clays, involving proper means to determine model parameters.

Complete specification of the model parameters requires the determination of (1) initial sizes and positions of yield surfaces together with associated plastic moduli, (2) elastic moduli and (3) volumetric hardening parameters. All of them can be evaluated by means of appropriate laboratory test programs. This procedure was proposed by Prevost (1980) and requires data from a conventional triaxial compression (CTC) test and a reduced triaxial extension (RTE) test. The basic idea of the procedure is that the model parameters are evaluated so as to match stress-strain relations and  $p - q$  diagram stress paths.

However, problems arise with the basic procedure, such as the overlapping of the yield surface, an unrealistic distribution of plastic moduli, and a lack of identification of parameters for a certain stress state. In some cases, these are serious. For example, the overlapping of the yield surface is not adequate to assure uniqueness of the constitutive relation. In fact a direct use of the conventional parameter evaluation procedure for soft clays results in most cases in the overlapping of yield surfaces.

In order to settle these problems, some new concepts are introduced to modify the procedure later in this chapter by which the model parameters are successfully determined for normally consolidated clays. In particular, the parameters are defined for a soil known as San Francisco Bay Mud. This is done because this clay is fairly typical of low plasticity clays and it is the most important material involved in the tunneling case history which will be used to calibrate the finite element program.

## 4.2 Rotationally Symmetric Stress Condition

The Prevost model implementation for rotationally symmetric stress conditions will be demonstrated in this chapter, and they include triaxial tests and consolidation tests. Because triaxial test data are used to identify model parameters, it is convenient to express the model stress-strain relation in the triaxial plane. It serves as a basis for the theoretical description of the model parameter determination procedure.

In order for the model to represent a soils anisotropy, the reference frame is fixed to a soil mass and the  $y$ -axis is taken in coincide with the vertical direction. Since  $\alpha_{ij}^{(m)}$  are not necessarily all equal to zero, the yield surface  $f_m$  is not symmetric with respect to the hydrostatic axis, that is, the yielding is anisotropic. Anisotropy of soils initially develops during consolidation, where no shearing components exist and the principal axes coincide with the physical axes. Therefore, the soil's anisotropy initially exhibits rotational symmetry about the  $y$ -axis,

$$\alpha_{yz} = \alpha_{zx} = \alpha_{xy} = 0 \quad (4.1a)$$

$$\alpha_{xx} = \alpha_{zz} = -\frac{1}{2}\alpha_{yy} \quad (4.1b)$$

for all  $m$ . In a particular situation of rotational symmetry where the principal axes coincide with the principal axes of anisotropy as well as the physical axes, the nested yield surfaces can be represented in the principal stress space. They are ellipsoids with a circular intersection to deviatoric planes and their main axes parallel to the hydrostatic axis. Equation 3.37 specifies that all the yield surfaces are centered along the

$\sigma_y$  axis on the deviatoric plane and plots an ellipse on the triaxial plane. Then, the yield function, equation 3.6, is simplified as

$$f_m = (q - \alpha^{(m)})^2 + c^2 (p - \beta)^2 - k_m^2 = 0 \quad (4.2)$$

where

$$q = \sigma_y - \sigma_x$$

$$\alpha = \frac{3}{2} \alpha_{yy} \quad (4.3)$$

in the triaxial test, the stress point travels along the  $\sigma_y$  axis in the deviatoric plane and stays on the triaxial plane. Therefore, the yield surface configuration and relative position of the stress point can be seen in the triaxial plane.

The state of the material can be described with reduced number of stresses and parameter components when it is rotationally symmetric.

$$s_{yy} = \frac{2}{3} (\sigma_y - \sigma_x) = \frac{2}{3} q \quad s_{xx} = s_{zz} = -\frac{1}{3} q \quad (4.4a)$$

$$\alpha_{yy} = \frac{2}{3} (\alpha_{yy} - \alpha_{xx}) = \frac{2}{3} \alpha \quad \alpha_{xx} = \alpha_{zz} = -\frac{1}{3} \alpha \quad (4.4b)$$

$$e_q = \frac{2}{3} (\epsilon_{yy} - \epsilon_{xx}) \quad (4.4c)$$

$$e_y = \epsilon_{yy} - \epsilon_{xx} = \frac{3}{2} e_q \quad (4.4d)$$

Derivatives of the yield function and plastic potential are

$$Q'' = 2c^2 (p - \beta), \quad P'' = 2c^2 (p - \beta) \pm \sqrt{6} \cdot A_m |q - \alpha| \quad (4.5a)$$

$$Q'_y = P'_y = 3 (s_{yy} - \alpha_{yy}) = 2 (q - \alpha) \quad (4.5b)$$

$$|Q'_{ij}| = 3 |s_{ij} - \alpha_{ij}| = \sqrt{6} |q - \alpha| \quad (4.5c)$$

$$Q_{mn} \dot{s}_{mn} = 2(q - \alpha) \dot{q}, \quad Q'' \dot{p} = 2c^2 (p - \beta) \dot{p} \quad (4.5d)$$

$$|Q_{ij}|^2 = 6(q - \alpha)^2 + \frac{4}{3}c^4 (p - \beta)^2 \quad (4.5e)$$

Incremental stress plastic strain relation can be written from equation 3.28:

$$\begin{pmatrix} \dot{e}_v^p \\ \dot{e}_q^p \end{pmatrix} = \begin{bmatrix} \frac{1}{H'} \frac{G P'' Q''}{|Q_{kl}|^2} & \frac{1}{H'} \frac{6 P''}{|Q_{kl}|^2} (q - \alpha) \\ \frac{1}{H'} \frac{6 Q''}{|Q_{kl}|^2} (q - \alpha) & \frac{1}{H'} \frac{4 (q - \alpha)^2}{|Q_{kl}|^2} \end{bmatrix} \begin{pmatrix} \dot{p} \\ \dot{q} \end{pmatrix} \quad (4.6)$$

Substituting equation 4.5 into 4.6, we have final form of the stress-strain relation in the triaxial plane:

$$\dot{e}_v = \frac{\dot{p}}{B} + \frac{1}{H'} \frac{(q - \alpha) \dot{q} + c^2 (p - \beta) \dot{p}}{(q - \alpha)^2 + \frac{2}{9}c^4 (p - \beta)^2} \left[ \frac{2}{3}c^2 (p - \beta) \pm \sqrt{6} A_m |q - \alpha| \right] \quad (4.7a)$$

$$\dot{e}_y = \frac{\dot{q}}{2G} + \frac{1}{H'} \frac{(q - \alpha) \dot{q} + c^2 (p - \beta) \dot{p}}{(q - \alpha)^2 + \frac{2}{9}c^4 (p - \beta)^2} (q - \alpha) \quad (4.7b)$$

These derivations are valid for all  $m$ . Equations 4.7a and 4.7b are the basis of the model parameter determination procedure. Note that if the associative flow rule is used,  $P'' = Q''$ , the constitutive matrix in equation 4.6 becomes symmetric for volumetric strain increment  $\dot{e}_v$  and deviatoric strain increment  $\dot{e}_q$ . But this is not the case for  $\dot{e}_v$  and  $\dot{e}_y$  in equation 4.7b, where  $e_y$  is strain deviator because of an adjustment of the constant factor  $2/3$ .

### 4.3 Consideration of Model Bulk Response

As indicated in equation 4.6, the Prevost model accounts for the coupling effect between the volumetric and deviatoric responses. Thus, the plastic volumetric strain  $\epsilon_v^p$  is influenced by both hydrostatic pressure  $p$  and deviatoric stress  $q$ . These contributions are examined individually in this section so as to provide simple loading conditions. Firstly, it is observed that the absence of deviatoric stress results in a simple  $p$  vs  $\epsilon_v^p$  relation like that for isotropic consolidation test. Secondly, assuming the effects of the mean pressure may be neglected during undrained shear; moreover, a relation between changes in shear stress and pore pressure is established. In contrast to these special cases of stress conditions, the bulk shear response for both drained and undrained loadings is considered later.

#### 4.3.1 Volumetric Response to Mean Stress

No shear stresses are induced in an isotropic consolidation test, and reference is useful for investigation of volumetric response of clays.

Without any shear stresses, all the yield surfaces center on the hydrostatic axis,  $\alpha_{ij} = 0$ , and the stress point moves along the same axis,  $s_{ij} = 0$ . When the stress point moves, all the surfaces inside of the current active yield surface are tangent to each other at the stress point and translate with the stress point.

Since no deviatoric stresses and strains and no anisotropy exist in isotropic consolidation, all the deviatoric components vanish in the

stress-strain relation, and equation 4.7a is simplified to

$$\dot{\epsilon}_v = \left( \frac{1}{B} + \frac{3}{H'} \right) \dot{p} \quad (4.8)$$

in which the plastic modulus acts as a plastic bulk modulus.

The plastic modulus  $H'_m$  in equation 3.57 simplifies to

$$H'_m = h'_m \pm B'_m \quad (4.9)$$

since  $|Q_{ij}| = \sqrt{3} Q''$  and  $Q'_{ij} = 0$ . A positive sign is taken for a loading consolidation in which the stress point moves toward a direction on the hydrostatic axis. Moreover, the stress point must satisfy  $Q'' > 0$  as a sufficient condition. On the other hand, a negative sign corresponds to unloading and  $Q'' < 0$ . Therefore, the plastic shear modulus  $h'_m$  and the plastic bulk modulus  $B'_m$  can be determined from the unloading and reloading stress-strain curves of isotropic consolidation test.

The translation of the yield surface  $f_m$  is defined by the Mroz translation rule, which was mentioned in Section 3.4.3. Equations 3.40 and 3.46 simplify in this case to

$$\delta\mu = \frac{3Q''^{(m)} \dot{p} - 2k_m \dot{k}_m}{Q''^{(m)} \mu''} \quad (4.10)$$

$$\mu'' = \frac{1}{3} \mu_{ij} \delta_{ij} = \frac{k_{m+1}}{c} - (p - \beta^{(m+1)}) \quad (4.11)$$

$$Q''^{(m)} = \frac{2}{3} c k_m \quad (4.12)$$

Equation 3.45 ends up as

$$\dot{\beta} = \delta\mu \mu_{ij} = \dot{p} - \dot{k}_m \quad (4.13)$$

The translation of  $f_m$  is simply defined in terms of changes in mean pressure and size of the yield surface  $f_m$ . Variable  $\dot{k}_m$  is governed by equation 3.50:

$$\dot{k}_m = \lambda k_m \dot{\epsilon}_v^p \quad (4.14)$$

When the stress point lies on the bounding surface  $f_p$ , the soil is normally consolidated for the applied stress. The plastic modulus is defined by equation 3.70,

$$H_p = 3\lambda p \quad (4.15)$$

in which  $\lambda$  is a slope of the curve relating the plastic volumetric strain and logarithmic mean pressure. The hardening rule follows the normal consolidation curve. The isotropic part of hardening is defined by

$$\dot{k}_p = \lambda k_p \dot{\epsilon}_v^p \quad (4.16)$$

and from equation 3.61 the kinematic part of hardening is

$$\frac{\dot{k}_p}{k_p} = \frac{\dot{\beta}(p)}{\beta(p)} = \frac{\dot{k}_m}{k_m} = \frac{\dot{\beta}(m)}{\beta(m)} \quad (4.17)$$

The solid line in Figure 4.1 indicates the relation between volumetric strain and mean pressure. This is calculated from the data of conventional consolidation tests on San Francisco Bay Mud conducted by Duncan (1962), assuming values of lateral pressure coefficient  $K_0$  after Brooker and Ireland (1965).

Using the unloading curve, the plastic moduli are calculated. The predicted behavior of the Bay Mud is in good agreement with the experi-

mental results. The same result is replotted in  $\epsilon_v$  vs  $\log p$  relation shown in Figure 4.2. The initial stress condition is selected such that void ratio  $e_c$  at preconsolidation pressure  $p_c$  is the same as the experimental value. And three percent of volumetric strain offset over  $p_0 = 0.2 \text{ kg/cm}^2$  is assumed to reach a normally consolidated state at  $p_c$ . The experimental normal consolidation line is slightly concave upwards, reflecting sensitivity of the Bay Mud, whereas the predicted line is straight since  $\lambda$  in equation 4.16 is a constant in the course of loading.

The model describes the hysteresis loops usually observed in experiments for loading reversal events although the comparison is difficult due to a lack of data. Once the stress point reaches the bounding surface  $f_p$  in reloading, the soil response comes back again to the normally consolidated state.

In Figure 4.3, the elasto-plastic bulk moduli for reloading process are assumed 10 percent less than those for the unloading process. This can be established by selecting appropriate values for  $h'_m$  and  $B'_m$  in equation 4.9 so that  $H'_m$  may have different values for the unloading and reloading processes. The hysteresis loop for loading reversals becomes smaller relative to the case where the plastic moduli are the same for unloading and reloading ( $B'_m = 0$ ).

#### 4.3.2 Pore Pressure Response to Shear Stress -- A Special Case

The undrained behavior of soil is characterized by deformation with constant volume. Since the volumetric strain increment is equal to zero

during the undrained test, the plastic volumetric strain increment  $\dot{\epsilon}_V^P$  is equal, but reversed in magnitude to the elastic volumetric strain increment  $\dot{\epsilon}_V^e$ . During shear of soft clay, pore pressure develops and the effective mean pressure is reduced. The mean pressure decrement  $\dot{p}$  causes negative elastic volumetric strain increment  $\dot{\epsilon}_V^e$  and, thus, a positive plastic volumetric strain increment  $\dot{\epsilon}_V^P$ . Therefore, the yield surface expands and plastic flow is inclined towards the positive hydrostatic axis while the soil is sheared. This is an elasto-plastic interpretation of soil behavior subject to undrained triaxial shear.

Now assume that volumetric plastic flow is caused only by the deviatoric stress but not by the mean pressure, resulting in a special stress path. In contrast to the isotropic consolidation in which no shearing components are present,  $Q_{ij}^i = 0$ , as discussed in the last section, the assumption of no mean pressure contribution leads to

$$\dot{p} = \frac{1}{H'} \frac{Q_{ij} \dot{\sigma}_{ij}}{|Q_{kl}|} (3Q'' + A_m |Q'_{st}|) \quad (4.18)$$

or

$$Q'' = \frac{2}{3} c^2 (p - \beta) = 0 \quad (4.19)$$

This means that the stress point always lies on the deviatoric semiaxis of the yield surface. The stress path under such circumstances draws a line which connects apexes of the deviatoric semi-axes of all the yield surfaces, as shown in Figure 4.4. Hence,  $\dot{\epsilon}_V^P$  is composed of the deviatoric and hydrostatic contribution. From equations 3.28 and 3.29,

$$p = \beta \quad (4.20)$$

With the help of equations 4.20 and 4.7a, the mean pressure increment can

be expressed by the deviatoric stress increment,

$$\dot{p} = -\frac{\sqrt{6}}{3} \frac{B}{H'_m} A_m \dot{q} \text{sign}(q - \alpha) \quad (4.21)$$

And equation 4.7a simplifies to

$$\dot{e}_y = \left[ \frac{1}{2G} + \frac{1}{H'_m} \right] \dot{q} \quad (4.22)$$

The mean pressure is related to the pore pressure  $u$  for the undrained triaxial test in an incremental expression,

$$\dot{p} = \frac{1}{3} \dot{q} - \dot{u} \quad (4.23)$$

Combining equations 4.21 through 4.23,  $A_m$  is obtained as

$$A_m = \frac{H'_m}{2\sqrt{6} B \text{sign}(q - \alpha)} \left[ \frac{\dot{u}}{\dot{e}_q} \left( \frac{1}{G} + \frac{2}{H'_m} \right) - \frac{3}{2} \right] \quad (4.24)$$

The plastic modulus  $H'_m$  associated with the yield surface  $f_m$  is written from equation 3.56 as

$$H'_m = h'_m \quad (4.25)$$

since  $Q^{(m)} = 0$ . The plastic modulus  $H'_m$  and the nonassociativity constant  $A_m$  can be evaluated from the experimental data of the undrained triaxial test. With the deviatoric stress-strain curve,  $H'_m$  can be defined by means of equation 4.22, and  $A_m$  can be determined from the pore pressure development by equation 4.24. The positions and sizes of yield surfaces are determined from the stress points on the compression and extension stress paths.

Figure 4.5(a) shows a typical stress-strain curve of a consolidated

undrained triaxial tests on San Francisco Bay Mud. The  $K_0$  value of consolidation phase is 0.7. Stress paths for compression and extension tests (CTC and RTE) are constructed such that the mean pressure at a stress point on the CTC path is the same at a point on the RTE path if the slopes of deviatoric stress strain curve are the same at these two points. Then they may satisfy the assumption of equation 4.19. The stress paths are shown in Figure 4.4 and the associated excess pore pressure development in Figure 4.5(b). Model parameters for 13 yield surfaces, including the bounding surface, are determined as shown in the upper rows of Table 4.1 as well as in Figure 4.4. The model predictions are shown in Figure 4.5, where excellent agreement is obtained for the stress-strain curves and excess pore pressure development.

It is a special case for the stress points always to stay on the apex of the deviatoric semiaxis of the yield surfaces. Prevost (1978) defined such a soil response as an undrained behavior handling with his model. Once the condition is accepted such that the mean pressure has no effect on the plastic volumetric strain, that is  $p = \beta$ , then the yield function 4.2 becomes independent of the mean pressure since the mean pressure term drops out. Thus the pressure nonsensitivity results.

$$f_m = \frac{3}{2} (s_{ij} - \alpha_{ij}^{(m)}) (s_{ij} - \alpha_{ij}^{(m)}) - k_m^2 = 0 \quad (4.26)$$

This says that the yield surface in the stress space is no longer an ellipsoid but a circular cylinder whose axes are parallel to the hydrostatic axis. The plastic potential surfaces are a set of conical shells whose axes coincide with the axes of the yield surfaces. The kinematic

hardening rule for nested yield surfaces, that is the Mroz translation rule, should be modified in this case to match the condition of  $p = \beta^{(m)}$ . The Mroz translation rule is decomposed into the projections onto the deviatoric subspace and the hydrostatic axis. The deviatoric part is used without modification. The translation of the yield surface along the hydrostatic axis is selected as a change in the mean pressure. Therefore the translation of the yield surface  $f_m$  can be written as

$$\dot{\xi}_{ij}^{(m)} = \delta\mu \mu'_{ij} + \dot{p} \delta_{ij} \quad (4.27)$$

The special case of soil behavior on the undrained triaxial test discussed above is useful primarily only to figure an implementation of the model. Although the yield function, equation 4.26, is applicable to the total stress analysis with good accuracy, the pressure term in the yield function cannot be ignored for an effective stress analysis. The contribution of the mean pressure as well as the plastic volumetric flow must be taken into account.

#### 4.3.3 Effects of Bulk Shear Interaction

A coupling between changes in shear stresses and involume is an important aspect of soil behavior. This characteristic is responsible for volumetric contraction due to shear for loose or soft soils and for volumetric expansion for dense or stiff soils. In the former case pore pressure increase results from the mean pressure decrease during the undrained test carried out on a saturated loose or soft soil. Such coupling effects can be described in terms of the coupling term in the constitutive equation

4.6. This is often referred to as pressure sensitivity, which is an important feature of soil plasticity. Nonassociativity is incorporated in the coupling terms.

Figures 4.6 and 4.7 indicate a comparison between predictions obtained from the pressure-sensitive and pressure-nonsensitive analyses. Duncan (1965) carried out undrained triaxial tests on the San Francisco Bay Mud, AC U-1 and AC U-2. Sample AC U-1 represents a soil element which is  $K_0$  consolidated with the major principal stress being vertical, and sheared by increasing axial compressive stress. Sample AC U-2 represents a soil element whose initial lateral pressure is higher than the axial stress, and sheared by increasing axial stress. The model parameters were determined from the experimental data according to the method to be explained in the next section.

For the pressure-nonsensitive analysis the yield functions have no pressure terms, and nonassociativity is ignored. Accordingly the coupling terms in constitutive equation vanish. In spite of the good prediction of stress strain response shown in Figure 4.6, the pore pressure development is poorly predicted for both tests of AC U-1 and AC U-2, as shown in Figure 4.7. Conventional stress paths are drawn in Figure 4.8, in which it is obvious that the pressure-nonsensitive analysis can not predict pore pressure development due to lack of accounting for the shearing - bulk interaction. The coupling effect can be simulated by means of the pressure-sensitive analysis, which is very important in effective stress analysis.

To test the model further, it is applied to a drained triaxial test

of Cook's Bayou Sand. Figure 4.9 is obtained with the model parameters referred to in Hughes and Prevost (1979). Volumetric expansion due to shear is simulated very well. It should be noted that the model prediction of sand dilatation does not result from the volumetric hardening of the overconsolidated side of the bounding yield surface, but is created by nonassociative hardening of the nested yield surfaces. Such flexibility in representing pressure sensitivity is considered as one of the major advantages of the Prevost model.

#### 4.4 Conventional Parameter Determination Procedure

A theoretical interpretation of the model parameters is given to help explain the conventional parameter determination procedure. This is needed later to examine and improve the procedure that is not perfectly applicable to soft clays.

##### 4.4.1 Interpretation of the Conventional Parameter Evaluation Procedure

Complete specification of the Prevost model parameters requires the determination of:

1. The initial positions and sizes of the yield surface  $f_m$ ,  $\alpha^{(m)}$ ,  $\beta^{(m)}$  and  $k_m$ ,
2. The plastic moduli associated with the yield surface  $f_m$ ,  $h_m'$ ,  $B_m'$  and  $A_m$ ,
3. The elastic shear and bulk moduli,  $G$  and  $B$ ,
4. The volumetric hardening parameters such as the power exponent  $n$  and the volumetric exponent  $\lambda$ .

Among the sets of model parameters, the first two are evaluated by means

of the parameter evaluation procedure. It is a major characteristic of the Prevost model that the model parameters can be derived entirely from the experimental results of conventional soil tests. Two types of parameter evaluation procedures have been developed, one from triaxial compression and extension tests, another from a simple shear test. The former are more useful because all the stresses are known in the triaxial test. For this reason the procedure based on the results of the conventional triaxial compression test (CTC) and the reduced triaxial extension test (RTE) are to be described in this section.

The unknowns to be defined are  $\alpha^{(m)}$ ,  $\beta^{(m)}$ ,  $k^{(m)}$ ,  $h'_m$ ,  $B'_m$  and  $A_m$  for every yield surface  $f_m$ . Since  $h'_m$  and  $B'_m$  are related to the plastic modulus  $H'_m$ , they are replaced by  $H'_{mC}$  and  $H'_{mE}$ , which are  $H'_m$  values at stress points on CTC and RTE stress paths, respectively. This leaves six unknowns to be determined. Fortunately, there are six conditions available. In view of Figure 4.10(a), two consistency conditions are derived from the geometry that the stress points C and E of CTC and RTE paths are on the yield surface  $f_m$ . At the same time, stress increments applied at C and E and corresponding strain increments obtained from the constitutive equations should coincide with the experimental stress-strain curve, Figure 4.10(b). The deviatoric and volumetric equations for stress points C and E provide four kinematic conditions. Therefore the six unknowns are solved with the six conditions. This is basic idea of the parameter evaluation procedure proposed by Prevost (1980, 1983), and supplemented by Sture (1981).

A distorted triaxial plane is introduced here for convenience. It is

a plane that the triaxial plane is elongated in the direction of the hydrostatic axis by a factor of the yield surface axis ratio  $c$ . In the distorted triaxial plane, all the yield surfaces are plotted as circles whose centers are at  $(c\beta^{(m)}, \alpha^{(m)})$ , as shown in Figure 4.10. The stress path of the triaxial compression test intersects a yield surface  $f_m$  at stress point C and the radius OC makes an angle  $\theta^C$  to the hydrostatic axis. Similarly stress point E has an angle  $\theta^E$  for the triaxial extension test.

The angles  $\theta^C$  and  $\theta^E$  are unknown and primary variables in identifying the parameters. Once they are found, every parameter of the model is ready to be determined. Accordingly all the conditions are reduced to solve for  $\theta^C$  and  $\theta^E$ . The model parameters are determined for their reference values corresponding to the reference mean pressure  $p_0$  at which the volumetric strain is reset. Kinematic parameters such as  $\alpha$ ,  $\beta$  and  $k$  follow the exponential rule,  $\alpha = \alpha_0 \exp(\lambda \epsilon_V^p)$ . Elastic and plastic moduli such as  $G$ ,  $B$ ,  $H'$ ,  $h'$ , and  $B'$  follow the power law, for example  $H' = H'_0 (p/p_0)^n$  as described in the last chapter.

#### 4.4.2 Consistency Conditions

Since stress points C and E are on the yield surface  $f_m$ ,

$$q - \alpha = k \sin\theta \qquad p - \beta = \frac{k}{c} \cos\theta \qquad (4.28)$$

In the expression of reference values with subscript 0,

$$q^C = \alpha_0 \exp(\lambda \epsilon_V^C) + k_0 \exp(\lambda \epsilon_V^C) \sin\theta^C \qquad (4.29a)$$

$$p^C = \beta_0 \exp(\lambda \epsilon_V^C) + \frac{k_0}{c} \exp(\lambda \epsilon_V^C) \cos\theta^C \qquad (4.29b)$$

and similarly for the stress point E ,

$$q^E = \alpha_0 \exp(\lambda \epsilon_V^E) + k_0 \exp(\lambda \epsilon_V^E) \sin \theta^E \quad (4.30a)$$

$$p^E = \beta_0 \exp(\lambda \epsilon_V^E) + \frac{k_0}{c} \exp(\lambda \epsilon_V^E) \cos \theta^E \quad (4.30b)$$

where  $\epsilon_V^C$  and  $\epsilon_V^E$  are plastic volumetric strain. Eliminating  $\alpha_0$  ,  $\beta_0$  and  $k_0$  from equations 4.29 and 4.30, an expression relating  $\theta^C$  and  $\theta^E$  is obtained.

$$\cos \theta^C - \cos \theta^E = R_{CE} (\sin \theta^C - \sin \theta^E) \quad (4.31)$$

Using formulas of trigonometric functions, the equation simplifies to

$$\tan \frac{\theta^C + \theta^E}{2} = -R_{CE} \quad (4.32)$$

or

$$\tan (\theta^C + \theta^E) = \frac{-2R_{CE}}{1 - R_{CE}^2} \quad (4.33)$$

where

$$R_{CE} = c \frac{p^C \exp(-\lambda \epsilon_V^C) - p^E \exp(-\lambda \epsilon_V^E)}{q^C \exp(-\lambda \epsilon_V^C) - q^E \exp(-\lambda \epsilon_V^E)} \quad (4.34)$$

#### 4.4.3 Kinematic Conditions

A strain increment is related to a stress increment at the stress points C and E through the constitutive equation. The stress-strain relation in equation 4.7 is rewritten in a distorted triaxial plane with the help of equation 4.28 and yields

$$\frac{\dot{e}_q}{q} = \frac{1}{2G} + \frac{1}{H'} \sin \theta \cdot T \quad (4.35a)$$

$$\frac{\dot{\epsilon}_v}{p} = \frac{1}{B} + \frac{1}{H'} \frac{2\cos\theta + \text{sgn} \cdot \sqrt{6} A_m \sin\theta}{3\gamma} \cdot T \quad (4.35b)$$

where

$$\gamma = \frac{\dot{p}}{q} \quad \text{and} \quad \text{sgn} = \text{sign}(q - \alpha) \cdot \text{sign}(p - \beta). \quad (4.36)$$

$$T = \frac{\sin\theta + c\gamma\cos\theta}{\sin^2\theta + \frac{2}{9}c^2\cos^2\theta} \quad (4.37)$$

Equations 4.35 are modified as

$$\frac{1}{X} = \left(\frac{p}{p_0}\right)^n \frac{\dot{\epsilon}_q}{q} - \frac{1}{2G_0} = \frac{1}{H'_0} \sin\theta \cdot T \quad (4.38a)$$

$$\frac{1}{Y} = \left(\frac{p}{p_0}\right)^n \frac{\dot{\epsilon}_v}{p} - \frac{1}{B} = \frac{1}{H'} \frac{2c\cos\theta + \text{sgn}\sqrt{6} A_m \sin\theta}{3\gamma} \cdot T \quad (4.38b)$$

Eliminating  $H'$  from above equations,

$$\frac{1}{\tan\theta} = \frac{1}{2c} \left( 3\gamma \frac{X}{Y} - \text{sgn}\sqrt{6} A_m \right) \quad (4.39)$$

Now the equation is applied to the stress points C and E .

$$\frac{1}{\tan\theta^C} = \frac{1}{2c} \left( 3\gamma^C \frac{X^C}{Y^C} - \text{sgn}^C \sqrt{6} A_m \right) \quad (4.40a)$$

$$\frac{1}{\tan\theta^E} = \frac{1}{2c} \left( 3\gamma^E \frac{X^E}{Y^E} - \text{sgn}^E \sqrt{6} A_m \right) \quad (4.40b)$$

$A_m$  can be eliminated to yield,

$$\frac{1}{\tan\theta^C} \pm \frac{1}{\tan\theta^E} = \frac{1}{2c} \left( 3\gamma^C \frac{X^C}{Y^C} \pm 3\gamma^E \frac{X^E}{Y^E} \right) \quad (4.41)$$

in which the composite sign is taken as opposite sign of  $(\text{sgn}^C) (\text{sgn}^E)$  .

A detailed description on sign selection rule is given in Table 4.2.

Equations 4.33 and 4.41 are to be solved for  $\theta^C$  and  $\theta^E$  simulta-

neously. The yield a quadratic equation with respect to  $\tan\theta^C$  or  $\tan\theta^E$  as well.

#### 4.4.4 Slope Condition

When  $\theta^C$  and  $\theta^E$  are to be solved, the position of stress points C and E should be predefined on the CTC and RTE curves. These stress points are selected such that the deviatoric stress-strain curves of CTC and RTE tests have the same slopes at C and E. Knowing positions of stress points C and E, the consistency condition and the kinematic condition are applied.

In spite of the simple idea of positioning stress points, this condition is too strict to impose on the model, especially for soft clays. This point will be discussed in detail in Section 4.5.3.

#### 4.4.5 Evaluation of Parameters

All the parameters are ready to be evaluated when  $\theta^C$  and  $\theta^E$  are known. From equations 4.28 and 4.29,

$$k_0 = \frac{q^C \exp(-\lambda \epsilon_V^C) - q^E \exp(-\lambda \epsilon_V^E)}{\sin\theta^C - \sin\theta^E} \quad (4.42)$$

$$\alpha_0 = q^C \exp(-\lambda \epsilon_V^C) - k_0 \sin\theta^C \quad (4.43a)$$

$$\beta_0 = p^C \exp(-\lambda \epsilon_V^C) - \frac{k_0}{c} \cos\theta^C \quad (4.43b)$$

From equation 4.39

$$A = \frac{1}{\sqrt{6} |\tan \theta^C|} \left[ 3\gamma^C \frac{X^C}{Y^C} \tan \theta^C - 2c \right] \quad (4.44)$$

in which

$$\tan \theta \cdot \text{sgn} = \tan \theta \cdot \text{sign}(\cos \theta) \cdot \text{sign}(\sin \theta) = |\tan \theta| \quad (4.45)$$

From equation 4.38a

$$H'_0 = XT \sin \theta \quad (4.46)$$

The expression of  $H'$  in equation 3.56 can be modified in the distorted plane and

$$H' = h' + \frac{\sqrt{2}}{3} c \frac{\cos \theta}{\sin^2 \theta + \frac{2}{9} c^2 \cos^2 \theta} B' \quad (4.47)$$

Using equations 4.46 and 4.47,  $B'$  and  $h'$  can be determined,

$$B'_0 = \frac{X^C T^C \sin \theta^C - X^E T^E \sin \theta^E}{\frac{\sqrt{2}}{3} c \left[ \frac{\cos \theta^C}{(\cos^2 \theta^C + \frac{2}{9} c^2 \sin^2 \theta^C)^{1/2}} - \frac{\cos \theta^E}{(\cos^2 \theta^E + \frac{2}{9} c^2 \sin^2 \theta^E)^{1/2}} \right]} \quad (4.48)$$

$$h'_0 = H'_0 - \frac{\sqrt{2}}{3} c \frac{\cos \theta^C}{(\sin^2 \theta^C + \frac{2}{9} c^2 \cos^2 \theta^C)^{1/2}} \cdot B' \quad (4.49)$$

Now all the model parameters have been determined.

#### 4.4.6 Flow Chart

Based on the mathematical interpretation of the model parameters, the procedure to derive the parameters from the conventional triaxial compression test (CTC) and the reduced triaxial extension test (RTE) are described in an itemized form as follows:

1. Select the bulk exponent  $n$  and the yield surface axis ratio  $c$ .
2. Select  $\lambda$  of  $\epsilon_V^P$  vs  $\log p$  curve from consolidation test.
3. Decompose the test data into deviatoric relation ( $q$  vs  $e_q$ ) and volumetric relation ( $p$  vs  $\epsilon_V$ ).
4. Select elastic moduli. They can be computed from the steepest initial slope of either CTC or RTE stress-strain curve.
5. Select stress points on the CTC stress path corresponding to the desired number of yield surfaces and compute piecewise secant moduli for every selected stress point on CTC path.
6. Find stress points on the RTE stress path at which the slope of the deviatoric stress-strain curve is the same as that for the stress point of concern on the CTC path.
7. Calculate piecewise secant moduli associated with stress point found on the RTE path.
8. Solve the equations 4.33 and 4.41 for  $\theta^C$  and  $\theta^E$ .
9. Calculate the model parameters  $k_0$ ,  $\alpha_0$ ,  $\beta_0$ ,  $H'_{0C}$ ,  $H'_{0E}$ ,  $h'_0$ ,  $B'_0$ , and  $A$  for the yield surface  $f_m$ .
10. Repeat steps 6 through 9 for the next yield surface up to before the bounding yield surface.
11. Set up the bounding yield surface according to the critical state concept.

The major parts of this procedure, namely steps 4 through 10, are incorporated into a program written by the author, REDUCT, to provide model parameters to minimize the time which might be spent for repeated trials needed for parameter determination.

## 4.5 Discussion on Problems with Model Parameters

The model parameters are calculated by means of the previously described procedure and checked against the theoretical values so that implementation of the procedure may be verified. The model accurately predicts the triaxial test data used for determining the parameters. However, more careful considerations are needed to analyze problems associated with parameters determination. The slope condition has been used in the conventional parameter determination procedure. The condition is examined in detail and found to give approximate locations of the calibrate points.

### 4.5.1 Justification of Model Parameters

The implementation of the parameter evaluation procedure is checked in this section. A hypothetical undrained behavior of clay in a triaxial test was introduced in Section 4.3.2. The CTC and RTE stress paths intersect each yield surface at the two ends of the deviatoric semiaxis. These stress points have the same mean pressure and the same slope of the stress-strain curves. Such a special feature of the hypothetical soil behavior allows one to analytically evaluate the model parameters. Thus, the theoretical values of the parameters are used to compare with the predicted values by the parameter determination procedure so that the implementation of the procedure may be calibrated. The stress paths and stress-strain curves of the hypothetical data were shown in Figures 4.4 and 4.5, respectively.

The model parameters predicted by the procedure are shown in each row in Table 4.1. The yield surface parameters such as  $\alpha^{(m)}$ ,  $\beta^{(m)}$  and  $k_m$  indicate good agreement with the expected values which have been derived analytically in that section. This agreement results from the consistency condition applied in the parameter determination procedure, whereas the plastic moduli such as  $h'_m$ ,  $B'_m$ ,  $H'_m$ , and  $A_m$  show rather poor agreement.

In view of the plastic modulus  $H'_m$  which is calculated for the CTC stress path, the predicted values are reasonably in agreement with those expected. Decomposition of  $H'_m$  into the plastic shear modulus  $h'_m$  and the plastic bulk modulus  $B'_m$  is not processed as it should be. Since the stress path was designed as  $p = \beta$ , which is equivalent to  $1/\tan\theta = 0$  at the intersection of each yield surface, the theoretical solution for the determination procedure does not exist for such a special case. Discretization of the stress-strain curve makes it possible to process the data for the determination of the model parameters. But still difficulty remains in obtaining parameters, especially in the evaluation of  $B'_m$ , reflecting very a large value of  $\tan\theta$  that affects the value of  $B'_m$ , whereas  $h'_m$  shows a reasonable value compatible with the exact value because  $h'_m$  is little affected by  $\tan\theta$ . The nonassociativity constant  $A_m$  is calculated from the CTC stress path. The correspondence between the exact and the predicted values is quite good.

Using the model parameters identified, undrained CTC and RTE tests are simulated to test the overall ability of the model prediction, in which the loading conditions are exactly the same as were used for the parameter

determination. The results are plotted in Figure 4.1. They reveal excellent prediction for the stress-strain relation and the pore pressure development.

Accordingly this result is thought to verify the parameter determination procedure developed herein for the Prevost model. Since the parameters are identified to fit CTC and RTE tests results, it is natural that the model should give a good prediction to follow these tests. However, the model parameters are not related to or responsible for loading conditions other than the triaxial tests considered for the parameter determination. It is difficult to draw from the CTC and RTE tests data the general properties of soil which are effective within entire stress field. The parameter satisfies the necessary conditions for the model implementation. Sufficient conditions are not considered through the parameter determination procedure so that problems are caused, as will be discussed next.

#### 4.5.2 Defective Aspect of the Model

The basic concept of the parameter evaluation procedure proposed by Prevost (1981) is expressed by the fact that the model parameters are determined so as to fit the experimental results. The idea is rather simple. With the parameters the model accurately follows the stress-strain curves that have been used for the parameter determination. In spite of this, some defective aspects must be recognized to properly apply the model.

(1) The parameters not unconditional

Equations 4.33 and 4.41 are solved for  $\theta^C$  and  $\theta^E$  with certain necessary conditions. For undrained stress paths of the CTC and RTE tests the solution is obtained such that  $(\text{sgn}^C)(\text{sgn}^E) > 0$ . This is equivalent to saying that the stress points lay in the first and the third quadrants with respect to the semiaxes of the yield surface as shown in Figure 4.12.

When the value of the consistency condition 4.33 becomes small relative to the kinematic condition 4.41, due to the value of  $R_{CE}$  in equation 4.34, no solution exists. Such a case happens when the mean pressure of the stress points on the CTC and RTE paths are very close to each other and stress points are plotted near the deviatoric semiaxis of the yield surface, as in the special case examined in Section 4.3.2. If the mean pressure of the extension test is larger than that of the compression test, then the solution is assured, as shown in Figure 4.12. In the early stage of loading the mean pressure has close values for the CTC and RTE tests and may result in some difficulty. No complete set of model parameters can be solved in such cases.

(2) Kinematic condition for RTE path found very strict.

When the stress points are plotted in the first and the third quadrants of the yield surface concerned, a discontinuous nonassociativity with a negative value is required to follow the stress paths. Nonassociativity was introduced to reduce plastic volumetric strain  $\dot{\epsilon}_V^P$ , as was explained in Section 3.4.5. Since the total volumetric strain increment

$\dot{\epsilon}_V$  is equal to zero for an undrained test, the plastic volumetric strain increment  $\dot{\epsilon}_V^P$  is in the opposite direction of elastic volumetric strain  $\dot{\epsilon}_V^E$ . Variable  $\dot{\epsilon}_V^P$  is negative due to a decrease in mean pressure, and hence  $\dot{\epsilon}_V^P$  orients positively on the hydrostatic axis. This situation is shown in Figure 4.12. Because nonassociativity parameter  $A_m$  is a constant for all the points on  $f_m$ , the stress point E on the RTE path should lie somewhere very close to the deviatoric semiaxis of  $f_m$ . This causes two types of problems: (1) overlapping of yield surfaces, and (2) unrealistic field moduli.

### (3) Overlapping of yield surfaces

In Figure 4.13 the stress point  $E_m$  on the RTE path moves with  $m$  toward the negative direction on the hydrostatic axis, and shifts the position of the outer yield surfaces to the left due to the reason described above. Then the spacing between the yield surfaces becomes small for the upper-right portion and eventually they begin to intersect. If the initial stress state exhibits a high anisotropy with a low  $K_0$  value and/or a high pore pressure parameter  $A_f$ , then the intersection of yield surfaces is more likely to occur. A similar problem is also seen in Figure 4.4. However, the yield surfaces do not intersect along the CTC and RTE stress paths since the consistency condition is imposed along those paths. Once the yield surface intersects, inversion of constitutive equation is no longer possible and the uniqueness of the solution for a new stress and strain state is not guaranteed. Suppose the nested yield surfaces are those in Figure 4.13. When a loading is applied such that the stress path

goes into the overlapping area shaded in the figure, the model is not able to deal with this situation because of a lack of the uniqueness in the stress-strain relation. This is a critical problem in applying the Prevost model, in particular for boundary value problems.

(4) Unrealistic field of plastic moduli results from the poor evaluation of  $B'_m$ .

$B'_m$  plays the role of a volumetric part of the plastic modulus  $H'_m$ , and the degree of its contribution depends on the relative distance of the stress point from the deviatoric semiaxis to the size of the yield surface. If the relative distance is small, and  $\tan\theta^E$  is close to infinity like that shown in Figure 4.12, it becomes hard to evaluate  $B'_m$ . The plastic bulk modulus  $B'_m$  with a large value relative to the plastic shear modulus  $h'_m$  is often obtained from undrained test data for soft clays. Then equation 3.56 suggests that a region of negative plastic moduli  $H'_m$  is developed on the right side of the yield surfaces,  $Q'^{(m)} < 0$ . This situation is shown schematically in Figure 4.14(a). The negative plastic modulus  $H'_m$  is responsible for a reverse flow and dilatation due to shear which is acceptable only outside of the critical state line. No stress paths are allowed to enter a region with negative  $H'_m$  in order to provide a realistic prediction of soil behavior. Because of the unrealistic field of the plastic moduli, limitations to the model applicability are inevitable. An example is provided in Figure 4.14(b), a stress path for the loading and unloading phase of a  $K_0$  consolidation. Upon unloading, the stress path AB enters the region with a negative plastic modulus and the model

prediction becomes ineffective.

(5) Different stress path predicted for extension test

The innermost yield surface bounds the elastic region within which no mean pressure change theoretically develops because of the constant volume condition of the undrained test. The stress path corresponding to the elastic region is parallel to the deviatoric axis or vertical, Figure 4.15(a). Therefore, the theoretical stress path reaches the elastic surface in the fourth quadrant as indicated with path R in the figure. However, a reduction of mean pressure is observed at the very beginning of the loading in the experimental results of the extension test, and the stress point actually reaches the elastic surface in the third quadrant as with path L. After the stress point touches the elastic surface, a plastic modulus is mobilized to develop a plastic strain, and the yield surfaces are translated with the stress point according to Mroz's translation rule. The currently active yield surface moves toward the conjugate point of the next outer yield surface. The conjugate points are located in the same quadrant of the respective semiaxis of yield surfaces. Consequently, the experimental stress path and the resulting model prediction are different, as shown in the illustration in the figure. The conditions are all the same for the two paths except for the location of the elastic yield surface. Path R reaches the elastic surface in the fourth quadrant, whereas path L does so in the third quadrant. Only minor differences are observed in the extension stress-strain curves in Figure 4.15(a), but there is a clear difference for the mean pressure change, Figure 4.15(b).

The limitations lie in the model prediction of the pore pressure development in the undrained extension test or for undrained unloading events in general.

(6) Model parameters not defined along a part of the extension stress path.

The conventional parameter evaluation procedure selects two stress points each on the CTC and RTE paths where the slopes of stress-strain curves are the same. The initial slope of the stress-strain curves are different and steeper for the RTE test than for the CTC test so that some stress points on the RTE path can not find their partner points on the CTC path. The model parameters cannot be determined with the lack of information. Such a situation occurs in the early stages of loading in the extension test.

The problems described previously derive mainly from inconformities between the model characteristics and the parameter evaluation procedure. The overlapping of yield surfaces and the unrealistic distribution of plastic moduli are especially important problems for a general application to analyze soil behavior. To circumvent these problems, some new concepts are developed.

#### 4.5.3 Examination of Slope Condition

The slope condition (Figure 4.16) used in the conventional model parameter evaluation procedure is examined in this section. The slope condition simply states that two stress points each on the CTC and RTE paths

are used to calibrate a yield surface where the slopes of the respective deviatoric stress-strain curves are the same.

The slope condition was first applied to the original version of the model by Prevost (1977), which was pressure-nonsensitive and used with pure kinematic hardening only. Total stress analyses for clays were carried out with this model. The slope condition was further applied to the effective stress approach, Prevost (1980). It was reported that the model parameters were successfully obtained to predict soil behavior in good agreement with the experimental results.

However, as has been described, difficulties arise in the evaluation of parameters for an effective stress analysis of soft clays. Direct application of Prevost's procedure is difficult for a normally consolidated or slightly overconsolidated clay whose pore pressure parameter at failure is close to unity. This requires further development.

Starting with the deviatoric stress strain relationship on the tri-axial plane, equation 4.7b gives

$$\dot{e}_y = \frac{\dot{q}}{2G} + \frac{3}{2H} Q'_Y \frac{Q'_Y \dot{q} + 3Q''\dot{p}}{|Q_{kl}|^2} \quad (4.50)$$

and using the power rule with a reference pressure  $p$ , we obtain

$$\left(\frac{p}{p_0}\right)^n \frac{\dot{e}_y}{q} = \frac{1}{2G_0} + \frac{3}{2H_0} Q'_Y \frac{Q'_Y + 3Q''\gamma}{|Q_{kl}|^2} \quad (4.51)$$

in which

$$e_y = \epsilon_y - \epsilon_x \quad (4.52a)$$

$$Q'_Y = 3(s_Y - \alpha_Y) = 2(q - \alpha) \quad (4.52b)$$

$$\gamma = \frac{\dot{p}}{\dot{q}} \quad (4.52c)$$

$$Q'' = \frac{3}{2}c^2 (p - \beta) \quad (4.52d)$$

Now the slopes of stress-strain curves are compared for the compression and extension tests.

$$\begin{aligned} \Delta &= \left[ 4 \left( \frac{p}{p_0} \right)^n \frac{\dot{e}_Y}{\dot{q}} \right]^C - \left[ 4 \left( \frac{p}{p_0} \right)^n \frac{\dot{e}_Y}{\dot{q}} \right]^E \\ &= \frac{6}{H_0^C} Q'_Y{}^C \frac{Q'_Y{}^C + 3Q''^C \gamma^C}{|Q_{k1}^C|^2} - \frac{6}{H_0^E} Q'_Y{}^E \frac{Q'_Y{}^E + 3Q''^E \gamma^E}{|Q_{k1}^E|^2} \end{aligned} \quad (4.53)$$

The slope condition is expressed as

$$\Delta = 0 \quad (4.54)$$

For the following discussion it is assumed for the sake of simplicity that  $H_0$  is a constant along the yield surface and  $c$  is  $3/\sqrt{2}$ , which yields  $|Q_{k1}|^2 = 6k^2$ . The equation 4.53 simplifies to

$$H_0 k^2 \Delta = (Q'_Y{}^C)^2 - (Q'_Y{}^E)^2 + 3[(Q'_Y{}^C Q''^C \gamma^C) - (Q'_Y{}^E Q''^E \gamma^E)] \quad (4.55)$$

Three types of simulations can be drawn from the above equation.

Case 1.  $Q'_Y{}^C = Q'_Y{}^E = 0$  then  $\Delta = 0$  (4.56)

This is a consolidation path. The stress path passes through the apex of hydrostatic semiaxis of yield surface and plastic strain develops in the

same direction of the hydrostatic pressure, Figure 4.17(a). The special case with  $\alpha_Y = 0$  corresponds to an isotropic consolidation.

$$\text{Case 2. } Q'_Y C = -Q'_Y E, \quad Q''_Y C_\gamma C = -Q''_Y E_\gamma E = \delta \quad \text{then } \Delta = 0 \quad (4.57)$$

This is the case of main concern. For  $\delta > 0$ , the second condition is rewritten as

$$(p^C - \beta) \left(\frac{\dot{p}}{q}\right)^C = -(p^E - \beta) \left(\frac{\dot{p}}{q}\right)^E \quad (4.58)$$

The slope of the stress path in  $p - q$  plane is proportional to the distance from the center of the yield surface along the hydrostatic semiaxis.

A special case with positive value of  $\delta$  in which

$$p^C - \beta = -(p^E - \beta) > 0$$

$$\text{and } \left(\frac{\dot{p}}{q}\right)^C = \left(\frac{\dot{p}}{q}\right)^E > 0 \quad (4.59)$$

is the drained behavior of the compression and reduced extension tests, Figure 4.17(b). Another case where

$$p^C - \beta = -(p^E - \beta) < 0$$

$$\text{and } \left(\frac{\dot{p}}{q}\right)^C = \left(\frac{\dot{p}}{q}\right)^E < 0 \quad (4.60)$$

corresponds to the drained behavior of the reduced compression and loading extension test, Figure 4.17(c).

When  $\delta$  is negative, the second condition of this case is related to undrained behavior, Figure 4.17(d), and written in the form of

$$(p^C - \beta) \left(\frac{1}{3} - a^C\right) = (p^E - \beta) \left(\frac{1}{3} - a^E\right) \quad (4.61)$$

where  $a^C$  and  $a^E$  are pore pressure parameters  $A$  in the undrained tri-

axial test. The pore pressure development is related to the inverse of the distance along the hydrostatic axis from the center of the yield surface, for the special situation

$$p^C = p^E = \beta \quad (4.62)$$

Stress points lie on the apex of shear semiaxis of the yield surface as is shown in Figure 4.17(e). When  $a$  is equal to  $1/3$  in equation 4.61, the stress points reflect shearing without coupling between the shear stress and mean pressure.

Case 3.  $Q'_Y{}^C = Q'_Y{}^E \neq 0, \quad Q''_{\gamma}{}^C = Q''_{\gamma}{}^E \quad \text{then} \quad \Delta = 0 \quad (4.63)$

Analogous to the second condition, this case is related to the drained behavior of loading compression and the reduced compression tests.

All the variety of stress paths are covered by equation 4.55 such that the slopes of the  $\epsilon_y$  vs  $q$  curve are the same at the stress points C and E. In this sense the slope condition seems to be suitable. However the violation of restrictions imposed on equation 4.55 causes an inadequacy of the slope condition and produces difficulty in the evaluation of the model parameters. The yield surface axis ratio  $c$  may not equal  $3/\sqrt{2}$  in general. A much smaller value of  $c$  is forcibly used for soft clays. The hardening modulus  $H_0$  is not a constant, but varies along the hydrostatic axis.

Among the various stress paths, only one in Figure 4.17(e) exactly satisfies these restrictions. Prevost (1978b) confined his undrained behavior to that path.

The conventional parameter evaluation procedure uses the slope condition in positioning the stress points, C and E, where a yield surface is calibrated. The slope condition is satisfactory within the theoretical framework of the model but it limits the capacity of the model application, especially for soft clays. The slope condition is not a required condition to obtain parameters. Instead, it will be used in the further development for a reference in finding the approximate positions of the points, C and E.

#### 4.6 Improved Evaluation of Model Parameters

In order to settle problems discussed previously, an attempt to improve the parameter determination for the Prevost model is described, considering the following points: loading history, field of plastic moduli and translation zone.

##### 4.6.1 Consideration of Loading History

Conventionally, the yield surface and associated plastic moduli are defined in terms only of two stress points on the CTC and RTE paths. This step implicitly assumes that the loading history undergone by a soil element is totally depicted in the stress-strain curves obtained from CTC and RTE tests on that soil. This may be true for most cases, but not in all. Consequently, no attention has been given to the relative configuration of the nested yield surfaces, thus often causing the overlapping of yield surfaces for soft clays in particular. If the loading history of soil elements is taken into account explicitly, the configuration of the yield

surfaces may be improved to avoid their overlapping. Since soft clays are usually subjected to  $K_0$  consolidation before being sheared, this process needs to be accounted for to draw a relative configuration of the nested surfaces.

During successive yielding of the soil, a stress point moves in the stress space while it stays on the yield surface. Since consolidation involves volumetric yielding, the stress point is on the bounding surface  $f_p$ , as shown in Figure 4.18(a). All the yield surfaces initially centered on the origin of stress space are tangential to  $f_p$  at the stress point on the  $K_0$  line. The volumetric hardening rule adopted conforms with the critical state. After consolidation, the stress may be kept constant for a period of time. A reduction of the void ratio results from an aging effect (Bjerrum 1973) in such circumstances, and this is responsible for the expansion of the yield surfaces, Figure 4.18(c). Now it is assumed that such expansion of yield surfaces occurs first from the outer yield surface and isotropically with respect to the origin of stress space, Figure 4.18(b). These expanded surfaces may express the line segment A'B in Figure 4.18(c). The outer surface expands more than the inner surfaces do, since the consolidation line is smoothly asymptote to the normal consolidation line at B. And thus overlapping of the yield surface is avoidable.

Consideration of  $K_0$  consolidation as a loading history can be useful for a substitution of the slope condition in the model parameter evaluation procedure. However, it leads to an overdetermination of the system when used together with the conventional parameter determination procedure. The

loading history consideration provides one more condition in determining the locus of the yield surface center besides the consistency condition, and thus  $\alpha^{(m)}$ ,  $\beta^{(m)}$  and  $k_m$  are solved at one time. The remaining three unknowns of  $h_m^I$ ,  $B_m^I$  and  $A_m$  do not satisfy the four kinematic conditions. Therefore, information less effective in parameter determination is ignored in order to obtain a complete set of solutions for the parameters. A good case in point is the condition on the nonassociativity constant  $A_m$  at stress point E on the RTE path. Such a measure results in a larger value of  $A_m$  relative to that obtained from the conventional procedure, thus the model prediction becomes less accurate for RTE stress path. This is believed to be the best way to eliminate the intersection of yield surfaces.

#### 4.6.2 Bulk Modulus Constraint

$H_m^I$  constitutes a field of moduli in the stress space. Unfortunately, the parameter determination procedure provides a poor evaluation, commonly with large values, of the plastic bulk modulus  $B_m^I$ . However, since the plastic bulk modulus is directly related to the volumetric response of the soil, information from consolidation tests is considered the most valuable in evaluating or modifying the plastic bulk modulus so that a realistic field of the plastic moduli may be constructed.

A path is considered such that it passes the apex points on the hydrostatic semiaxis of the yield surfaces shown as  $C_m C_p$  and  $E_m E_p$  in Figure 4.19. This is a path of consolidation which produces the plastic volumetric strain  $\dot{\epsilon}_v^P$ , but not the plastic deviatoric strain  $\dot{\epsilon}_v^D$ . The plastic moduli

$H'_m$  changes its value along the yield surface with the extreme values at points  $C_m$  and  $E_m$ .

$$H'_m = 3 \frac{\partial k}{\partial \epsilon_v} \frac{p}{k} \quad (4.64)$$

The  $\dot{\epsilon}_v$  vs  $\dot{p}$  relation along those paths can be expressed by

$$\dot{\epsilon}_v = \left( \frac{1}{B} + \frac{3}{H'_m} \right) \dot{p} = \frac{1}{B_{ep}^{(m)}} \dot{p} \quad (4.65)$$

where  $B$  and  $B_{ep}^{(m)}$  are the elastic bulk modulus and the elastic plastic bulk modulus, respectively. The value of  $B_{ep}^{(m)}$  on  $f_1$  is equal to  $B$  because  $H'_1 = \infty$ .

Mroz, et al. (1978) introduced an interpolation rule to calculate plastic moduli  $H'_m$  in terms of its values on  $f_1$  and  $f_p$  yield surfaces. Similarly the elastic plastic bulk modulus  $B_{ep}^{(m)}$  is interpolated in terms of  $B$  and  $B_{ep}^{(p)}$  along the paths  $C_m C_p$  and  $E_m E_p$  and shown in Figure 4.19,

$$B_{ep}^{(m)} - B_{ep}^{(p)} = \left| \frac{k_p - k_m}{k_p - k_1} \right|^\gamma (B - B_{ep}^{(m)}) \quad (4.66)$$

where  $\gamma$  is a material constant. Assuming the same value of  $\gamma$  for the two paths, a condition is obtained that the distribution of the plastic modulus  $H'_m$  should satisfy

$$H_{mE} (H_{pC} + 3B) = H_{mC} (H_{pE} + 3B) - 3(H_{mC} - H_{mE}) \quad (4.67)$$

$H_{mC}$  and  $H_{mE}$  are related to model parameters  $h'_m$  and  $B'_m$  which are constants over the yield surface  $f_m$ .

$$H_{mC} = h'_m + B'_m \quad (4.68a)$$

$$H_{mE} = h'_m - B'_m \quad (4.68b)$$

Therefore, the magnitude of the model parameters,  $h'_m$  and  $B'_m$ , can be defined.

The interpolation rule and the reference value of  $B_{ep}^{(p)}$  have an important role in this approach. An example of  $B_{ep}$  variations with relative size of yield surface  $k_m/k_p$  are shown in Figure 4.20, which are calculated from the unloading phase of the consolidation tests. Although  $B_{ep}^{(p)}$  at  $E_p$  is not defined, a small negative value could be used without causing problems. Because of the large value of  $B$  compared to that of  $B_{ep}^{(p)}$ ,  $B_{ep}$  at  $C_p$  is always larger than but not very different from  $B_{ep}$  at  $E_p$ . This leads to a comparable magnitude of the model parameters  $h'_m$  and  $B'_m$  and positive plastic modulus  $H'_m$  for the entire stress space within  $f_p$  except for the vicinity around the stress point  $E_p$  on  $f_p$ .

Stress points on CTC and RTE paths can be found such that the bulk modulus constraint is satisfied through the parameter determination procedure, and a reasonable distribution of the plastic moduli is obtained.

Note that the bulk modulus constraint is a necessary condition to eliminate the unrealistic distribution of plastic moduli. Stress points on CTC and RTE paths at high stress levels can not satisfy the bulk modulus constraint since the slope of stress-strain curve is flattened so that the plastic moduli  $H'_m$  in such a situation becomes small relative to the bulk modulus  $B_{ep}^{(m)}$  for consolidation. This type of difficulty results from an attempt to simulate soil behavior corresponding to the flattened part of stress-strain curve by means of the high level nested yield surfaces. The

bounding surface can follow the stress point in such a situation.

#### 4.6.3 Transition Zone at Low Stress Levels

The initial tangent of the stress-strain curve for an extension test is generally different from and higher than that for a compression test. This fact is derived from the inherent anisotropy of soil which is created during consolidation (Duncan 1965, Hansen 1980). When this anisotropy is to be accounted for in the model parameter determination, a difficulty occurs with the slope condition. Since the maximum slope of the compression curve is generally less than the slope of the extension curve, data points can not be found on the compression curve such that its slope is the same as the slope of data points on the extension curve. This is shown in Figure 4.21 in which  $E_i^C$  and  $E_i^E$  are initial tangents of  $q - e_y$  curves for compression and extension tests, respectively. A stress point B can be found on the extension curve, the slope of which  $E_B^E$  is equal to  $E_i^C$ . Then there is no partner point on the compression curve for a point on the segment AB of extension curve. The stress point corresponding to C may be selected as point A but still the slope of the stress-strain curve associated with  $f_m$  surface can not be defined, and the respective parameters are not obtained. Direct application of the conventional procedure for  $f_m$  often results in the intersection of the yield surfaces, and as a result certain model parameters are undefined.

Even if the loading history is considered in lieu of the slope condition, this problem also happens for the region within  $f_t$  and along path segment AB. This region is referred to as a transition zone bounded by

the transition yield surface  $f_t$ . As illustrated in Figure 4.18, outside of the transition surface the stress state has been affected by the aging effect, but inside of  $f_t$  it has not. Therefore the yield surface  $f_t$  is in the transition state of the aging influence.

One possible solution is to assume elastic and plastically rigid behavior within the transition yield surface  $f_t$ . However this is not successful because the transition zone is a direct reflection of the anisotropy in the stress-strain relation and is not negligible. The higher the yielding anisotropy of soil is, the larger the transition zone becomes. Therefore it is necessary to develop a modified parameter determination procedure for the transition zone.

A yield surface  $f_m$  which is within the transition zone is to be identified from information of stress points A and C in Figure 4.21. Instead of applying the kinematic conditions at point A, which are not defined, the tangent condition of contacting yield surfaces is issued from equation 3.38:

$$\frac{\sigma_{ij} - \xi_{ij}^{(m)}}{k_m} = \frac{\sigma_{ij} - \xi_{ij}^{(t)}}{k_t} \quad (4.69)$$

where  $\sigma_{ij}$  is a stress at A. The yield surface  $f_t$  bounding the transition zone is assumed to have already been identified. Equation 4.69 is projected onto the triaxial plane and yields the distorted  $q - cp$  plane, and

$$\theta_m^A = \theta_t^A \quad (4.70)$$

where  $\theta_t^A$  an angle between radius  $O_t A$  and the hydrostatic axis. From

the consistency condition, equation 4.33, which simply states that stress points A and C stay on the  $f_m$ , we obtain

$$\tan(\theta^A + \theta^B) = \frac{-2R}{1 - R^2} \quad (4.71)$$

So  $\theta_m^C$  is solved and the  $f_m$  is fully determined.

Now derivatives of stress-strain curve at point C give the values of

$$\frac{1}{X_B} = \left(\frac{p}{p_0}\right)^n \left(\frac{\dot{\epsilon}}{q}\right)_B - \frac{1}{2G_0} \quad (4.72a)$$

$$\frac{1}{Y_B} = \left(\frac{\dot{p}}{p}\right)^n \left(\frac{\dot{\epsilon}_v}{p}\right)_B - \frac{1}{B_0} \quad (4.72b)$$

$$\gamma_B = \left(\frac{\dot{p}}{q}\right)_B \quad (4.73)$$

And the plastic moduli at C can be calculated by

$$H_m^C = X \sin\theta^C \frac{\sin\theta^C + c \gamma_C \cos\theta^C}{\sin^2\theta^C + \frac{2}{9} c^2 \cos^2\theta^C} \quad (4.74)$$

$H_m^C$  is expressed in terms of two independent parameters,  $h'_m$  and  $B'_m$ .

$$H_m^C = h'_m + \frac{\sqrt{2}}{3} c \frac{\cos\theta^C}{(\sin^2\theta^C + \frac{2}{9} c^2 \cos^2\theta^C)^{1/2}} \cdot B'_m \quad (4.75)$$

According to the bulk modulus constraint, equation 4.67,  $h'_m$  and  $B'_m$  are related to each other:

$$a_1 h'_m + a_2 B'_m = a_3 \quad (4.76)$$

where  $a_1$ ,  $a_2$  and  $a_3$  are constants. Equations 4.75 and 4.76 are solved simultaneously for  $h'_m$  and  $B'_m$ . The nonassociativity parameter

$A_m$  is defined in the same manner as in the conventional method.

$$A_m = \frac{1}{\sqrt{6} |\tan \theta^c|} \left| 3\gamma_C \frac{X_C}{Y_C} - 2c \right| \quad (4.77)$$

Thus, parameter identification for the transition zone is completed.

#### 4.6.4 Model Prediction with New Model Parameters

With considerations given to the stress history, the bulk modulus constraint and the transition zone, measures to improve the model parameter determination procedure have been discussed. It is difficult to take everything into account since the procedure is no longer a matter of simple routine. Judgement is necessary to establish model parameters.

Because the quantity of information on soil behavior is usually much greater than the number of parameters incorporated in the model, a prediction of the model and its initialization process can be improved by introducing new parameters. Mould (1983) did so for the purpose of permitting greater flexibility for positioning the yield surfaces. However, such an approach does not seem appropriate because an increase in the number of model parameters requires a proportional increase in the complexity.

The model parameters are identified for San Francisco Bay Mud which is normally consolidated under  $K_0 = 0.5$ . The parameters were obtained using the improved procedure and a given set of triaxial test data (Table 4.3). Figure 4.22 shows a configuration of yield surfaces. The stress-strain curves and stress paths for both compression and extension tests are shown in Figure 4.23.

Model predictions show good agreement with the original data for the CTC test, but it is not quite as good for the RTE test. The predicted stress-path corresponding to the extension test depends somewhat on the original path since the condition on the nonassociativity was ignored for the RTE outside of the transition zone.

#### 4.7 Summary and Conclusions

The model parameter determination procedure and associated problems were described, and the procedure was modified so that the model may be applied to soft clays.

The capability of the model to predict soil behavior was examined for volumetric response to mean pressure and pore pressure development due to undrained shear. A coupling between shear stress and volume change was discussed in view of the model prediction for a pore pressure development in an undrained test and a dilatation of sand in a drained test.

Model parameters have been conventionally determined such that the model may follow the CTC and RTE test results. The idea is simple, but the model provides a good prediction for the loading conditions that have been used for the parameter determination. However, problems are often encountered during a model parameter evaluation with the conventional procedure, especially for soft clays, such as the overlapping of the yield surfaces, unrealistic distribution of plastic moduli, parameters undefined, and so on. These problems are not acceptable for a numerical implementation of the model. Accordingly, the procedure to evaluate the model para-

meters were modified to settle the problems with consideration of the loading history, the bulk modulus constraint, and the transition zone. In this approach the procedure is no longer a matter of simple routine, but requires judgements to be made. Although the model does not follow the calibration data of CTC and RTE test exactly, it provides satisfactory predictions for undrained triaxial tests on a soft clay of San Francisco Bay Mud.

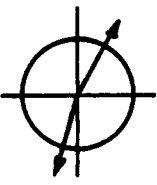
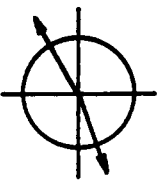
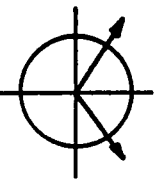
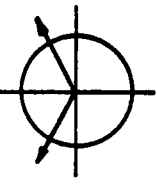
The loading conditions concerned in this chapter were limited to and identical to the conditions used for the parameter determination. The loading conditions other than the above will be examined later.

Table 4.1 Prevost Model Parameters Identified from a Special Case of Triaxial Test

$G = 61.333$      $B = 163.55$      $n = 1.0$      $c = 1.50$   
 $\sigma_{x_0} = \sigma_{z_0} = 0.8$      $\sigma_{y_0} = 1.0$      $\tau_{ij} = 0$     up: exact  
down: predicted

m	$\alpha^{(m)}/\sigma'_{y_0}$	$\beta^{(m)}/\sigma'_{y_0}$	$k_m/\sigma'_{y_0}$	$h'_m/\sigma'_{y_0}$	$B'_m/\sigma'_{y_0}$	$H'_m/\sigma'_{y_0}$	$A_m$ ( $\times 10^{-2}$ )
2	0.2081	0.8000	0.0920	357.6	0.0	357.6	0.0
	0.2081	0.7943	0.09236	1378.0	-19172.0	273.2	-10.02
3	0.1673	0.8000	0.1327	117.4	0.0	117.4	-2.347
	0.1706	0.7865	0.1310	169.8	-553.4	113.2	-2.362
4	0.1650	0.7560	0.2250	62.34	0.0	62.34	-1.874
	0.1604	0.7583	0.2315	65.84	-64.55	60.00	-1.739
5	0.1545	0.7560	0.2975	39.71	0.0	39.71	-1.469
	0.1557	0.7344	0.3004	34.17	66.22	38.86	-1.634
6	0.1500	0.7360	0.3465	24.37	0.0	24.37	-0.9573
	0.1500	0.7174	0.3472	22.43	29.37	29.17	-0.7825
7	0.1445	0.7072	0.4135	14.54	0.0	14.54	-0.6203
	0.1443	0.6940	0.4138	13.56	76.64	16.15	-0.5813
8	0.1405	0.6872	0.4565	9.713	0.0	9.713	-0.4790
	0.1394	0.6762	0.4557	12.97	-61.50	11.25	-0.2934
9	0.1375	0.6712	0.4865	7.050	0.0	7.050	-0.3990
	0.1376	0.6606	0.4869	7.715	21.19	8.191	-0.3415
10	0.1355	0.6576	0.5085	5.092	0.0	5.092	-0.2927
	0.1360	0.6488	0.5091	4.991	58.46	5.995	-0.3232
11	0.1335	0.6424	0.5325	3.192	0.0	3.192	-0.2352
	0.1338	0.6344	0.5329	4.064	25.67	4.428	-0.2665
12	0.1310	0.6176	0.5630	1.621	0.0	1.621	-0.1708
	0.1301	0.6123	0.5622	2.833	-12.96	2.665	-0.0406
13	0.1280	0.5872	0.5900	1.484	0.0	1.484	-0.2784
	0.1285	0.5818	0.5905	1.207	-2.137	1.192	-0.3215
P	0.126	0.5376	0.6235	0.0	0.0	0.0	0.0
	0.126	0.5376	0.6235	0.0	0.0	0.0	0.0

Table 4.2 Sign Selection Rule in Model Parameter Evaluation Procedure

Case	1	2	3	4
Stress path				
$\text{Sgn}^C$	+	-	+	-
$\text{Sgn}^E$	+	-	-	+
$\text{sgn}^C \cdot \text{sgn}^E$	+	+	-	-
$\tan\theta^C$	+	-	+	-
$\tan\theta^E$	+	-	-	+
$\tan\theta^C \cdot \tan\theta^E$	+	+	-	-
$\tan\theta \cdot \text{sgn}$	+	+	+	+

note:  $\text{sgn} = \text{sign}(p-\beta) \cdot \text{sign}(q-\alpha)$

$$\tan\theta = \frac{q-\alpha}{c(p-\beta)}$$

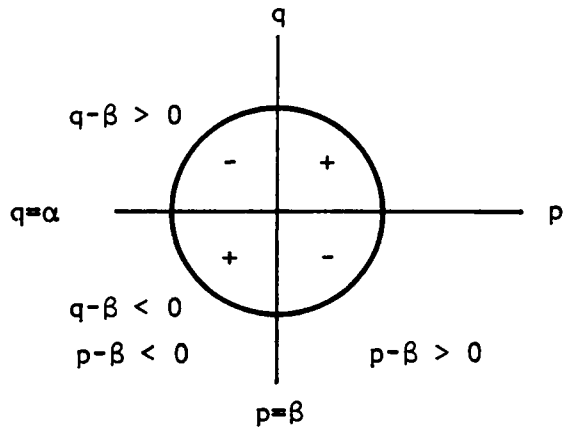


Table 4.3 Prevost Model Parameters for San Francisco Bay Mud

(  $K_0 = 0.5$  )

$G/\sigma'_{v_0} = 72.9$      $B/\sigma'_{v_0} = 145.8$      $n = 1.0$      $\lambda = 10.6$      $c = 1.0$

m	$\alpha^{(m)}/\sigma'_{v_0}$	$\beta^{(m)}/\sigma'_{v_0}$	$k_m/\sigma'_{v_0}$	$h'_m/\sigma'_{v_0}$	$B'_m/\sigma'_{v_0}$	$A_m$
2	0.4733	0.6539	0.0296	1104	65.97	-0.477
3	0.4589	0.6469	0.0456	564.1	44.86	-0.448
4	0.4330	0.6345	0.0743	273.4	33.48	-0.431
5	0.3908	0.6143	0.1211	114.6	27.27	-0.327
6	0.3339	0.5870	0.1843	57.98	25.75	-0.230
7	0.260	0.553	0.264	26.08	9.48	-0.118
8	0.201	0.556	0.385	7.34	9.44	-0.141
9	0.124	0.523	0.462	2.33	9.68	-0.147
10	0.104	0.510	0.489	0.64	0.40	-0.155
11	0.0858	0.500	0.5143	0.0	0.0	0.0

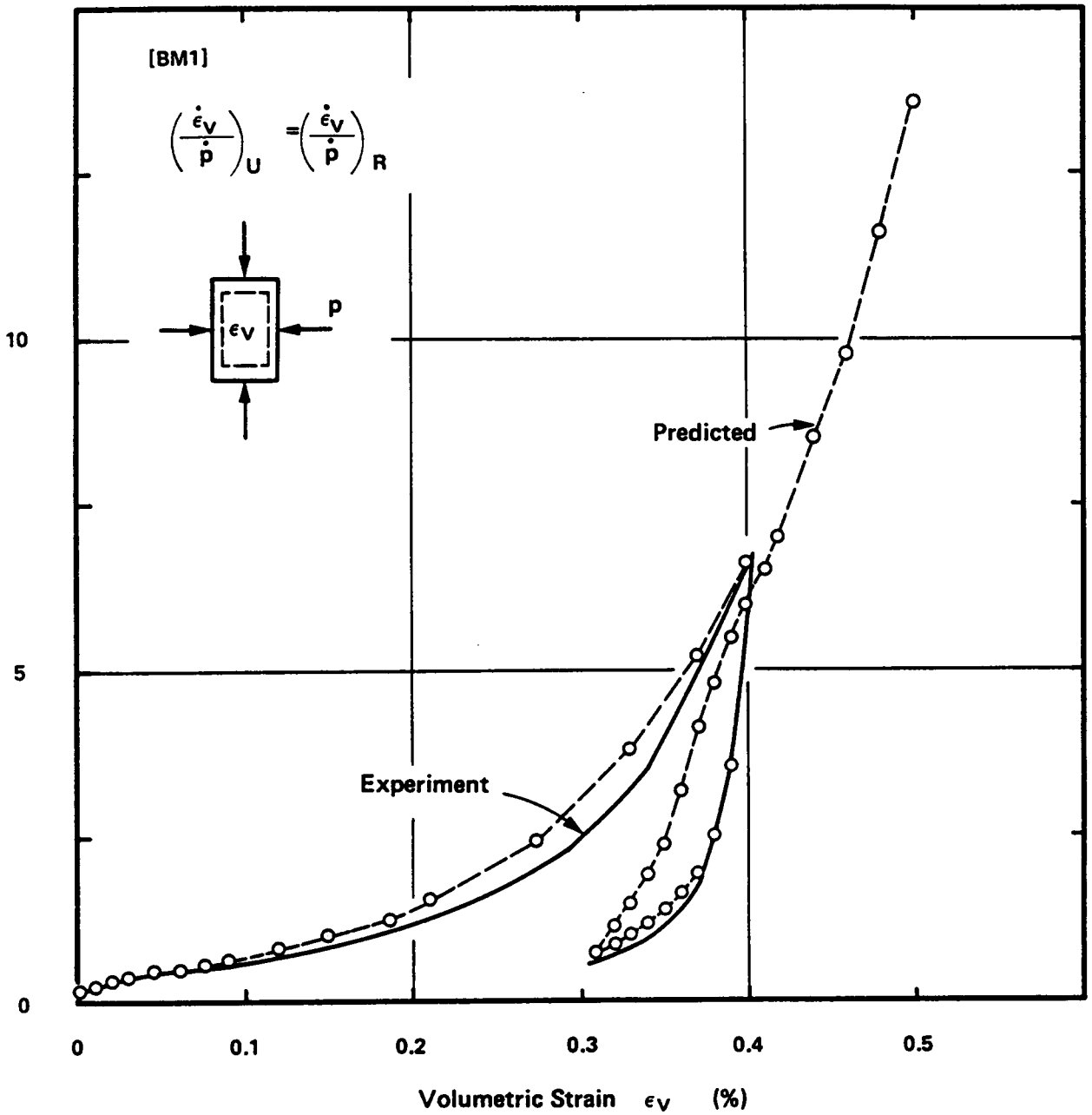


Figure 4.1 Volumetric Strain vs Mean Pressure Relation of Consolidation Test (Data Modified after Duncan 1962)

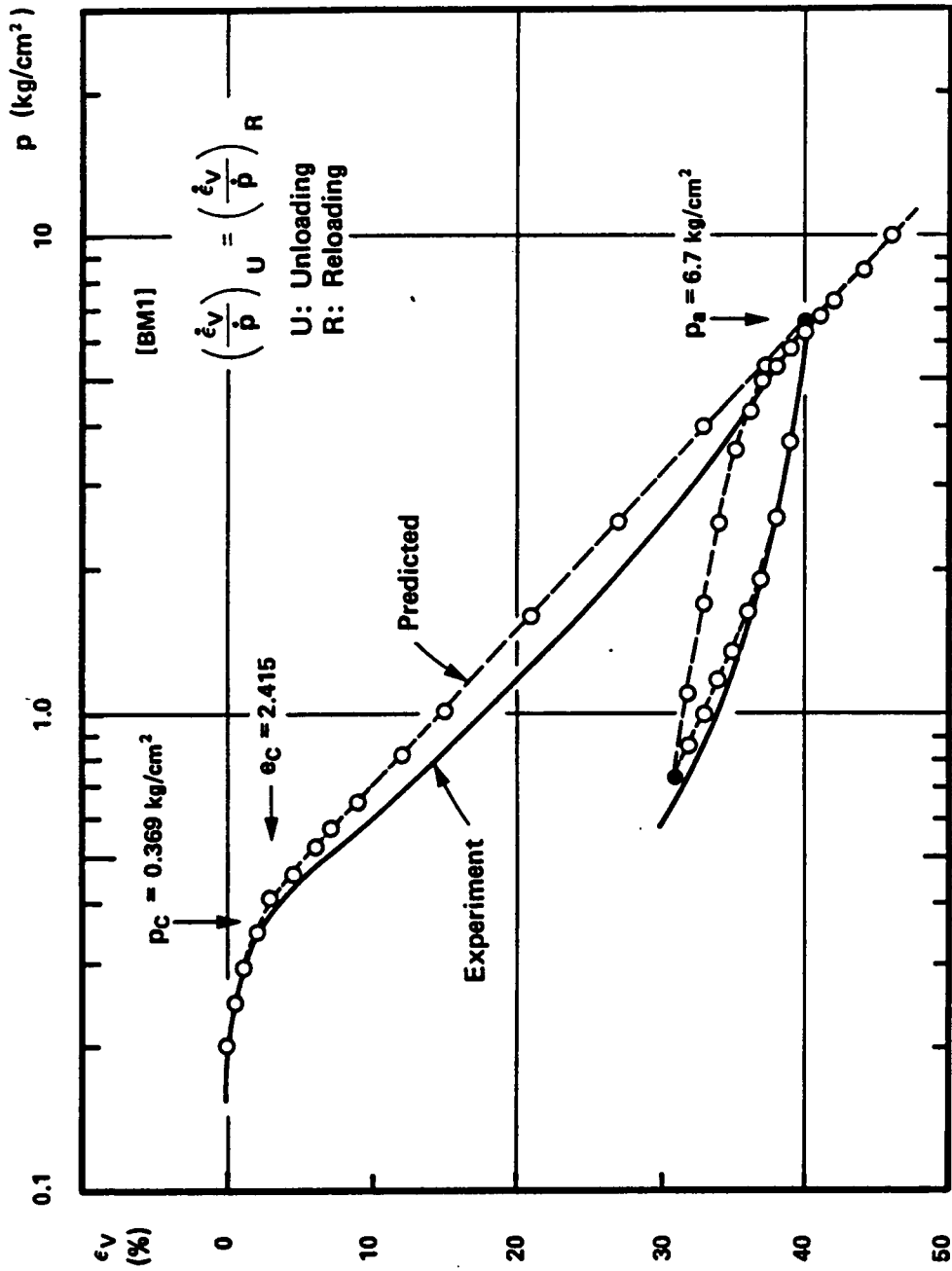


Figure 4.2 Relation between Volumetric Strain and Logarithm of Mean Pressure of Consolidation Test (Data Modified after Duncan 1962)



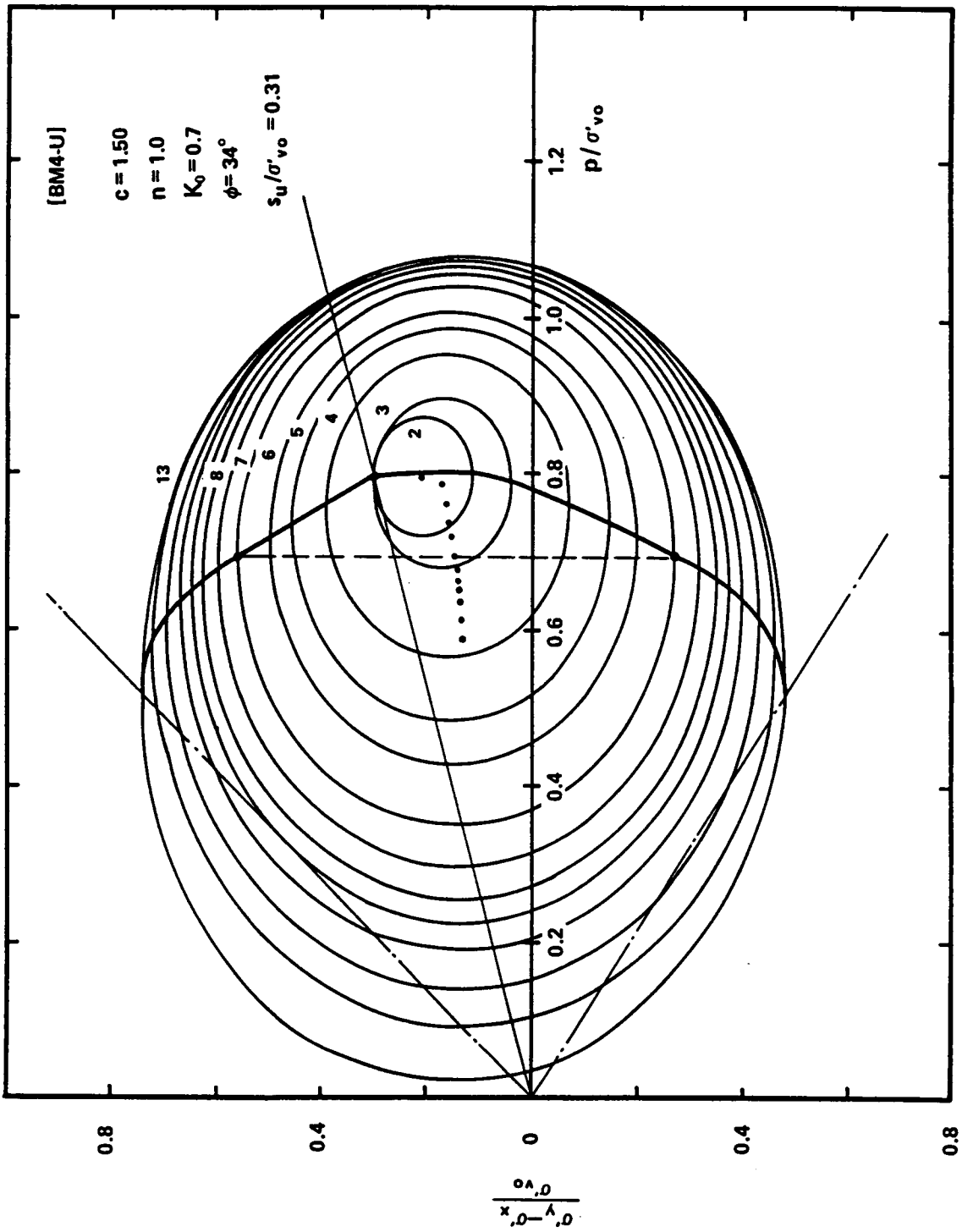


Figure 4.4 Stress Paths and Yield Surfaces for a Hypothetical Undrained Behavior on Triaxial Test

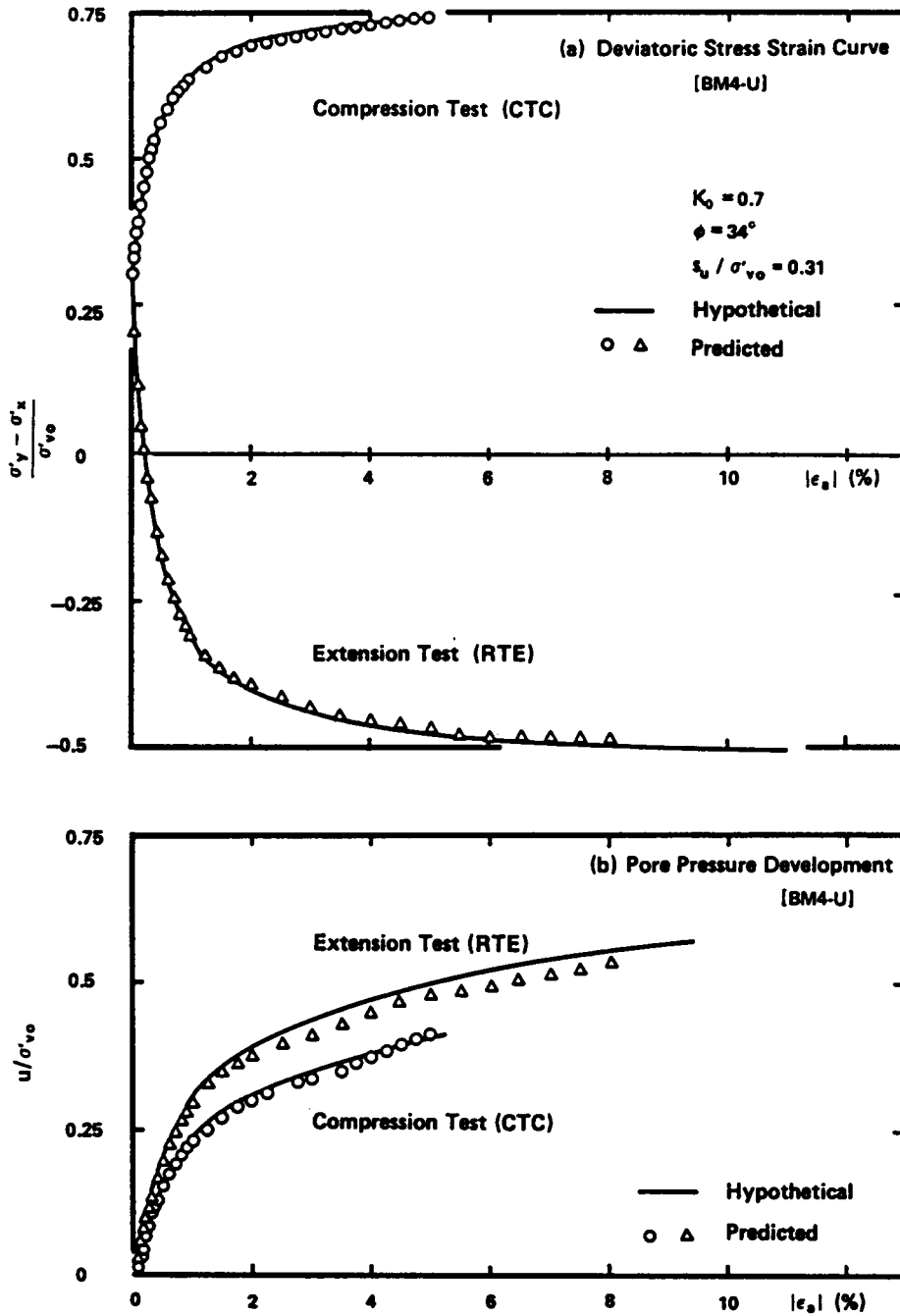


Figure 4.5 Stress-Strain Curve and Excess Pore Pressure Development for a Triaxial Test

$\sigma_y - \sigma_x$  (kg/cm<sup>2</sup>)

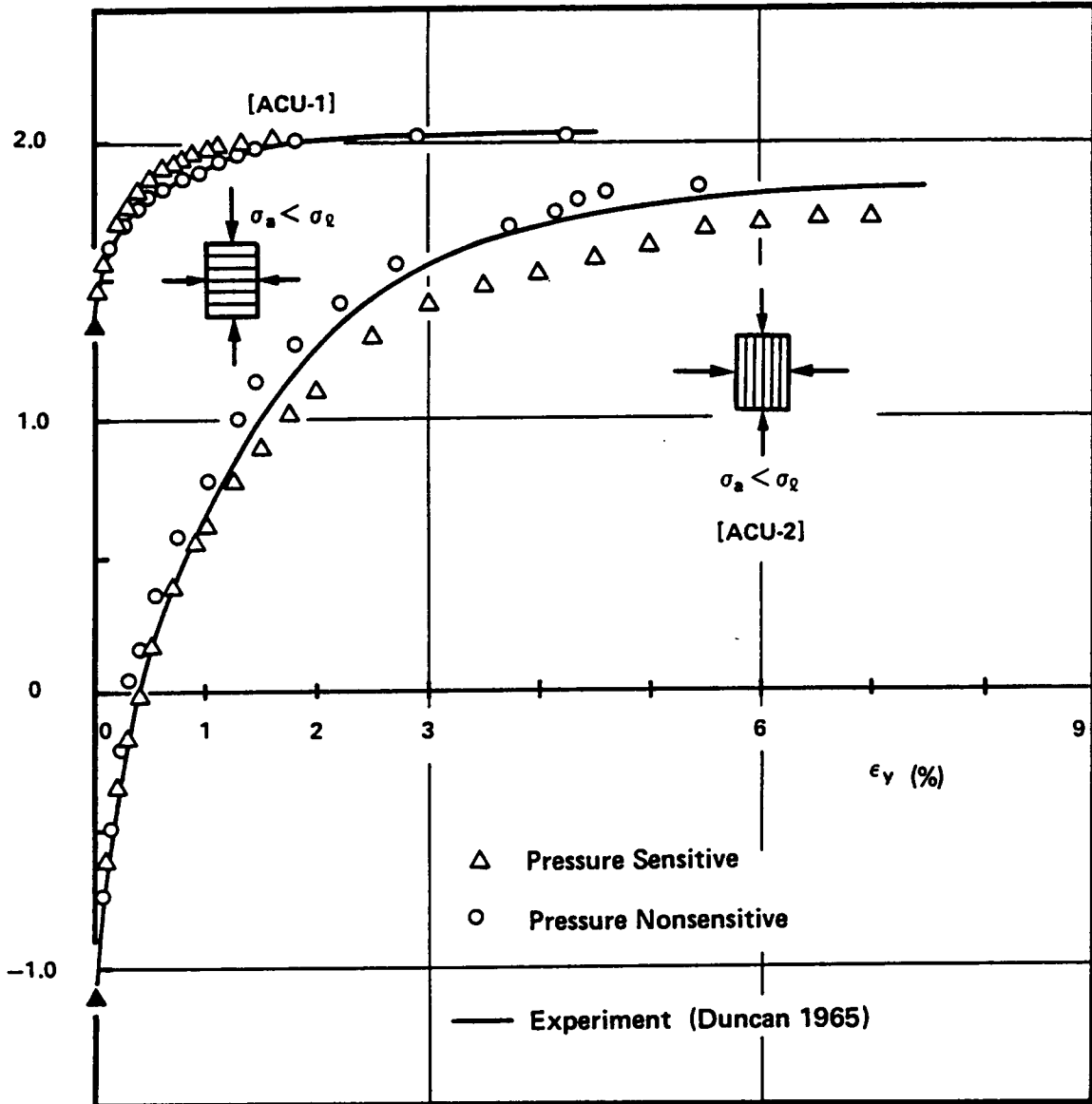


Figure 4.6 Comparison of Stress-Strain Curves Predicted by Pressure Sensitive and Pressure Nonsensitive Models Simulating Undrained Triaxial Tests

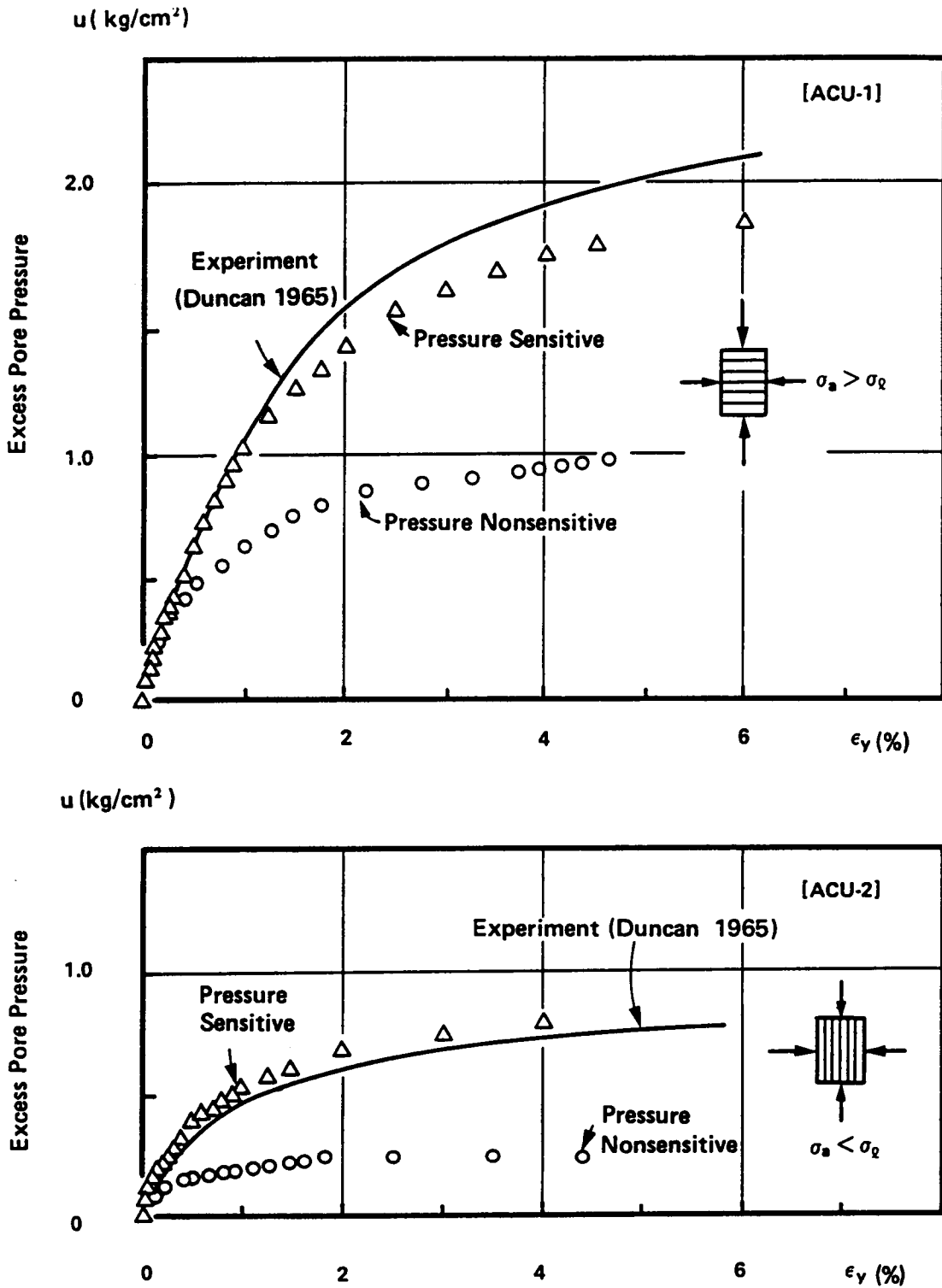


Figure 4.7 Comparison of Excess Pore Pressure Development Predicted by Pressure Sensitive and Pressure Nonsensitive Models Simulating Undrained Triaxial Tests

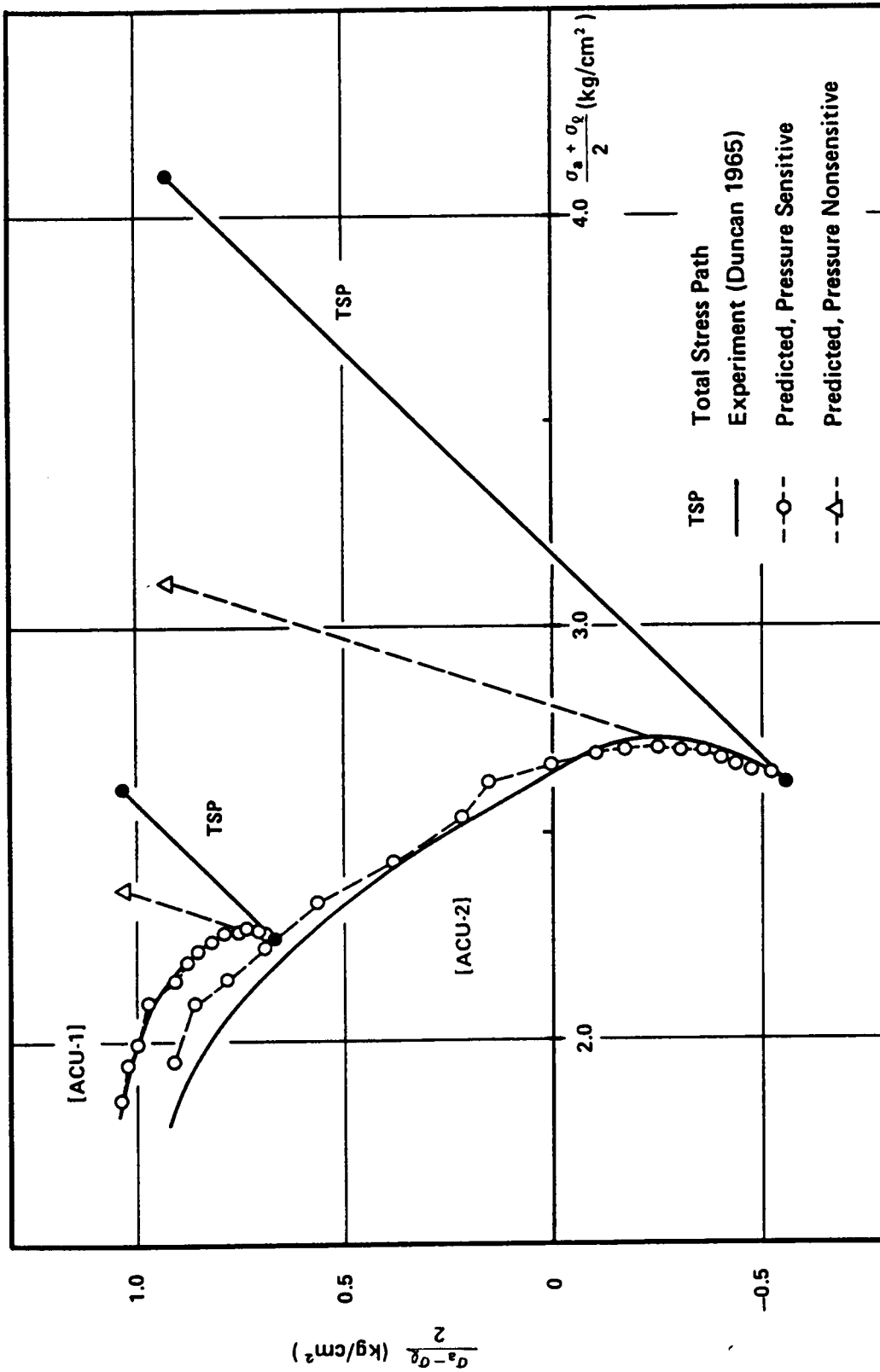


Figure 4.8 Comparison of Conventional Stress Paths for Pressure Sensitive and Pressure Nonsensitive Models Simulating Undrained Triaxial Tests

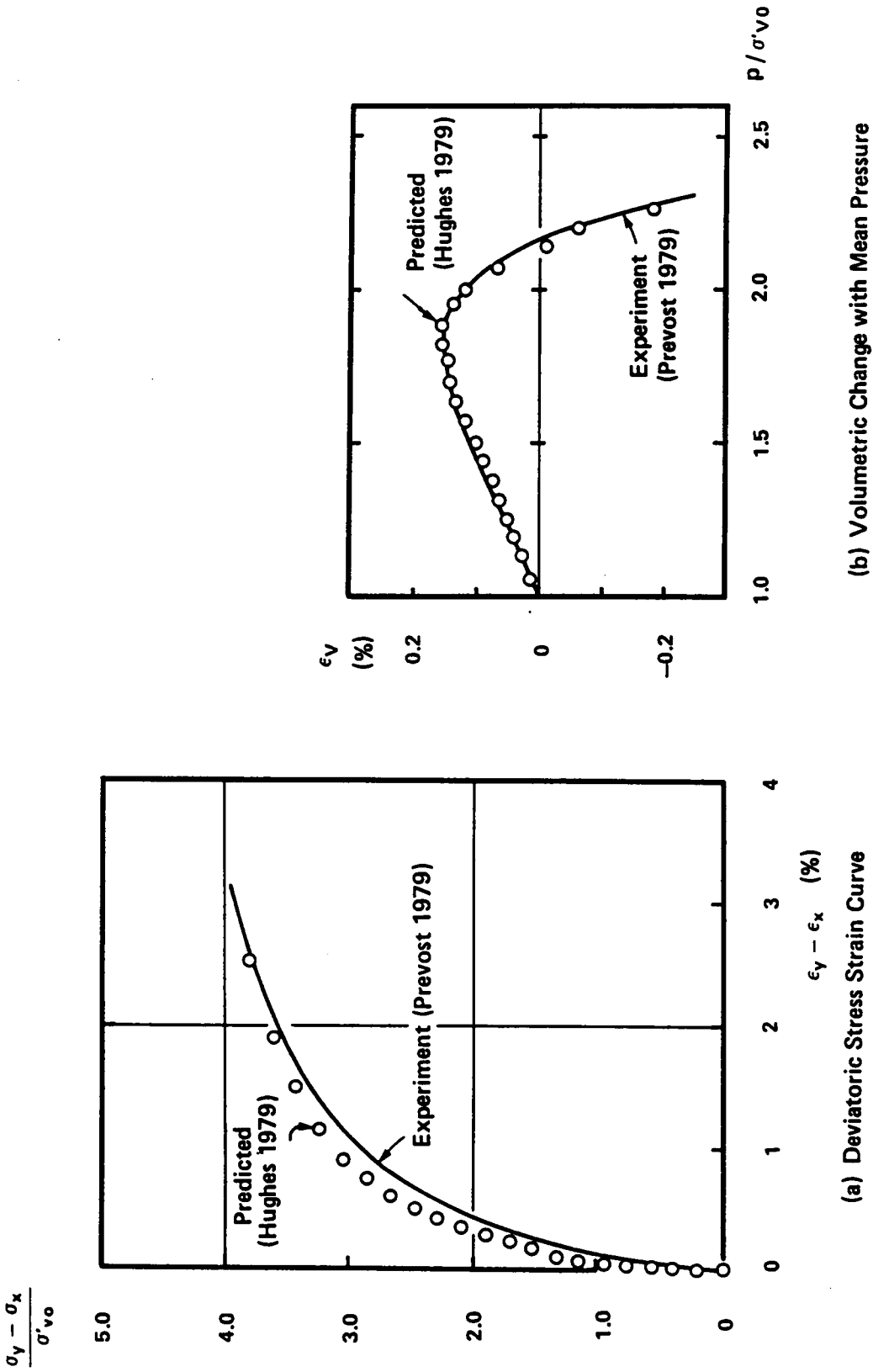
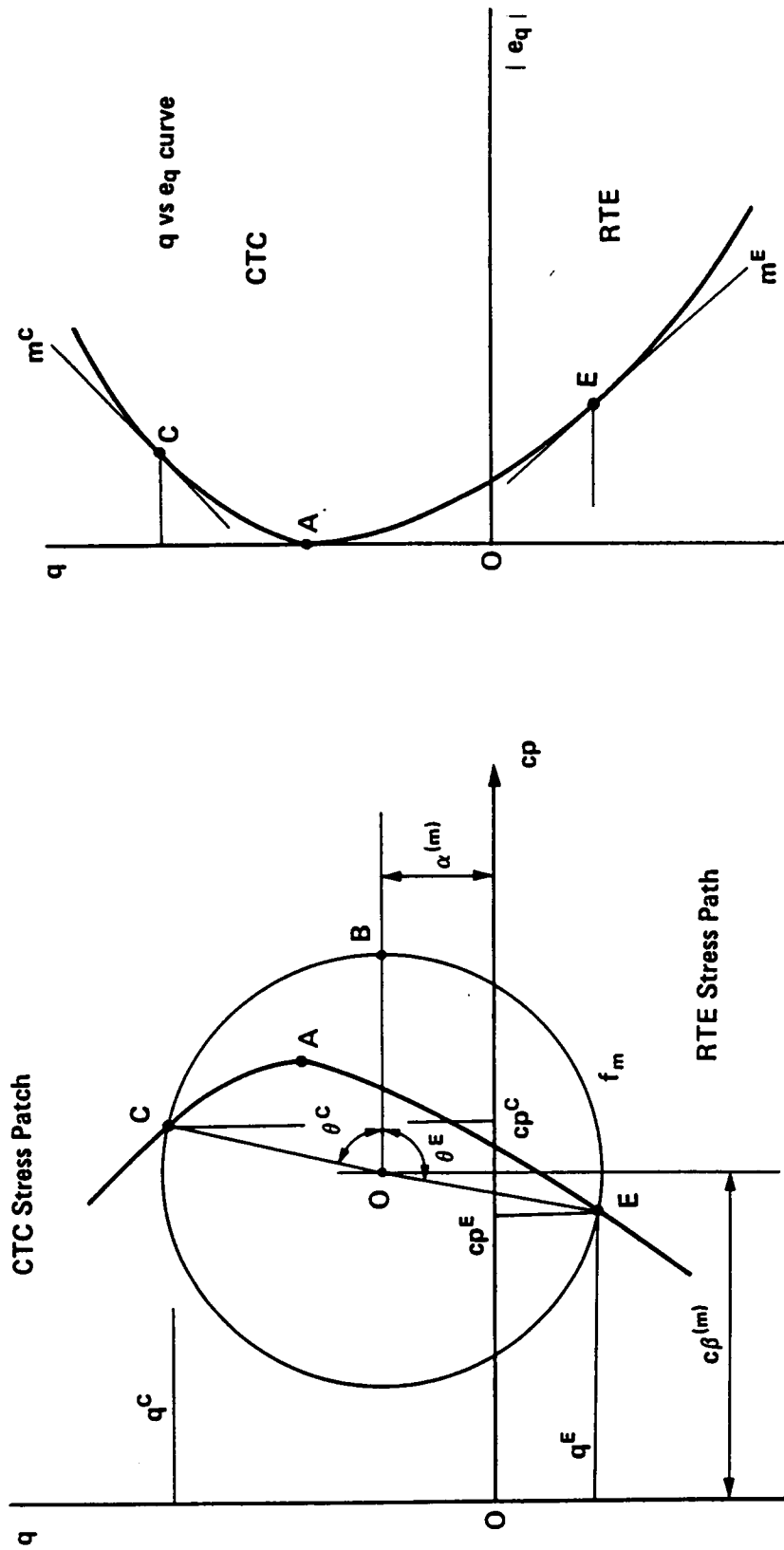


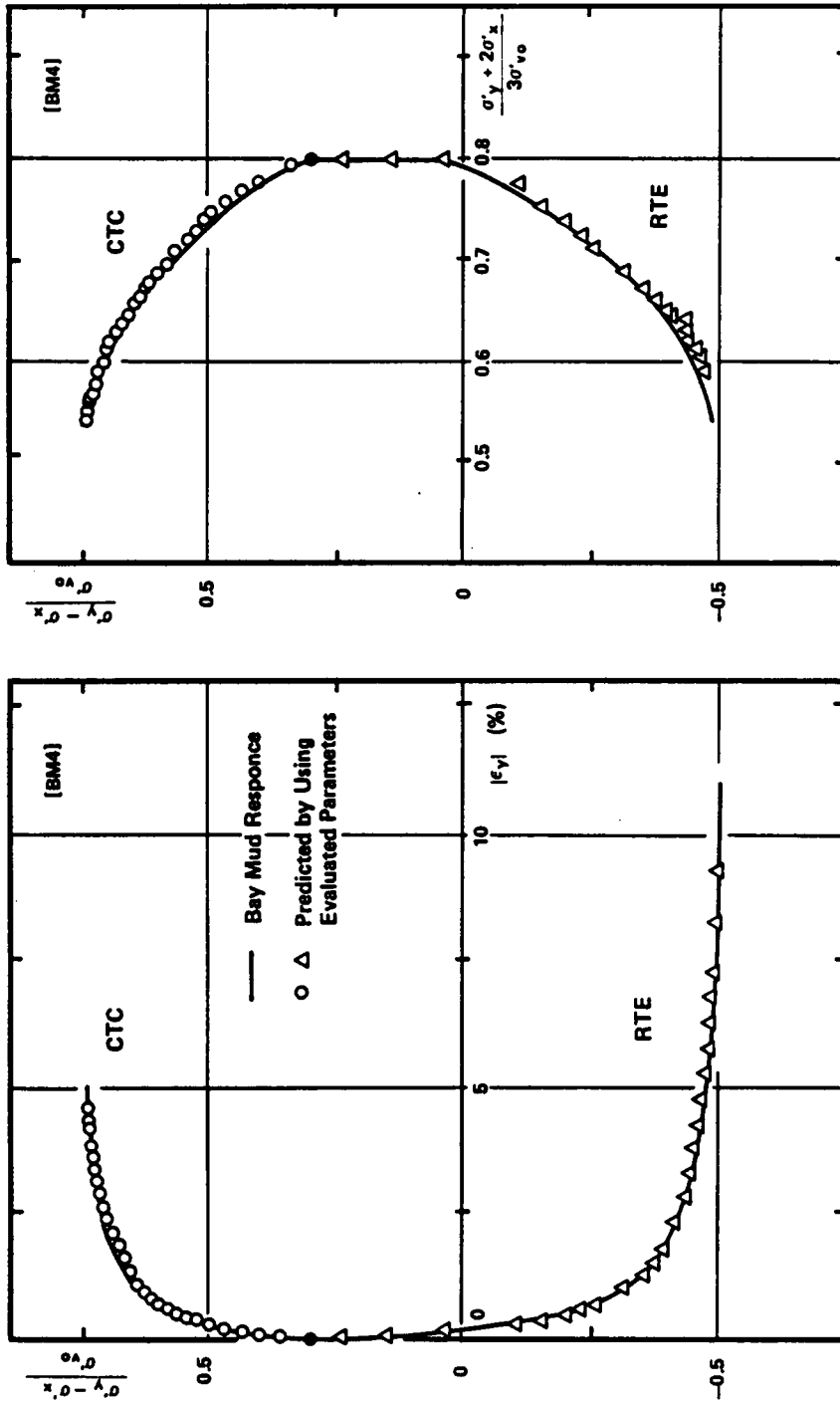
Figure 4.9 Predicted Shearing Deformation and Dilatation of Sand on Drained Triaxial Test with Model Parameters Referred to Hughes (1979)



(a) Distorted Triaxial Plane (q-cp Plane)

(b) Deviatoric Stress Strain Curve

Figure 4.10 Model Parameter Evaluation Procedure on Distorted Triaxial Plane associated with Stress-Strain Curve



(b) Effective Stress Paths

(a) Deviatoric Stress Strain Relations

Figure 4.11 Comparison of Predicted Stress-Strain Curves and Stress Paths with Calibration Data

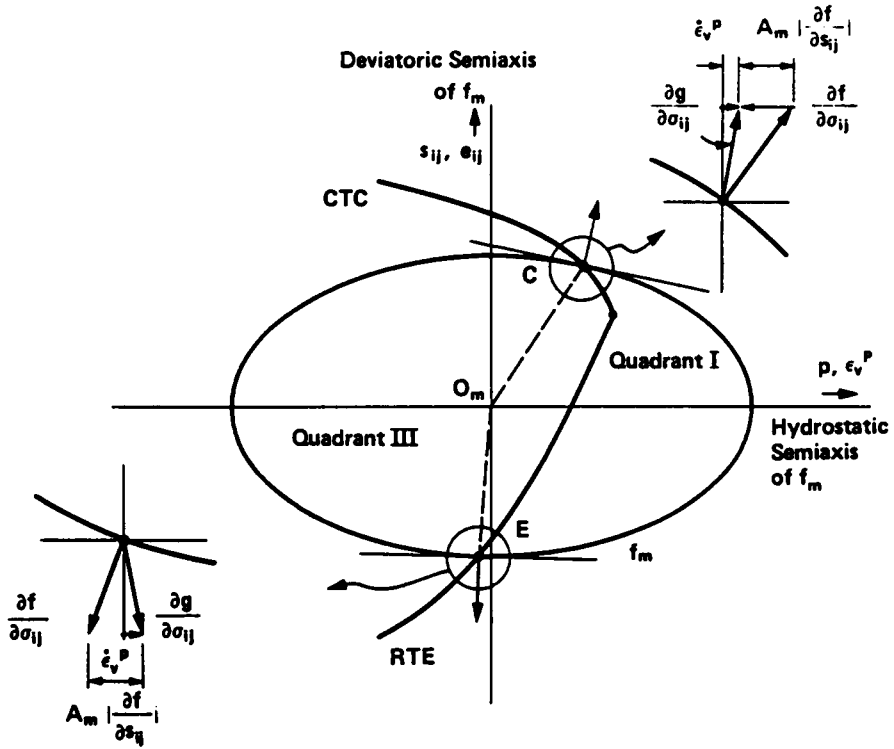


Figure 4.12 Position of Stress Points on  $f_m$  in Relation to Nonassociative Flow Rule

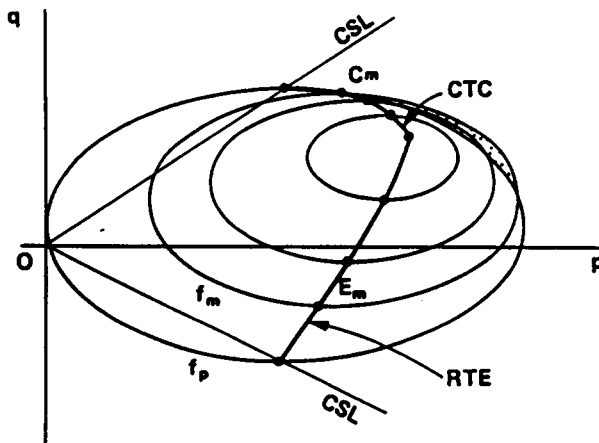
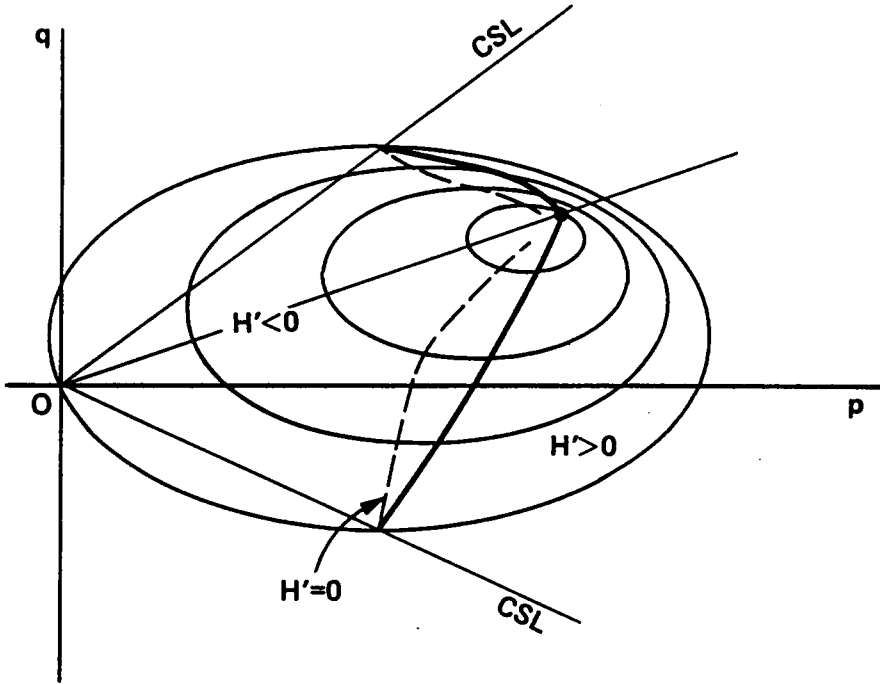
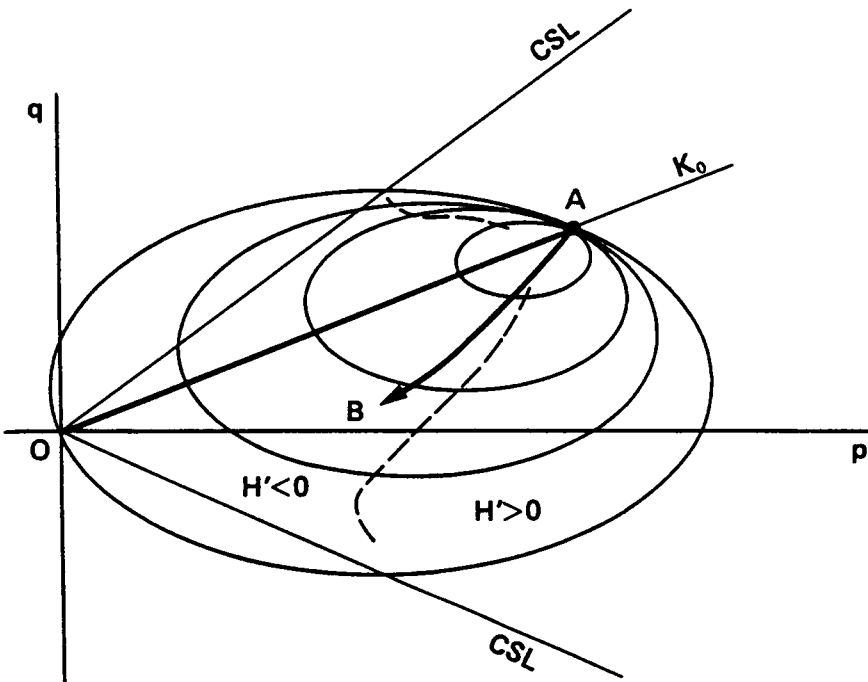


Figure 4.13 Overlapping of Yield Surfaces

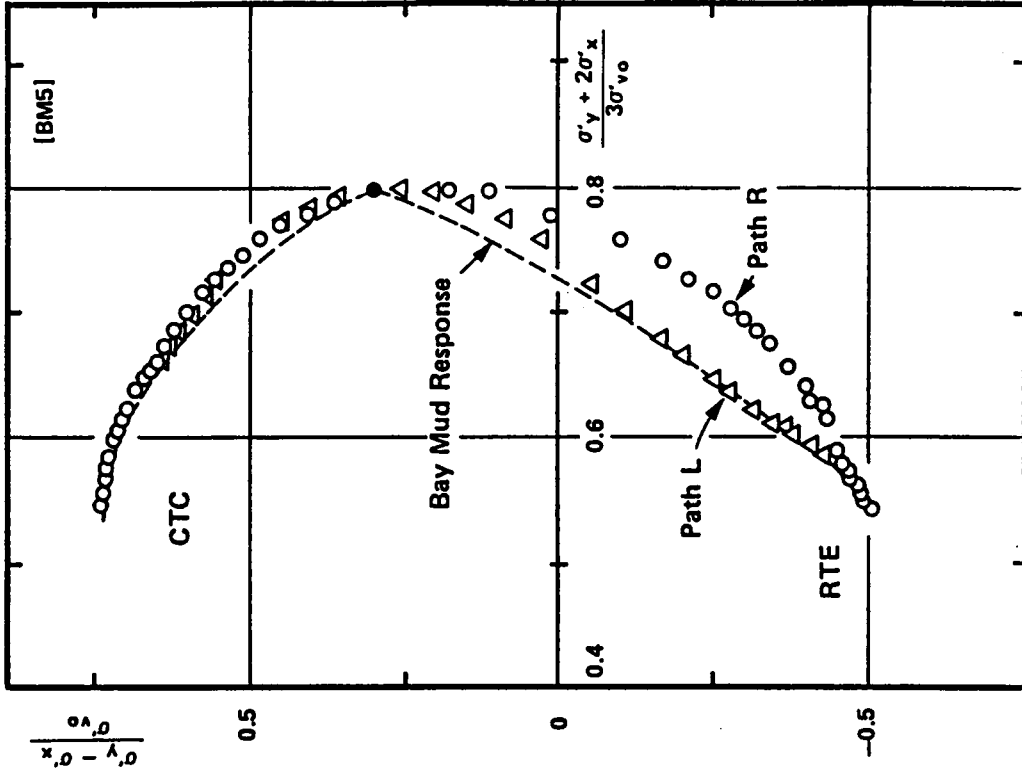


(a) Distribution of  $H'$  Associated with  $f_m$  in  $q - p$  plane

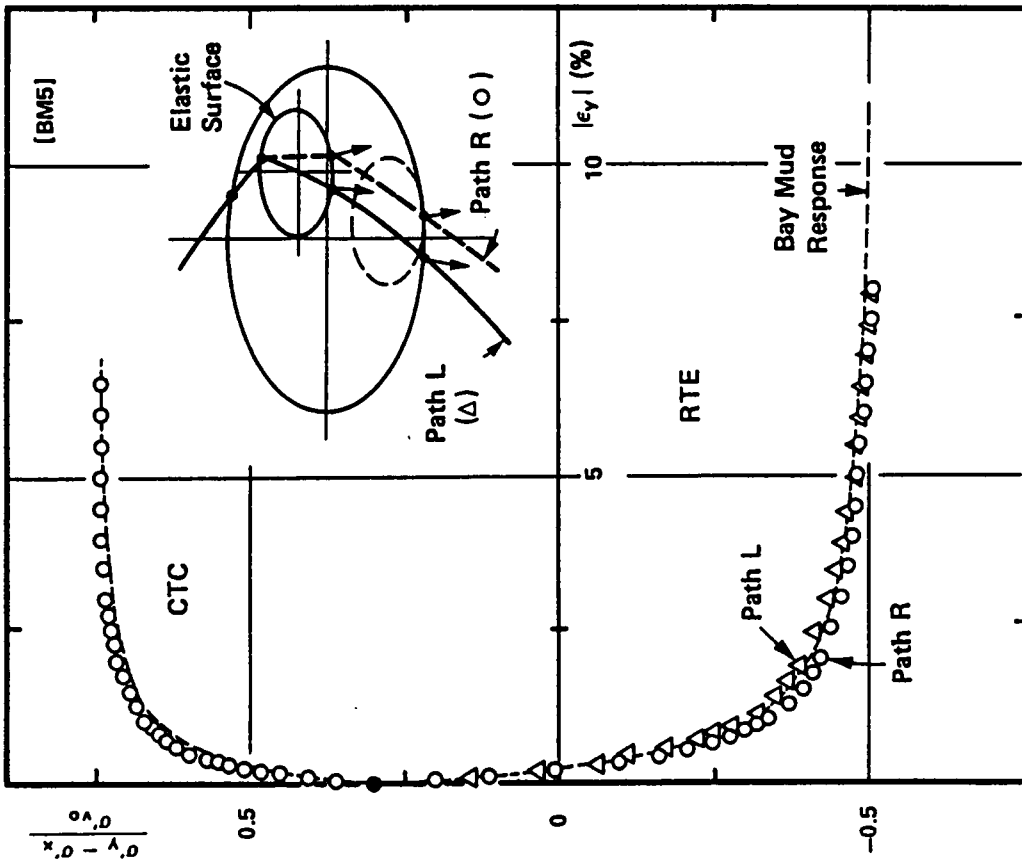


(b) A Stress Path encountering negative  $H'$

Figure 4.14 Unrealistic Distribution of Plastic Moduli

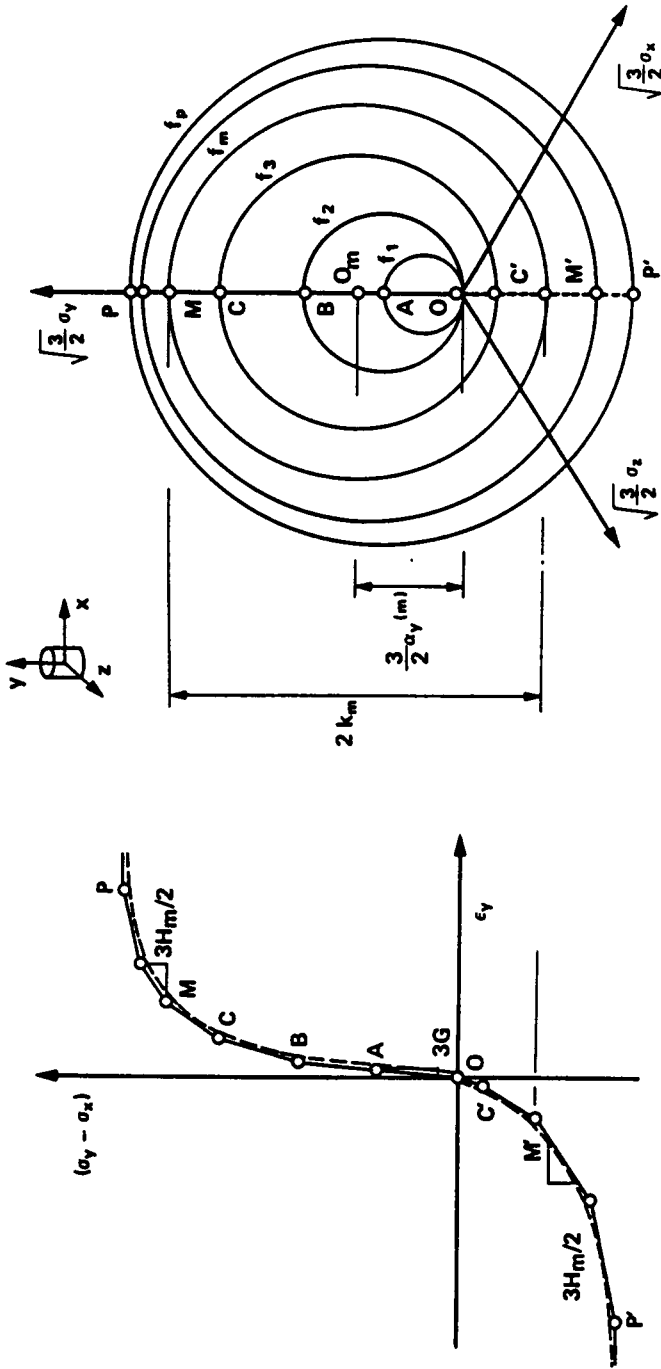


(a) Deviatoric Stress Strain Curves



(b) Effective Stress Paths

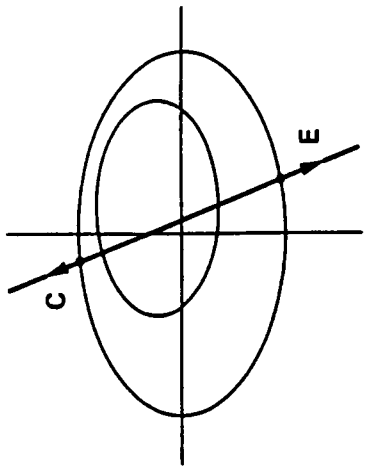
Figure 4.15 Effect of Routing of Stress Path with regard to Yield Surface Configuration



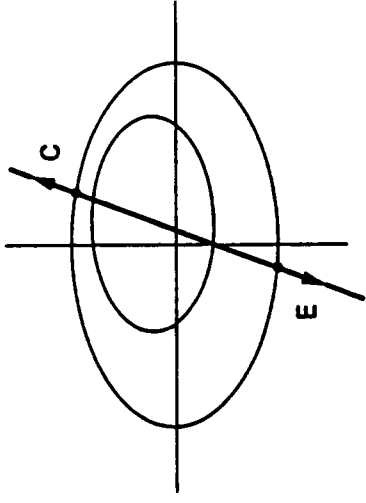
(a) Stress-Strain Curve Approximated by Linear Segments

(b) Representation in Stress Space

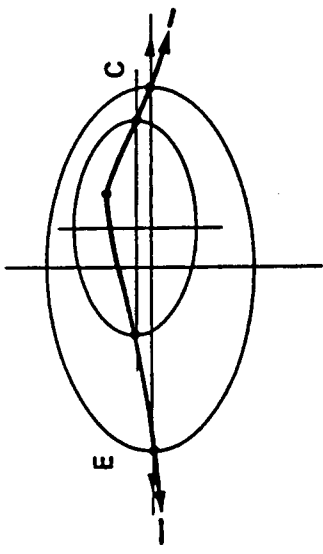
Figure 4.16 Shear Moduli Evaluation of Pressure Nonsensitive Model after Prevost (1977)



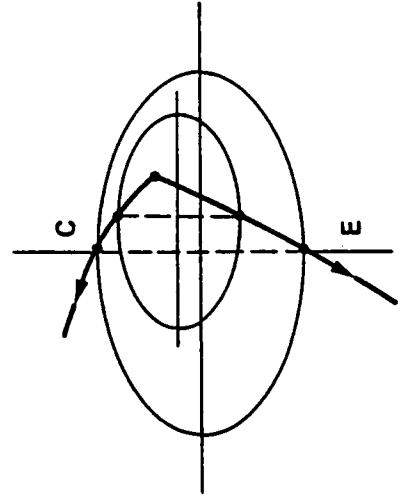
(c) Drained Reduced Compression/  
Loading Extension



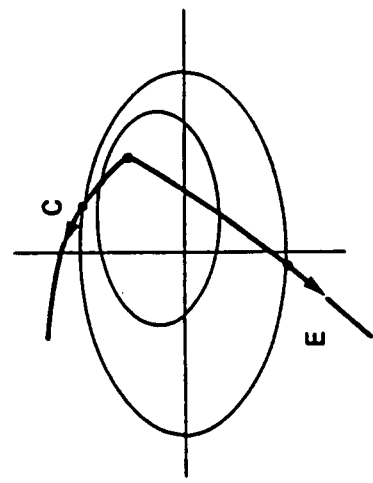
(b) Drained Compression/  
Reduced Extension



(a) Consolidation with Isotropic  
Volume Change



(e) Special Case of Undrained  
Triaxial Compression/Extension



(d) Undrained Compression/  
Extension

Figure 4.17 Various Stress Paths associated with Slope Condition

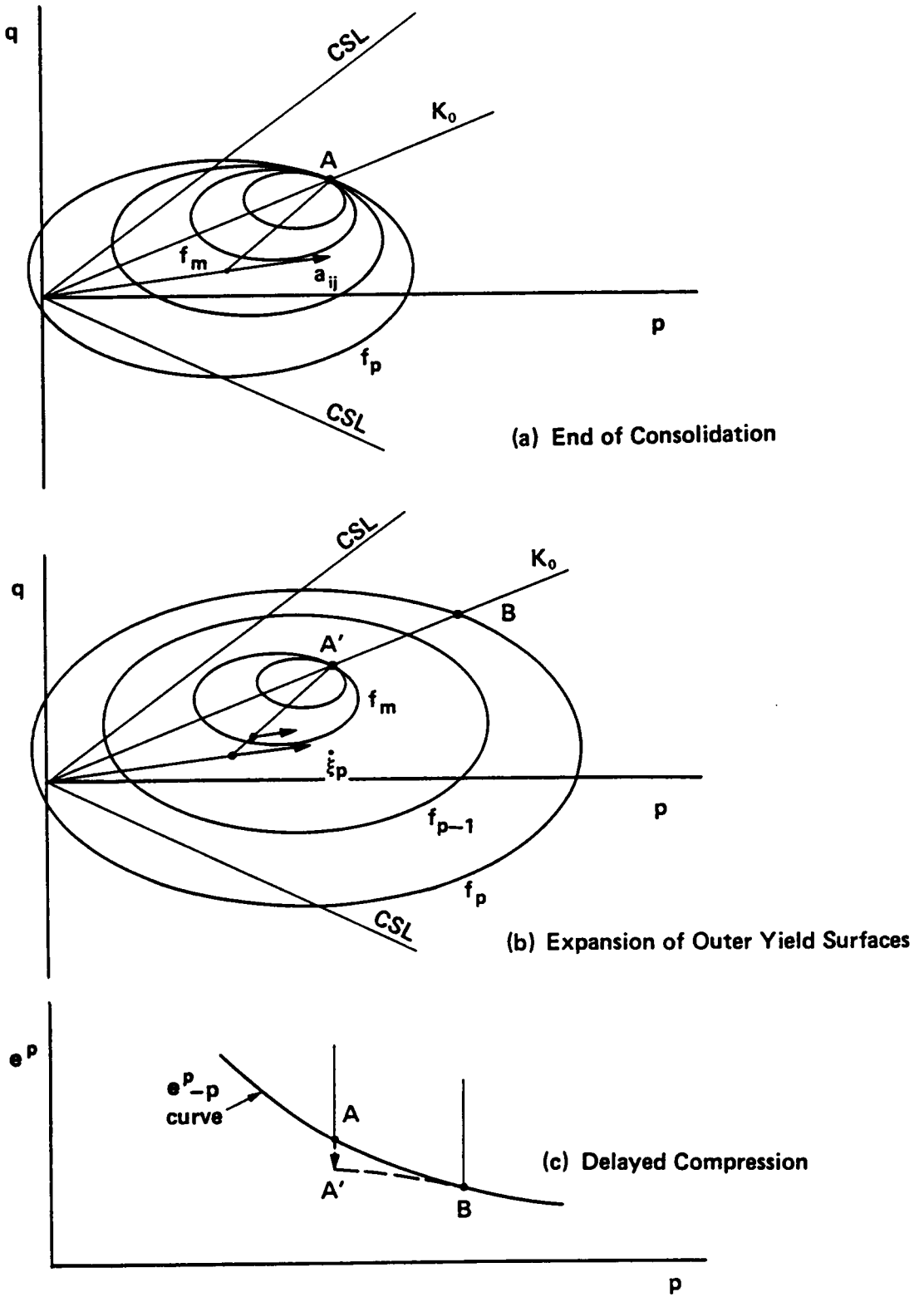


Figure 4.18 Expansion of Yield Surface due to Delayed Compression after Consolidation



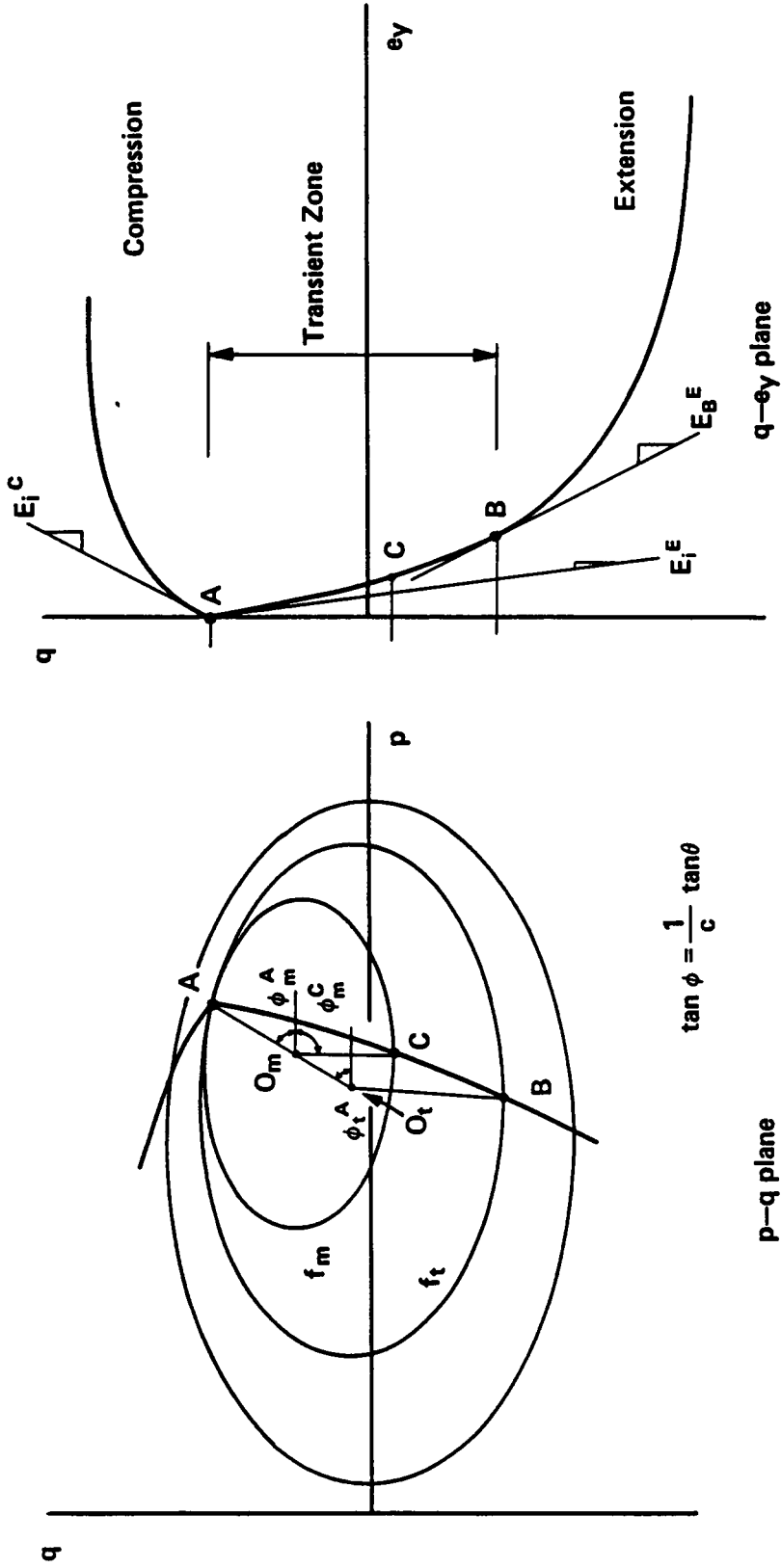


Figure 4.21 Description of Transition Zone reflecting Initial Soil Anisotropy

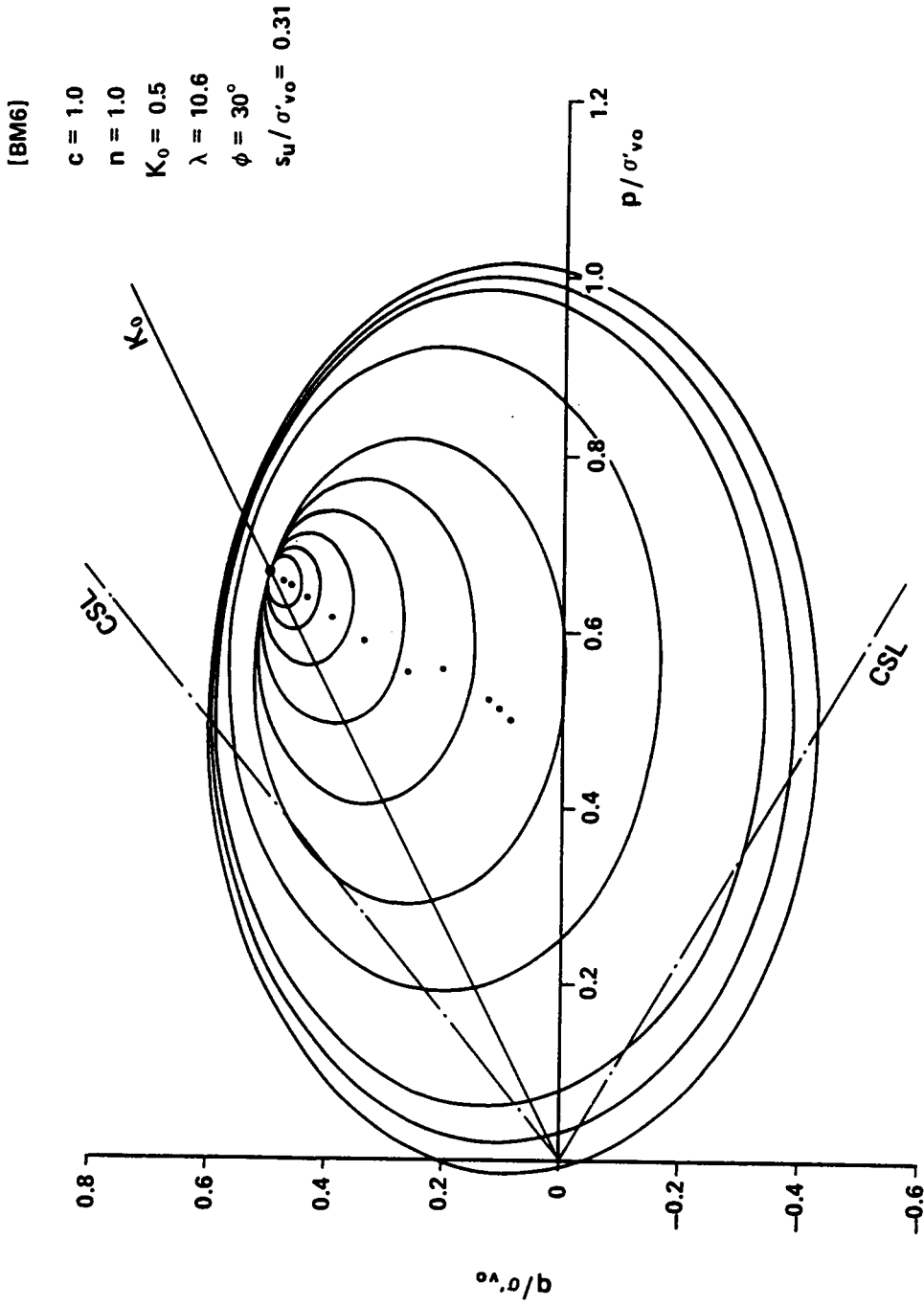


Figure 4.22 Yield Surface Configuration of San Francisco Bay Mud Obtained by Modified Parameter Evaluation Procedure

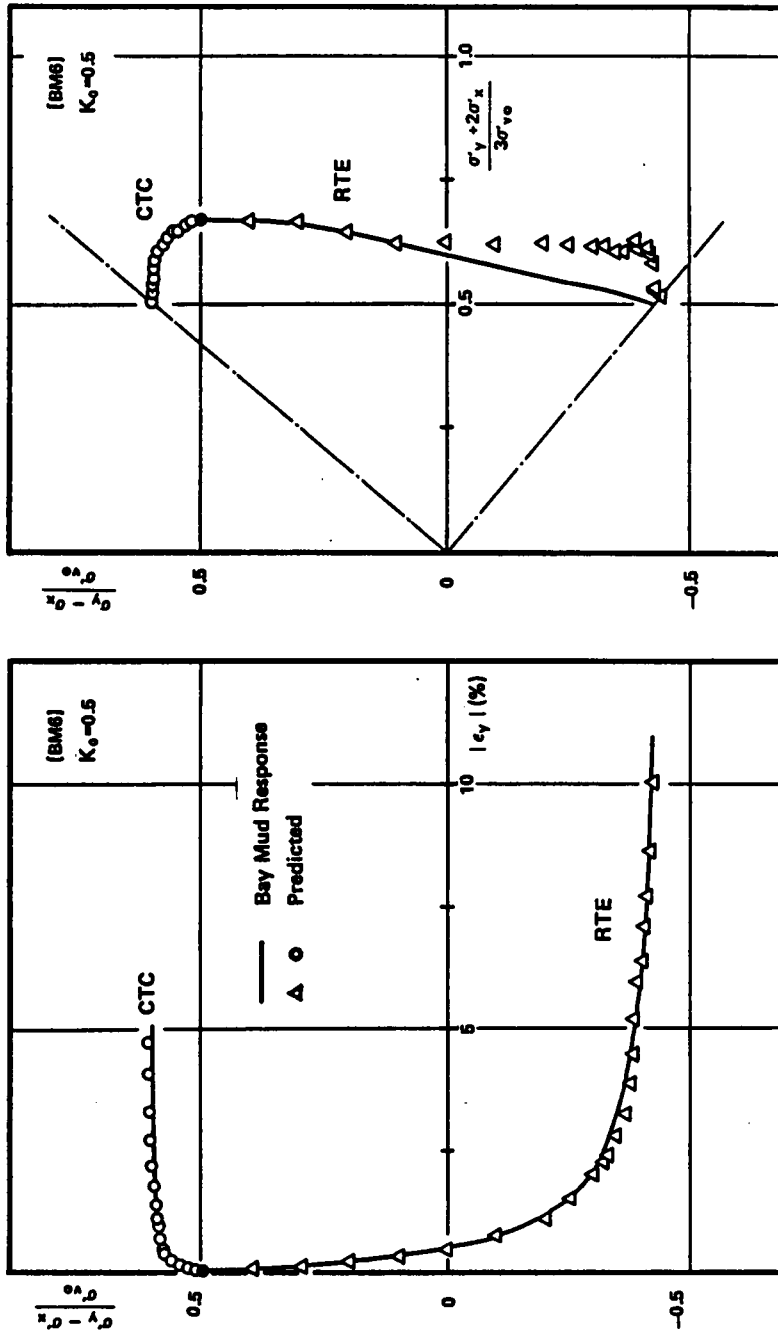


Figure 4.23 Predicted Response of San Francisco Bay Mud on Triaxial Tests

## Chapter 5

### APPLICABILITY OF PREVOST MODEL TO SAN FRANCISCO BAY MUD

#### 5.1 Introduction

The Prevost model capabilities are described in the preceding chapters. This model is discussed in relation to San Francisco Bay Mud in this chapter. This soil is significant with respect to the N-2 case history which is the subject of the analytical studies in the Chapters 7 and beyond. The behavior of Bay Mud is well known, and a large quantity of experimental data are available for it. With such information available, a detailed examination of the Prevost model applicability to the Bay Mud is set forth in this chapter.

The first step involves determining the model parameters. Since there is scatter in the data for engineering properties of the Bay Mud, a set of representative soil constants are selected and checked against the observed behavior. In the comparison of the predicted and experimental results, it is shown how the Prevost model predicts the Bay Mud behavior.

#### 5.2 Description of San Francisco Bay Mud

San Francisco Bay Mud is composed of sediments of the Late Quaternary Age overlying bedrock in San Francisco Bay. The sediments consists of materials washed out from the surrounding hills and brought down the rivers that enter the Bay. The youngest of the sediments is called San Francisco Bay Mud. Below this deposit is the Merritt colluvium sand layer which is

underlain by stiff clay called Old Bay Mud. The changes in sea level during the Late Pleistocene Epoch caused erosional unconformities in the sand layer and the top of the Old Bay Mud. Thus, the thickness of San Francisco Bay Mud varies, with values reaching as much as 150 ft.

San Francisco Bay Mud, often referred to as simply Bay Mud or Recent Bay Mud, is typically a soft silty clay, which is essentially normally consolidated, very compressible, moderately sensitive, with low undisturbed strength and with interbedded thin lenses of fine sand. This soil has been the subject of much study over the years and accumulated information is available on its engineering properties (Bonaparte and Mitchell 1979), Duncan 1965).

Normalized behavior can be assumed for the Bay Mud (Duncan 1965, Kavazanjian and Mitchell 1980). The undrained strength ratio  $s_u/\sigma'_v$  as defined in triaxial compression tests is 0.30 - 0.38, which is consistent with other clays (Ladd, et al. 1977). The shear strength almost proportionally increases with depth except in the upper portions of Bay Mud where it is often overconsolidated due to desiccation. The effective friction angle  $\phi'$  is found to be about  $34^\circ$  on an average. Seed, et al. (1964), Duncan (1965), and Denby (1978) measured the pore pressure parameter  $A_f$  in undrained triaxial compression tests and gave values about unity at failure. In contrast, the  $A_f$  parameter is 0.7 - 0.8 for extension loading (Duncan 1965).

Duncan and Buchignani (1976) gave a relationship between the modulus number  $K (E/s_u)$ , overconsolidation ratio OCR and plasticity index PI

for clays. With average values of Bay Mud,  $K$  will fall between 300 - 500.

Duncan (1965) performed tests to define the anisotropy of Bay Mud. Defining a ratio of strength obtained from a vertical compression test to that from an extension test, he obtained a value of 0.78. This value is consistent with the relation between anisotropic strength ratio and  $P_1$  given by Ladd, et al. (1977) for other clays. Hansen (1980) studied modulus anisotropy for Bay Mud and found the ratio of the modulus in compression to that in extension of 2.11. This is on the high side of values shown for other clays.

The coefficient of lateral earth pressure at rest  $K_0$  for Bay Mud has been measured in situ. Denby (1978) found  $K_0$  values from the self-boring pressuremeter tests from 0.5 to 0.6. Lacerda (1976) measured slightly higher values in long term lab tests. The actual  $K_0$  value of Bay Mud apparently lies between 0.5 and 0.7.

Compression index values,  $C_c$ , are found from 0.8 to 1.8 reflecting a high compressivity of Bay Mud. The recompression index,  $C_r$ , is about one tenth of  $C_c$ , in the range of 0.10 - 0.15. The natural water content is about 90 percent with a void ratio,  $e_0$ , of around 2.4.

More details on the geotechnical properties of the Bay Mud can be obtained in the report published by Bonaparte and Mitchell (1979).

### 5.3 Prevost Model Representation

A set of Prevost model parameters is to be identified for the San

Francisco Bay Mud in terms of the engineering properties described in the previous section.

### 5.3.1 Interpretation of Undrained Triaxial Test Results

In order to evaluate the Prevost model parameters for the Bay Mud, it is necessary to have both stress-strain curves and excess pore pressure development curves which are obtained from the triaxial compression and extension tests.

In this approach it is useful to assume that a hyperbolic curve approximates a deviatoric stress-strain curve of the Bay Mud. Duncan, et al. (1980) have shown that the hyperbolic representation of the Bay Mud deformation properties is reasonable. For this approach, an initial tangent to the curve and an asymptotic value fully determines the hyperbolic relation. A modulus,  $K$ , is selected as 360 to define the initial Young's modulus, based on the previous discussion. The undrained shear strength  $s_u$  is assumed to be equivalent to 0.37 times effective overburden pressure  $\sigma'_v$ , and equal effective friction angle is assumed to be 30 degrees.

As noted, the Bay Mud exhibits modulus and strength anisotropy. For this work, the anisotropic modulus and strength ratios are taken as 2.1 and 0.8, respectively. Strains at failure are five percent and 11 percent for the triaxial compression and extension tests, respectively. Accordingly, the stress-strain curve is more brittle for compression than for extension. Because the soil yields in a ductile mode in extension, the undrained extension strength is taken to be 0.97 of the asymptote

for the extension case.

Excess pore pressure developments are assumed in a similar fashion to those observed in the experiment with  $A_f$  values of 0.93 and 0.66 for the triaxial compression and extension tests, respectively. The initial stress condition is defined assuming the lateral pressure coefficient of 0.7 at rest.

The stress-strain curves and effective stress paths are determined in consideration for the triaxial compression (CTC) and the reduced triaxial extension (RTE) cases. For these triaxial test data, Prevost model parameters are evaluated by means of the procedures described in Chapter 4. The parameters obtained for the Bay Mud are shown in Table 5.1, where sixteen yield surfaces are identified.

### 5.3.2 Calculation of Prevost Model Predictions for Simple Loadings

A computer program has been developed so that stress-strain predictions can be calculated using the Prevost model. When either stresses or strains are given, the corresponding unknowns are solved. The program is named PRVCNST, and its functions and description for use are explained in detail in Appendix B. The program is used in this chapter to simulate Bay Mud response in various laboratory tests. The predictions are compared with the experimental results to check if the Prevost model is capable of accurately representing the Bay Mud behavior. Figure 5.1 shows the stress paths in the tests to be analyzed.

#### 5.4 Undrained Behavior in Triaxial Tests

The triaxial compression and extension tests to be simulated have also been used for the parameter determination. In such circumstances, it is expected that the prediction will be reasonable. Accordingly, it is demonstrated in Figures 5.2 and 5.3 that predictions for both stress-strain curves and effective stress paths agree very well with the experimental data.

Failure occurs on the critical state lines for both the CTC and RTE loading paths (Figure 5.1), and thus the ultimate strength of the corresponding path was predicted correctly. In the course of loading, a smooth yielding and a gradual excess pore pressure development are seen in Figures 5.2 and 5.3. The yielding process is modeled well using a multi-yield surface model, in particular, for a case where the initial stress state with a relatively high  $K_0$  value of 0.7 is sufficiently far from the outmost bounding surface. If it is too close, as in the case with a small  $K_0$  value, predictions of the Prevost model will not be very different from a single yield surface model. Note the predicted deviatoric stresses are found slightly larger than the experimental data as shown in those figures.

Figures 5.4 and 5.5 show the model predictions extended to include an unloading cycle. Starting with initial stress of  $K_0 = 0.7$ , (1) shear stress is reduced to a hydrostatic stress; then (2) it is increased with vertical stress in compression to near failure; (3) reversal loading is imposed by reducing the vertical stress until near failure in extension. The stress-strain curve and stress path of the original data in the triaxial

tests are shown together in the figures.

CTC stress-strain curve of (2) after shear stress reduction plots just under the original curve (Figure 5.4). In contrast, the ordinary CTC curve predicted falls on the opposite side in which no loading reversals are involved, as noted earlier. The predicted CTC response with loading reversal becomes less stiff relative to that without it. This is caused since the elastic range is shifted down the vertical shear stress axis during the unloading process (1), and yielding occurs at a lower shear stress level in the reloading process (2), causing a larger deformation. The same thing is found if the stress-strain curve corresponding to reversal loading (3) is compared with the original curve, where a Bauehinger effect is predicted. The kinematic hardening representation in the Prevost model yields a reasonable behavior for the Bay Mud.

A predicted effective stress path is shown in Figure 5.5 for the same loading sequence. With the effect of shear reduction (1), the CTC path (2) stays to the left of the original path. This illustrates the development of excess pore pressure which is much higher in an early stage than that for the ordinary CTC path without the loading reversal. As failure is approached, excess pore pressure developments become about the same for the CTC paths with and without the loading reversals. This phenomenon is attributed to the little change in the critical stress state with the different processes of yielding.

The reversal loading path (3) is nearly vertical, suggesting that there is minimal excess pore pressure on the second loading reversal. This is

not consistent with typical soft clay behavior (Ladd, et al. 1977). In face, repeated cyclic loading is difficult to model (Pande and Zienkiewitez 1982). Fortunately, for the advanced shield case, repeated cycles of loading need not be considered.

### 5.5 Drained Behavior on Oedometer Test

Bay Mud response to oedometer test loading is predicted using the same model parameters as before and is comparable to the experimental results obtained by Denby (1978).

The initial state of the model is assumed to be at a void ratio of 2.05 with a OCR of 1.4 for a preconsolidation pressure of  $1.11 \text{ kg/cm}^2$  ( $108.8 \text{ kN/m}^2$ ). Calculated consolidation and rebound lines are plotted in Figure 5.6. They demonstrate a good agreement which is encouraging since model parameters are essentially obtained from other loading programs than those in this test.

Figure 5.7 shows calculated variation of the ratio of the horizontal stress to the vertical for the oedometer test, noted as  $K_0$ , for both the loading and rebound responses. At the beginning of the loading,  $K_0$  values fluctuate. This is due to the fact that the initial configuration of the yield surfaces is crowded, and the soil passes from an overconsolidated to a normally consolidated region. Subsequently the  $K_0$  value stabilizes to a nearly constant value of 0.56. This is consistent with the experimental values of Denby (1978) and Lacerda (1976).

With reduction of the vertical stress, larger  $K_0$  values are calcu-

lated. They are plotted against the overconsolidation ratio (OCR) in Figure 5.8. In the lower portion of the figure, some general reference data are shown for purposes of comparison with the calculations. No specific data are available for this phase of behavior for Bay Mud. However, the general trends agree with those predicted.

In simulation of the oedometer test, the normally consolidated phase is controlled by the bounding surface during the swelling phase by intermediate nested yield surfaces. They allow the model to successfully predict the Bay Mud behavior.

## 5.6 Undrained Behavior in Plane Strain Shear Test

In contrast to the triaxial or oedometer tests where a rotational symmetry exists, all the three normal stress and strain components are independent in the plane strain test. This situation represents a special challenge to the model.

Duncan (1965) carried out a series of plane strain tests on the Bay Mud. Both vertical and horizontal loading plane strain tests were conducted. His results fall in a band as shown in Figures 5.9 and 5.10. The initial stress condition of the tests used a  $K_0$  consolidation of 0.5. For this reason the Bay Mud model parameters for  $K_0 = 0.5$ , which have been shown in Table 4.3 of the Chapter 4, are to be used instead of the model parameters with  $K_0 = 0.7$  for this section. The predicted stress-strain curves are in approximate agreement with the experimental results (Figure 5.9).

Figure 5.10 shows a comparison of excess pore pressure developments between the prediction and the observation. They agree quite well. It is notable that in the vertical and horizontal loading pore pressure curves in Figure 5.12, jumps occur in the predicted data at high stress levels. These result from the transition from the plastic state represented by the nested yield surfaces to that by the bounding surface. As discussed in Sections 3.4.5 and 3.5.3, plastic moduli associated with those yield surfaces have different roles and thus an inconsistency is temporarily created. This is inevitable unless the conformity of functions for every yield surfaces is assured. The recent published versions of the Prevost model (Hughes and Prevost 1979, Prevost 1982a) are ignored volumetric yielding associated with the bounding surface and employed the same method for specifying plastic moduli as for the nested surfaces. This is a deviation. On the other hand, Mroz, et al.(1978) applies the volumetric yielding concept for every yield surface inclusive of the bounding surface in their model. The Prevost model being used in this thesis is a combination of the two approaches. In spite of the inconsistency. The model used herein yields reasonable results with the exception of the jumps referred to above.

## 5.7 Model Response to Multicubical Test

Sinram (1983) carried out undrained multicubical tests on the Bay Mud. He attempted to follow the stress path subjected in soil elements near an inflated pressuremeter. Two typical test results are considered herein to simulate with the Prevost model.

Figure 5.11(a) explains the hypothetical stress state of a soil element which is closely located to the side of a pressuremeter. As the pressuremeter is inflated with increasing radial stress  $\sigma_r^T$ , the tangential stress  $\sigma_\theta^T$  decreases with a constant mean normal stress. Plane strain conditions are assumed to exist normal to vertical stress  $\sigma_z^T$ .

Stress conditions in the pressuremeter problem may be idealized in a cubical soil element as shown in Figure 5.11(b). An incremental stress  $\dot{\sigma}_r^T$  is applied in the  $r$ -direction while the same amount of stress  $\dot{\sigma}_\theta^T$  is reduced in the  $\theta$ -direction. The soil element is subjected to a pure shear stress state in the  $r$ - $\theta$  plane. In addition, vertical deformation is constrained so as to establish a plane strain condition in the  $r$ - $\theta$  plane. This loading in the cubical test is a kind of plane strain, but is different from the previously studied plane strain test in that the direction of the loading stress does not coincide with the anisotropy of the soil.

#### 5.7.1 Cubical Shear on Isotropically Consolidated Bay Mud

One of the two multicubical test results selected from Sinram's work uses an initial isotropic consolidation stress state shown in Figure 5.12(a). The loading method and the total stress path of loading for both loading and unloading are shown in Figure 5.12(b) and (c).

The Prevost model parameters in Table 5.1 are used in the prediction. The initial stresses of the model are designated by a  $K_0$  of 0.7 in Figure 5.13(A), whereas the stress state with  $K_0 = 1$  is employed in the

experiment. To create the model's initial stress state identical to that used in the experiment, imaginary loading steps of a drained extension and a consolidation are introduced as are steps (B) and (C) shown in Figure 5.13. After stress adjustments of the model, undrained shear of step (D) in Figure 5.13 is imposed in accordance with the stress path applied in the experiment.

Predicted and observed stress-strain curves and pore pressure changes are shown in Figure 5.14. The effective stress,  $\sigma'_r$ , and effective stress path are shown in Figure 5.15. The predicted stress path agrees well with the experimental results, but poorer agreement is obtained for the unloading phases. Only the trends for the vertical effective stress variation,  $\sigma'_z$ , are predicted; absolute magnitudes are too high relative to those measured (Figure 5.16). This stress represents the one generated in the "plane strain" axis, which models the vertical axis in the field.

#### 5.7.2 Cubical Shear on Anisotropically Consolidated Bay Mud

In the anisotropic consolidation phase of a cubical shear test (Sinram 1983), a  $K_0 = 0.6$  was used. The initial stress condition and the loading procedure are shown in Figure 5.17. As noted earlier, the model parameters have been established for  $K_0$  value of 0.7. Thus, a stress adjustment is again required to create the initial stress condition of  $K_0 = 0.6$  for the model representation, as shown in step (B) in Figure 5.18.

The observed and predicted stress-strain curve, the mean pressure changes, the effective stress variations and the effective stress path are

given in Figures 5.19 to 5.21. The same basic trends in success and lack of success in modeling the observed behavior are observed here as in the isotropic consolidated case.

## 5.8 Summary and Conclusions

The Prevost model has been examined to see how it predicts behavior of the San Francisco Bay Mud as observed in experiments obtained from various laboratory tests. The engineering properties of the Bay Mud in general were reviewed in the literature. With these data the stress-strain curves and pore pressures in undrained triaxial tests are hypothetically constructed. Then Prevost model parameters are determined by means of the parameter evaluation procedure described in Chapter 4. Two sets of the Bay Mud parameters are used with initial stress conditions of  $K_0 = 0.7$  and  $0.5$ .

Prevost model applicability to Bay Mud is examined for a variety of stress paths created in the laboratory tests. They include the undrained triaxial tests, the oedometer tests, the undrained plane strain tests, and the undrained multicubical tests. Both drained and undrained behavior, loading and unloading and stress paths on and out of the triaxial plane, are involved in the simulations. In the majority of cases the Prevost model predictions were found to represent well the trends of the Bay Mud behavior observed in the experiments.

Through the simulations of various types of soil test, the Prevost model has demonstrated its capabilities to accurately predict behavior of

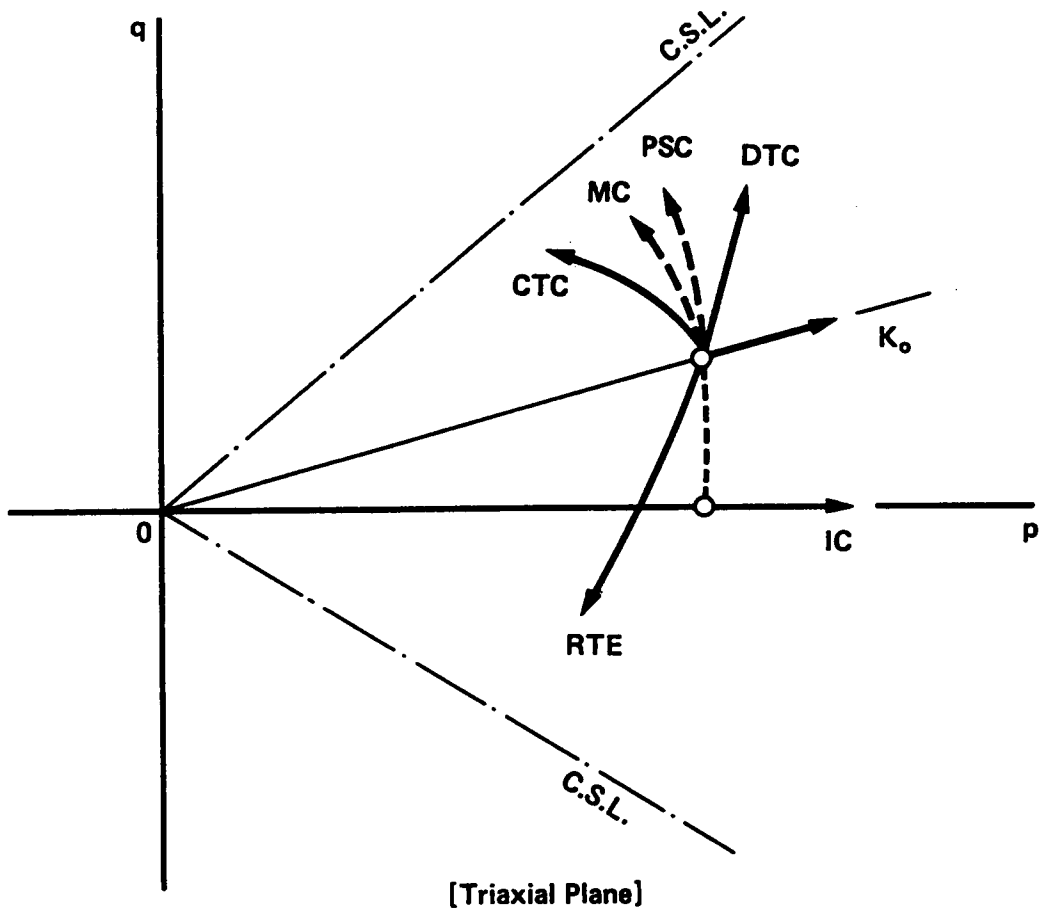
the Bay Mud. The model parameters are known to have been calibrated reasonably. Therefore the model can confidently be applied in later tunneling analyses.

Table 5.1 Prevost Model Parameters for San Francisco Bay Mud

(  $K_0 = 0.7$  )

$G/\sigma'_{v_0} = 61.33$      $B/\sigma'_{v_0} = 122.66$      $n = 1.0$      $\lambda = 8.68$      $c = 1.0$

m	$\alpha^{(m)}/\sigma'_{v_0}$	$\beta^{(m)}/\sigma'_{v_0}$	$k_m/\sigma'_{v_0}$	$h'_m/\sigma'_{v_0}$	$B'_m/\sigma'_{v_0}$	$A_m$
2	0.2480	0.8104	0.035	120.0	-1600	-1.0
3	0.2496	0.8131	0.060	100.0	-1200	-0.8
4	0.2120	0.8071	0.1014	89.03	-622.3	-0.6590
5	0.1790	0.7944	0.1395	63.53	-148.2	-0.4876
6	0.1684	0.7207	0.2377	45.69	-97.78	-0.2989
7	0.1610	0.6981	0.3050	33.42	-68.78	-0.2169
8	0.1543	0.6923	0.3517	23.25	-43.57	-0.1753
9	0.1463	0.6628	0.4164	15.57	-29.45	-0.1348
10	0.1409	0.6475	0.4579	11.17	-22.18	-0.1133
11	0.1387	0.6346	0.4885	8.254	-17.56	-0.0949
12	0.1366	0.6255	0.5103	6.048	-12.91	-0.0817
13	0.1343	0.6147	0.5338	3.893	-9.458	-0.0664
14	0.1302	0.5985	0.5625	2.171	-6.322	-0.0478
15	0.1281	0.5803	0.5901	0.984	-4.781	-0.0146
16	0.1165	0.5397	0.6235	0.0	0.0	0.0



**Legend:**

- CTC** Conventional Triaxial Compression Test
- RTE** Reduced Triaxial Extension Test
- MC** Multicubical Compression Test (Not in Triaxial Plane)
- PSC** Plane Strain Compression Test (Not in Triaxial Plane)
- DTC** Drained Triaxial Compression Test
- K<sub>0</sub>** Anisotropic (K<sub>0</sub>) Consolidation Test
- IC** Isotropic Consolidation Test

Figure 5.1 Various Stress Paths to be examined for San Francisco Bay Mud

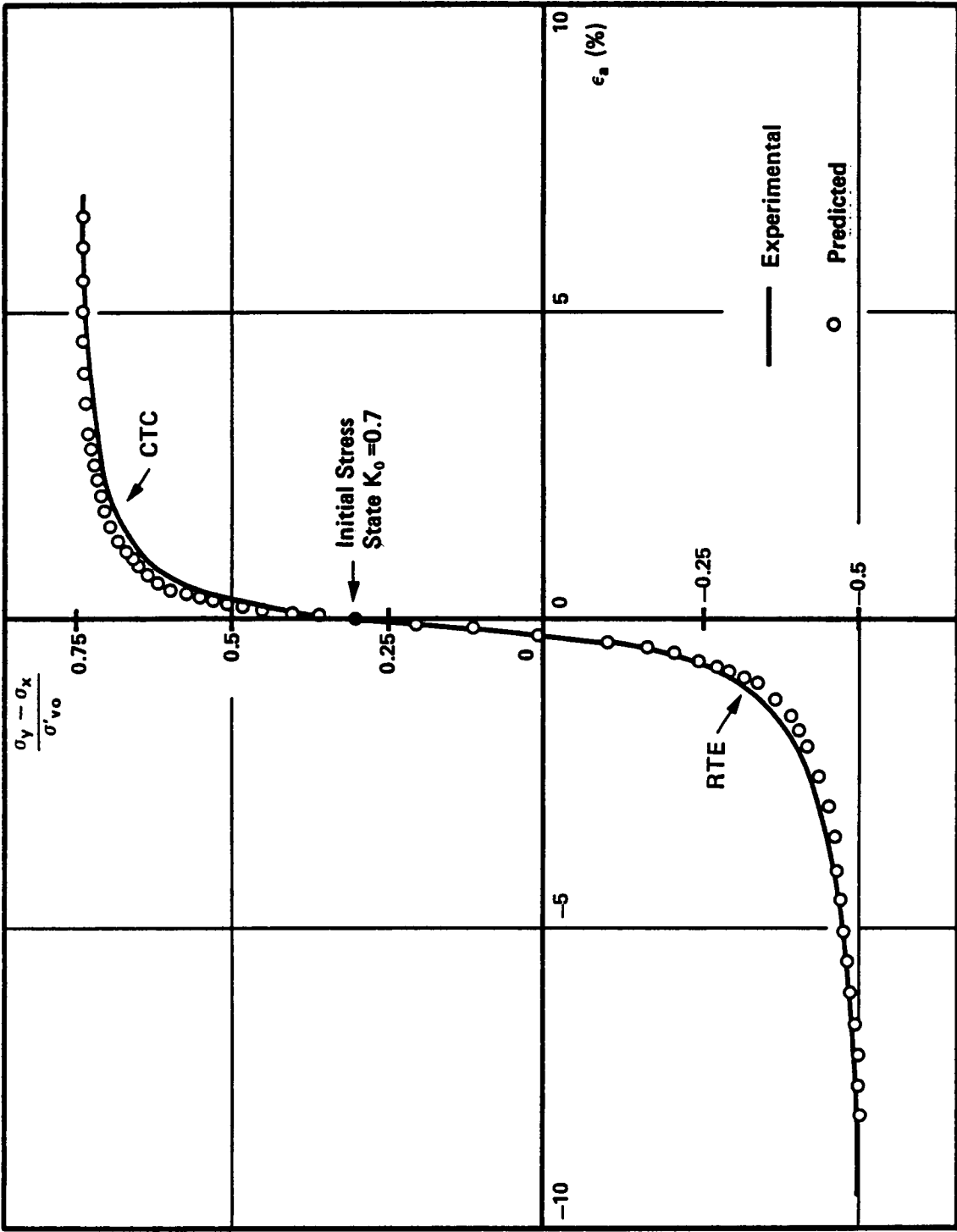


Figure 5.2 Stress-Strain Relation in Triaxial Compression (CTC) and Extension (RTE) Tests of Bay Mud (  $K_0 = 0.7$  )

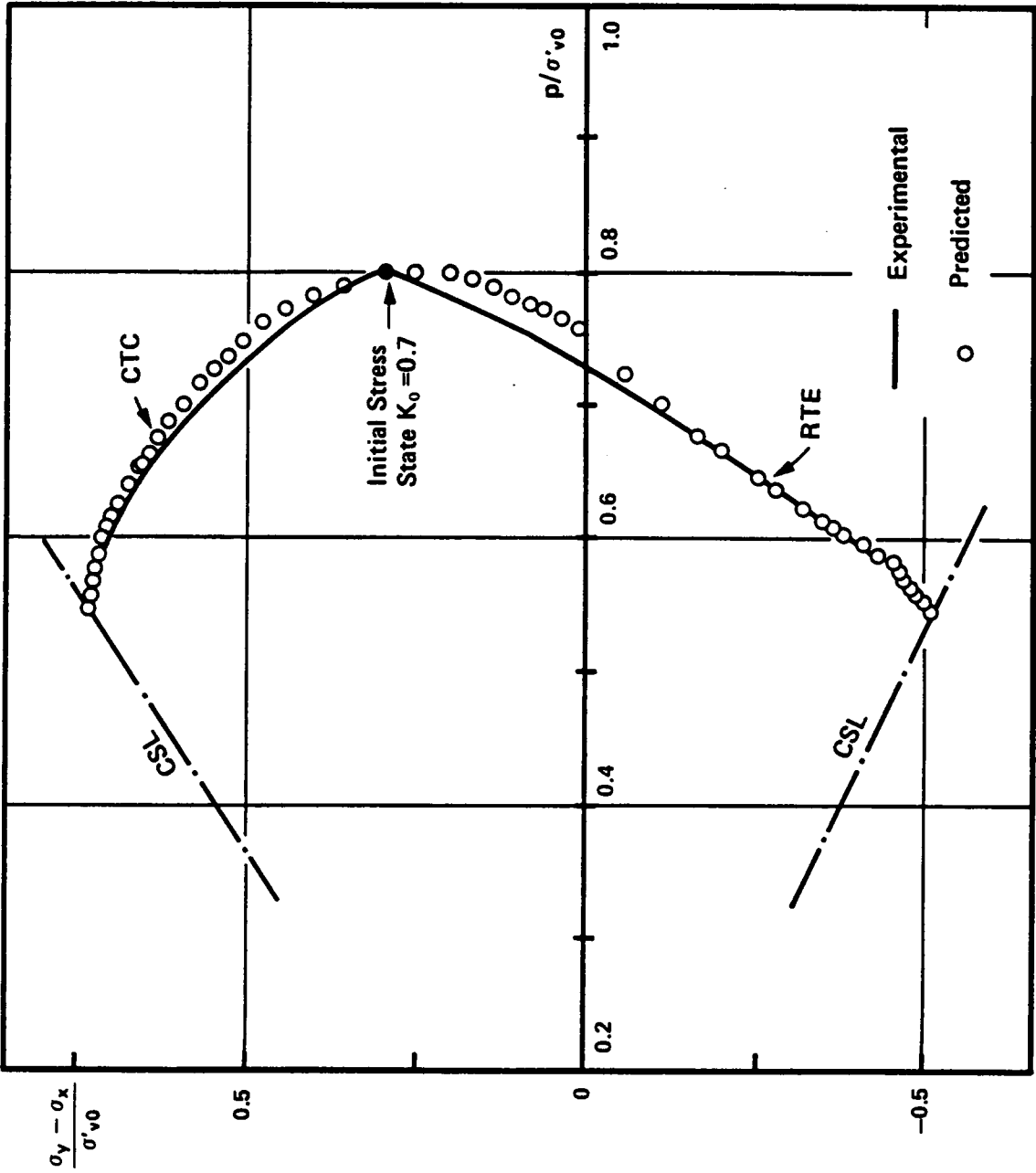


Figure 5.3 Effective Stress Paths in Triaxial Compression (CTC) and Extension (RTE) Tests on Bay Mud (  $K_0 = 0.7$  )

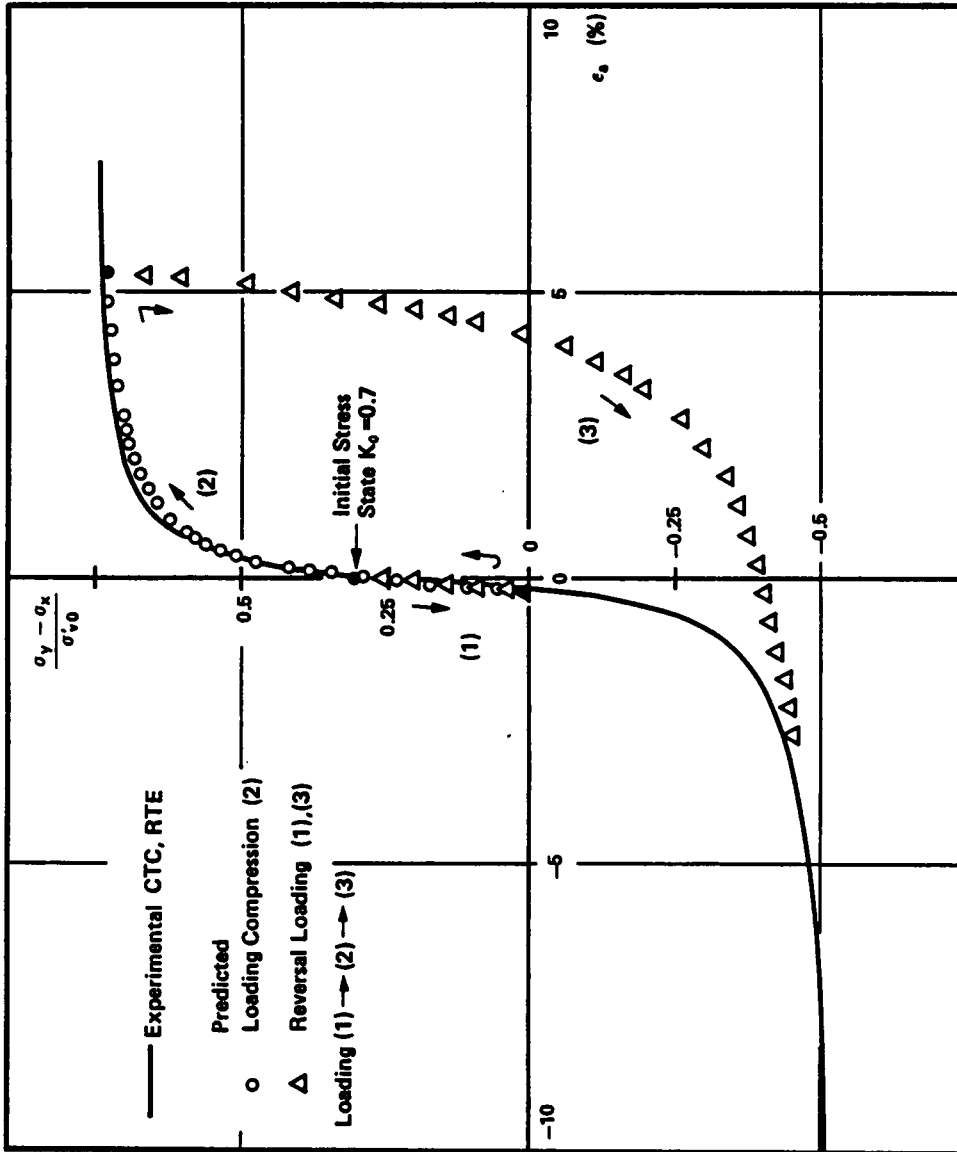


Figure 5.4 Predicted Stress-Strain Curve in Triaxial Test with Loading Reversals

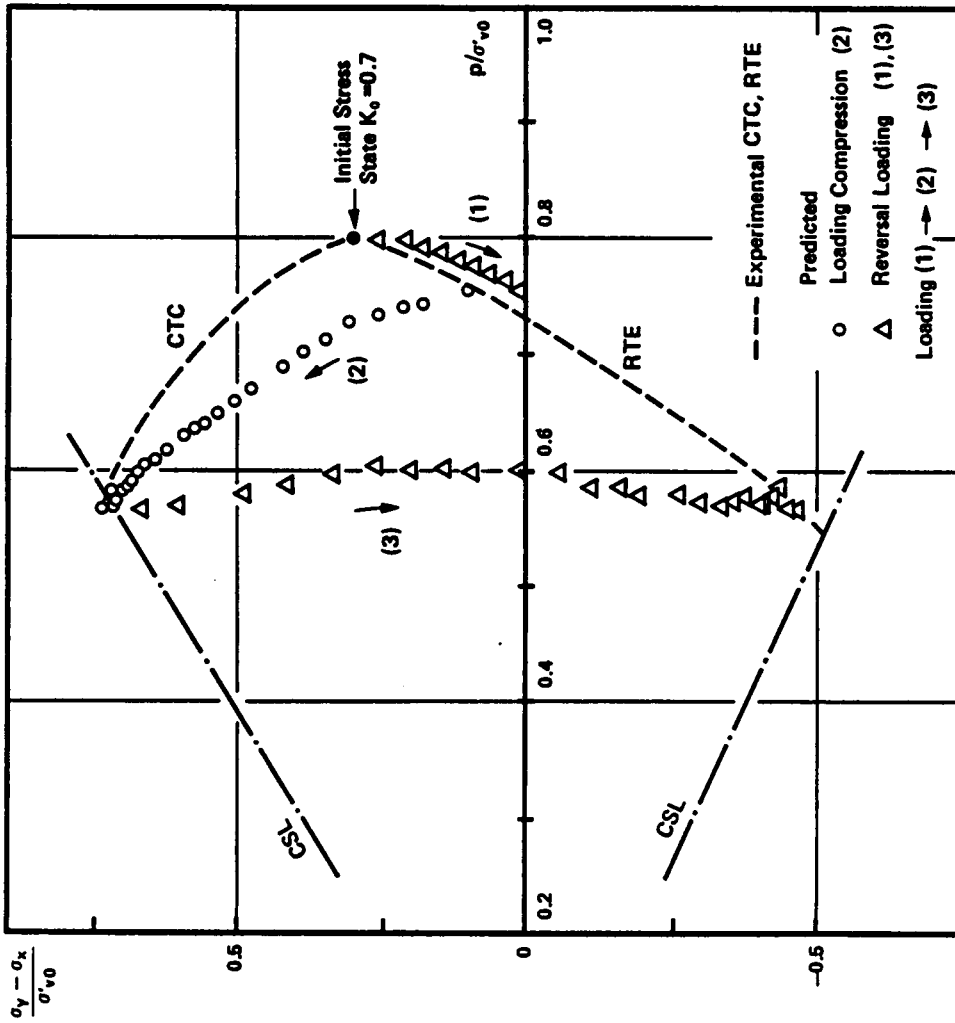


Figure 5.5 Predicted Effective Stress Path in Triaxial Test with Loading Reversals

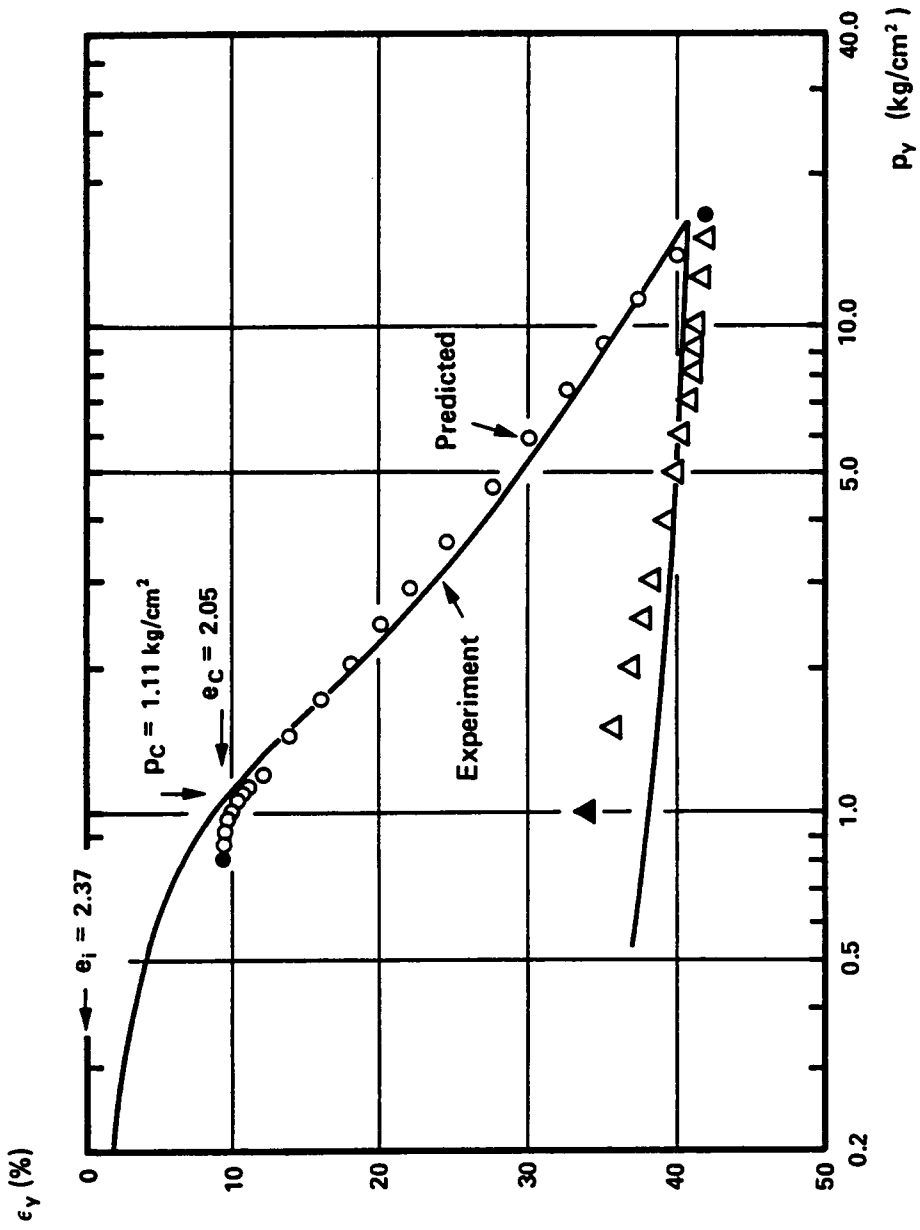


Figure 5.6 Predicted and Experimental Consolidation Curves of Oedometer Test  
( after Denby 1977 )

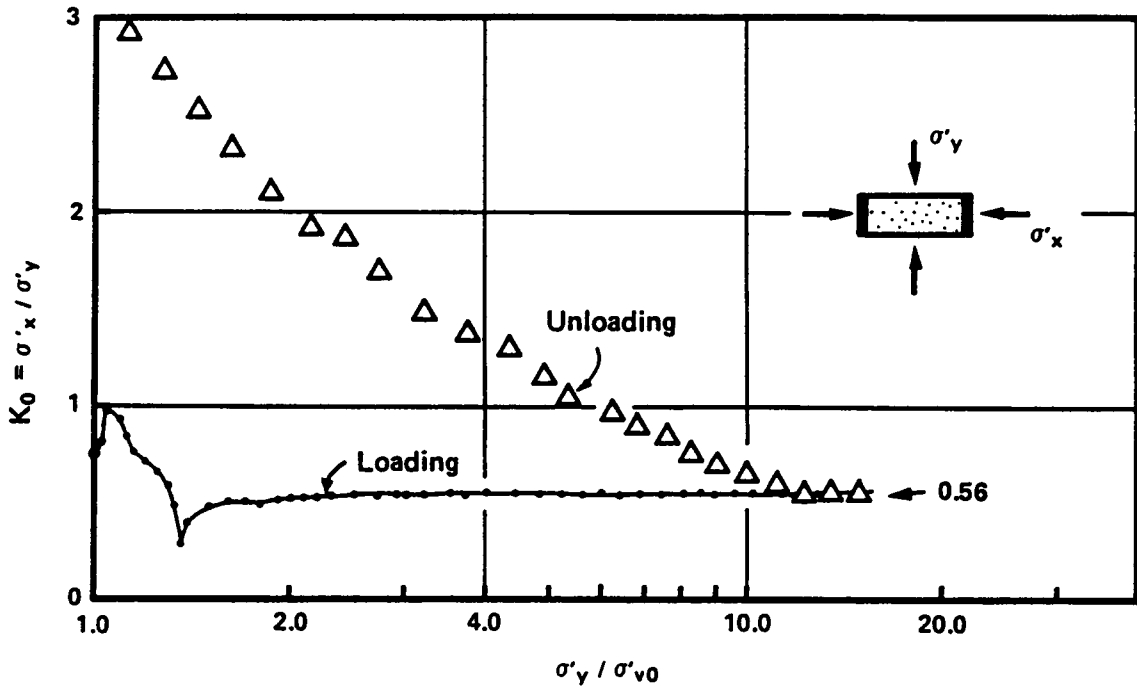


Figure 5.7 Ratio of Horizontal to Vertical Stresses in Oedometer Test

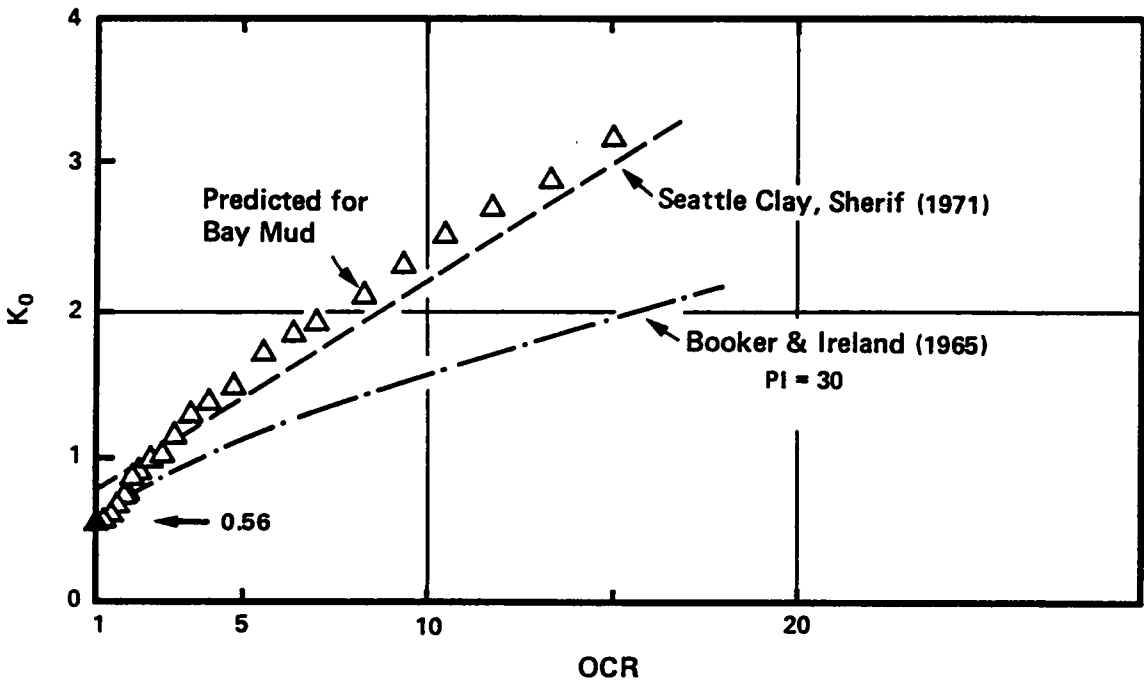


Figure 5.8  $K_0$  Values in Overconsolidated Range of Oedometer Test

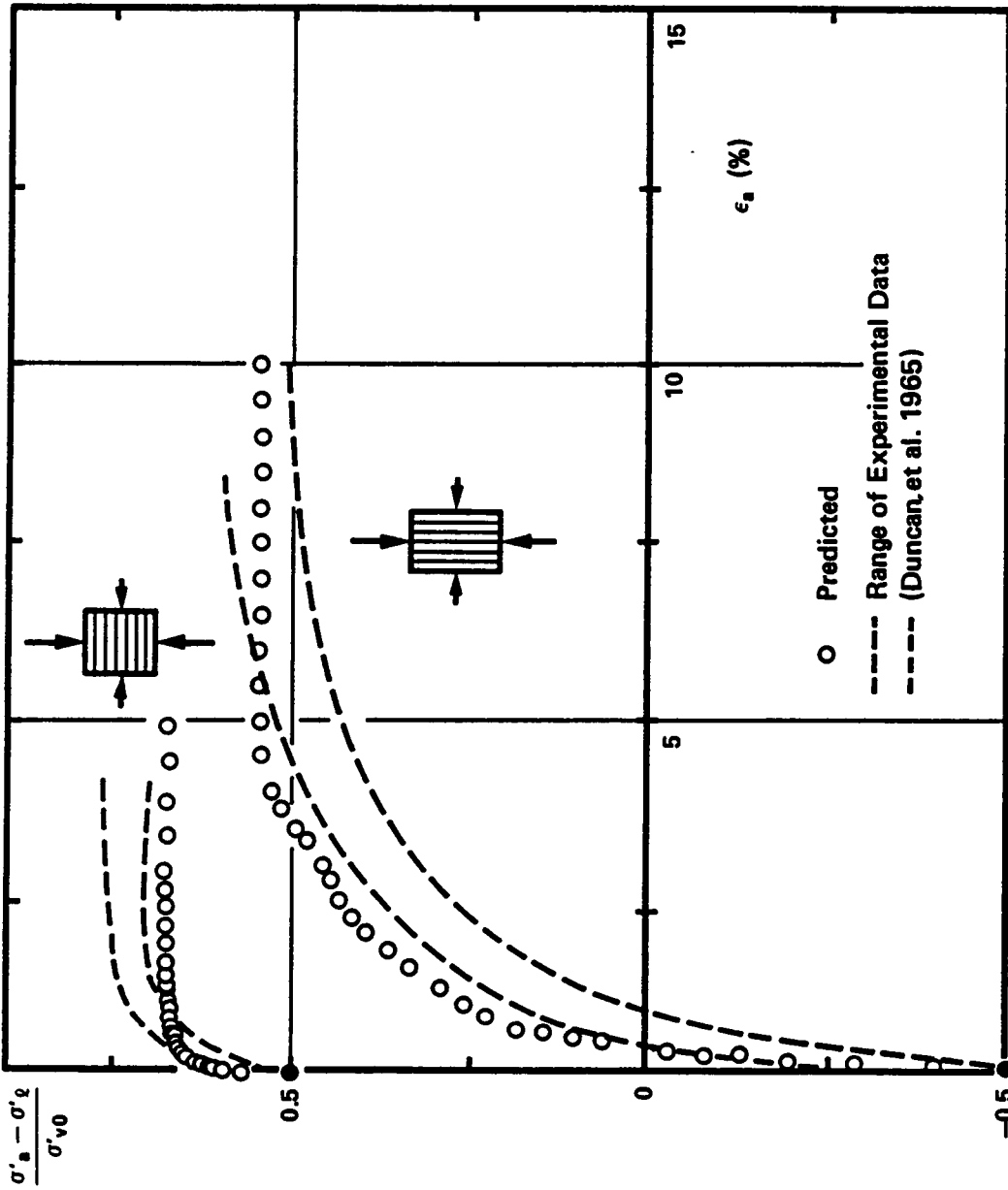


Figure 5.9 Stress-Strain Relation in Plane Strain Tests of Bay Mud (  $K_0 = 0.5$  )

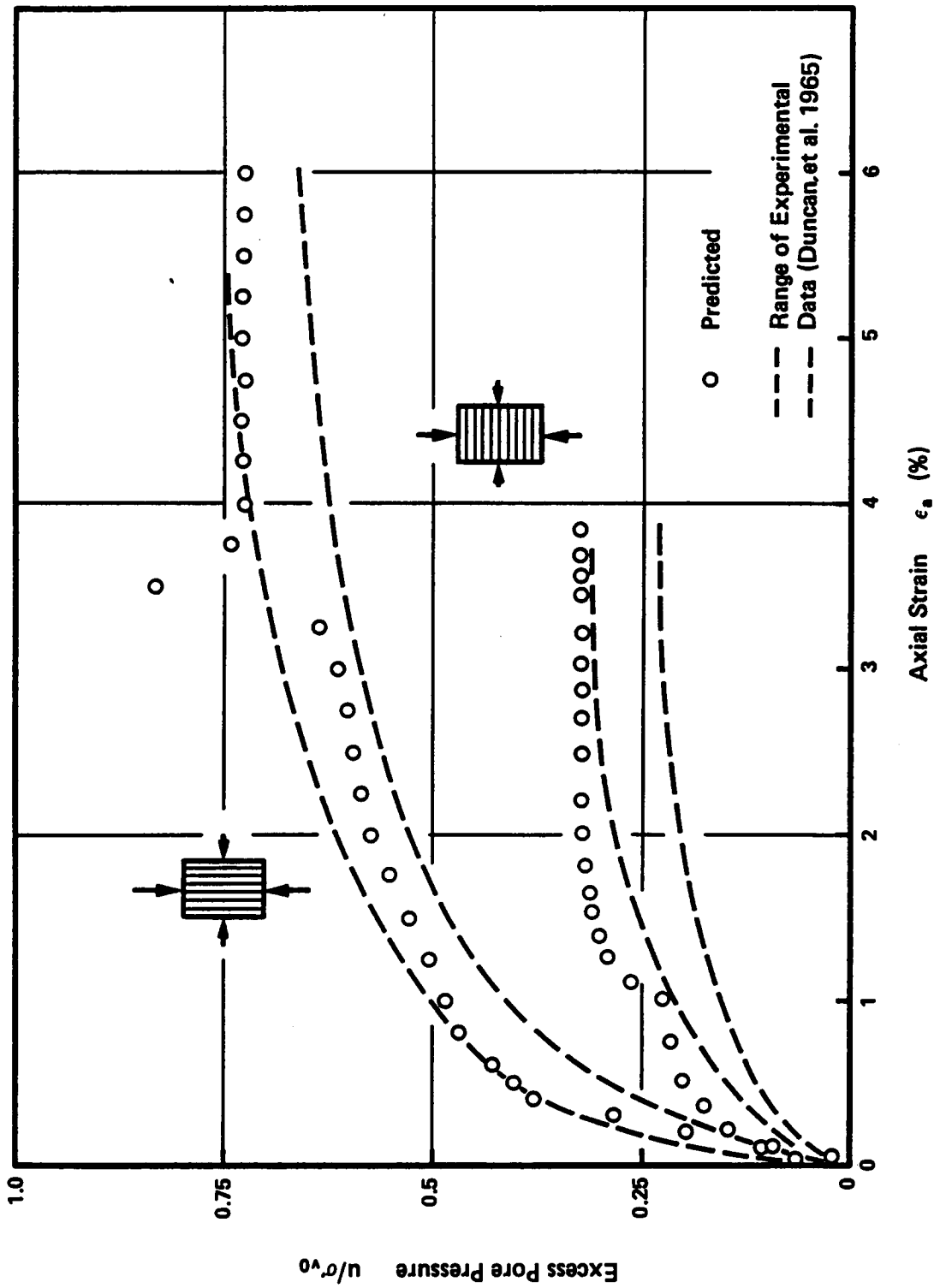


Figure 5.10 Excess Pore Pressure Development in Plane Strain Test of Bay Mud (  $K_0 = 0.5$  )

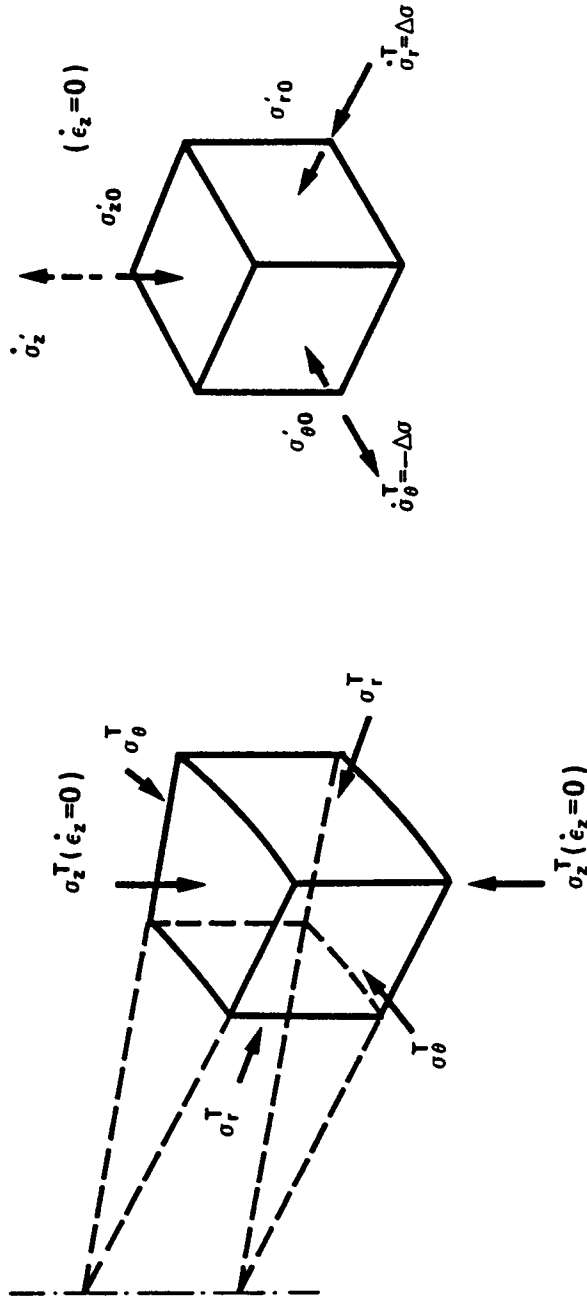
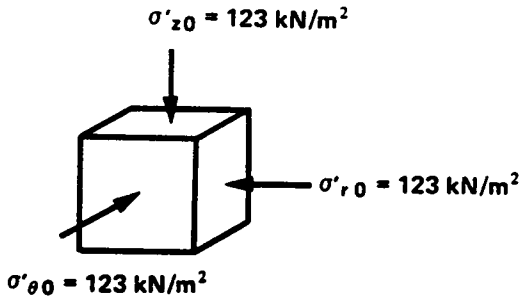
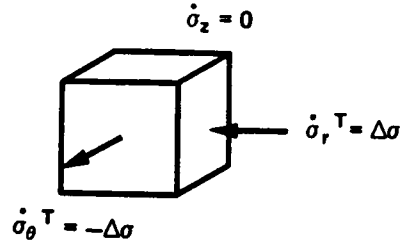


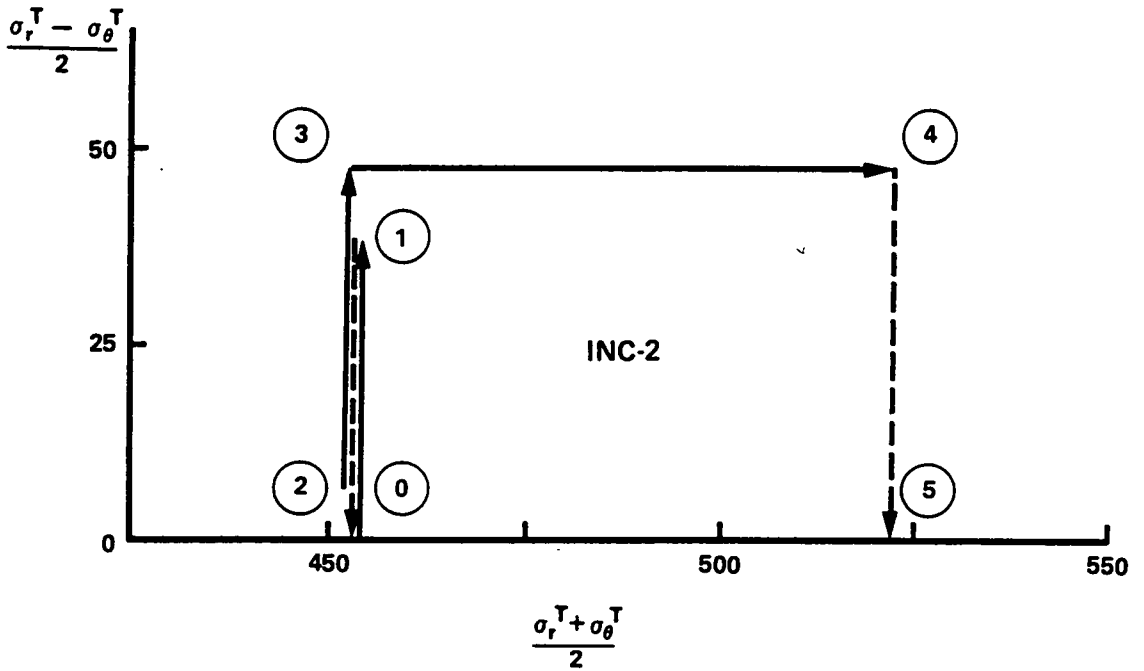
Figure 5.11 Explanation of Stress State associated with Pressuremeter and Multicubical Tests



(a) Initial Stresses  
(Isotropic Consolidation)

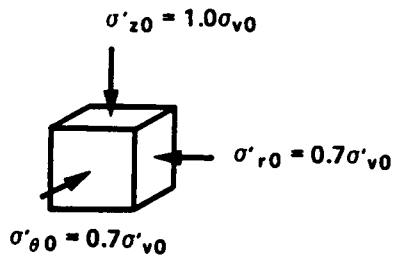


(b) Applied Stresses

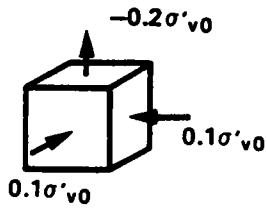


(c) Total Stress Path of Loading

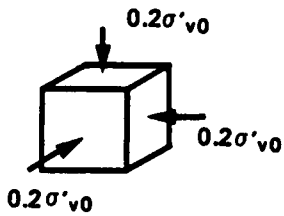
Figure 5.12 Multicubical Test for Isotropically, Normally Consolidated (INC) Bay Mud



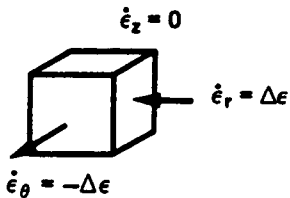
(A) Initial Stresses



(B) Drained Extension



(C) Consolidation



(D) Undrained Shear

INC-2

———— Undrained Path

- - - - - Drained Path

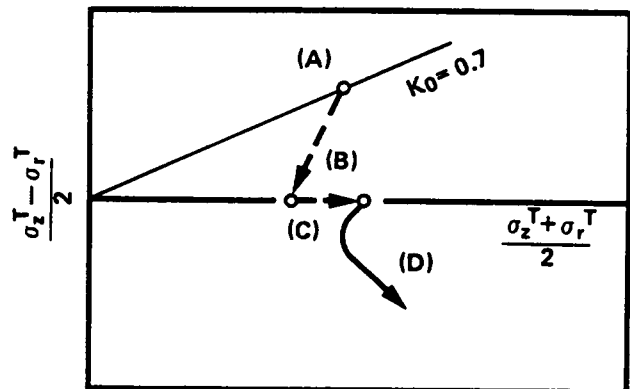
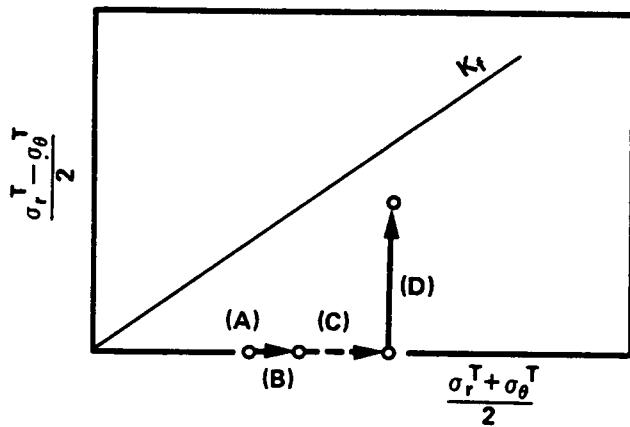


Figure 5.13 Preparation of Prevost Model for INC Bay Mud

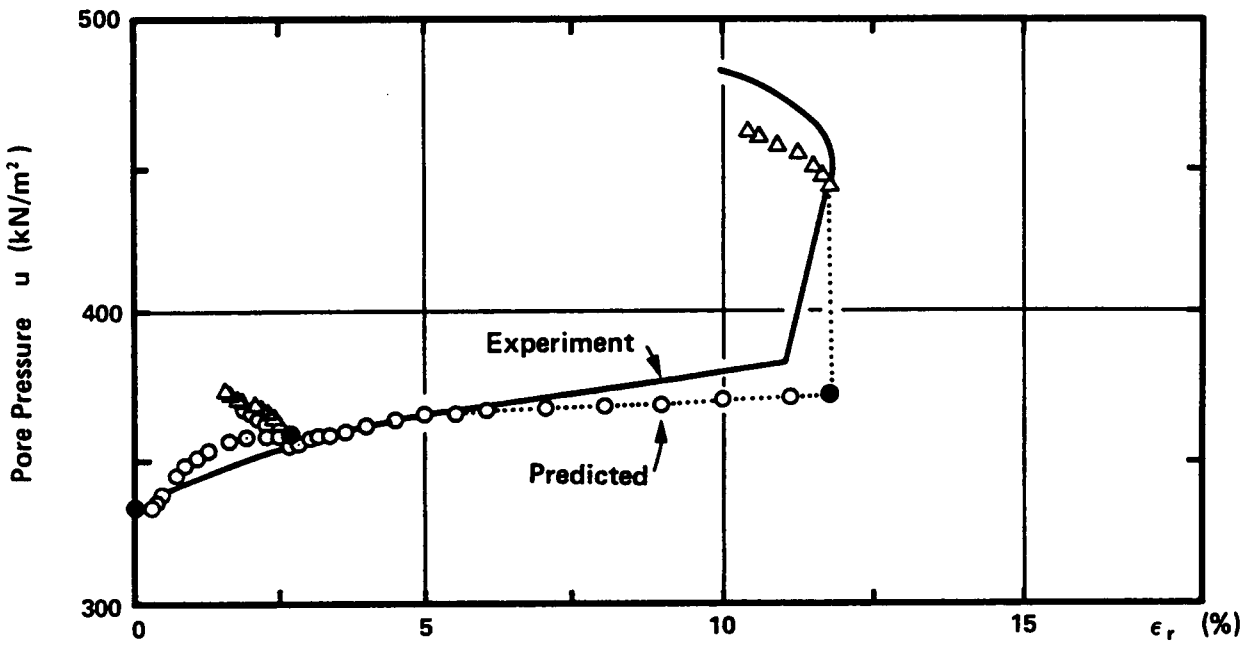
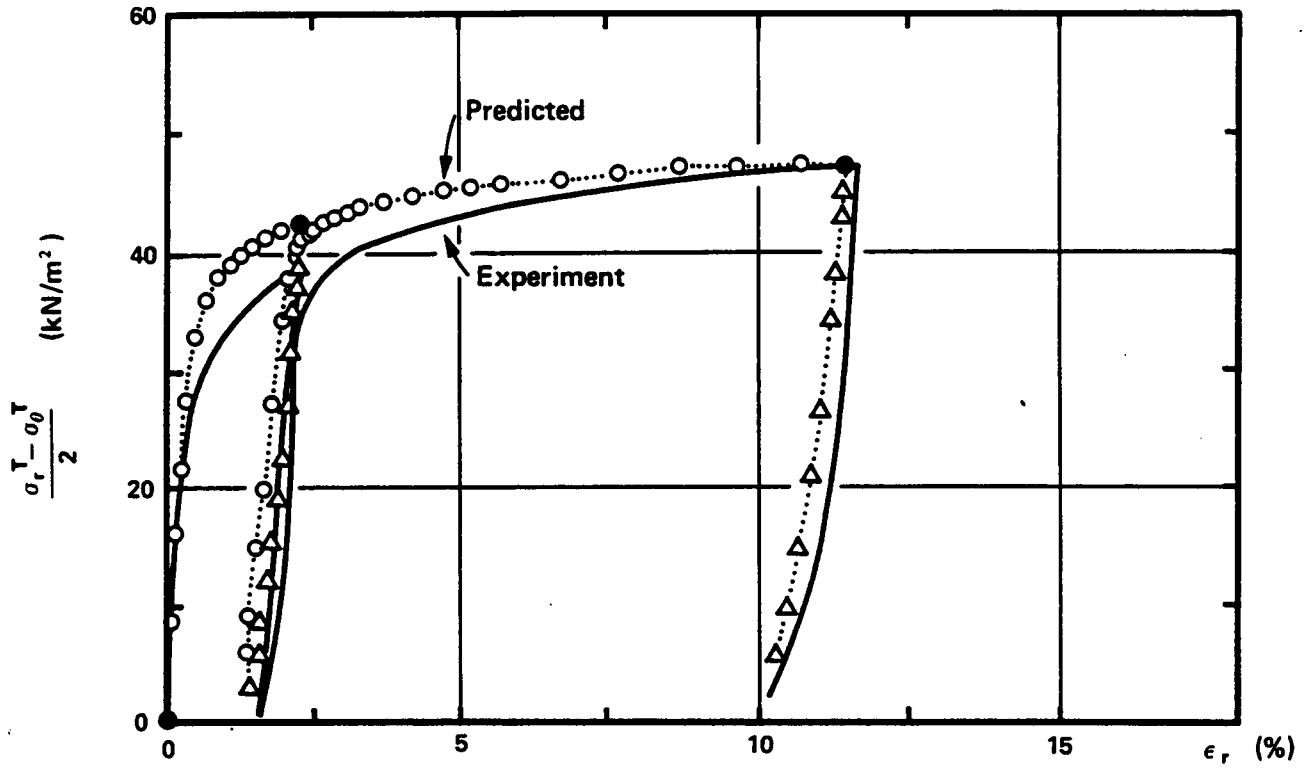


Figure 5.14 Stress-Strain Curve and Pore Pressure Changes in Multicubical Test, INC Bay Mud

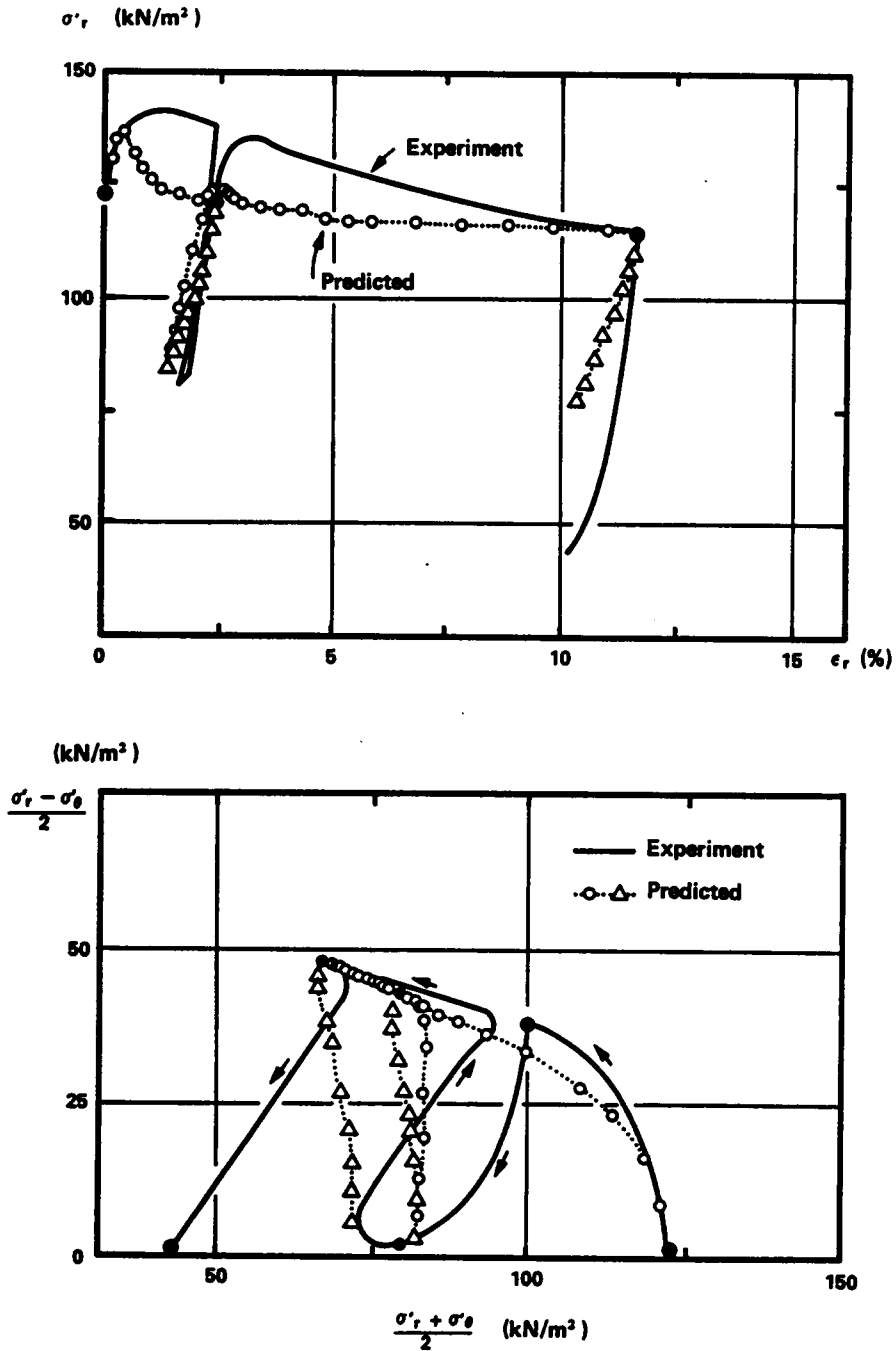


Figure 5.15 Variation of Effective Loading Face Stress and Effective Stress Path in Multicubical Test, INC Bay Mud

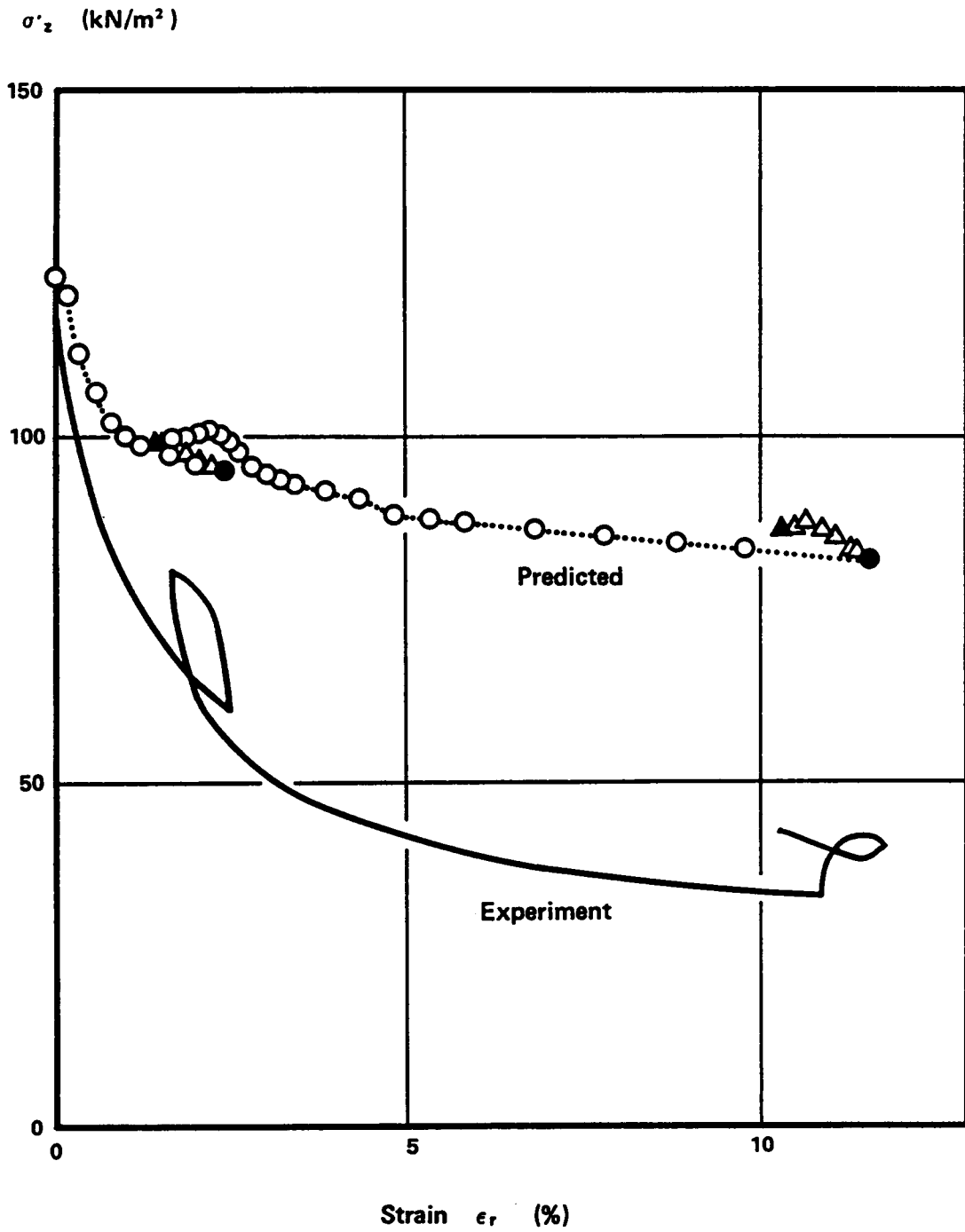
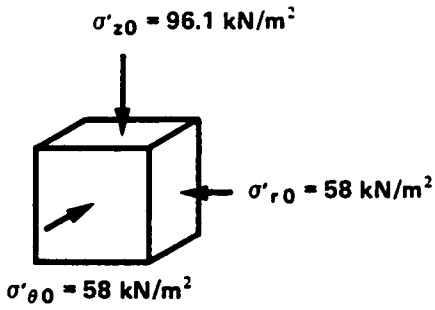
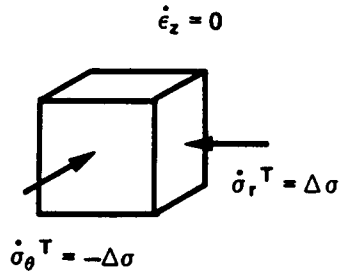


Figure 5.16 Variation of Effective Vertical Stress in Multicubical Test, INC Bay Mud

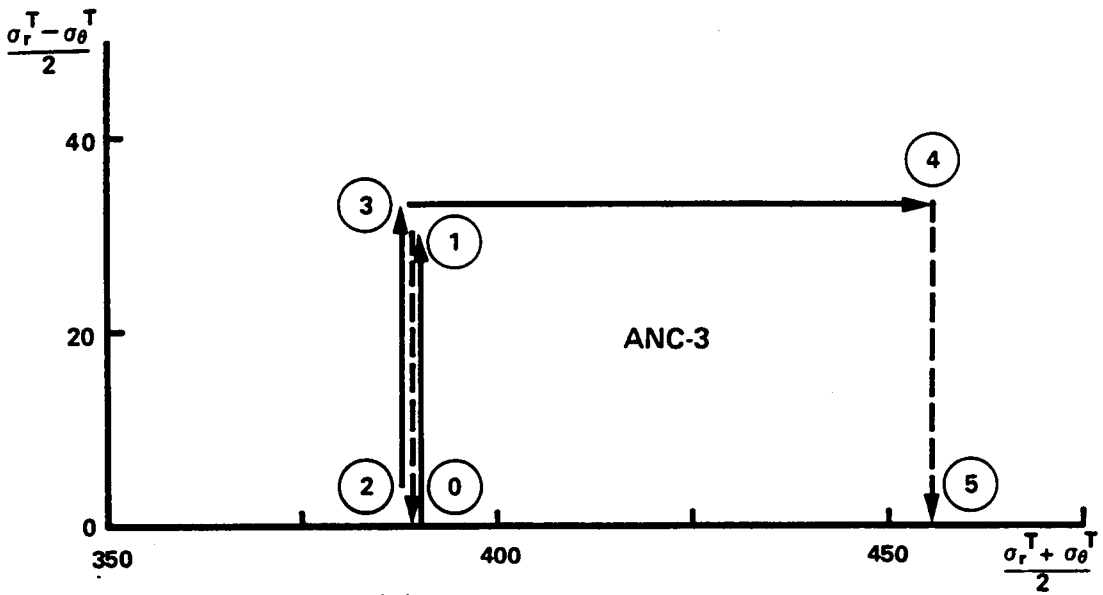


(a) Initial Stresses



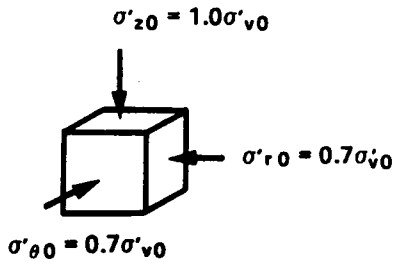
(b) Applied Stresses

(Anisotropic Consolidation  $K_0 = 0.6$ )



(c) Total Stress Path of Loading

Figure 5.17 Multicubical Test for Anisotropically, Normally Consolidated (ANC) Bay Mud

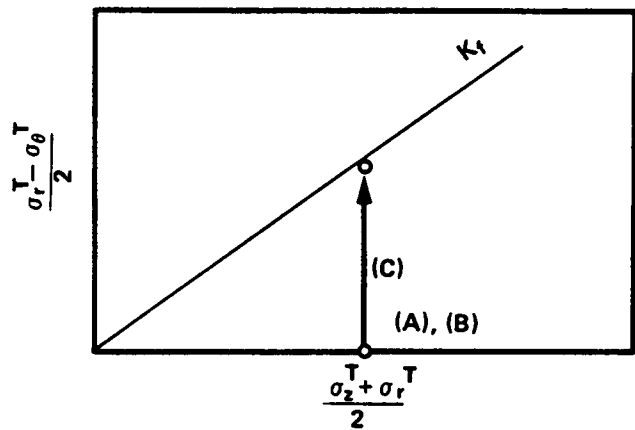
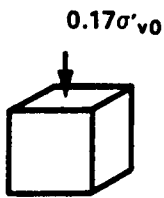


ANC-3

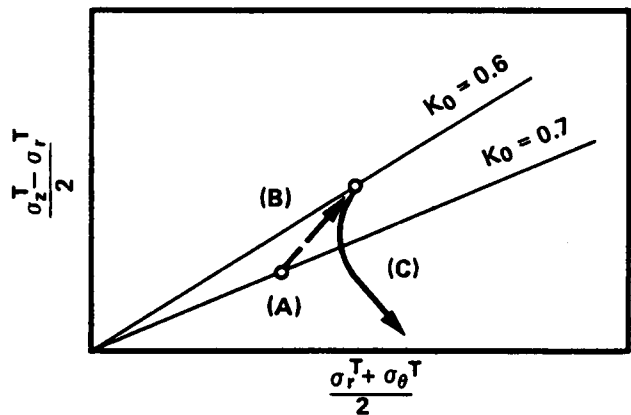
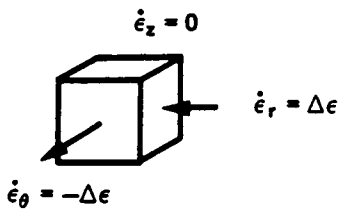
— Undrained Path

- - - - - Drained Path

(A) Initial Stresses



(B) Drained Compression



(C) Undrained Shear

Figure 5.18 Preparation of Prevost Model for ANC Bay Mud

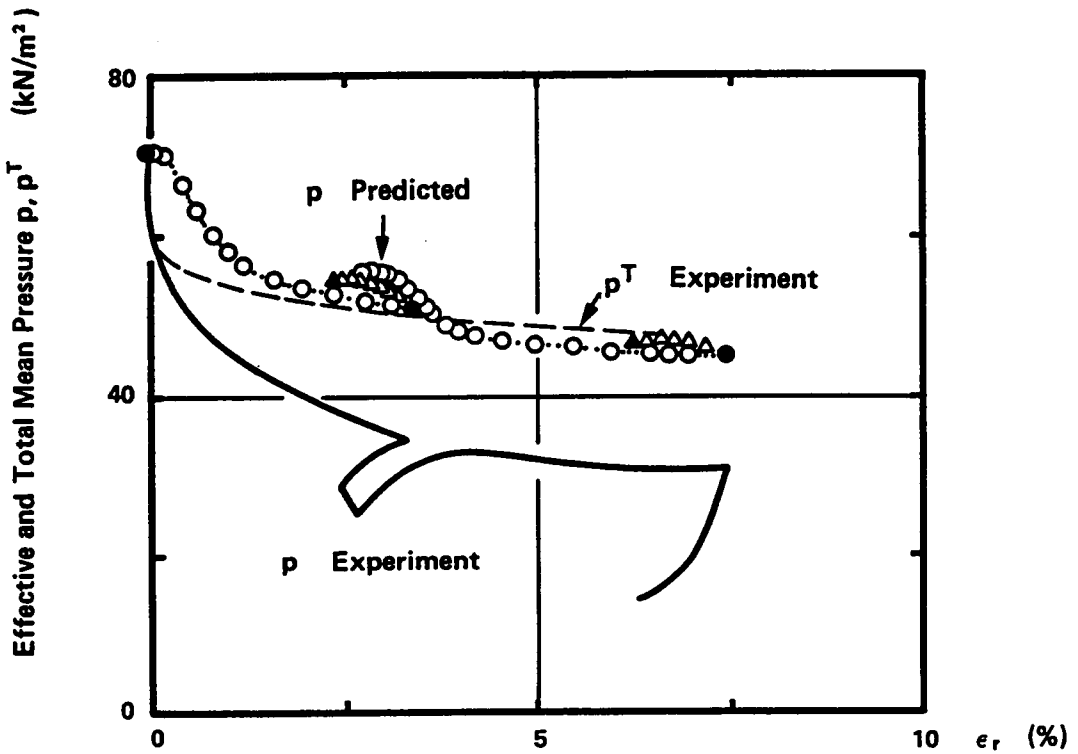
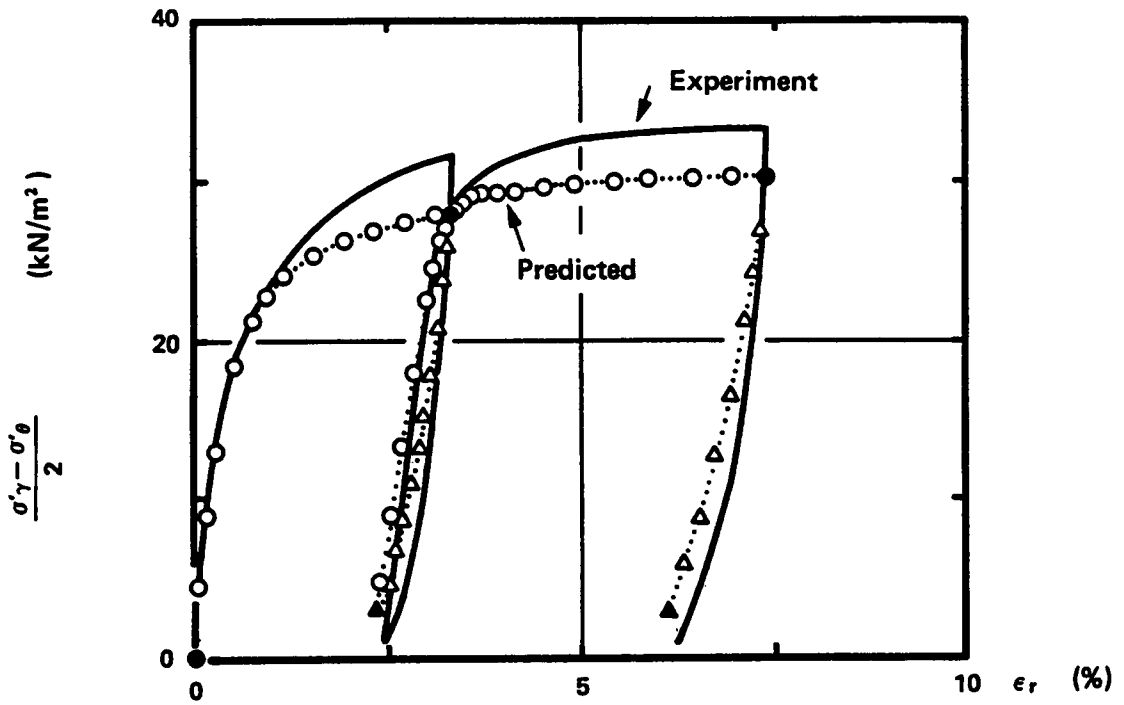


Figure 5.19 Stress-Strain Curve and Mean Pressure Changes in Multicubical Test, ANC Bay Mud

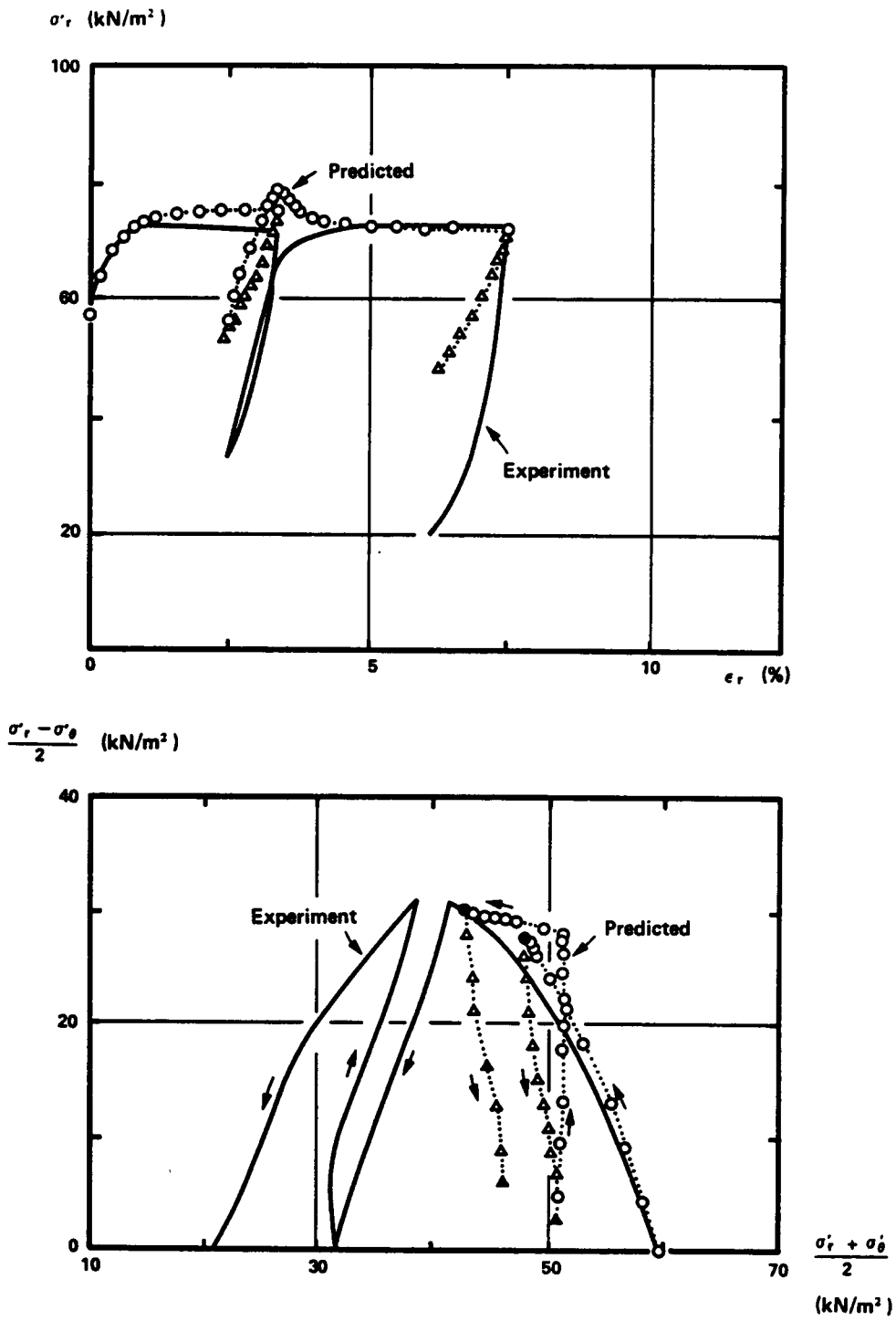


Figure 5.20 Variation of Effective Loading Face Stress and Effective Stress Path in Multicubical Test, ANC Bay Mud

$\sigma'_z$  (kN/m<sup>2</sup>)

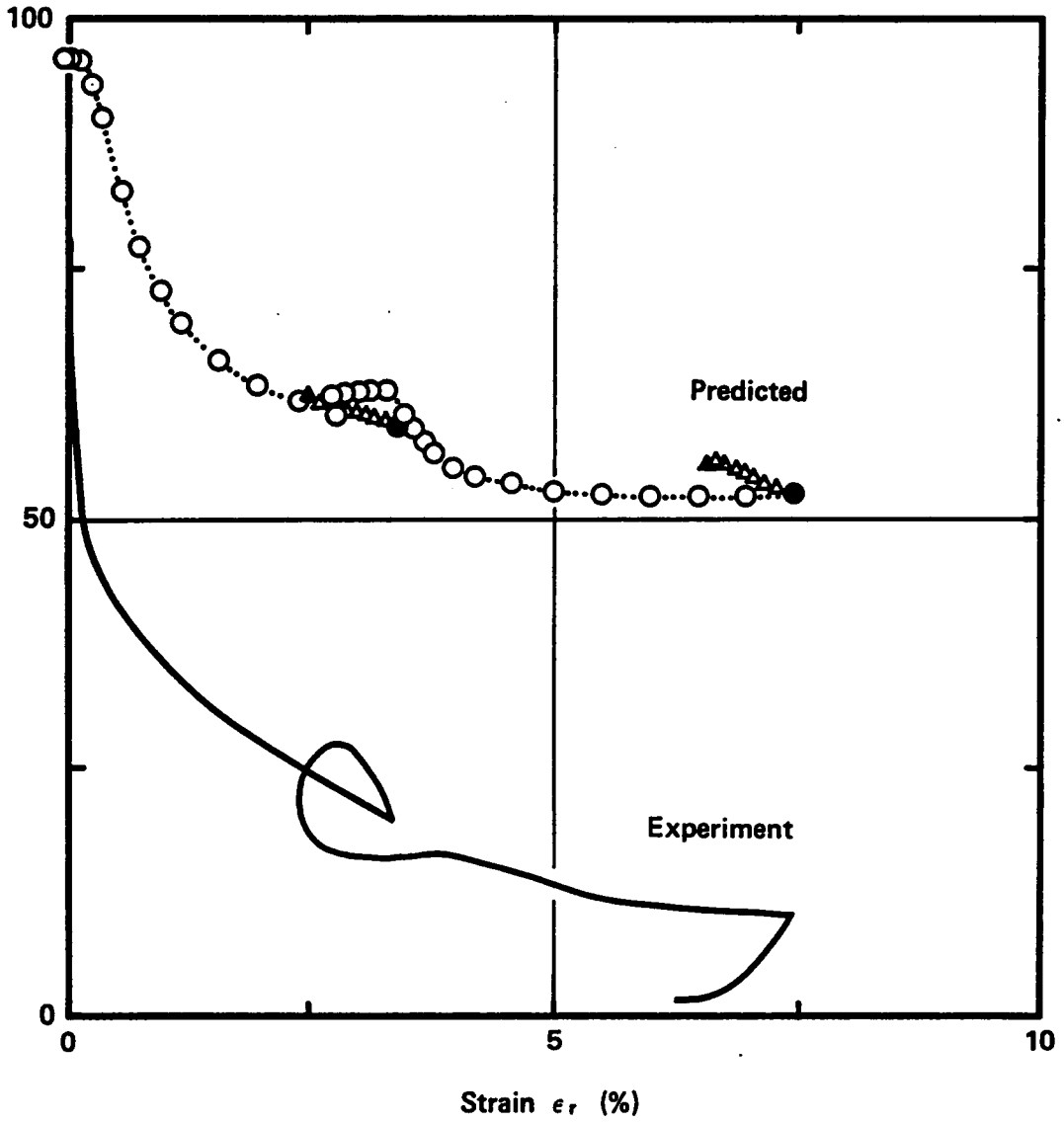


Figure 5.21 Variation of Effective Vertical Stress in Multicubical Test, ANC Bay Mud

## Chapter 6

### DEVELOPMENT OF FINITE ELEMENT CODE FOR USE IN SHIELD TUNNELING SIMULATION

#### 6.1 Introduction

The basis for the finite element code is developed in this chapter. The special considerations that are required for application of the program to the problems that are encountered in the shield tunneling are described.

First, it is necessary to incorporate the elasto-plastic formulation of the Prevost model in the program to deal with the material nonlinearity. Second, in advanced shield tunneling deflections of the ground due to the initial heave and the inward soil movements due to the tail void closure may, at least locally, induce large strains; thus, a large deformation formulation is taken into account. Third, as time-dependent responses of ground movements are observed in the field due to the generation and dissipation of excess pore pressure, a consolidation must be considered and adopted into the program.

#### 6.2 Finite Element Formulation

The basis of the finite element formulation in terms of the displacement method is described briefly to explain further developments in this chapter.

### 6.2.1 Elasto-plastic and Nonlinear Elastic Constitutive Equations

A general constitutive equation can be written in the following form:

$$\dot{\sigma}_{ij} = C_{ijkl} \dot{\epsilon}_{kl} \quad (6.1)$$

Stress  $\sigma_{ij}$  and strain  $\epsilon_{ij}$  are selected in accordance with the reference frame. In a small deformation theory,  $\sigma_{ij}$  and  $\epsilon_{ij}$  are implicitly defined as the Cauchy stress and the Lagrangian linear strain, respectively. However, special attention is required for large deformations, as will be discussed later.

$C_{ijkl}$  is a tensor which constitutes the material's characteristic with respect to the deformation and strength of the material. The constitutive equation for the Prevost model is given in equation 3.36. If one allows the plastic modulus  $H'$  in equation 3.36 to be infinite, then a constitutive equation is obtained for an isotropic elastic material which is equivalent to equation 3.29.

The elastic form of the constitutive equation is of interest inasmuch as a nonlinear elastic model is used herein for certain granular soils in case history studies. Two independent parameters appear in the constitutive tensor of an isotropic elastic material. A nonlinear elastic model uses these same parameters, but they may not be constant. As stresses are increased in the material, values of elastic constants are reduced so as to figure the nonlinear stress-strain relation observed in the laboratory tests. Duncan and Chang (1970) employed a hyperbola to approximate the stress-strain curve, and combined this with a dependency on the confining pressure (Janbu 1963) and the Mohr-Coulomb failure criteria to complete

the Duncan-Chang hyperbolic soil model. Duncan, et al.(1980) modified the model so as to take the volumetric contribution into account.

The complete expression for the tangent modulus of the Duncan-Chang model is

$$E_t = K p_a \left( \frac{\sigma_3}{p_a} \right)^n \left[ 1 - \frac{R_f (1 - \sin \phi) (\sigma_1 - \sigma_3)}{2 c \cos \phi + 2 \sigma_3 \sin \phi} \right]^2 \quad (6.2)$$

where  $E_t$  is the tangent Young's modulus,  $K$  and  $n$  are constant,  $p_a$  is the atmospheric pressure, and  $c$  and  $\phi$  are strength constant.

In this thesis, sandy deposits are modeled by means of this approach, since the parameters can be estimated from the limited amount of data available for these soils.

### 6.2.2 Integration Formulation

The finite element formulation of the displacement method starts with differential equations of stress equilibrium:

$$\frac{\partial \sigma_{ij}^T}{\partial x_j} - F_i = 0 \quad (6.3)$$

where  $x_i$  are the coordinate in Cartesian reference system  
 $\sigma_{ij}^T$  are the components of the total nominal stress tensor  
 $F_i$  are the components of body force.

The essential and natural boundary conditions are

$$d_i = 0 \quad \text{on } S_E \quad (6.4)$$

$$\sigma_{ij}^T n_j = -T_i \quad \text{on } S_N \quad (6.5)$$

respectively, where  $d_i$  and  $n_i$  are components of displacements and an outward normal of the surface. The whole boundary surface consists of  $S_E$  and  $S_N$ .

Let  $d_i$  and  $d_i + \delta d_i$  be displacement fields which satisfy the essential boundary condition of equation 6.4, then the equilibrium equation 6.3 and the natural boundary condition of equation 6.5 can be written in the integrated form

$$\int_V \{ \sigma_{ij}^T \delta \epsilon_{ij} + F_i \delta d_i \} dV + \int_S T_i \delta d_i dS = 0 \quad (6.6)$$

This expression will be referred to repeatedly when the incorporation of the consolidation and large deformation theories is considered.

### 6.2.3 Finite Element Approximation

An approximate solution of equation 6.6 may be obtained by an application of the finite element technique. Discretization of unknown displacement  $d_i$  allows for the integral equation to be written in a set of linear homogeneous equations.

Let  $[N_d]$  be a shape function for displacements,

$$\{d\} = [N_d]^T \{\delta\} \quad (6.7)$$

where  $\{\delta\}$  is a vector that contains values of nodal displacements. After calculating the gradients of  $\{d\}$ , substitution into the integral equation 6.6 yields

$$[K] \{d\} = \{f\} \quad (6.8)$$

where  $\{f\}$  is a nodal force vector and  $[K]$  is a stiffness matrix.

The homogeneous nodal displacement-force relation form of equation 6.8 is not changed even after additional ideas are introduced associated with a coupling formulation of the consolidation theory and an Eulerian formulation of the large deformation theory. The final form of stiffness matrix  $[K]$  will appear with several parts.

$$[K] = [K_{vol}] + [K_{dev}] + [K_{und}] + [K_{flow}] + [K_{init}] \quad (6.9)$$

$[K_{vol}]$  and  $[K_{dev}]$  are volumetric and deviatoric contributions which are corresponding to equations 3.34a and 3.34b, respectively.  $[K_{und}]$  is derived from the bulk modulus of pore fluid.  $[K_{flow}]$  comes from contribution of pore water flow which is dealt with in the consolidation theory. The last term  $[K_{init}]$  is the initial stress stiffness matrix which is required in the large deformation analysis. The last two terms are the subjects of the next two sections.

### 6.3 Pore Fluid Flow and Consolidation

The essential parts of the theory of consolidation will be outlined in this section as incorporated in the finite element program. Comparisons of the predicted results with closed form solutions will demonstrate the validity and accuracy of the program.

#### 6.3.1 Consolidation Theory

The compression of soils under a load due to a squeezing out of the pore water is called consolidation. Terzaghi (1925) explained this phenomenon for the case of one-dimensional consolidation, and it was later

generalized to three dimensions by Biot (1941).

The analytical expression of the consolidation problem requires field and constitutive coupled equations based on the mixed formulation. A solution may be obtained numerically by use of the finite element method for complicated boundary value problems. Christian (1968) derived a variational form and solved for static stress distribution for undrained, incompressible soils, and Sandhu and Wilson (1969) proposed a finite element procedure for an elastic medium in more general form. Booker and Small (1975) used a different approach for the problem of elasto-plastic consolidation considering various yield conditions of soil. Prevost (1981, 1982c) proposed a similar method to analyze transient behavior of an elasto-plastic porous media. Finally, Johnston (1981) followed Booker's approach to combine consolidation theory with the Cam Clay soil model. The same method will be used in this thesis with the Prevost model. The complete mathematical formulation can be seen in Booker and Small (1975) and Small, et al. (1976).

### 6.3.2 Governing Equations and Integral Formulation

Biot's equation was derived from the following considerations: (1) the stress equilibrium, (2) the constitutive relation between effective stresses and strains, (3) Darcy's law which governs pore water flow, (4) continuity conditions. Condition (1) has been shown in equation 6.3. The other conditions lead to the following equation:

$$\dot{\sigma}_{ij} = \dot{\sigma}_{ij}^T - \dot{u}\delta_{ij} = C_{ijkl} \dot{\epsilon}_{kl} \quad (6.10)$$

$$v_i = -\frac{k_{ij}}{\gamma_w} \frac{\partial u}{\partial x_j} \quad (6.11)$$

$$\frac{\partial v_i}{\partial x_i} = -\frac{\partial \epsilon_v}{\partial t} \quad (6.12)$$

where  $u$  is the pore pressure  
 $v_i$  are the components of the superficial velocity  
 $k_{ij}$  are the coefficients of permeability tensor  
 $\gamma_w$  is the unit weight of water  
 $t$  denotes the time.

Boundary conditions are required to be set forth for the pore pressure in addition to the boundary conditions for displacements given in equations 6.3 and 6.4.

$$u_i = 0 \quad \text{on} \quad S_{Eu} \quad (6.13)$$

$$n_i v_i = 0 \quad \text{on} \quad S_{Nu} \quad (6.14)$$

For a kinematically admissible virtual displacement  $\delta d_i$  and virtual pore pressure  $\delta u$ , the governing equations 6.10 through 6.12 and associated natural boundary condition 6.14 can be written in a weak form integral expression that is similar to the equation 6.6.

$$\int_V \{ -C_{ijkl} \dot{\epsilon}_{kl} \delta \epsilon_{ij} + \dot{u} \delta \epsilon_v \} dV + \int_V \dot{F}_i \delta d_i dV + \int_S \dot{T}_i \delta d_i dS = 0 \quad (6.15)$$

$$-\int_V \left\{ k_{ij} \frac{\partial u}{\partial x_i} \frac{\partial \delta u}{\partial x_j} + \frac{\partial \dot{\epsilon}_v}{\partial t} \delta u \right\} dV = 0 \quad (6.16)$$

where  $T_i$  is the surface traction. These two equations are mathematically equivalent to those found in the Biot theory.

### 6.3.3 Finite Element Approximation

Similar to the approach in Section 6.2.3 where the integral form of governing equations is reduced to a set linear homogeneous equations, the equations 6.15 and 6.16 will be approximated with discretization.

$$\mathbf{u} = \{N_u\}^T \{q\} \quad (6.17)$$

where  $\{N_u\}^T$  is a shape function for the pore pressure and  $\{q\}$  includes nodal values of pore pressure. It is recommended that the order of  $N_u$  is lower than that of  $N_d$  by one, so that a matching of stress and pore pressure distributions may be obtained (Johnston 1981, Christian 1977).

After substituting equations 6.7 and 6.17 to the coupled equations 6.12 and 6.13, the final form of equations for an element is obtained in a form of

$$[K] \{\dot{\delta}\} + [L]^T \{\dot{\delta}\} = \{\dot{f}\} \quad (6.18a)$$

$$-[L] \{\dot{\delta}\} - \beta \Delta t [\phi] \{\dot{q}\} = \Delta t \{n\} + \Delta t [\phi] \{q_0\} \quad (6.18b)$$

where  $[L]$  and  $[\phi]$  are coefficient matrices which control volumetric response,

$\{n\}$  is a vector reflecting gravity effects,

$\{q_0\}$  is the pore pressures at the beginning of the increment,

$\beta$  is the time integration parameter.

In view of the coefficient matrices of the above equation, the rows and columns associated with the pore pressure degrees of freedom  $\dot{q}$  appear besides the ordinary stiffness matrix  $[K]$ . Moreover the overall coefficient matrix is symmetric  $\{f\}$  is an ordinary load vector. The coupling

term  $[L]$  controls the interaction between volumetric response of soil and pore pressure changes.

An eight-noded quadrilateral element with a pore pressure degree of freedom at the corner nodes (Q8P4) will be used hereafter to implement this formulation.

#### 6.3.4 Time Integration

The time integration rule used for equation 6.18b is defined in terms of the value of  $\beta$ , which may vary from zero of a purely explicit scheme to one that is purely implicit. When  $\beta = 0.5$ , it corresponds to a trapezoidal rule, and when  $\beta = 2/3$  it corresponds to a parabolic rule. Booker and Small (1975) showed that for  $\beta$  greater than or equal to one half, the solution is unconditionally stable. Johnston (1981) and Finno (1983) used  $\beta = 0.5$  in their tunnel analyses in which the Cam Clay soil model was incorporated.

Hughes, et al. (1979) developed an implicit-explicit operator splitting method, which enables an efficient treatment of kinematic constraints in transient analysis. Prevost (1982c) applied that method to solve consolidation problems of elasto-plastic media represented by the Prevost model. He used a backward difference scheme in time integration which is equivalent to  $\beta = 1.0$ . This thesis also employs the Prevost model, but the time integration method with  $\beta = 0.5$  will be used according to the Booker and Small (1975) approach.

In addition to the importance of the value of  $\beta$ , the time integra-

tion step size,  $\Delta t$ , has an influence on stability and accuracy. It depends on the drainage path length, permeability of soil and pore pressure gradient. The initial time step is selected in this thesis to be an order of  $10^{-4}$  for nondimensional time,  $T$  (the time factor in the one-dimensional consolidation theory). The time step can be increased throughout the marching process without losing numerical stability if  $\beta \geq 1/2$ . with the value of  $\beta$  being 0.5, five time increments are taken to cover a tenfold increase in time in all calculations.

In order to determine if the formulation is accurate, some results of numerical experiments for particular consolidation problems are demonstrated in the following sections.

### 6.3.5 Hydrostatic Pressure and Seepage

As a start, the new program must predict steady state pore pressure distributions in the pressure of steady seepage. Predictions for special cases with hydrostatic pressure and steady seepage flow are given by the finite element program and shown in Figures 6.1 and 6.2. Exact pressure distributions are also shown in the figures for comparison.

In Figure 6.1(a), the water table in a level ground is initially at the level of base (1). It is raised by head of  $3h$  to the ground surface (H) and kept at this level. After a period of time long enough to stabilize the pressure the final distribution of hydrostatic pressure is calculated. The pore pressures are predicted accurately. The  $\{n\}$  vector in equation 6.18b found properly evaluated. The water table in the left of

pervious soil zone rises by  $3h$  from  $L$  to  $H$  in height as shown in Figure 6.1(b). After steady state of seepage flow is established, the predicted pressure gradient is found as expected.

Figure 6.2 demonstrates a situation with radial flow. The finite element program accurately predicts flow fields in a steady state. These studies show that the term involving  $[\phi]$  matrix in the equation 6.18b is correctly accounted for. In this case the soil is idealized as rigid for given small seepage forces involved, and thus the coupling term represented by  $[L]$  matrix is negligible.

### 6.3.6 One-Dimensional Consolidation

One-dimensional consolidation occurs when a uniform load is applied to a clay layer and drainage is allowed to occur in the vertical direction only. Settlement occurs with time as excess pore pressure is allowed to dissipate. In this section linear and nonlinear consolidation processes are concerned.

If the soil skeleton is assumed to behave elastically, the consolidation process can be analyzed with Terzaghi's theory. The solution is given in a form that the excess pore pressure  $u$  is related to its initial value  $u_0$ .

$$u = Bu_0 \tag{6.19}$$

where

$$B = \sum_{m=1}^{\infty} \frac{2}{M} \left( \sin M \frac{Y}{H} \right) e^{-M^2 T} \tag{6.20}$$

$$M = \frac{\pi}{2} (2m + 1) \tag{6.21}$$

$$T = \frac{c_v t}{H^2} \quad (6.22)$$

$c_v$  is the coefficient of consolidation and is equal to  $k_y/\gamma_w m_v$ . The vertical permeability  $k_y$  and the constrained compressibility  $m_v$  are assumed to be constant. The degree of consolidation is given by

$$U = 1 - \sum_{m=1}^{\infty} \frac{2}{M^2} e^{-M^2 T} \quad (6.23)$$

Equations 6.19 and 6.23 are plotted in Figures 6.3 and 6.4. The results of finite element analyses using five Q8P4 elements are also shown in the figures. There is excellent agreement with the theoretical values. All the terms in the equations 6.18a and 6.18b are involved in this calculation and thus the coupled formulation of the finite element method used in this thesis is verified.

Davis and Raymond (1965) modified the Terzaghi's consolidation theory and introduced nonlinearity to the consolidation process. The results of oedometer test on normally consolidated soils show that void ratios plot as straight lines against the logarithm of applied pressures. This leads to the constrained compressibility  $m_v$  approximately proportional to the inverse of the pressure  $p$ . The coefficient of consolidation in this case is relatively constant and it may be assumed that the decrease in permeability is proportional to the decrease in compressibility. The solution obtained is dependent on the ratio of the initial pressure  $\sigma_{yi}$  to the final pressure  $\sigma_{yf}$  :

$$\frac{\sigma_{yf} - u}{\sigma_{yf}} = \left( \frac{\sigma_{yf}}{\sigma_{yi}} \right)^{-B} \quad (6.24)$$

where  $B$  is the same as in equation 6.20. It is interesting to note that the degree of consolidation  $U$  in this nonlinear process of consolidation is found the same as that in Terzaghi's theory, equation 6.23.

Similar to the power law of equation 3.32, the permeability is assumed to change with pressure:

$$k_{ij} = k_{ij0} \left(\frac{p}{p_0}\right)^{-n} \quad (6.25)$$

where  $k_{ij0}$  is permeability at a reference pressure. The exponent  $n$  is the same as before. When the value of  $n$  is given unity for the permeability and the bulk modulus, the consolidation process becomes equivalent to that investigated by Davis and Raymond (1965).

Excess pore pressures in the nonlinear consolidation are calculated for a ratio  $\sigma_{yi}/\sigma_{yf}$  of two. Excess pore pressure distributions and their variation with time are demonstrated in Figures 6.5 and 6.6, respectively. Those predicted by Terzaghi's theory are also shown in the figures. Three Q8P4 elements are used to follow the process in which the bulk modulus and the permeability are updated at every time integration process. In spite of the coarse mesh scheme, the predicted results agree very well with the theoretical values. Therefore it is considered that the integration scheme employed in this thesis effectively deals with nonlinear soil behavior.

### 6.3. Two-Dimensional Consolidation

Solutions to the Biot's equation are found only for problems with very simple boundary conditions. The case of a strip load on an infinite

elastic half space was solved by Schiffman, et al.(1969). Later Gibson, et al.(1970) solved for the problem of a strip or circular load on an elastic layer on the rigid base.

The finite element mesh used is shown in Figure 6.7. The drainage is allowed only at the surface. Figure 6.8 shows the computed dimensionless excess pore pressure as a function of the dimensionless time factor  $T$ . The results are presented as ratios of excess pore pressure to its initial value at a point below the load. The closed-form solution for the case of a half space is plotted in the figure. They agree very well.

The numerical solutions also predict an increase in excess pore pressure beyond the initial value which occurs at the early stage of consolidation. This phenomenon is known as the Mondel-Cryer effect and is characteristic of the coupled consolidation theory. Cryer (1962) found such a phenomenon with respect to the pore pressure at the center of saturated sphere of the soil. It is explained as an oscillation due to the process of total stress transfer (Schiffman, et al. 1969).

### 6.3.8 Pseudo-Three-Dimensional Condolidation

The coupled formulation with respect to a consolidation analysis for three-dimensional conditions is available. However, only a plane strain version is used in this thesis and it must serve to approximate any three-dimensional effects in shield tunneling. To handle this, it is proposed that a simplified out-of-plane drainage in the expression of volumetric equilibrium be considered while the plane strain deformation is reserved.

As illustrated in Figure 6.9, the out-of-plane drainage is assumed such that the pore pressure decreases linearly to vanish in a certain drainage length  $l_{eq}$  transverse to the plane of analysis. Darcy's law is applied to the out-of-plane flow and thus the integration form of volumetric expression, equation 6.16, gains another term.

$$-\int_V \left\{ k_{ij} \frac{\partial u}{\partial x_j} \frac{\partial \delta u}{\partial x_i} + \frac{\partial \dot{\epsilon}_v}{\partial t} \delta u + \frac{k_z}{\gamma_w l_{eq}} (u - u_0) \delta u \right\} dV = 0 \quad (6.26)$$

Discretization leads to a matrix expression similar to equation 6.18b.

$$-[\mathbf{L}]\{\dot{\delta}\} - \beta \Delta t ([\phi] + [\phi_z])\{\dot{\mathbf{q}}\} = \Delta t (\{\mathbf{n}\} + \{\mathbf{n}_z\}) + \Delta t ([\phi] + [\phi_z])\{\mathbf{q}_0\} \quad (6.27)$$

where

$$[\phi_z] = \int_V \{N_u\} \frac{k_z}{\gamma_w l_{eq}} \{N_u\}^T dV \quad (6.28)$$

$$\{\mathbf{n}_z\} = \int_V \{N_u\} \frac{k_z}{\gamma_w l_{eq}} u_0 dV \quad (6.29)$$

$\{N_u\}$  is the shape function for the pore pressure same as before.

Effects of the out-of-plane drainage are shown in Figure 6.9. Three different values are selected for the drainage length  $l_{eq}$  while the permeability  $k_z$  is the same as that in the region of concern. An infinitely long  $l_{eq}$  results in one-dimensional consolidation. For smaller values of  $l_{eq}$ , the consolidation is accelerated significantly and the three-dimensional effect in the consolidation process is accounted for to some degree. It is difficult to select an appropriate  $l_{eq}$  for specific problems, although it is reasonable to assume that  $l_{eq}$  is the distance to a point where the pore pressure is little affected by the applied load  $\Delta\sigma$ .

### 6.3.9 Summary

The coupled formulation of consolidation theory is herein described. The theory is incorporated into the finite element program to compute pore pressure variations in a problem with a complicated boundary value problem. Simple cases were examined to obtain numerical solutions for comparison with closed-form solutions. Because agreement is obtained, it is concluded that the consolidation process is accurately calculated in the finite element analysis.

## 6.4 Large Deformations

A finite element formulation with large deformation theory is discussed in this section. In soils, the modulus gets smaller as the soil approaches failure. This can result in a large deformation of soil mass. In shield tunneling, soils adjacent to the tunnel are subject to a wide range of strain levels depending on the performance. For advanced shield tunneling, soils are forced to deform near the shield face in the initial heaving stage and near the shield tail upon the tail void closure. The deformation for such situations may be large enough to be analyzed in consideration of the large deformation formulation.

### 6.4.1 Reference Frame

Two possible reference frames, Lagrangian and Eulerian descriptions, are used to cope with geometrically nonlinear problems due to large deformations. In a Lagrangian approach, the coordinate system remains fixed in

space. Displacements are referred to the original configuration. This method takes nonlinear terms of Lagrangian strain into account and leads to an asymmetric stiffness matrix (Zienkiewicz 1977).

In contrast, an Eulerian approach employs the coordinate system which is fixed on the material. This method is approximated by taking small load increments so as to enable the use of linear Eulerian strain while updating the coordinates after each increment. McMeeking and Rice (1975) used this approach to incorporate the constitutive relation which had been proposed by Hill (1959) to adapt for large deformations, and this is the method used here.

#### 6.4.2 Large Deformation Form of Constitutive Equation

Yamada and Wifi (1977) discussed the relationship between different measures of stress. It is important to adopt an appropriate stress definition in the variational form of the finite element formulation. The method applied by McMeeking and Rice (1975) is followed here.

The equilibrium equation 6.3 and its integral form, equation 6.6, are conveniently written in terms of Lagrangian nominal stress  $\sigma_{ij}$ . A material derivative of nominal stress  $\dot{\sigma}_{ij}$  is simply related to the Jaumann derivative of the Cauchy stress  $\overset{*}{\sigma}_{ij}$ :

$$\overset{*}{\sigma}_{ij} = \dot{\sigma}_{ij} + \sigma_{ik} \omega_{kj} + \sigma_{jk} \omega_{ki} \quad (6.30)$$

where  $\omega_{ij}$  is skew tensor. The Jaumann derivatives of the Kirchoff and Cauchy stress,  $\overset{*}{\tau}_{ij}$  and  $\overset{*}{\sigma}_{ij}$ , are related to each other by an equation,

$$\tau_{ij}^* = \sigma_{ij}^* + \sigma_{ij} \epsilon_{kk} \quad (6.31)$$

In the large deformation formulation stress and strain in the constitutive equation 6.1 must be the Jaumann derivative of the Kirchoff stress  $\tau_{ij}^*$  and the Eulerian stress  $\tilde{\epsilon}_{ij}$ . Substituting equations 6.30 and 6.31 into the integral form of governing equation 6.6, the final expression is given in a form

$$\int_V \left\{ \tau_{ij}^* \delta \tilde{\epsilon}_{ij} + \frac{\partial \delta v_k}{\partial X_i} \sigma_{ij} \frac{\partial v_k}{\partial X_j} - 2\delta \tilde{\epsilon}_{ki} \sigma_{ij} \tilde{\epsilon}_{kj} + F_i \delta d_i \right\} dV + \int_S T_i \delta d_i dS = 0 \quad (6.32)$$

Performing discretization for the displacement field using equation 6.7, the above equation can be written in an approximate form of matrix notation.

$$([K] + [K_\sigma]) \{\dot{\delta}\} = \{\dot{f}\} \quad (6.33)$$

where  $[K_\sigma]$  is called an initial stress stiffness matrix arising from the second and third terms of the integrand for the volumetric integration.

### 6.4.3 Stress Corrections

In order to represent large deformations, additional terms appear beyond the small deformation approach to correct stresses matching the current state of reference. The effects of these terms will be examined.

The Jaumann derivative of stress, equation 6.30, serves the stress corrections due to rigid rotation. An element is considered such that it is initially prestressed with  $\sigma_x$  in the x-direction as shown in Figure 6.10. Then this element is rotated through  $90^\circ$  without deformation. A new state after rotation of angle  $\theta$  may be analyzed by means of Mohr's

circle. Computed results for three different angle increment  $\dot{\theta}$  are compared with the theoretical values in the figure. Prescribed nominal stresses may not change with rigid rotation. Although exact corrections are not expected, considerable improvements are obtained due to the terms with spin tensor in the Jaumann derivative in equation 6.30.

Figure 6.11 gives the effects of the stress corrections in addition to the rigid rotation. An elastic element is subjected to vertical compression and lateral shear simultaneously. The computed stresses are plotted against the vertical deformation which is represented by linear Lagrangian strain  $\epsilon_y$ . Starting with a small deformation presentation, Figure 6.11 compares the effects of a series of stress corrections which involve the updating of coordinates  $[X_{up}]$ , the initial stress stiffness matrix  $[K_\sigma]$ , the rigid rotation  $[\omega]$ , the volumetric correction to follow the equation 6.31  $[\epsilon_v]$ , and the residual or unbalanced load correction  $[\sigma_0]$ . It is seen that the effects of updating coordinates and volumetric correction are significant in this particular case. However, it depends on the situation as to which term may significantly contribute to the stress correction.

Johnston (1981) commented that because intermediate strains are anticipated in tunnel analysis, all of the stress correction terms may not be taken into consideration. He finally applied only the updating of the nodal coordinates in his tunnel analyses. However, a thorough formulation for a large deformation scheme does not require significant computational efforts, and therefore, all the correction terms are accounted for in the analyses in this thesis, except the residual load correction.

#### 6.4.4 Large Deformation Analysis of One-Dimensional Consolidation

A one-dimensional elastic consolidation is analyzed with consideration given to large deformations. Figure 6.12 compares the computed settlements at the loading surface by means of the large and small deformation analyses. Differences in the final settlement are large when the surcharge pressure is large.

The final theoretical settlement  $\delta$  with large deformations is given in the following equation:

$$\frac{H - \delta}{H} = \exp\left(-\frac{\Delta\sigma}{E}\right) \quad (6.34)$$

The values of  $\delta/H$  are shown in Table 6.1 in which the predicted values are compared with the theoretical values. They agree very well, and the formulation of large deformation theory in the program is verified for this condition.

In view of the settlement curves, it is noted that the final settlement is reached earlier for the large deformation analysis than for the small deformation analysis. This can be attributed to the progressively shorter drainage paths that result from updating the coordinates. Carter, et al. (1977) presented these trends in their finite element results.

#### 6.4.5 Summary

A large deformation formulation with finite element methods is outlined, which leads to a symmetric stiffness matrix and enables problems involving large strains to be solved accurately. This feature of the

finite element program will be used in the tunnel analyses.

## 6.5 Incorporation of Elasto-plastic Constitutive Law

In addition to the fore-mentioned features, it is necessary to incorporate the Prevost model into the finite element program.

### 6.5.1 Deviatoric Yielding under Plane Strain Condition

In the plane strain analysis, loading processes are described in terms of in-plane stress  $\sigma_y$  and  $\sigma_x$ , while the out-of-plane strain  $\epsilon_z$  is fully constrained. Thus a mixed representation of a stress state appears in the constitutive relation. This is a possible cause of sensitivity that occasionally leads to numerical instability in the calculation of the constitutive equation. Such a problem will be discussed from the viewpoints of hardening associated with both the deviatoric yielding and the volumetric yielding. The deviatoric yielding under the plane strain condition is first examined.

Figure 6.13 pictures the octahedral plane which includes the deviatoric semiaxis of the Prevost model yield surface, that is,  $p = \beta$ . Relative configurations of yield surfaces are also shown in the figure for the Cam Clay model and the Von Mises and Mohr-Coulomb yield criteria. The Prevost model yield surface shares with other criteria the stress point C which is on the stress path of the triaxial compression test. In contrast, the Prevost model yield surface is calibrated against the Mohr-Coulomb yield criteria along the triaxial extension test path at point E.

A stress path associated with the plane strain test may deviate from the triaxial plane CE . For a perfectly compressible material that has no lateral deformation when it is loaded uniaxially, the stress path caused by the plane stress test stays on the triaxial plane as a particular case. On the other hand, the perfectly incompressible material follows the stress path of

$$\sigma_z = \frac{1}{2} (\sigma_x + \sigma_y) \quad (6.35)$$

in the plane strain test. This is true even after yielding occurs if no volumetric changes are involved. Equation 6.35 determines a stress path of OD in Figure 6.13 which is referred to as an incompressive line.

The stress path encounters the Prevost model yield surface at D , whereas it reaches the Mohr-Coulomb yield surface at F . Yielding in this situation occurs less at a shear stress level for the Mohr-Coulomb criteria than it does for the Prevost model.

Actual stress paths associated with the plane strain test fall in the range between the above mentioned two extremes, that is, some place on the arc CD of the yield surface. It is assumed that a Prevost model consists of a single cylindrical yield surface for which the volumetric term and the anisotropy are neglected, that is  $c = 0$  and  $\alpha_{ij} = 0$  in the yield function of equation 3.6. This becomes equivalent to the Von Mises yield criteria. The outward normal of the yield surface is always perpendicular to the hydrostatic axis and thus no plastic volumetric strains are involved. With such circumstances an undrained plane strain test is simulated, one in which a constant volume is assured during shear. The material is assumed to be elastically compressible with  $\nu^e = 0.3$  . Further an isotropic hard-

ening with a constant plastic shear modulus is assumed for yielding behavior. The computed stress paths projected onto the octahedral plane are shown in Figure 6.14.

An elastic response yields a straight stress path within the region bounded by the yield surface. Once the yield surface is reached, a plastic flow occurs to modify the stress state. During the yielding process the predicted incremental lateral stress  $\dot{\sigma}_z$  may be larger than the incremental loading stress  $\dot{\sigma}_y$  so that the stress point moves toward the incompressible state line. As the plastic state matures, the stress path asymptotes the incompressible state line. The smaller the plastic shear modulus is, the faster the stress point approaches the incompressible state line.

For a special case of elastic-perfectly plastic behavior,  $H' = 0$ , the stress point moves along the yield surface because no hardening is present. It should be noted that failure of the material does not occur at the point where the yield surface is first reached, but it does when an incompressible stage is established because of the plastically incompressive nature of yielding. A mathematical explanation of the failure has been given in Section 3.2.7, in which the elasto-plastic modulus was examined. The failure occurs when the elasto-plastic stiffness  $C_{ijkl}^{e-p}$  becomes singular. It happens when the direction of the incremental total strain  $\dot{\epsilon}_{ij}$  coincides with that of the normal of yield surface  $Q_{ij}$ . Due to the contribution of the incremental elastic strain components  $\dot{\epsilon}_{ij}^e$ ,  $\dot{\epsilon}_{ij}$  is not parallel to  $Q_{ij}$  except the point on the incompressible state line. Figure 6.14 shows that the elastic-perfectly plastic response is in conformity with the theoretical consideration. This serves as one piece

of evidence that the elasto-plastic formulation is adequate.

The stress paths in the figure are calculated under a totally strain-controlled loading procedure to establish the volumetric constraint and the plane strain condition. This avoids a mixed representation of the constitutive equation. However this is not the case with ordinary plane strain loading procedures. Loading stress  $\sigma_y$  and lateral stress  $\sigma_z$  are given while out-of-plane strain  $\epsilon_z$  is fully constrained as shown in Figure 6.15(d).

The predicted stress path with the ordinary loading procedure is shown in Figure 6.15(a) with the same conditions as employed in the previous discussion and with  $H'/2G = 0.1$ . This is different from that shown in Figure 6.14, and significant fluctuations of the stress path appear. When the stress point overshoots the incompressible state line, negative incremental out of plane stress  $\dot{\sigma}_z$  is calculated in spite of the positive loading  $\dot{\sigma}_y$  being applied. However it becomes stable with oscillation about the incompressible state line as the plastic state are in full development. In contrast to the isotropic hardening case, the oscillation of the stress path for the kinematic hardening case is not stabilized as shown in Figure 6.15(b), which is obtained in the exactly the same situation except for the hardening rule.

The loading stress increment used is unchanged in the course of the loading process. However, the loading increment becomes smaller relative to the size of the yield surface in case of the isotropic hardening where the yield surface expands with hardening. This is not the case for the

kinematic hardening. The relative magnitude of the applied incremental stress is considered responsible for the degree of fluctuation of the stress path to be predicted.

The loading increments used in these cases are about one percent of the size of yield surface  $k$ . It is practically difficult to apply a smaller increment in the finite element analysis from the viewpoint of computational efforts. Therefore fluctuations similar to the ones discussed here may be anticipated in the results obtained for boundary value problems.

#### 6.5.2 Volumetric Yielding under Plane Strain Condition

Prediction of stresses under the plane-strain condition is found sensitive to the size of the loading increment relative to the size of the yield surface when the deviatoric or volumetric yielding was concerned.

Volumetric yielding is examined for an ellipsoidal yield surface with isotropic hardening like the Cam Clay model. It is assumed that a soil is initially in an isotropic stress state and undergoes a drained shear in a plane strain condition.

Figure 6.16 shows stress-strain curves and stress paths for four different loading increments. Both the stress-strain curves and the stress paths exhibit significant fluctuations. As the loading increment decreases, the predicted values are improved with more stable and reasonable trends. This result gives a clue as to how to select the loading increment to obtain a reasonable prediction for shearing. However, it is often difficult

to employ such a small loading increment like the smallest one in the finite element analysis on boundary value problems. Therefore it is concluded that certain errors may be included in the results obtained with a practical loading increment, but that these should be minimized.

### 6.5.3 Bearing Capacity of Footing

In order to demonstrate the validity of the finite element program with the elasto-plastic formulation, a classical problem of the bearing capacity of footing is investigated. This type of problem has been studied for the Prandtl-Reuss material (Hill 1950) and for the Mohr-Coulomb material (Sokolovski 1965). Finite element analyses of the same problem are presented by Chen (1975), Yamada and Wifri (1977), Small, et al. (1976), and Carter, et al. (1977). This section concerns itself with the case of a Prandtl-Reuss material, which is an incompressible, isotropic, and elastic-perfectly plastic. The Von Mises yield criteria is used to lead to  $H' = 0$ . The finite element mesh used is the same as that used before in Figure 6.7. The limit load of the bearing capacity for this situation is  $(2 + \pi) B s_u$ , where  $B$  and  $s_u$  are the width of the footing and undrained strength of the soil, respectively.

Figure 6.17 shows the predicted footing settlements. The results that are calculated with the large deformation theory yield a better response of the footing near the ultimate state. In the first trial in this case, the stress point often overshoots the yield surface and violates the consistency condition. Such an incompatible condition may be improved by scaling (Chen 1975) and unbalanced load corrections (Zienkiewicz 1977).

Taking advantage of these techniques, the resulting settlement curve is shown in Figure 6.18. Thus, considerable improvements are obtained.

Figure 6.19 shows the development of zones where soils have yielded with respect to the pressure applied on the footing. It is seen that a shear band develops from the edge of the footing under it. Figure 6.20 pictures the velocity field at the bearing pressure close to the ultimate load. It resembles the Prandtl solution though the mesh scheme is not fine enough for direct comparison.

In view of the results of a footing analysis on the bearing capacity which predicts the ultimate bearing pressure accurately, it is concluded that the finite element program incorporating an elasto-plastic formulation is able to provide accurate predictions up to the state close to soil failure.

#### 6.5.4 Partially Drained Plane Strain Test

With the constitutive law of the Prevost model coupled with the consolidation theory, the finite element program can deal with the elasto-plastic time dependent behavior of the soil. To examine this, plane strain tests with partial drainage are investigated in this section. In this case the distance of the drainage path and loading rate are selected as parameters to picture the response of a soil subjected to shear and consolidation simultaneously. The loading rate is defined by

$$\omega = \frac{d\epsilon_y}{dT} \quad (6.36)$$

where  $T$  is dimensionless time ( $C_v t/H^2$ ),  $\epsilon_y$  is strain in the loading direction. The Prevost model parameters to be used here are those shown in Table 4.3. The undrained plane strain response for this soil was examined in the Section 5.5.

Fully drained and fully undrained stress paths are shown in Figure 6.21. The initial stress state is on the  $K_0$  line. However, the critical state line where the soil fails is not known because the figure is not a  $p - q$  diagram but the conventional stress path. Both undrained and drained paths exceed the Mohr-Coulomb yield criteria, which is explained with the help of Figure 6.13. For the fully undrained plane strain compression test, the stress point projected on the octahedral plane moves along the line  $OD$  of the incompressible state line. The stress point first reaches the Mohr-Coulomb yield surface at point  $F$  and later the Prevost yield surface at point  $D$ . The Prevost model predicts that soils fail at the point  $D$  which is beyond the Mohr-Coulomb yield surface. The ratio  $OD/OF$  is about 1.35. Magnifying the  $K_f$  line of the Mohr-Coulomb yield criteria in Figure 6.21 by 1.35, a new  $K_f$  line of the Prevost model approximates the failure point  $D$  back in Figure 6.13. Incidentally, the undrained path terminates close to the  $K_f$  line of the Prevost model as is seen in Figure 6.21.

Free drainage is allowed at the top, bottom and side faces of the specimen of the plane strain test as shown in Figure 6.22. Twenty-five Q8P4 elements model one quarter portion of the specimen. The principal stress orientations and distribution of volumetric strain  $\epsilon_v$  are shown in the figure at the instance when the vertical strain  $\epsilon_y$  reaches 2.5

percent. The undrained stress-strain curve of plane strain test is available in the Figure 5.9 for the same Prevost model. The 2.5 percent of the strain corresponds to a state very close to the failure in the undrained test. High volumetric strains are found on the margin of the specimen, in particular along the loading face. In contrast, little changes are predicted in the center portion of the specimen. No significant rotations of the principal stresses are indicated.

Figure 6.23 shows stress paths followed by four elements selected in the specimen. The element [a] is located near the center of the specimen and exhibits a stress path very similar to the fully undrained path. On the other hand, the corner element [d] plots a path analogous to the drained path. The other element [b] and [c] yield intermediate paths. They are likely undrained in the early stages and then switch to a drained-like response in the later stages of the test.

The response of the soil appears to vary with location, and may be caused by the different distances of drainage paths. The effects of the loading rate are demonstrated in Figure 6.24, in which isochrones are drawn for three different loading rates,  $\omega = 1$ ,  $1/10$  and  $1/100$  at the time of 2.5 percent vertical strain. It is clearly shown that excess pore pressures do not dissipate when the loading is fast, as is the case of  $\omega = 1$ . Significant parts of excess pore pressure have dissipated for the slow loading of  $\omega = 1/100$ .

Figure 6.25 shows stress paths for the same element for the three loading rates. When loading is fast, the response is undrained. Slow

loading causes the stress path to be about the drained path. Overall stress-strain curves are compared with the undrained and drained curves in Figure 6.26.

These studies show that the finite element program can predict a partially drained response of soil. When drainage is allowed during loading, the soil's response is calculated such that it falls in between an undrained and a drained response. A longer distance of the drainage path and higher loading rate results in a response more like the undrained behavior.

#### 6.5.5 Consolidation of Clay Layer between Sand Strata

This section deals with the combined scheme of a potentially undrained material like a clay and drained material like sands in a finite element configuration. Sands, or clays with short-term loading, can be modeled by means of the ordinary element which concerns an effective stress approach without pore pressure changes, or a total stress approach. On the other hand, sands with high-rate loading or clays with long-term loading should be modeled by the element that takes the coupling formulation of consolidation theory into account.

Drained materials and/or the total stress approach are represented by the variational form of equation 6.6, whereas undrained material with an effective stress approach is governed by other variational forms of the equations 6.15 and 6.16. If both of the above are present in the same finite element configuration, some additional procedures are required to combine them and to adjust the boundary conditions.

Figure 6.27 shows the ground profile used to study the consolidation of a clay layer which lies between two sand strata. The top fill and the bottom soil are sand layers modeled as drained materials. The intermediate stratum is Bay Mud. A Q8 element with the Duncan-Chang nonlinear elastic model is used to represent the fill and the colluvium, while Q8P4 Prevost model element is used to model the Bay Mud. The Prevost model parameters used here are those given in Table 4.3. The water table is assumed to be 10 feet below the ground surface. A surcharge pressure of 500 psf is loaded on the ground surface at the time of zero.

Effective vertical stress  $\sigma'_y$  and pore pressure  $u$  are shown with a depth in Figure 6.27 for the initial state, and at the times 30 minutes and 25 days after the load is placed. It is demonstrated that excess pore pressures are generated in the Bay Mud layer immediately after the loading, while no changes in pore pressure exist in the drained layers.

Figure 6.28 shows the consolidation settlement curves at the top of each layer. More than two inches of settlement at the ground surface is predicted. The predicted settlement can be compared to the settlement calculated from the compressibility of the Bay Mud, using typical values of 1.2 and 0.12 for the compression index  $C_c$  and the recompression index  $C_r$ , respectively, and an overconsolidation ratio of 1.2 assumed for the Bay Mud. 2.4 inches of the surface settlement is obtained at the ground surface which is close to the predicted value.

In view of the results shown in the Figures 6.26 and 6.27, it can be considered that the finite element program properly deals with the combined

problem of drained and undrained/consolidation conditions.

#### 6.5.6 Summary

Elasto-plastic formulation is incorporated into the finite element program. The elasto-plastic analysis is numerically sensitive to the size of the loading increment when the plane strain condition is imposed, and it is necessary to employ small loading increments. The results of the analysis of the footing-bearing capacity problem demonstrate good agreement with the classical plasticity theory. The effects of drainage length and loading rate are examined. Both the undrained and drained materials are successfully combined together in a finite element analysis. It is concluded from the series of examination that the newly developed program is applicable to boundary value problems.

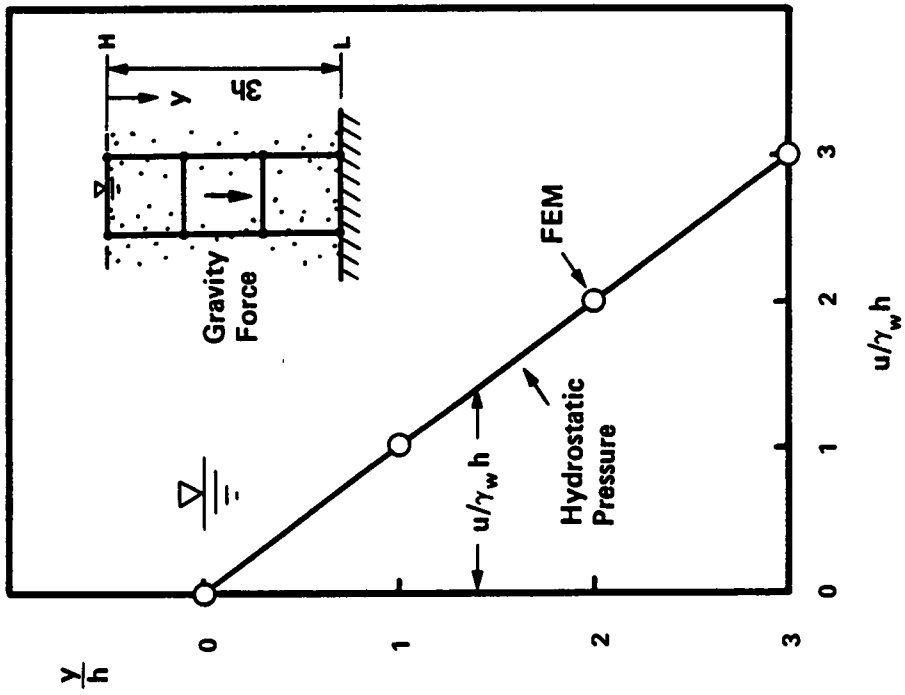
#### 6.6 Summary and Conclusions

A finite element code has been developed for use in the shield tunneling analysis. The finite element formulation used in the program is founded on the ordinary displacement method, and is extended to facilitate more features so that the program may accurately simulate soil behavior found important to shield tunneling. Three major features are incorporated in the finite element program: (1) elasto-plastic formulation of the material nonlinearities; (2) large deformation formulation coping with the geometric nonlinearity; and, (3) the coupling formulation of the constitutive equations with the pore fluid flow equation to solve the consolidation problems.

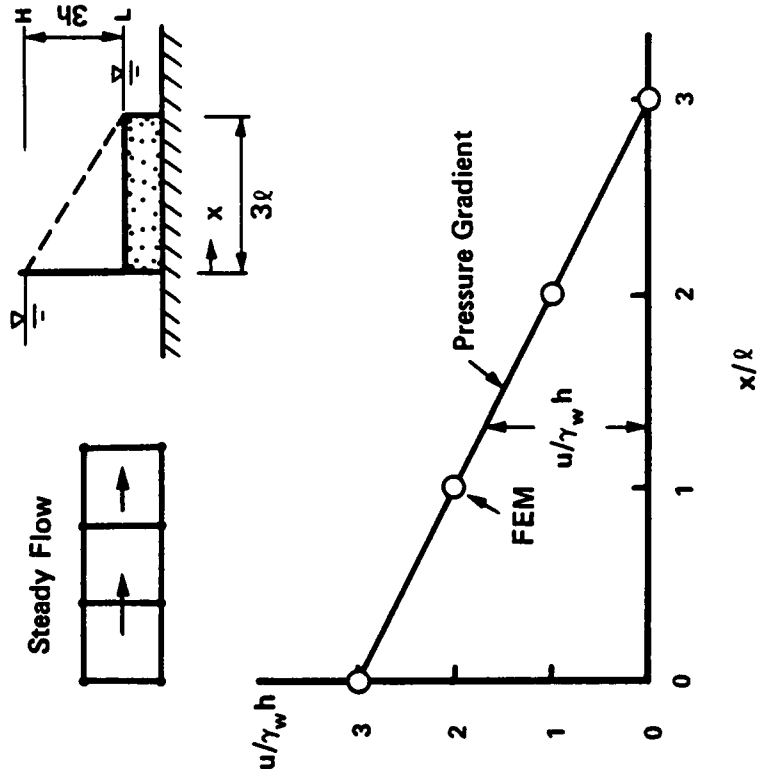
The essential parts of the theories underlying the new formulation are outlined. The program is examined for each of the three features as well as their combination. In view of the results it is concluded that the extended version of the finite element program is correctly formulated and that it can be used in an analysis of the shield tunneling.

Table 6.1 Comparison of Strains due to Final Settlements in 1-D Consolidation Predicted by means of Large Deformation Theory  $\delta/H$

Load $\Delta\sigma/B$	Closed Form Solution $\delta/H$		FEM $\delta/H$	
	Small Deformation	Large Deformation	Small Deformation	Large Deformation
0.1	0.0429	0.0419	0.0429	0.0420
0.2	0.0857	0.0821	0.0857	0.0826
1.0	0.4285	0.349	0.4285	0.355



(A) Hydrostatic Pressure



(B) Pressure Gradient

Figure 6.1 Steady State of Pore Pressure, Hydrostatic Pressure and Seepage

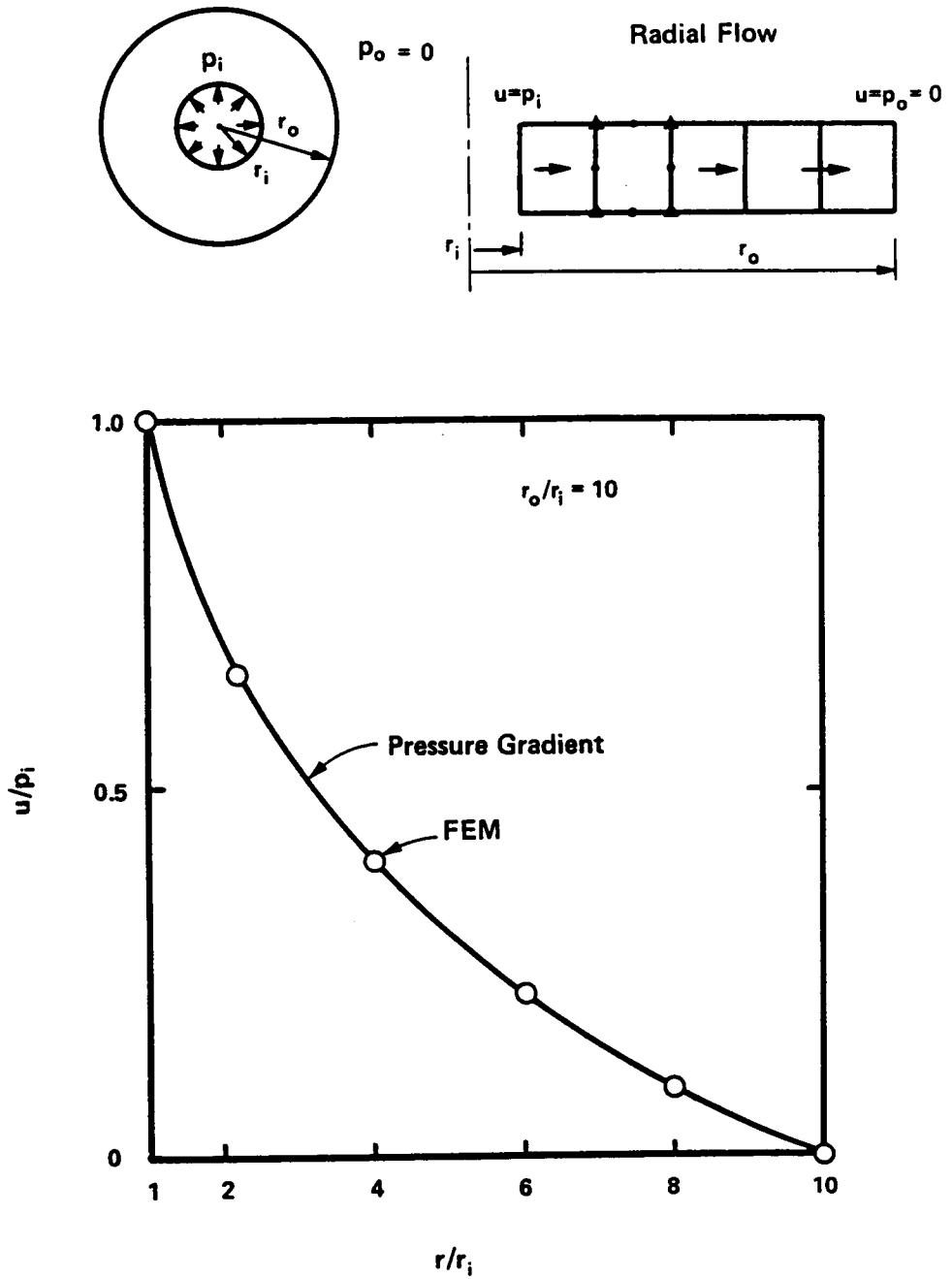


Figure 6.2 Steady State of Pore Pressure, Radial Flow

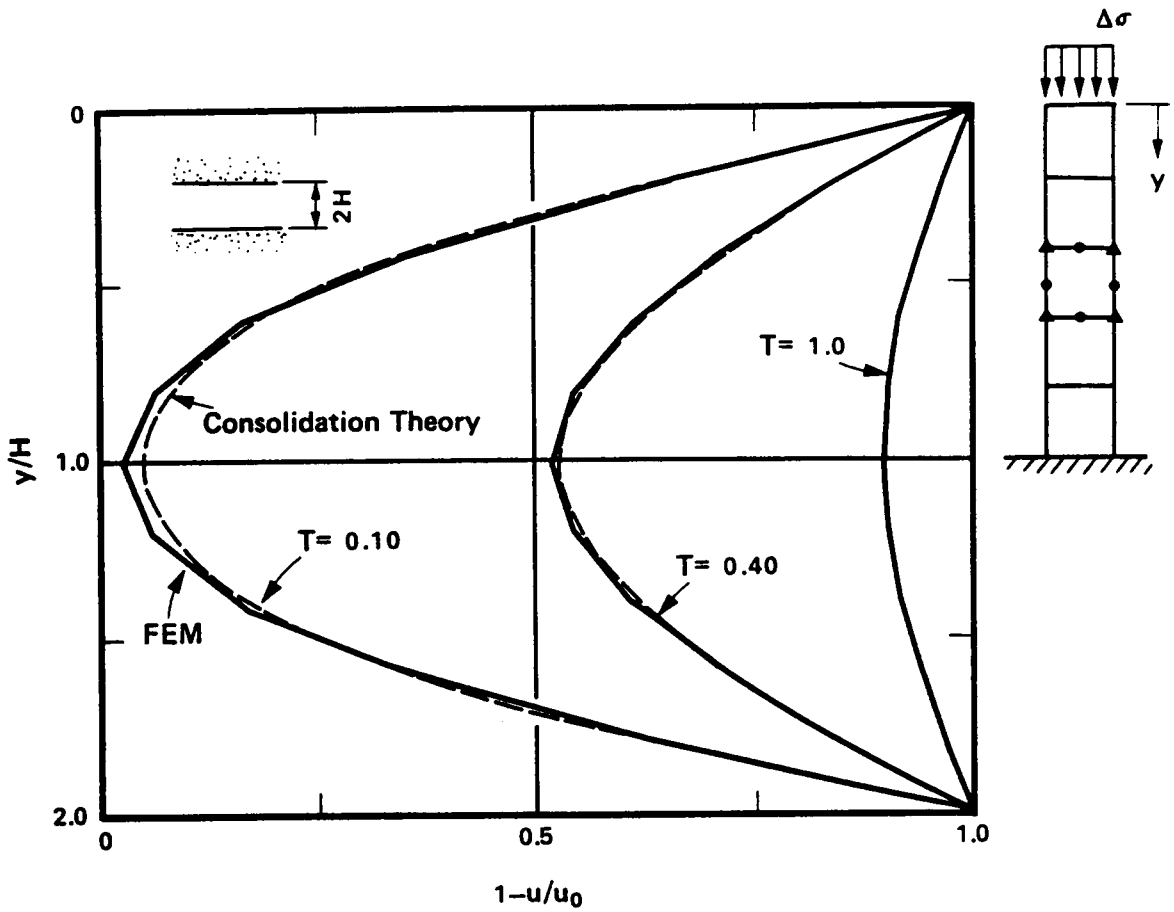


Figure 6.3 Excess Pore Pressure Distributions for One-Dimensional Consolidation

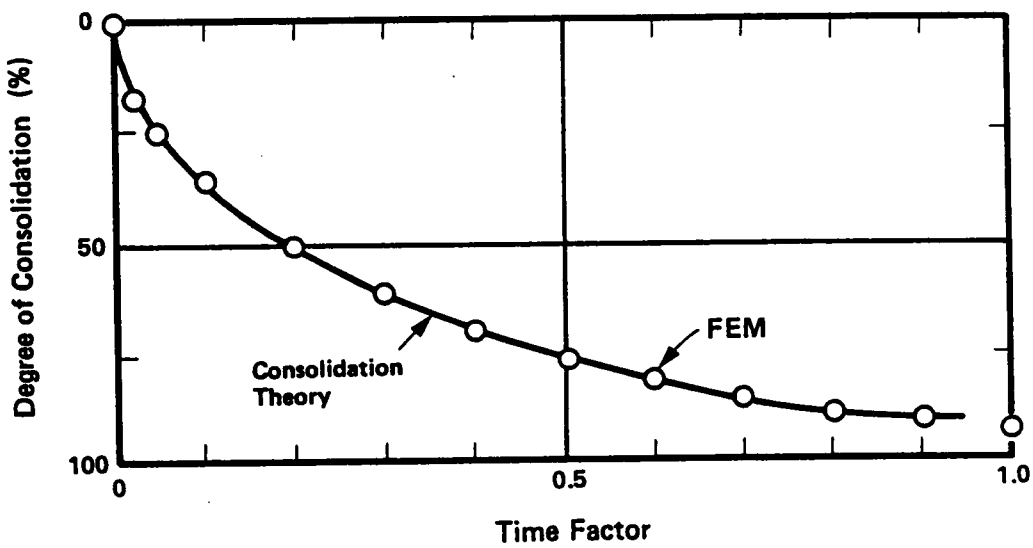


Figure 6.4 Degree of Consolidation for One-Dimensional Consolidation

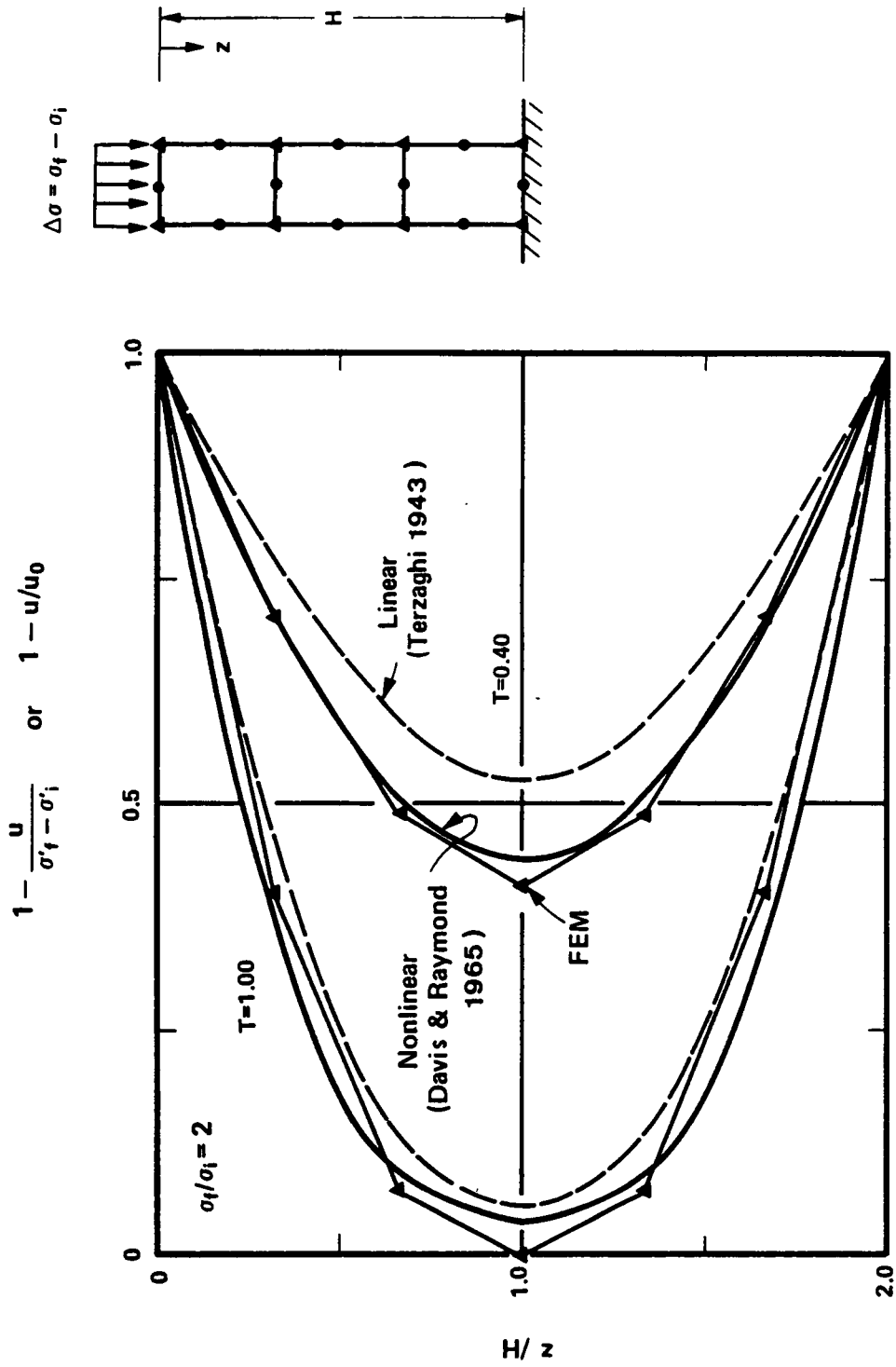


Figure 6.5 Excess Pore Pressure Distribution for Nonlinear One-Dimensional Consolidation

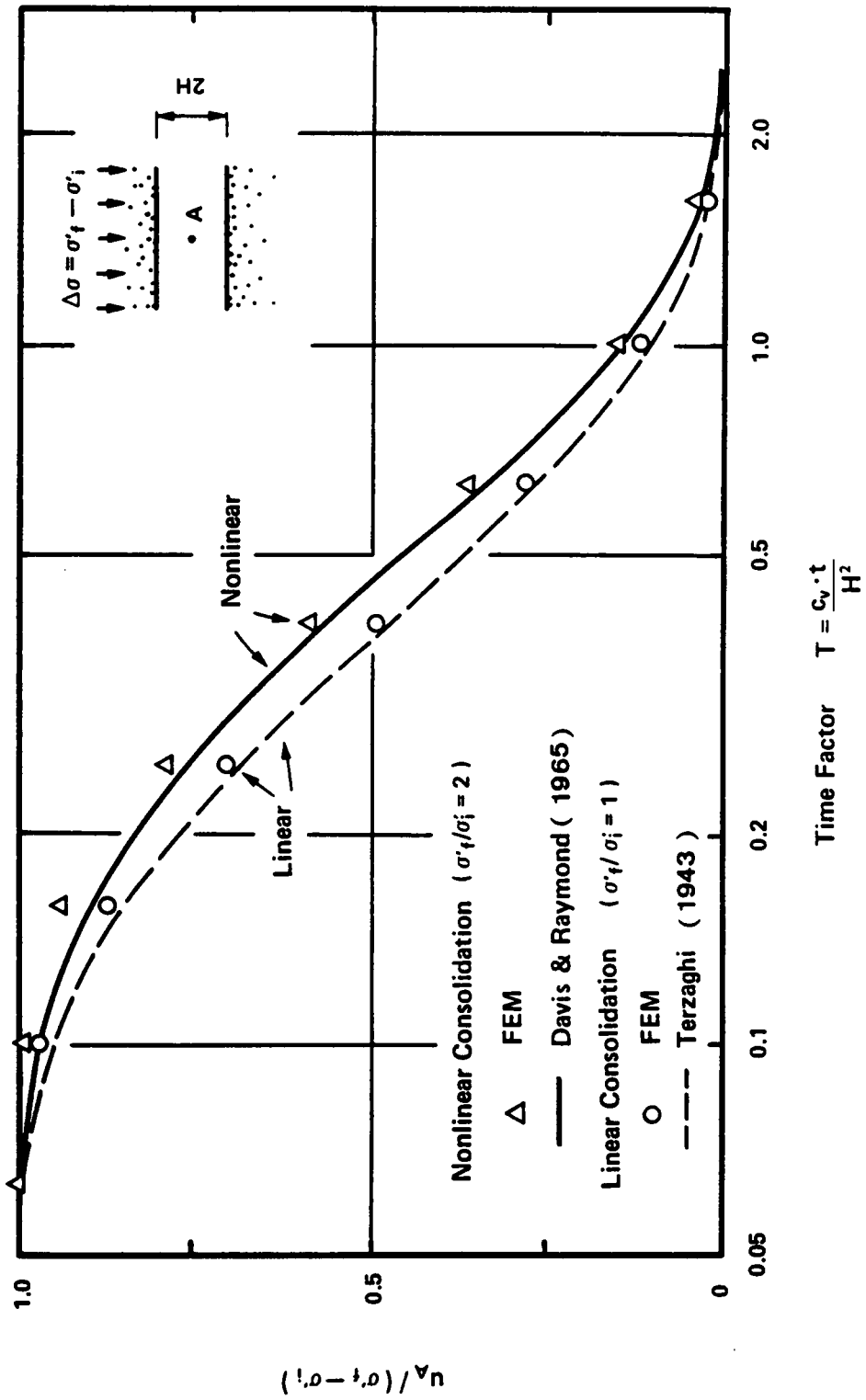


Figure 6.6 Time Dependent Variation of Excess Pore Pressure for Nonlinear One-Dimensional Consolidation

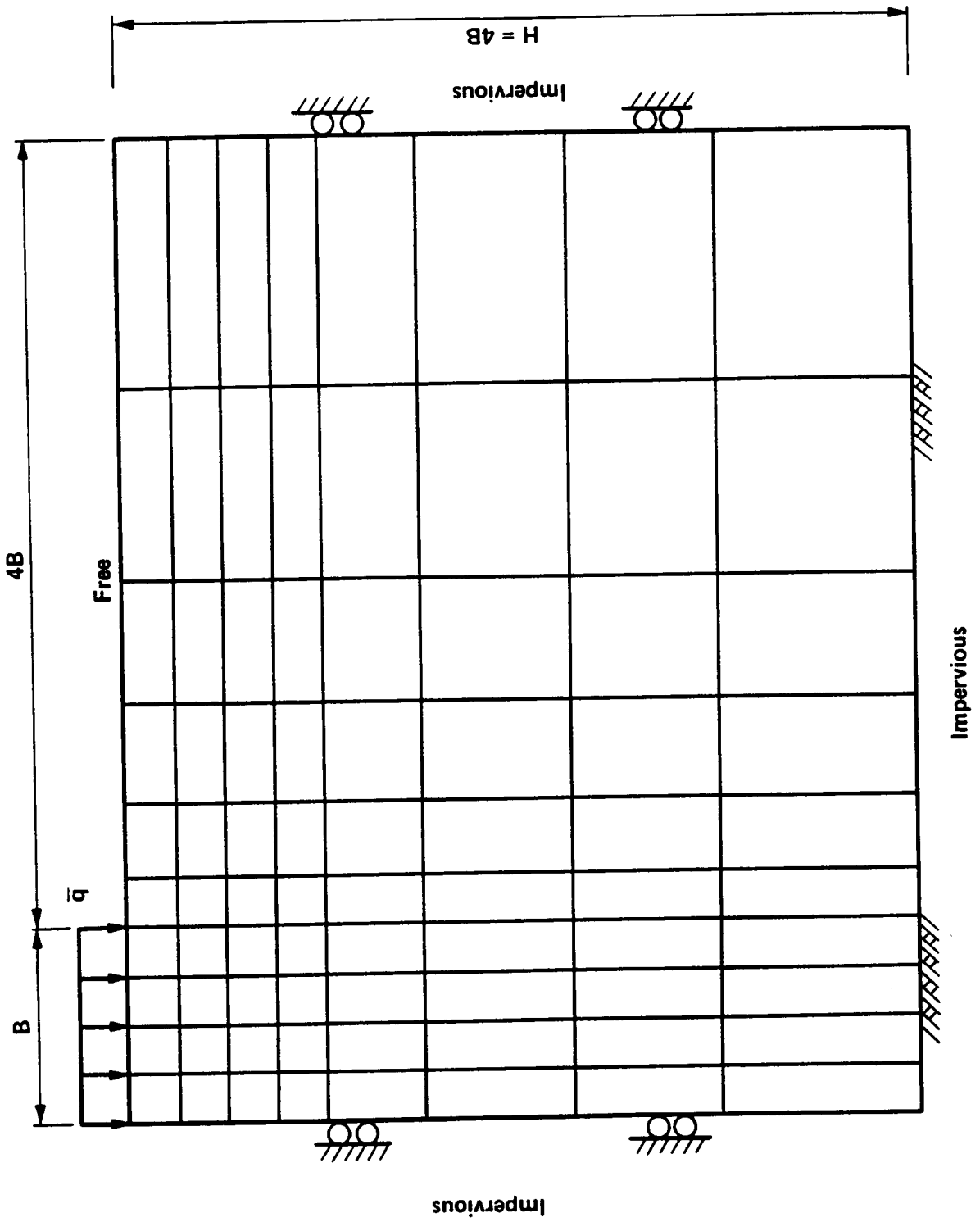


Figure 6.7 Finite Element Idealization of a Strip Load on Ground Surface

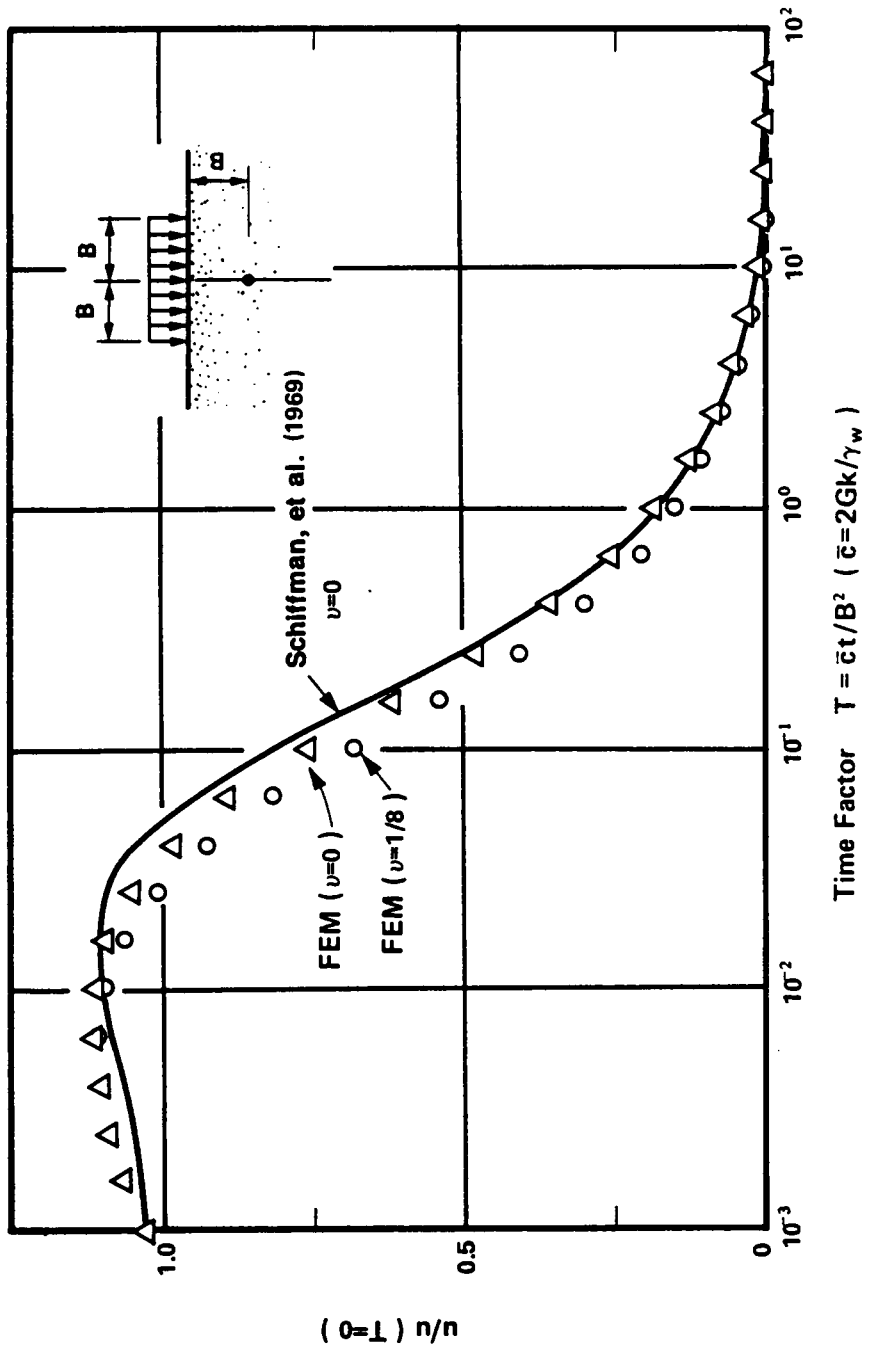


Figure 6.8 Dimensionless Excess Pore Pressure Changes under a Strip Loading

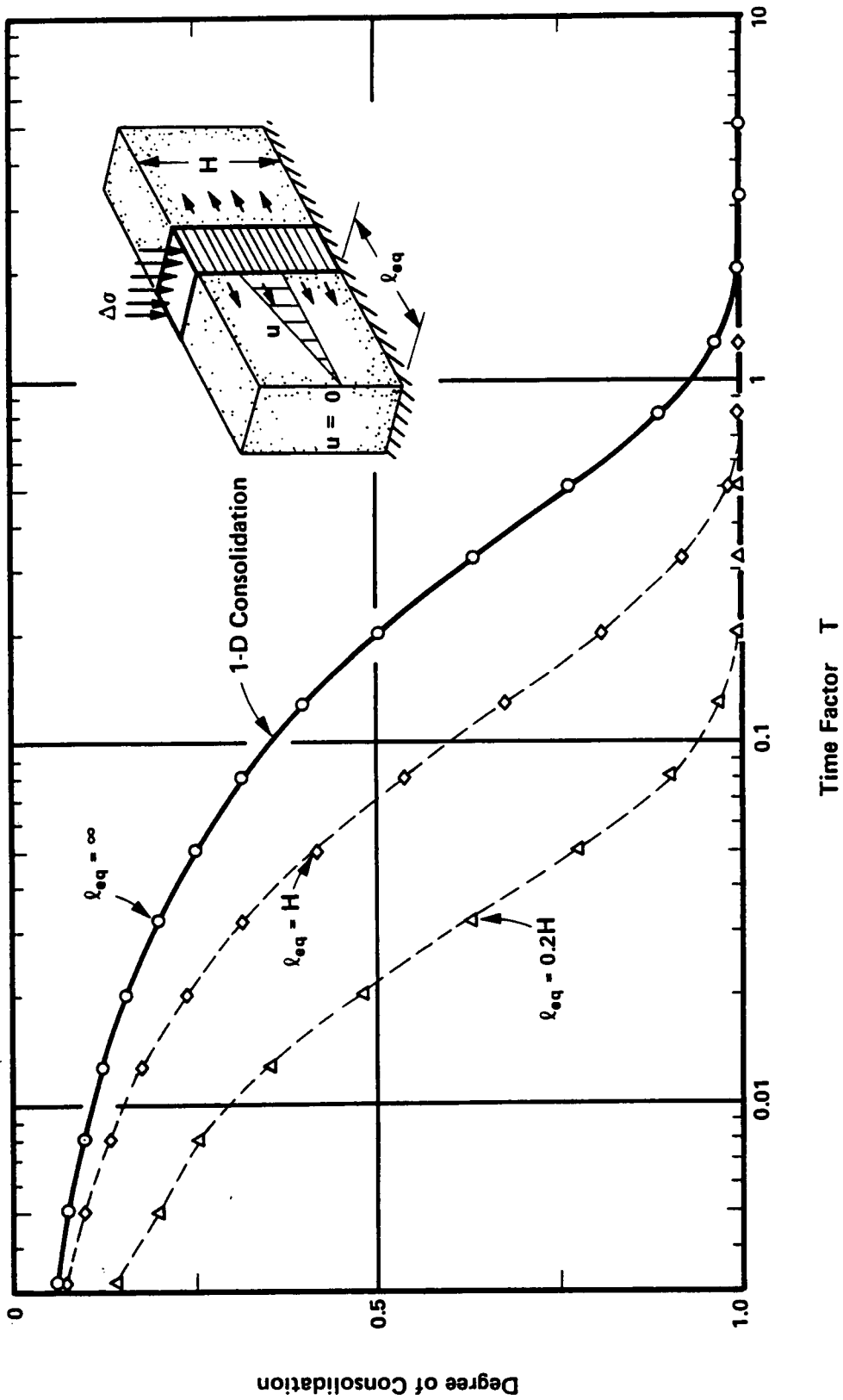


Figure 6.9 Acceleration of Consolidation due to Out-of-Plane Drainage

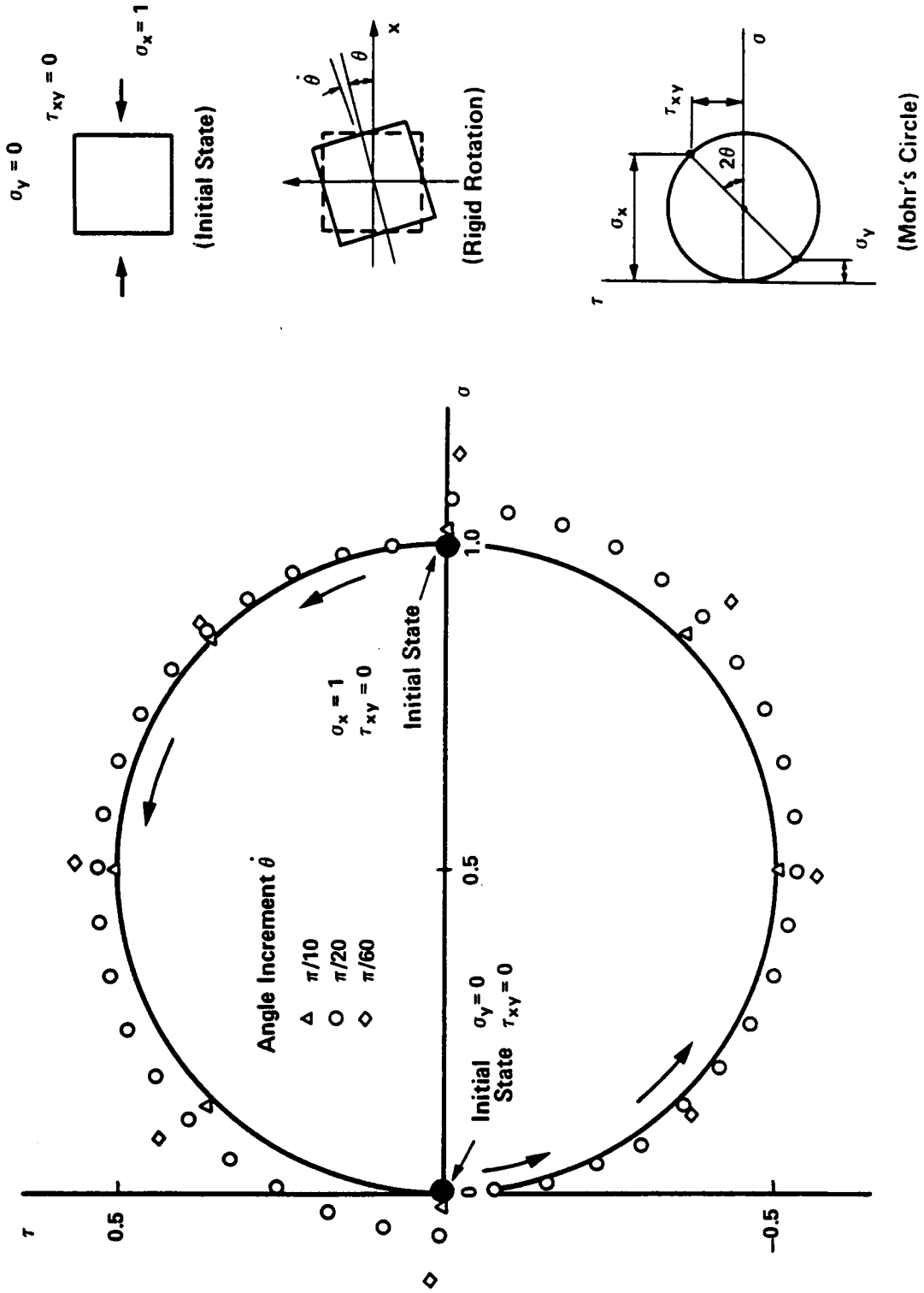


Figure 6.10 Stress Correction due to Rigid Rotation

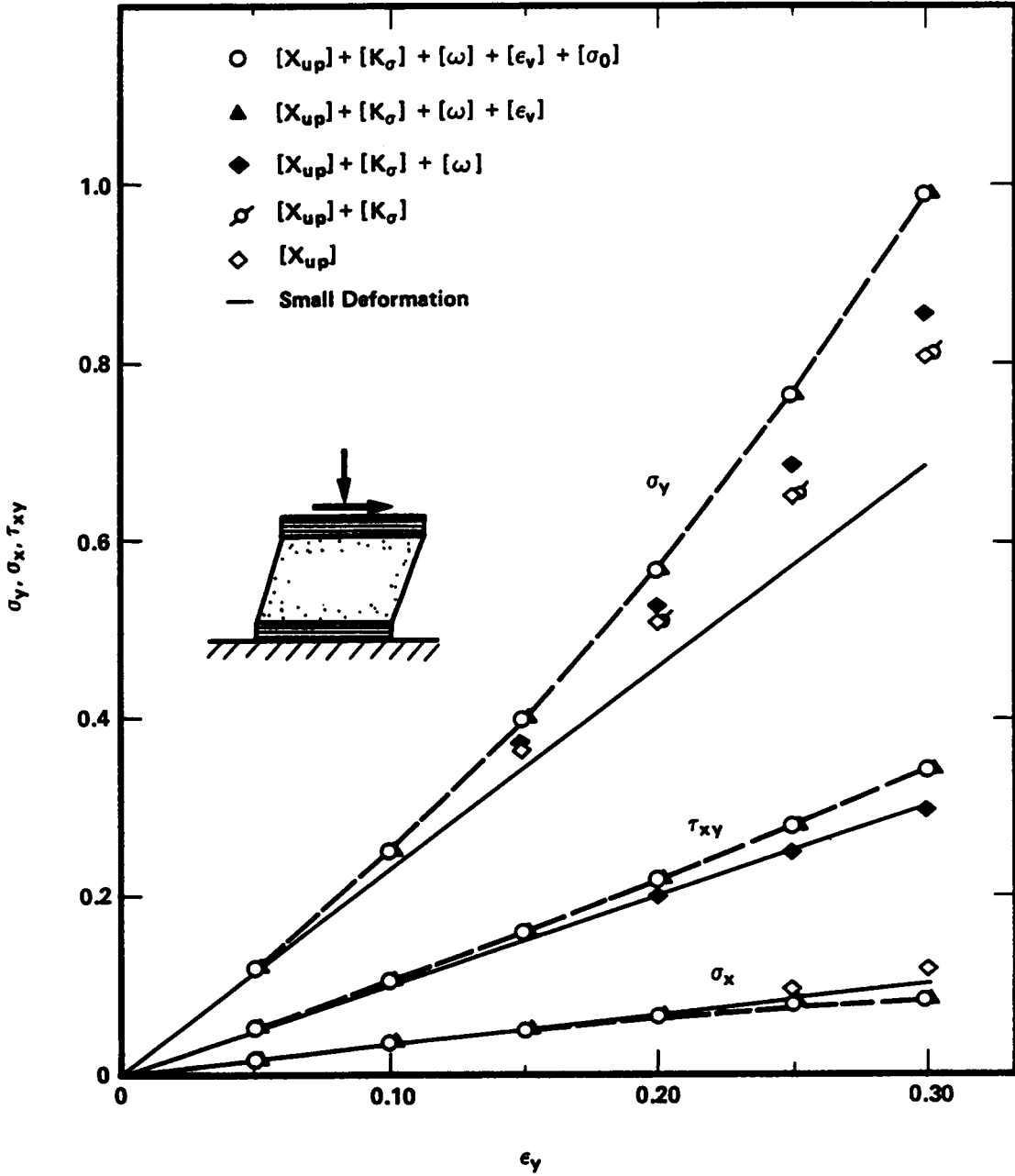


Figure 6.11 Various Stress Corrections in Simple Shear Stress State

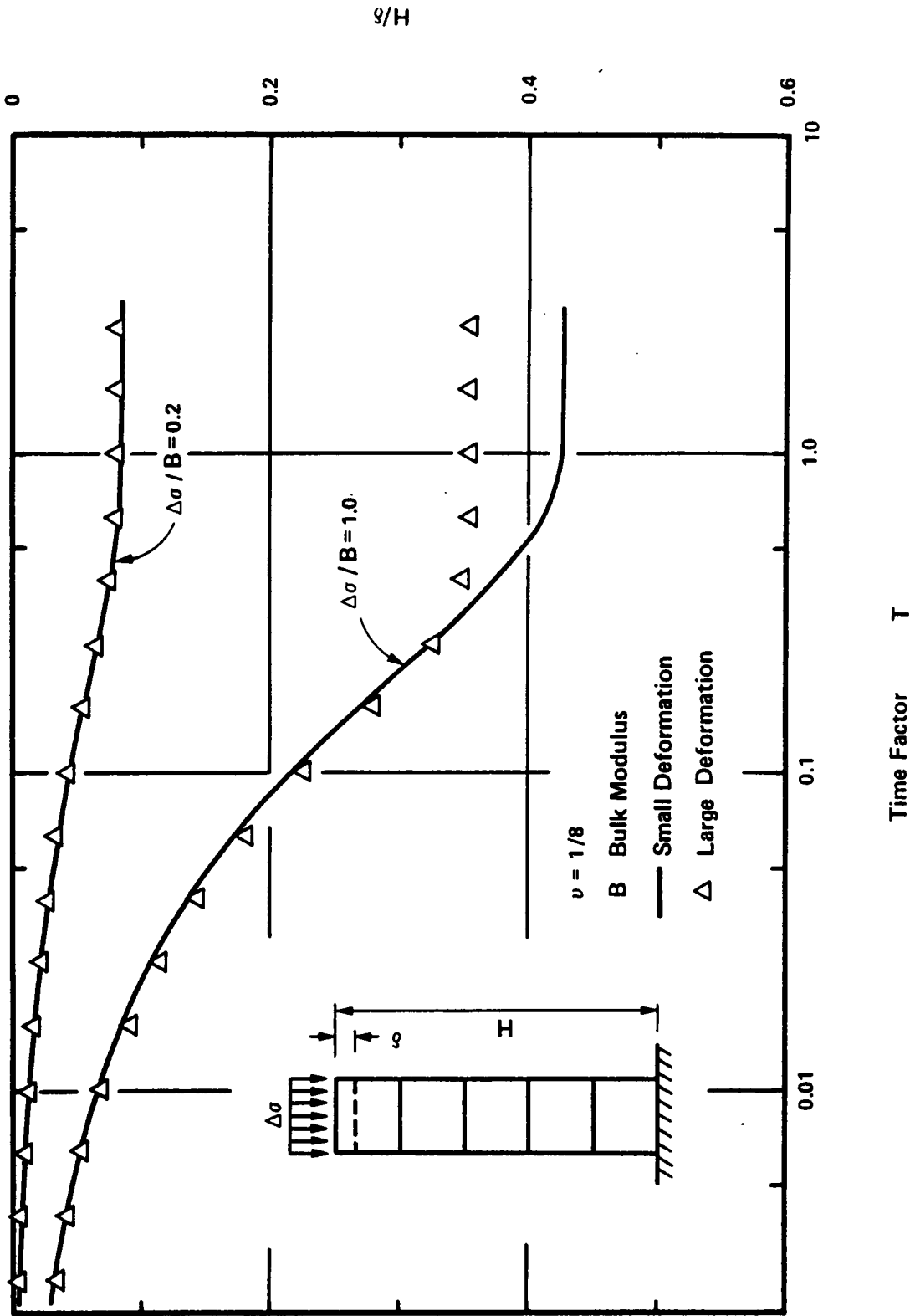
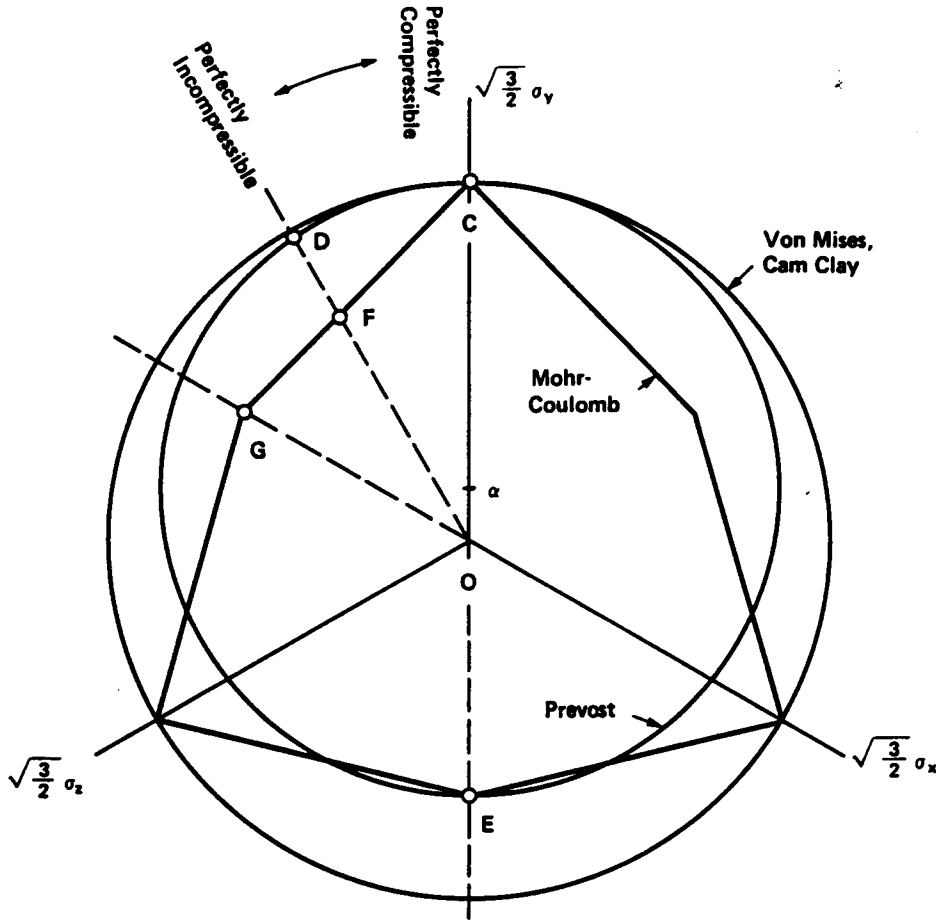


Figure 6.12 Comparison of One-Dimensional Consolidation between Small and Large Deformation Analyses



Loading Paths and Calibration Points on Mohr-Coulomb Yield Criteria		$q/p = \sqrt{3} J_2 / p$
C	CTC	$6 \sin \phi' / (3 - \sin \phi')$
E	RTE	$6 \sin \phi' / (3 + \sin \phi')$
F	Undrained Plane Strain Compression	$3 \sin \phi' / \sqrt{3 + \sin \phi'}$

Figure 6.13 Yield Surfaces of Various Yield Criteria on Octahedral Stress Plane

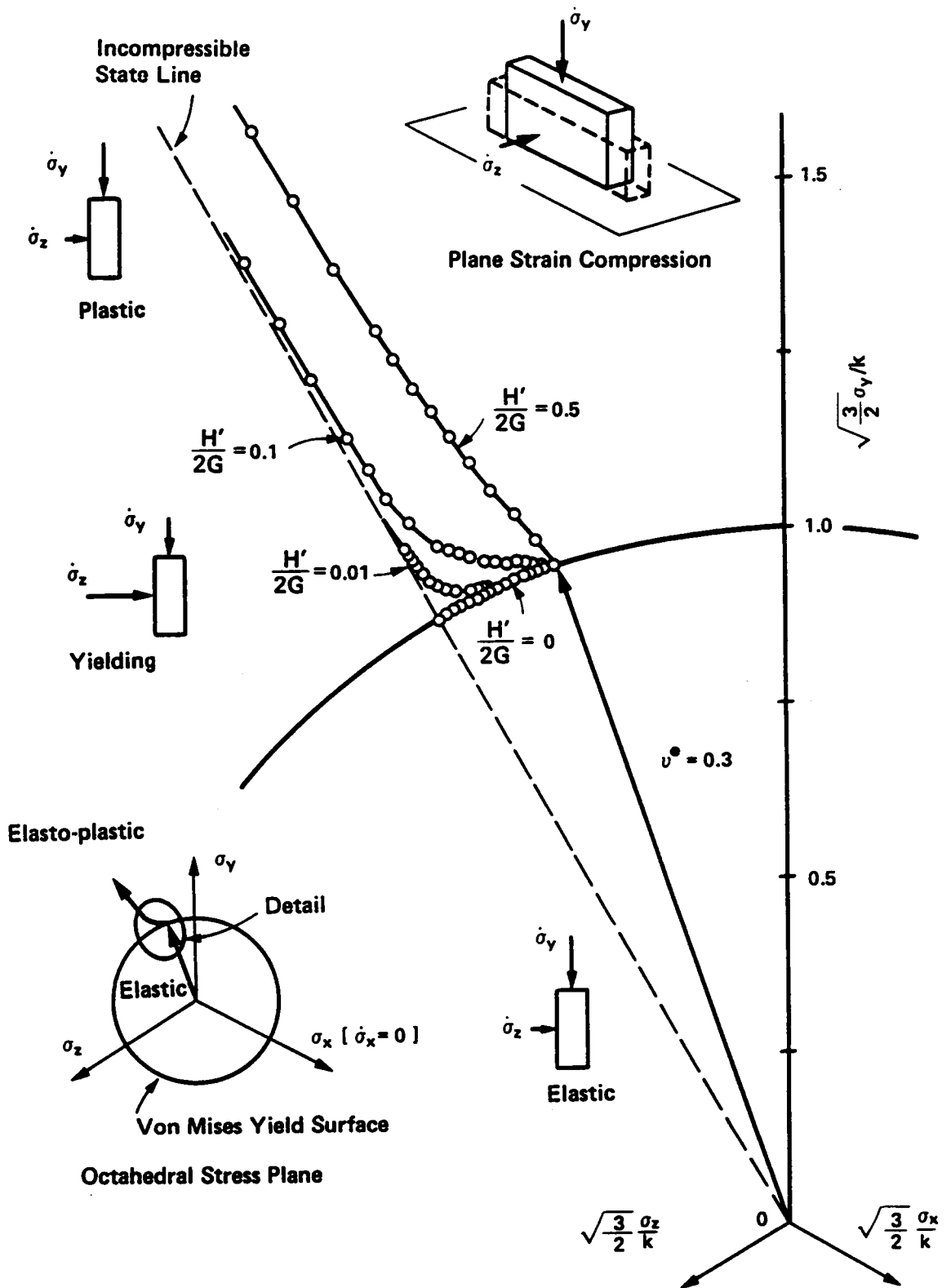
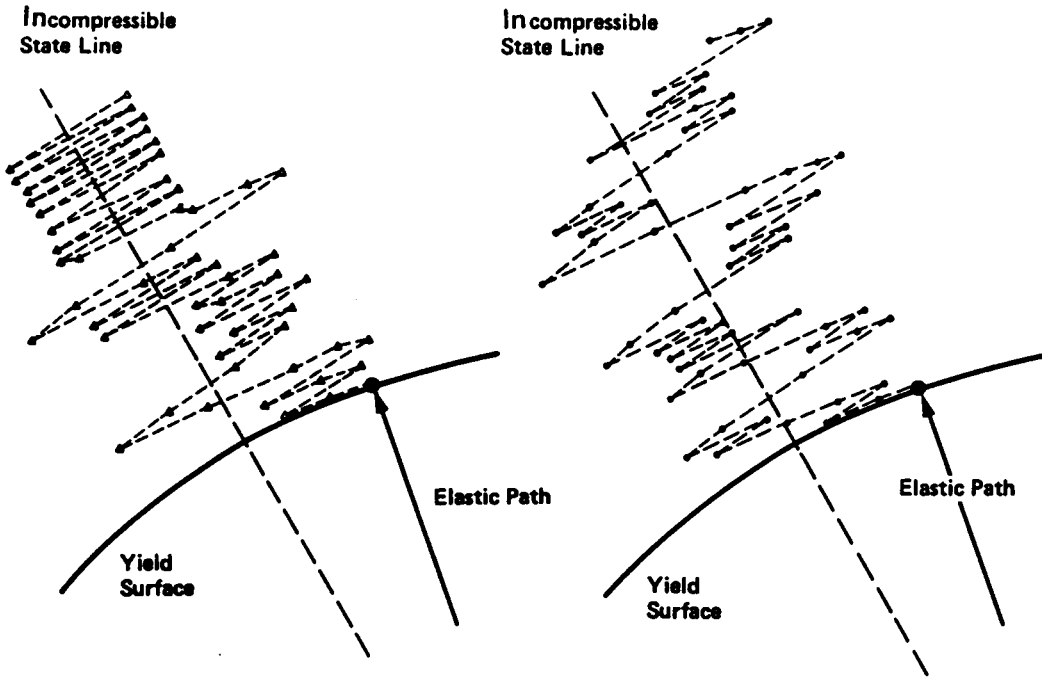
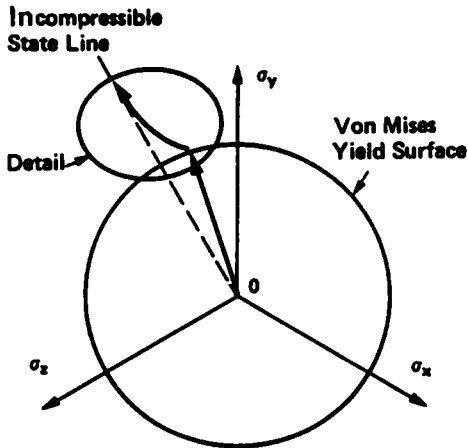


Figure 6.14 Analysis of Strain Controlled Undrained Plane Strain Test with Linear Isotropic Hardening

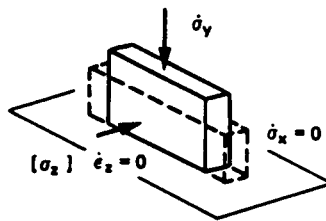


(a) Isotropic Hardening

(b) Kinematic Hardening



(c) Stress Path on Octahedral Plane



(d) Plane Strain Compression Test

Figure 6.15 Comparison of Stress Paths in Plane Stress Test between Isotropic and Kinematic Hardening Rules

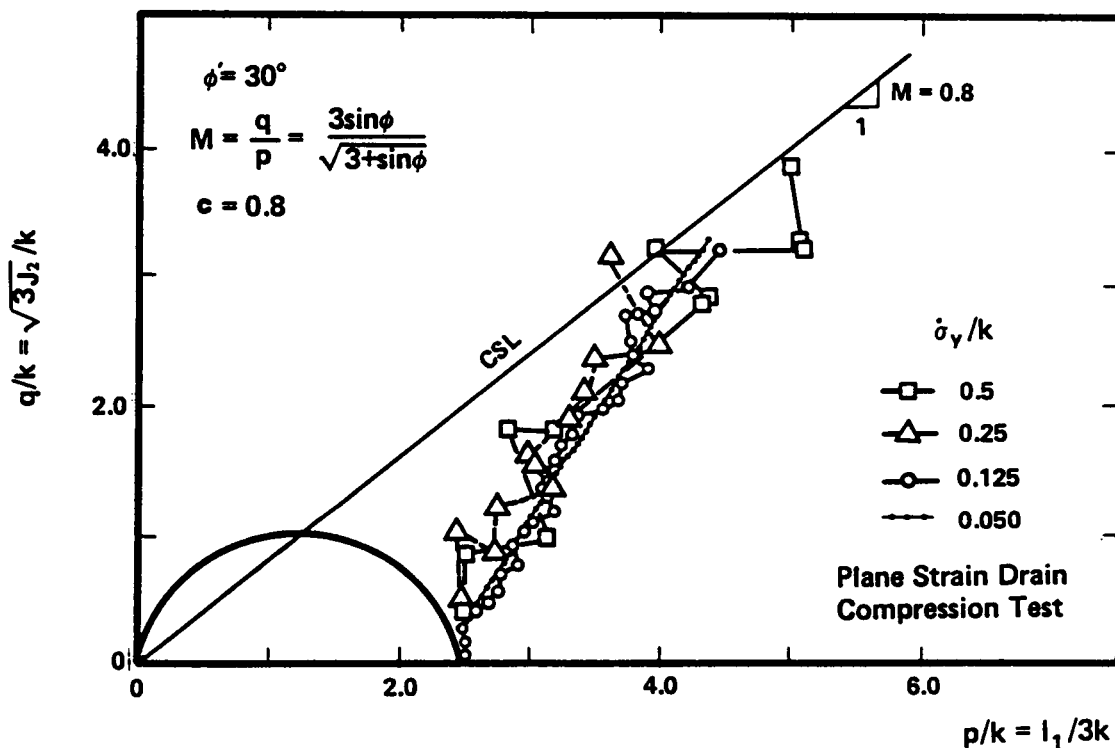
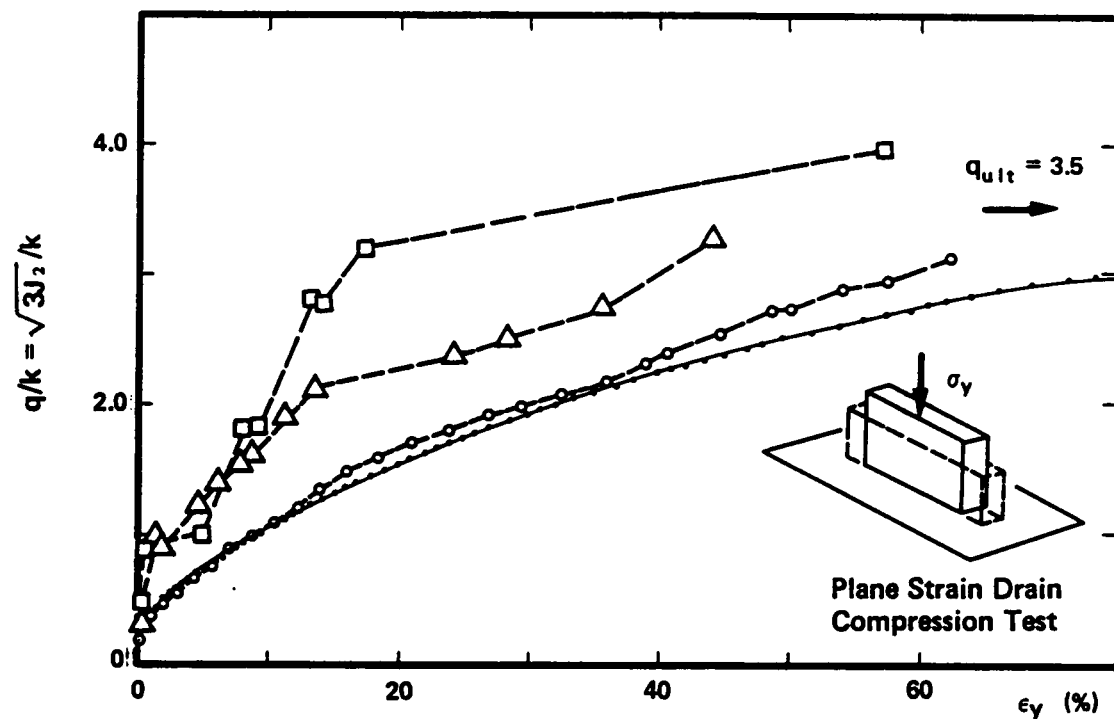


Figure 6.16 Stress-Strain Curves and Stress Paths in Drained Strain Test with Different Loading Increments

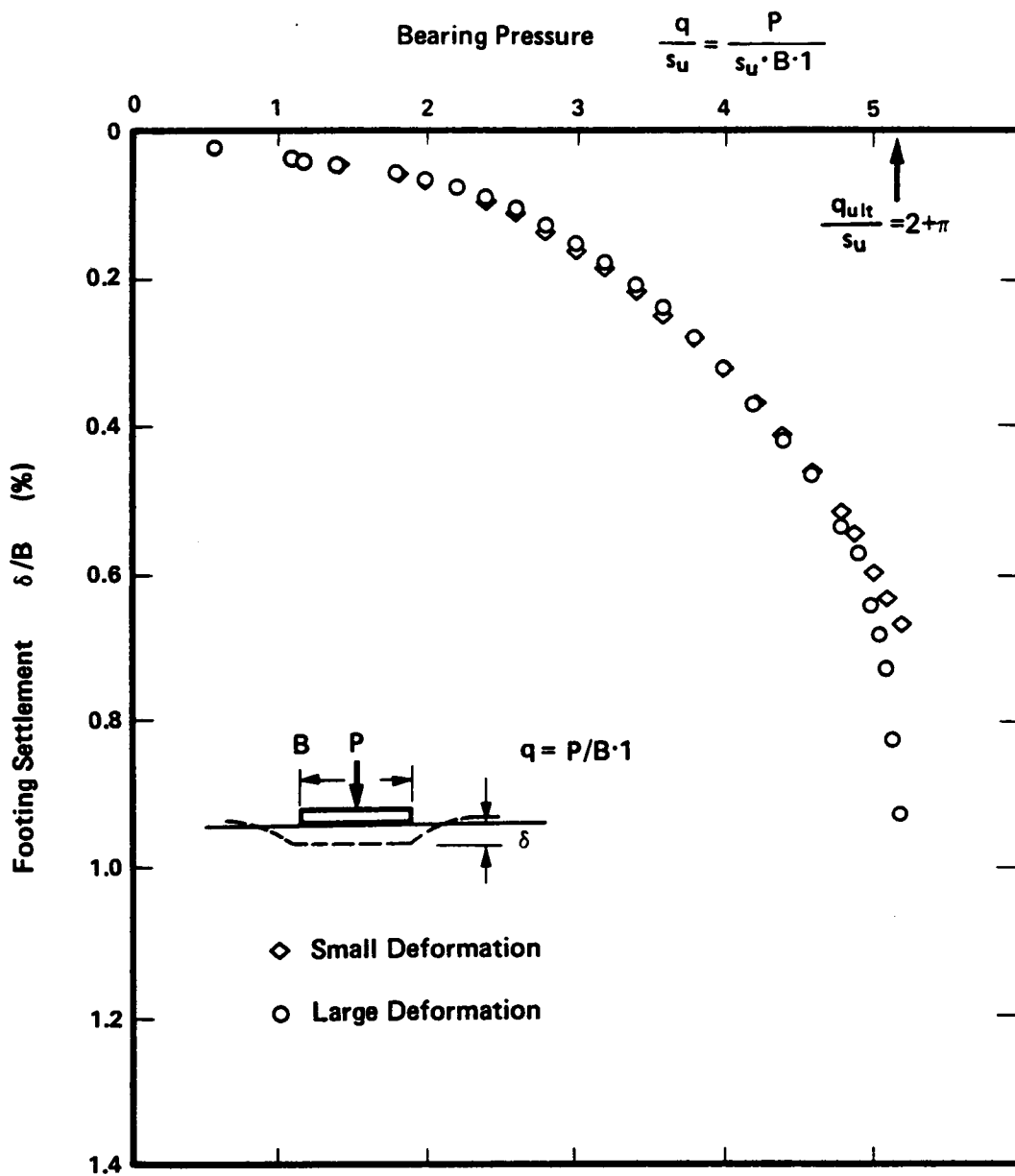


Figure 6.17 Footing Settlement Curves

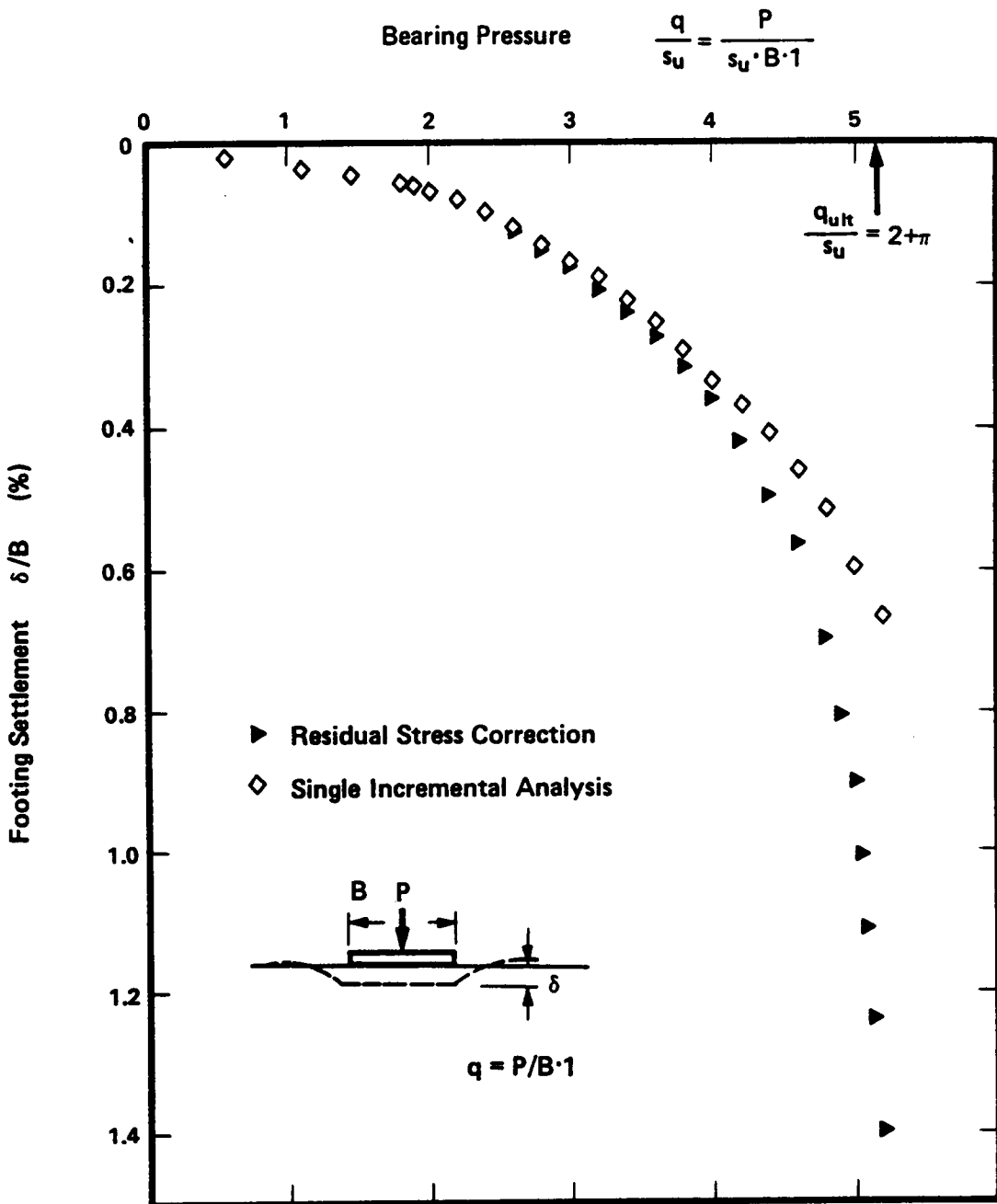


Figure 6.18 Corrected Footing Settlement Curves

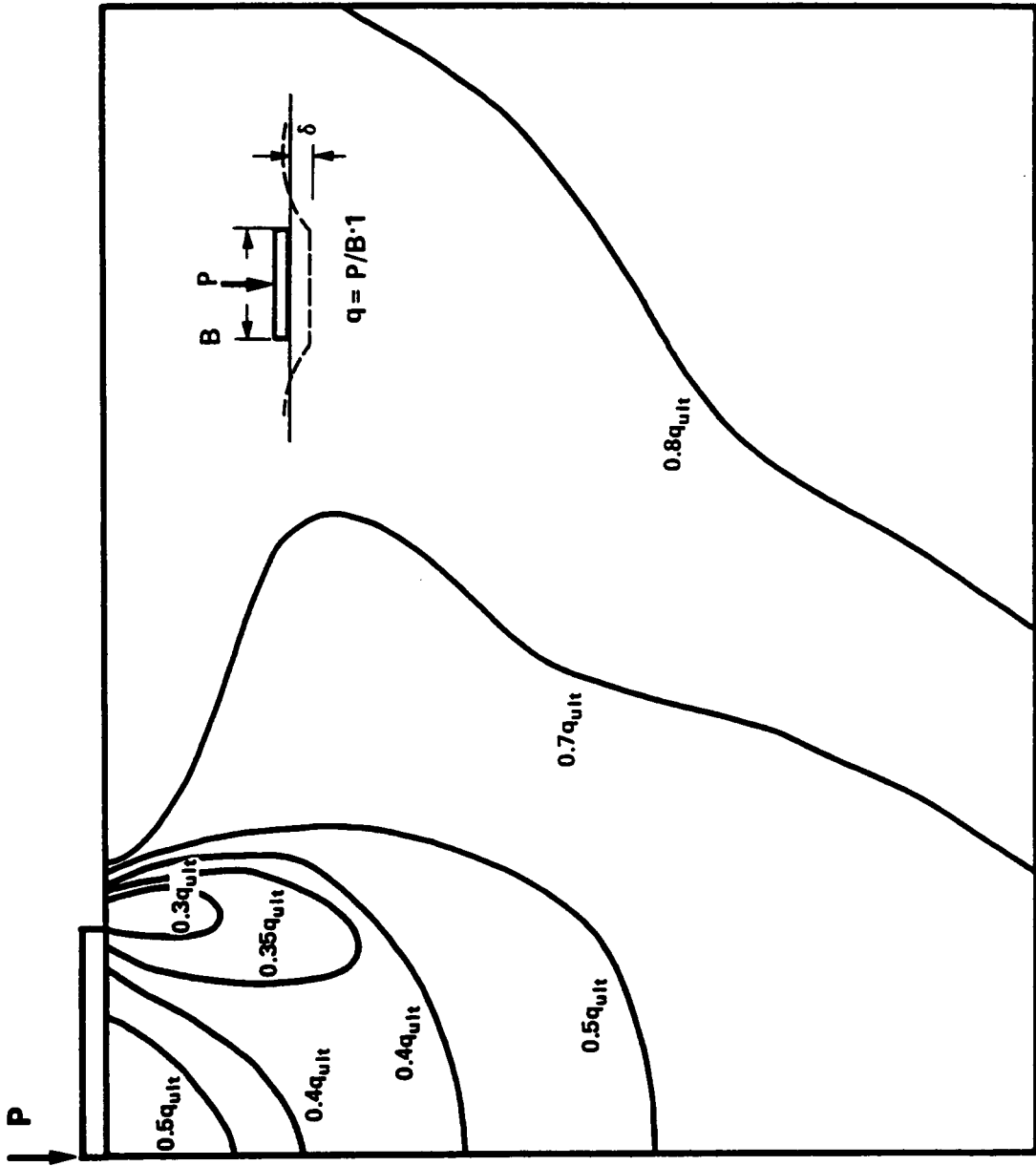


Figure 6.19 Development of Yielded Zone of Footing Bearing Problem

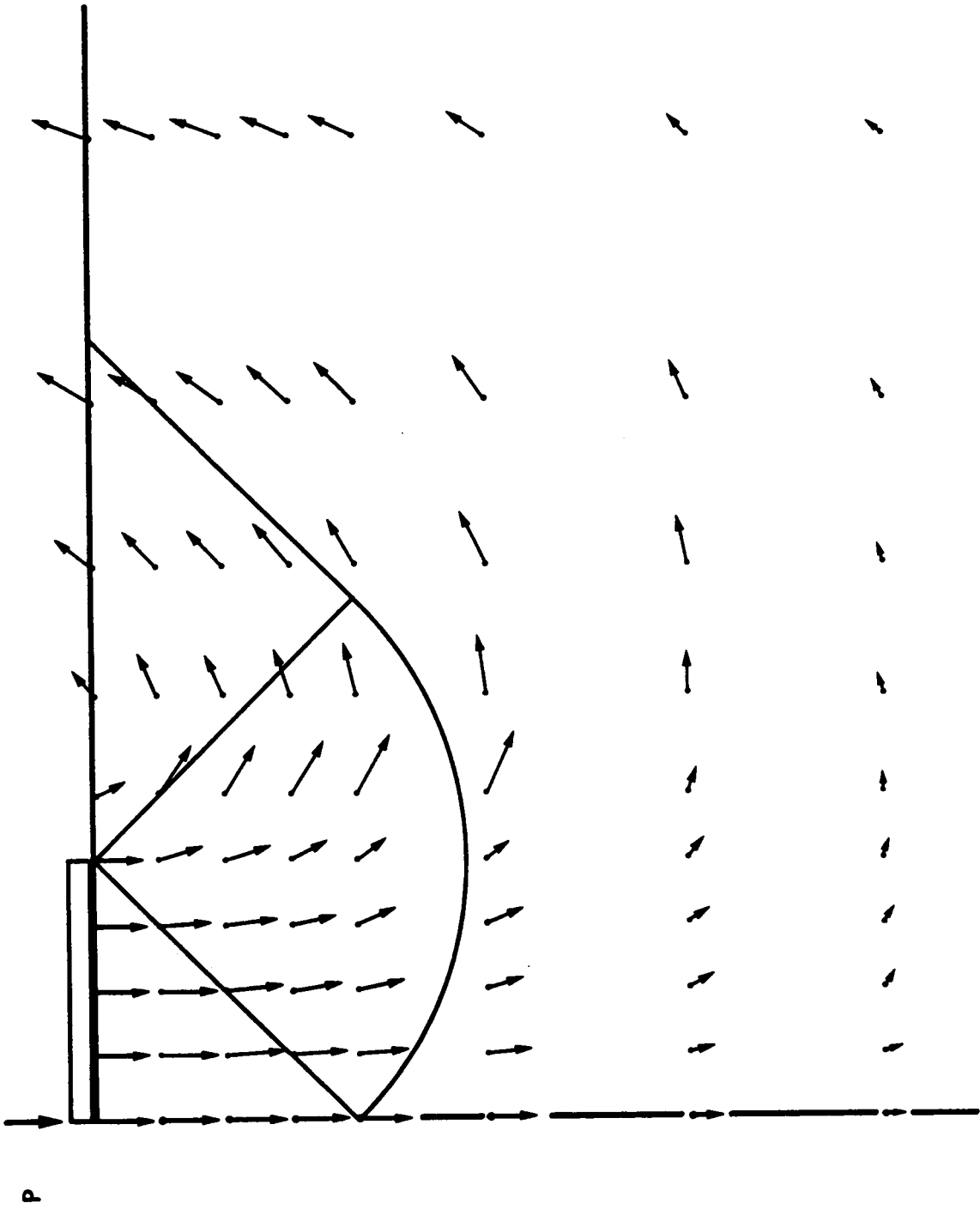


Figure 6.20 Velocity Field in Footing Bearing Problem

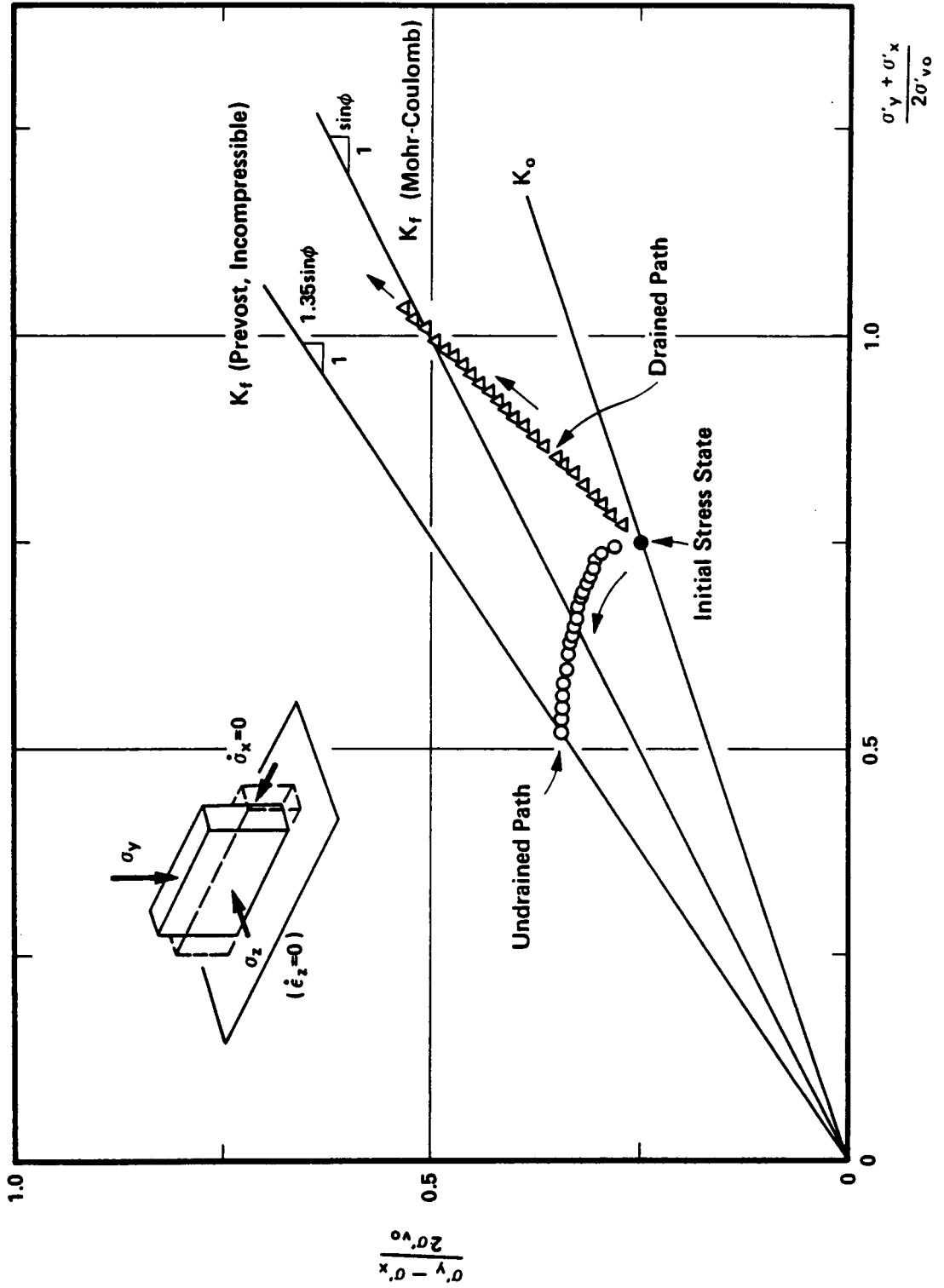
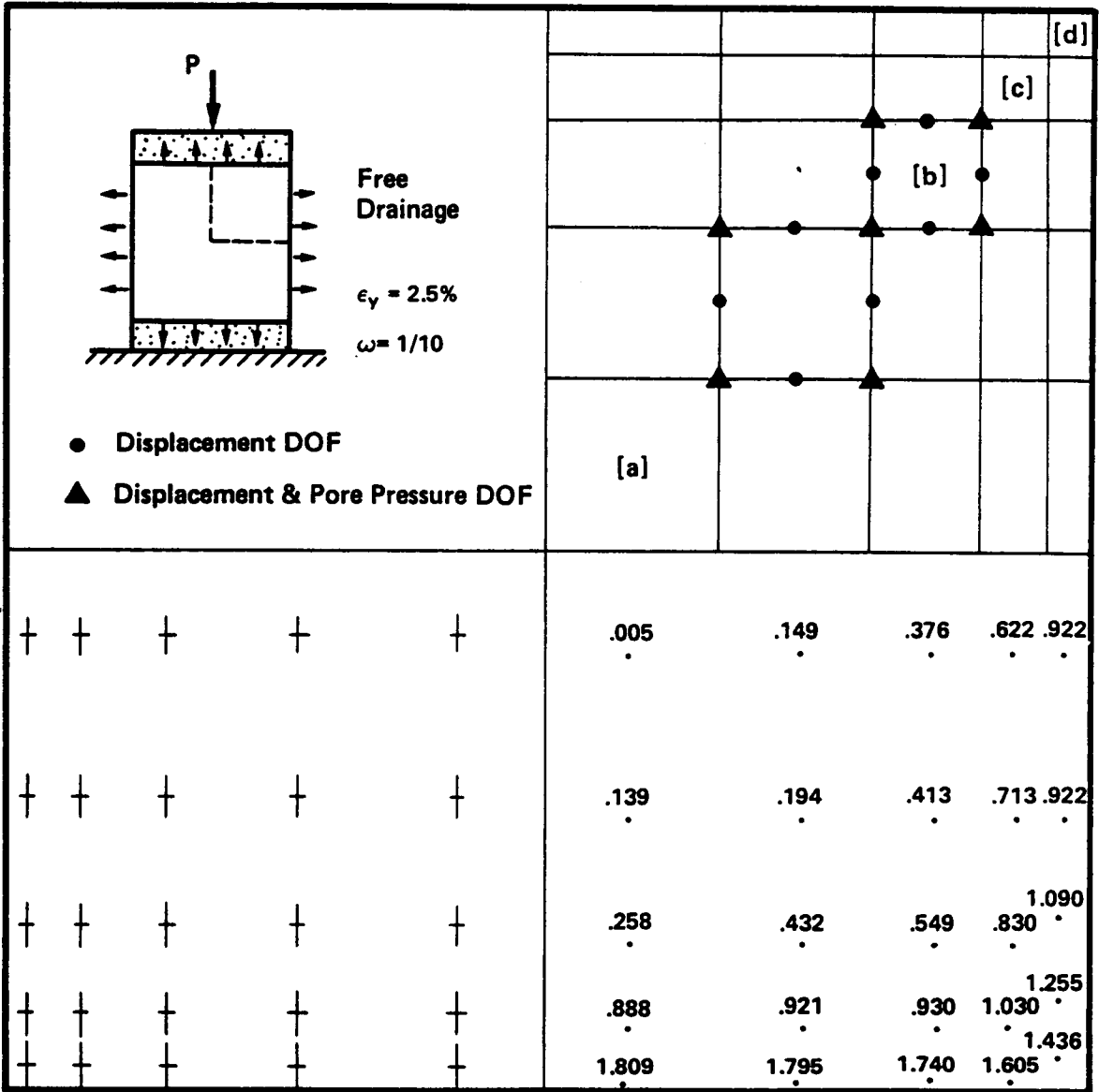


Figure 6.21 Undrained and Drained Stress Paths of Plane Strain Test on Bay Mud



(a) Principal Stress Distribution

(b) Volumetric Strain  $e_v$  (%)

Figure 6.22 Plane Strain Test with Free Surface Drainage

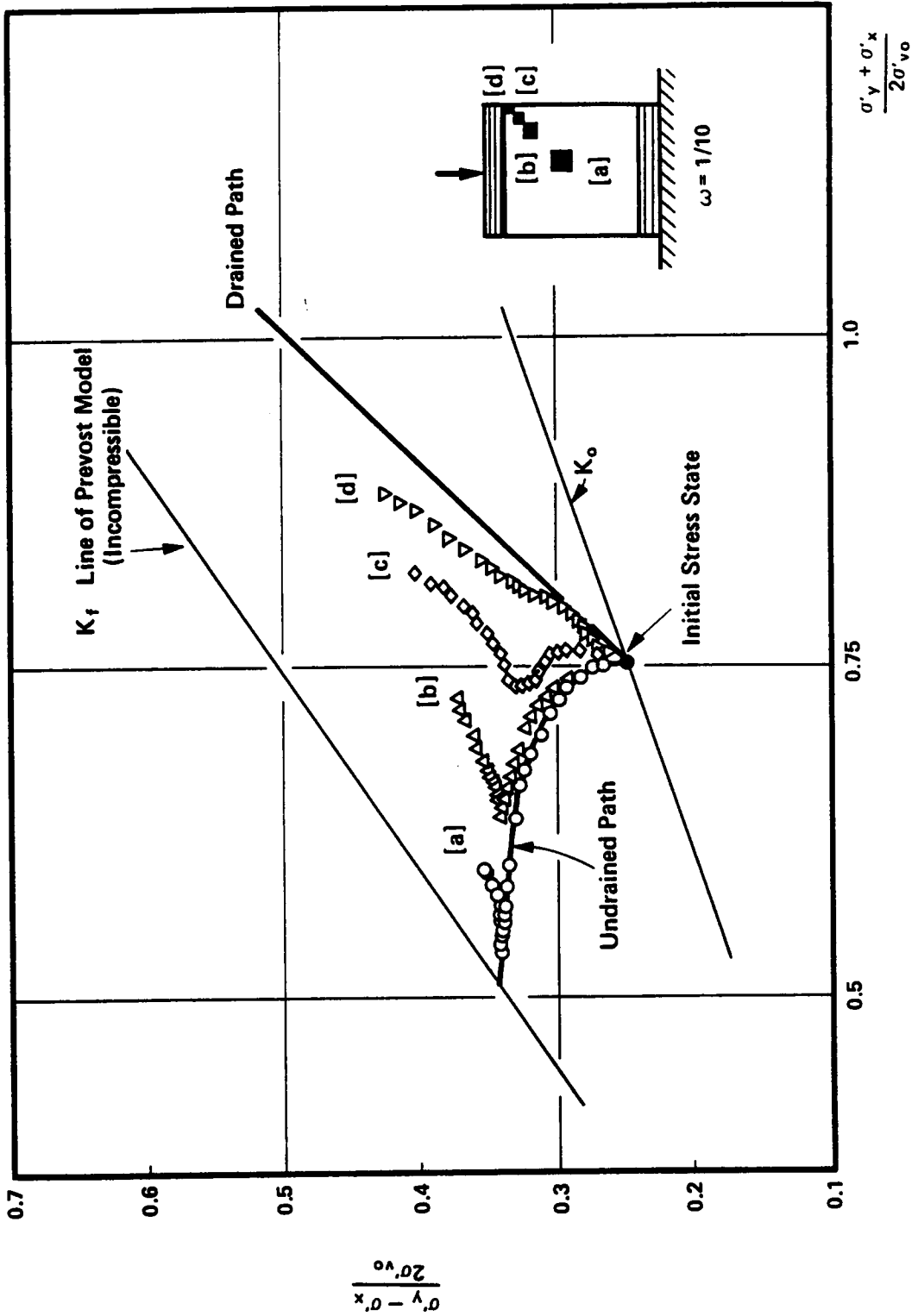


Figure 6.23 Stress Paths Predicted for Various Locations of Plane Strain Test with Free Surface Drainage

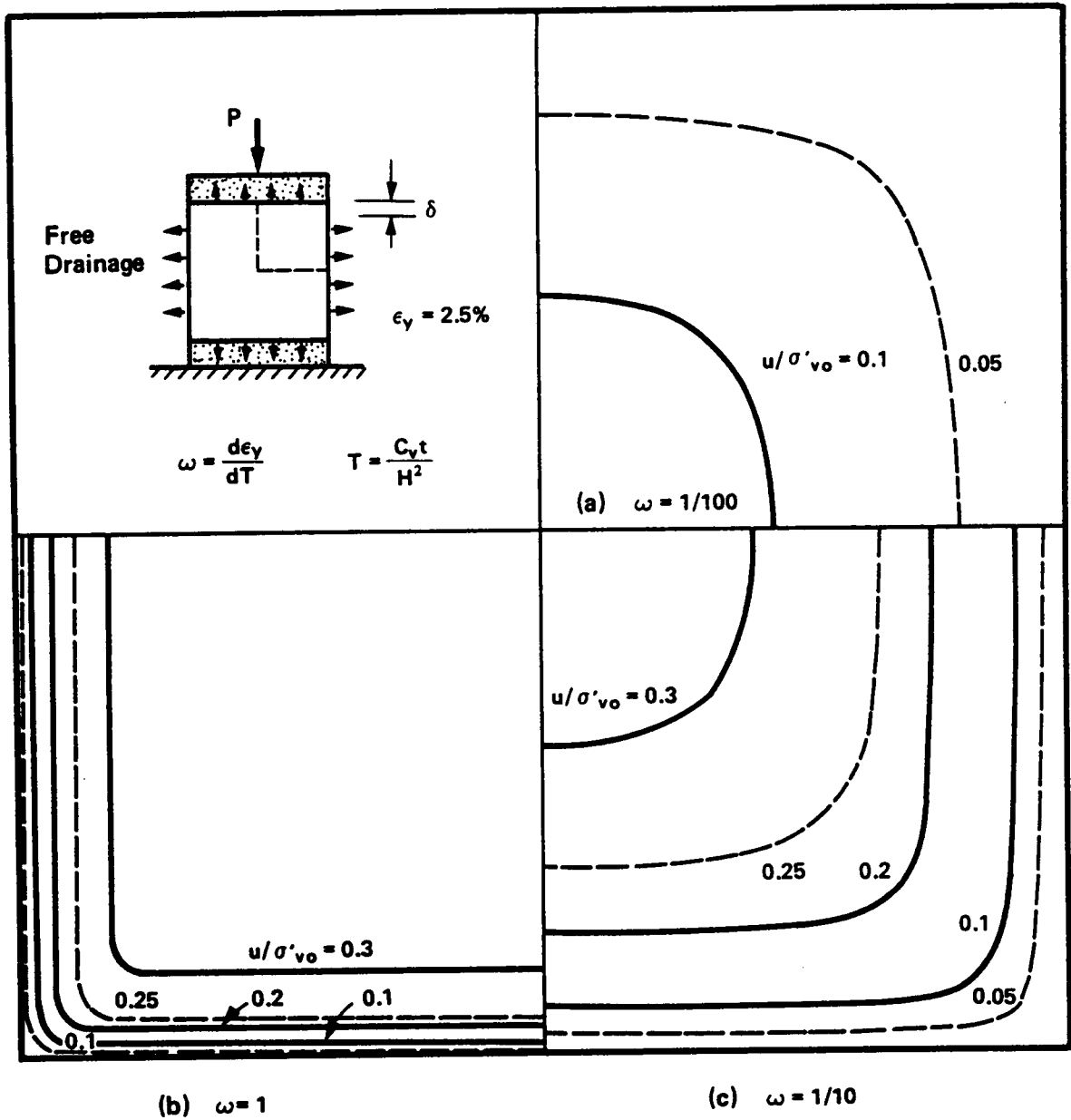


Figure 6.24 Variation of Excess Pore Pressure with Loading Rate in Plane Strain Test with Free Surface Drainage

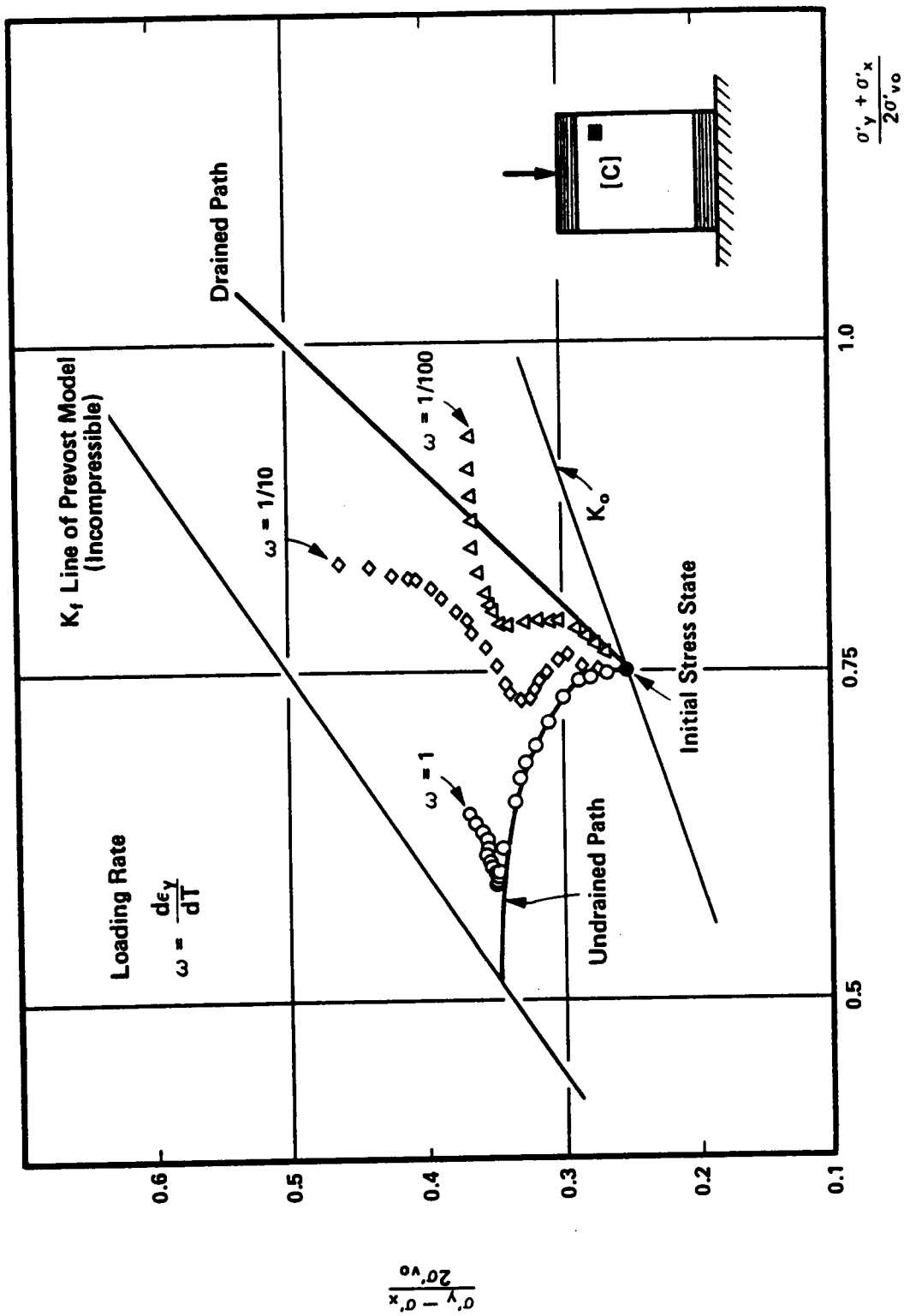


Figure 6.25 Stress Paths Predicted for Different Loading Rates in Plane Strain Test with Free Surface Drainage

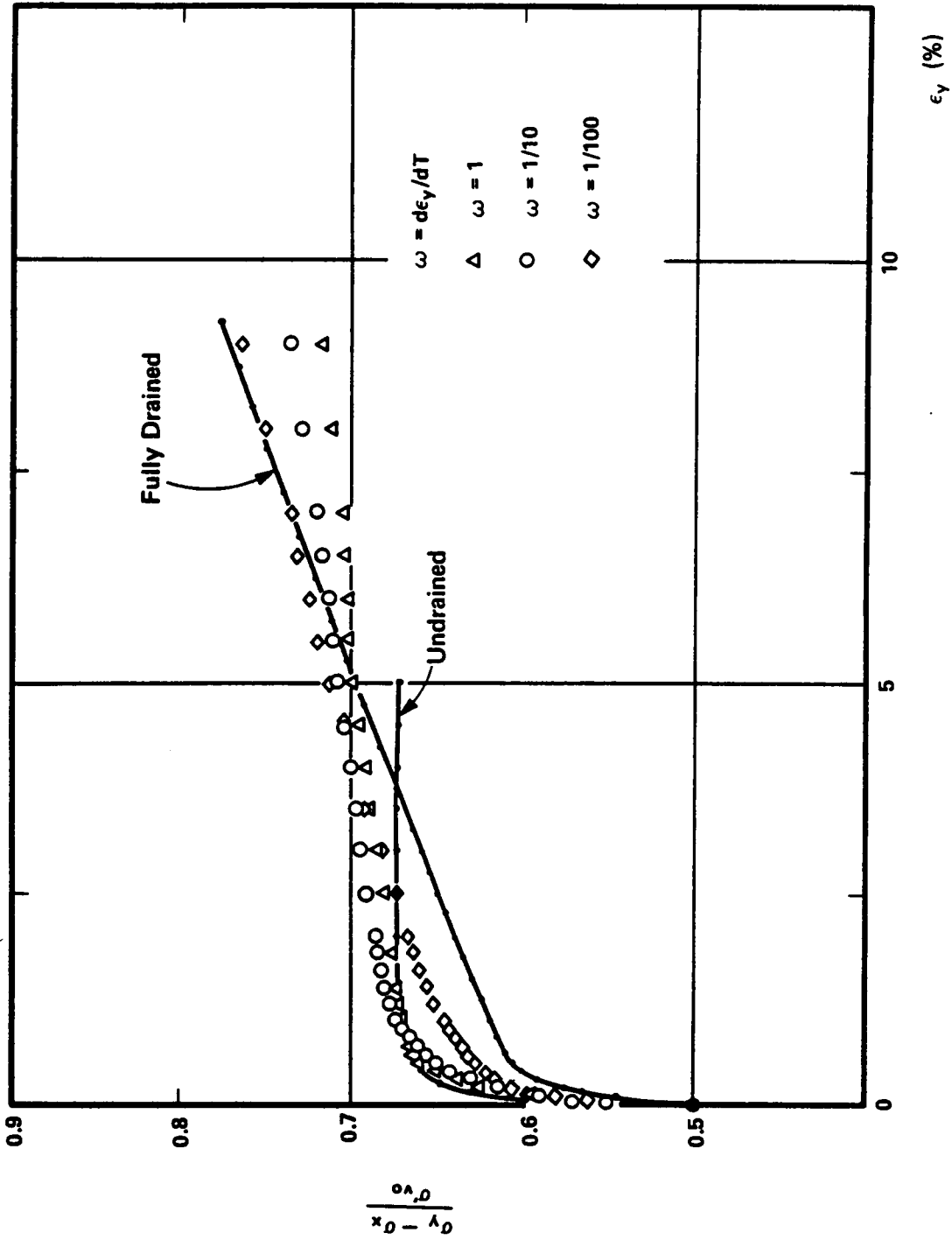


Figure 6.26 Stress-Strain Curves Predicted for Different Loading Rates in Plane Strain Test with Free Surface Drainage

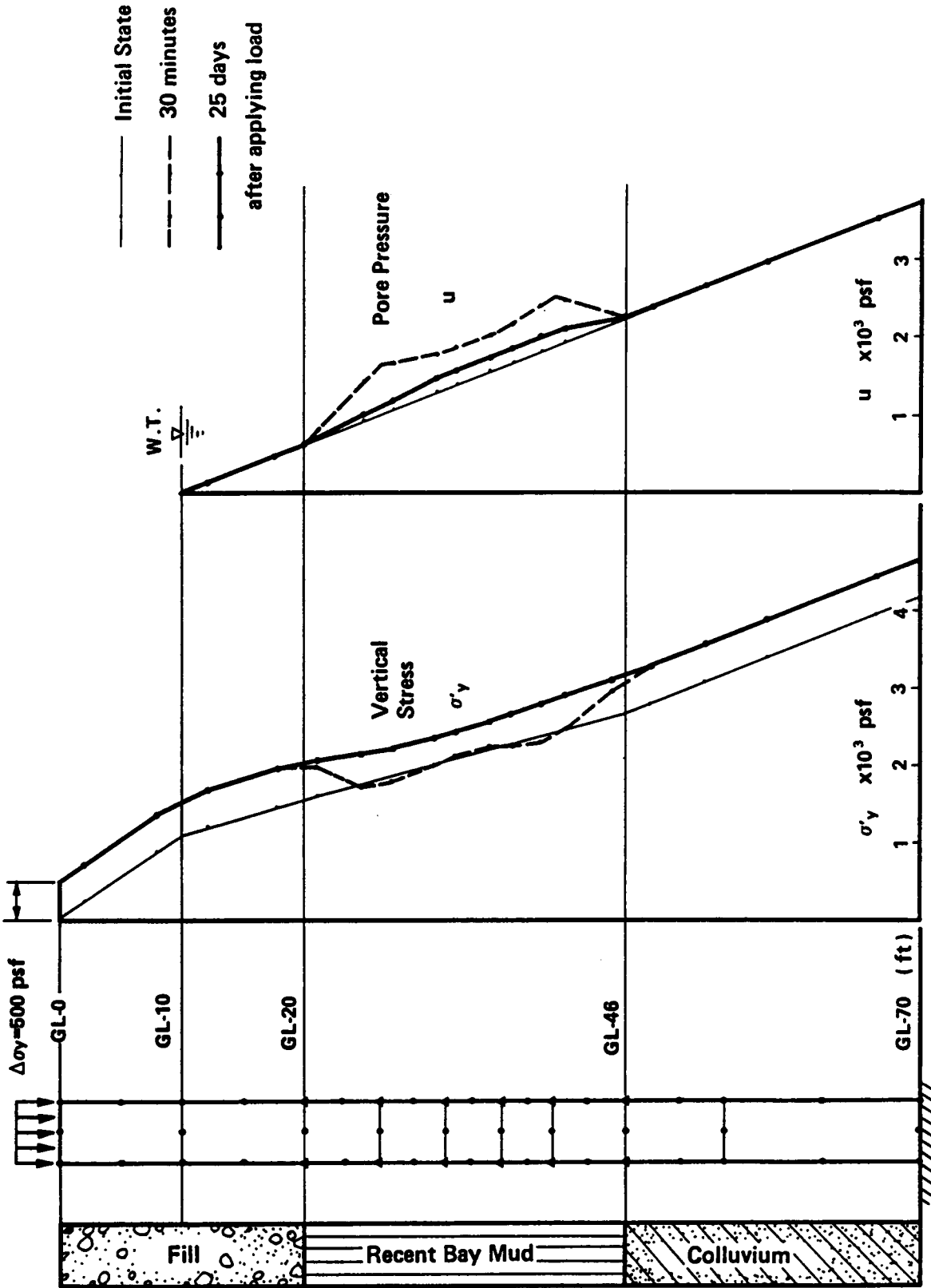


Figure 6.27 One-Dimensional Consolidation Problem of Mixed Ground Profile with Drained and Hardly Drained Subsoils

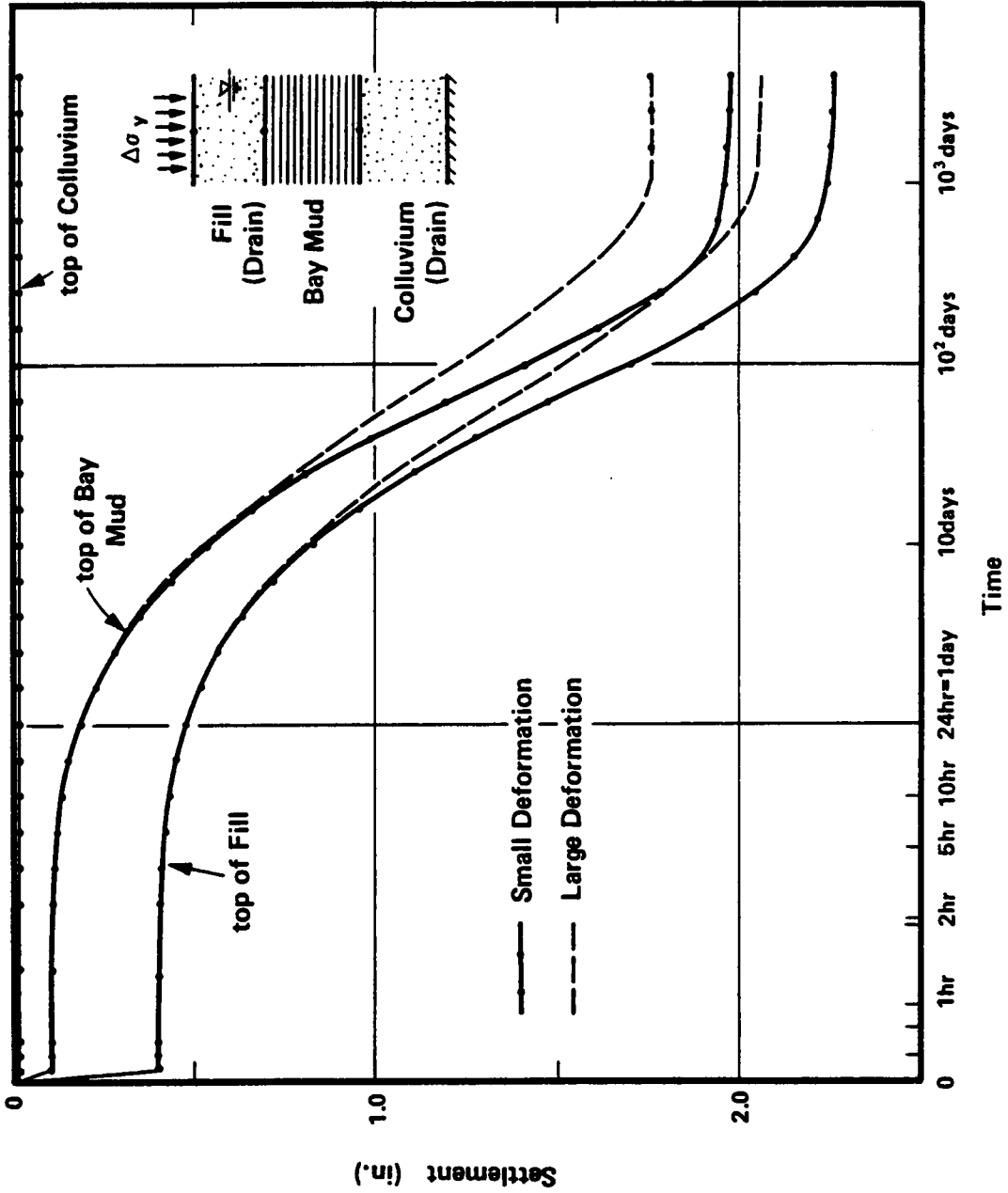


Figure 6.28 Ground Settlement Curves of Consolidation of Mixed Ground Profile with Drained and Hardly Drained Subsoils

## Chapter 7

### FINITE ELEMENT ANALYSES OF THE N-2 PROJECT

#### 7.1 Introduction

General observed ground movements caused by the EPB shield at the N-2 tunnel project are summarized in Chapter 2. The results clearly showed the initial heaving effect induced in the EPB process. Of particular interest was the fact that at each of the three instrument lines, a different amount of heave occurred, which could be correlated with the level of pressure measured on the bulkhead inside the shield.

A plane strain finite element analysis in a transverse section to the tunnel alignment is employed to simulate the EPB process, including loading stages for heaving, tail void closure, liner installation and consolidation. The Bay Mud is modeled by the Prevost elasto-plastic model to carry out an effective stress analysis coupled with pore pressure variation. An incremental, iterative analysis with large deformation theory is employed.

Ground movements were measured at three lines, Line 2, 3 and 4, at the N-2 project. Of the three, Line 4 provides the most complete set of data and the behavior for Line 4 is first examined for comparison with the predictions. The comparison between the ground movements at the three lines is studied later.

#### 7.2 Finite Element Idealization of the N-2 Tunnel

The basic conditions in the N-2 tunnel analysis are described in this

section. The theoretical background has been fully discussed in the preceding chapters. Only the soil properties and the analytical procedures which are considered essential are to be described in this section.

#### 7.2.1 Soil Properties and Idealization of the N-2 Tunnel, Line 4

As noted earlier, the soil at the site consists of fill followed by cohesive Recent Bay Mud, overlying a dense sandy colluvium deposit. The finite element mesh in Figure 7.1 takes this into account. The top two rows of elements in the mesh correspond to the fill and the bottom two rows to the colluvium. The middle rows of elements represent the Recent Bay Mud layer through which the N-2 tunnel was driven.

A drained response is assumed for the fill and the colluvium. A non-linear elastic hyperbolic model is used for these materials. Material parameters for the fill and the colluvium layers are shown in Table 7.1. Finno (1983) introduced parameters for these soils by making reference to the work done by Duncan, et al. (1980). The parameters in Table 7.1 are taken from Finno (1983) with minor revisions.

The middle layer of the soil profile represents the Recent Bay Mud, which is simulated by means of the Prevost soil model. Chapter 5 demonstrated the capacity of the Prevost model to model Bay Mud behavior as observed in laboratory test. Parameters for this model are given in Chapter 4 in Table 4.3. These parameters are appropriate for the tunnel problem except that it was found necessary to reduce the moduli of the Bay Mud by 30 percent in order to generate more reasonable patterns of

behavior. All other parameters such as yielding and hardening characteristics are unchanged from Table 4.3.

In the Bay Mud, excess pore pressure developed due to the stresses induced by tunneling. Changes in pore pressure with time are accounted for in the analysis. Pore pressure degrees of freedom are added and coupled with the deformation resistance of the Q8P4 soil elements.

The variation of soil properties with depth in the Bay Mud are in proportion to the effective overburden stress. In this case, only one set of the Prevost model parameters is needed to describe the whole region of the Bay Mud. Although the top portion of the Bay Mud layer is thought to be slightly overconsolidated, this was neglected for simplicity.

The coefficient of permeability of the Bay Mud in the vertical direction  $k_v$  is assumed to be 0.0028 ft/day ( $1 \times 10^{-6}$  cm/sec), which is a typical value for Bay Mud and the same as the value used by Finno (1983) in his analyses of the N-2 project. The permeability in the horizontal direction  $k_H$  should be greater than that in the vertical direction since the presence of sand and silt lenses were reported within the Bay Mud. A value of  $k_H$  five times greater than that of  $k_v$  was used. Evidence to support this ratio is given by Kavazanjian (1980) and Benoit (1983). Nonlinearity of permeability with void ratio changes is taken into consideration.

During the heaving stage, out-of-plane drainage was taken into consideration. In a true plane strain analysis pore pressure flow is fully confined without any flux in the longitudinal direction. However, the

heaving process results in a localized development of a very high excess pore pressure in soils to the side and in front of the shield. Thus pore pressure dissipation toward the front is likely to be present. Hirata and Aritome (1983) showed with field data excess pore pressure around an advanced shield to exist about two diameters ahead of the shield face. Therefore an equivalent out-of-plane drainage length of 24 ft. (7.3 m) was used in the N-2 analyses.

The ground water table is assumed at 10 ft. (3.0 m) below the ground surface as shown in Figure 7.1. The bottom boundary of the mesh configuration fully constrains nodal displacements along the boundary, and only vertical displacements are allowed at the side boundaries. The domain concerned with the analysis is 70 ft. (21.2 m) in depth and 80 ft. (24.2 m) in width. Total degrees of freedom of the system are 720, of which 93 are inactive due to the displacement constraints of the boundary conditions.

### 7.2.2 Analytical Procedure Simulating Tunnel Construction

Tunnel construction simulation consists of five stages, which are modeled as different loading steps. Figure 7.2 explains the procedure.

As the first step initial stress and pore pressure in the ground are set up assuming a  $K_0$  condition of 0.5. The initial heaving effect is simulated by applying a distributed pressure along the periphery of the shield as shown in step 2. The heaving pressure is radial so as to produce outward displacements in the adjacent soils. Finno (1983) applied an elliptically distributed normal pressure to the tunnel perimeter based on

the results of longitudinal finite element analyses. The distribution of the heaving pressure for this work is shown in Figure 7.3(a). One hour was allowed for each step to increase the average heaving pressure by 60 psf (2.9 kPa). This is consistent with the fact that heaving occurs in the field over a protracted period of time. The heaving stage is considered completed when the predicted maximum lateral displacement reaches that observed at the closest inclinometer line to the tunnel. Twelve to 28 increments were required to complete the heaving process depending upon the different levels of heaving for the three locations. The time allowed for the heaving loading is believed to be roughly consistent with the time required in the field for the full heaving pressure front to develop at any given point.

Loading step 3 in the simulation accounts for the effect of the tail void closure. Inward movements of the soil are induced by applying an unloading pressure around the tunnel periphery, and several schemes for this were considered. Finno (1983) applied a uniform pressure and considered the tail void to be closed when the inward movement at the crown closed the theoretical tail void gap of 3 in. (7.6 cm) for the N-2 shield. However, his results considerably overpredicted the movements near the shield that were observed in the field. It was concluded that the discrepancy was partly due to a lack of accounting for the void filling effects of the liner grouting and inadequacies in the Cam Clay soil model. The latter has been improved by means of applying the Prevost soil model. The former can be improved by introducing more realistic loading conditions to represent the tail void closure.

After a number of studies, an elliptic distribution of unloading pressure is employed as shown in Figure 7.3(b). The preference of this pressure is discussed in detail in Chapter 9. These pressures are applied in a series of increments until the calculated lateral deflections of the soil fall in the same level as those observed in the field. The total time allowed for pore pressure dissipation in step 3 in the analysis is about 3 hours, which is consistent with that associated with the time required for closure in the N-2 field results. Depending on the amount of the heave and the inward movement to close the tail void, 12 to 23 increments are needed to complete the loading steps for the tail void closure.

Once the tail void is filled, the remaining residual stresses in the soil are transferred to the liner so that the inner surface of the tunnel may be free from tractions. This process is simulated in the loading step 4. Prior to applying the tractions, the liner elements are activated so as to represent the equivalent liner stiffness against ring compression. Surface tractions along the shield periphery are calculated in terms of stresses in the adjacent soils and then loaded on the liner. The weights of the liner and other machinery in the tunnel are loaded at the same time. They are typically 30 percent of the weight of the excavated soil. Only small displacements are induced during this step due to the rigidity of the liner even though a large amount of stress rearrangement takes place. The liner installation process is completed in 7 loading increments in the analysis.

Excess pore pressure develops in the Bay Mud during the loading stages and time must be allowed for dissipation. This process is analyzed by

means of 14 to 20 time integration steps; the total elapsed time for pore pressure equilibration is 250 days to 1 year.

### 7.3 Ground Response at Instrument Line 4

The results of the instrument Line 4 were best documented and represented an average of all those observed. Thus this line is examined first in terms of comparisons between the predicted and observed results for each construction stage.

#### 7.3.1 Heaving Process

An average heaving pressure of 1260 psf (60.7 kPa) is applied to induce the same lateral displacements in soils as those observed for the field. Figure 7.4 shows the predicted and observed lateral displacements along the instrument lines 4B and 4E, which are 6.4 ft. (2.0 m) and 18 ft. (5.5 m) in distance from the tunnel centerline, respectively. A good agreement is observed. Displacements in the Bay Mud layer predominate while those in the overlying fill and the underlying colluvium are small.

Figure 7.5 demonstrates the predicted displacement pattern in the form of a deformed finite element mesh. Only small upward heaves are predicted in the overlying fill above the tunnel, and less than 0.25 in. (0.64 cm) occurs at the surface. The degradation of movements at the level of the springline and the invert with distance from the tunnel is shown in Figure 7.6. The data predicted by the FEM analysis are bounded by and follow the trend of the field data.

### 7.3.2 Tail Void Closure

An average unloading pressure of 1500 psf (72.2 kPa) is applied on the tunnel periphery to produce lateral displacements similar to those observed (Figure 7.7). The agreement between the observed and predicted results is very good and far better than the early results obtained by Finno (1983).

Figure 7.8 shows the deformed mesh. Whereas the heaving caused little movement vertically, there are significant settlements in the crown area due to void closure. Relatively smaller lateral movements occur, so that the effects of the initial heaving still remain in the area to the side of the tunnel. In the comparison of the predicted subsurface movements with the field data, only the lateral displacements are available for stages of the heaving and the tail void closure. The agreements for these stages are encouraging.

### 7.3.3 Surface and Deep Ground Movements

Surface movements at the tunnel centerline were measured for all construction stages. Figure 7.9 gives the variation of the surface movement with time for tunnel construction and a period of 300 days thereafter. Magnitudes of the predicted surface heaves agree well as do the long term settlements. It is worth noting that during liner installation a small upward displacement is predicted. This is due to the reduction of gravity force since the load of the tunnel is far lighter than that of the soil mass it replaces. This small effect was not picked up in the field data.

Figure 7.10 gives a comparison of the predicted and observed surface settlement troughs and there is generally good agreement. Three hundred days after tunneling, the observed trough exhibits a shaper curvature than that predicted. The reason for this is not known.

The deformed mesh plot after full consolidation is shown in Figure 7.11. Comparing it with Figure 7.8, it is found that increases in settlement occur within a wide area in the region.

Deep ground movements are shown in vector forms in Figure 7.12 comparing the predicted and observed displacements. In most cases the displacements agree well. It should be noted that Clough, et al. (1982a) point out that the measured vertical movements are much less reliable than the horizontal movements because of the nature of the instrumentation.

Considering the correlation of predicted ground movements to those observed at Lint 4, it is concluded that the proposed finite element procedures reasonably model the EPB tunneling effect on ground movements.

#### 7.3.4 Predicted Excess Pore Pressures and Stress Levels

Contours of computed values of excess pore pressures and stress levels within the Bay Mud are shown in Figures 7.13 and 7.14, respectively, with respect to each construction stage.

As heaving is completed, excess pore pressures develop, concentrating in the vicinity of the springline. Excess pore pressures higher than 600 psf (28.9 kPa) are predicted just beside the shield. This is enough head

increase so that when added to the water table level at 10 ft. (3 m) below the ground surface, the local pore pressure head will be at or above the ground. In fact, instrument casings in the Bay Mud shows rapid rises in water level near the ground surface. Upon tail void closure, a rearrangement of the excess pore pressure occurs. The maximum value decreases while the region with high value extends away from the tunnel. Negative pore pressures are predicted at the crown and the invert. This is in conformity with the instrumented observations that soils above the crown expand (Atkinson and Pott 1977a, Cording and Hansmire 1975). Liner installation causes changes in stress distribution but excess pore pressures are not changed very much.

Stress level is defined as a ratio of the radius of the current stress point to that of the critical state line projected on the octahedral plane in stress space, as explained in Section 5.3. It is an indication of how close a soil is to failure. Stress level is 0.73 for the initial stress state before tunneling and is 1.0 if a soil reaches failure. Stress levels for different stages of simulation are shown in Figure 7.14.

At the heaving stage the stress levels indicate increases above the original values in the soil above the crown and below the invert. These are due to increases in the vertical stresses in the soils there. Decreases in stress levels in the vicinity of the springline result from that the heaving increases confining pressure of soils, reducing the shear stress.

At the stages of the tail void closure and liner installation, stress

levels in locations 45 degrees from the springline increase considerably. Soils between the crown and the springline are close to failure. After long term consolidation, stress levels are decreased in general. This is due to an increase shear strength of the soil caused by the void ratio decrease during consolidation.

Variations of excess pore pressures and stress levels predicted for each construction stage are descriptive features of ground response to tunneling. The heaving effect, as a characteristic of advanced shield, has both an advantage and a disadvantage: high excess pore pressure development and stress level reduction, respectively. The former is responsible for a larger consolidation settlement while the latter provides a higher stiffness of the soil.

#### 7.4 Comparisons of Ground Response for Instrument Lines 2, 3 and 4

The finite element analysis of Line 4 conditions gave a series of reasonable predictions which agreed well with the observation data. To further test the procedures it is useful to examine Lines 2 and 3 since the behavior at Line 4 falls between the two extremes at Lines 2 and 3.

##### 7.4.1 Lateral Displacements and Settlements

Lateral displacements measured by inclinometers at Lines 2 and 3 are used as the calibration for the heaving and closure condition, as they were for Line 4. Figure 7.15 shows a comparison of the predicted and observed lateral displacements for all three Lines, 2, 3 and 4. The

maximum values must be the same since the heaving pressure is calibrated in this way. However, the fact that the entire profiles of lateral deflections agree quite well is an independent check. As noted earlier in Chapter 2, the differences in response have been attributed to the use of different thrusting levels at the three lines. Table 7.2 gives the average heaving pressures needed in the analyses to duplicate the field behavior. The average heaving pressure at Line 3 is more than 2.5 times larger than that at Line 2. Average thrusting pressures from the actual shield operation are also shown in the table. They are calculated from the readings of shield jack forces recorded in passing the instrumentation lines, with a subtraction of the average adhesion along the shield perimeter. The thrusting pressure acts in the axial direction of the tunnel, whereas the heaving pressure in the analysis is applied in the transverse direction. Therefore a comparison of their absolute values is not appropriate, but their ratios are likely an indication for correlation between the thrusting and heaving pressures. The ratios are about 80 percent for all the three lines.

Figure 7.16 gives the predicted and observed lateral displacements at tail void closure. Again the predicted results agree well with the observed data. A significant amount of lateral displacements remain in the Bay Mud; ground movements toward the tunnel are predicted at Line 2 where the smallest heaving deflection was induced. Such inward movements are common for the conventional shields. The other two lines remain displaced away from the tunnel.

Variation of surface settlement at the centerline with time is shown

for the three instrument lines in Figure 7.17, and the predicted final settlements are compared with the field data. Even though the final settlements fall in a relatively small range, the ground movements corresponding to the preceding construction stages are quite different. This suggests that construction practice influences the ground movement greatly. The initial heave and the consolidation settlement are the largest at Line 3, whereas the immediate settlement at Line 2 exceeds the others. This issue is discussed in more detail in the next sections. Note that settlements at the time of shield passage were not measured at Line 2 and 3 and so quantitative comparison is not possible for them.

Figures 7.18 and 7.19 compare vectors of predicted final displacements with those observed at Lines 2 and 3, respectively. The predicted displacement has the same trend as the observed ground movements. Similar to Figure 7.12 for Line 4, the soils above the tunnel settle downwards and those below the tunnel rise very little. Lateral displacement adjacent to the springline are different between instrument lines reflecting different levels of the initial heave.

Relative displacements can be computed as a change in displacements from the heaving stage to the final state and are shown in Figure 7.20. This reflects primarily the effect of tail void closure. The relative displacements are essentially similar in their direction for Lines 2, 3 and 4, in spite of the fact that there were very different heaving levels. Therefore, it appears that the ground movements for the stages following the heaving are caused by means of the same mechanism, one which is independent upon the initial effects.

Displacement patterns at the heaving and the consolidation stages are found in deformed meshes (Figures 7.21 and 7.22 for Lines 2 and 3, respectively). These can be compared with Figures 7.5, 7.8 and 7.11 for Line 4. Upward movements below the invert are found relatively large for Line 2. This is due to the presence of the greatest thickness of the Bay Mud at that location.

#### 7.4.2 Earth Pressures and Liner Stresses

Using the stresses and the pore pressures predicted at the stress points closest to the tunnel, normal stress distributions are calculated along the tunnel periphery. Those predicted for the heaving stage for all lines are shown in Figure 7.23 together with the initial at-rest earth pressure. The earth pressures relative to at-rest increase largely around the springline albeit only slightly at the crown and the invert. The earth pressure distributions at the tail void closure are shown in Figure 7.24. Higher than at-rest pressures remains at the springline, but those at the crown and invert are lower. Some fluctuations are found in the final pressure distribution probably because predictor-corrector type iteration applied in the analyses is not sufficient to achieve full stabilization in stress agreement in soils. This is especially true for soils close to failure just like the area near the crown where high stress levels have been mobilized.

The earth pressure is interesting since it may be surprising that the advanced shield heaving effect influences the distribution. For conventional tunnels, Eden and Bozozuk (1969) showed that two thirds of the

overburden pressure existed on the liner for a tunnel in stiff clay. Yamamoto, et al.(1978) measured similar earth pressures. The field data generally indicate that the earth pressure on the liner for a conventional shield is reduced below that before shield driving, consistent with the evaluation method proposed by Terzaghi (1943). However, the earth pressure predicted for the Lines 2, 3 and 4 are larger than, or the same as, the initial pressure at the vicinity of the springline, reflecting the nature of the advanced shield.

Figure 7.25 shows predicted stress distribution induced in the liner at Line 4. Axial stress, bending stress and out-of-plane shear stress are calculated from stresses at the stress points in the liner elements. The axial stresses are high in compression, particularly at the crown, invert and springline, while the bending stresses are relatively small. The sign of bending stress changes between locations near the springline and the crown and invert. Although there is a lack of field data on the liner stress, the predicted axial and bending stress distributions are similar to those obtained by Yamamoto, et al.(1978).

The axial and bending stress distributions are compared for Lines 2, 3 and 4 in Figure 7.26. Stresses increase with the level of heaving at the springline, but it is not so simple at the crown and the invert. Line 2 exhibits a special response. Since Bay Mud is very deep there, the stress distribution may be sensitive to the soil profile.

As consolidation proceeds, the axial stress increases at the springline, and decreases at the crown and invert as shown in Figure 7.27. The

amounts of their changes, however, are not significant relative to the changes in the bending stress. Consolidation also leads to increases in the bending stress.

#### 7.4.3 Changes in Tunnel Diameter

During the consolidation stage, the tunnel diameter changes with movements of the surrounding ground. Measured field data are available for the comparison with the predicted diameter changes. However, the presence of equipment in the shield did not allow the diameter to be measured immediately after the liner was installed. For this reason, the field data are only available from five to eight days after the shield passage.

The three succeeding figures, Figures 7.28 to 7.30, show a comparison of the diameter changes with time for Lines 2, 3 and 4, respectively. Field data indicating the vertical diameter at Line 2 were not obtained.

Generally, the predicted diameter variation with time follows the observed trend well. The vertical diameter shortens with time, while the horizontal is lengthened. The magnitudes of the vertical diameter shortening is slightly larger than that of the horizontal lengthening. The changes are also different in magnitude for the three instrumentation lines. Their relative magnitudes are in the same order as of the heaving levels.

The range of the diameter changes is from 0.03 percent of the tunnel diameter at Line 2 to 0.3 percent at Line 3. The deformations of the tunnel in the predicted results are found to mostly stop within one month.

Eden and Bozozuk (1969) showed in their field data that 0.1 percent of the tunnel diameter change was measured in one month after the shield passage. Yamamoto, et al. (1978) also collected many field data on the liner deformation of tunnels constructed in soft clays and presented evidence that  $D/200$  to  $D/50$  were observed in diameter changes. The field data of the N-2 project are plotted in that range.

#### 7.4.4 Predicted Excess Pore Pressures and Stress Levels

Excess pore pressures and stress levels mobilized at stages of heaving and liner installation are shown in Figures 7.31 to 7.33 for all the lines. It is interesting to note that stress level contours after the completion of heaving are quite different for the three instrument lines (Figure 7.31). As described in Section 7.3.4, the heaving pressures cause a reduction of stress level in the vicinity of the springline but an increase at the crown and the invert. These effects vary from line to line depending upon the level of heaving.

Shear zones with high stress levels develop in the direction 45 degrees to the vertical after tail void closure. Such zones are commonly observed for conventional shields (Cording and Hansmire 1975, Murayama and Matsuoka 1969). The shear zone is clearly shown in the contour of stress levels after liner installation in Figure 7.32.

For Lines 2 and 3 very high stress levels are mobilized in a part of the shear zone close to the tunnel. On the other hand, relatively moderate stress levels are predicted for Line 4. This fact suggests that the

construction performance at Line 4 was more successful in causing less disturbance in the ground.

Figure 7.33 gives excess pore pressure development up to the time of liner installation. These values are important since they are a direct cause of consolidation settlements. The pore pressures vary from being small at Line 2 to large at Line 3, reflecting the levels of heaving pressure for the respective locations. Reflecting to Figure 7.17, it is found that the consolidation settlements are well correlated to the level of developed excess pore pressure.

#### 7.4.5 Soil Volume Balance about Shield

Suppose a line which is located on the shield perimeter before shield driving, is termed a reference line. It expands out of the shield as heaving is produced, and then shrinks with inward movements of soils in response to tail void closure. Since, at most, small movements on the shield periphery during consolidation are expected because of the presence of the liner, the position of the soil periphery after the liner installation can be considered to be the final situation.

The volumes displaced by the various construction activities are illustrated for Line 4 in the right-hand side of Figure 7.34. A dotted zone in the figure indicates a soil volume corresponding to the relative displacement from the heaving to the liner installation stages. This is explained as the soil volume which is lost during the tail void closure process, and termed volume loss  $V_L$ . Similarly, a heaving volume  $V_H$

is defined as a soil volume calculated by the expansion of the reference line due to heaving. All numbers for soil volume,  $V_H$  and  $V_\ell$ , are scaled assuming that the tail void volume  $V_{TV}$  is 100 percent. Variations of the soil volume changes for each construction stage are schematically shown on the left side of the figure with respect to the ground response predicted at Line 4.

At the initial stage, the reference line is the shield perimeter by definition. After the heave, a heaving volume for Line 4 is created of 42 percent of  $V_{TV}$ . It is followed by an inward movement of the reference line as the tail void closes. Since the tail void closure and the liner installation are completed in a short term, the soil response to those events takes place in an essentially undrained condition without volume changes in the soil, and the soil mass of the heaving volume keeps its volume unchanged even after liner installation. The net tail void volume not filled by soil displacement is 62 percent of  $V_{TV}$ . This part may reasonably be considered to have been filled with grouting materials due to the backfill grouting of the liner, termed grouting volume  $V_G$ . The final net volumetric balance of the soil is found to be 4 percent of the heave at Line 4.

Results of similar considerations on the soil volume balance are demonstrated for Lines 2 and 3 in Figure 7.35. Reflecting the differences in heaving levels, only an 18 percent  $V_H$  is found for Line 2, but a value of 136 percent is computed for Line 3. In contrast to the uneven heaving volumes, volume loss due to the tail void closure are close for both lines with amounts of 64 percent and 68 percent. These are more

than 1.5 times larger than that calculated at Line 4, suggesting that grouting volumes for these lines are only 36 percent and 32 percent, respectively. The net volumetric balances end up with a 46 percent reduction at Line 2 and a 68 percent heave in Line 3.

It is interesting to note that even though differences exist in the final net volumetric balance, the final surface settlements observed in the field were substantially the same (Figure 7.17). This reflects differences in ground movements due to consolidation, which makes the final movements similar. Consolidation movements for Line 3 were the largest and these negated the initially effective movements of the large heaving at this Line.

Figure 7.36 shows the variation of surface movements with relation to the soil volume balance associated with respective construction stages. As the surface heave becomes larger, the reference volume increases, and consolidation settlements increase. The data show that the three lines had different component responses. Line 3 had the least heave and consolidation effect, but the largest tail void loss. Line 3 had the largest heave, but also the highest consolidation effect. Finally, Line 4 had an intermediate heave and consolidation but a low tail void loss. All of these factors taken together give the whole picture of the behavior of ground movements.

## 7.5 Summary and Conclusions

Using the finite element code developed for this research, procedures

and results of analyses for the N-2 tunnel project are described. A plane strain analysis method is employed for the transverse section of the tunnel. The finite element simulation is checked against measured ground response at three instrumentation lines in the N-2 project. The predicted results are compared with the field data in all ways possible and good agreement is found for every case at all the construction stages. The analytical procedure is thus believed realistic and reasonable for the advanced shield tunnel analysis.

The analyses also provide detailed information which is not available otherwise, such as pore pressure changes, stress levels, liner stresses, and volumetric considerations. These are used to explain the differences and similarities of the behavior at the three lines. The results show that the tradeoff in levels of heaving and the subsequent settlement is not simple. Each line had some different contribution in regard to heave, void closure and consolidation. To clarify this situation, parametric studies are done in the next chapter.

Table 7.1 Material Parameters of Nonlinear Pseudo-elastic Model for Fill and Colluvium

	Fill	Colluvium
Poisson ratio	0.30	0.35
Poisson ratio at failure	0.49	0.49
Failure ratio	0.95	0.90
Effective friction angle (degrees)	30°	20°
Cohesion (psf)	250	1000
Modulus exponent	0.50	0.40
Modulus constant	200	945
lateral earth pressure coefficient	0.5	0.8
Total unit weight (pcf)	110	125

Table 7.2 Relation between Average Heaving Pressure and Shield Thrusting Pressure

Average Pressure	Line 2	Line 3	Line 4
Initial	3307 <sup>psf</sup>	3307 <sup>psf</sup>	3307 <sup>psf</sup>
End of Heaving	3958	4957	4465
Applied Heaving Pressure $\bar{p}_H$	651	1650	1158
Thrusting Pressure of Shield Jacks	821	2147	1369
Ratio	80%	77%	84%

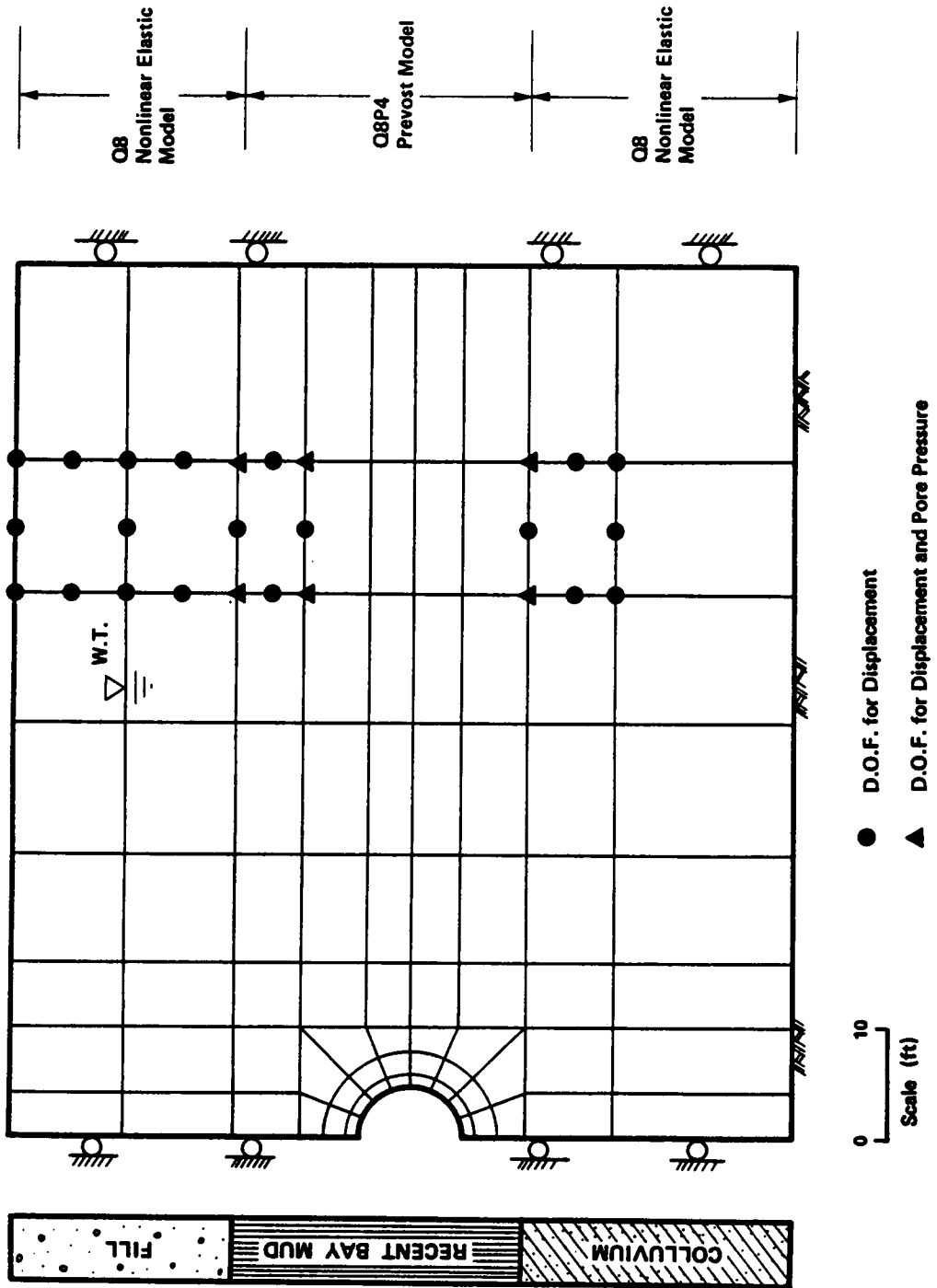


Figure 7.1 Finite Element Mesh for N-2 Tunnel Simulation, Line 4

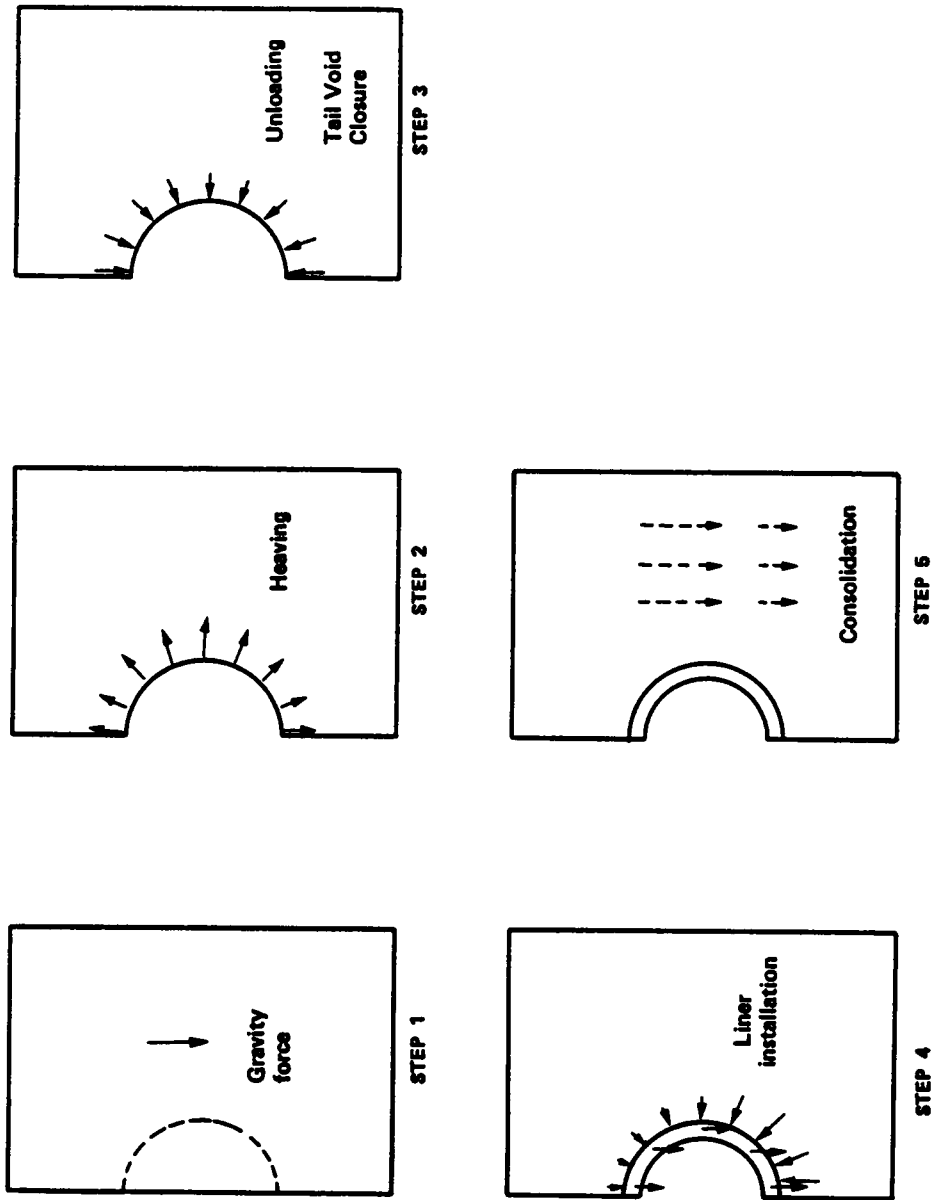
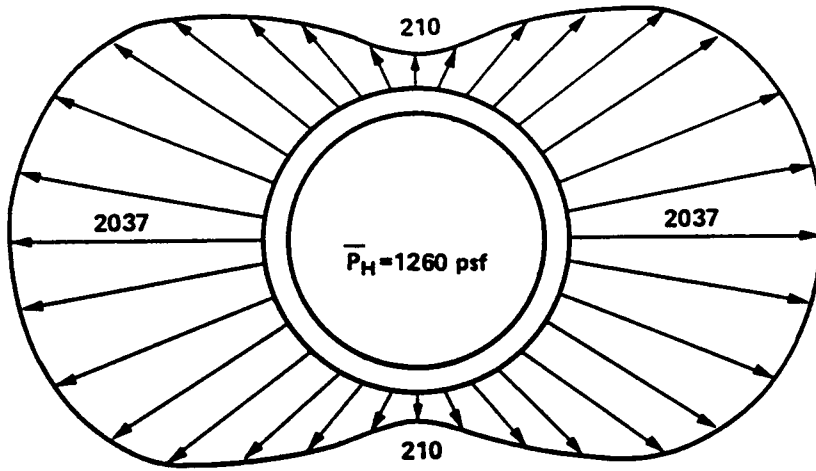
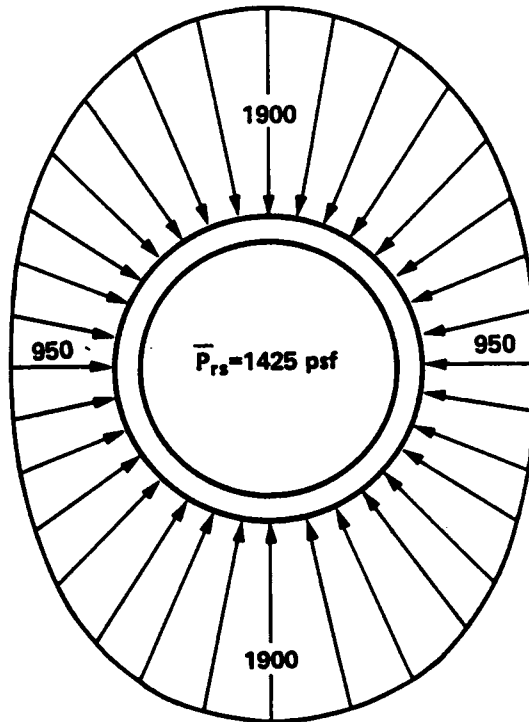


Figure 7.2 Analytical Procedure Modeling Tunnel Construction Stages



(a) Heaving Pressure Distribution (psf)  
(Average Pressure  $\bar{P}_H = 1260 \text{ psf}$ )



(b) Unloading Pressure of Stress Relief at Tail Void (psf)  
(Average Pressure  $\bar{P}_{rs} = 1425 \text{ psf}$ )

Figure 7.3 Pressure Distribution applied along Tunnel Periphery  
for Modeling of Heaving and Tail Void Closure, Line 4

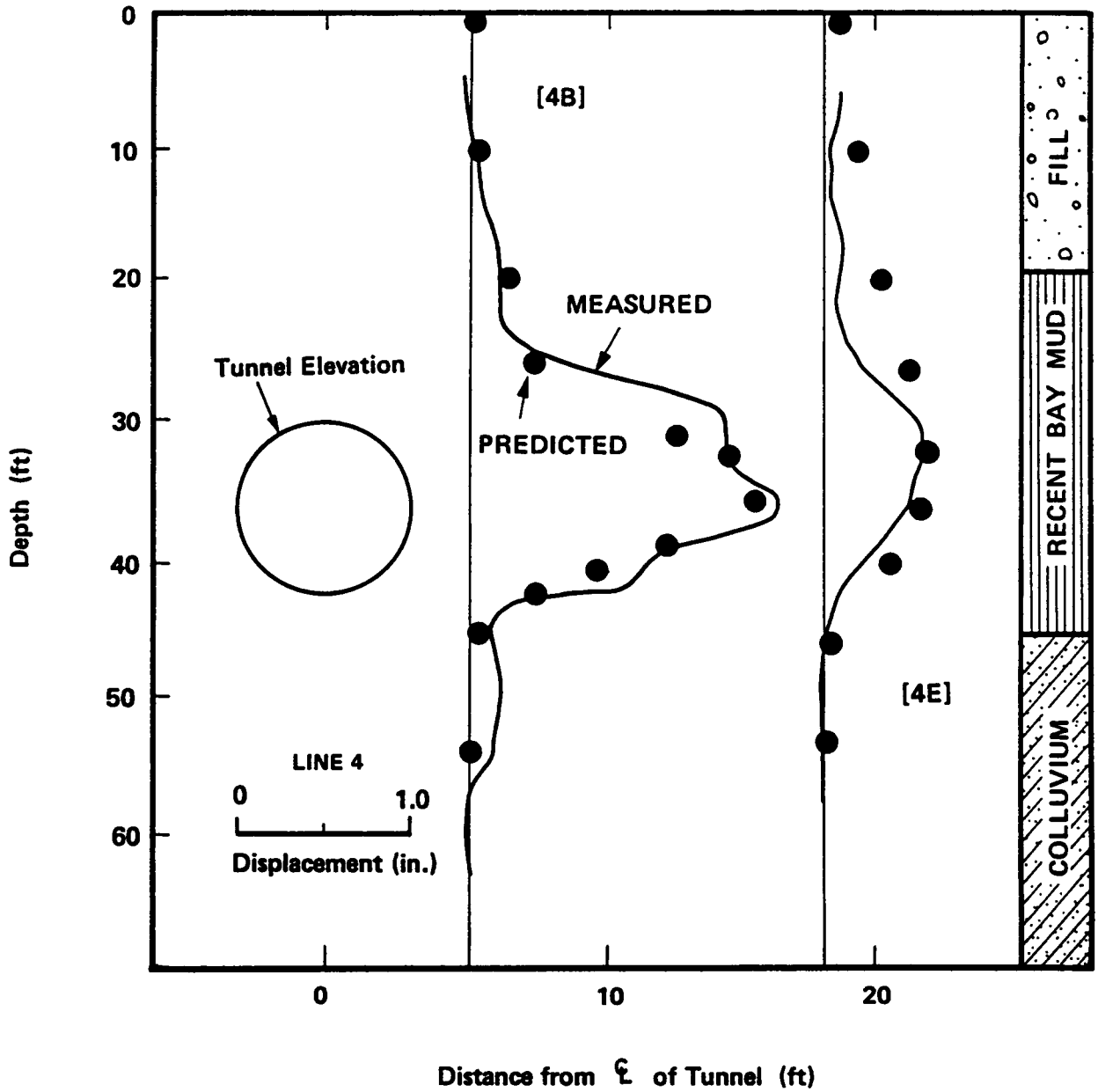


Figure 7.4 Predicted and Observed Lateral Displacements after Heaving, Line 4

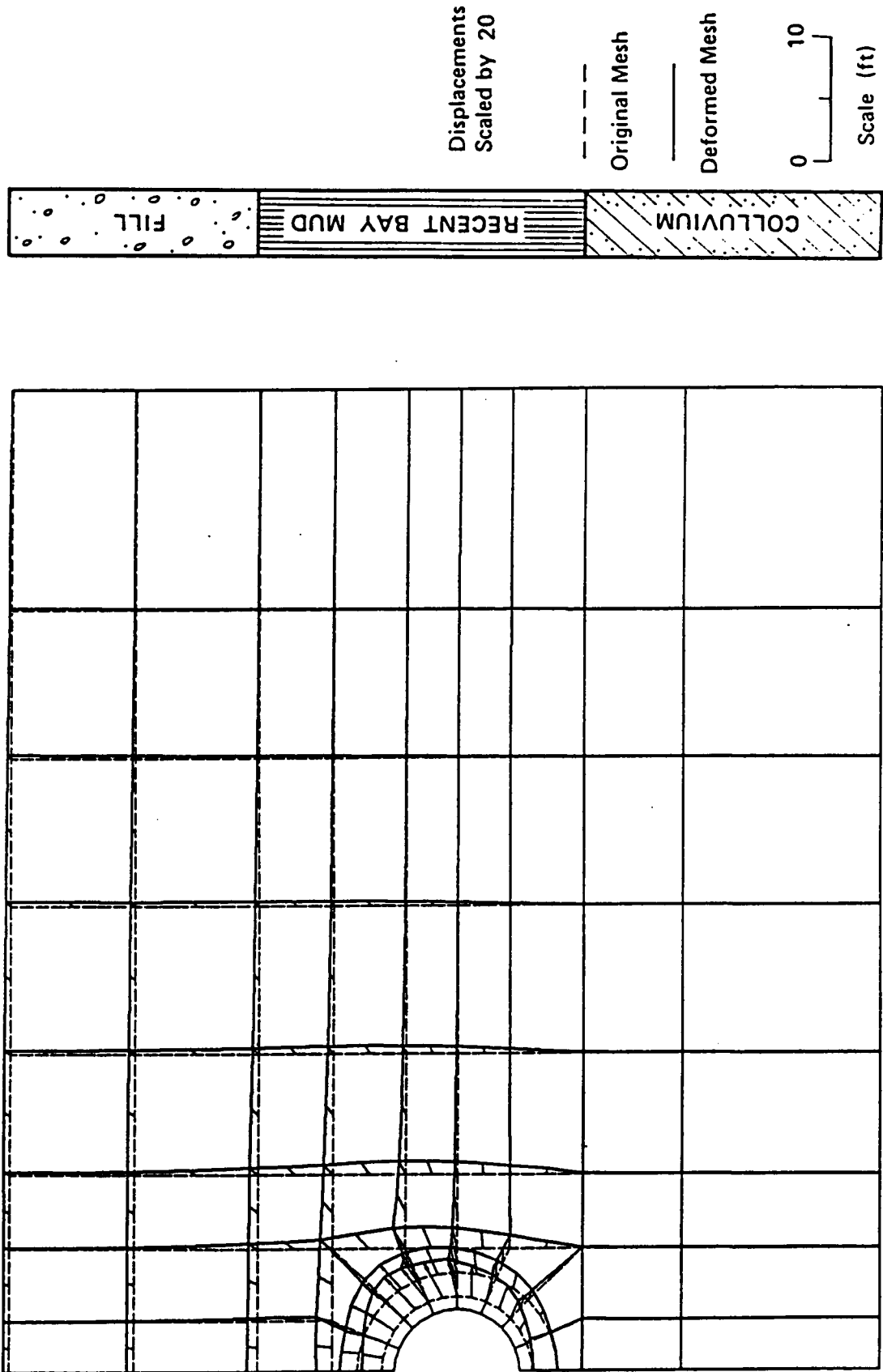
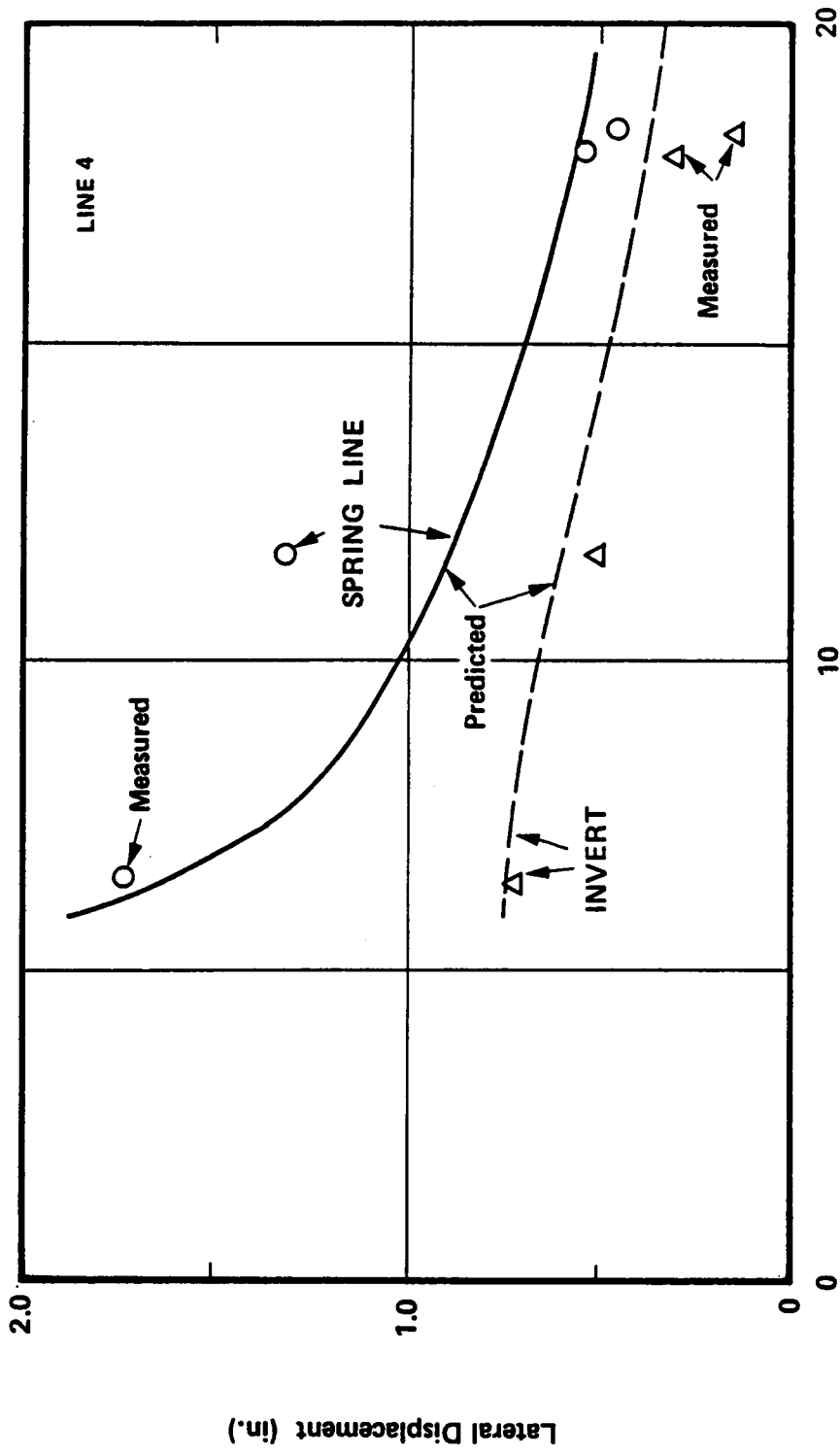


Figure 7.5 Predicted Displacement Field after Heaving, Line 4

LINE 4



Distance from  $\xi$  of Tunnel (ft)

Figure 7.6 Predicted and Observed Lateral Displacement Degradation with Distance from Tunnel at Springline and Invert, Line 4

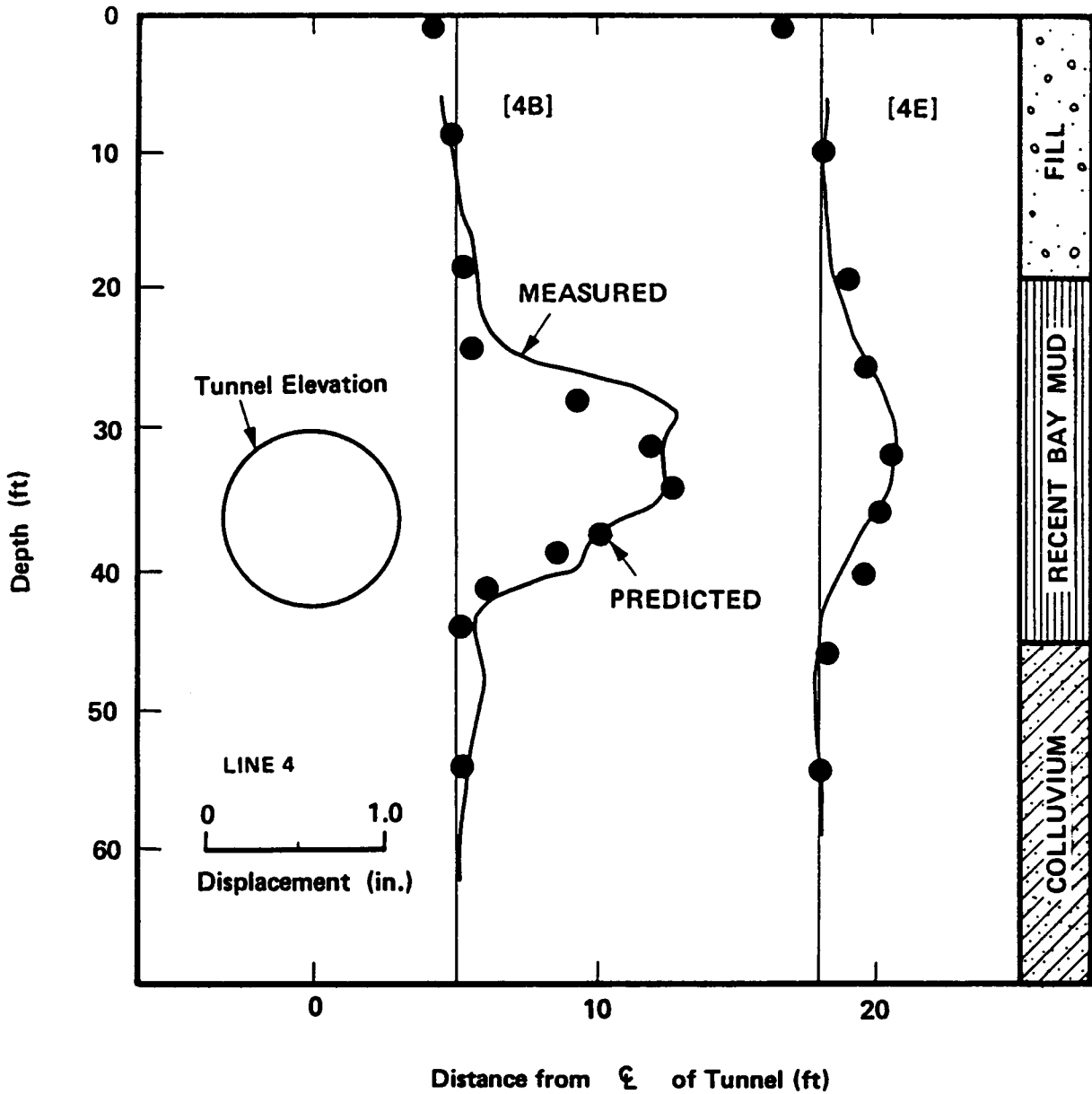
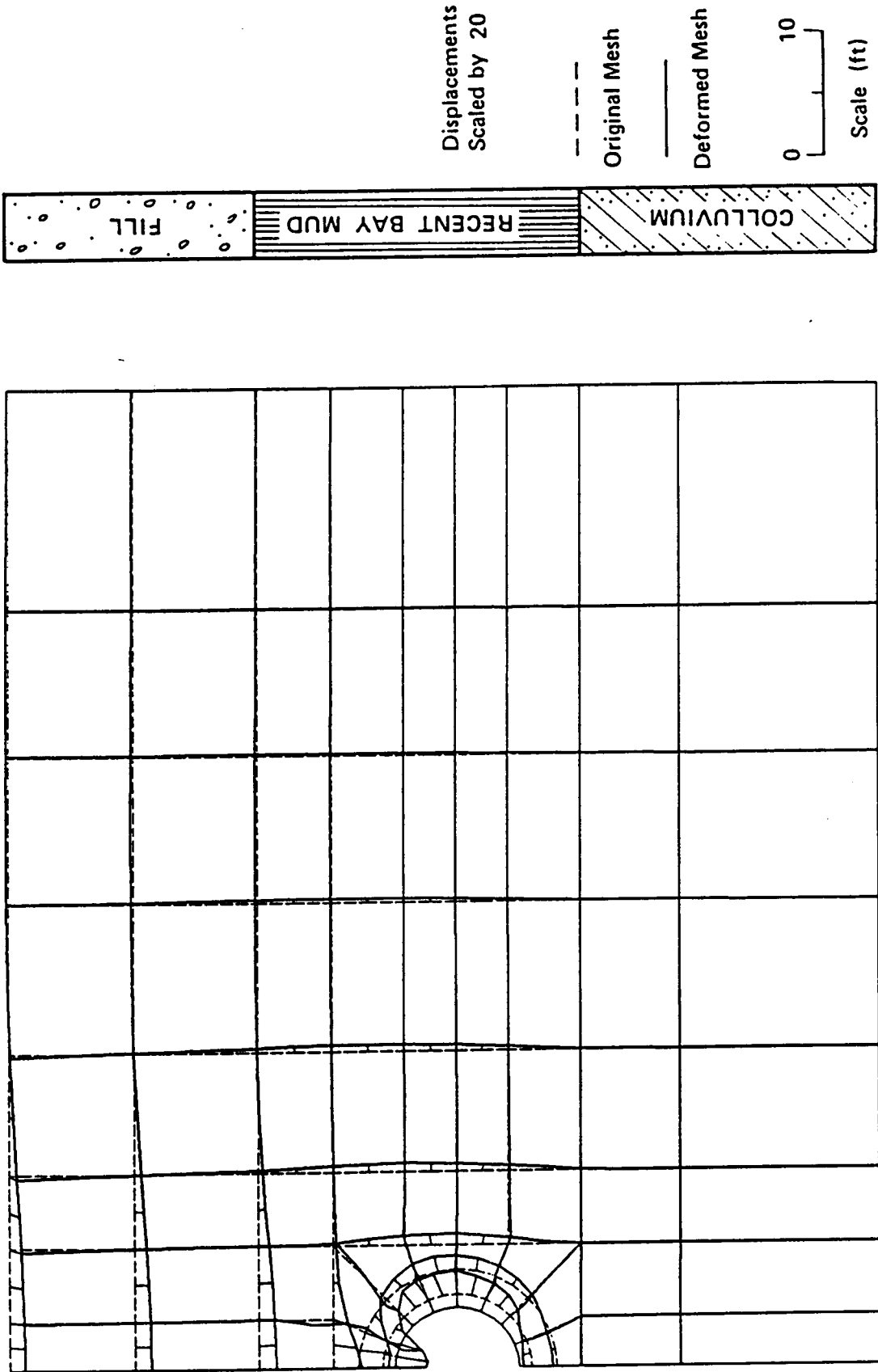


Figure 7.7 Predicted and Observed Lateral Displacements after Tail Void Closure, Line 4



LINE 4

Figure 7.8 Predicted Displacement Field at Liner Installation, Line 4

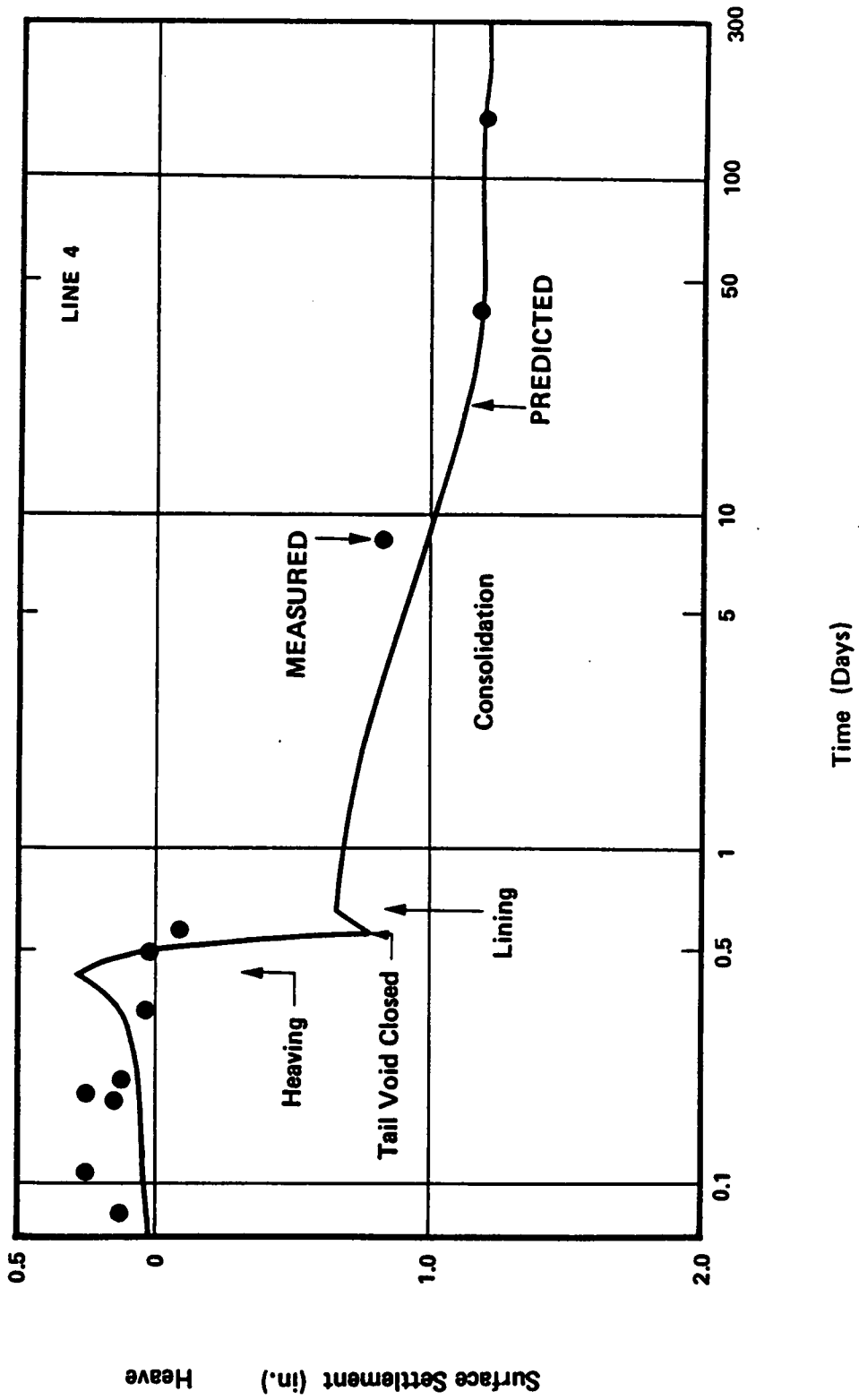


Figure 7.9 Predicted and Observed Variation of Centerline Surface Movement with Time, Line 4

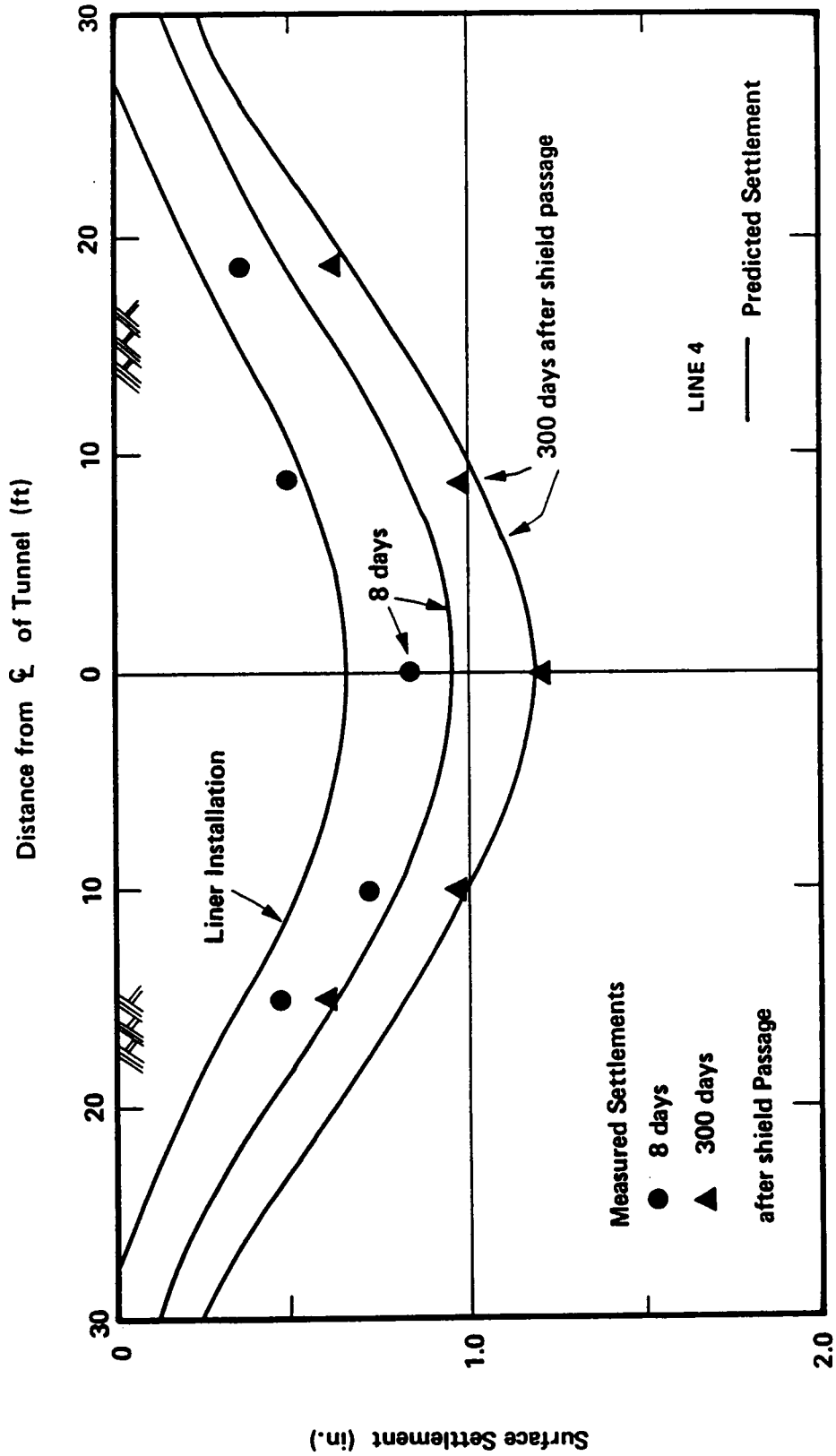
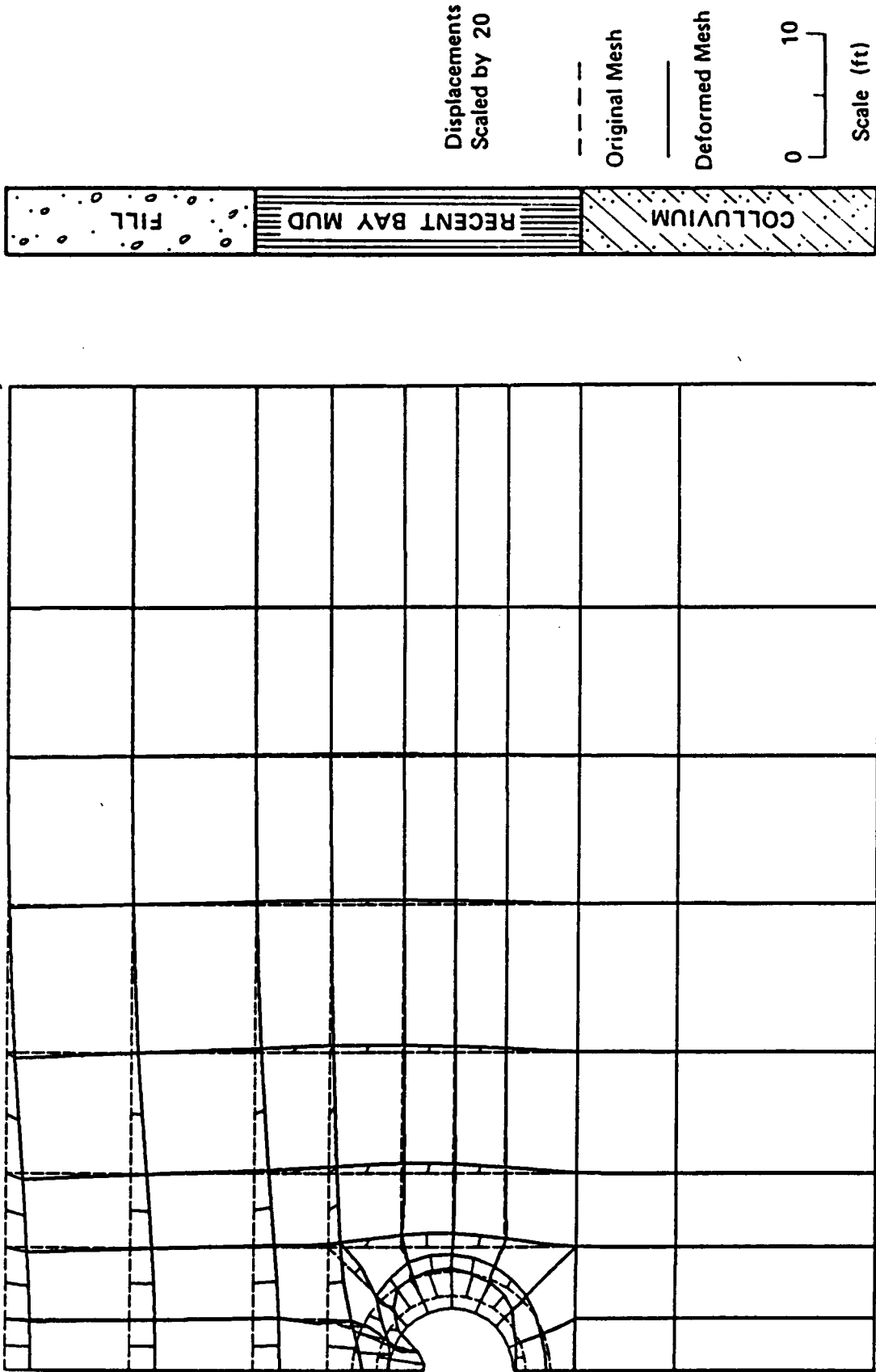


Figure 7.10 Predicted and Observed Shape of Surface Settlement Trough, Line 4



LINE 4

Figure 7.11 Predicted Displacement Field after Consolidation, Line 4

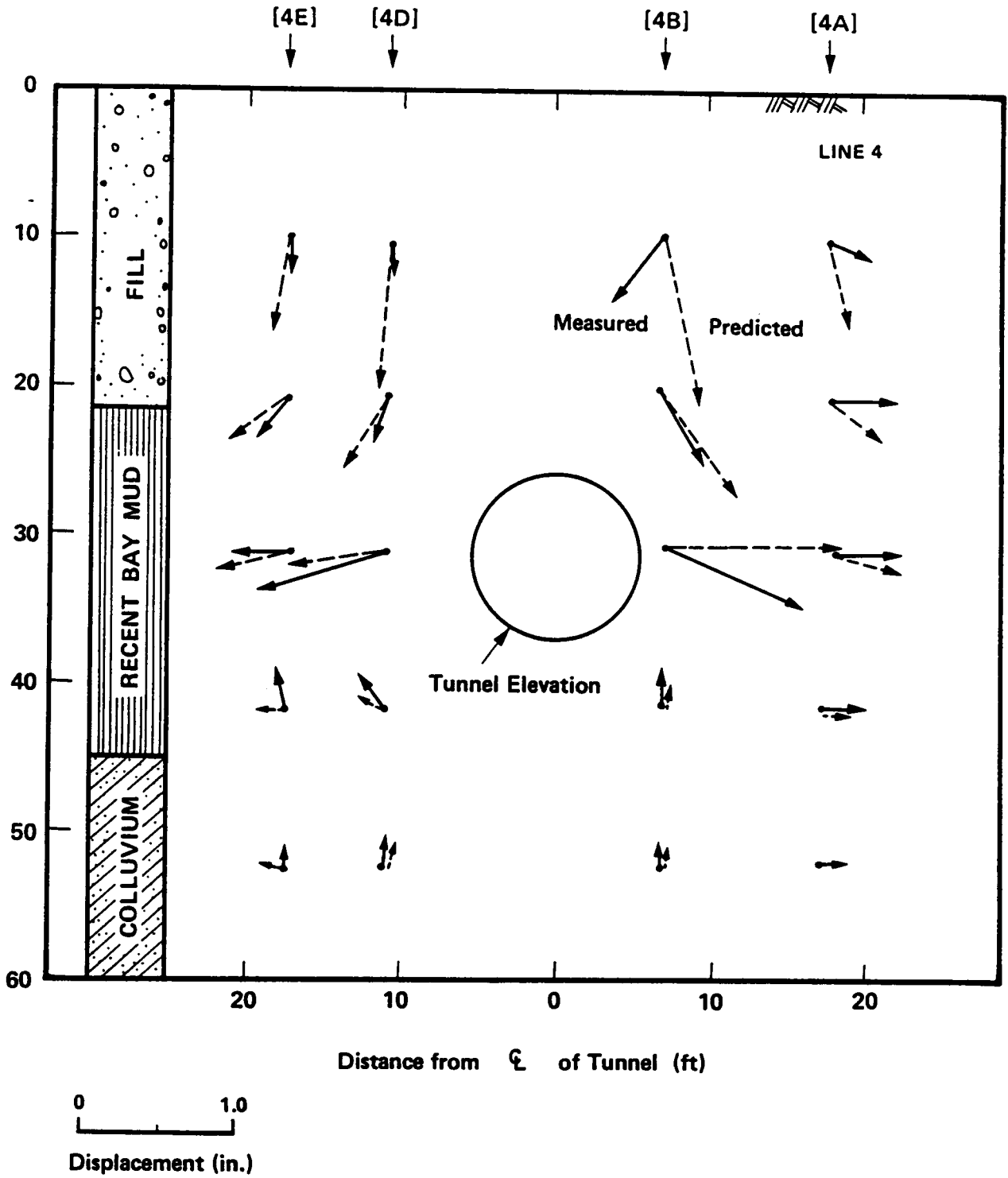


Figure 7.12 Predicted and Observed Displacement Vecotrs after Consolidation, Line 4

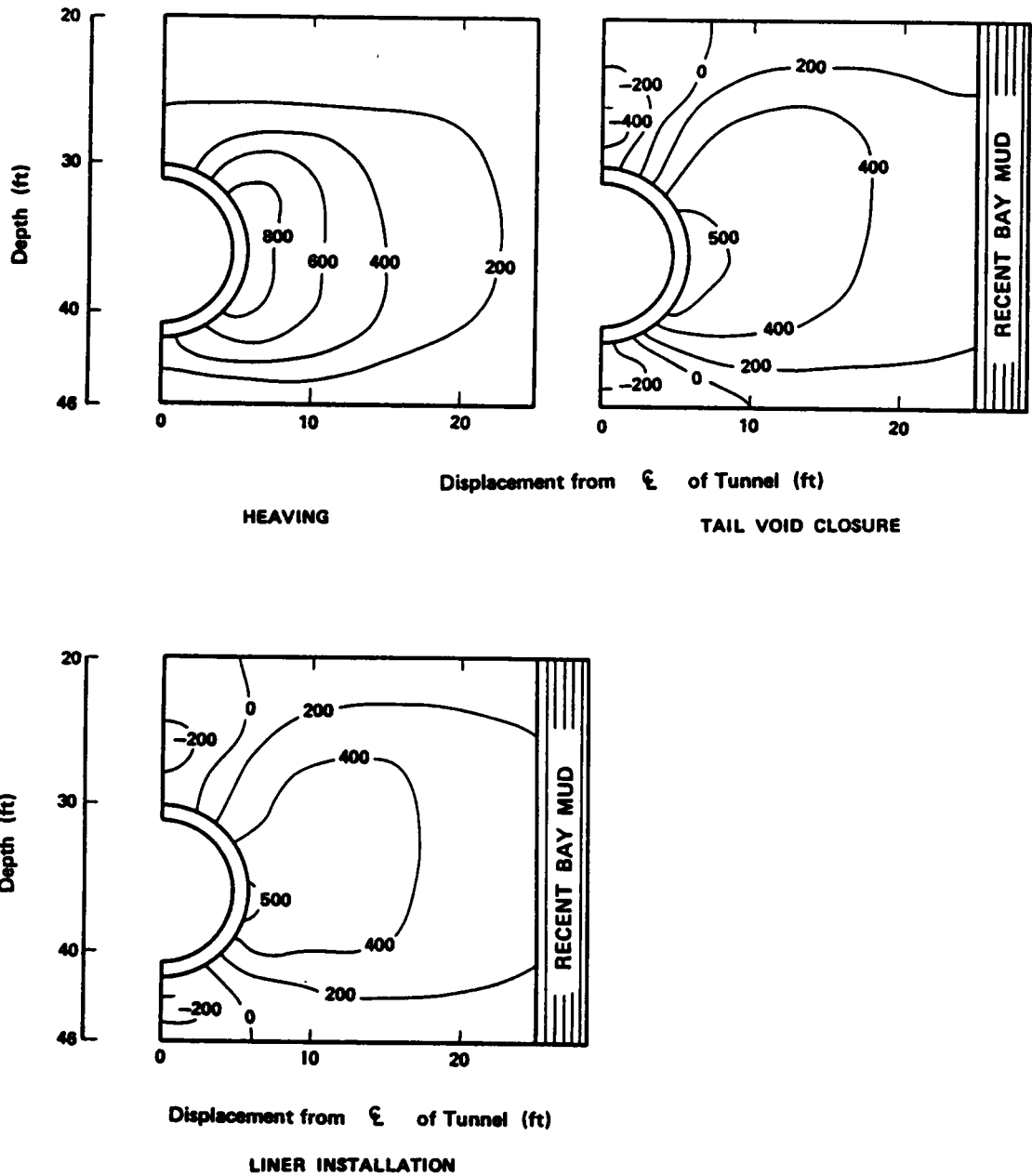


Figure 7.13 Variation of Pore Pressure Development Predicted for Different Loading Stages, Line 4

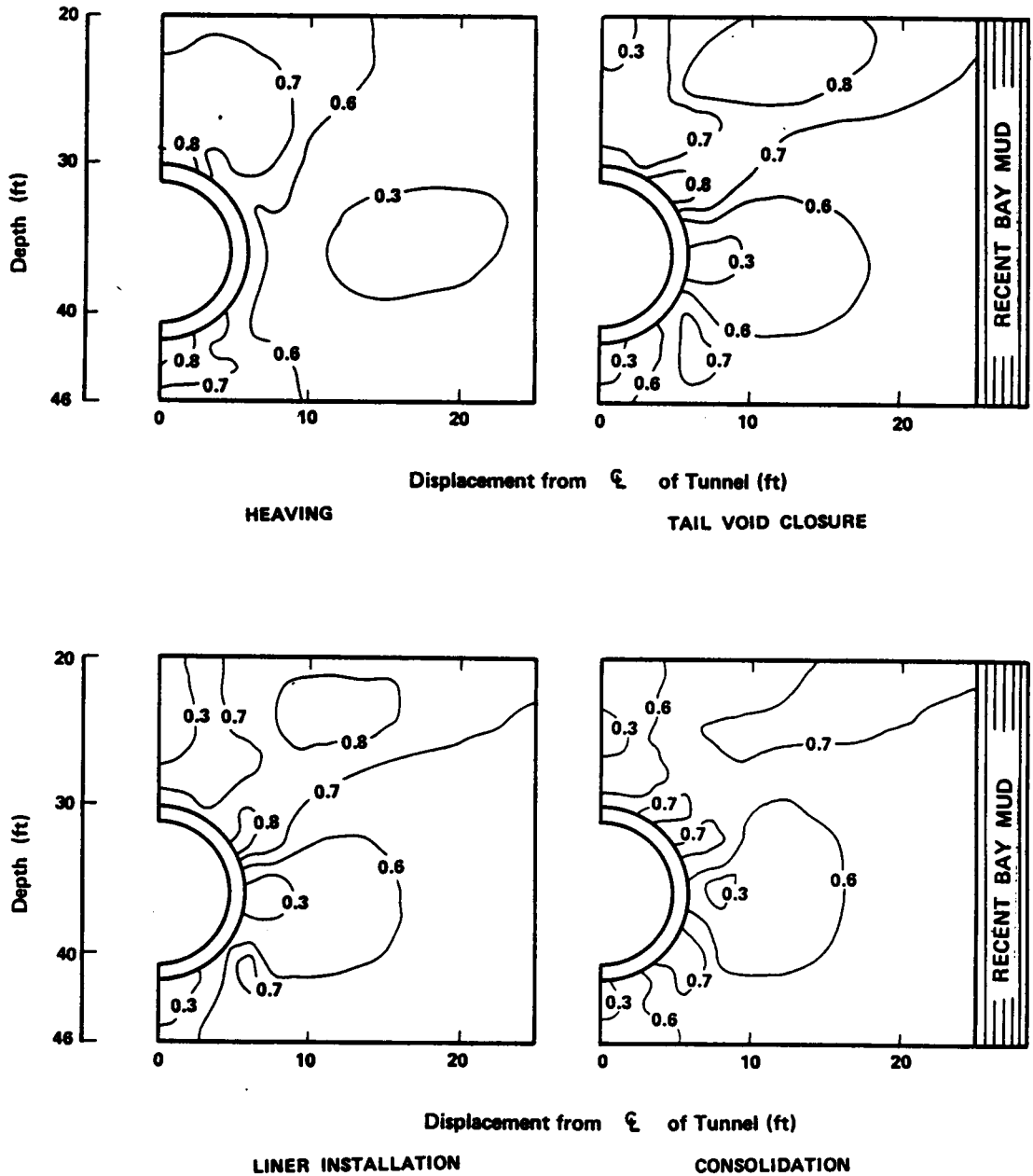


Figure 7.14 Variations of Stress Level Distributions Predicted for Different Loading Stages, Line 4

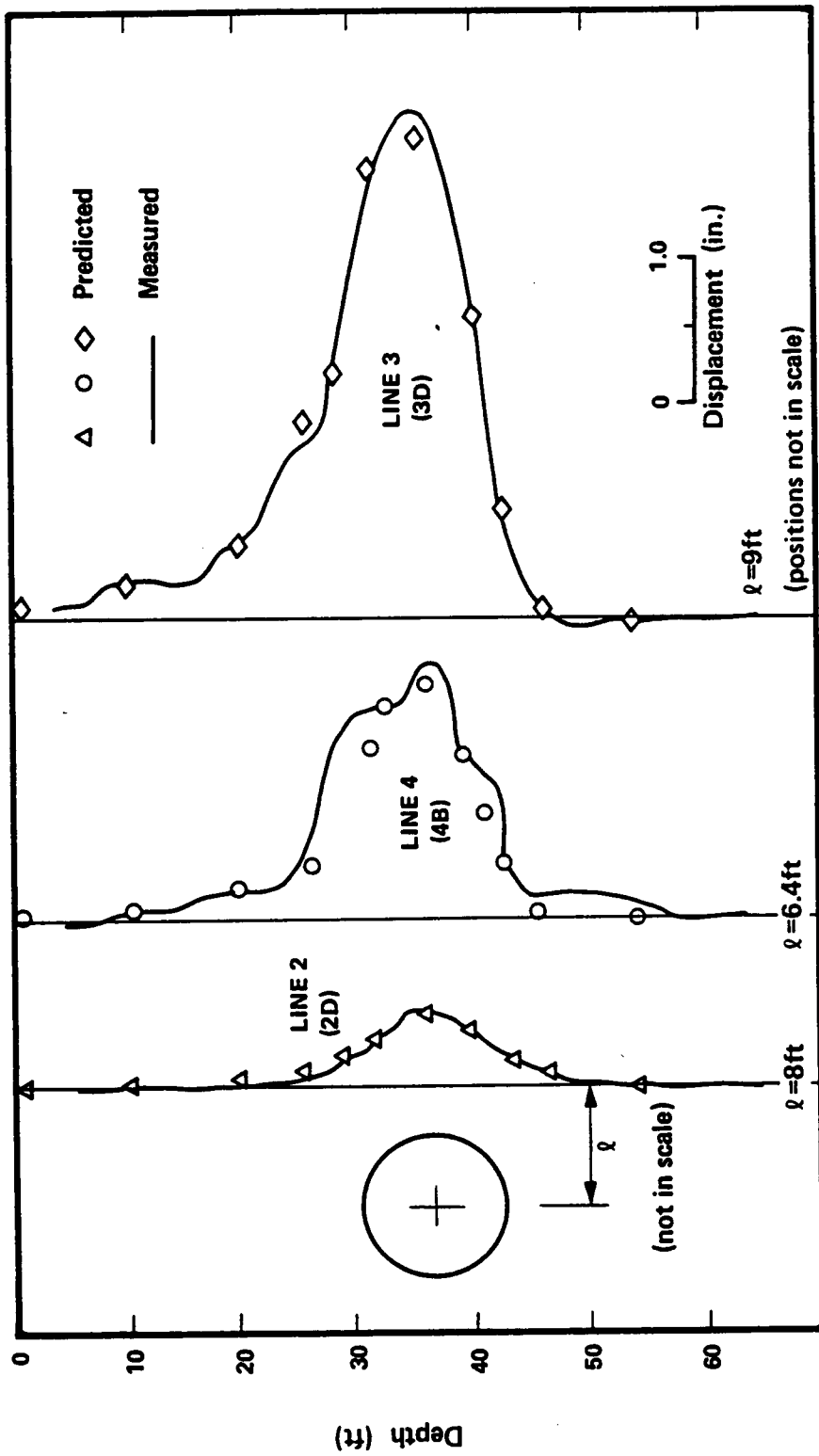


Figure 7.15 Comparison of Lateral Displacements after Heaving between Lines 2, 3 and 4

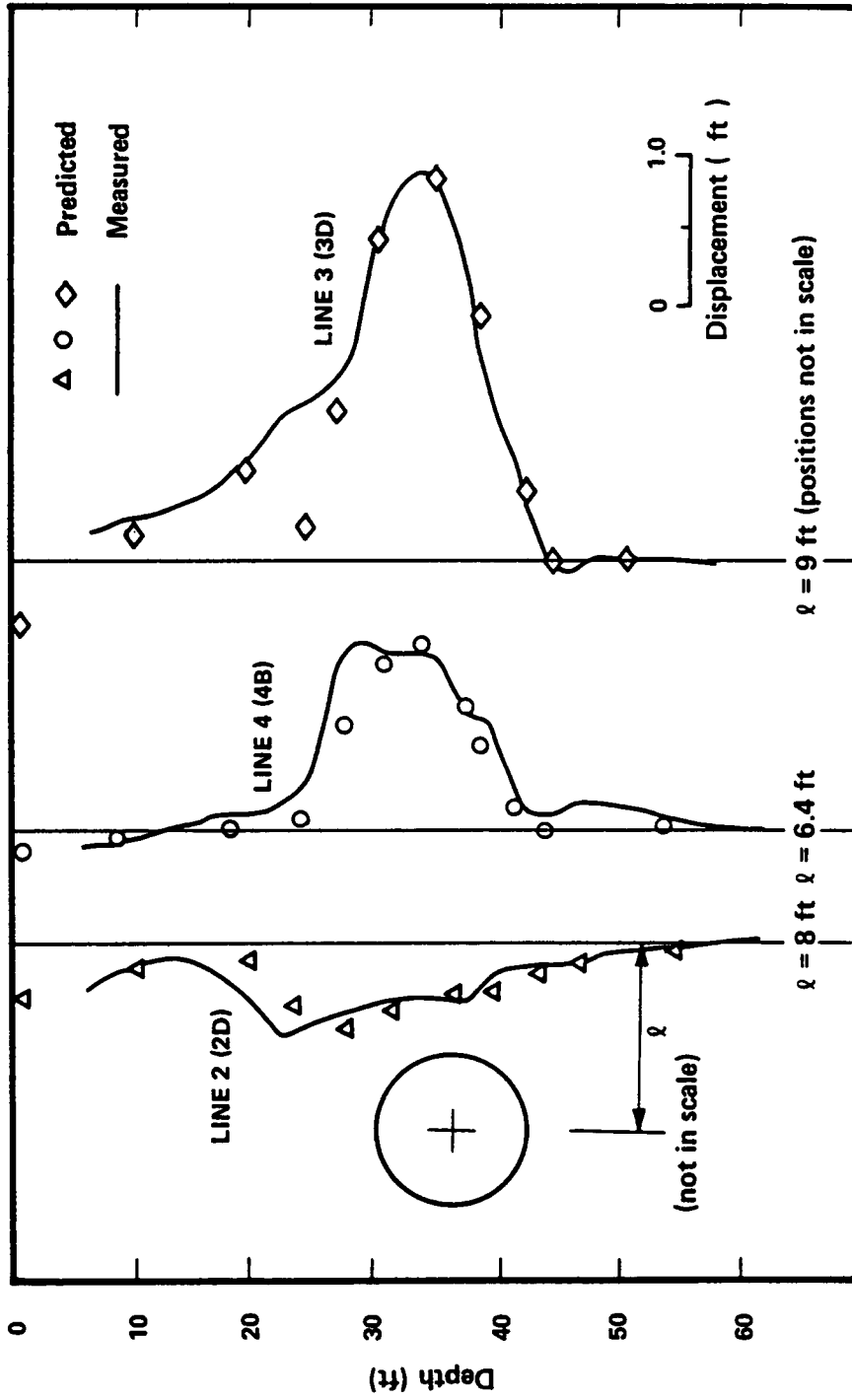


Figure 7.16 Comparison of Lateral Displacements after Tail Void Closure between Lines 2, 3 and 4

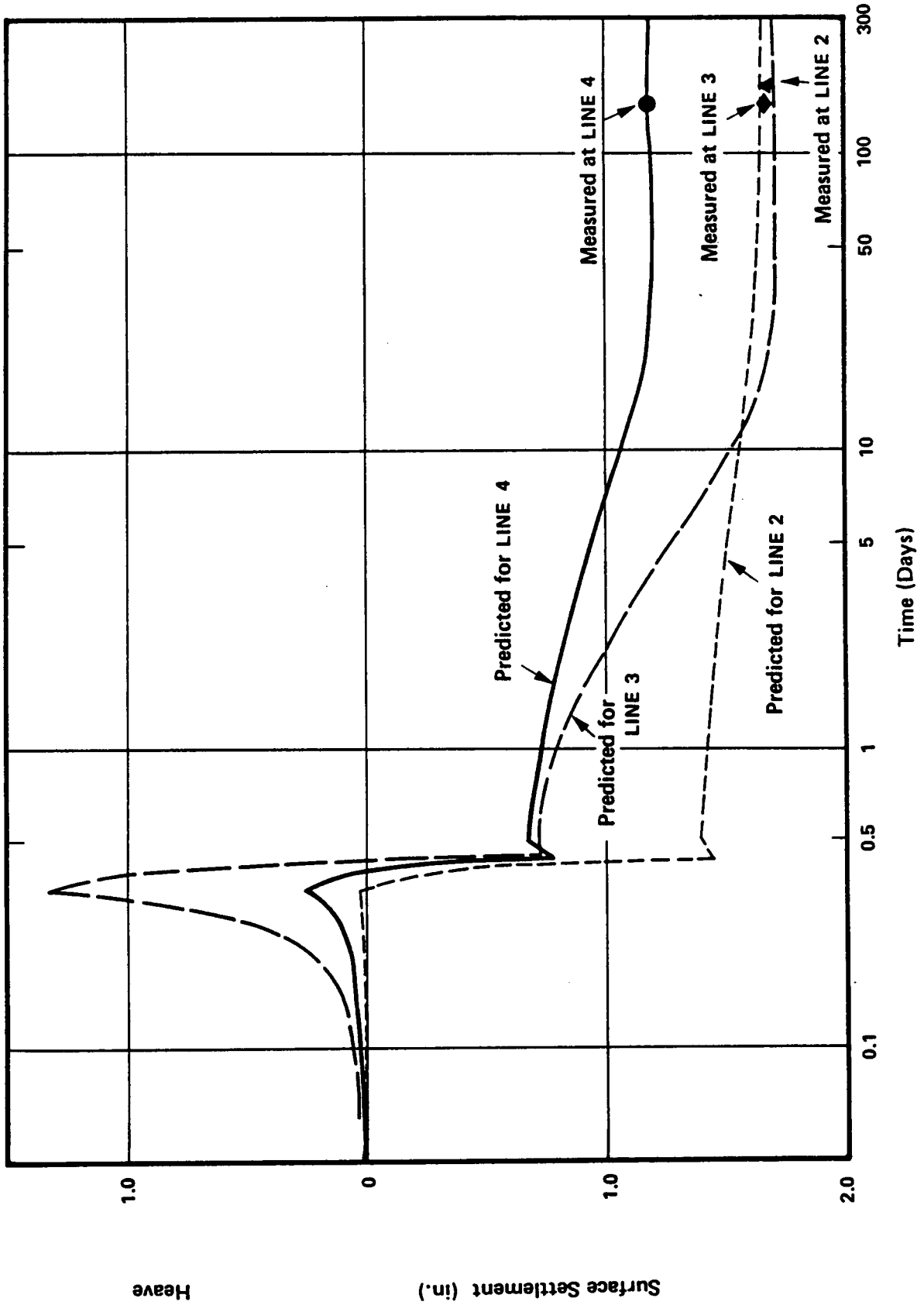


Figure 7.17 Variation of Centerline Surface Settlement for Lines 2, 3 and 4

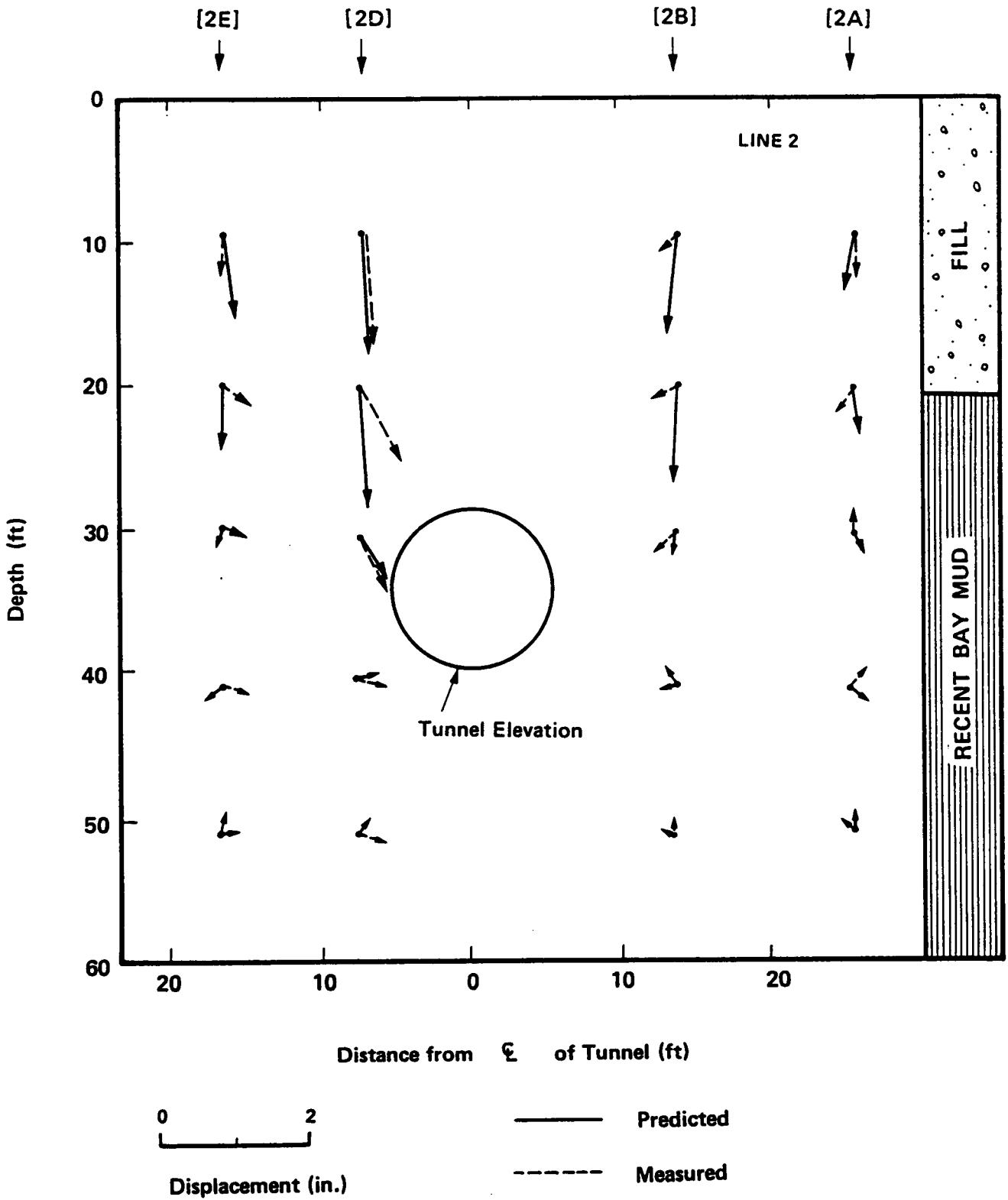


Figure 7.18 Predicted and Observed Displacement Vectors after Consolidation, Line 2

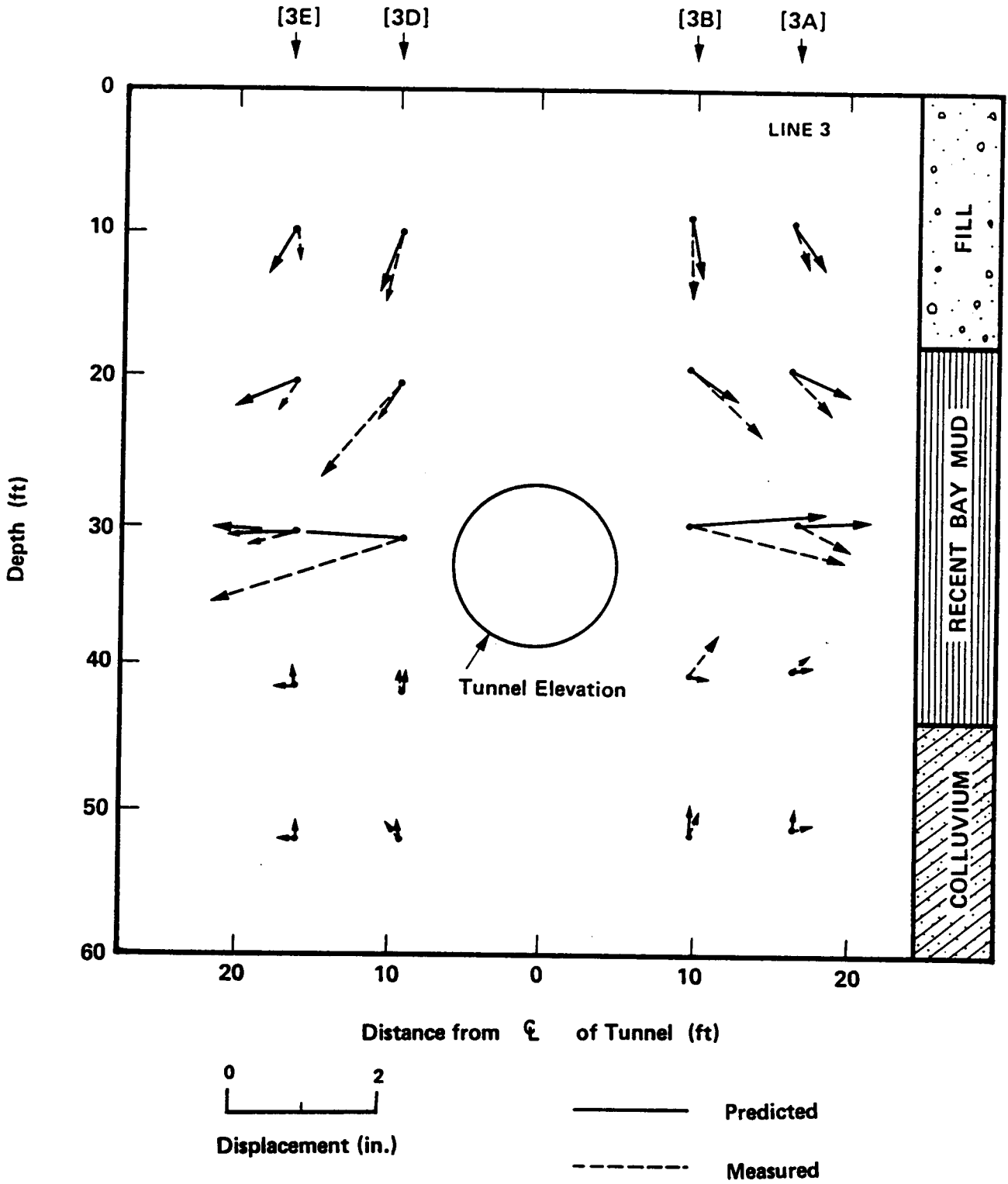


Figure 7.19 Predicted and Observed Displacement Vectors after Consolidation, Line 3

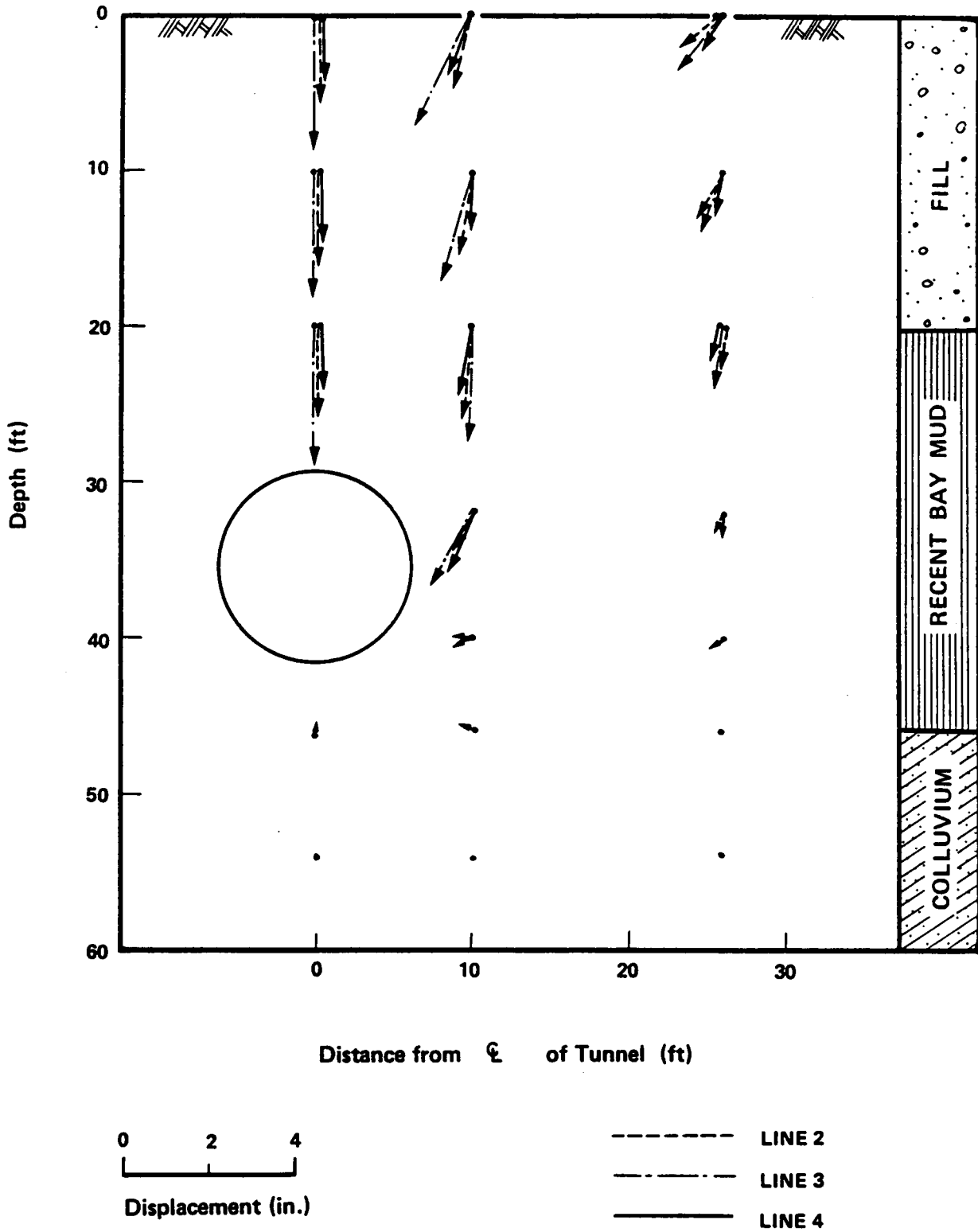


Figure 7.20 Vectors of Predicted Displacements after Consolidation Relative to Heaving Stage, Line 2, 3 and 4

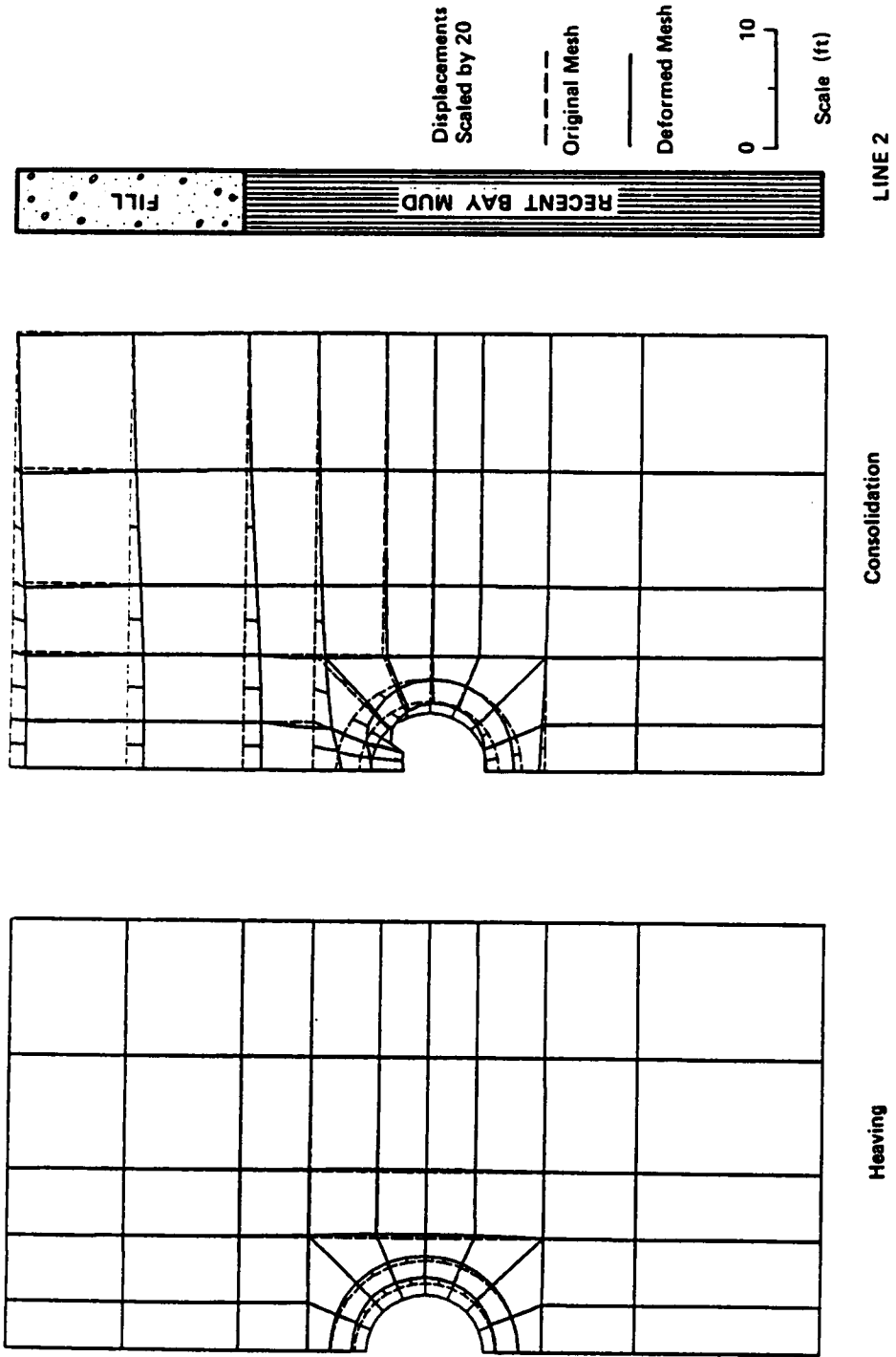


Figure 7.21 Predicted Displacement Fields after Heaving and Consolidation, Line 2

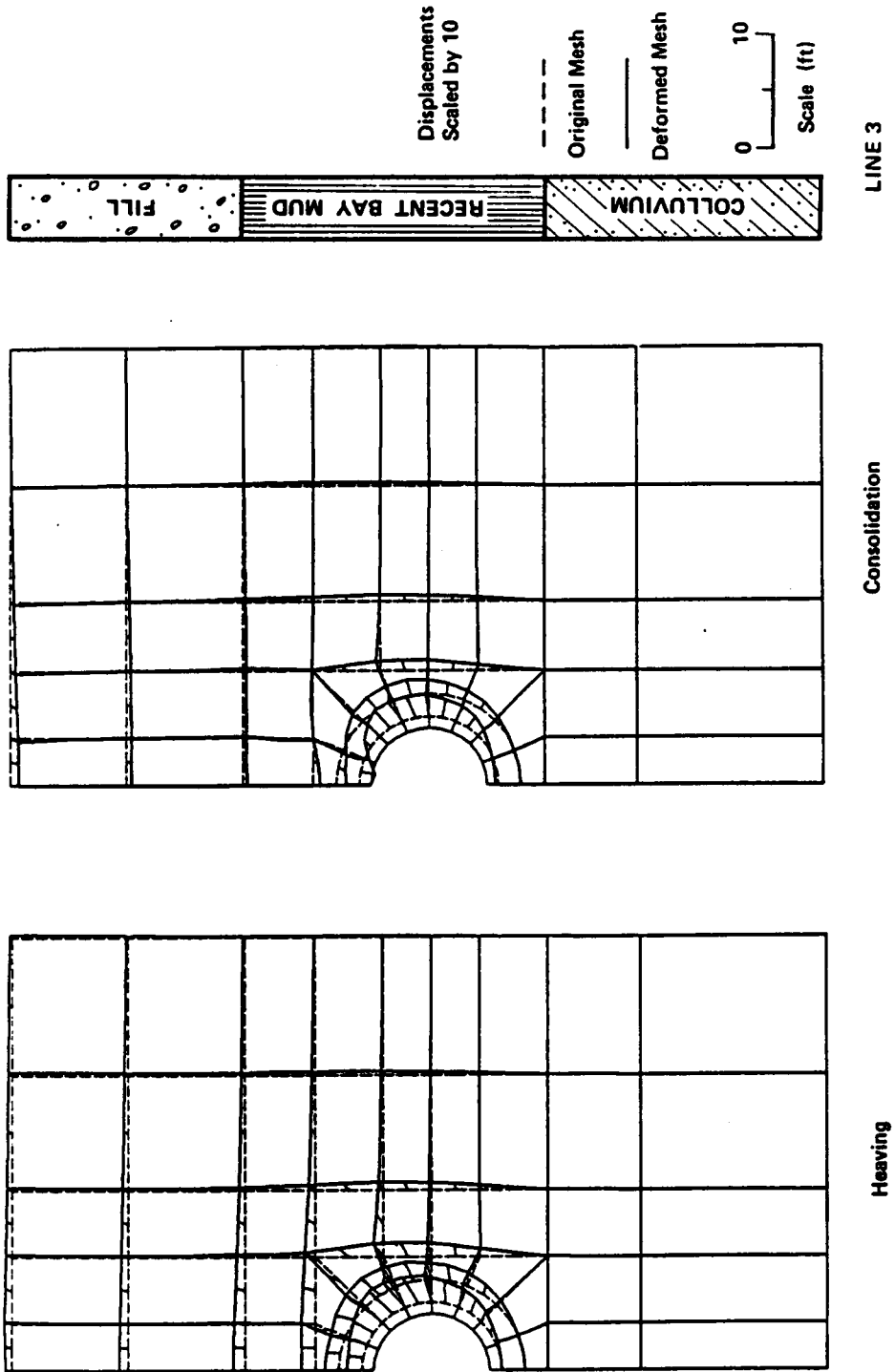


Figure 7.22 Predicted Displacement Fields after Heaving and Consolidation, Line 3

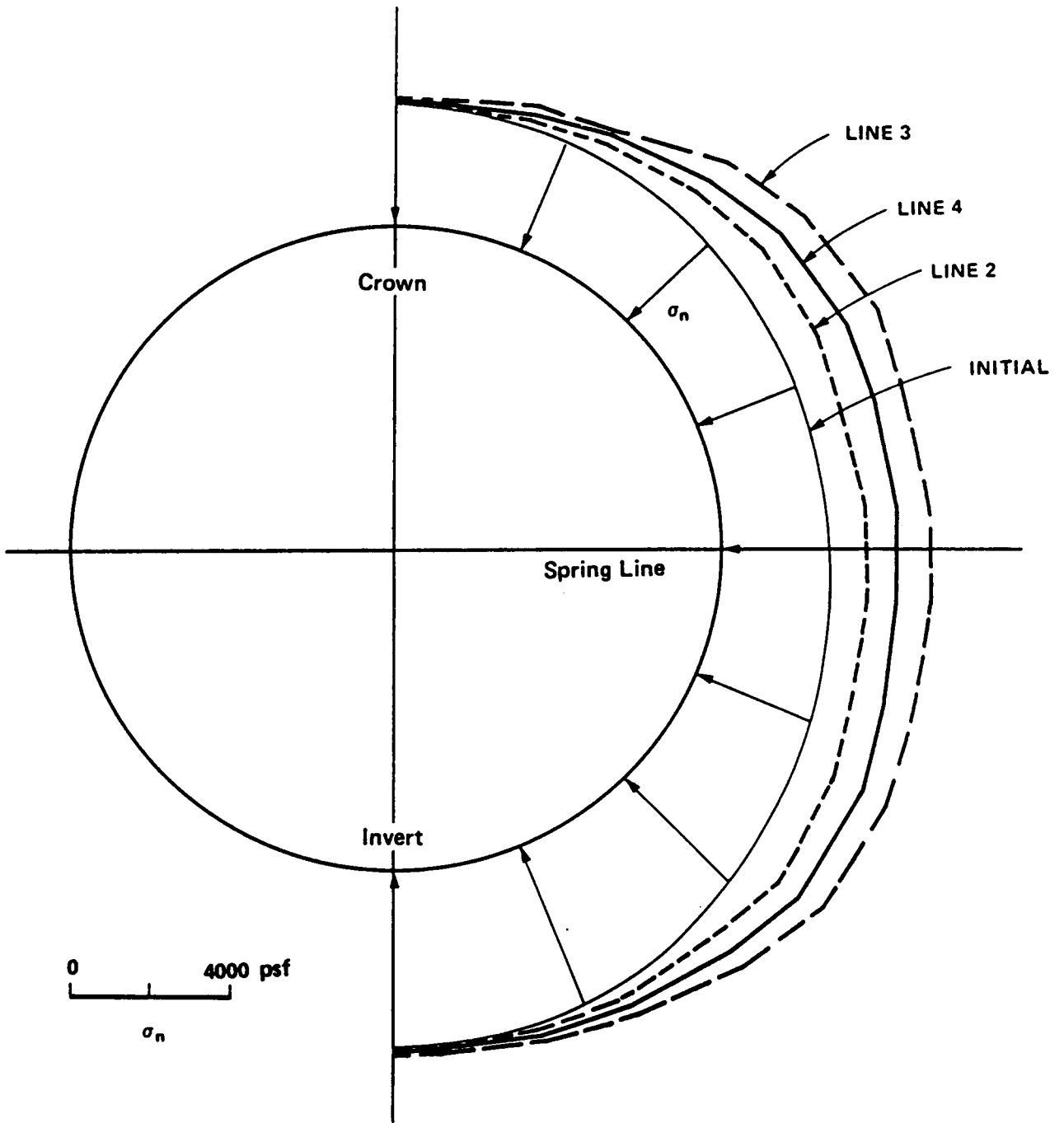


Figure 7.23 Predicted Pressure Distributions Normal to Shield Periphery after Heaving, Lines 2, 3 and 4

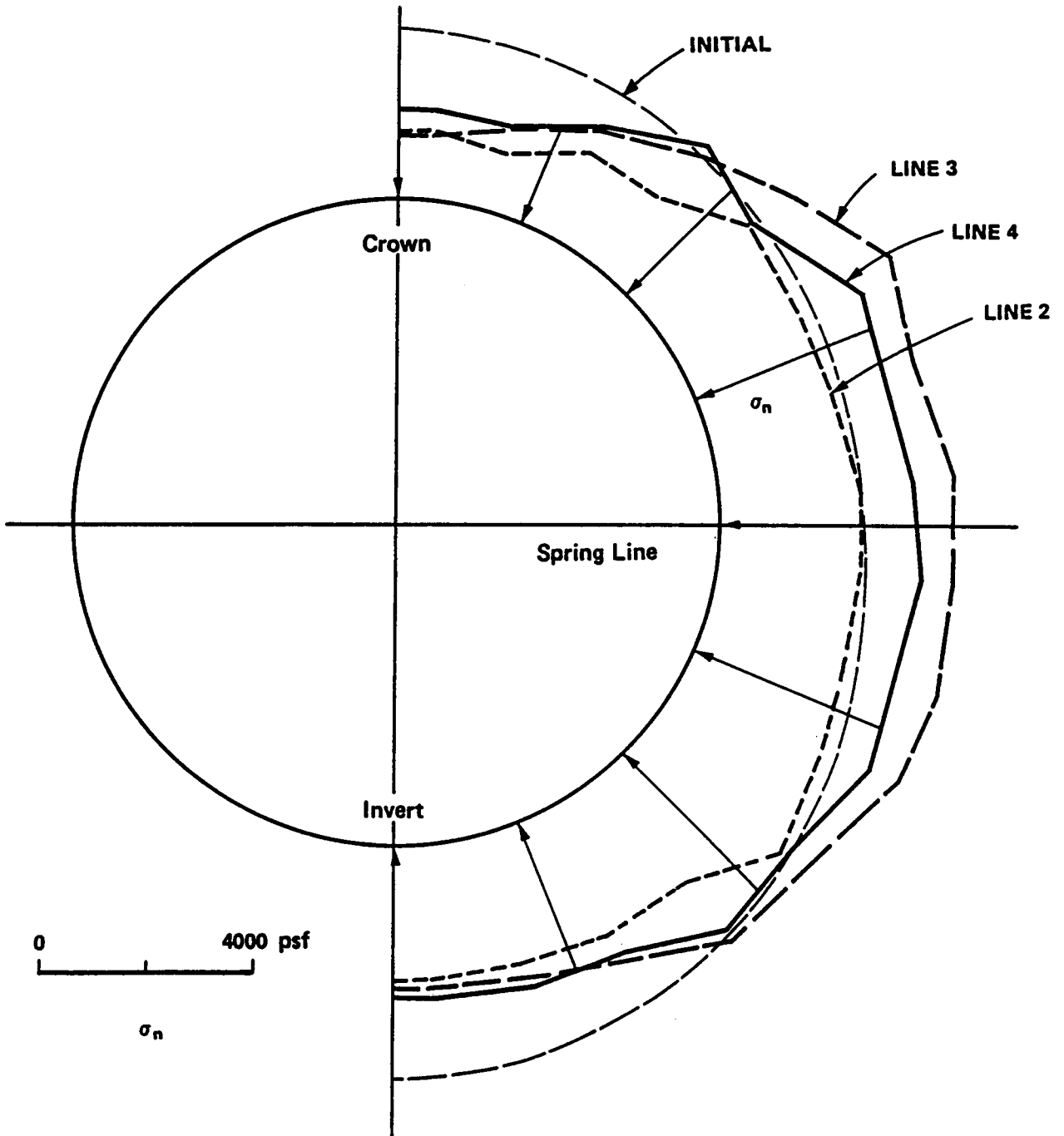


Figure 7.24 Predicted Pressure Distributions Normal to Tunnel Liner at Tail Void Closure, Lines 2, 3 and 4

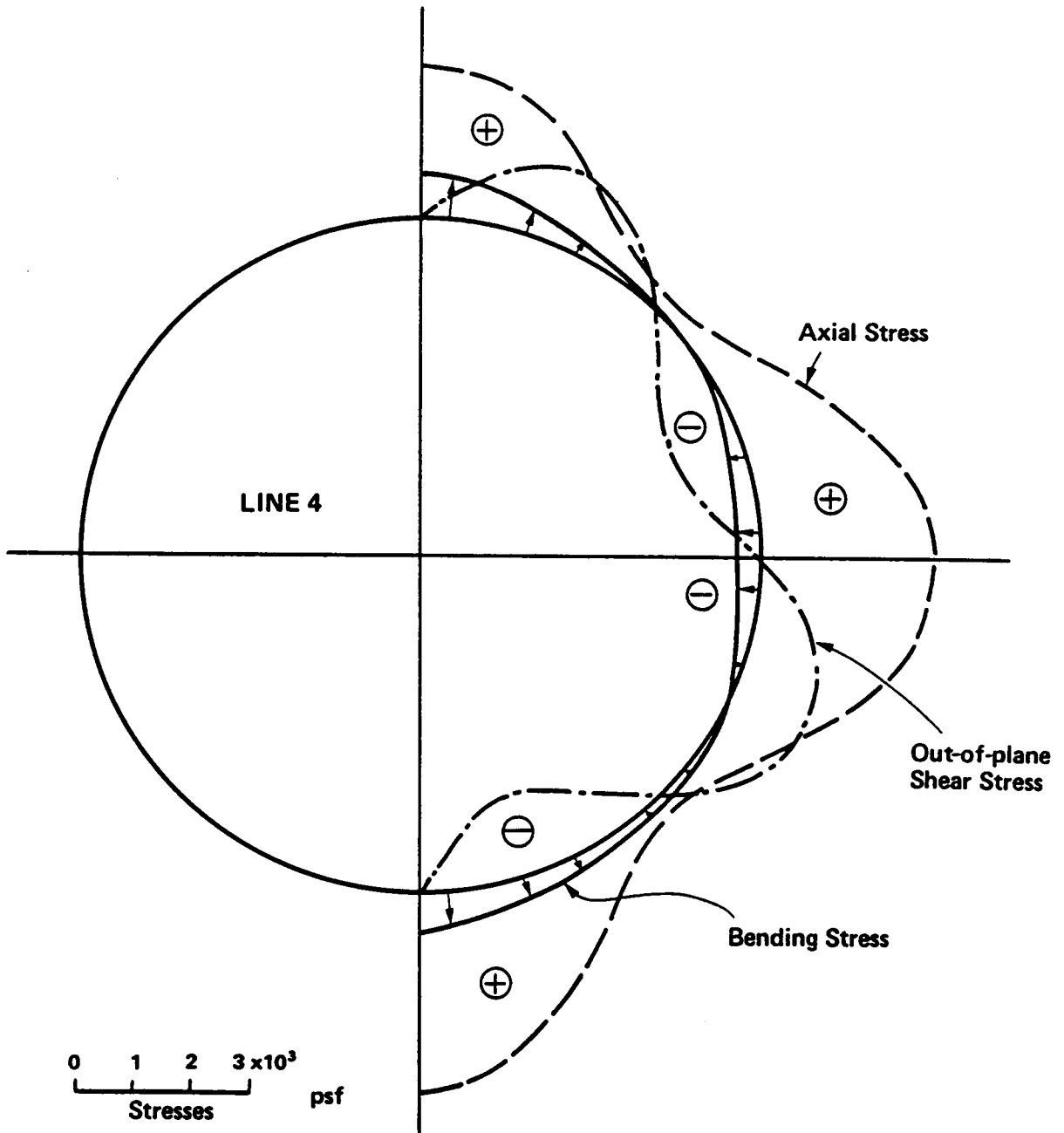


Figure 7.25 Predicted Stress Distributions Induced in Tunnel Liner after Liner Installation, Line 4

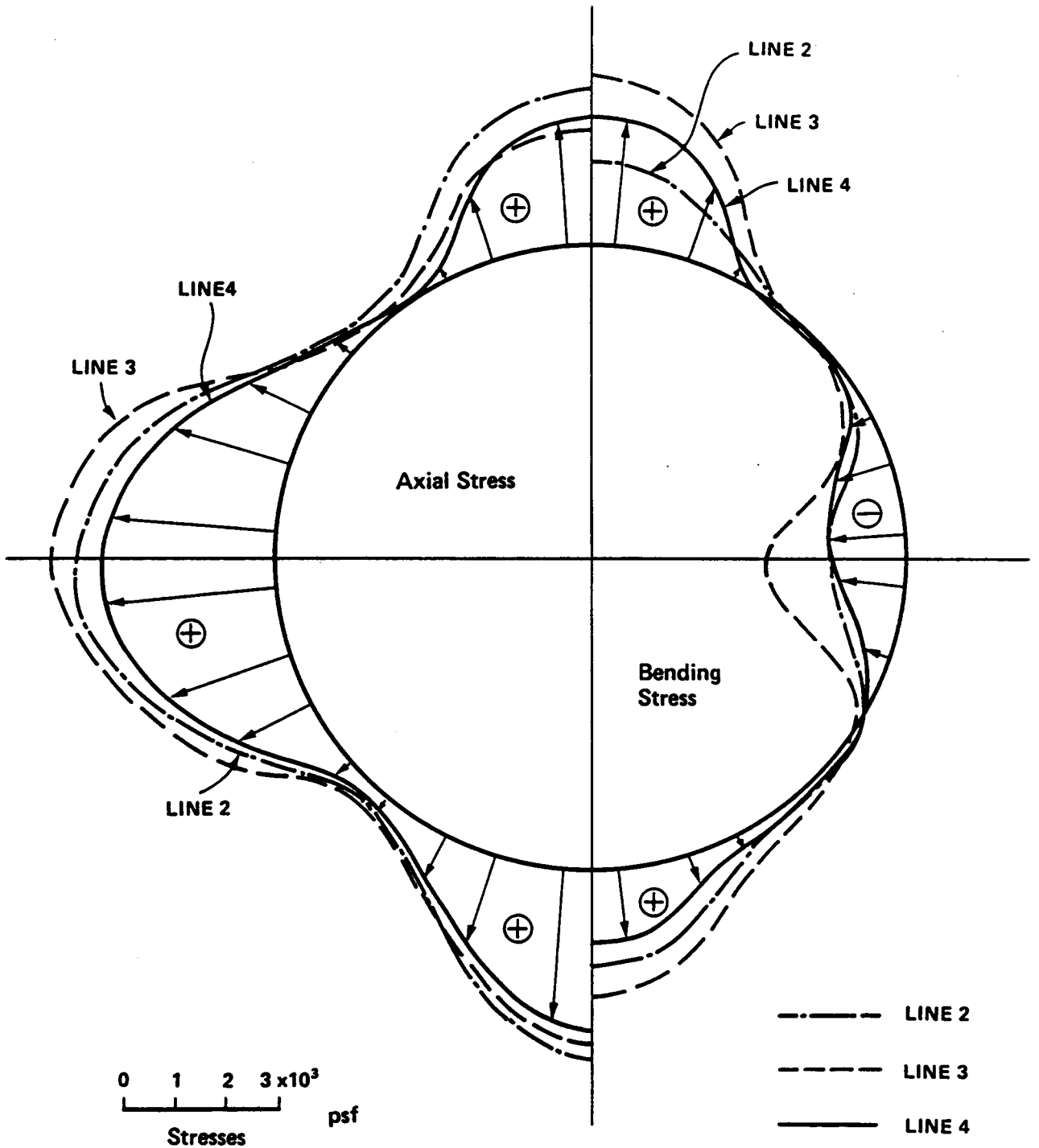


Figure 7.26 Comparisons of Predicted Axial and Bending Stress Distributions after Liner Installation for Lines 2, 3 and 4

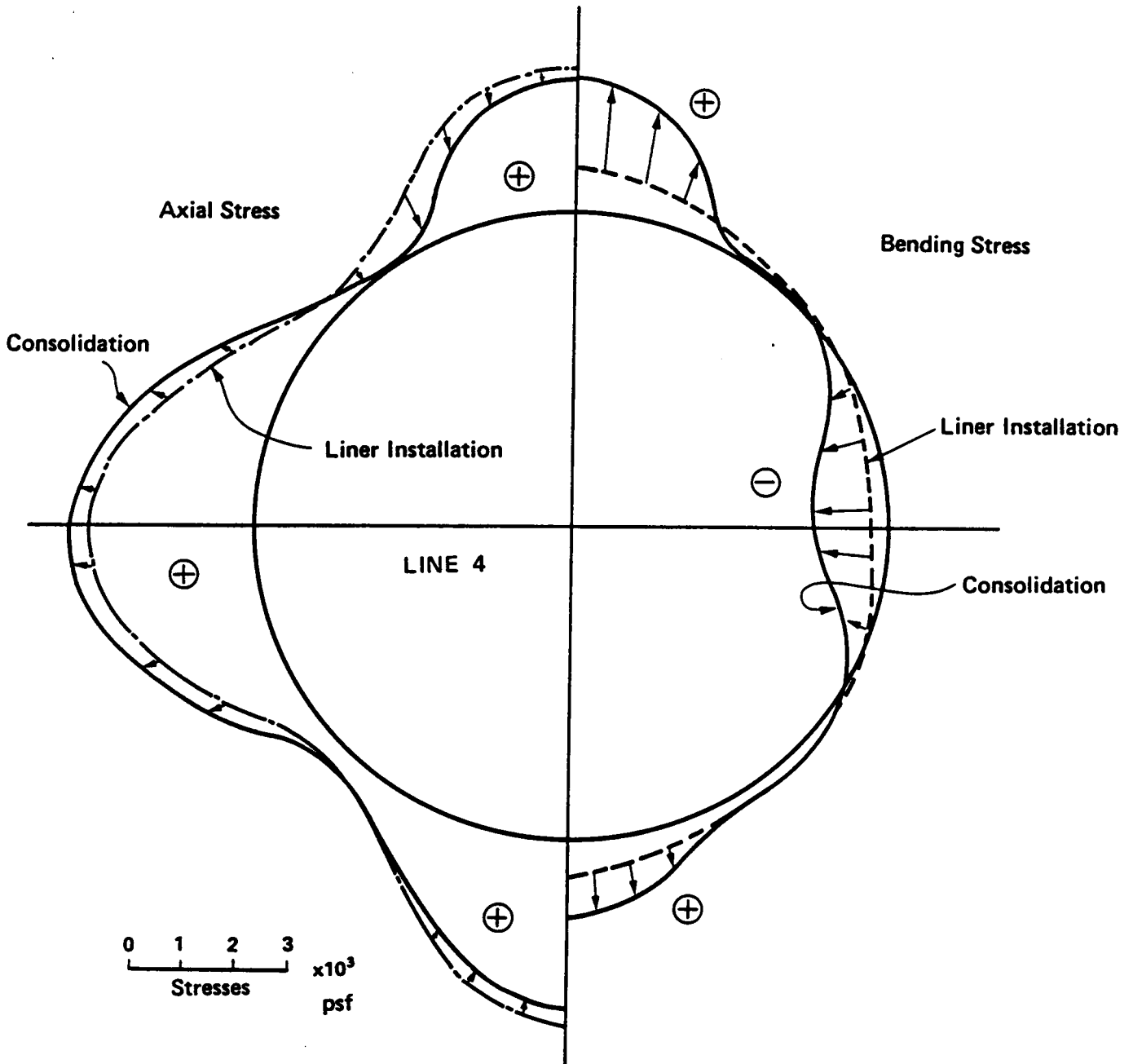


Figure 7.27 Changes in Predicted Axial and Bending Stress Distributions during Consolidation of Ground, Line 4

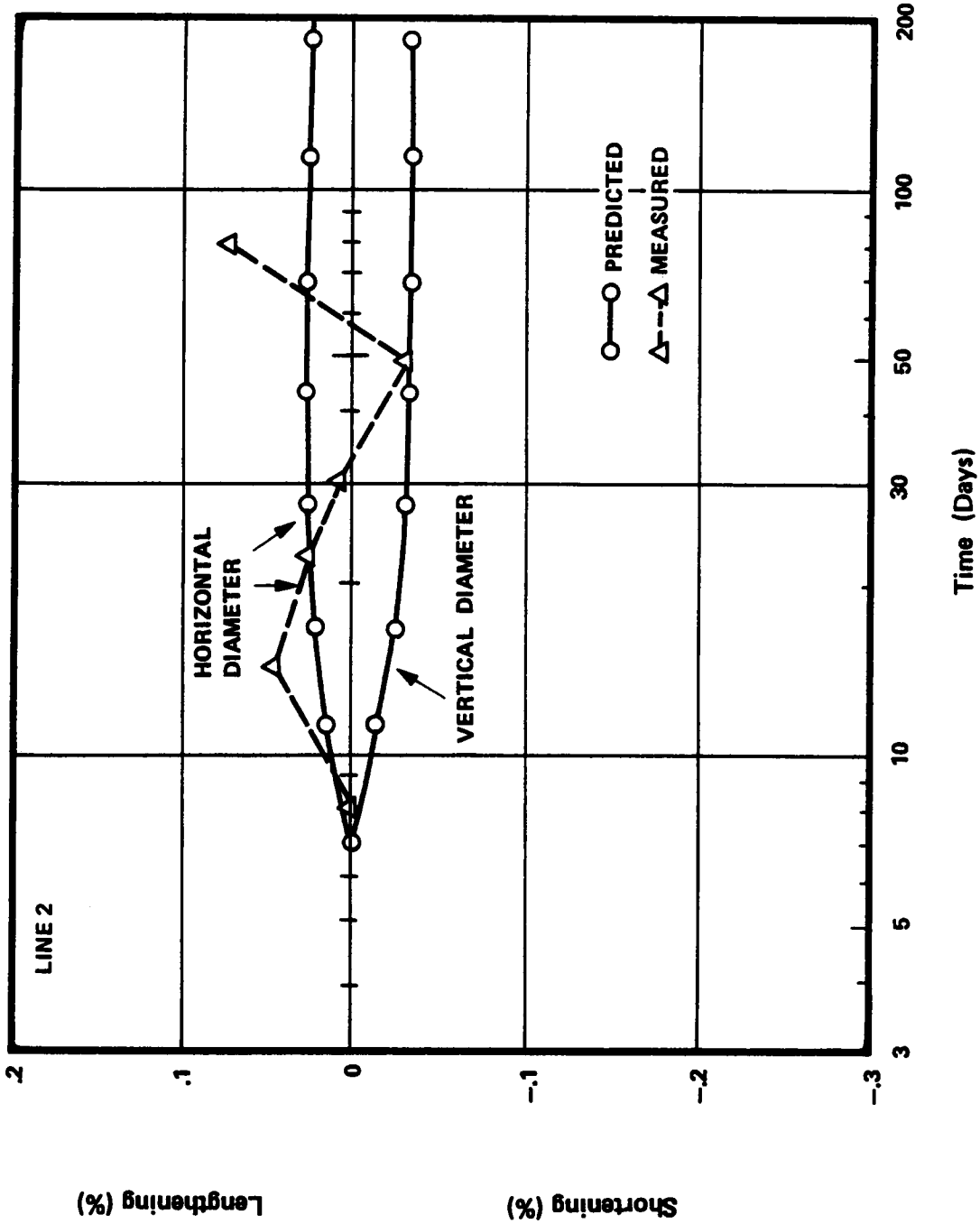


Figure 7.28 Predicted and Observed Liner Diameter Changes, Line 2

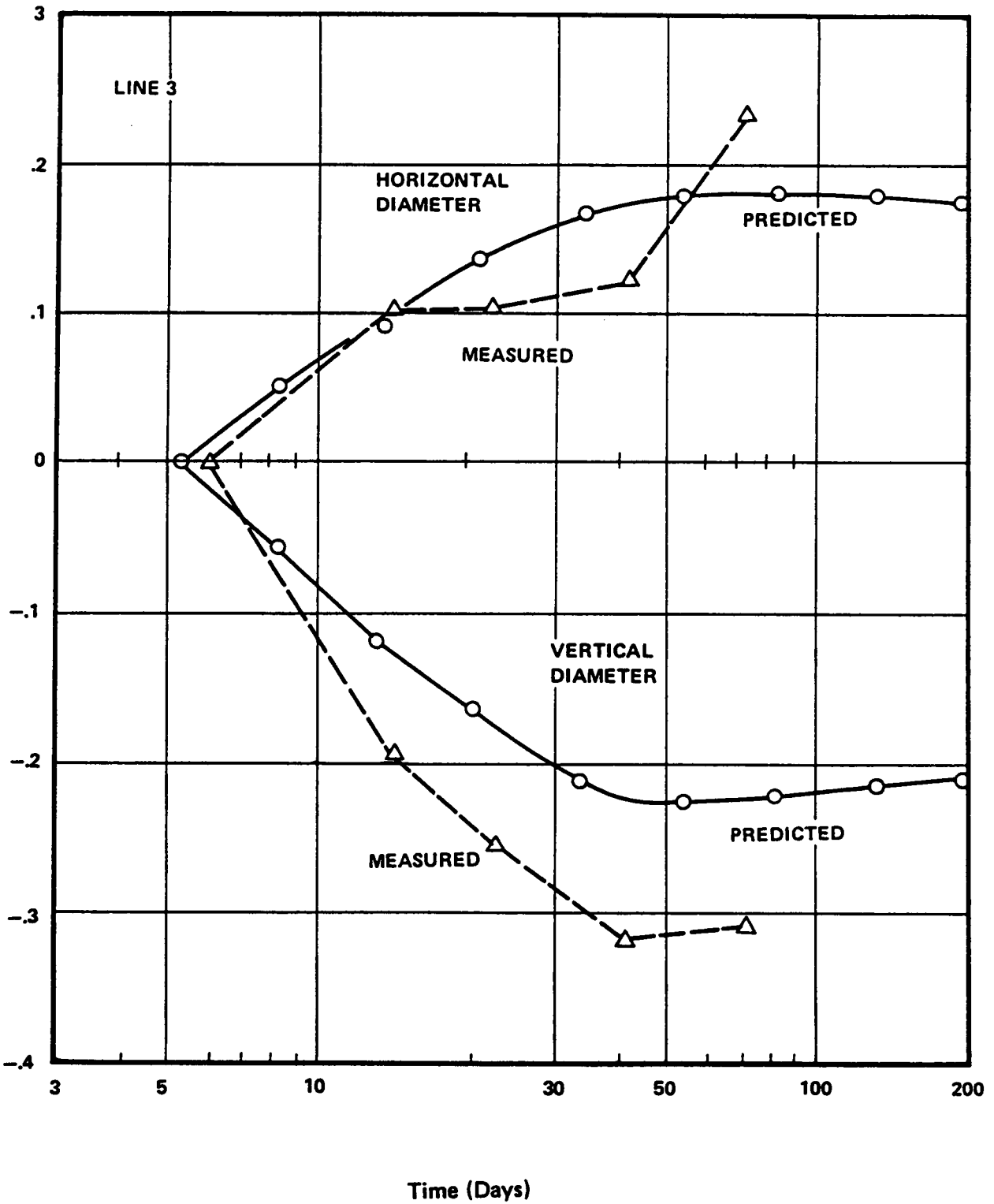


Figure 7.29 Predicted and Observed Liner Diameter Changes, Line 3

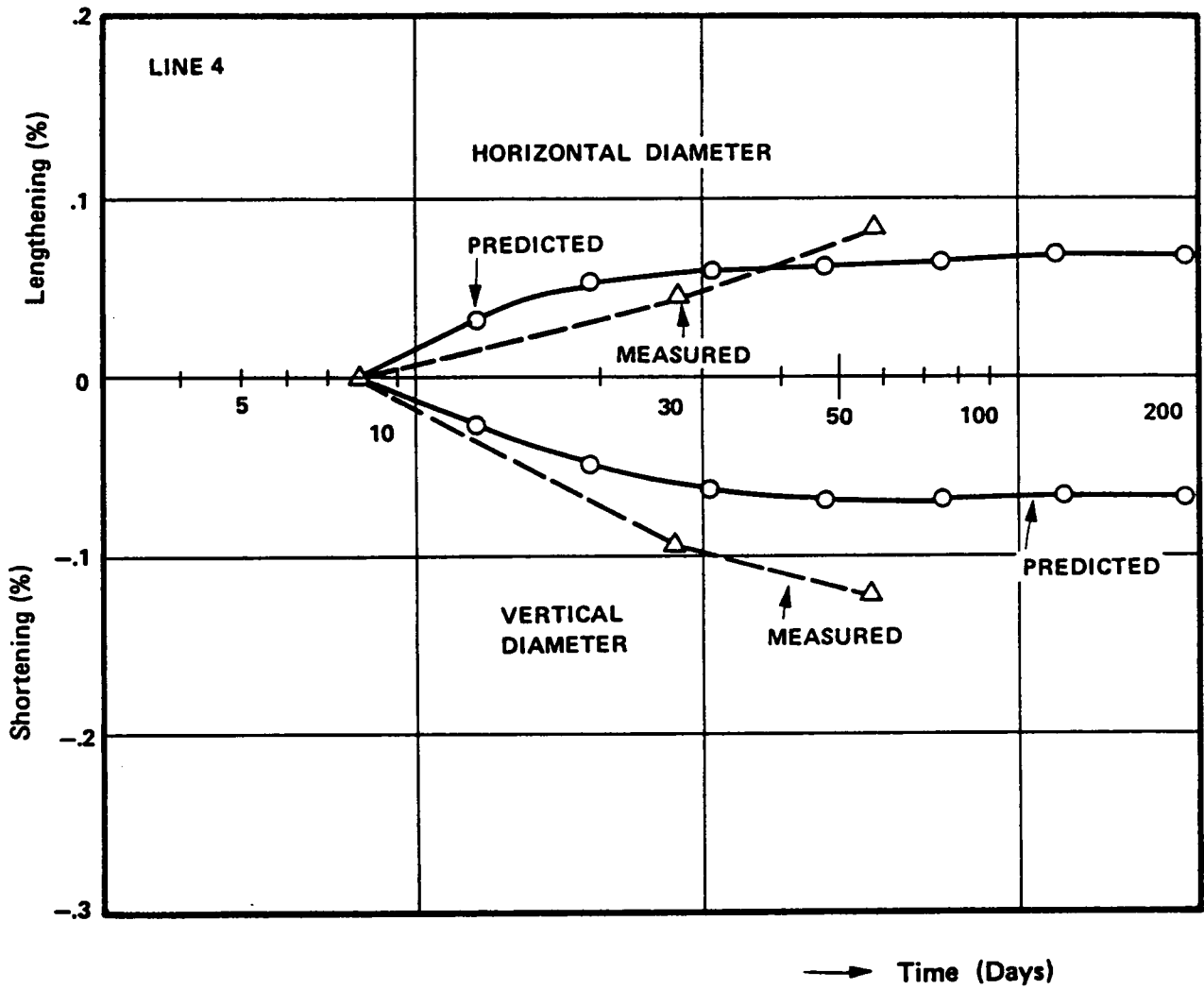


Figure 7.30 Predicted and Observed Liner Diameter Changes, Line 4

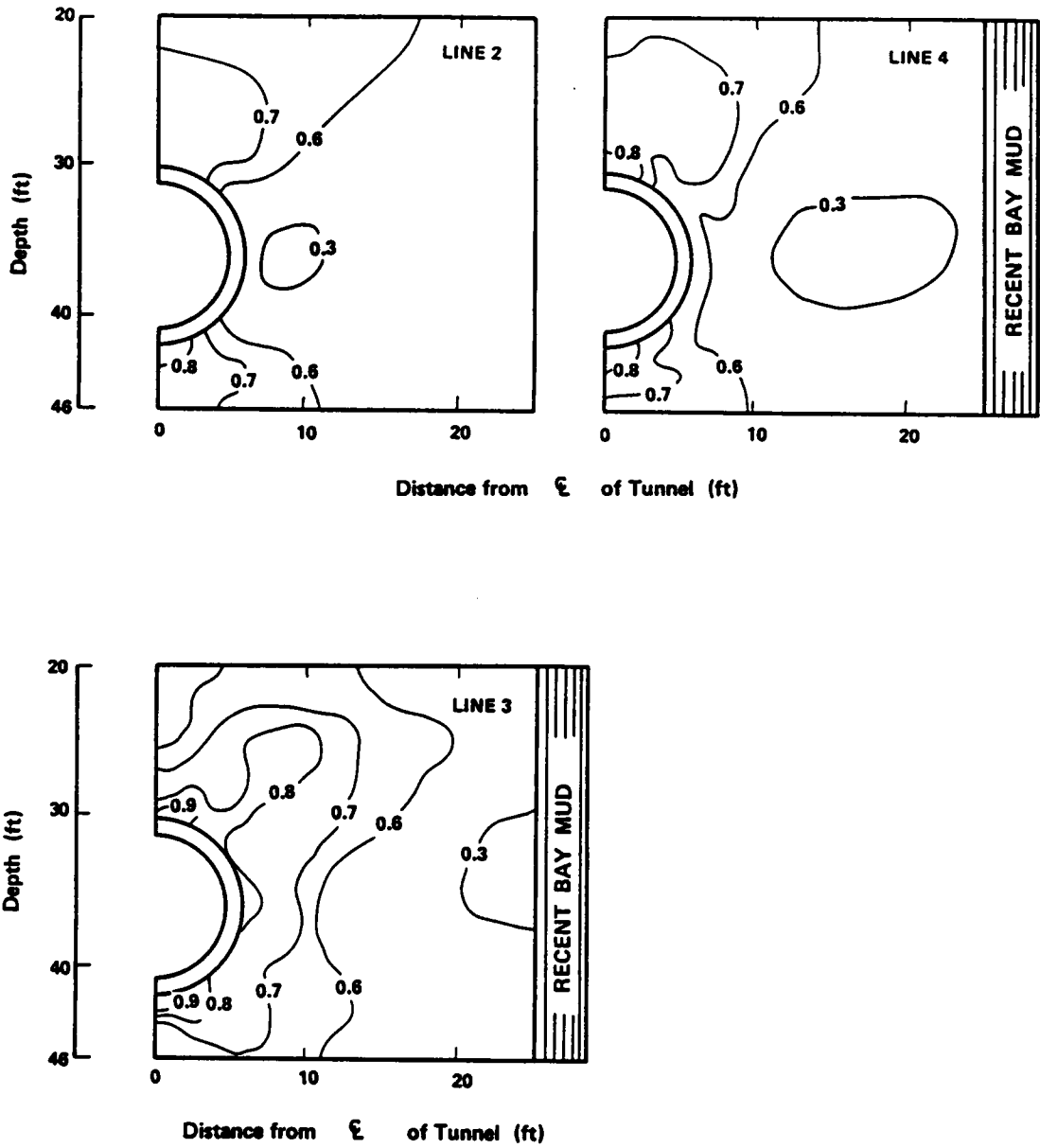


Figure 7.31 Contour of Stress Levels after Heaving, Lines 2, 3 and 4

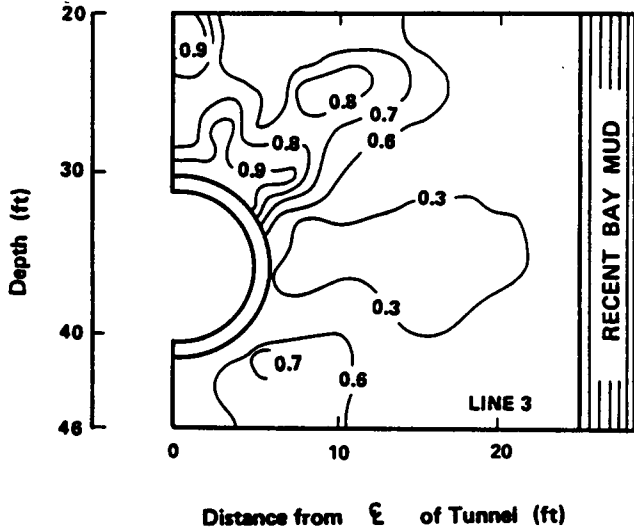
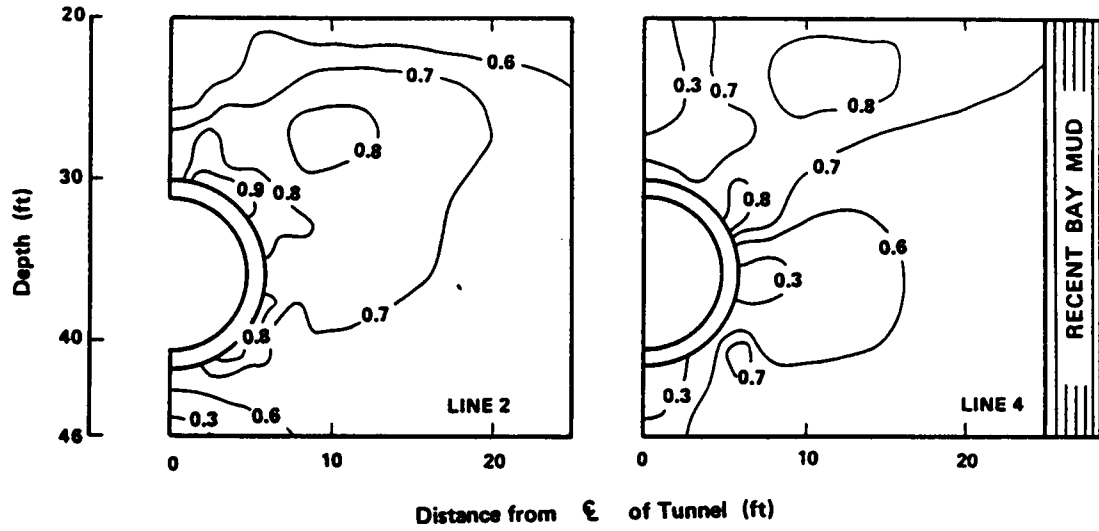


Figure 7.32 Contour of Stress Levels after Liner Installation, Lines 2, 3 and 4

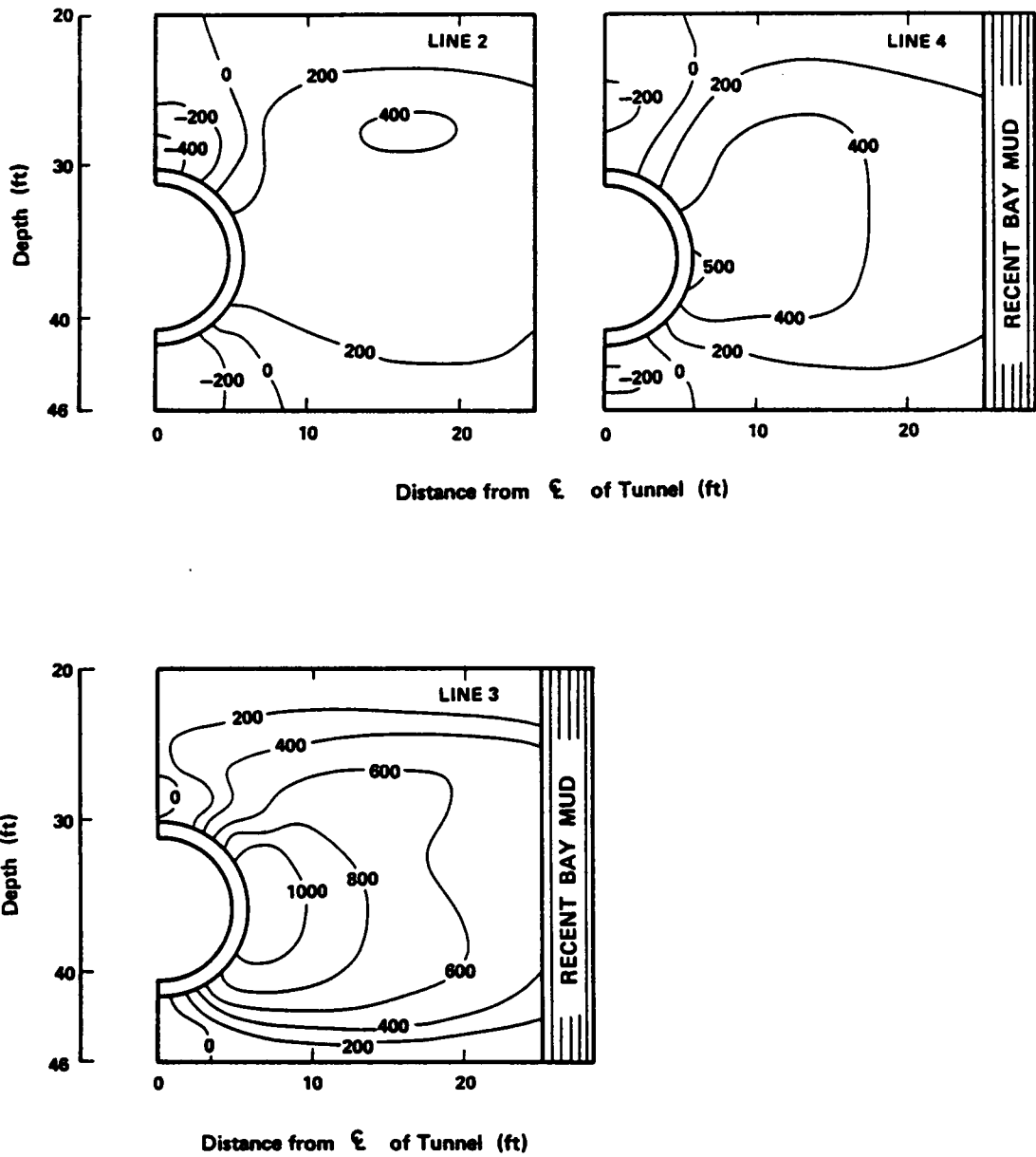
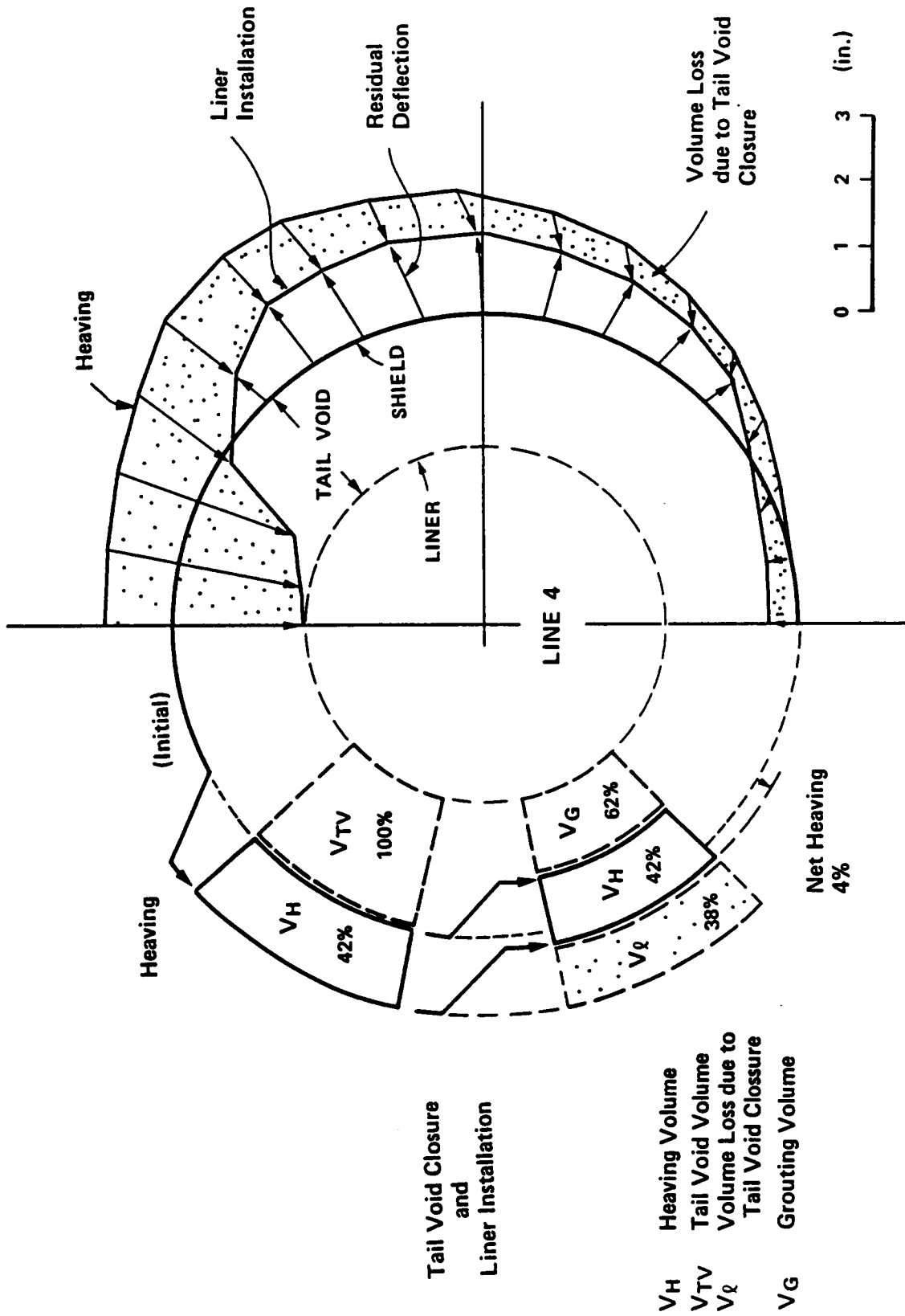


Figure 7.33 Excess Pore Pressure Development after Liner Installation, Lines 2, 3 and 4 (psf)



Displacements

Volume Compensation

Figure 7.34 Soil Volume Balance around Shield, Line 4

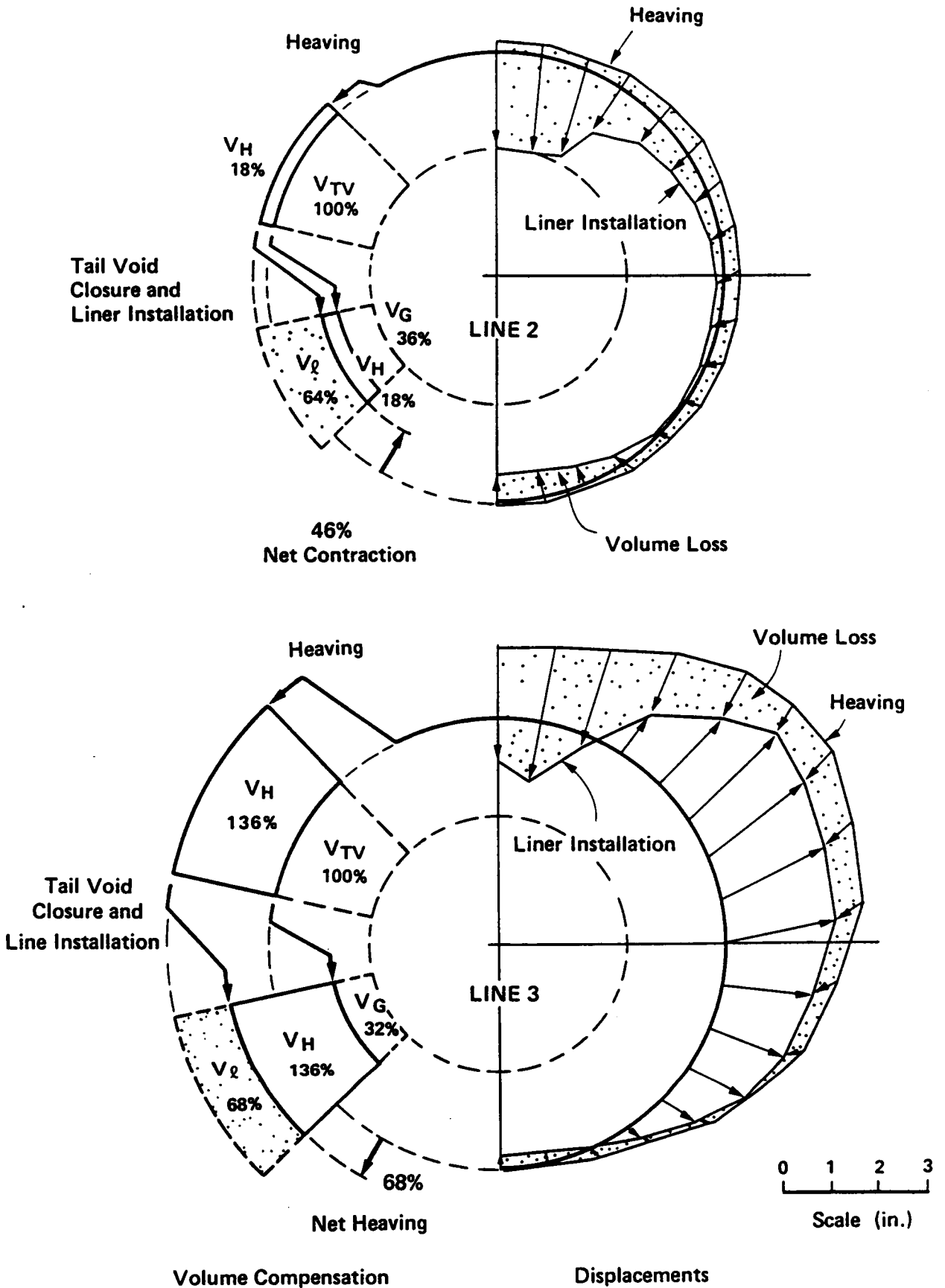


Figure 7.35 Soil Volume Balance around Shield, Lines 2 and 3

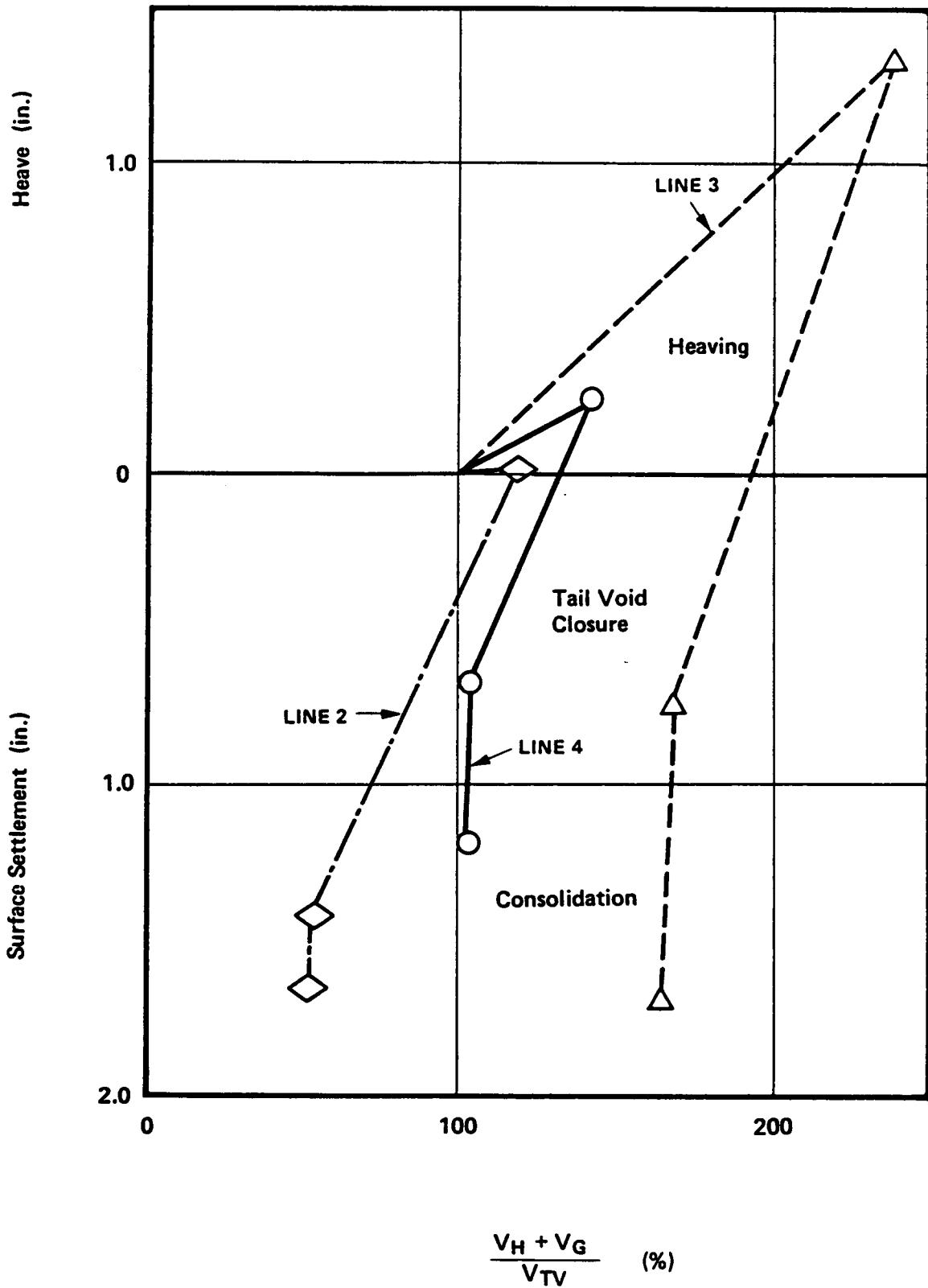


Figure 7.36 Relation between Surface Movements and Reference Soil Volume about Shield

## Chapter 8

### PARAMETRIC STUDIES OF EPB SHIELD TUNNELING

#### 8.1 Introduction

The findings presented in the last chapter suggest the importance of initial heaving and volume loss upon tail void closure. This chapter is concerned with quantifying the relative effects of the initial heaving and the backfilling of the tail void.

##### 8.1.1 Objectives

The heaving effect is considered as one of the most advantageous aspects of the advanced shield. It is not known, however, how much of the heaving level should be applied when the shield machine is operated. It can easily be imagined that applying too much heaving might bring adverse effects on tunneling performance. On the other hand, full release of stresses at the face will result in ground movements similar to those caused by the open-faced conventional shield. In between these extremes an optimum level of heaving should be present. To examine this, a series of parametric studies are carried out.

Another important factor in the ground movements, the tail void closure, is also examined from the point of view of the volume loss upon tail void closure. The actual mechanism of the tail void closure is complex and linked in practice with the soil stand-up time and the procedures and promptness of grouting. However, this is quantified in the analyses as an

unloading process limited by a certain volume loss which is influenced by the grout volume.

Figure 8.1 explains the volumetric consideration of soil movements for construction stages of the advanced shield tunneling analysis. As is discussed in the last chapter, volume of soil  $V_H$  is supplied from the front of and to the side of the shield face during heaving. As the tail void begins to impact the situation, the soils move into the void, subtracting from the heaving volume an amount of volume loss  $V_\ell$ . The soils of volume  $V_H$  may not change the volume during the process of tail void closure as shown in the figure. The part of the theoretical tail void volume which remains unoccupied by soils due to inward movement, denoted as  $V_G$ , is considered filled with grouting material injected. The sum of volumes  $V_\ell$  and  $V_G$  is equal to the tail void volume  $V_{TV}$ , which is unique for each shield.

### 8.1.2 Analytical Procedures

The procedures and assumptions of the analyses are basically equivalent to those applied in the N-2 tunnel analyses of the last chapter. Brief explanations are provided for the differences adopted.

In contrast to the soil conditions for the N-2 tunnel analyses the soil profile concerned in this chapter is assumed to be a homogeneous Bay Mud clay layer with a depth of seventy feet over the rigid base. A twelve-foot diameter shield tunnel to be constructed is placed in this layer 36 feet below the ground surface. The tail void of the shield is assumed to

be three inches and thus the tail void volume  $V_{TV}$  is 8.2 percent of the face excavation volume of the shield. The mesh used in the finite element analyses is identical to that shown in Figure 7.1, which was used in the N-2 tunnel analyses. The characteristics of the Bay Mud are the same as in the previous work assuming a normalization relative to the overburden pressure for compressibility and strength. Loading procedures for the construction stages are exactly the same as those applied in the N-2 analyses as illustrated in Figure 7.2.

The heaving process is modeled by applying a pressure outward of the shield, the distribution of which is shown in Figure 7.3(a). The level of heaving is designated in terms of the values of average heaving pressure. Among the loading steps of the heaving process, six levels of the heaving pressure are selected to use in further analyses for subsequent stages. They include zero, 0.127, 0.222, 0.317, 0.360, and 0.397 in terms of  $\bar{p}_H / p_V$ .

Stress relief at the tail void is modeled by applying pressure oriented inward to the tunnel. The pressure distribution is non-uniform as shown in Figure 7.3(b). A degree of volume loss calculated from soil movements is taken as a parameter to define the effects of different conditions of tail void closure. As explained before, this does not result in releasing all of the stresses, since the remainder are transferred to the liner so as to assure a stress-free boundary on the inner surface of tunnel liner. The additional weight of the tunnel liner and the equipment are put together on the liner at this stage of the liner installation. They are equal to 30 percent of the excavated soil weight.

Through the loading stages, the soils around the shield are disturbed and develop excess pore pressure. Consolidation is the last stage of the construction sequence in the analysis to allow the pore pressures to dissipate.

## 8.2 Effects of Heaving Pressure Level

The heaving level is taken as a parameter, while tail void loss is unchanged, in determining the heaving effects on the subsequent stages.

### 8.2.1 Completion of Heaving and Tail Void Closure

As the heaving pressure is increased, outward movements of soil take place. This relation is shown in Figure 8.2. The heaving volume  $V_H$ , normalized with respect to the tail void volume  $V_{TV}$ , is plotted for the average heaving pressure  $\bar{p}_H$ , which is normalized by the effective overburden pressure  $p_V$  at the depth of the shield springline. An increment of the nondimensional heaving pressure of 0.0159 is applied with an iteration in the incremental analysis. Twenty-nine loading steps are used to draw the heaving volume development curve to yield a 100 percent increase, as shown in Figure 8.2.

The rate of heaving volume increase becomes larger when the heaving pressure grows higher since a higher stress level mobilized in soils results in the reduction of soil resistance to deformation. A 20 percent of heaving volume is calculated for the heaving pressure of 0.2. However, a pressure twice that, 0.4, is responsible for more than four times the

heaving volume, 82 percent.

Distribution of displacements around the tunnel for the three heaving pressures are shown in the left side of Figure 8.3. In spite of the fact that the soil is homogeneous clay, the shape of the deformation distributions are similar to those obtained for the N-2 tunnel analyses.

After heaving, the tail void effect is modeled so as to reach a fixed amount of volume loss. The volume loss in this section is fixed at 40 percent of the tail void volume  $V_{TV}$ , with reference to the volume loss of 38 percent calculated at Line 4 in the N-2 tunnel analysis. Then the net heaving volume is an amount of the initial heaving volume minus 0.4 of the volume loss. This situation is shown by triangles in Figure 8.2. The analyses use 12 to 18 unloading steps to assure the specified volume loss of  $0.4 V_{TV}$  for the tail void closure process.

Redistribution of stresses due to the liner installation provides additional small deflections of soil; the final positions are shown on the right side of Figure 8.3. Net inward movements of soil at the crown and the invert are not very different for three of the levels of heaving pressure, whereas those around the springline are quite different according to the level of heaving pressure. This situation was observed in the instrumentation results for the N-2 project. Such a trend suggests that settlement above the tunnel centerline may not be greatly different as a result of the different heaves; there is likely to be more influence on settlements away from the tunnel.

### 8.2.2 Development of Ground Surface Settlements

The final ground surface settlements at the completion of consolidation are shown in Figure 8.4 for the six levels of initial heaving pressure. A classical bowl shape of settlement trough is observed. The maximum settlements above the tunnel centerline are essentially the same for all cases with a nondimensional heaving pressure up to 0.317. But cases of very high heaving pressure result in smaller settlements (see  $\bar{p}_H / p_V$  of 0.360 and 0.397 in the figure).

For all cases in Figure 8.4 the shape of the settlement trough is approximately represented by the normal distribution curve and an inflection point can be calculated. A distance to the inflection point  $l_{inf}$  may be considered as an index of the width of settlement trough. The trough width is shown in Figure 8.5 in the normalized form with respect to the tunnel diameter  $D$ . A trend of narrowing the settlement trough with increasing heaving pressure is illustrated (see also Figure 8.4).

Surface movements at the centerline are shown in Figure 8.6 as a function of time. In this figure nondimensional settlements are plotted against a nondimensional time factor which is similar to the one used in the consolidation theory. In defining the time factor  $T$ , the tunnel diameter  $D$  and a coefficient of consolidation  $\bar{c}$  based on the soil's elastic shear modulus are applied as a reference length and a reference consolidation property, respectively.

Development of the surface settlements is shown in the figure for all the construction stages of tunneling. Applying higher heaving pressure

results in a larger surface heave in the heaving stage as expected, and this is then followed by a smaller immediate settlement due to the tail void closure. However, a larger long-term settlement results from consolidation of the ground. It is interesting to note that even though an amount of surface movements differ for each loading stage, the final settlements are almost the same in amount except cases for the very high heaving pressure.

Small upward movements are seen during the stage of liner installation just after the tail void closure. The reason for this is that the resultant force of the liner loading acts in an upward direction since excavation loads have applied to make the inner tunnel surface free from any tractions produce a bouyant force. As the excavation load varies with the heaving pressure initially applied, the upward movements are not the same in strict expression. However, they are practically the same as seen in the figure.

Final settlements in the figure are reached at different times. This trend is clear for the surface movement with a smaller heaving pressure which takes a longer consolidation time. This may be due to several reasons, the most likely of which is the time required for the stress rearrangement which takes place in the surrounding soil of the tunnel as consolidation proceeds.

### 8.2.3 Pore Pressure Development and Stress Level Mobilized

Figure 8.7 gives distributions of excess pore pressure at the liner

installation stage for four of the heaving cases. For the case of no heaving pressure,  $\bar{p}_H / p_V = 0$ , or with a small heaving pressure, the highest pore pressures develop in a region away from the tunnel at the level of the springline. Higher heaving pressures lead to higher pore pressure levels which are concentrated adjacent to the tunnel at the springline. These high pore pressures lead to the higher consolidation settlements noted in Figure 8.6.

Figure 8.8 gives four charts of the stress level distribution in the soil at the time of liner installation for the corresponding heave cases covered in Figure 8.7. It can be seen that high level stresses are mobilized just above the tunnel springline for no or small heaving pressure cases. In contrast, intensive stress mobilization does not occur for cases with moderate heaving.

#### 8.2.4 Relative Surface Settlement between Construction Stages

Using the results for the stages of heaving, tail void closure, and consolidation, surface settlements due to each consecutive stage may be considered. Figure 8.9 shows surface movements for a nondimensional heaving pressure  $\bar{p}_H / p_V$  of 0.317, and a volume loss at tail void closure  $V_L / V_{TV}$  of 0.4.

Upon the completion of heaving, an upward movement of the ground surface is observed. The profile of the surface heave shown in the figure is slightly different from that observed for the N-2 tunnel project since the maximum upward heave does not occur at the tunnel centerline as was

the case at the N-2 site. Apparently, the top layer of sandy fill at the N-2 site has a relatively high deformation resistance and acts as a beam, forcing a maximum heave at the centerline. In support of the profile obtained in Figure 8.9, it may be noted that Finno (1983) obtained a similar result for a homogeneous clay deposit using a different soil model. For the homogeneous clay, the upward displacement is a maximum at a position about two tunnel diameters away from the centerline. Such a profile is derived partly from the effects of the elliptic distribution of heaving pressure.

Tail void closure leads to surface settlement near the tunnel centerline, whereas further away heaves remain. A classical bowl shape of the surface settlement develops only towards the final stage of construction. A relative displacement between the heaving and the tail void closure stages may be referred to as immediate settlement because the volume loss of 0.4 of the tail void volume created immediately reflects the surface settlement, while soils behave largely undrained. On the other hand, the difference in settlements between the tail void closure and the final stages is due to consolidation and volume change.

One effect which shows clearly in Figure 8.9 is that the width of the settlement trough gets broader through the process of immediate settlement and consolidation. This is especially true for the case of the long-term settlement.

Surface settlements after the heaving stage are depicted in Figure 8.10. The figure shows the surface settlement at the tunnel centerline

relative to the upward surface displacement during the heaving stage. The total surface settlement is divided into immediate and consolidation phases. The results show that as long as the heaving pressure is zero or small, the immediate settlement is about two thirds of the total settlement. The ratio of immediate to consolidation settlements is altered only if the heaving pressure increases. Once the heaving pressure exceeds  $0.3$  of  $p_v$ , the consolidation settlement becomes far more important. This suggests that the heaving effect is self-limiting since the larger the heave, the larger the consolidation settlement.

Figure 8.11 shows the variation of volume loss at the ground surface with respect to the heaving pressure applied. The ground surface volume loss is represented in terms of ratios of soil volume lost with surface settlement occurring after heaving to that at the tail void. The volume ratio is about unity upon the tail void closure, indicating that the volume loss occurring at the ground surface is virtually the same as that occurred at the shield tail. This is because the settlements caused by the tail void closure occur in the short term where the soils behave in an undrained fashion without volume change. In contrast to the equal volume losses for the immediate settlement, long term settlements appear to magnify the volume loss due to the ground surface settlement. After consolidation settlements are completed, two to three times of the tail void volume is lost at the ground surface. The consolidation settlement is responsible for the volume loss in excess of the immediate volume loss, as is shown in the figure. As the heaving pressure increases, the consolidation effect on the surface volume loss increases. In particular, it becomes more

important if the heaving pressure exceeds 0.2 of  $p_V$ . This result reinforces the idea of limiting the validity of the heaving effect.

#### 8.2.5 Discussion of Results

Six levels of the heaving pressure were considered in the analyses with a fixed amount of 40 percent of the tail void volume  $V_{TV}$  assumed to be lost upon tail void closure. It was observed that the use of different levels of heaving pressure leads to different ground movements in subsequent loading stages. When higher heaving pressures are applied, larger initial upward surface movements are caused, followed by smaller immediate settlements upon the tail void closure and larger long term settlements due to consolidation of soils are attributed.

The benefits of the heaving effects lies in two areas:

1. If the heaving is large enough, the maximum settlement can be reduced.
2. The extent of the surface settlement trough is reduced using heaving.

The first of these points requires careful consideration to fully appreciate the heaving impact. As noted earlier, the analytical results clearly show that while heaving can reduce settlements, it is a self-limiting process, because for each increment of heave, there is an additional consolidation settlement. The choice of the optimum amount of heave is made difficult by the interaction of the short term and long term effects. Of course, in the field the options may be partially controlled by concerns that large heaves are unacceptable in terms of the impact they may cause on utilities or adjacent structures.

Minowa (1981) has written that experience with the EPB shield suggests that surface settlements are minimized with heaving of about two percent of the shield face volume. A comparable result was achieved in the parametric studies using the heaving pressure of 0.222 . Thus, it appears that experience supports the idea of using a level of heaving which leads to relatively small consolidation settlements.

### 8.3 Effects of Volume Loss upon Tail Void Closure

This section deals with tail void loss to see its effect on the ground movements while the heaving level remains at a constant level.

#### 8.3.1 Tail Void Closure and Volume Loss

Tail void closure involves soil movement into the void when the tail of the shield passes. It is complicated by the process of grouting the void; grouting may or may not effectively fill the void depending upon the response of the soil to the reduction of support as the shield advances. This process causes a stress arrangement at and around the shield tail. The modeling procedure used herein are described in Figure 7.3.

It is useful to refer to Figure 8.1 to explain the construction stages of grouting and liner installation. The tail void lies between the shield shell and the tunnel liner. It may be filled by soil or grouting material or some combination thereof. Neither the actual stress distribution nor the displacement distribution are known along the interface of the in-move soil and the grouting material. For this discussion, the parameter which

will be used to characterize the closure is the volume loss which occurs on the closure. This is convenient since in the field, the tail void volume and grouting volumes are used to describe the problem, and their quantities are all related. Volume loss as used herein describes the net volume of the inward movement of the soil into the tail void which is not halted by grouting. Thus,  $V_l = V_{TV} - V_G$  as illustrated in Figure 8.1.

A case with the normalized heaving pressure of 0.222 is selected as the base to evaluate the effects of volume loss. That amount of heaving pressure is considered close to the limit of causing major soil disturbance as was discussed in the last section. The heaving volume for this case is about 22 percent of tail void volume  $V_{TV}$  according to Figure 8.2. Using the same type of expression, Figure 8.12 shows the reduction of the heave volume with the average releasing pressure  $\bar{p}_{rs}$  normalized by the effective overburden pressure  $p_v$ . The axis on the right side is the volume loss relative to the heaving level.

Volume loss increases slowly when the releasing pressure is small. But it increases at a high rate for higher releasing pressure ranges. Such a response of the volume loss development is derived mainly from the reversal yielding of soil elements which are characterized by the kinematic hardening rule of the Prevost model. Twenty-three loading steps are applied in the analyses to obtain a volume loss of 60 percent of  $V_{TV}$ . Among them seven levels of volume loss are chosen as marked in the figure for further analyses.

### 8.3.2 Development of Ground Surface Settlement

A higher volume loss created upon the tail void closure logically causes more ground movement and a larger surface settlement. This is indicated in Figure 8.13, where the final surface settlements are shown for cases with different volume losses. Unlike the surface settlement pattern where the trough grows narrower with heaving pressure, the settlement trough becomes deeper with volume loss. The maximum settlement along the tunnel centerline is a direct reflection of the volume loss.

Figure 8.14 shows the development of the surface settlement at the tunnel centerline with time elapsed in tunnel construction. As the final settlement grows with the volume loss, both the immediate and long term settlements become larger when the volume loss becomes larger. Figure 8.15 shows nondimensional excess pore pressure distribution at the stage of liner installation for four different levels of volume losses. As the volume loss increases, the maximum excess pore pressure developed in the vicinity of the springline decreases. Surface settlement is likely to be greatly influenced by the spreading of moderate excess pore pressures rather than by the development of high excess pore pressure in a limited area. A negative excess pore pressure develops at the crown and the invert with increasing volume loss.

The final settlement is seen to be reached at more or less the same time for all cases as consolidation has been completed (Figure 8.14). This is different from the effect of heaving pressure, where greater heaves lead to shorter times to complete settlement.

### 8.3.3 Immediate Settlement and Consolidation Settlement

Figure 8.16 shows variations of the immediate and consolidation settlements together with the total settlement with respect to volume loss upon tail void closure. A negative value of immediate settlement is seen in Figure 8.16 for the case with no volume loss. The surface rises responding to the bouyant force caused by the excavation load at the liner installation stage. Development of the immediate settlement is approximately proportional to the volume loss (Figure 8.16). The consolidation settlement also increases with the volume loss but it is very slow compared to the rate of the immediate settlement. The total settlement increases approximately proportional to the volume loss.

Figure 8.17 shows a volumetric expression of the surface settlement as an alternative of the previous figure. The soil volume of the surface settlement relative to the heaving stage is normalized by the tail void volume and is plotted against the normalized volume loss. The immediate settlement gives a linear relation between the volume of the surface settlement and the volume loss at the shield tail since soils behave undrained without volume change during the process of immediate settlement.

In both cases concerning the maximum surface settlement in Figure 8.16 and the volume of surface settlements in Figure 8.17, the consolidation settlement is greater than the immediate settlement when the volume loss upon tail void closure is small. But the immediate settlement becomes important when the volume loss increases. The degree of contribution of the immediate and consolidation settlements may vary with the initial

heaving pressure, though the effects of volume loss on increase settlements is considered basically the same.

#### 8.3.4 Discussion of Results

Volume loss as a result of tail void closure is a direct source of surface settlement and the most important factor to control the ground movement caused by shield tunneling. At least some limitation of ground loss can be achieved by grouting. In the practice of grouting, the pressure and volume of injection can be controlled. The purpose of grouting is to fill the tail void with a grouting material, usually cement bentonite mixture, so that soils are prevented from moving toward the liner to create a volume loss of soil. It is common to grout with the same amount volume as the tail void volume. Even though such execution is reportedly performed in most tunnel constructions, a volume loss usually occurs, because the soil has actually moved inward and cannot be readily pushed back. Typically the use of excess pressure simply contracts the liner rather than pushing the soil outwards. Further, this may actually disturb the soil and enhance the consolidation effects.

An alternative to grouting is the newly proposed cast-in-place concrete lining method (Matsuo and Makino 1980). This uses a heavy lining form which bears the fluid concrete pressure pressed by thrust jack forces as the shield advances. The tail void is filled with the concrete simultaneously as the void opens since the concrete is fluid and under high pressure. This method has been shown to be effective, but considerable sophistication in shield operation is inevitable and causes a reduction in productivity.

Another innovation involves the immediate injection of the tail void in which the grout injection is carried out during the shield movement as the void opens. The grouting is done from inside of the shield machine through the tail seal. It is possible to provide effective control of the tail void backfill in this method although, again, the process is costly. Excellent results of ground movement control are reported in the literature (Yoshizawa, et al. 1984).

#### 8.4 Summary and Conclusions

Parametric studies have been carried out in this chapter to see the effects of the initial heaving at the shield face and the volume loss at the shield tail supposing a shield tunnel is constructed in a homogeneous clay layer. The heaving and volume loss were found in the previous chapter to be important factors which affect the ground movement around the shield tunnel. In particular, the heaving effect is a characteristic of close-faced shield tunneling methods such as the EPB shield and the slurry shield.

The parametric studies show that the heaving process can be used to reduce the magnitude of the maximum settlement and the extent of the settlement trough. However, the heaving effect is self-limiting in that the more it is used, the larger are the long term consolidation settlements. It appears that a moderate amount of heave is preferable to optimize the beneficial effects of heaving.

Volume loss is caused by an insufficient volume of grouting materials to replace the tail void, and it leads directly to ground settlements. In

fact, the soil volume due to the surface settlement is nearly proportional to the volume loss at the shield tail. Therefore, it is best to fill the tail void completely and immediately after the tail void is created with shield advancement.

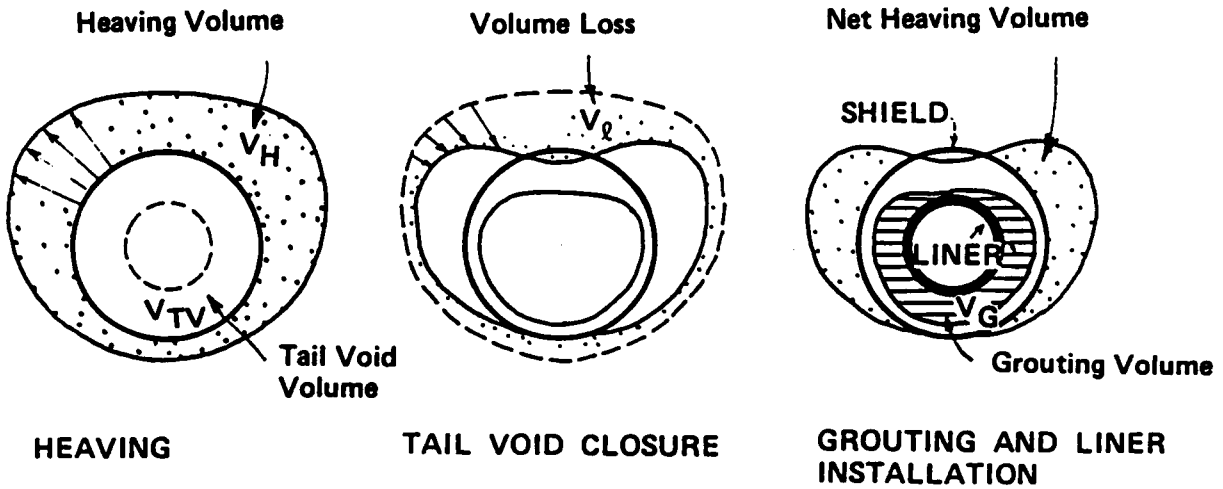
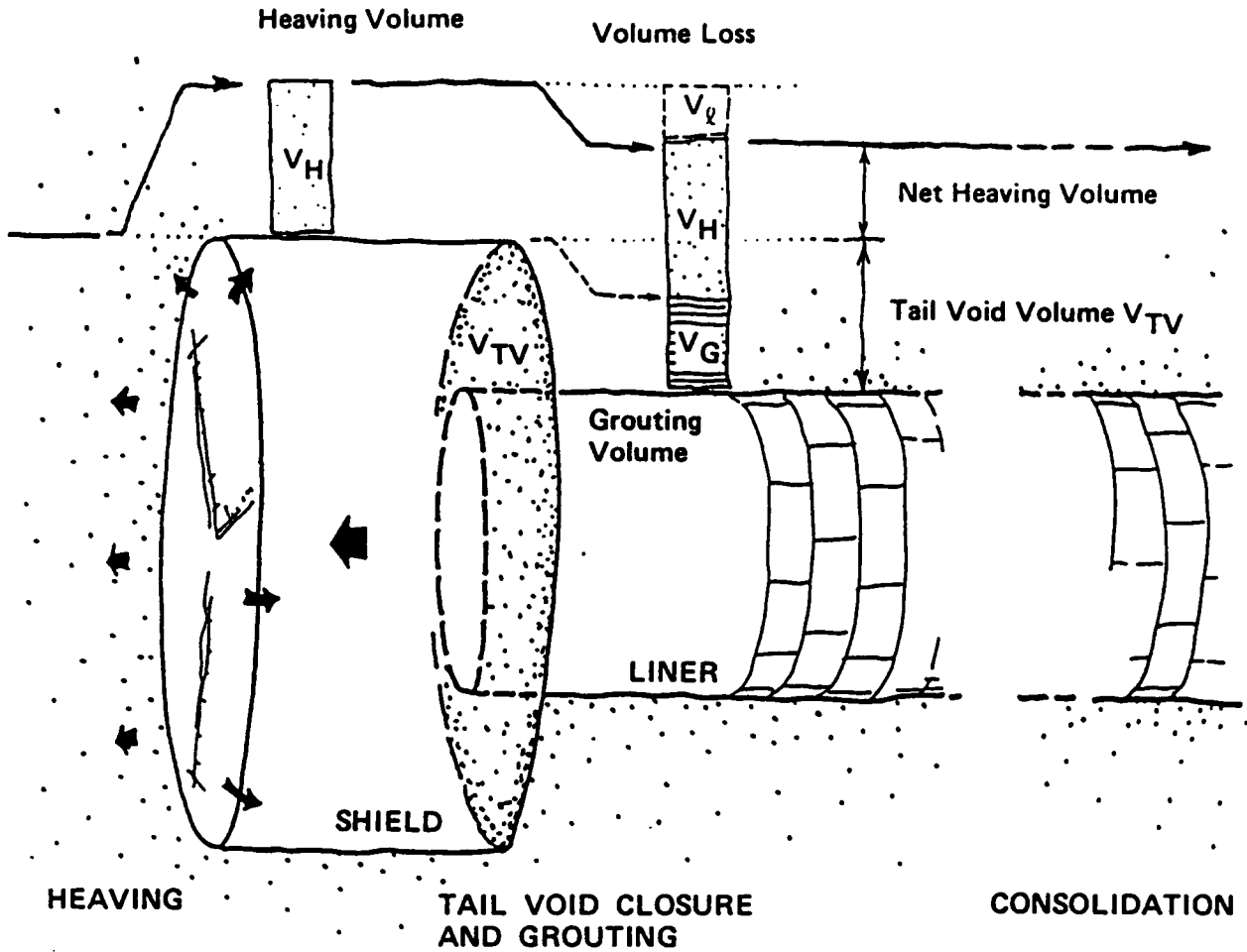


Figure 8.1 Volume Consideration of Soil Movement around the Shield due to Heaving and Tail Void Closure

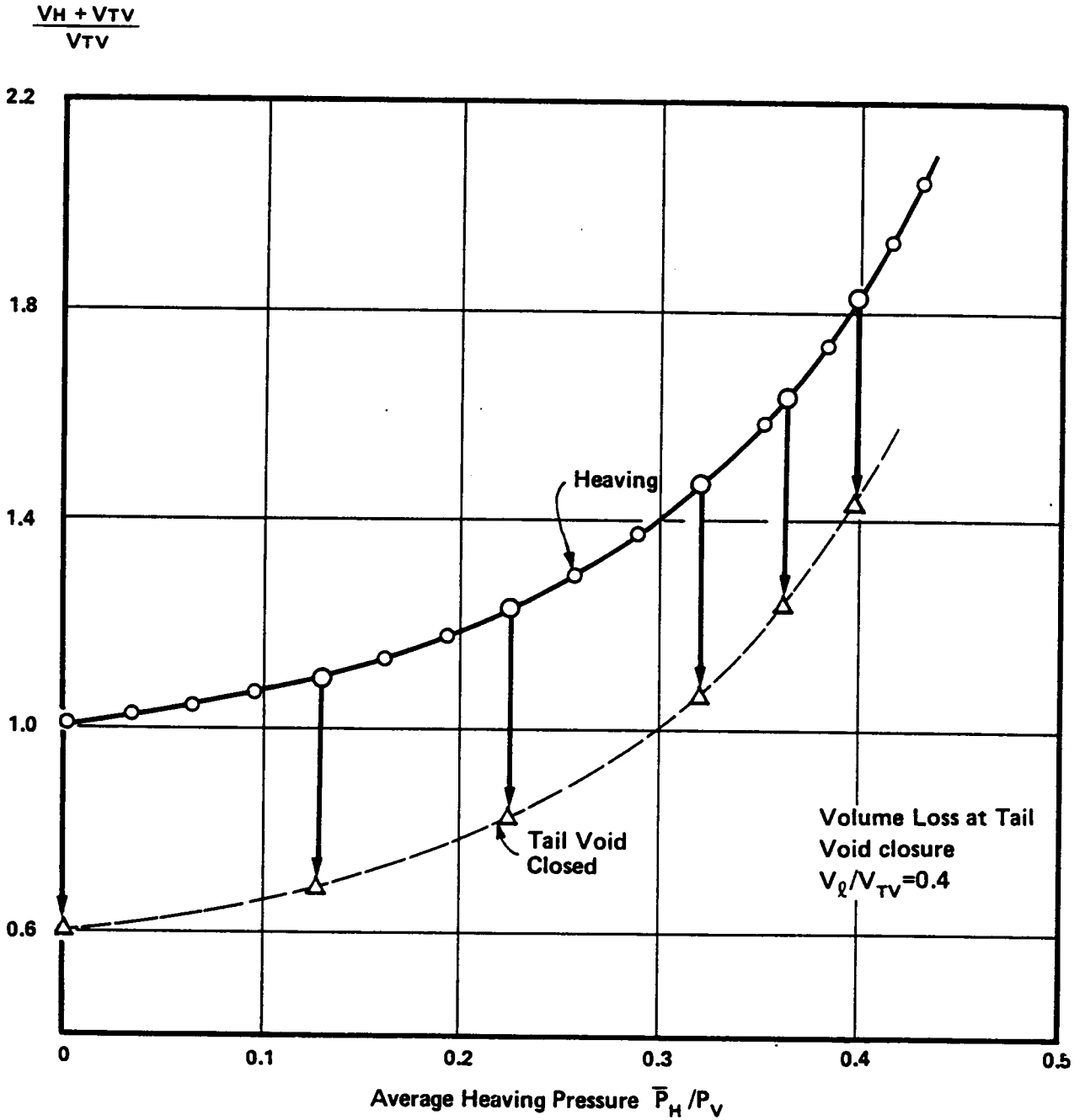


Figure 8.2 Normalized Heaving Volume Varying with Normalized Average Heaving Pressure

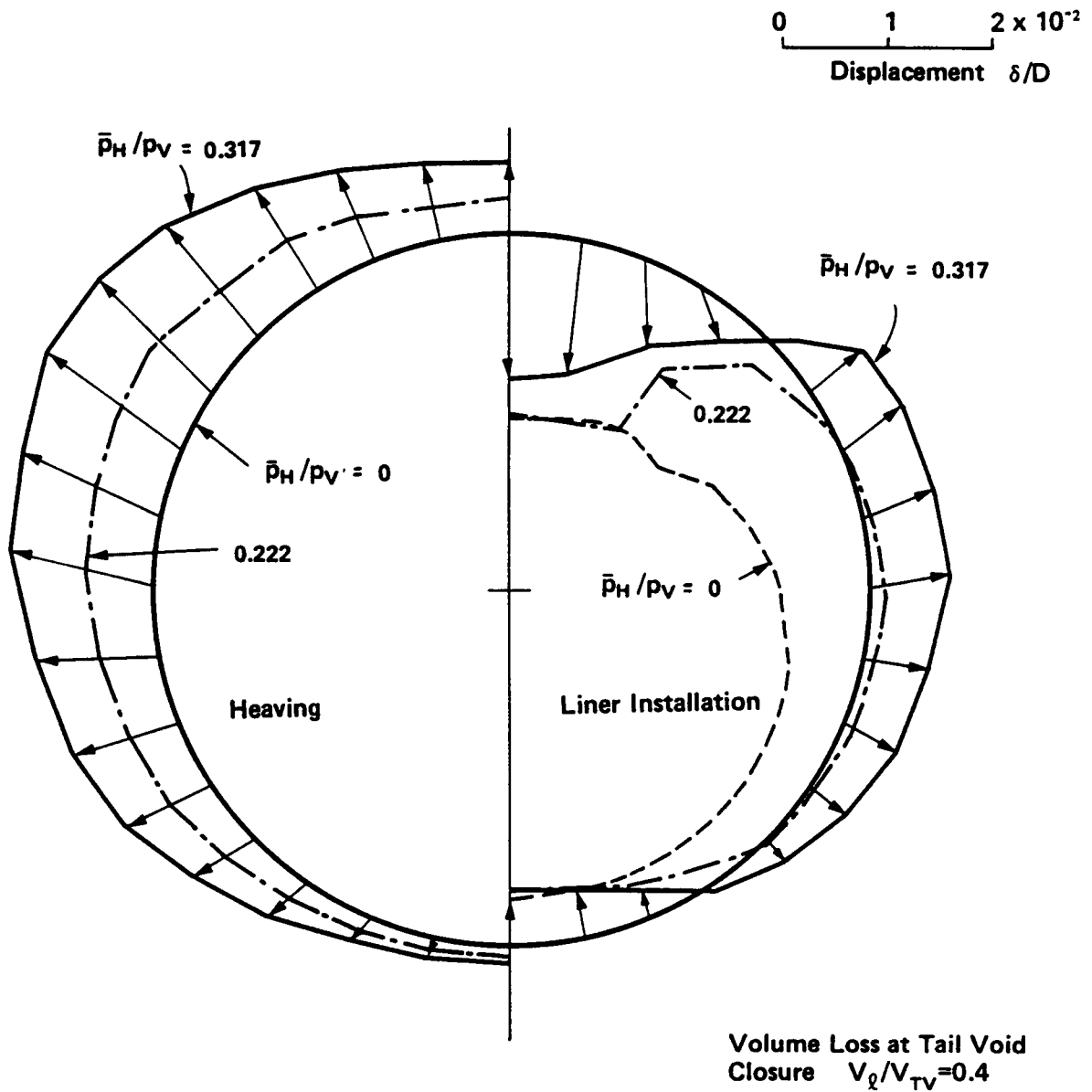


Figure 8.3 Displacements of Soils around the Shield at Heaving and Liner Installation Stages for Three Levels of Heaving Pressure

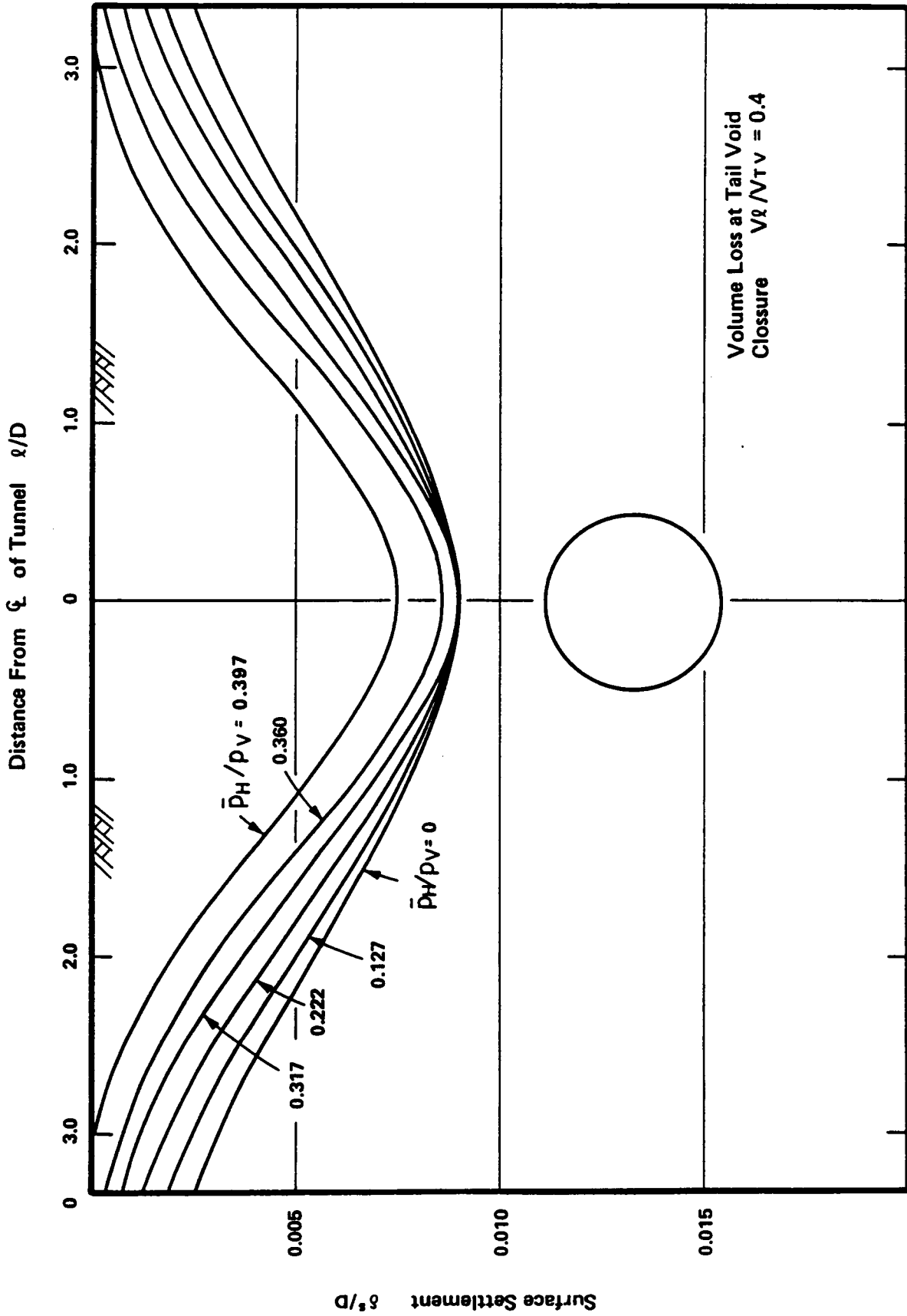


Figure 8.4 Settlement Curves at Ground Surface for Different Heaving Pressure

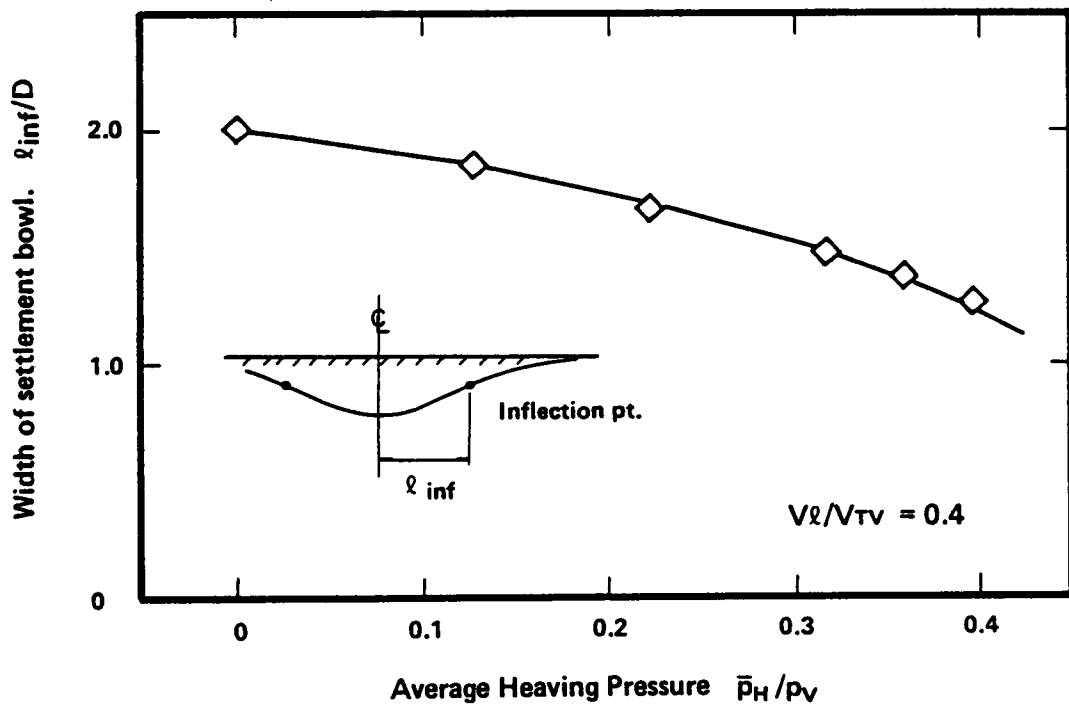


Figure 8.5 Widths of Settlement Bowl at Ground Surface as Positions of Inflection Points

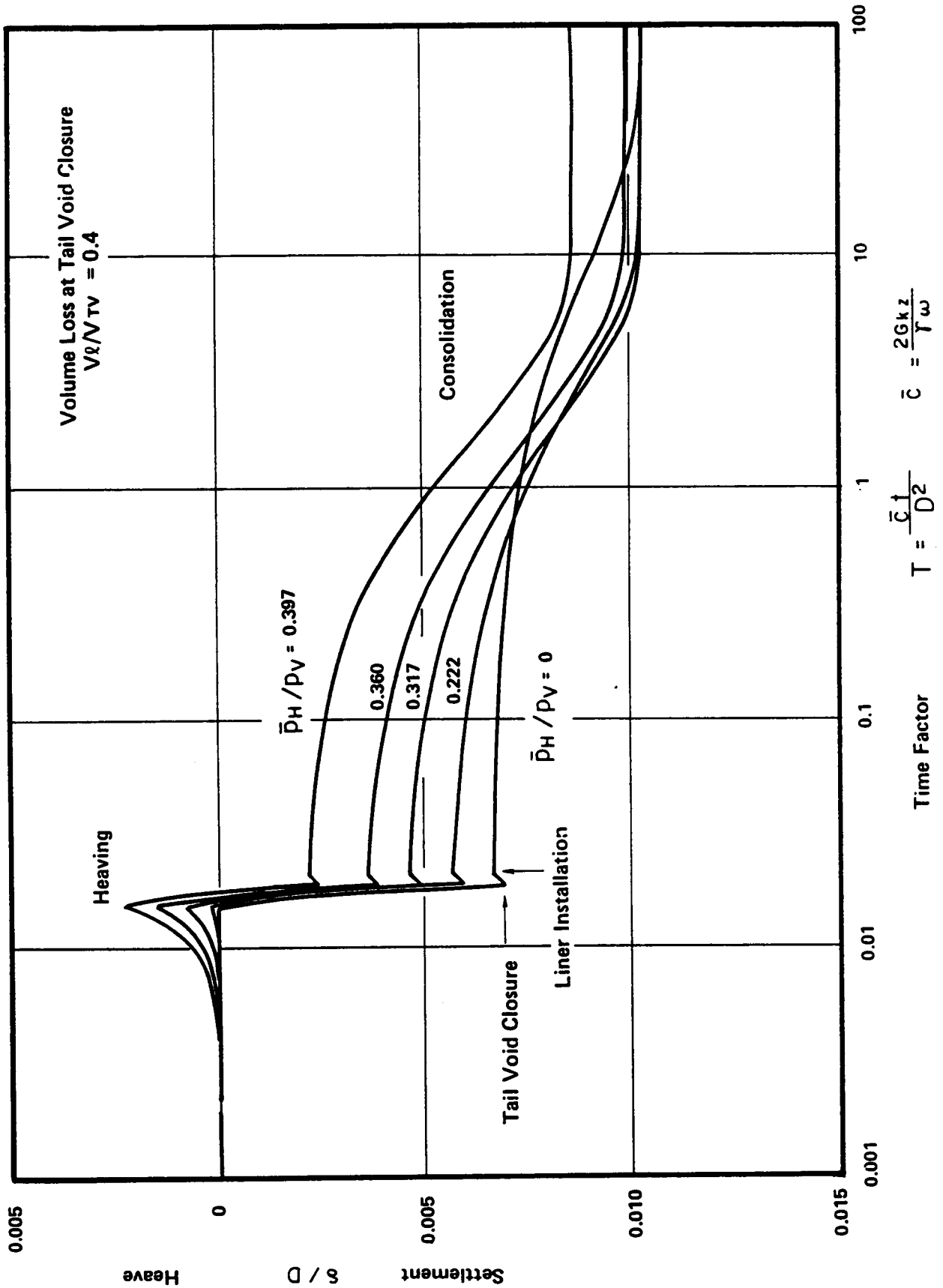


Figure 8.6 Centerline Surface Movements Varying with Time Needed for Construction Stages for Different Heaving Pressures

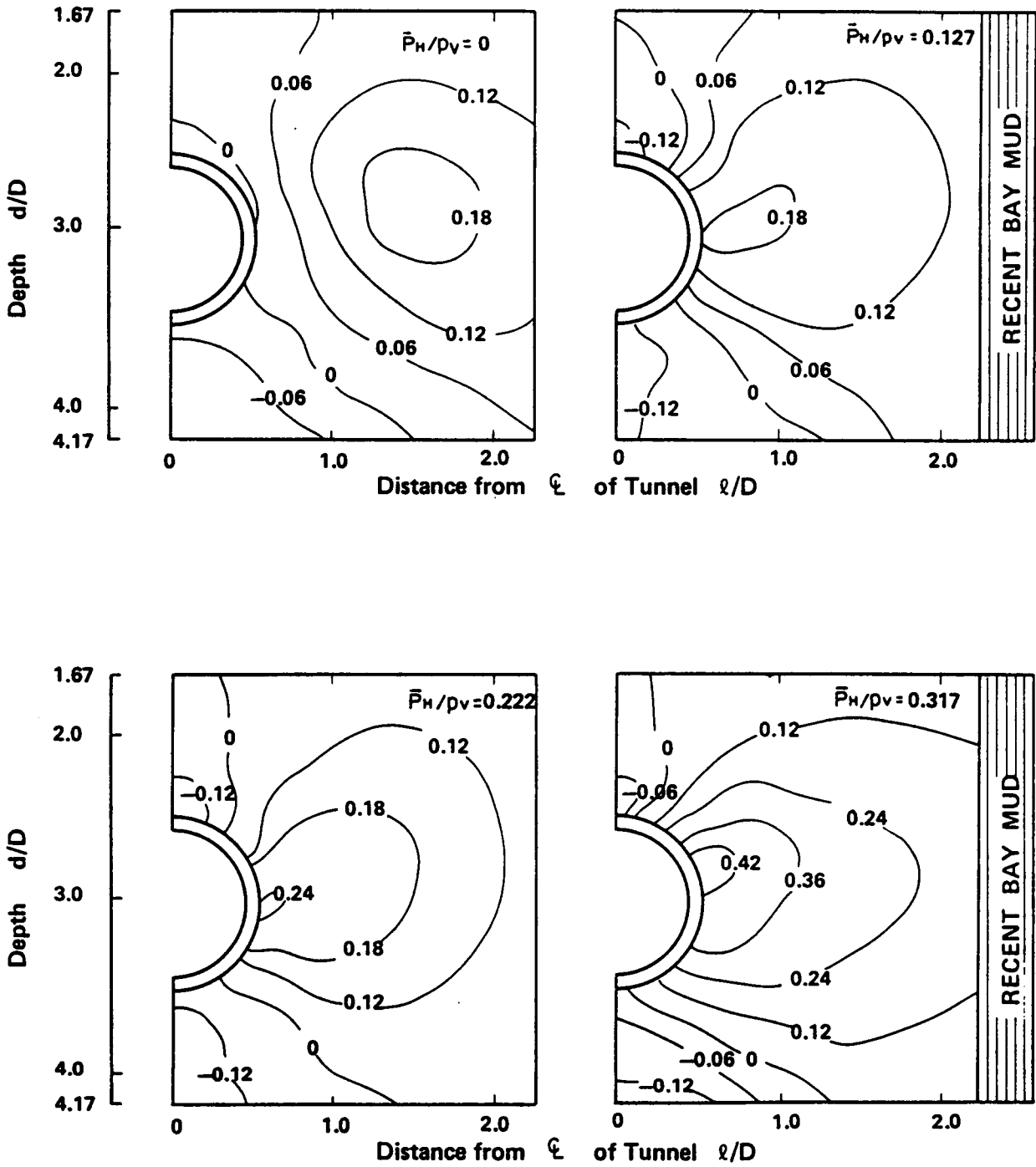


Figure 8.7 Nondimensional Excess Pore Pressure Development upon Liner Installation for Different Heaving Pressures ( $V_\ell/V_{TV} = 0.4$ )

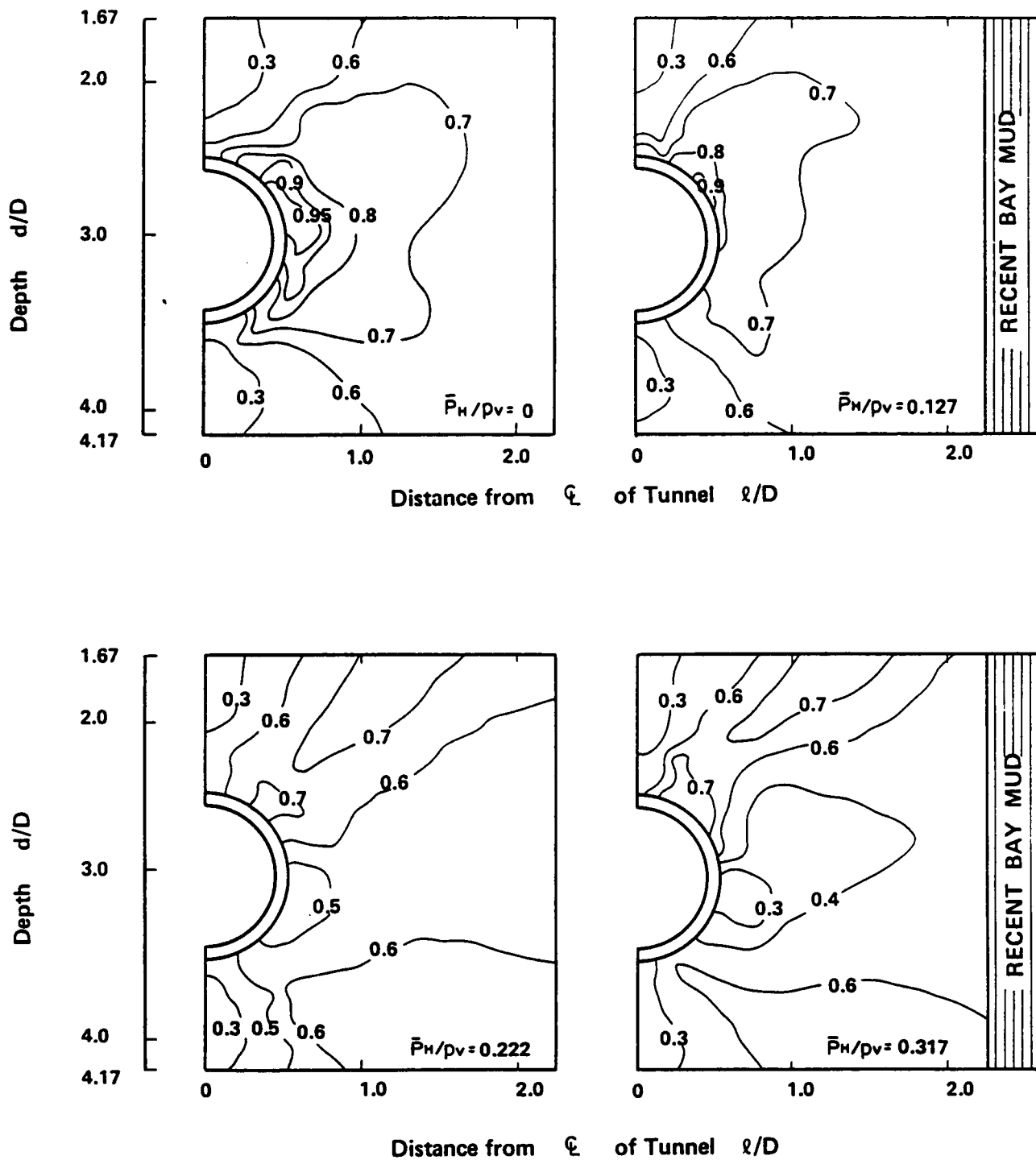


Figure 8.8 Stress Level Distributions in Subsoil upon Liner Installation for Different Heaving Pressures ( $V_\ell/V_{TV} = 0.4$ )

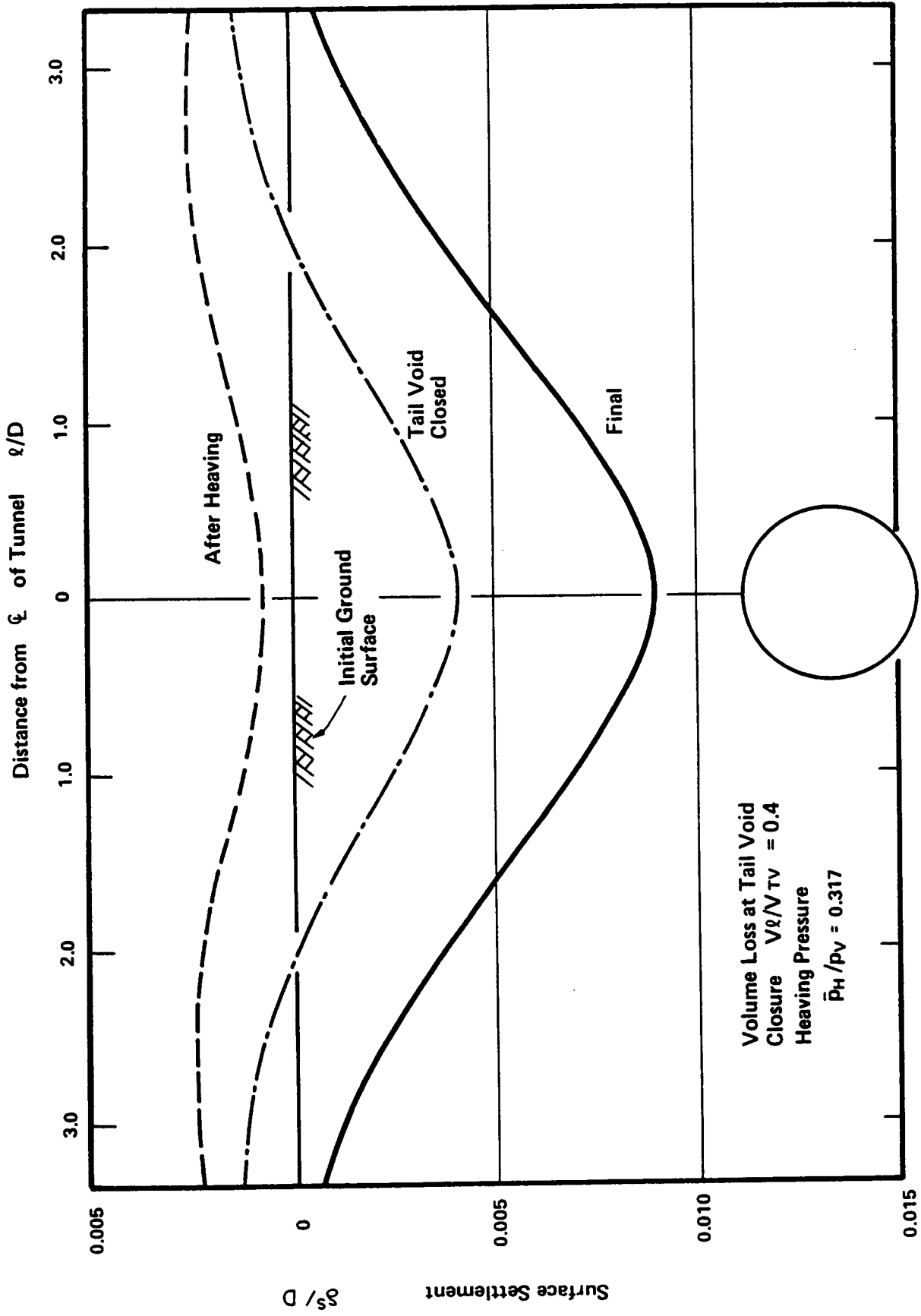


Figure 8.9 Surface Movement Profile at Heaving, Tail Void Closure and the Final Stages

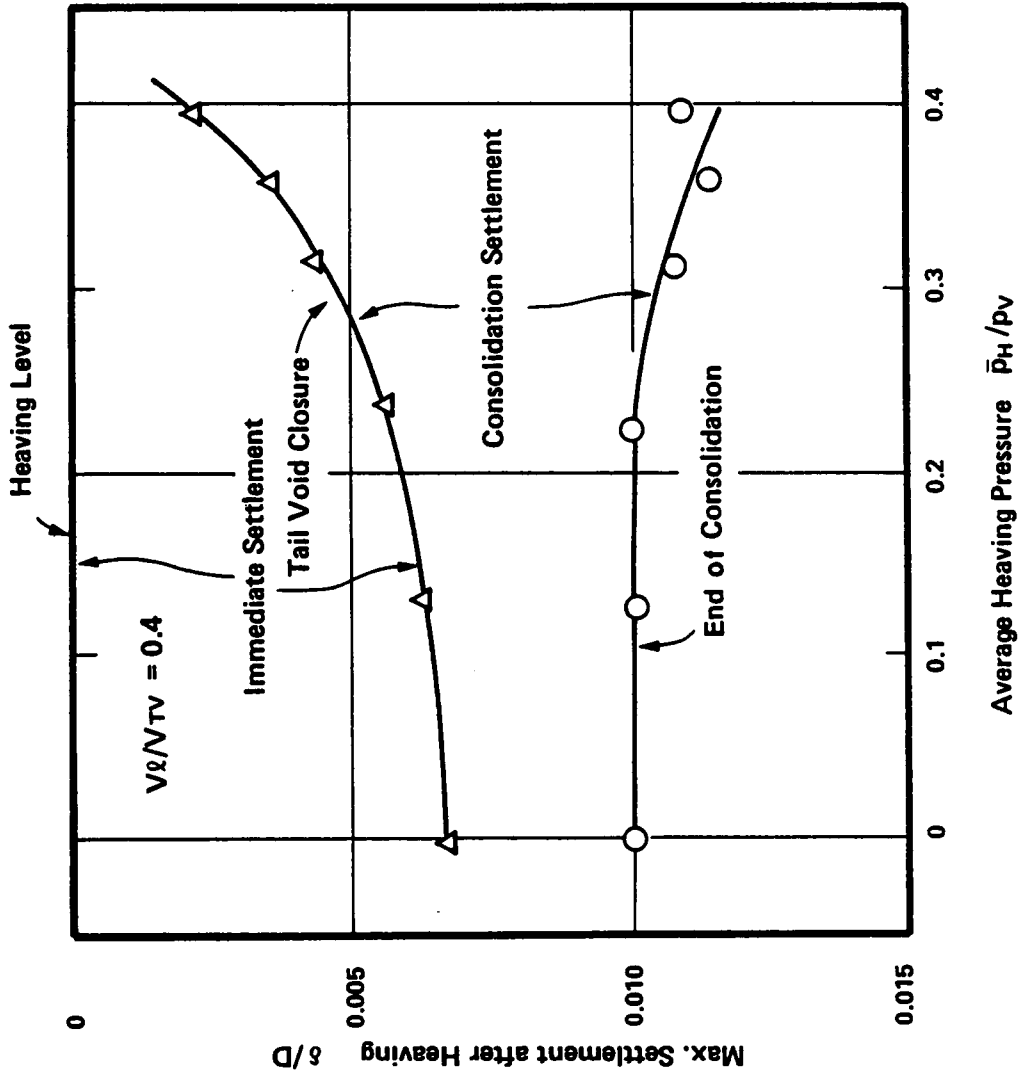


Figure 8.10 Maximum Surface Settlements at Tail Void Closure and End of Consolidation Stages Relative to Surface Heave for Different Heaving Pressures

Ratio of Volume Loss at Ground Surface to Tail Void Volume Loss upon Closure (  $V^s/V_{TV}$  )

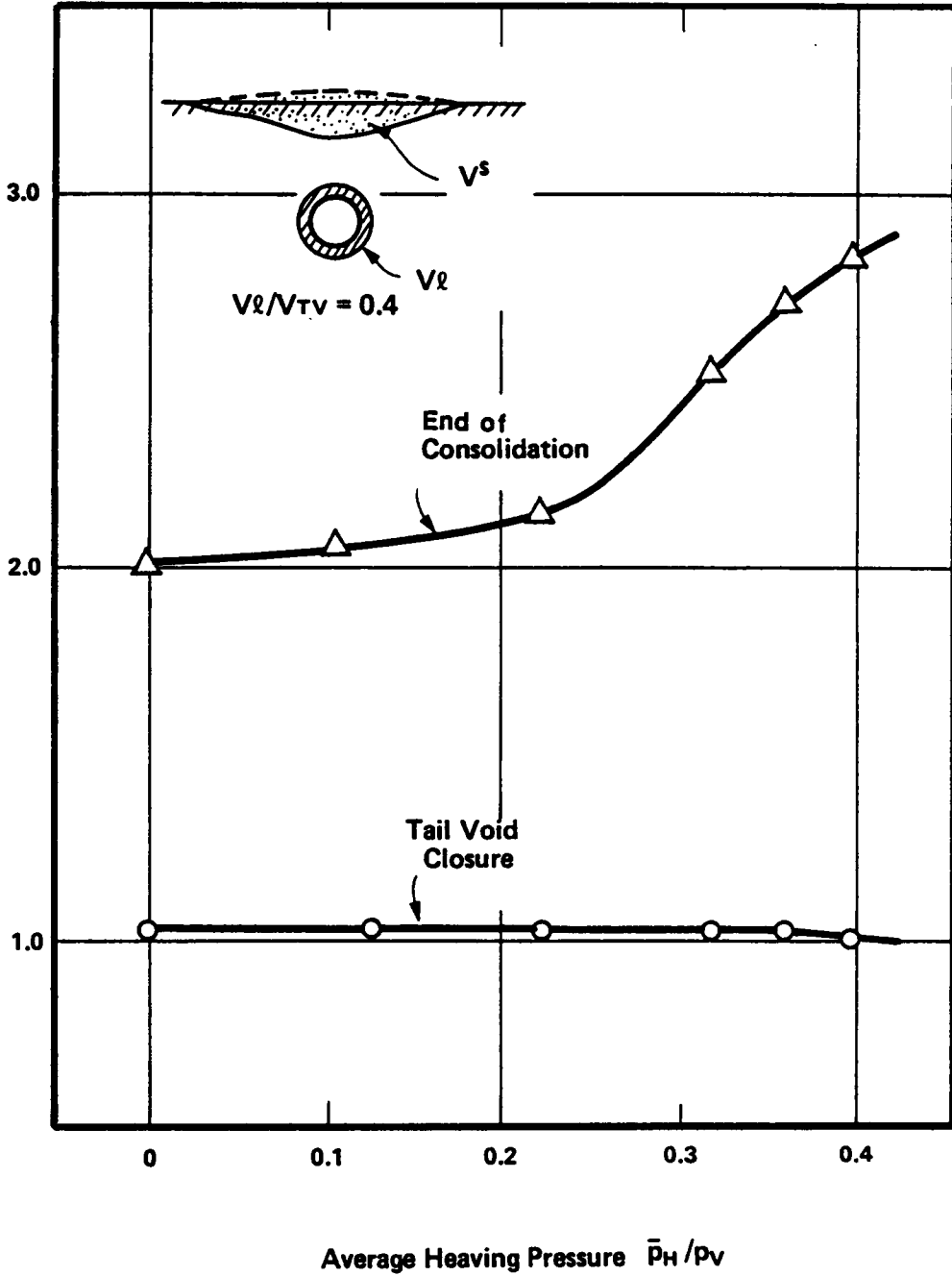


Figure 8.11 Variation of Ratio of Volume Loss due to Surface Settlement to That Occurred upon Tail Void Closure with Heaving Pressure

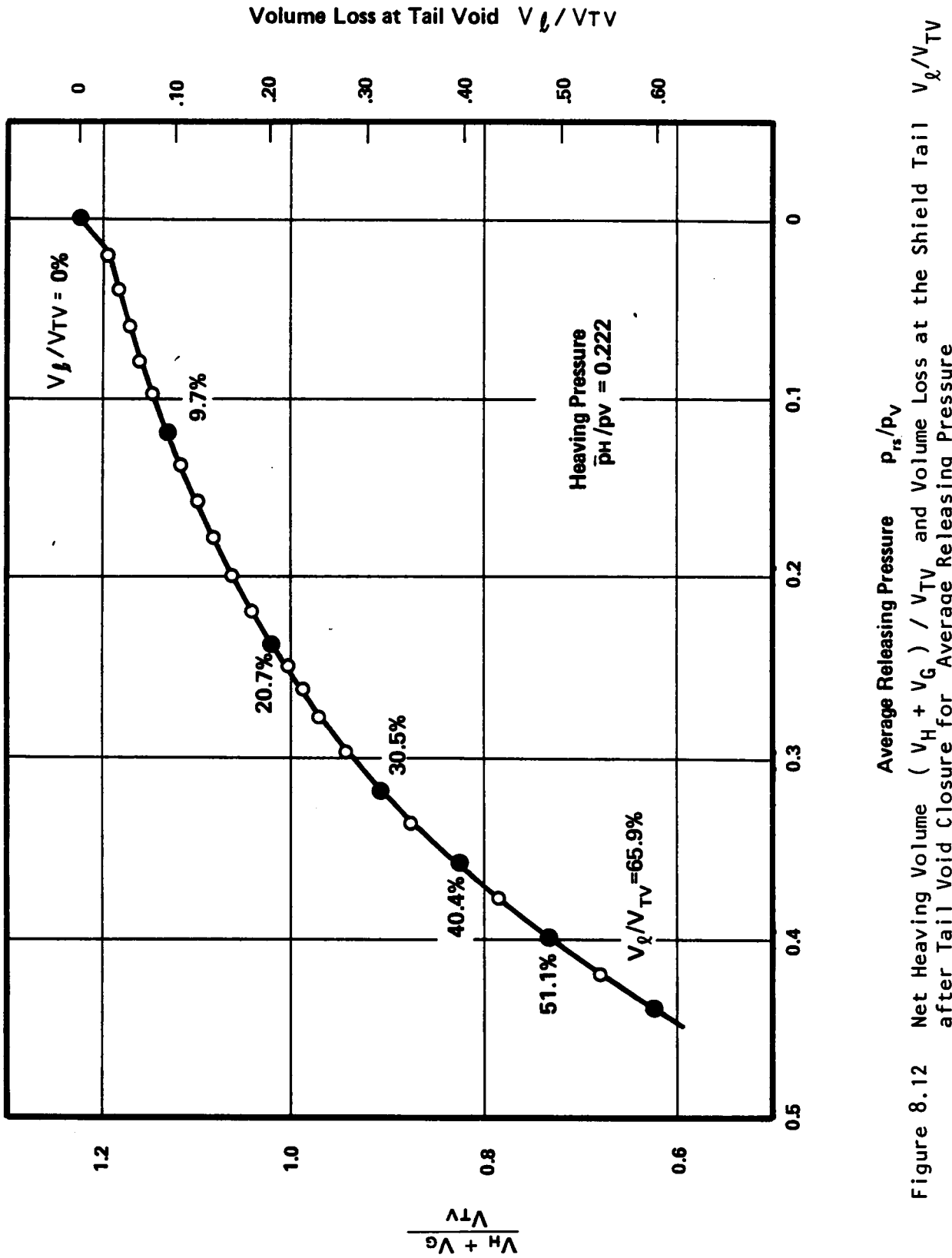


Figure 8.12

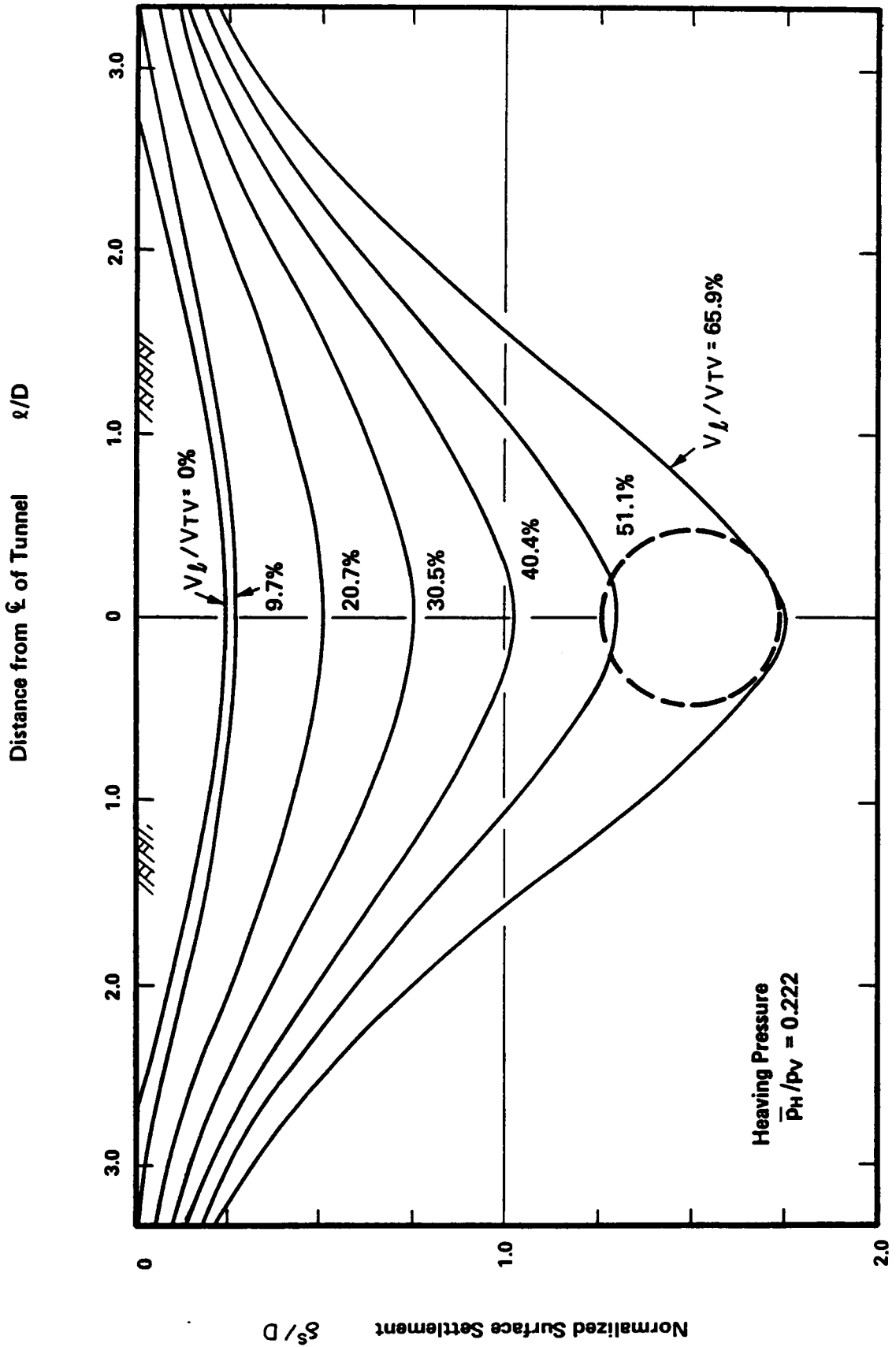


Figure 8.13 Settlement Curves at Ground Surface for Different Tail Void Volume Losses upon Closure

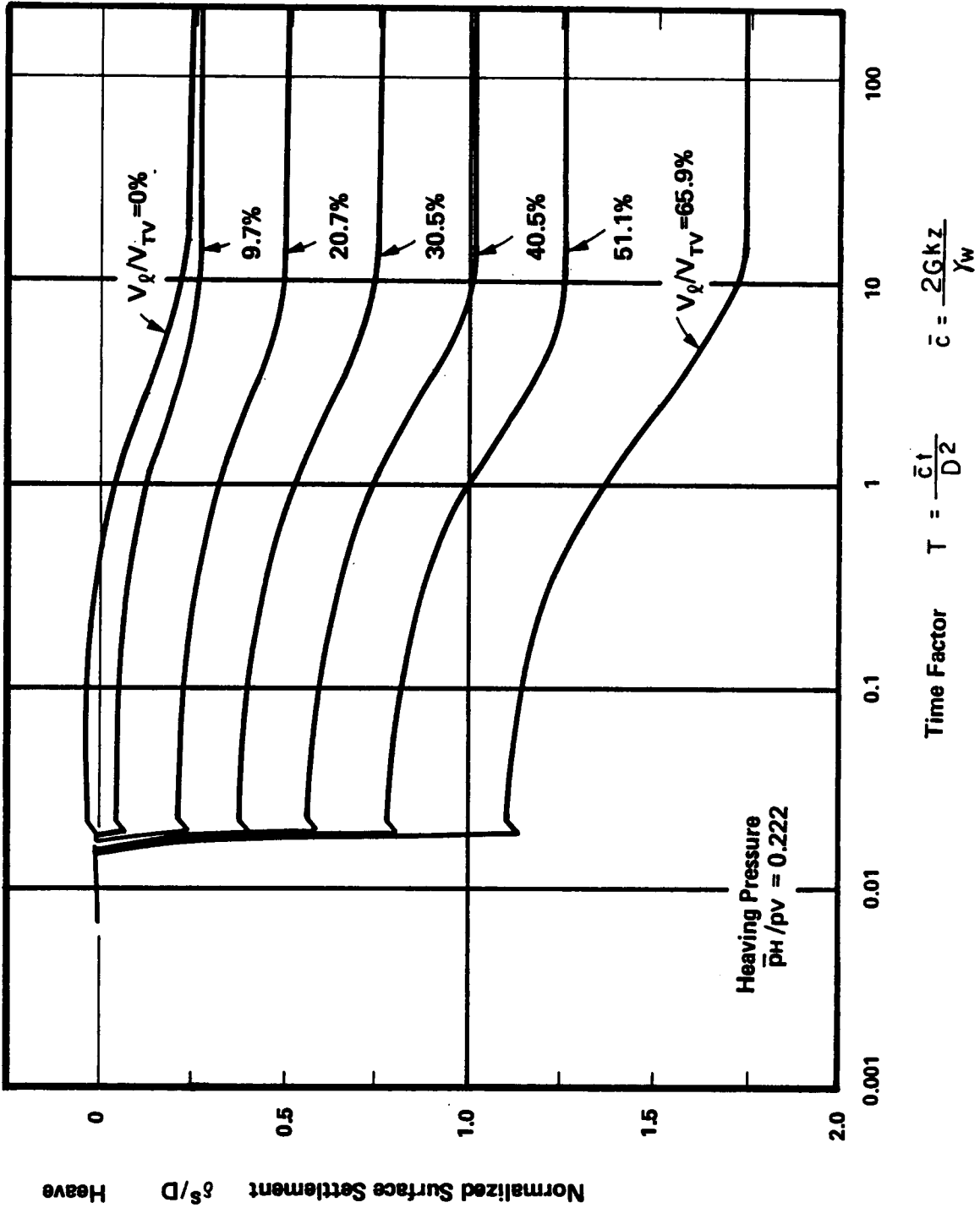


Figure 8.14 Centerline Surface Movements Varying with Time Needed for Construction States for Different Tail Void Volume Losses at Closure

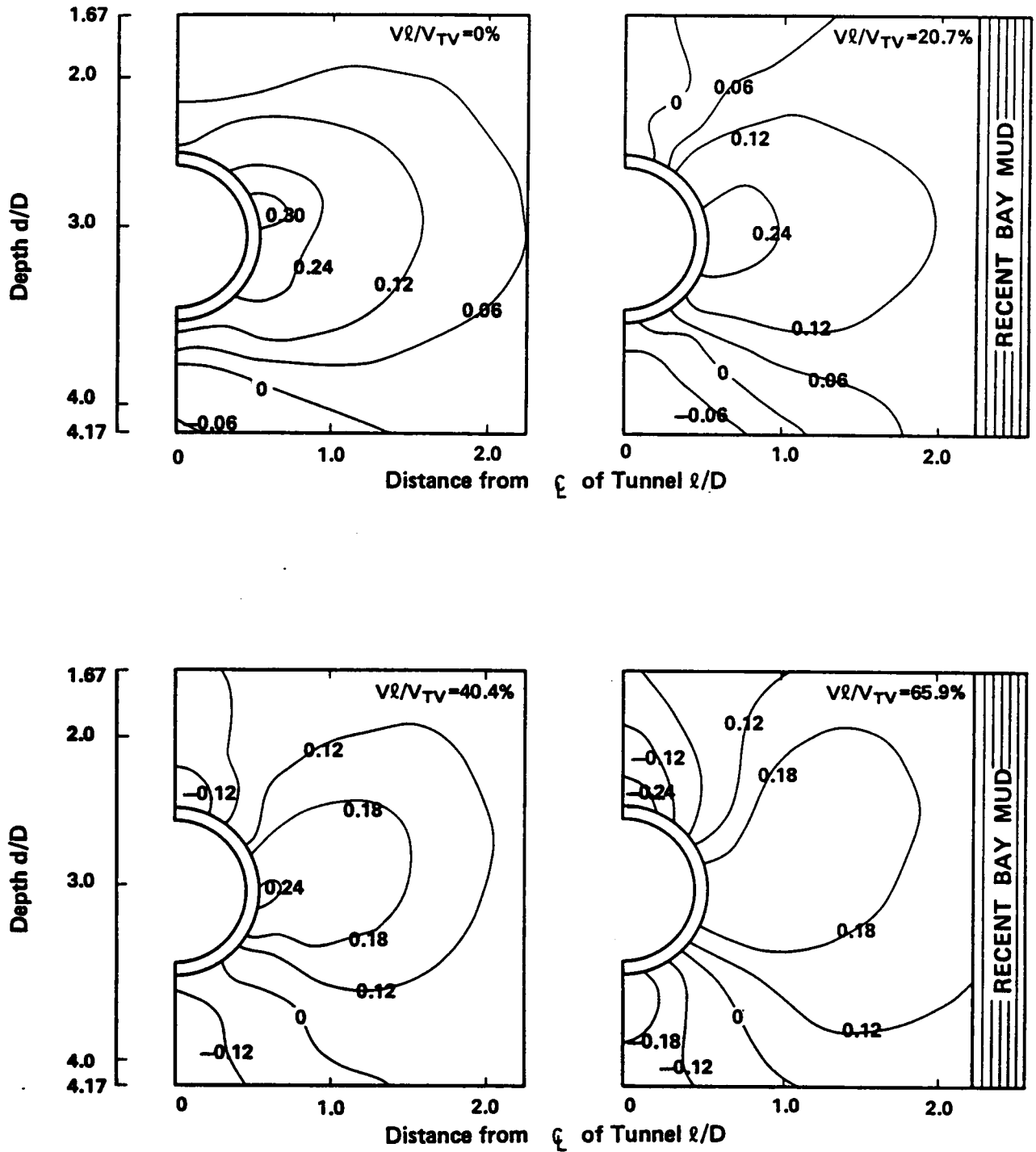


Figure 8.15 Nondimensional Excess Pore Pressure Development at Liner Installation Stage for Different Tail Void Volume Losses upon Closure ( $\bar{p}_H/p_V = 0.222$ )

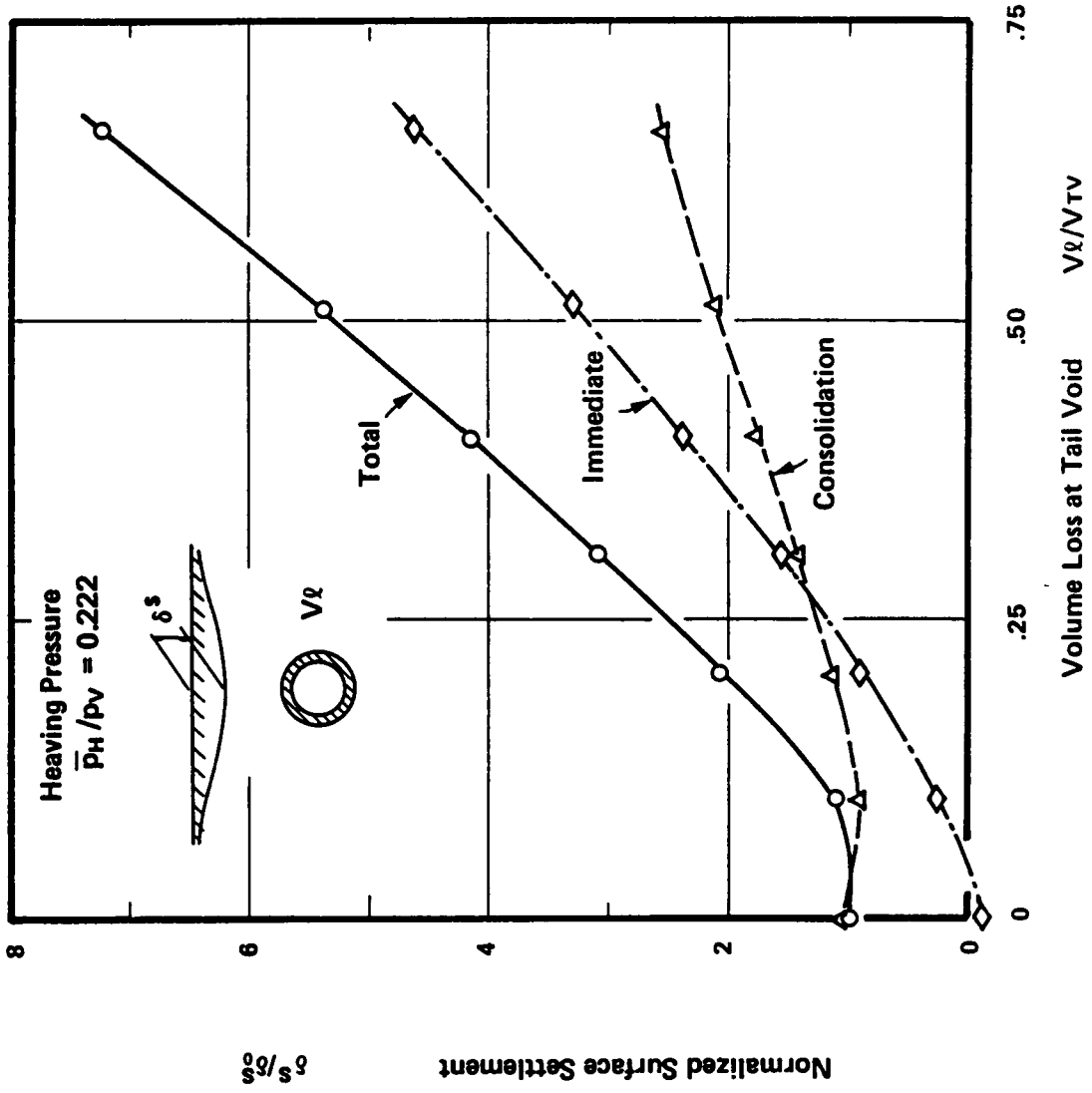


Figure 8.16 Normalized Maximum Surface Settlements for Different Tail Void Volume Losses upon Closure

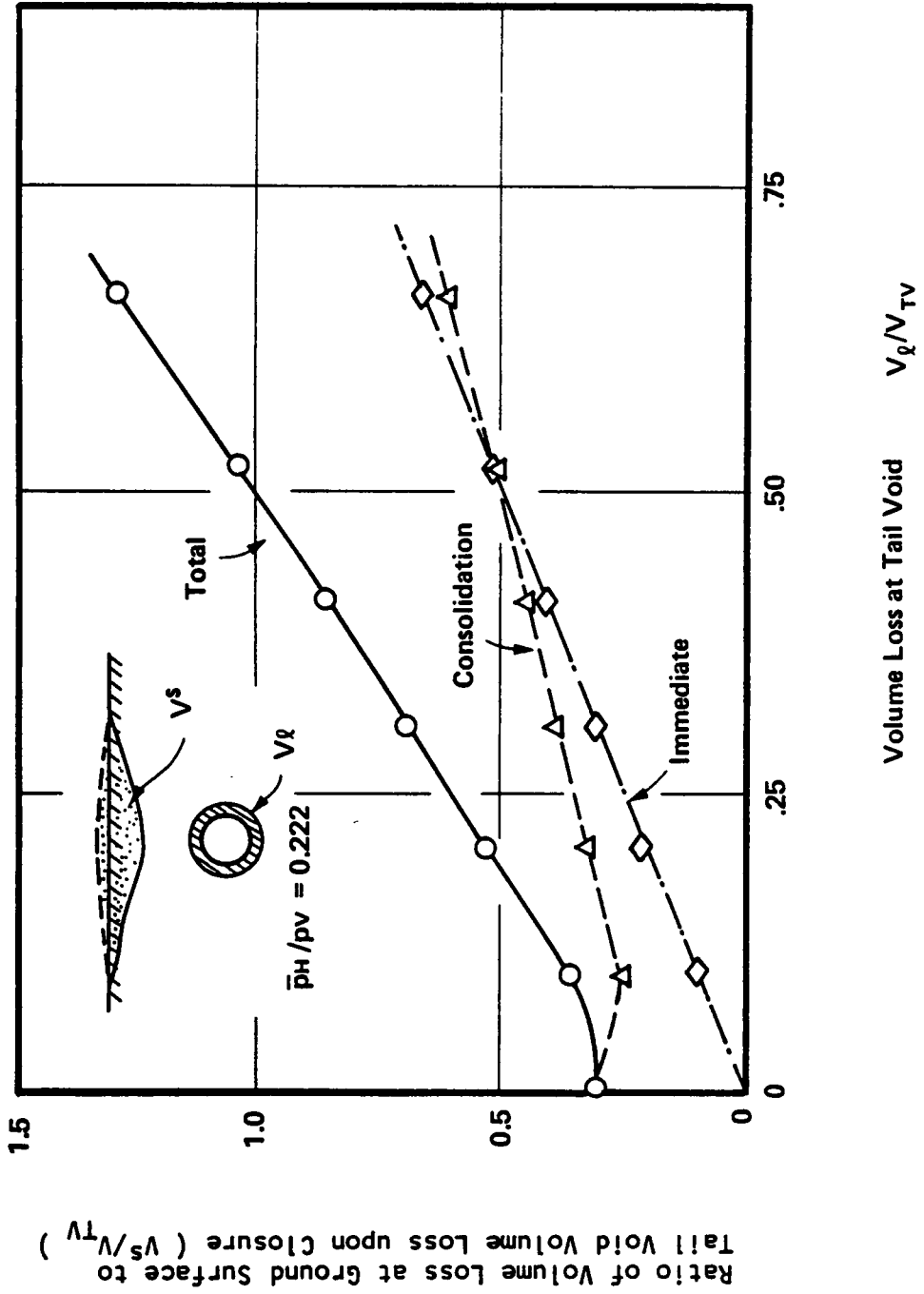


Figure 8.17 Variation of Ratio of Volume Loss due to Surface Settlement to That Occurred upon Tail Void Closure

## Chapter 9

### EFFECTS OF DIFFERENT PROCEDURES FOR MODELING ADVANCED SHIELD TUNNELING

#### 9.1 Introduction

The process of the FEM analysis of shield tunneling involves not only careful modeling of the soil behavior, but also a proper means of simulation of the tunneling processes. The latter of the two problems is addressed in this chapter. Simulation of the tunneling processes is complicated by the facts that the modeling is done in two dimensions, although it is to a degree three dimensional, and that portions of the problem are indeterminate. For example, if an advanced shield causes heaving in the soil, it is a result of a volume balance (soil excavated vs shield advance), and the volume balance is along the longitudinal axis of the tunnel. The analysis only addresses the transverse effects of the volume balance. Thus the project is reduced to simulating the effect of the process, and not the process itself. The tail void-grouting problem is also very difficult to rigorously quantify. First, we do not even know exactly how to quantify a soil which closes in to the void upon shield advance, nor how effective the grouting is in pushing the soil back away from the shield. To solve these issues leads to the use of trial techniques tempered by engineering judgement.

#### 9.2 Loading Models for Heaving and Tail Void Closure Stages

There are five loading stages in the analysis of the advanced shield tunnel construction as was shown in Figure 8.2. The modeling procedures

for the initial stress setup, the liner installation and consolidation are almost self-determined, whereas methods to simulate the heaving effect caused by the shield, and the closure of the tail void with the attendant void grouting have not yet been properly defined.

Ground movements during the heaving stage are usually simulated in FEM analyses by applying a radial heaving pressure to the periphery of the tunnel opening. Tail void closure is usually modeled by applying an unloading pressure which reduces the stress on the shield periphery. The different types of these pressure distributions to be discussed herein are shown in Figure 9.1. Those on the left half are used in the tunnel analyses for the N-2 project and extended parametric studies in the last two chapters. Those on the right half were employed by Finno (1983) in his tunnel analyses. His predicted ground movements agreed well with the observed data in the field except in the case of movements close to the tunnel during the tail void closure.

The heaving pressure distributions used for this work (II) and that of Finno (1983) (I) are very similar except in their magnitudes at the springline and directions near the crown or invert. Under the same average heaving pressure, the pressure at the springline for distribution II is smaller by about 27 percent than for distribution I. Also, the pressure for I is normal to the shield perimeter, but the direction of the heaving pressure near the crown/invert deviates from the normal for II. The latter approach is designed to reflect the effects of normal pressure and the shearing stress components which act on the tunnel opening.

Finno (1983) applied a simple, radial uniform unloading pressure in an attempt to simulate the soil movements during the tail void closure. Herein, an oval distribution of unloading pressure to the shield is used (Figure 9.1(b)). The ratio of the pressure at the crown to that at the springline is two. The basis for this choice lies in the appreciation of certain facts, and the use of engineering intuition. First, it is known that the tail void is actually a nonuniform gap. Due to the nature of the shield tunneling process, the gap is the largest in the crown and invert areas and smaller on the sides. Thus, the closure must be larger in the crown and invert areas than on the sides. Second, all efforts to model tail void closure using a uniform pressure have failed to yield satisfactory predictions. Thus, a nonuniform pressure distribution is a logical choice, and the one chosen herein is simple to apply and reasonably fits the criteria to generate the expected relative closure levels needed around the tail void.

Analytical procedures other than modeling of the heaving and the tail void closure are exactly the same as those used by Finno (1983). Conditions and soil properties for these analyses are the same as those used in the N-2 analyses of Chapter 8, although out-of-plane drainage is not used for simplicity.

### 9.3 Predicted Ground Responses Obtained from Different Procedures

#### 9.3.1 Lateral Displacement Profile

At the completion of heaving the lateral displacements shown in

Figure 9.2 are obtained for the proposed method (II) and Finno's method (I). For comparison, the field data from the N-2 case are also plotted. The two predicted heaving patterns are not greatly different and both agree reasonably well with the observed data. Looking at the details, the heaving deflection in the Bay Mud is predicted slightly better by the new method (II).

Contrary to the heaving stage, the procedures of this investigation and those of Finno (1983) lead to a definite difference after the tail void is closed (Figure 9.3). The two predictions of ground movements utilize the same average unloading pressure in simulating the tail void closure. However, only the displacements obtained in the new method agree well with the observed data. Therefore, the new method with an oval distribution of the unloading pressure is felt to be more appropriate than that of the uniform distribution.

### 9.3.2 Surface Movements

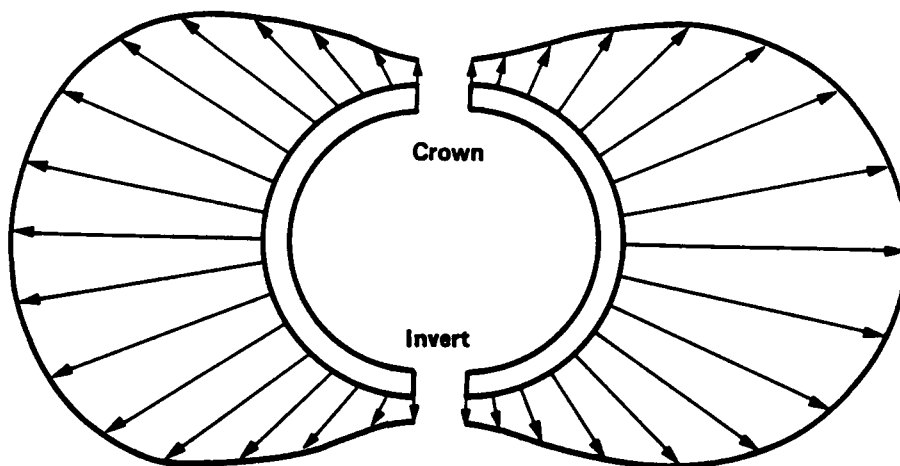
Figure 9.4 shows variations of predicted and observed centerline surface settlement curves with time up to 300 days after the shield passage. While the two predicted settlement curves show similar trends, the results based on the proposed method are in slightly better agreement with the observed data than the other method's results are. The relative lack of influence of the method of tail void closure on the centerline surface settlement reflects the fact that this point is far enough away from the tunnel to be significantly influenced by details of the modeling of the tail void problem. This is particularly true since in both cases about

the same amount of void closure was achieved at the crown of the tunnel.

While the centerline surface settlement is not strongly influenced by the different tail void closure, the shape of the surface settlement trough is. Figure 9.5 shows the comparison between the results obtained by the different loading procedures. The trough profile predicted by the uniform unloading pressure is not in good agreement with the observed data. It exaggerates the settlement trough. On the other hand, the trough predicted by the new method demonstrates a very good fit with the observed data.

#### 9.4 Summary and Conclusions

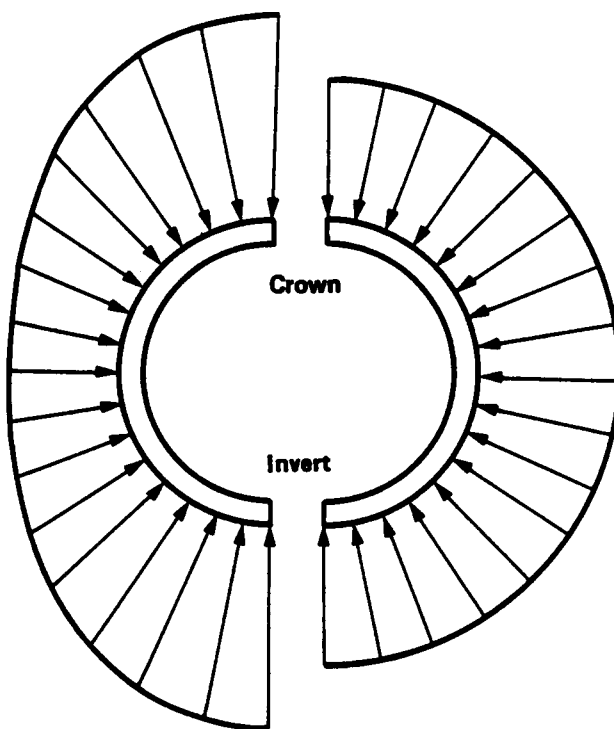
The importance of proper loading procedures for simulating the heaving and tail void closure stages is described. Two different methods to model these loading stages are examined, one of which is new to this thesis and is employed in Chapters 7 and 8 for the analyses of the N-2 project and the extended parametric studies, respectively. The results obtained from the new method demonstrate good predictions relative to the observed data. Therefore it is concluded that the new procedures for modeling the heaving and the tail void closure is effective in providing accurate predictions of the ground behavior due to advanced shield tunneling.



**Heaving Pressure II  
(Present Work)**

**Heaving Pressure I  
(Finno 1983)**

**(a) Heaving Pressure Distribution**



**Oval Unloading Pressure  
(Present Work)**

**Uniform Unloading Pressure  
(Finno 1983)**

**(b) Unloading Pressure Distribution to Stress Relief at Tail Void**

**Figure 9.1 Different Types of Pressure Distribution Simulating Heaving and Tail Void Closure**

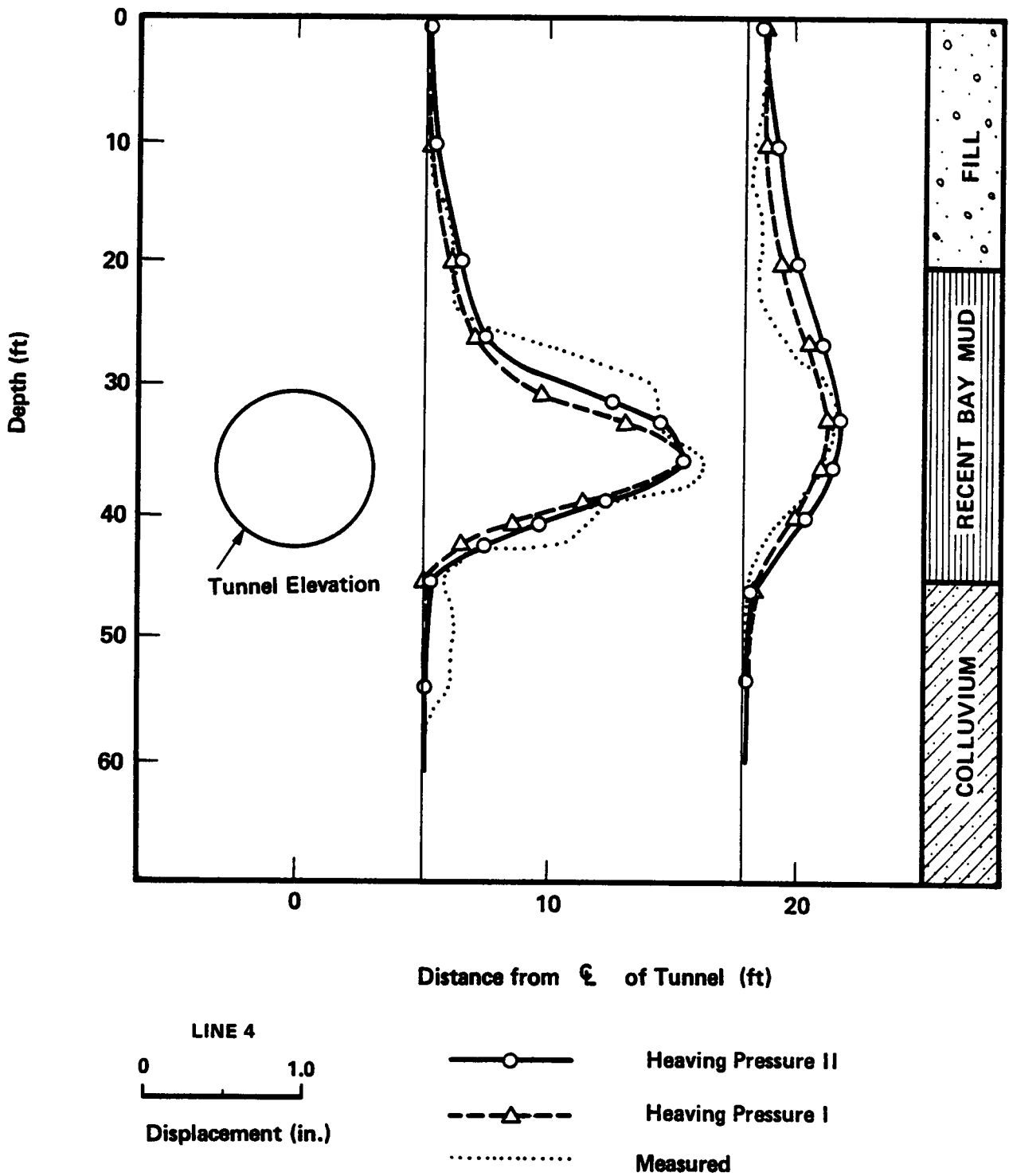


Figure 9.2 Comparison of Lateral Displacements after Heaving between Proposed and Other Loading Methods, Line 4

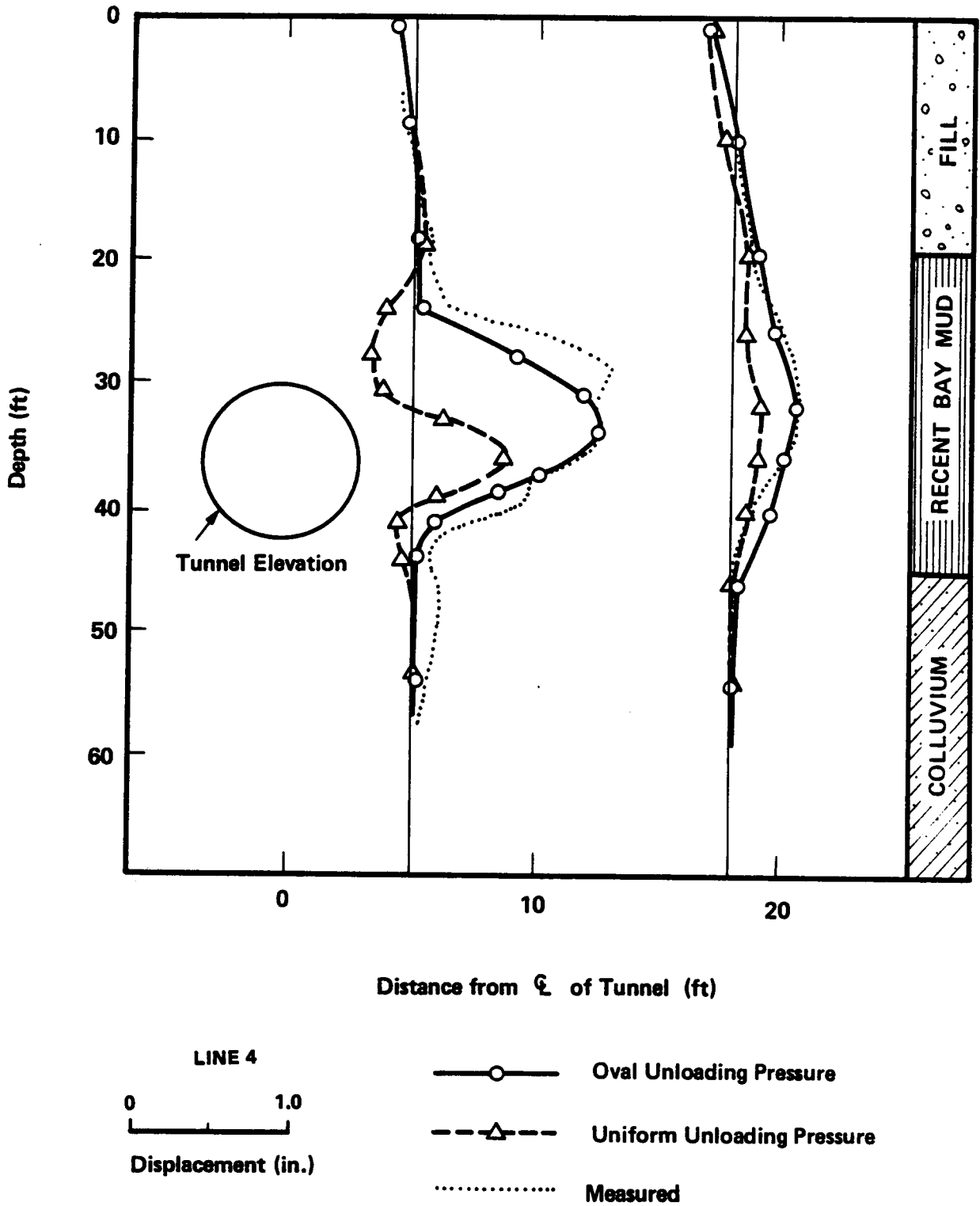


Figure 9.3 Comparison of Lateral Displacements after Tail Void Closure between Proposed and Other Loading Methods, Line 4

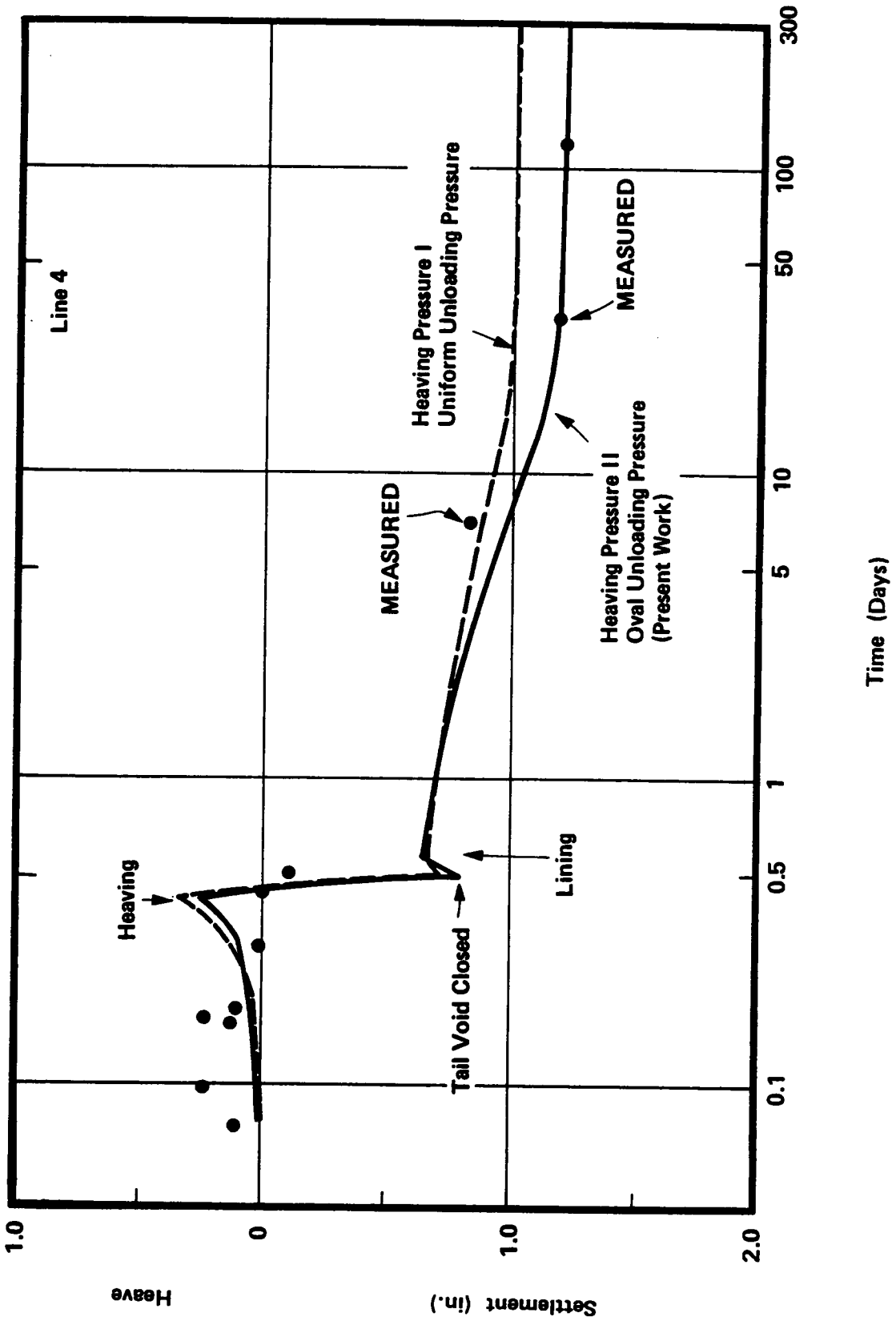


Figure 9.4 Comparison of Centerline Surface Movements between Proposed and Other Loading Methods, Line 4

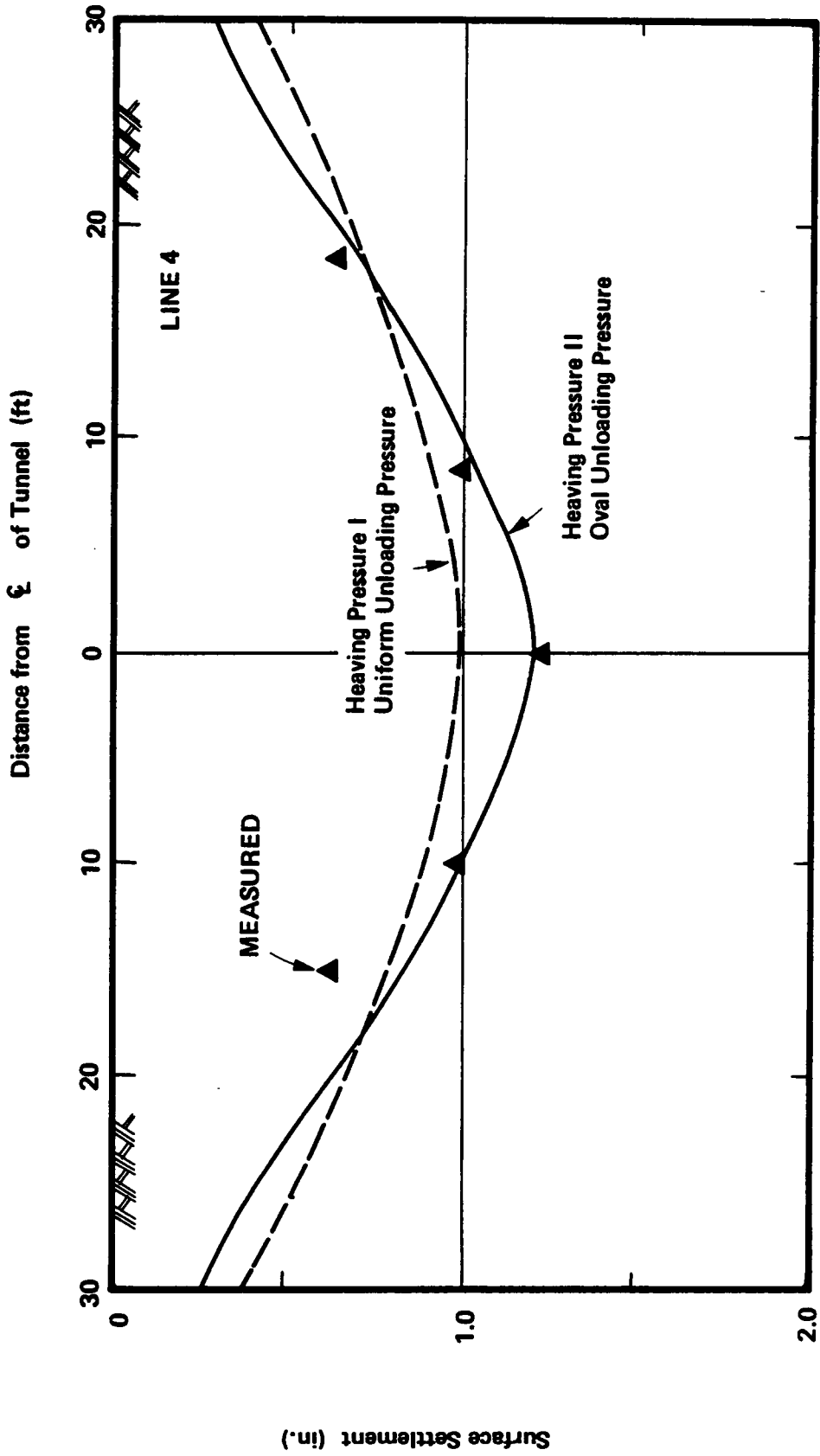


Figure 9.5 Comparison of Shapes of Surface Settlement Trough between Proposed and Other Loading Methods, Line 4

## Chapter 10

### COMPARISON OF RESULTS PREDICTED WITH DIFFERENT TYPES OF SOIL MODEL

#### 10.1 Introduction

To this point in this thesis, the Prevost soil model has been used. In previous analyses of soil tunneling by other authors, many different types of soil models have been used, and in most cases reasonable predictions for some aspects of tunnel behavior have been obtained. This raises a number of questions:

1. What effect does the type of soil model used have on predicted behavior?
2. Are certain aspects of tunneling induced movements not sensitive to the soil model? If so, which ones?
3. Is the type of soil model significant in the prediction of advanced shield tunnel processes?

To answer these questions, finite element analyses of the N-2 tunnel project are examined using two models with different characteristics from the Prevost model. The analyses are directed at Line 4 of the N-2 tunnel project since the behavior monitored there was the most complete obtained in this case history (Clough, et al. 1982a).

Two models which are widely used in geotechnical applications are considered in the comparative study. One is a simple total stress, nonlinear elastic model which uses variable moduli in an elastic formulation to simulate nonlinearity. The other is the well-known Cam Clay approach which was used extensively by Finno (1983) in his study of the N-2 project. In the case of the Cam Clay model, the results of Finno (1983) are used directly.

In the nonlinear pseudo-elastic model, a hyperbola approximates the primary loading stress-strain curve, and an equation for the slope of this curve defines the tangent modulus of elasticity. Failure is characterized by lowering the elastic modulus to a very small value; failure conditions are defined by the Mohr-Coulomb criteria. The basic idea for this model was originally proposed by Duncan and Chang (1970), although the version used here is a variation of that model developed by Hansen (1980), who incorporate an anisotropic response of clay. Only total stress conditions are considered in this case.

The Prevost and Cam Clay models are elasto-plastic models in contrast with the nonlinear elastic model. Although these models are both based on an effective stress analysis with the critical state concept (Schofield and Wroth 1968), they apply different hardening rules: kinematic and isotropic hardening, respectively. The kinematic hardening rule allows for a smooth yielding of the soil under reversal loading, while in isotropic hardening only an elastic response is observed.

Soils around a tunnel are subject to loading reversal during advanced shield tunneling as the loading moves from heaving to closure of the tail void. From the theoretical view point, the Prevost model would appear to be preferable for such stress conditions; however, it is not known what differences actually exist in the results of the analysis when the different models are used.

As much as possible, similar analytical conditions and procedures in tunnel simulation are adopted for the three model cases so that the results

may be compared easily.

## 10.2 Brief Description of Soil Models

A variation of the nonlinear pseudo-elastic Duncan-Chang model (Hansen model) and the Cam Clay model are introduced.

### 10.2.1 Nonlinear Anisotropic Pseudo-elastic Model

The nonlinear pseudo-elastic model presented by Duncan and Chang (1970) uses a hyperbolic curve to approximate the primary loading stress-strain curve. Parameters which characterize the curve are determined from triaxial compression test results. By differentiating the hyperbolic stress-strain relation a tangential modulus is obtained in terms of the current shear stress level. Allowances are also made for the effects of confining pressure and failure.

This approach was extended by Hansen (1980) to allow for an anisotropy of clays following the experimentally observed loading response of clays (Figure 10.1). It allows stress-strain data to be implemented in simple forms with a few extra parameters over the conventional Duncan-Chang version. It can be readily used in a finite element analysis of a wide variety of undrained loading problems in clays. Hansen applied the model in FEM analyses of the response of excavations in clays supported by a braced wall, and obtained reasonable behavior. This model is used for the analyses herein with only minor modifications.

Hansen's model has several important features beyond the Duncan-Chang

model. Quite importantly, it includes anisotropic behavior. The anisotropy is linked to the angle of the major principal stress reorientation,  $\beta$ , during loading. For in situ initial stress conditions, the major principal stress  $\sigma_1$  is in the vertical direction. In loading, additional stresses are induced to alter the direction of  $\sigma_1$  from the vertical. Therefore, the reorientation angle,  $\beta$ , is measured from the vertical to the new  $\sigma_1$  orientation. Anisotropy of both the shear strength and the modulus is defined in terms of  $\beta$ .

Figure 10.1 illustrates the stress-strain curves of the triaxial test for the phases of loading compression ( $A \rightarrow R$ ) and unloading ( $R \rightarrow E$ ). During the compression the major principal stress lies in the vertical direction and this leads to  $\beta = 0^\circ$ . In contrast, a 90 degree reorientation of the major principal stress occurs in the extension test because the lateral pressure exceeds the vertical at point B. The stress-strain curves of compression ( $\beta = 0^\circ$ ) and extension ( $\beta = 90^\circ$ ) loadings are the basic relationship in Hansen's model, and they are approximated by means of hyperbola as depicted in Figure 10.1. They are defined by a simple equation:

$$2|\bar{q} - \bar{q}_0|_\beta = \frac{\gamma_{max}}{\frac{1}{E_{i\beta}} + \frac{R_f \cdot \gamma_{max}}{(|\bar{q} - \bar{q}_1|_f)_\beta}} \quad (10.1)$$

where  $\beta$  has a value of 0 or 90.

The variation of undrained shear strength is defined by the equation proposed by Bishop (1966),

$$s_{u\beta} = s_{u0} (1 - A_s \sin^2\beta)(1 - B_s \sin^2 2\beta) \quad (10.2)$$

Hansen notes that values of the ratio of strength in the extension test  $\beta = 90^\circ$  to that in the compression test  $0^\circ$ ,  $K_s$ , vary from 0.22 to 0.76. Normally consolidated clays with a low plasticity index are more anisotropic than clays with a high plasticity index. For Bay Mud, Hansen (1980) gave a  $K_s$  value of 0.76, which means that the undrained strength of the Bay Mud is not very anisotropic.

The ratio of initial modulus for  $\beta = 90^\circ$  to that for  $\beta = 0^\circ$  is termed the anisotropic modulus ratio  $K_E$ . Values of  $K_E$  vary from 0.69 to 2.0 for most clays, with the majority being 1.2 or larger. A value of 1.25 was used in the tunnel analyses.

In the Hansen model, the tangent modulus is computed from the slope of the hyperbolic curve analogous to the Duncan-Chang approach. Expressions for the tangent moduli for  $\beta = 0^\circ$  and  $\beta = 90^\circ$ , or  $E_{t0}$  and  $E_{t90}$  are

$$E_{t0} = E_{i0} \left( \frac{1}{E_{i0}} + \frac{R_f \gamma_{max}/2}{2(s_{u0} - q_i)} \right) \quad (10.3)$$

$$E_{t90} = E_{i90} \left( \frac{1}{E_{i90}} + \frac{R_f \gamma_{max}/2}{2(s_{u90} + q_i)} \right) \quad (10.4)$$

where  $R_f$  is the strength factor relating the asymptotic hyperbolic principal stress difference to the actual principal stress difference at failure.  $R_f$  is assumed to be independent of rotation angle  $\beta$ . The maximum shear strain,  $\gamma_R$ , is used as the strain parameter because it affords a measure of the total amount of shear distortion, independent of the stress or strain conditions. Thus, it provides a consistent parameter for any  $\beta$  imposed by any change in stresses. Further, it is noted that the value of the principal stress difference is referenced to the initial anisotropic

state of stress,  $(\bar{q} - \bar{q}_i)$ , but undrained strength is referenced to a value of zero principal stress difference,  $s_{u_0}$  or  $s_{u_{90}}$ .

Finally, in the Hansen model, the variation of tangent modulus is described as follows with a parameter  $A_E$  normalized by  $E_{t_0}$  and  $E_{t_{90}}$ :

$$(E_{t\beta} - E_{t_0}) / (E_{t_0} - E_{t_{90}}) = \sin^2\beta + A_E \sin 2\beta \quad (10.5)$$

$A_E$  can be -0.20 to -0.25. A summary of all the model parameters established for the Hansen model for Bay Mud are shown in Table 10.1.

Although the Hansen model effectively accounts for anisotropy, for a virgin stress paths starting from the initial stress condition, once loading reversal is encountered, it simply reverts to linear elasticity. Such a response is not realistic for tunnel analyses, and for this reason the model's response to loading reversals is changed for this work such that the stress-strain curve is approximated by a hyperbola whose asymptotic value is the shear strength  $s_{u(90-\beta)}$  in equation 10.2.

Stress level is defined for the nonlinear elastic model as a ratio of mobilized shear stress to marginal shear strength over the initial shear stress:

$$\eta_H = \frac{\bar{q} - \bar{q}_i}{s_u - \bar{q}_i} \quad (10.6)$$

where  $\bar{q} = (\sigma_1^T - \sigma_3^T)/2$ .  $\bar{q}_i$  is an initial value of  $\bar{q}$ . In the above equation  $\bar{q}$ ,  $\bar{q}_i$  and  $s_u$  are used after modification of the principal stress rotation.

### 10.2.2 Cam Clay Model

The Cam Clay model is a rate-independent, isotropic, elasto-plastic, nonlinear, effective stress soil model. The version to be used in this chapter is the so-called modified Cam Clay model (Roscoe and Buland 1968), which is minor variant of the original Cam Clay model developed over a 20 year period at Cambridge University. In this theory, the state of stress in a soil element is defined by the soil's void ratio  $e$ , the mean effective normal stress  $p$ , and the octahedral shear stress  $q$ . As it is an elasto-plastic model, the soil response is governed by the specification of a yield surface, the flow rule and hardening rule analogous to that for the Prevost model.

The model applies an elliptic yield surface defined by

$$\frac{q^2}{M^2} + P(P - P_c) = 0 \quad (10.7)$$

where  $p_c$  is the preconsolidation pressure and  $M$  is a slope of projection of the critical state line onto the  $p - q$  plane. The yield surface is shown in Figure 10.2. The associative normality flow rule is employed. The plastic volumetric strain  $\epsilon_v^p$  is selected as a hardening parameter which controls the isotropic expansion of the yield surface in conformity with the soil's isotropic consolidation response.

The Cam Clay model is fully established if the following five parameters are defined:  $\lambda$  and  $\kappa$ , the slopes of the virgin line and rebound line, respectively, for the isotropic consolidation test;  $M$ , the slope of the critical state line in  $p - q$  plane;  $G$ , the elastic shear modulus; and,  $e_{cs}$ , the critical void ratio for unit pressure. Johnston (1981)

combined the Cam Clay model constitutive law with the pore fluid flow equation so that pore pressure change may be taken into consideration. Thus, it becomes possible to evaluate consolidation due to the excess pore pressure dissipation, which is important in soil response to tunneling. Finno (1983) defined Cam Clay model parameters for the San Francisco Bay Mud, summarized in Table 10.2. No new analyses with the Cam Clay model were carried out in this research; rather the results of Finno (1983) are used directly.

Although differences between the Cam Clay model and the Prevost model have been described in Section 3.1, major differences are reviewed briefly here. The Prevost model used the same type of volumetric hardening principle as the Cam Clay model does because they are both founded on the critical state concept. Both use similar elliptic yield surfaces, but the Prevost model has many yield surfaces so that it can express more precisely complicated behavior particular to soils. While the Cam Clay model is based on the associative normality flow rule, the Prevost model applies the nonassociative flow rule. The nonassociativity concept is introduced to improve the ability to predict the pore pressure development which is generated in the soil due to shear. As the Cam Clay model applies an isotropic hardening rule, the yield surface expands in any direction as the soil hardens. Within the region enclosed by the yield surface, the soil element acts as elastic. However, this is not realistic if a loading reversal occurs. This defect was addressed by applying the kinematic hardening rule in the Prevost model. Combining multi-yield surfaces with the kinematic hardening rule, the Prevost model predicts a plastic flow

from the very beginning of a loading reversal.

### 10.3 Conditions in Tunnel Analysis

Most of the conditions employed here in the N-2 tunnel analysis are the same as those used in Finno's analysis (1983) so that his results may be fairly compared.

The finite element mesh is the same one shown in Figure 8.1 except for the case with a nonlinear elastic model. Unlike the Prevost or Cam Clay models which use eight node quadrilateral elements (Q8), the nonlinear elastic model uses five node quadrilateral elements (Q5). Differences in the geometry of the meshes are expected to have a negligible effect on the outcome of the study.

Of course, it is difficult to insure that material properties of the Bay Mud for different soil models are consistent. A basic assumption is introduced to bridge the problem, namely, that the Bay Mud is a clay with normalized properties. Thus, the undrained strength of the Bay Mud and its moduli increases with an effective overburden pressure.

As in the preceding chapters of the N-2 tunnel analysis, the ordinary Duncan-Chang soil model is employed for the overlying fill and underlying colluvium layers for all analyses. Their material properties are shown in Table 10.3. Drained conditions are assumed to apply.

Loading procedures, which simulate tunnel construction sequences in advanced shield tunneling, are the same as those that Finno used in his

work. Although the last chapter showed that it might not be the best loading procedure, it is used in order to maintain consistency. A uniformly distributed unloading pressure is applied to model the tail void closure. The tail void is considered closed when the inward movement of the soil at the crown reaches the size of the tail void gap, which was 3 inches for the N-2 tunnel case. Pressure distributions are shown on the right half of Figure 9.1. Overall loading procedures for tunnel construction simulation at Line 4 of the N-2 project are indicated in Table 10.4. The analyses with the Prevost model required the finest division of incremental loading so that numerical problems such as instabilities were avoided in the course of the loading.

#### 10.4 Comparison of Predicted Ground Response

Results of the ground response to the shield tunneling analyzed using the three soil models are described. Effects of applying different soil models are being investigated, and comparisons are made focusing on the soil behavior to figure out the effectiveness of each model. These involve displacements, surface settlements, pore pressure development, and mobilized stresses in the ground.

##### 10.4.1 Lateral Displacements

Lateral displacements of the ground are calculated from the results of the analyses at the locations where the inclinometers were placed to the side of the tunnel, about 7 feet (2.1 m) and 18 feet (5.5 m) from the centerline. Figure 10.3 illustrates the predicted ground movements

by the three soil models after the completion of the heaving stage. Field observation data are also shown for comparison. The maximum deflection at the springline coincides in all cases since this is a fixed calibration point so that the magnitude of the heaving pressure is defined to complete the heaving stage. The results are not unreasonable for any of the models, except that the nonlinear elastic model definitely overestimates ground movements at the farthest inclinometer line.

A more careful observation shows that the vertical extent of the deflections at the closest inclinometer increases in the order of the Prevost, Cam Clay, and nonlinear elastic models. There are small differences here because a form of unloading occurs. To the side of the tunnel in the springline vicinity, the heaving increases the lateral stress while the vertical stress is relatively unaffected. This causes the shear stress level to decrease and unloading conditions are thereby created. In this case the Cam Clay and nonlinear elastic models act as a simple elastic material, while the Prevost model accounts for the plastic flow from the beginning of shear stress reduction. This leads to differences in the predicted behavior. Elastic behavior provides a wider vertical extent of the deflection.

The same trend is found at the farthest inclinometer line. The smallest displacements are predicted by the Prevost model, whereas the largest by the nonlinear elastic model. An elastic soil response produces a broader influential area and ends up with a slower degradation of lateral displacement with increasing distance from the tunnel. This is shown in Figure 10.4 in comparison for the three soil models. The Prevost model

yields the most realistic prediction.

Lateral displacements after the tail void closure are compared in Figure 10.5 for the three cases. In view of the distribution of displacements in the Bay Mud, none of the predictions are close to the observed data at the nearest inclinometer location. A better agreement is obtained at the farthest inclinometer but the differences remain. The problems here lie in the fact that the method used to simulate the tail void closure by applying uniform unloading pressure is not consistent with the field situation. This shows that no soil model accurately predicts the behavior close to the tunnel when the field loadings are incorrectly modeled. However, it is notable that the "error" diminishes with the distance from the loading so that at the outermost inclinometer reasonable agreement is obtained.

Figure 10.6 shows the deformation of the tunnel periphery during the heaving and tail void closure. The figure demonstrates movements of soils close to the shield during the heaving and tail void closing processes. Note that, as designed, inward movements of the soil at the crown reached about three inches to close the tail void. The largest downward movement occurred at the crown and the displacements at the springline remained in the outward deflection for all the cases.

#### 10.4.2 Ground Surface Movements

Upward heaves and subsequent settlements of the ground surface directly above the tunnel centerline are shown in Figure 10.7. The surface movements

predicted for the three models are plotted against the time elapsed for the actual construction work covering the entire tunneling process. The observed data are also shown.

The Prevost and Cam Clay models yielded similar predictions for every construction stage, whereas the nonlinear elastic model provided unique results. The nonlinear elastic model significantly overestimated the initial heave, and the final settlement was too small compared to the observed data. This latter problem is related to the fact that the nonlinear elastic model did not incorporate the consolidation effects. Both the Prevost and Cam Clay models provided good predictions for surface movements.

Measured and predicted values of the surface settlements for a transverse section at a period of 150 days following the shield passage are given in Figure 10.8. The hyperbolic model poorly predicts the settlements. This is primarily due to the fact that it overpredicted the initial heave and was unable to account for the consolidation effects. The Prevost and Cam Clay models are found to reasonably predict settlements within a range of observed data, but in both cases the extent of the settlement trough is slightly overpredicted, and the curvature is not in full agreement with that observed. The reason for the overprediction lies, in part, in the incorrect simulation of the tail void closure process. As shown in earlier chapters, a nonuniform tail void closure leads to more reasonable predictions.

### 10.4.3 Variation of Pore Pressure and Stress Levels

It is useful to consider the distribution of excess pore pressure and stress levels around the tunnel for the different soil models. It is noteworthy that stress level is defined in different ways for the nonlinear and elasto-plastic soil models. The nonlinear elastic model employs the principal stress difference to define the stress level, while the Prevost and Cam Clay model use deviatoric stress to measure the distance to the critical state. Thus, a direct comparison between predicted stress levels is not always possible, but the variation of stress levels can be compared.

Figure 10.9 shows stress level distributions after heaving for the three models. An area with low stress levels is found at the vicinity of the springline for all. As mentioned before, this is due to the fact that the heaving pressure increases the confining pressure of the soils in that area, thereby reducing stress levels. On the other hand, the heaving pressure increases the shear stresses at the crown and the invert making the stress levels there higher. This is found in the results for all three soil models.

Excess pore pressure developments for the Prevost and Cam Clay models after heaving are shown in the left half of Figure 10.10. The basic features are similar for the two cases, but the extent and the magnitude of pore pressures are larger for the Prevost model. For example, excess pore pressure at the springline is about 40 percent higher for the Prevost model than for the Cam Clay model. This is related to the fact that the soil in the Prevost model behaves plastically, accounting for a pore pressure

development due to shear, while in the Cam Clay model the soil goes into an elastic phase near the springline.

The effect of the tail void closure in terms of excess pore pressure distributions is given in the right half of Figure 10.10. Negative excess pore pressure develops at the crown and the invert for both cases. The only obvious difference is found near the springline, where the excess pore pressure is smaller for the Prevost model than for the Cam Clay model. The excess pore pressures developed at this stage are responsible for the subsequent consolidation settlements. These settlements for the Cam Clay model case are larger and take a longer time than for the Prevost model, as depicted in Figure 10.7.

Stress levels after the tail void closure are shown in Figure 10.11. Different distributions of stress levels are obtained for the three models. Soils reach failure in the shear zone for the nonlinear elastic model, at locations beside the tunnel 45 degrees from the springline for the Prevost model, and at the crown for the Cam Clay model, respectively. However, regions with a high stress level are limited to an area just within the vicinity of the tunnel for all cases.

Stress level distributions for the Cam Clay and Prevost model end up with similar patterns when the consolidation stage is completed, as shown in Figure 10.12. As excess pore pressure is dissipated with time, the effective mean pressure increases and volumetric strain grows. Then the volumetric hardening is mobilized and the yield surfaces expand, leading to reduced stress levels.

#### 10.4.4 Stress Paths

Variation of the stress state is easily pictured by means of the stress path. Conventional stress paths of soil elements adjacent to the crown, springline and invert are shown in Figures 10.13 and 10.14. Effective stress paths are compared between the results for the Prevost and Cam Clay models. Total stresses are calculated by adding pore pressure on the effective stresses obtained from the Prevost model analyses so that they can be compared with the stress path predicted by the nonlinear elastic model. The conventional stress path is useful to envision the effects of stress reversals (Lambe and Marr 1979), although the intermediate principal stress is not involved in this case (Pender 1980).

General patterns of the stress path found in the figures as follows. Soil above the crown and below the invert respond in a similar manner. Heaving induces increased shear and causes the soils to move towards failure (pt. H). As the tail void is closed, the soils in these areas undergo a reduction of vertical stress and a principal stress rotation of 90 degree (pt. H). Liner installation and consolidation, pts. L and C, cause only slight changes in stresses. The soil at the springline undergoes two reversals of principal stresses during the heaving and tail void closure stages. The heaving pressure increases confining pressure of the soil to reach the stress condition at pt. H. The large reduction of horizontal stress during tail void closure causes a reduced compression stress state at pt. T in the soil, and there is a second principal stress reorientation. Subsequent loadings slightly increase the mean pressure without large changes in shear stress.

When Figure 10.13 is used to compare effective stress paths obtained for the Prevost and Cam Clay models, it is found that in spite of similar stress variations during the heaving stage, the stress path obtained for the Prevost model in the subsequent stages stays to the left of that for the Cam Clay model and exhibits smaller shear stresses. This is explained by the fact that the magnitude of the unloading pressure to close the tail void was smaller by 18 percent for the Prevost model than for the Cam Clay model (Table 10.4).

The  $K_0$  lines above and below the hydrostatic axis are shown in Figure 10.13. The region within these lines can be considered as an elastic region for the Cam Clay model. An effective stress path with elastic response to undrained shear which does not alter their effective mean pressure significantly is represented by a line close to the vertical. The stress paths predicted by the Cam Clay model are close to the vertical except at the top and bottom ends where the stress paths deviate from the vertical because of plastic flow involved. In contrast to the stress paths of the Cam Clay model, that of the Prevost model moves to the left, and the mean stresses predicted by the Prevost model are smaller than those predicted by the Cam Clay model, particularly at the crown and the invert.

Figure 10.14 compares total stress paths obtained from the Prevost and nonlinear elastic model analyses. They do not agree closely but show the same general trends.

## 10.5 Summary and Conclusions

In order to develop the proper finite element modeling procedures which enables the prediction of the ground response associated with advanced shield tunneling, an adequate soil model must be used to obtain realistic soil behavior. Three soil models were examined herein and the predictions were checked where possible using the field observed data for the N-2 project.

According to the predicted lateral displacements and the surface settlement profiles, the Prevost model and the Cam Clay model yielded similar results for the long term settlements with consolidation effects, whereas the nonlinear elastic model provided poor prediction. This model is considered inadequate for an advanced shield tunneling because: (1) it overpredicts the initial heave as shield approaches; and, (2) it is based on the total stress approach and cannot simulate the pore pressure changes induced by tunneling.

Both the Prevost and Cam Clay models predicted the elasto-plastic behavior of the soil, but the predicted soil behaviors are different. Unloading conditions with reducing stress levels are created in certain areas during tunneling activities. In such a situation the Cam Clay model behaves elastic, whereas the Prevost model predicts a elasto-plastic response accounting for the yielding and excess pore pressure changes. This phenomenon appears in the variation of stress levels and stress paths.

As a whole, both the Prevost and the Cam Clay models yielded reasonable behavior trends. Either is suitable from a practical perspective to

use in simulation of advanced shield tunneling. However, the Prevost model predicts details of the soil response better than the Cam Clay model does.

Table 10.1 Material Parameters of Nonlinear Pseudo-elastic Model accounting for Anisotropy of Recent Bay Mud

		Recent Bay Mud
Poisson Ratio	$\nu$	0.49
Poisson Ratio at Failure	$\nu_f$	0.49
Failure Ratio	$F_R$	0.90
Anisotropic Strength Ratio	$K_s$	0.76
Undrained Strength		
Horizontal (psf)	$S_{U0}$	$130 + 0.235 \sigma'_v$
Vertical (psf)	$S_{U90}$	$99 + 0.179 \sigma'_v$
Anisotropic Modulus Ratio	$K_E$	1.25
Modulus Constant		
Horizontal	$K_0$	$0.166 S_{U0}$
Vertical	$K_{90}$	$0.274 S_{U90}$
Parameters for Anisotropic Strength Variation	$A_s$ $B_s$	0.234 0.077
Parameter for Anisotropic Modulus Variation	$A_E$	- 0.20
Modulus Exponent	$n$	0.0
Lateral Earth Pressure Coefficient	$K_0$	0.5
Total Unit Weight (pcf)	$\gamma_t$	105

Table 10.2 Material Parameters of Cam Clay Model for Recent Bay Mud (Finno 1983)

		Recent Bay Mud
Slope of Isotropic Rebound	$\kappa$	0.043
Slope of Isotropic Compression	$\lambda$	0.326
Void Ratio at Critical State and Unit Pressure	$e_{cs}$	3.72
Slope of Critical State Line $6\sin\phi / (3-\sin\phi)$	$M$	1.2
Modulus Multiplier ( $G/S_u$ )	$m$	120
Unit Weight (pcf)	$\gamma_t$	105
Normalized Factor	$c/p$	0.30
Coefficient of Permeability ( $K_H = 100k_v, F_t/\text{Day}$ )	$K_H$	0.28

Table 10.3 Material Parameters of Nonlinear Pseudo-elastic Model for Fill and Colluvium

		Fill	Colluvium
Poisson Ratio	$\nu$	0.30	0.35
Poisson Ratio at Failure	$\nu_f$	0.49	0.49
Failure Ratio	$F_R$	0.90	0.90
Effective Friction Angle (Degrees)	$\phi$	30	20
Cohesion (psf)	$c$	300	1000
Modulus Exponent	$n$	0.5	0.40
Modulus Constant	$K$	400	945
Lateral Earth Pressure Coefficient	$K_0$	0.5	0.8
Total Unit Weight (pcf)	$\gamma_t$	110	125

Table 10.4 Loading Conditions regarding to Tunnel Construction Stages for Different Types of Soil Model

Construction Stages	1	2 *4	3
Soil Model for Bay Mud	Prevost	Cam Clay	Nonlinear Elastic
Computer Program Used	JFSEST	JFEST (Finno 1983)	SOILSTRA (Hansen 1980)
Heaving			
No. of Loading Increments	20 steps	10 steps	10 steps
Average Heaving Pressure *1	1200 psf	1200 psf	1200 psf
Average Incremental Pressure	60 psf	120 psf	120 psf
Time Elapsed	10 hrs	10 hrs	-
Unloading			
No. of Loading Increments	23 steps	17 steps	13 steps
Average Release Pressure *2	1725 psf	2040 psf	1950 psf
Average Incremental Pressure	75 psf	120 psf	150 psf
Time Elapsed	1.7 hrs	2.5 hrs	-
Liner Activation			
No. of Loading Increment	7 steps	7 steps	5 steps
Time Elapsed	1.0 hr	1.0 hr	
Consolidation			
No. of Time Integration Steps *3	16 steps	21 steps	-
Time Elapsed	about 300 days	more than 1 yr	

\*1 Heaving pressure is distributed elliptically with the maximum pressure at spring line and the minimum at crown and invert.

\*2 Releasing pressure is distributed uniformly along tunnel periphery.

\*3 Time interval is increasing exponentially to plot evenly in logarithmic scale.

\*4 Reference to Finno 1983.

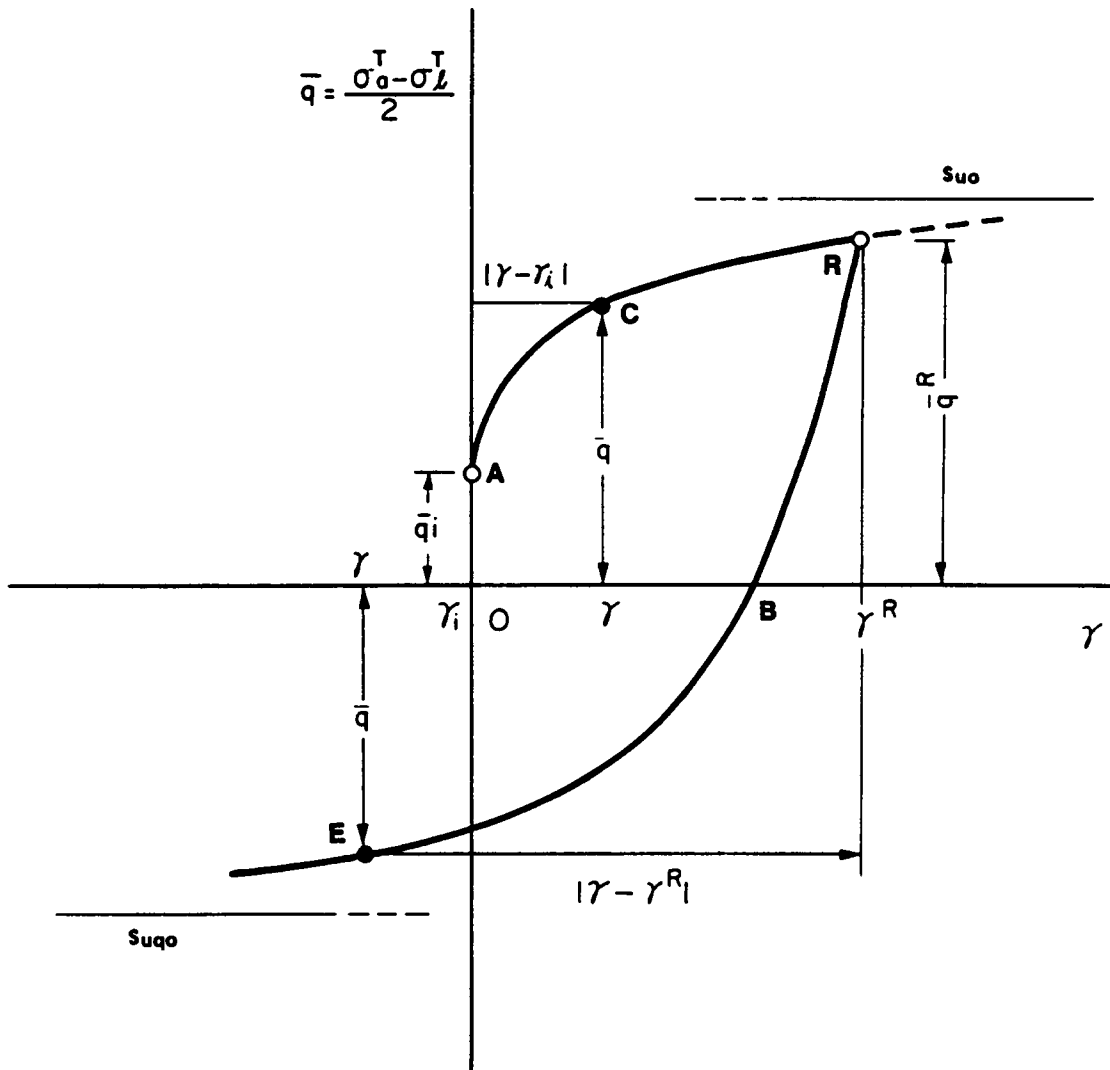


Figure 10.1 Hyperbolic Stress-Strain Approximation for Compression and Extension Tests for Nonlinear Pseudo-elastic Model

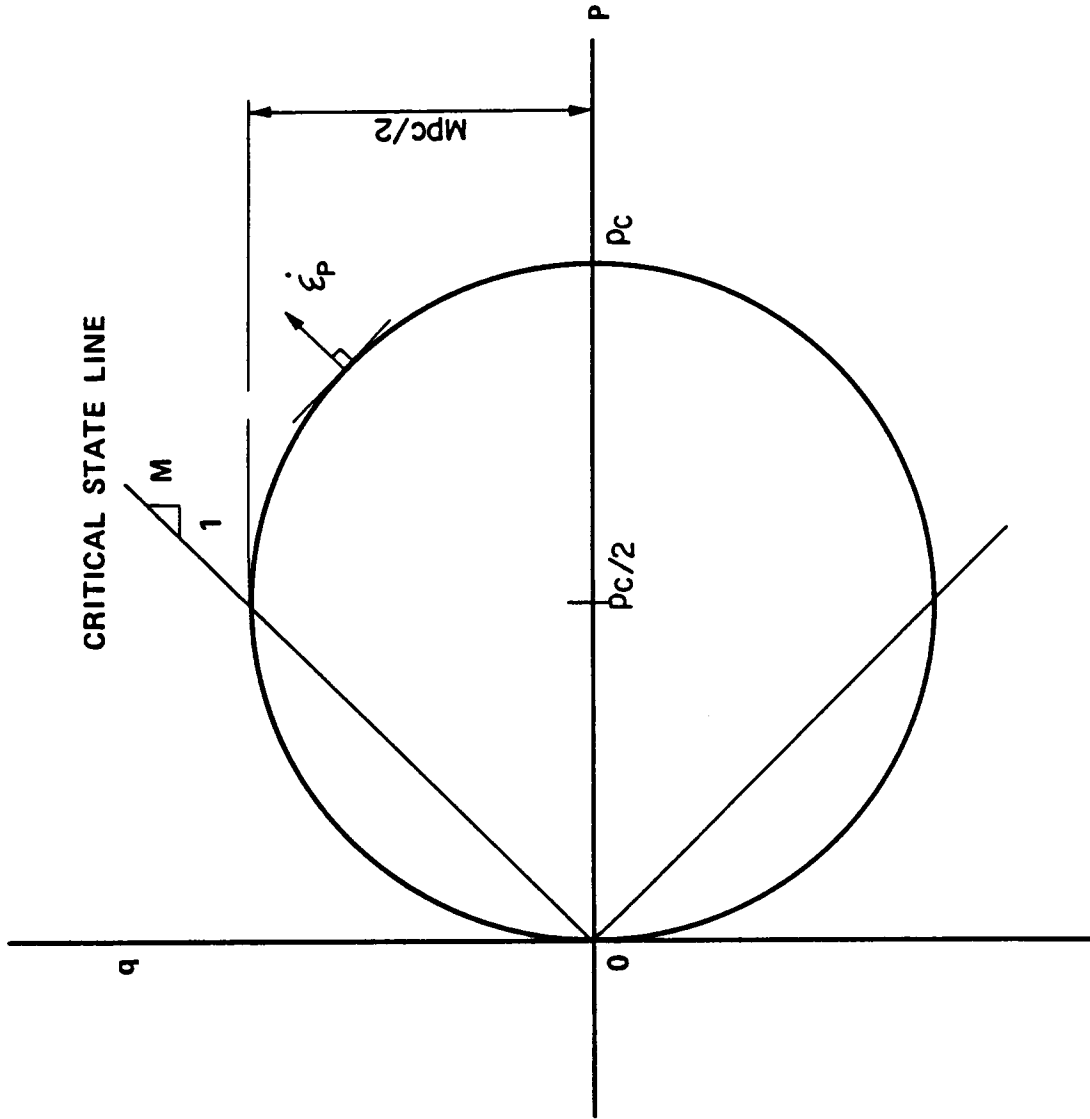


Figure 10.2 Yield Surface of Cam Clay Model in Triaxial Stress Plane

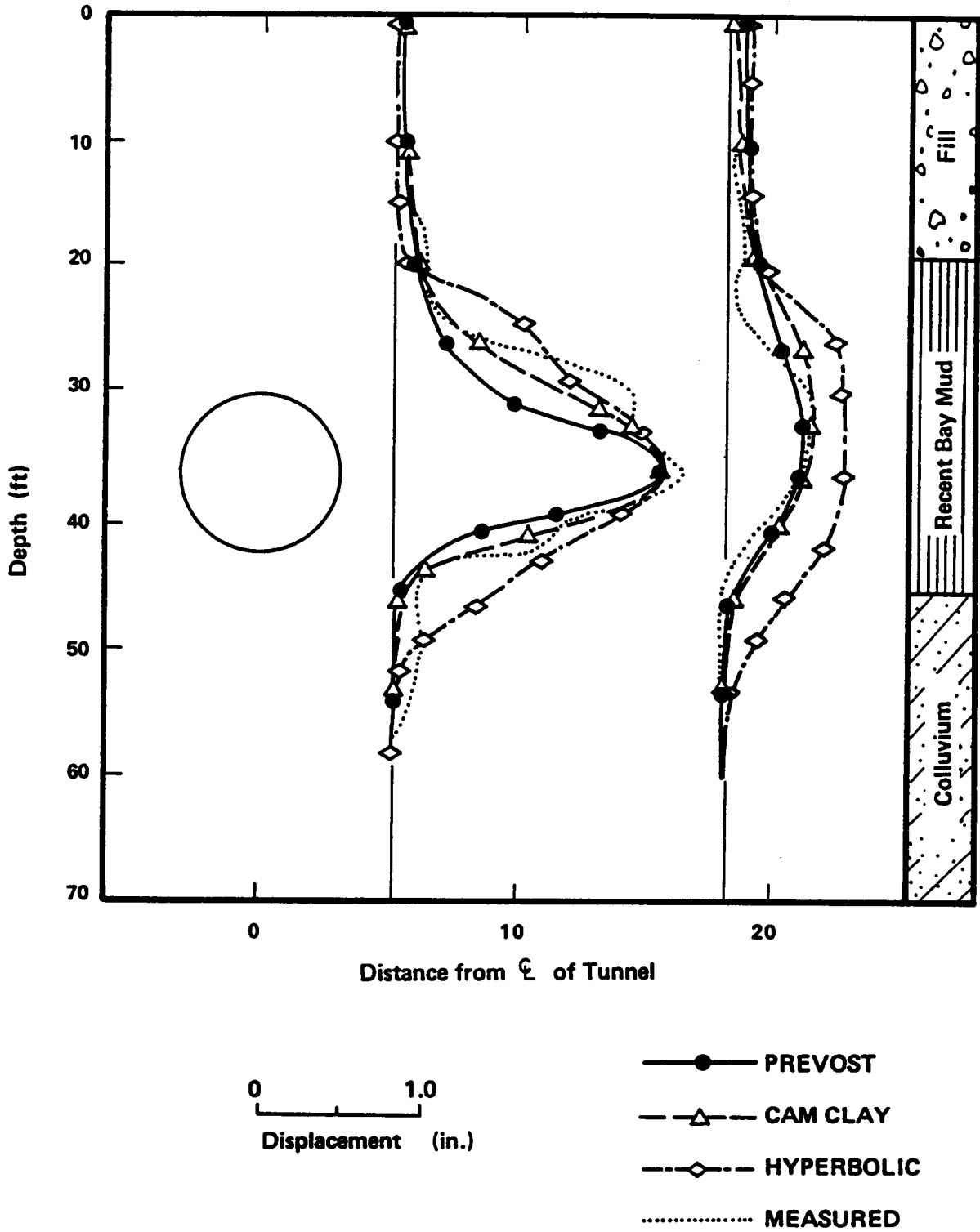


Figure 10.3 Comparison of Lateral Displacements after Heaving for Different Soil Models, Line 4

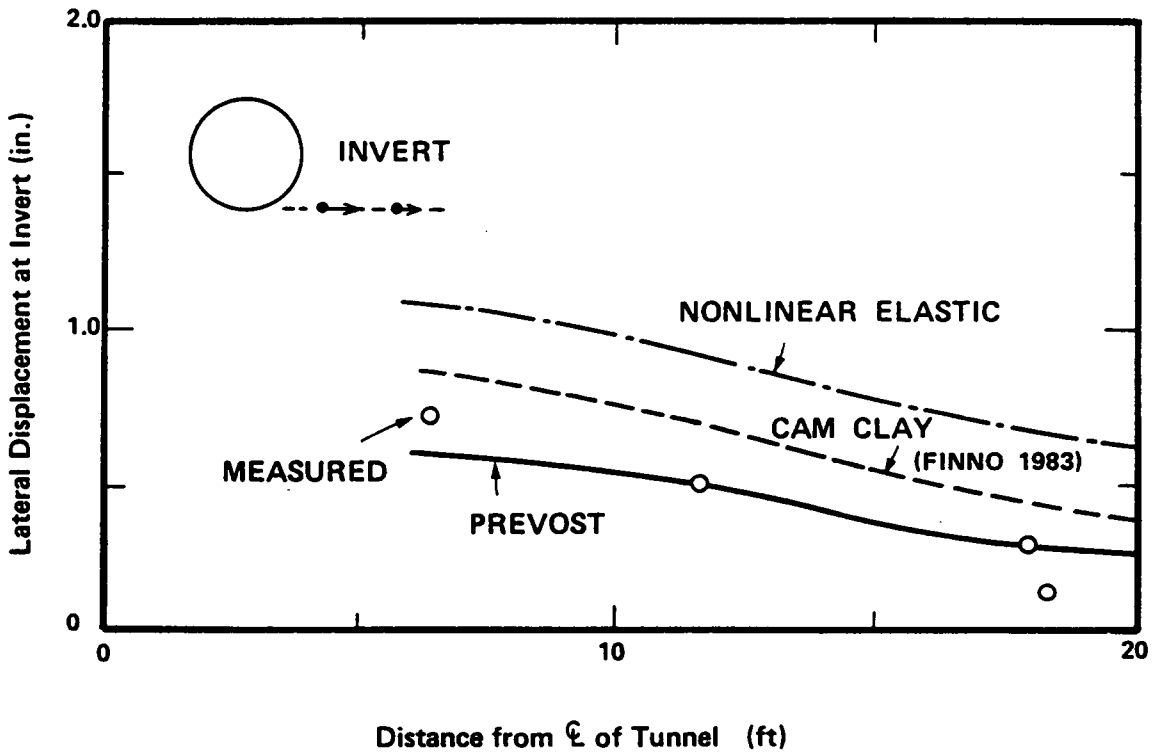
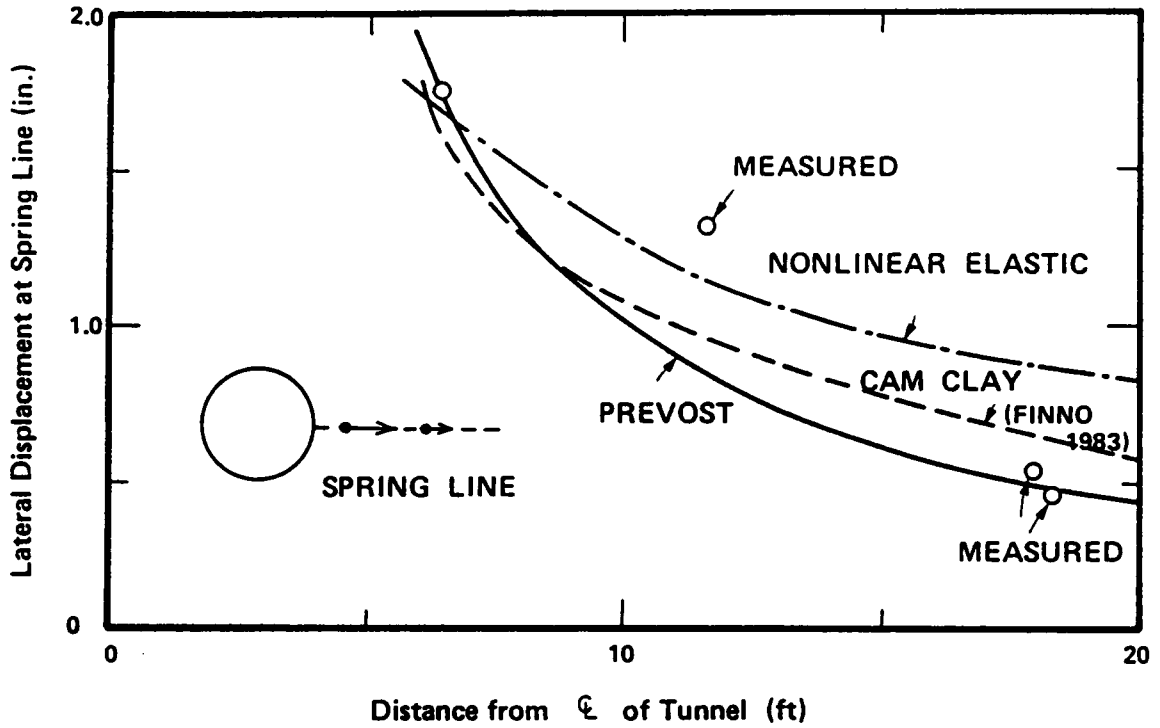


Figure 10.4 Comparison of Lateral Displacement Degradation at Springline and Invert for Different Soil Models, Line 4

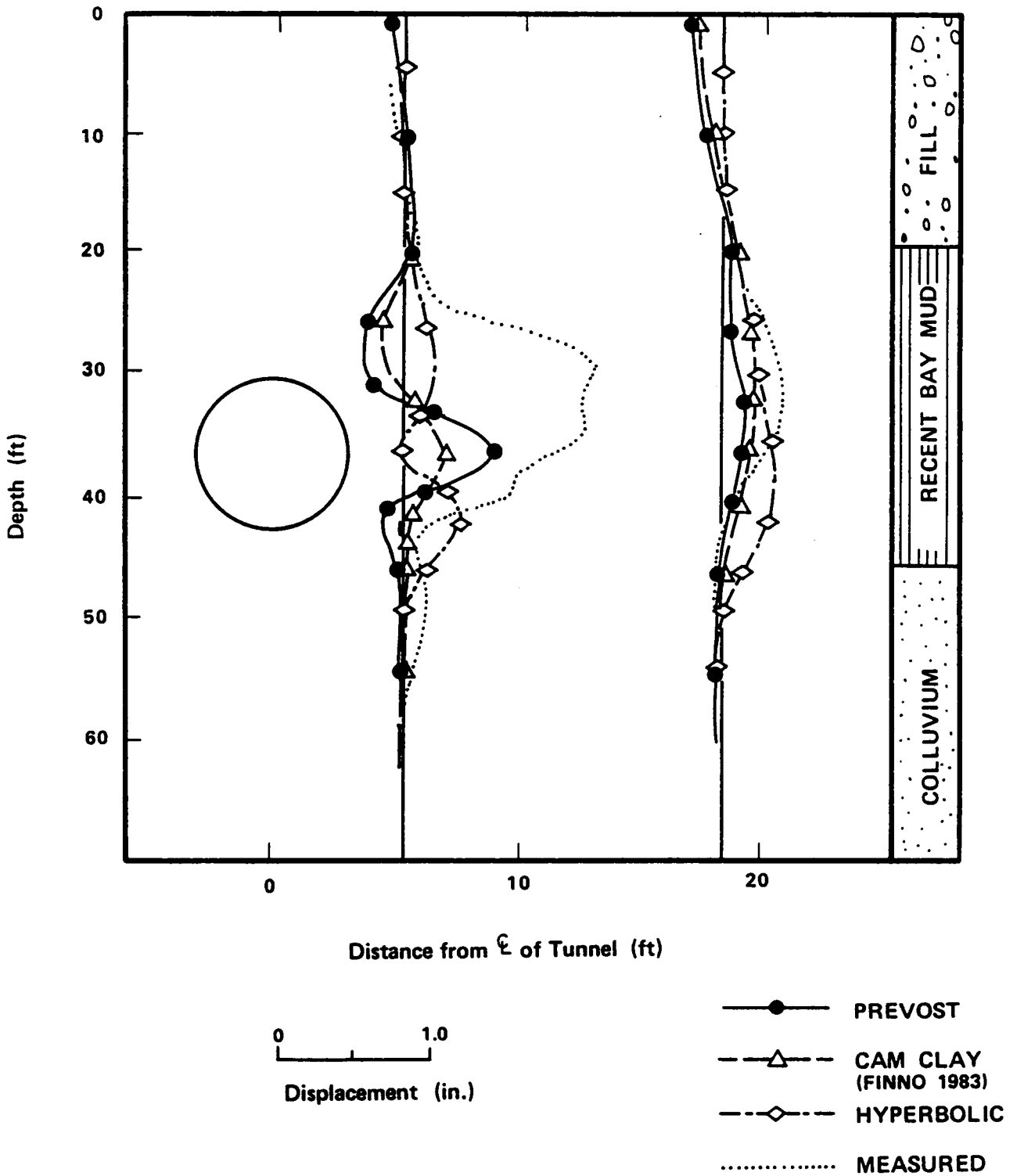


Figure 10.5 Comparison of Lateral Displacements after Tail Void Closure for Different Soil Models, Line 4

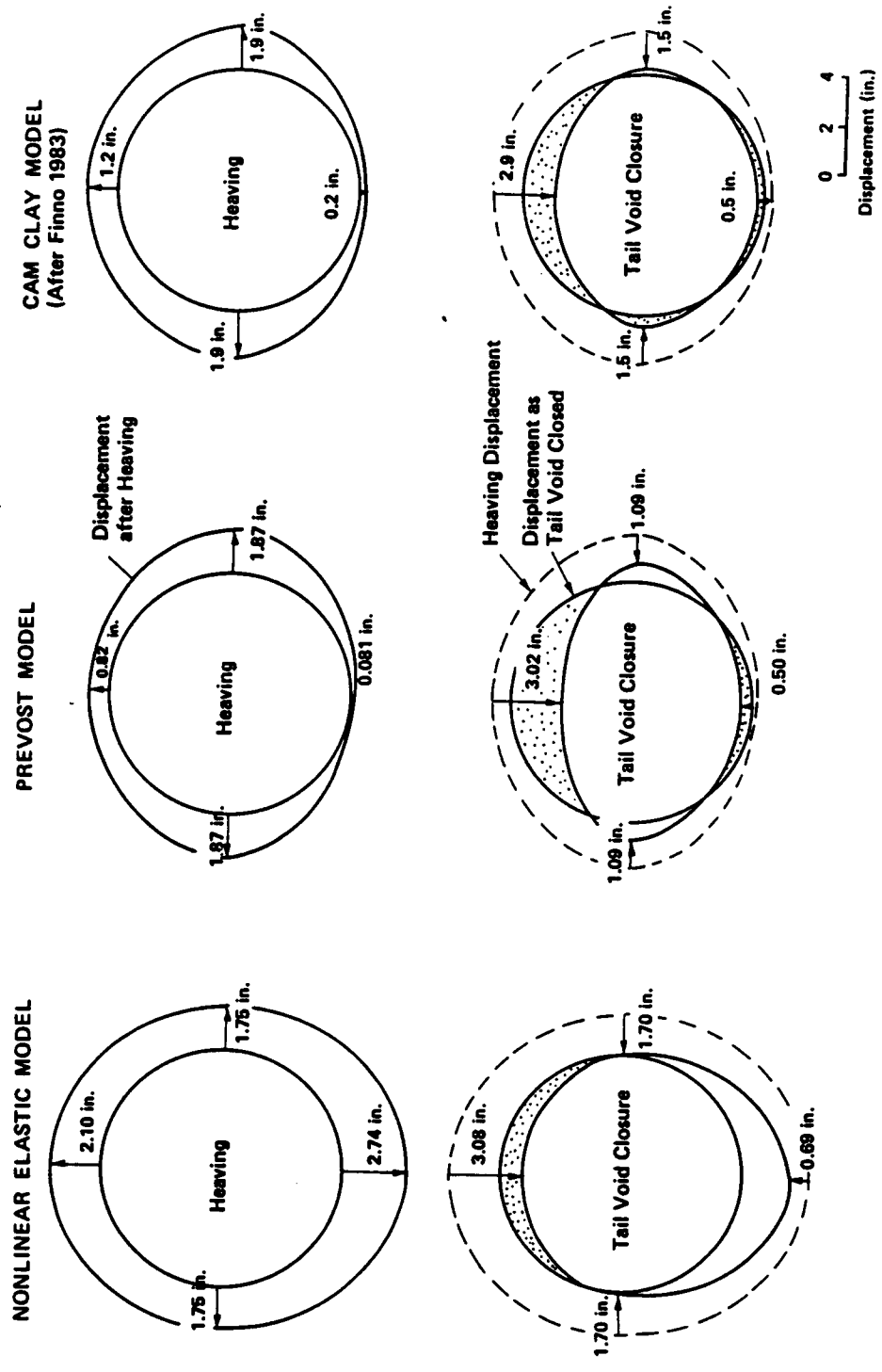


Figure 10.6 Comparison of Movements of Soil Close to Tunnel after Heaving and Tail Void Closure Predicted by Different Soil Models, Line 4

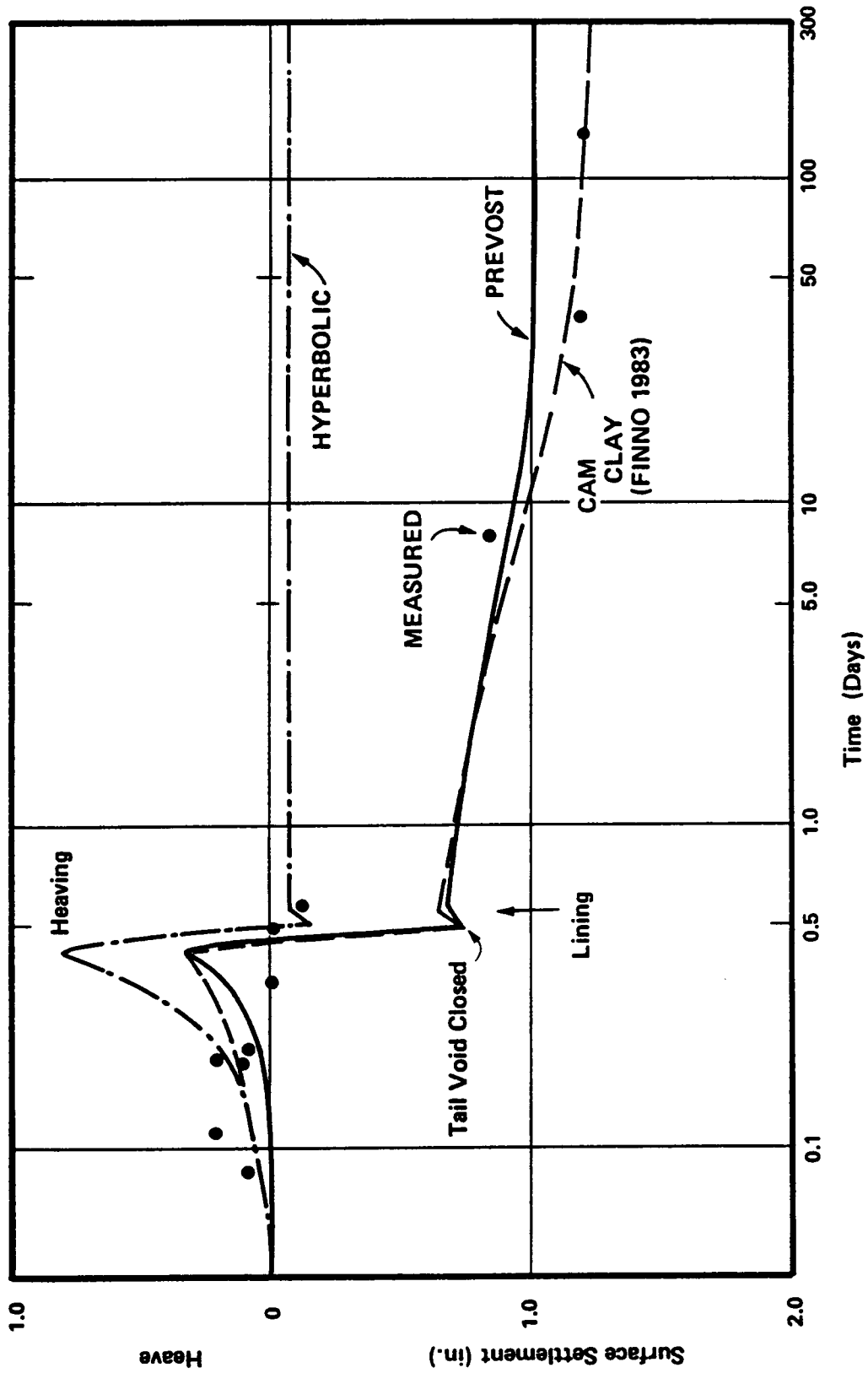


Figure 10.7 Comparison of Variation of Centerline Surface Movements with Time Predicted by Different Soil Models, Line 4

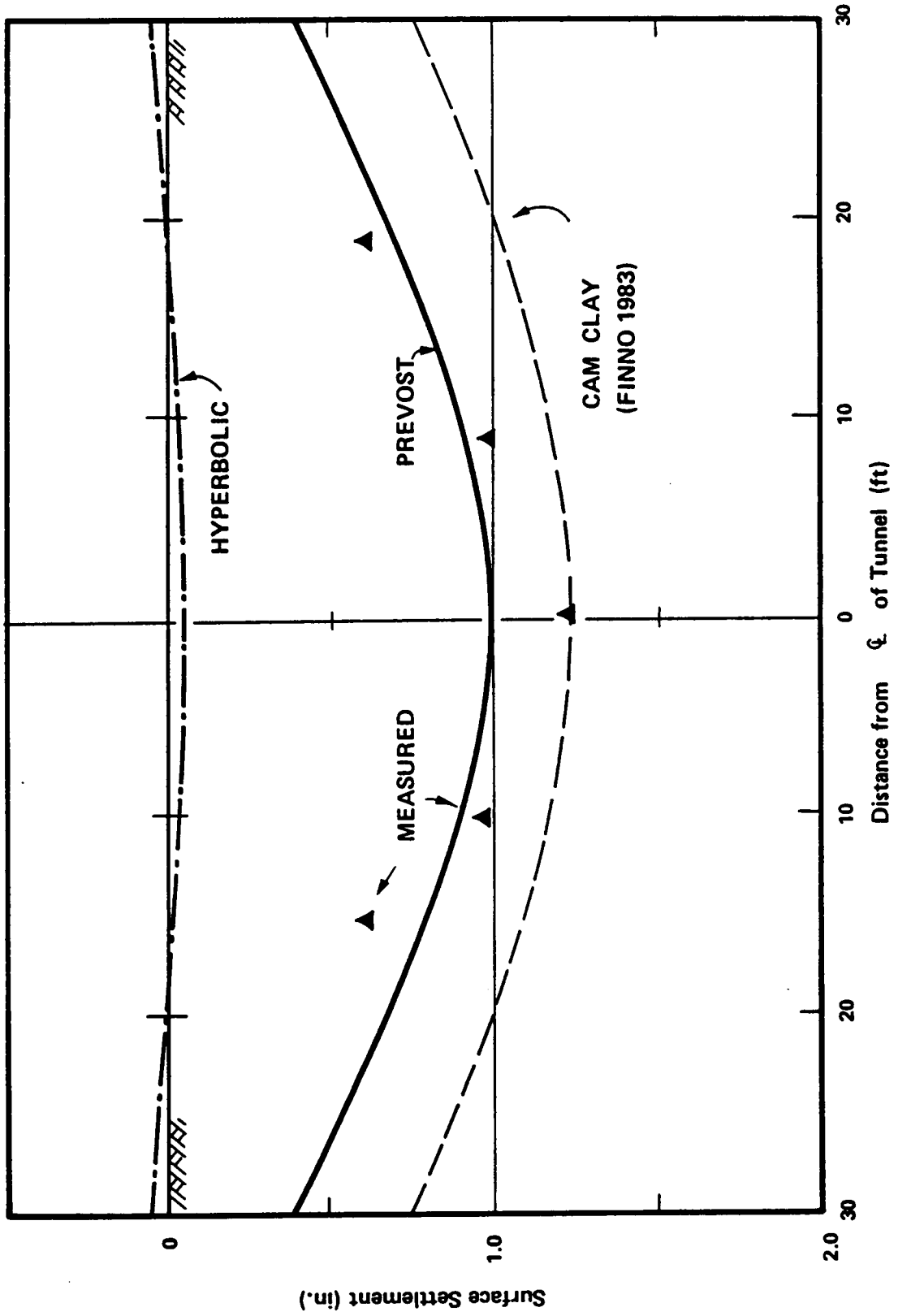


Figure 10.8 Comparison of Shape of Surface Settlement Trough Predicted by Different Soil Models, Line 4

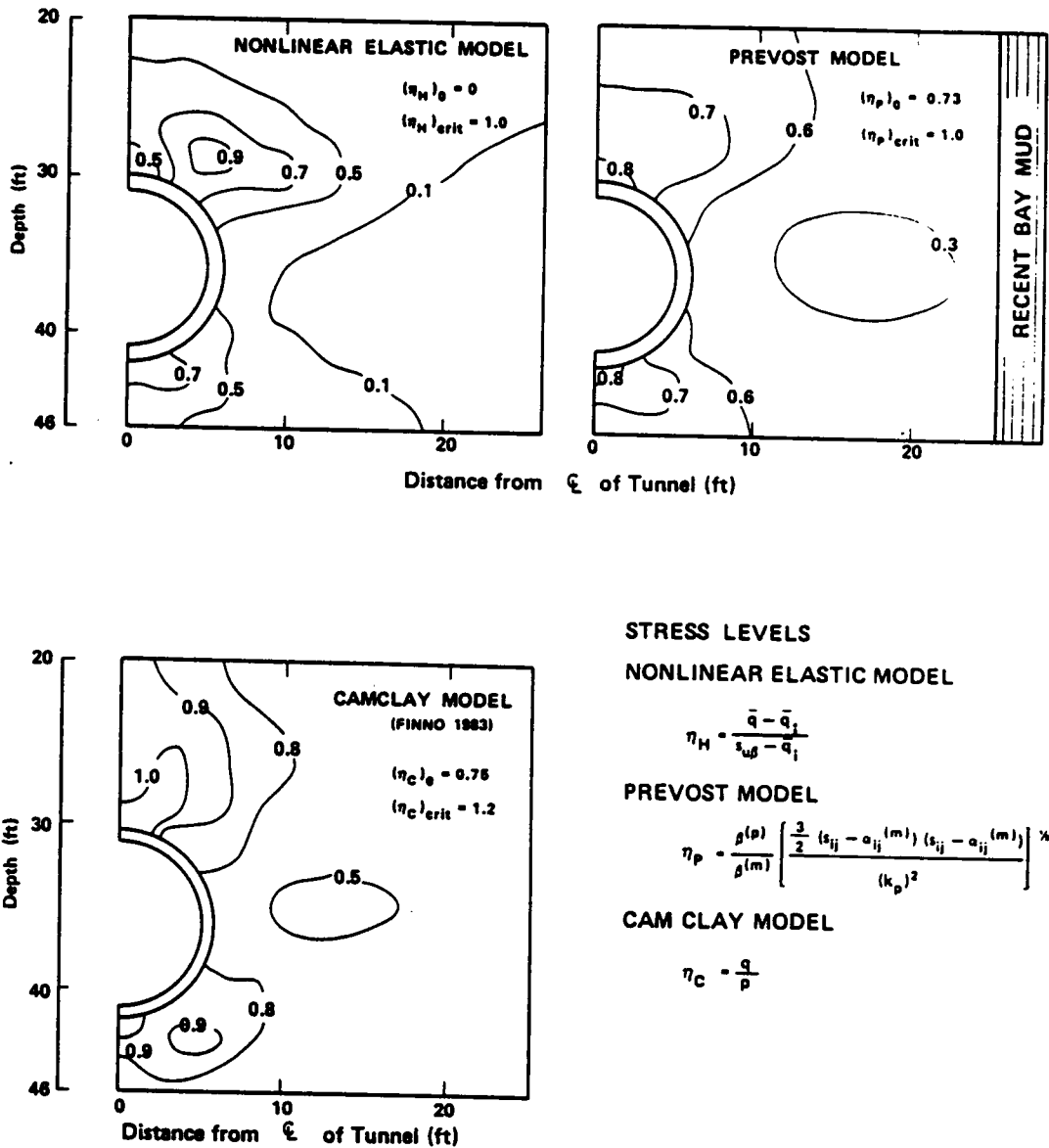


Figure 10.9 Comparison of Stress Level Distributions after Heaving Predicted by Different Soil Models, Line 4

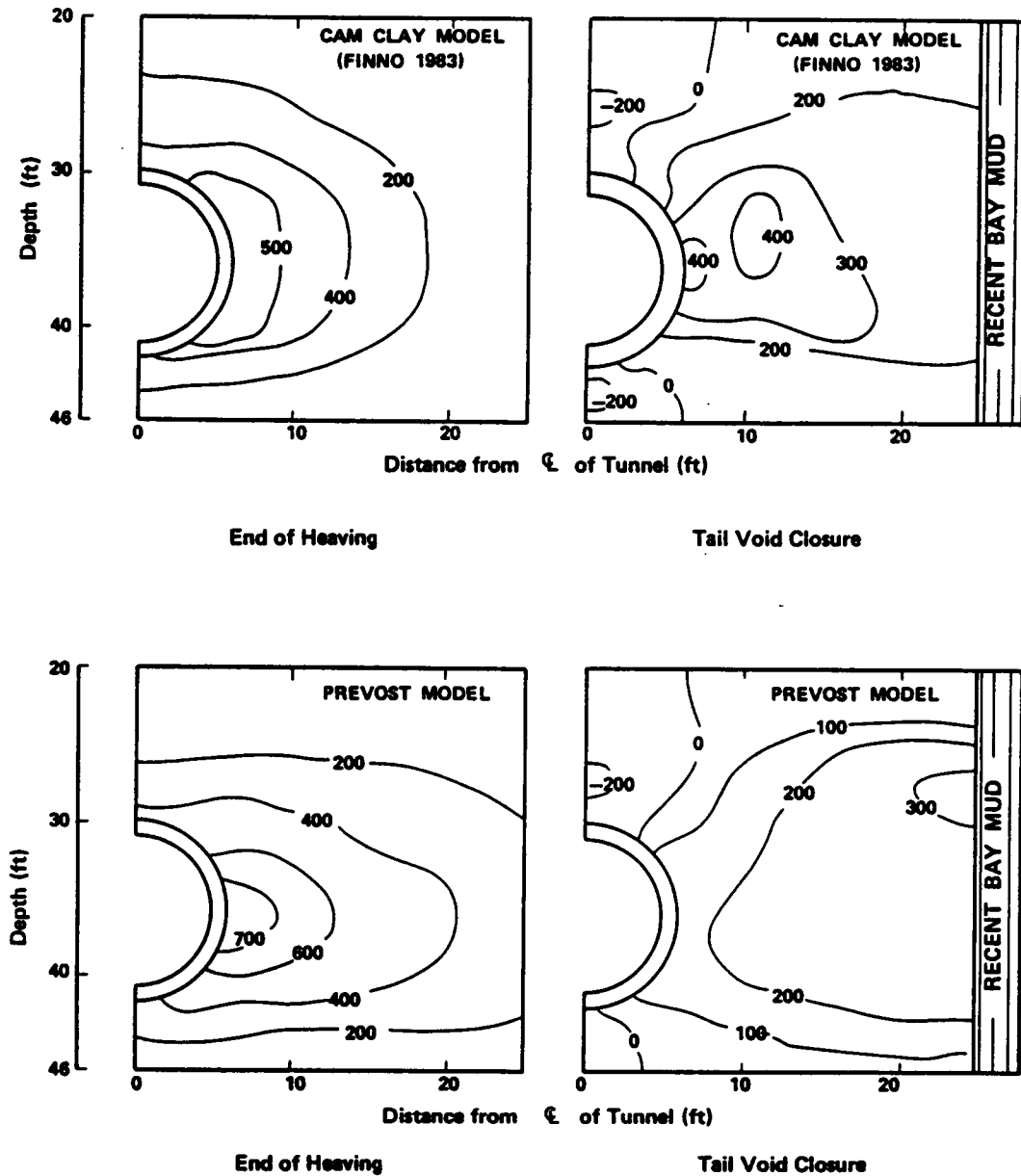


Figure 10.10 Comparison of Variation of Pore Pressure Developments Predicted by Different Soil Models, Line 4 (psf)

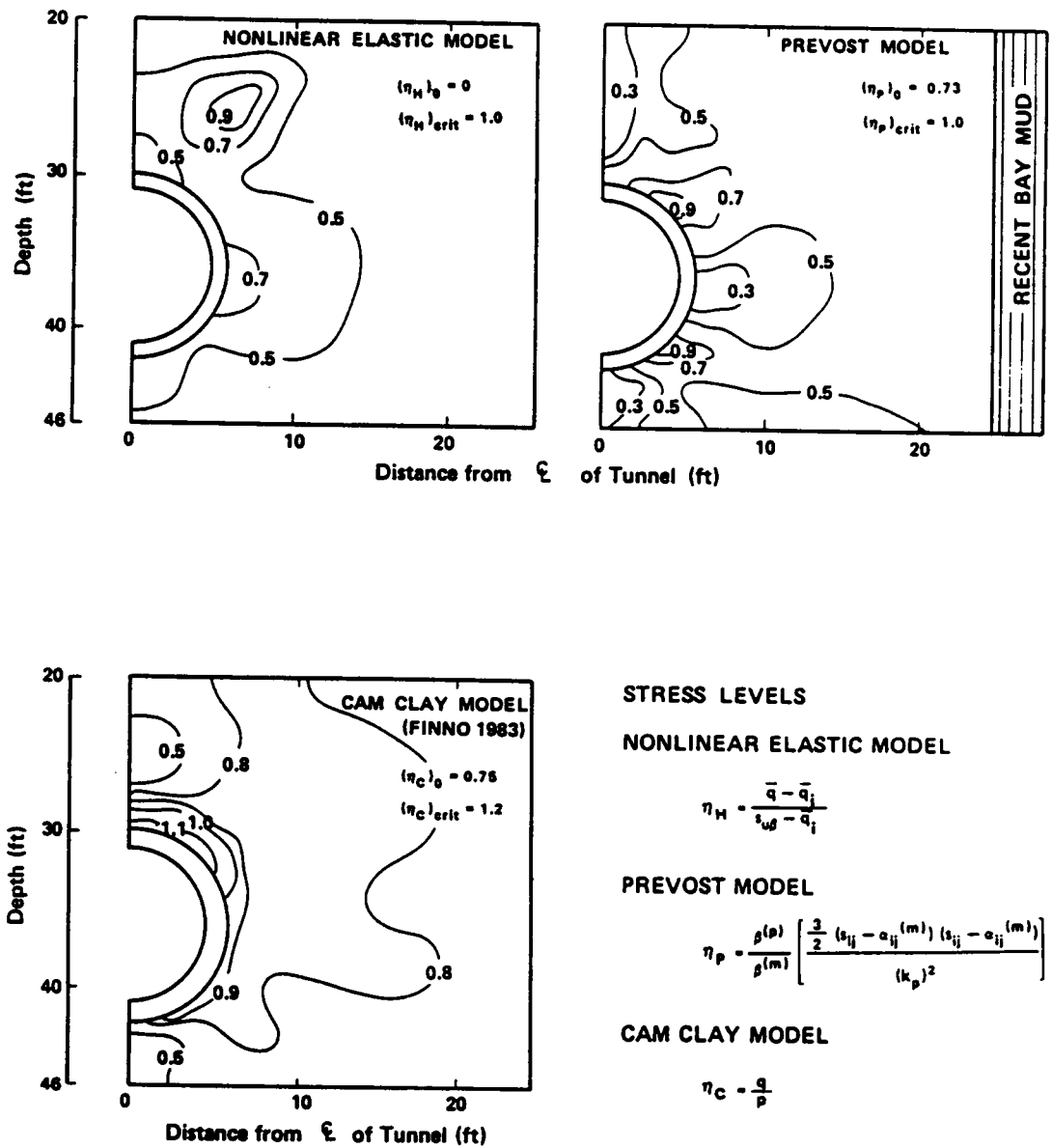


Figure 10.11 Comparison of Stress Levels after Tail Void Closure Predicted by Different Soil Models, Line 4

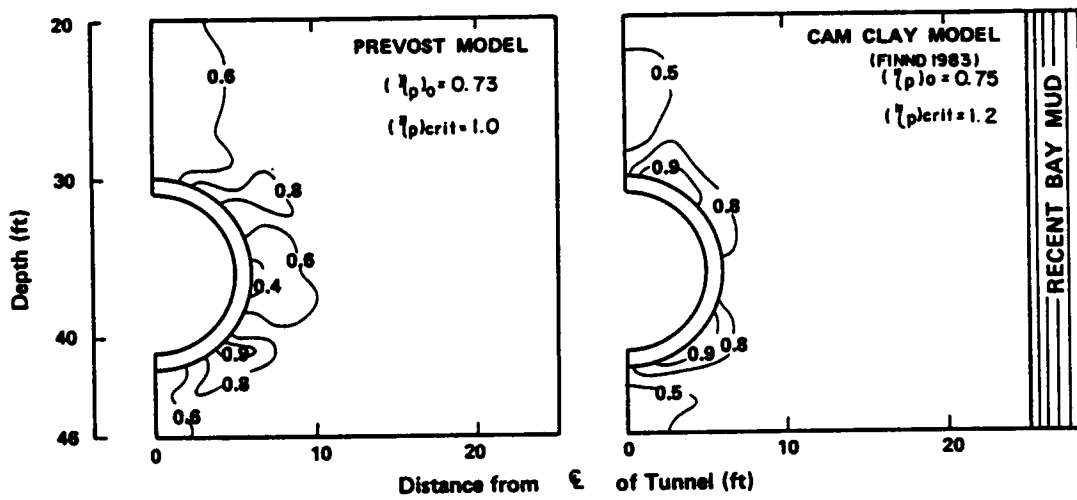


Figure 10.12 Comparison of Stress Level Distributions after Consolidation Predicted by Prevost and Cam Clay Models, Line 4

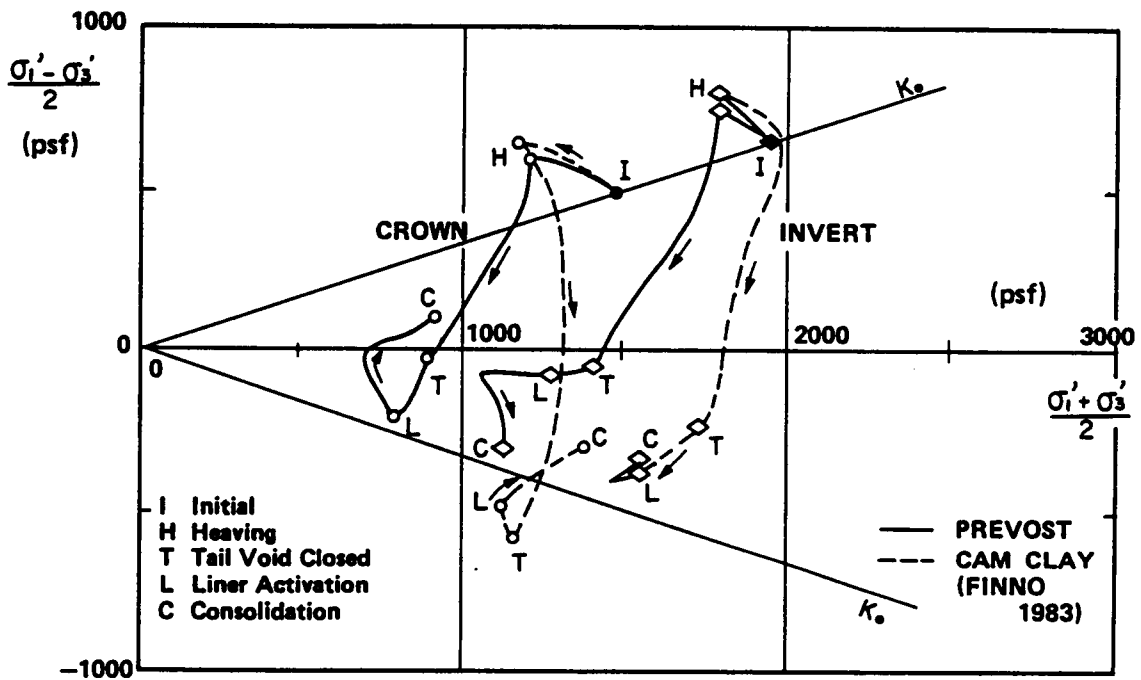
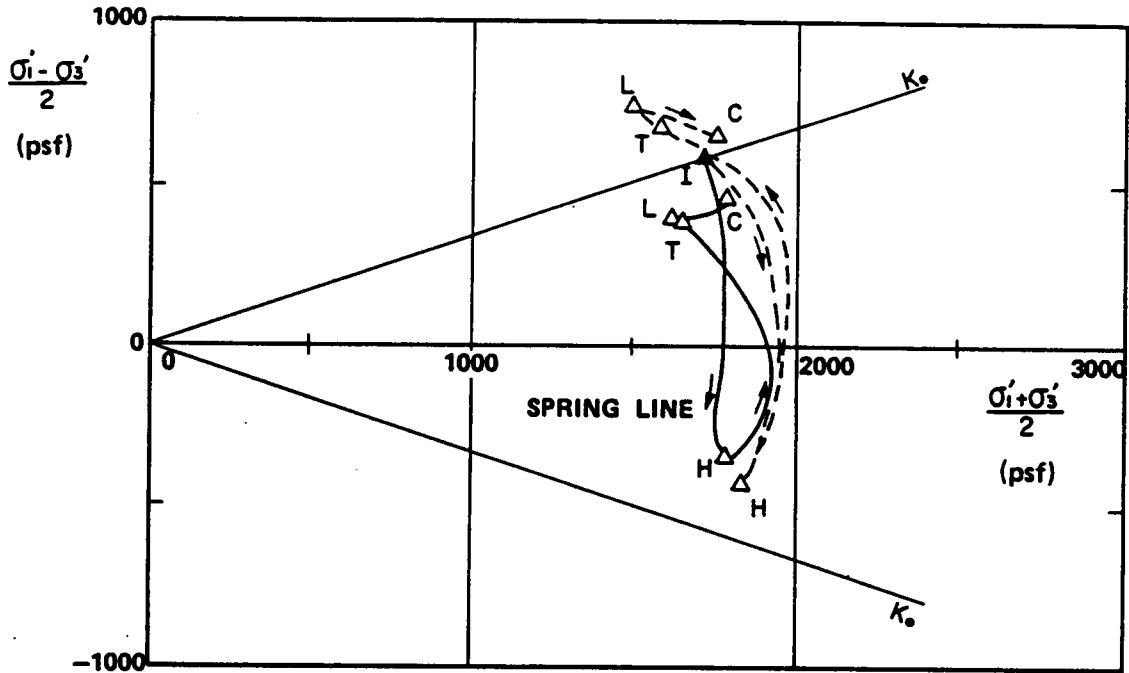


Figure 10.13 Comparison of Effective Stress Paths Predicted by Prevost and Cam Clay Models, Line 4

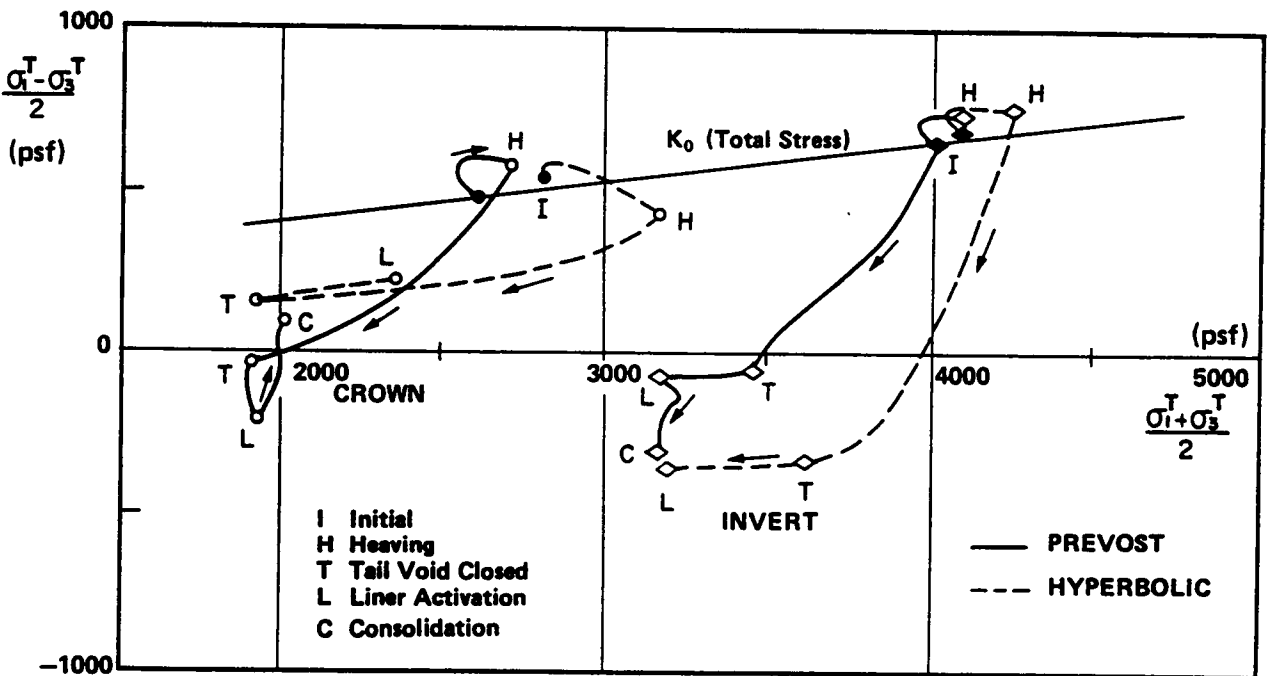
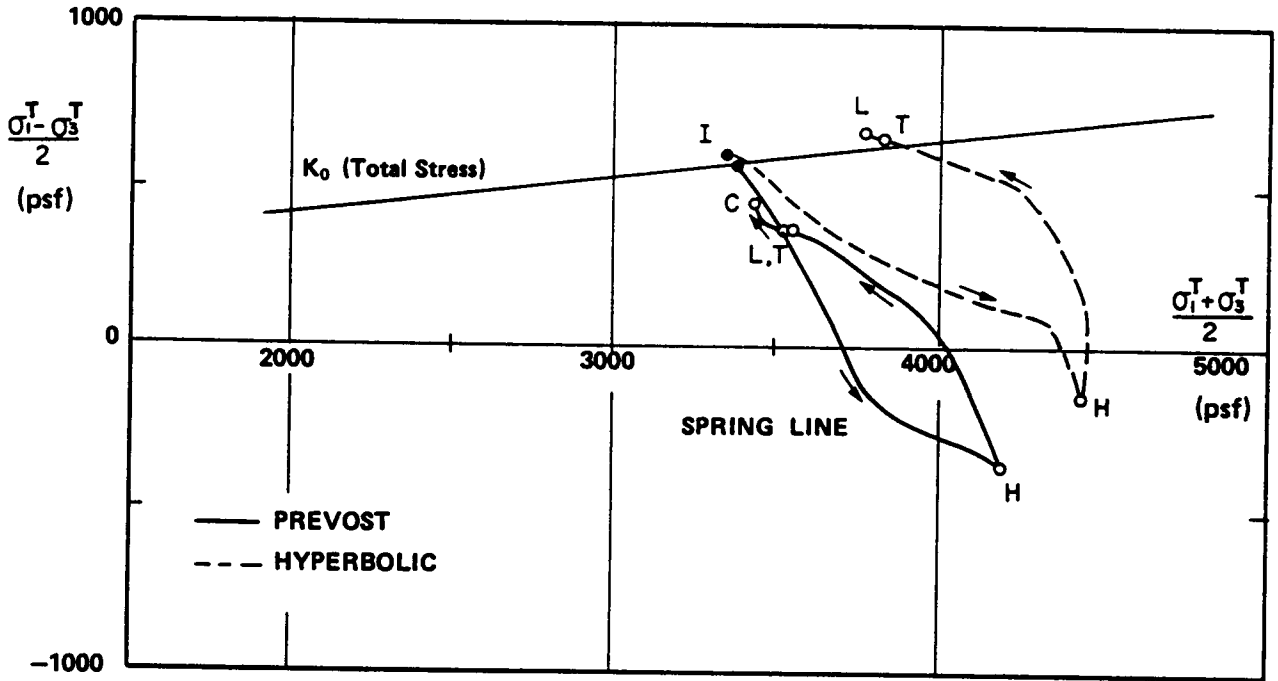


Figure 10.14 Comparison of Total Stress Paths Predicted by Prevost and Nonlinear Elastic Models, Line 4

## Chapter 11

### CONCLUSIONS

Advanced shield tunneling techniques have become increasingly popular because they allow close control of soil and water movements, even in difficult soils. Control of ground movements during tunneling is one of the major issues related to construction in an urban environment. Experience has shown that advanced shields are able to control ground settlements better than conventional shields. However, methods for prediction of ground movements to be induced by advanced shield tunneling are not satisfactorily established, and not enough is known of the mechanics of ground behavior during advanced shield tunneling. An accurate prediction of ground movements is not possible unless complete knowledge is obtained for causes and effects associated with tunneling performance. This thesis describes a research program devoted to the study of ground response to advanced shield tunneling in soft clays by means of finite element analyses. The study involves:

1. Reviewing case histories of advanced shield tunneling in soft clays and related research works.
2. Developing a finite element code to simulate advanced shield tunneling, while taking into account the inelastic behavior of soil and excess pore pressure development and dissipation.
3. Calibrating the program code by comparing the predicted ground movements with those observed for the N-2 tunnel project.
4. Performing a series of parametric studies to clarify the relative influence of the effects of initial heaving, volume loss upon tail void closure, and long term consolidation.

The first advanced shield project in the United States was the N-2

tunnel project in San Francisco for the construction of a 12-foot diameter 3,000 foot long tunnel in 1981. An EPB shield was used to drive through a soft clay, locally called Bay Mud. The project was instrumented, and a complete set of observed data are available to display ground movements induced by the tunneling. The data showed a unique response of soils such that the soils initially moved away from the shield as it approached, then moved back toward the tunnel, and finally exhibited a long-term settlement. Such ground movements were typical for the three instrument lines monitored, but interestingly their magnitudes were not identical. The amount of initial heaving was found correlated with the observed differences in behavior at the three instrument lines.

Considering the observed behavior at the N-2 site and elsewhere, it was felt that the FEM program to be used for advanced shield tunneling study should have the following features:

1. Modeling for the construction sequence of advanced shield tunneling.
2. An elasto-plastic soil model to follow realistic soil behavior patterns.
3. A capability for representing time-dependent effects due to pore pressure changes.
4. A capability to handle large deformation effects.

The final program developed has all of these desired characteristics and is believed to be suitable for the research study.

The major problem in soil modeling revolved around how to treat the behavior of soft clays, since these soils are often the most likely to lead to large movements in shield tunneling. Various types of elasto-plastic types of models were considered, and three were directly compared:

nonlinear elastic, Cam Clay and Prevost techniques. Of these the Prevost model was found to do the best job in predicting all aspects of behavior, and it was selected for use in the research where modeling of clays was required.

The Prevost model is a multi-yield surface elasto-plastic model with a kinematic hardening rule so that it may predict inelastic soil responses even under loading reversals. This is important to advanced shield tunneling in that a significant loading reversal occurs in transition from the initial heave effect to the tail void closure. This feature of the model made it possible to explain effects of the initial heave on the subsequent ground settlements. Three chapters in this thesis are devoted to the Prevost model to describe its development, code implementation, and calibration for modeling clay.

Modification of the model was made for it to handle the pressure-sensitive behavior of clay since the original version was found to be inadequate. This option was needed herein since both drained and undrained behavior of clay had to be modeled in order to predict pore pressure development and its dissipation. In addition, it was found that a general process of parameter determination for the Prevost model did not exist. A new procedure was proposed to circumvent this problem.

Capabilities of prediction by the Prevost model were carefully investigated for the response of San Francisco Bay Mud under a variety of stress paths using data that were available from laboratory results. It was shown that the Prevost model satisfactorily represents the Bay Mud for both

undrained and drained behavior. This result was encouraging, and the Prevost model representing the Bay Mud was used for the studies of the N-2 case history.

The Prevost model was coupled with the consolidation theory in the FEM program so that time-dependent effects might be evaluated. This allowed long-term ground settlements generated as a result of pore pressure dissipation to be predicted. Also, the program was developed to include large strain effects to be able to handle large strains which occurred during heaving and tail void closure.

In addition to proper modeling of the soil behavior, for accurate results to be obtained it was also necessary that the physical loading effects of an advanced shield be simulated reasonably. This involved setting up initial ground stresses, heaving effects during shield advance, tail void closure and grouting, liner installation and subsequent long-term pore pressure dissipation. Of these, the most difficult to define were the heaving effects and tail void closure with grouting. In the first place, these factors were to some degree three dimensional, while the modeling was done with a two-dimensional FEM program. Secondly, the actual processes were indeterminate and little was known about the details of them in the field. In the end, procedures were developed by trial and engineering judgement and shown to predict reasonable results. The predictions with the new methods were shown to be superior to those used in previous studies.

Using the FEM program and the proposed loading simulation procedures,

the ground response to the N-2 tunneling was simulated. The predicted results showed excellent agreement with those observed at every instrument line of the N-2 project. The analyses suggest that both the initial heave and the immediate settlement are quite influential with respect to the final settlement after consolidation. The satisfactory prediction of the N-2 behavior is taken to verify the program from a practical application standpoint.

The conclusions of this research work are summarized as follows:

1. The Prevost model accurately represents behavior of the San Francisco Bay Mud for a variety of stress paths which include both drained and undrained loadings.
2. Model parameters for the Bay Mud are successfully obtained by means of the modified parameter evaluation procedure proposed in this thesis.
3. Loading procedures proposed and used in the analyses are found reasonable to model the heaving and tail void closure stages.
4. The FEM program developed for this research was determined to be valid for a simulation of advanced shield tunneling. Excellent agreement of the predicted data with the observed of the N-2 project are obtained.
5. The initial heaving level and volume loss upon the tail void closure are important factors which affect subsequent ground settlements. The volume loss upon the tail void closure leads only to adverse effects, increases the surface settlement, and widens the trough indicating a larger influential area. On the other hand, the initial heaving reduces the trough width and generally reduces the surface settlement.

6. The effects of initial heaving are not simple in that the heave does not automatically compensate for settlements. More of the effects of heave go into lateral movements than into vertical ones, and the heaving process generates excess pore pressures which cause consolidation settlements. This results in the fact that with the initial heave, long-term consolidation settlement increases while immediate settlement decreases.
7. A moderate level of the initial heaving is the best for the shield operation from the point of view of positive ground control in tunneling. According to the results of parametric studies, the heaving should be in a range of two percent of excavation volume, where soil disturbance effects are minimized. Such a guideline is consistent with that evolved by practitioners in the field.
8. A comparison of the predictions by three different soil models -- the Prevost, Cam Clay and nonlinear elastic models -- shows that the first two models are most effective for use in tunneling analyses. The nonlinear elastic model was found inadequate since the soil model with the total stress approach can not deal with consolidation. Finally, the Prevost model predicted details of the soil response better than did the Cam Clay model.

## BIBLIOGRAPHY

1. Adachi, T., Y. Mochida, T. Tamura, "Tunneling in Fully-Saturated Soft Sedimentary Rocks," 3rd International Conference on Numerical Methods in Geotechnics, Aachen, Vol. 2, 1979, pp.599-610
2. Atkinson, J. H., D. M. Potts, "Subsidence above Shallow Tunnels in Soft Ground," Journal of the Geotechnical Engineering Division, ASCE, Vol. 103, GT4, April, 1977a, pp.307-325
3. Atkinson, J. H., D. M. Potts, "Stability of a Shallow Circular Tunnel in Cohesive Soil," Geotechnique 27, No. 2, 1977b, pp. 203-215
4. Atkinson, J. H., D. M. Potts, "Calculation of Stresses of Deformations around Shallow Circular Tunnels in Soft Ground by the Methods of Associated Field," Computer Method in Tunneling Design, Institution of Civil Engineers, 1978
5. Atkinson, J. H., P. L. Bransby, "The Mechanics of Soils - An Introduction to Critical State Soil Mechanics," McGraw Hill, University Series in Civil Engineering, U. K., 1978
6. Attewell, P. B., "Engineering Contract, Site Investigation and Surface Movements in Tunneling Works, Soft-Ground Tunneling-Failures and Displacement," A. A. Balkema, 1981, pp.5-12
7. Baker, R., C. S. Desai, "Consequence of Deviatoric Normality in Plasticity with Isotropic Strain Hardening," International Journal for Numerical and Analytical Methods in Geomechanics, Vol. 6, 1982, pp.383-390
8. Banerjee, P. K., A. S. Stipho, "Associated and Non-Associated Constitutive Relations for Undrained Behavior of Isotropic Soft Clays," International Journal for Numerical and Analytical Methods in Geomechanics, Vol. 2, 1978, pp.35-56
9. Banerjee, P. K., A. S. Stipho, "An Elasto-Plastic Model for Undrained Behavior of Heavily Overconsolidated Clays," International Journal for Numerical and Analytical Methods in Geomechanics, Vol. 3, 1979, pp.97-103
10. Benoit, J., "Analysis of Self-boring Pressuremeter Tests in Soft Clay," Thesis presented to Stanford University in partial fulfillment of the requirements of the degree of Doctor of Philosophy, Stanford, CA, August, 1983
11. Boit, M. A., "General Theory of Three-Dimensional Consolidation," Journal of Applied Physics, Vol. 12, February, 1941, pp.155-164
12. Bishop, A. W., "The Strength of Soils as Engineering Materials," Sixth Rankine lecture, Geotechnique, Vol. 17, No. 2, 1966, pp.91-130

13. Bjerrum, L., "Problems of Soil Mechanics and Construction on Soft Clays and Structurally Unstable Soils," General Report, Session No. 4, Proceedings, 8th International Conference on Soil Mechanics and Foundation Engineering, Vol. 4, 1973, pp. 111-159
14. Blight, G. E., "Soil Mechanics Principles in Underground Mining," Journal of Geotechnical Engineering, ASCE, Vol. 110, No. 5, May, 1984, pp.567-581
15. Bonaparte, R., J. K. Mitchell, "The Properties of San Francisco Bay Mud at Hamilton Air Force Base, California," Department of Civil Engineering Report, University of California, Berkeley, CA, 1979
16. Booker, J. R., "Numerical Method for the Solution of Biot's Consolidation Theory," Quarterly Journal of Mechanics and Applied Mathematics, Vol. XXVI, Part 4, 1973, pp.457-470
17. Booker, J. R., J. C. Small, "An Investigation of the Stability of Numerical Solution of Biot's Equations of Consolidation," International Journal of Solids Structure, Vol. 11, 1975, pp.907-917
18. Brebbia, C. A., "The Boundary Element Method for Engineering," Pentech Press, London, 1978
19. Breth, H., "Tunnelling in Soft Ground," Proceedings, 9th International Conference on Soil Mechanics and Foundation Engineering, Vol. 3, Tokyo, 1977, pp.463-468
20. Brom, B. B., H. Bennermark, "Stability of Clay at Vertical Opening," Journal of the Soil Mechanics and Foundation Division, ASCE, Vol. 93, SM1, January, 1967, pp.71-94
21. Brooker, E. M., H. O. Ireland, "Earth Pressure at Rest Related to Stress History," Canadian Geotechnical Journal, Vol. 11, No. 1, February, 1965, pp.1-15
22. Burland, J. B., "The Yielding and Dilatation of Clay," Correspondence, Geotechnique, Vol. 15, No. 2, 1965, pp.211-214
23. Carter, J. P., J. R. Booker, E. H. Davis, "Finite Deformation of an Elasto-Plastic Soil," International Journal for Numerical and Analytical Methods in Geomechanics, Vol. 1, 1977, pp.25-43
24. Carter, J. P., J. R. Booker, J. C. Small, "The Analyses of Finite Elasto-Plastic Consolidation," International Journal for Numerical and Analytical Methods in Geomechanics, Vol. 3, 1979, pp.107-129
25. Chen, W. F., "Limit Analysis and Soil Plasticity," Elsevier Scientific Publishing Co., 1975
26. Cheung, Y. K., L. G. Tham, "Numerical Solution for Biot's Consolidation of Layered Soil," Journal of Engineering Mechanics, Vol. 109, No. 3, June, 1983, pp.669-679

27. Christian, J. T., "Undrained Stress Distribution by Finite Elements," Journal of Soil Mechanics and Foundation Engineering Division, ASCE, Vol. 94, SM6, November, 1968, pp.1333-1345
28. Christian, J. T., J. W. Boehmer, P. P. Martin, "Consolidation of a Layer under a Strip Load," Journal of Soil Mechanics and Foundation Division, ASCE, Vol. 98, SM7, July, 1972, pp.693-707
29. Christian, J. T., "Two or Three Dimensional Consolidation," Chapter 12 in 'Numerical Methods in Geotechnical Engineering,' edited by Desai and Christian, 1977, pp.399-426
30. Carter, J. P., J. R. Booker, "Elastic Consolidation around a Lined Circular Tunnel," Research Report No. R426, The University of Sydney, November, 1982, 47p
31. Clough, G. W., "Finite Element Analyses of Soil-Structure Interaction in U-Frame Locks," Thesis presented to University of California, Berkeley in partial fulfillment of the requirement of the degree of Doctor of Philosophy, Berkeley, California, September, 1969
32. Clough, G. W., "Advanced Soil and Soft Rock Tunneling Technology in Japan," Stanford University Technical Report No. CE-252, October, 1980
33. Clough, G. W., "Innovation in Tunnel Construction and Support Techniques," Bulletin of the Association of Engineering Geologists, Vol. XVIII, No. 2, May, 1981, pp.151-167
34. Clough, G. W., J. M. Duncan, "Finite Element Analyses of Retaining Wall Behavior," Journal of the Soil Mechanics and Foundation Division, ASCE, Vol. 97, SM12, December, 1970, pp.1657-1673
35. Clough, G. W., B. Schmidt, "Design and Performance of Excavations and Tunnels in Soft Clay," A State-of-the-Art Paper, International Symposium on Soft Clays, Bangkok, 1977
36. Clough, G. W., L. A. Hansen, "Clay Anisotropy and Braced Wall Behavior," Journal of the Geotechnical Engineering, ASCE, Vol. 107, GT7, July, 1981, pp.893-913
37. Clough, G. W., R. J. Finno, B. P. Sweeney, E. Kavazanjian, "Development of a Design Technology for Ground Support for Tunnels in Soil - Vol. III, Observed Behavior of an Earth Pressure Balance Shield in San Francisco Bay Mud," Report prepared for the U. S. Department of Transportation, Stanford University, February, 1982a
38. Clough, G. W., R. J. Finno, B. P. Sweeney, "Ground Deformation Induced by an Earth Pressure Balance Shield in Silts and Clays," Tunneling Technology, December, 1982b, pp.1-11
39. Clough, G. W., B. P. Sweeney, R. J. Finno, Closure, Journal of Geotechnical Engineering, ASCE, Vol. 110, No. 2, February, 1984, pp.306-307

40. Cording, E. J., W. H. Hansmire, "Displacements Around Soft Ground Tunnels," General Report: Session IV, Tunnels in Soil, 5th Panamerican Buenos Aires, November, 1975
41. Cryer, C. W., "A Comparison of the Three-Dimensional Consolidation Theories of Biot and Terzaghi," Quarterly Journal of Mechanics and Applied Mathematics, Vol. XVI, Part 4, 1963, pp.401-412
42. Dafalias, Y. F., "Materials with Vanishing Elastic Region," International Journal for Numerical and Analytical Methods in Geomechanics, Vol. 6, 1982, p.389
43. Dafalias, Y. F., E. P. Popov, "A Model of Nonlinearly Hardening Materials for Complex Loading," Acta Mechanica, Vol. 21, 1975, pp.173-192
44. Dafalias, Y. F., E. P. Popov, "Cyclic Loading for Materials with a Vanishing Elastic Region," Nuclear Engineering and Design, Vol. 41, 1977, pp.293-302
45. Dames and Moore Consulting Engineers, "Supplementary Soils Report, North Shore Ourfall, Consolidation Project Contracts N1, N2, and N4 San Francisco, CA.," November, 1977, p.64
46. Davis, E. H., G. P. Raymond, "A Non-linear Theory of Consolidation," Geotechnique, Vol. 15, No. 2, June, 1965, pp.161-173
47. Davis, E. H., M. J. Gunn, R. J. Mair, H. N. Seneviratne, "The Stability of Shallow Tunnels and Underground Openings in Cohesive Material," Geotechnique 30, No. 4, 1980, pp.397-416
48. Davis, R. O., G. Mullenger, "A Rate-Type Constitutive Model for Soil with a Critical State," International Journal for Numerical and Analytical Methods in Geomechanics, Vol. 2, 1978, pp.255-282
49. Denby, G. M., "Self-Boring Pressuremeter Study of the San Francisco Bay Mud," Thesis presented to Stanford University in partial fulfillment of the requirements for the degree of Doctor of Philosophy, 1978
50. Dendrou, B. A., S. A. Dendrou, "A Finite Element - Boundary Integral Scheme to Simulate Rock-Effects on the Liner of an Underground Intersection," Proceedings, 3rd International Seminar on Boundary Element Methods, Irvine, California, July, 1981, pp.593-608
51. Desai, C. S., H. J. Siriwardane, "A Concept of Correction Functions to Accounting for Non-Associative Characteristics of Geologic Media," International Journal for Numerical and Analytical Methods in Geomechanics, Vol. 4, 1980, pp.377-387
52. DiMaggio, F. L., I. S. Sandler, "Material Model for Granular Soils," Journal of Engineering Mechanics Division, ASCE, Vol. 97, No. 3, 1971

53. Doherty, W. P., E. L. Wilson, R. L. Taylor, "Stress Analysis of Axisymmetric Solids Utilizing Higher-Order Quadrilateral Finite Elements," Report No. SESM 69-3, Structural Engineering Laboratory, University of California, Berkeley, CA, 1969
54. Drucker, D. C., W. Prage, "Soil Mechanics and Plastic Analysis or Limit Design," Quarterly Applied Mechanics, Vol. 10, No. 2, 1952, pp.157-165
55. Drucker, D. C., R. E. Gibson, D. J. Henkel, "Soil Mechanics and Work Hardening Theories of Plasticity," Transaction, ASCE, Vol. 122, 1957, pp.338-346
56. Duncan, J. M., Consolidation Tests Performed at the University of California, Berkeley, Published in 'The Properties of San Francisco Bay Mud at Hamilton Air Force Base, California' by Bonaparte and Mitchel (1979), 1962
57. Duncan, J. M., "The Effect of Anisotropy and Reorientation of Principal Stresses on the Shear Strength of Saturated Clay," Ph. D. thesis, the University of California, Berkeley, 1965
58. Duncan, J. M., C. Y. Chang, "Nonlinear Analysis of Stress and Strain in Soils," Journal of the Soil Mechanics and Foundation Division, ASCE, Vol. 96, SM5, September, 1970, pp.1629-1653
59. Duncan, J. M., A. L. Buchignani, "Failure of an Underwater Slope in San Francisco Bay," Journal of the Soil Mechanics and Foundations Division, ASCE, Vol. 99, No. SM5, September, 1973
60. Duncan, J. M., P. Byrne, K. S. Wong, P. Mabry, "Strength, Stress-Strain and Bulk Modulus Parameters for Finite Element Analyses of Stresses and Movements in Masses," Report No. UCB/GT/80-01, University of California, Berkeley, CA, 1980
61. Eden, W. J., M. Bozozuk, "Earth Pressures on Ottawa-Outfall Sewer Tunnel," Canadian Geotechnical Journal, Vol. 6, 1969, pp.17-32
62. Editorial Staff, Civil Engineering, "Tunnelling, Japan Takes the Lead," Civil Engineering, February, 1981, pp.20-24
63. Editorial Staff, McGraw Hill, "Japanese giant tests management ideas on first U. S. tunnel jobs," Engineering New Record, September 20, 1979, pp.64-65
64. Editorial Staff, McGraw Hill, "Kudos for Japanese on U. S. Bore," Engineering News Record, July 16, 1981, pp.56-59
65. Eisenstein, Z., F. El-Nahhas, S. Thomson, "Strain Field Around a Tunnel in Stiff Soil," Proceedings, 10th International Conference on Soil Mechanics and Foundation Engineering, Stockholm, 1981, pp.283-288

66. Finno, R. J., "Response of Cohesive Soil to Advanced Shield Tunneling," Thesis presented to Stanford University in partial fulfillment of the requirement for the degree of Doctor of Philosophy, Stanford, CA, July, 1983
67. Fujita, K., "On the Surface Settlement Caused by Various Methods of Shield Tunneling," Vol. 4, Proceedings, 10th International Conference on Soil Mechanics and Foundation Engineering, Stockholm, 1981, pp.609-610
68. Fujiwara, T., Y. Hanyuda, Y. Yamashita, "Study on Suitability of Ground for Earth Pressure Type Shield," Bulletin of Technical Research Institute, Ohbayashi Corporation, No. 23, 1981, pp.82-86
69. Fujiwara, T., Y. Hanyuda, Y. Yamashita, "Field Experiments on Foam-Injected Shield Tunneling Method," Proceedings, 36th Annual Conference of Japan Society of Civil Engineers, Vol. 3, 1981, pp.358-359
70. Fujiwara, T., Y. Yamashita, "Elasto-Plastic-Viscous Analysis for Rock Tunnel Excavation by Finite Element Method," Proceedings, 18th Japan National Conference on Soil Mechanics and Foundation Engineering, June, 1983, pp.530-531
71. Fukuda, Y., S. Ichida, "The Present Status of Mechanization in Shield Tunneling," Tsuchi-no-Kiso, Japan Society of Soil Mechanics and Foundation Engineering, Vol. 32, No. 1, January, 1984, pp.23-28
72. Ghaboussi, J., W. H. Hansmire, H. W. Parker, K. J. Kim, "Finite Elements Simulation of Tunneling Over Subways," Journal of the Geotechnical Engineering Division, ASCE, Col. 109, No. 3, March, 1983, pp.318-334
73. Gibson, R. E., R. L. Schiffman, S. L. Pu, "Plane Strain and Axially Symmetric Consolidation of a Clay Layer on a Smooth Impervious Base," Quarterly Journal of Mechanics and Applied Mathematics, Vol. XXIII, Part 4, 1970, pp.505-520
74. Goodman, R. E., R. L. Taylor, T. L. Brekke, "A Model for the Mechanics of Jointed Rock," Journal of the Soil Mechanics and Foundation Division, ASCE, Vol. 94, SM3, May, 1968, pp.637-659
75. Green, A. E., "Hypoelasticity and Plasticity," Proceedings of Royal Society, No. 234, 1956, pp.46-59
76. Hansen, L. A., "Prediction of the Behavior of Braced Excavation in Anisotropic Clay," Dissertation submitted to the Department of Civil Engineering and the Committee of Graduate Studies of Stanford University in partial fulfillment of the requirement for the degree of Doctor of Philosophy, April, 1980
77. Hansen, L. A., G. W. Clough, "Characterization of the Undrained Anisotropy of Clays," Proceedings, Conference on Application of Plasticity and Generalized Stress-Strain Relation in Geotechnical Engineering, ASCE Special Publication, 1980

78. Hansmire, W. H., "Discussion on Measured Soil Response to EPB Shield Tunneling," *Journal of Geotechnical Engineering*, ASCE, Vol. 110, No. 2, February, 1984, pp.305-306
79. Hansmire, W. H., E. J. Cording, "Field Measurement of Ground Displacements about a Tunnel in Soil," UILU-ENG-75-2021, submitted to Washington Metropolitan Area Transit Authority, Washington, D. C., September, 1975
80. Hanya, H., "Ground Movement due to Construction of Shield-Driven Tunnel," *Proceedings, 10th International Conference on Soil Mechanics and Foundation Engineering*, Vol. 4, Tokyo, 1977, pp.759-790
81. Hashimoto, S., "Instrumentation and Construction of Twin Shield Tunnel in Soft Ground," Ph. D. Dissertation submitted to the University of Tokyo, May, 1984
82. Hoyaux, B., B. Ladanyi, "Gravitational Stress Field around a Tunnel in Soft Ground," *Canadian Geotechnical Journal*, Vol. 7, 1970, pp.54-61
83. Henkel, D. J., "The Shear Strength of Saturated Remoulded Clays," *Research Conference on Shear Strength of Cohesive Clays at University of Colorado*, ASCE, June, 1966, pp.533-554
84. Heuer, R. E., "Catastrophic Ground Loss in Soft Ground Tunnels," *Proceeding, Rapid Excavation and Tunneling Conference*, Las Vegas, 1976, pp.278-295
85. Hill, R., "The Mathematical Theory of Plasticity," Clarendon Press, Oxford, 1950
86. Hill, R., "Some Basic Principles in the Mechanics of Solids without a Natural Time," *Journal of Mechanics and Physics of Solids*, No. 7, 1959, pp.209-225
87. Hirata, T., Y. Aritome, "Ground Movement Observation due to Subway Construction in Osaka, Japan by EPB Shield," *The Foundation Engineering and Equipment*, Vol. 11, No. 10, Japan, October, 1983, pp.101-111
88. Hoeg, K., J. T. Christian, R. V. Whitman, "Settlement of Strip Load on Elastic-Plastic Soil," *Journal of Soil Mechanics and Foundation Division*, ASCE, Vol. 94, SM2, March, 1968, pp.431-445
89. Hughes, T. J. R., K. S. Pister, R. L. Taylor, "Implicit-Explicit Finite Element in Nonlinear Transient Analysis," *Computer Methods in Applied Mechanics and Engineering*, 17/18, 1979, pp.159-182
90. Hughes, T. J. R., J. H. Prevost, "DIRT II - A Nonlinear Quasi-Static Finite Element Analysis Program," *Division of Engineering and Applied Mechanics*, California Institute of Technology, 1979
91. Hvorslev, M. J., "Physical Component of the Shear Strength of Saturated Clays," *Proceedings, Research Conference on Shear Strength of Cohesive Soils*, ASCE, 1969, pp.169-273

92. Ishihara, K., "Performances of EPB Shield and Water Pressure Balance Shield," Recent Development of Shield Tunneling, Vol. 6, Japan Project Research, 1978
93. Ito, T., M. Hisatake, "Analytical Study of NATM," Proceedings, 10th International Conference on Soil Mechanics and Foundation Engineering, Vol. 1, Stockholm, 1981, pp.311-314
94. Iwan, I. D., "On a Class of Models for the Yielding Behavior of Continuous and Composite System," Journal of Applied Mechanics, Transaction, ASME, Vol. 34, No. E3, 1967, pp.612-617
95. Janbu, N., "Soil Compressibility as Determined by Oedometer and Triaxial Tests," European Conference on Soil Mechanics and Foundation Engineering, Wiesbaden, Germany, Vol. 1, 1963, pp.19-25
96. Jones, R. M., "Plasticity," Lecture notes, ESM 6070, Virginia Polytechnic Institute and State University, 1982
97. Johnston, P. R., "Finite Element Consolidation Analyses of Tunnel Behavior in Clay," Thesis presented to Stanford University in partial fulfillment of the requirement for the degree of Doctor of Philosophy, Stanford, CA, 1981
98. Kasalik G., "Three-Dimensional Finite Element Analysis of Advanced and Conventional Shield Tunneling," Thesis presented to Stanford University in partial fulfillment of the requirements for the degree of Doctor of Philosophy, Stanford, CA, 1981
99. Katzenbach, R., H. Breth, "Nonlinear 3-D Analysis for NATM in Frankfurt Clay," Proceedings, 10th International Conference on Soil Mechanics and Foundation Engineering, Vol. 1, Stockholm, 1981, pp.315-318
100. Kavazanjian, E., J. K. Mitchell, "Time-Dependent Deformation Behavior of Clays," Journal of the Geotechnical Engineering, ASCE, Vol. 106, GT6, June, 1980, pp.611-630
101. Kawamoto, T., K. Okuzono, "Analysis of Ground Surface Settlement due to Shallow Shield Tunnels," International Journal for Numerical and Analytical Methods in Geomechanics, Vol. 1, 1977, pp.271-281
102. Kitamura, M., S. Ito, T. Fujiwara, "Shield Tunneling Performance and Behavior of Soft Ground, Osaka, Japan," Rapid Excavation and Tunnel Conference, Proceedings, Vol. 1, 1981, pp.201-220
103. Kobayashi, T., "Studies on Soil Remove Control with Advancement of Closed-faced Shield Tunneling," Proceedings, 29th Japan Symposium on Soil Mechanics, Tokyo, November, 1984, pp.59-64
104. Kobayashi, T., Y. Nishimatsu, "Studies on Displacement of Soft Ground Caused by Driving of Shield Tunnel," Proceedings, Japan Society of Civil Engineers, No. 328, December, 1982, pp.77-88

105. Konder, R. L., "Hyperbolic Stress-Strain Response: Cohesive Soils," *Journal of the Soil Mechanics and Foundation Division, ASCE*, Vol. 89, SM1, January, 1963, pp.115-143
106. Krieg, R. D., "A Practical Two Surface Plasticity Theory," *Journal of Applied Mechanics, Transaction of ASCE*, September, 1975, pp.641-646
107. Kurosawa, S., "Earth Pressure Balance Shield Tunneling," *Journal of the Construction Division, ASCE*, Vol. 107, No. C04, December, 1981, pp.609-618
108. Lacerda, W. J., "Stress Relaxation and Creep Effects on the Deformation of Soils," PH. D. Thesis, University of California, Berkeley, 1976
109. Ladd, C. C., R. Foott, K. Ishihara, F. Schlosser, H. G. Poulos, "Stress-deformation and Strength Characteristics," *Proceedings, 9th International Conference of Soil Mechanics and Foundation Engineering*, Vol. 2, Tokyo, July, 1977, pp.421-494
110. Lade, P. V., J. M. Duncan, "Elastoplastic Stress-Strain Theory for Cohesionless Soil," *Journal of Geotechnical Engineering Division, ASCE*, Vol. 101, GT10, 1974, pp.1037-1053
111. Lambe, T. W., W. A. Marr, "Stress Path Method; Second Edition," *Journal of Geotechnical Engineering, ASCE*, Vol. 105, GT6, June, 1979, pp.727-738
112. Lo, K. Y., edited, "Tunneling in Soil and Rock," *Proceedings of two sessions at GEOTECH '84, ASCE, Atlanta, May, 1984*
113. Lo, K. Y., R. K. Rowe, "Prediction of Ground Subsidence due to Tunneling in Clays," *Research Report, GEOT-10-82, Engineering Science, The University Western Ontario, London, Canada, July, 1982*
114. Mair, R. J., M. J. Gunn, M. P. O'Reilly, "Ground Movements around Shallow Tunnels in Soft Clay," Vol. 4, *Proceedings, 10th International Conference on Soil Mechanics and Foundation Engineering, Stockholm, 1981, pp.323-328*
115. Matsui, T., N. Abe, "Introduction to Constitutive Law of Soils; Elasto-Plastic Formulation and Its Application," *Tsuchi-to-Kiso, Japan Society of Soil Mechanics and Foundation Engineering*, Vol. 31, No. 11, November, 1983, pp.97-105
116. Matsumoto, K., M. Fujiwara, T. Katatsu, "Measurements due to Excavation by Soil Pressure Type Shield," *Proceedings, 16th Japan Conference on Soil Mechanics and Foundation Engineering, 1981, pp.1525-1532*
117. Matsuo, S., M. Makino, "Place-in-cast Concrete Lining in Shield Tunneling Method," *Journal of Mechanical Construction and Machinery*, September, 1980, pp.45-50
118. McMeeking, R. M., J. R. Rice, "Finite-Element Formulations for Problems of Large Elastic-Plastic Deformation," *International Journal of Solids Structure*, Vol. 11, 1975, pp.601-616

119. Miki, G., "Effects of Shield Tunneling on Surrounding Ground and Structures," Edited, Proceedings of 29th Symposium of Japan Society of Soil Mechanics and Foundation Engineering, October, 1984
120. Miki, G., T. Saito, H. Yamazaki, "The Principle and Field Experience of a Slurry Mole Method for Tunneling in the Soft Ground," Presented at Specialty Session 1, 'Tunneling in the Soft Ground,' 9th International Conference on Soil Mechanics and Foundation Engineering, Tokyo, 1977
121. Mindline, R. D., "Stress Distribution around a Tunnel," Proceedings, ASCE, Vol. 65, 1939, pp.619-642
122. Minowa, T., "Excavated Soil Discharge Control of EPB Shield and Its Operation Method," 2nd Symposium on Tunneling Technology, 'Status quo of Slurry Shield and EPB Shield Technology; Japan Tunnel Association, February, 1981
123. Miyamoto, Y., K. Naito, S. Yamamoto, H. Nagi, "Construction Control of Slurry Shield Work at Gravelly Ground," Proceedings, 29th Japan Symposium on Soil Mechanics and Foundation Engineering, 1984, pp.11-16
124. Moretto, O., "Deep Excavations and Tunnelling in Soft Ground," Record of Technical Session, Main Session 4, Vol. 4, 7th International Conference on Soil Mechanics and Foundation Engineering, Mexico, 1969, pp.325-328
125. Mori, A., K. Akagi, "Consolidation Phenomena of Normally Consolidated Clays due to the Disturbance Caused by Undrained Shear," Proceedings, Japan Society of Civil Engineers, Vol. 335, July, 1983, pp.117-125
126. Mould, J. C., "Stress Induced Anisotropy in Sand and the Evaluation of a Multi-Surface Elasto-Plastic Material Model," Partial fulfillment of the requirements for the degree of Doctor of Philosophy, University of Colorado, October, 1983
127. Mroz, Z., "Non-Associated Flow Laws in Plasticity," Journal of Mechanics, Vol. 11, No. 1, March, 1963
128. Mroz, Z., "On the Description of Anisotropic Workhardening," Journal of Mechanics and Physics in Solids, Vol. 15, 1967, pp.163-175
129. Mroz, Z., "An Attempt to Describe the Behavior of Metals under Cyclic Loads Using a More General Workhardening Model," Acta Mechanica, No. 7, 1969, pp.199-212
130. Mroz, Z., "On Hypoelasticity and Plasticity Approaches to Constitutive Modeling of Inelastic Behavior of Soils," International Journal for Numerical and Analytical Methods in Geomechanics, Vol. 4, 1980, pp.45-55
131. Mroz, Z., "On Two Limiting Cases of a Multisurface Hardening Model," International Journal for Numerical and Analytical Methods in Geomechanics, Vol. 6, 1982

132. Mroz, Z., N. C. Lind, "Simplified Theory of Cyclic Plasticity," Acta Mechanica, Vol. 22, 1975, pp.131-152
133. Mroz, Z., V. A. Norris, O. C. Zienkiewicz, "An Anisotropic Hardening Model for Soils and Its Application to Cyclic Loading," International Journal for Numerical and Analytical Methods in Geomechanics, Vol. 2, 1978, pp.203-221
134. Mroz, Z., V. A. Norris, O. C. Zienkiewicz, "Application of an Anisotropic Hardening Model in the Analysis of Elasto-Plastic Deformation of Soils," Geotechnique, Vol. 29, No. 1, 1979a, pp.1-34
135. Mroz, Z., V. A. Norris, O. C. Zienkiewicz, "Simulation of Behavior of Soils under Cyclic Loading by Using More General Hardening Rule," University of Swansea Report, 1979b
136. Mroz, Z., V. A. Norris, O. C. Zienkiewicz, "An Anisotropic, Critical State Model for Soils Subject to Cyclic Loading," Geotechnique, Vol. 31, No. 4, 1981, pp.451-469
137. Mroz, Z., V. A. Norris, "Elastoplastic and Viscoplastic Constitutive Models for Soils with Application to Cyclic Loading," Soil Mechanics-Transient and Cyclic Loads, Edited by G. N. Pande and O. C. Zienkiewicz, Chapter 8, John Wiley & Sons, 1982, pp.173-217
138. Murayama, S., S. Matsuoka, "On the Settlement of Granular Media Caused by a Local Yielding in the Media," Proceedings, Japan Society of Civil Engineers, Vol. 172, 1969, pp.31-42
139. Naito, K., "The Earth Pressure Balance Shield: Case Studies, Current Research, Future Prospects," Underground Space, Vol. 8, No. 2, 1984, pp.89-94
140. Naito, K., "The Earth Pressure Balance Shield Technology," Tunnel and Tunneling, in press, 1985
141. NAVFAC DM-7, Design Manual; Soil Mechanics, Foundation and Earth Structures, Department of the Navy, March 1971, revised, March 1974
142. O'conner, W., K. Naito, T. Shirasuna, "San Francisco N-2 Sewer Main Tunnel Project," International Tunneling Symposium "Underground Space and Technical Transfer," Minnesota University, Minneapolis, October, 1983
143. Okuzono, K., "Backfill Grouting in Shield Tunneling in Questionnaires," Proceedings, 6th Symposium on Tunneling Technology, 'Backfill Grouting in Shield Tunneling,' Japan Tunneling Association, September, 1984, pp.37-48
144. O'Reilly, M. P., B. M. New, "Settlements above Tunnels in the United Kingdom - Their Magnitude and Prediction," Tunneling '82, The Institute of Mining and Metallurgy, 1982, pp.173-181

145. O'Rourke, T. D., "Guideline for Tunnel Lining Design," Edited, The Technical Committee on Tunnel Lining, the Underground Technology Research Council, May, 1984
146. Orr, T. L. L., J. H. Atkinson, C. P. Wroth, "Finite Element Calculation for the Deformation around Model Tunnel," Computer Methods in Tunnel Design, Institution of Civil Engineers, 1978, pp.121-144
147. Osaimi, A. E., G. W. Clough, "Pore-Pressure Dissipation During Excavation," Journal of the Geotechnical Engineering, ASCE, Vol. 105, GT4, April, 1979, pp.481-497
148. Osaka City Bureau of Civil Engineering, Japan, "Technical Statement of Large-scale Slurry Shield Tunneling Method, Hirano River Project of Underground Regulation Reservoir Construction," 1984
149. Palmer, J. H. L., D. J. Belshaw, "Deformation and Pore Pressures in the Vicinity of a Precast, Segmented, Concrete-Lined Tunnel in Clay," Canadian Geotechnical Journal, Vol. 17, 1980, pp.174-184
150. Pande, G. N., O. C. Zienkiewicz, "Soil Mechanics - Transient and Cyclic Loads," Edited, John Wiley & Sons, 1982
151. Peck, R. B., "Deep Excavations and Tunneling in Soft Ground," State-of-the-Art Report, Seventh International Conference on Soil Mechanics, and Foundation Engineering, Mexico City, State-of-the-Art Volume, 1969, pp.225-281
152. Peck, R. B., "State of the art: Soft-Ground Tunneling," Proceedings of Technical Session, Tunnelling in Soil and Rock, Geotech III Specialty Conference, ASCE, Atlanta, May, 1984, pp.1-11
153. Peck, R. B., A. J. Hendron, B. Mohraz, "State of the Art of Soft Ground Tunneling," Proceedings, 1st Rapid Excavation and Tunneling Conference, Vol. 1, 1972, pp.259-286
154. Pender, M. J., "A Model for the Behaviour of Overconsolidated Soil," Geotechnique, Vol. 28, No. 1, 1978, pp.1-25
155. Pender, M. J., Discussion on "Stress Path Methods: Second Edition," Journal of the Geotechnical Engineering, ASCE, Vol. 7, GT9, September, 1980
156. Peterson, E., P. Frobenius, "Soft-ground Tunneling Technology on the BART Project," Civil Engineering, ASCE, October, 1971, pp.72-76
157. Phillips, A., R. L. Sierakowski, "On the Concept of the Yield Surface," Acta Mechanica, Vol. 1, 1965, pp.29-35
158. Pietruszczak, St., Z. Mroz, "On Hardening Anisotropy of K-Consolidated Clays," International Journal for Numerical and Analytical Methods in Geomechanics, Vol. 7, 1983, pp.19-38

159. Pietruszczak, St., Z. Mroczka, "Application of an Anisotropic Hardening Model to Analyses of Axisymmetric Footing," International Journal for Numerical and Analytical Methods in Geomechanics, in press, 1984
160. Poorooshasb, H. B., I. Holubec, A. N. Sherbourne, "Yielding and Flow of Sand in Triaxial Compression: Part I," Canadian Geotechnical Journal, Vol. III, No. 4, 1966, pp.179-190
161. Poorooshasb, H. B., I. Holubec, A. N. Sherbourne, "Yielding and Flow of Sand in Triaxial Compression: Part II and III," Canadian Geotechnical Journal, Vol. IV, No. 4, 1967, pp.376-397
162. Prager, W., "Recent Development in the Mathematical Theory of Plasticity," Journal of Applied Physics, Vol. 22, 1949, pp.235-241
163. Prager, W., "The Theory of Plasticity - A Survey of Recent Achievement," Proceedings, Institution of Mechanical Engineers, Vol. 169, 1955, pp.41-47
164. Prevost, J. H., "Mathematical Modeling of Monotonic and Cyclic Undrained Clay Behavior," International Journal for Numerical Analytical Method in Geomechanics, Vol. 1, 1977, pp.195-216
165. Prevost, J. H., "Anisotropic Undrained Stress-strain Behavior of Clays," Journal of the Geotechnical Engineering Division, ASCE, Vol. 104, GT8, August, 1978a, pp.1075-1090
166. Prevost, J. H., "Plasticity Theory for Soil Stress-strain Behavior," Journal of the Engineering Mechanics Division, ASCE, Vol. 104, EM5, October, 1978b, pp.1177-1198
167. Prevost, J. H., "Mathematical Modeling of Soil Stress-Strain-Strength Behavior," 3rd International Conference on Numerical Method in Geomechanics, Aachen, April, 1979, pp.347-361
168. Prevost, J. H., "Constitutive Theory for Soil," Proceeding of the Workshop on Limit Equilibrium, Plasticity and Generalized Stress-Strain Relation in Geotechnical Engineering, McGill University, May, 1980, pp.745-814
169. Prevost, J. H., "Consolidation of an Elastic Porous Media," Journal of the Engineering Mechanics Division, ASCE, Vol. 107, EM1, February, 1981, pp.169-186
170. Prevost, J. H., "DYNA-FLOW: A Nonlinear Transient Finite Element Analysis Program," Department of Civil Engineering, Princeton University, January, 1981, Revised July, 1982a
171. Prevost, J. H., "Two Surface Versus Multi-Surface Plasticity Theories: A Critical Assessment," International Journal for Numerical and Analytical Method in Geomechanics, Vol. 6, 1982b, pp.323-338
172. Prevost, J. H., "Nonlinear Transient Phenomena in Saturated Porous Media," Computer Methods in Applied Mechanics and Engineering, Vol. 20, 1982c, pp.3-18

173. Prevost, J. H., "Nonlinear Transient Phenomena in Elastic-Plastic Soils," *Journal of the Engineering Mechanics Division, ASCE*, Vol. 108, EM6, December, 1982d, pp.1297-1311
174. Prevost, J. H., "Constitutive Equation for Pressure Sensitive Soils: Theory, Numerical Implementation, and Examples," Personal communication, June, 1983
175. Prevost, J. H., K. Höeg, "Effective Stress-Strain-Strength Model for Soils," *Journal of the Geotechnical Engineering Division, ASCE*, GT3, Vol. 101, March, 1975, pp.259-278
176. Prevost, J. H., K. Höeg, "Plasticity Model for Undrained Stress-Strain-Strength Behavior," 9th International Conference on Foundation Engineering and Soil Mechanics, Tokyo, Japan, 1977, pp.255-261
177. Prevost, J. H., T. J. R. Hughes, M. F. Cohen, "Analysis of Gravity Offshore Structure Foundation," *Journal of Petroleum Technology*, February, 1980, pp.199-209
178. Prevost, J. H., B. Cuny, T. J. R. Hughes, R. F. Scott, "Offshore Gravity Structure: Analysis," *Journal of the Geotechnical Engineering Division, ASCE*, Vol. 107, GT2, February, 1981, pp.143-165
179. Prevost, J. H., T. J. R. Hughes, "Finite-Element Solution of Elastic-Plastic Boundary-Value Problems," *Journal of Applied Mechanics, ASME*, Vol. 48, March, 1981
180. Roscoe, K. H., A. M. Schofield, A. Thurairajah, "Yielding of Clays in States Wetter than Critical," *Geotechnique*, Vol. 13, No. 3, 1963, pp.211-239
181. Roscoe, K. H., J. B. Burland, "On the Generalized Stress-Strain Behavior of 'Wet' Clay," *Engineering Plasticity*, Cambridge University Press, 1968, pp.535-609
182. Rowe, R. K., G. J. Kack, "A Method of Estimating Surface Settlement above Tunnels Constructed in Soft Ground," *Canadian Geotechnical Journal*, Vol. 20, No. 1, 1983a
183. Rowe, R. K., G. J. Kack, "Some Application for Analysis in the Estimation of Settlements Caused by Tunneling," *Canadian Geological Journal*, Vol. 20, No. 2, 1983b
184. Saito, J., T. Fujiwara, K. Naito, "Elasto-plastic FEM Analyses on Ground Movement Surrounding of Shield Tunnel," *Bulletin of Technical Research Institute, Ohbayashi Corporation*, No. 7, 1973, pp.112-116
185. Saito, J., Y. Hanyuda, R. Fujiwara, Y. Yamashita, "Present Status and Problems in Construction by Mechanical Blind Shield Method (Earth Pressure Balance Shield)," *Bulletin of Technical Research Institute, Ohbayashi Corporation*, No. 20, 1980, pp.61-64

186. Saito, J., T. Fujiwara, Y. Hanyuda, T. Tanaka, "Experiments on Continuous Transportation of Excavated Soils in Foam-injected Shield Tunneling," Bulletin of Technical Research Institute, Ohbayashi Corporation, Vol. 27, 1983, pp.107-111
187. Sakurai, S., "Direct Strain Evaluation Technique in Construction of Underground Opening," 22nd U. S. Symposium on Rock Mechanics, MIT, 1981
188. Sasaki, M., "Mechanism of Face Stability during EPB Shield Tunneling," 2nd Symposium on Tunneling Technology, 'Status quo of Slurry Shield and EPB Shield Technology,' Japan Tunnel Association, February, 1981
189. Sasaki, M., M. Tanaka, "Face Stability and Ground Condition for Advanced Shield Method," Shield Tunneling Methods and Ground Condition, Japan Society of Soil Mechanics and Foundation Engineering, 1981, pp.87-104
190. Schiffman, R. L., A. T. F. Chen, "An Analysis of Consolidation Theories," Journal of Soil Mechanics and Foundation Division, ASCE, Vol. 95, SM1, January, 1969, pp.285-312
191. Schofield, A. N., C. P. Wroth, "Critical State Soil Mechanics," McGraw Hill, 1968
192. Seed, H. B., I. Noorany, I. M. Smith, "Effect of Sampling and Disturbance on the Strength of Soft Clays," Soil Mechanics and Bituminous Materials Research Laboratory, Report No. TE64-1, University of California, Berkeley, 1964
193. Shimizu, N., S. Sakurai, "Application of Boundary Element Method for Back Analysis Associated with Tunnelling Problems," Proceedings, 5th International Conference on Boundary Elements, Hiroshima, Japan, November, 1983, pp.645-655
194. Sinram, A., "Behavior of San Francisco Bay Mud to Cubical Shear," Engineer's degree thesis submitted to Stanford University, 1983.
195. Skempton, A. W., "The Pore-Pressure Coefficient A and B," Geotechnique, Vol. 4, No. 4, 1954, pp.143-147
196. Small, J. C., J. R. Booker, E. H. Davis, "Elasto-Plastic Consolidation of Soil," International Journal of Solids Structure, Vol. 12, 1976, pp.431-448
197. Sokolovski, V. V., "Statics of Granular Media," Pergomon Press, New York, 1965
198. Sture, S., "Model by Prevost, Part 6, Workshop on Evaluation of Constitutive Parameter for Geological Materials," Symposium on Implementation of Computer Procedure and Stress-Strain Laws in Geotechnical Engineering, Chicago, August, 1981

199. Takeyama, T., S. Kotake, M. Takano, "Shield Tunneling Methods and Ground Conditions; Ground Settlement," Tsuchi-to-Kiso, Journal of Japan Society of Soil Mechanics and Foundation Engineering, Vol. 26, No. 3, 1978
200. Tan, D. Y., G. W. Clough, "Ground Control for Shallow Tunnels by Soil Grouting," Journal of the Geotechnical Engineering Division, ASCE, Vol. 106, GT9, September, 1980, pp.1037-1057
201. Terzaghi, K., "Erdbaumechanik auf bodenphysikalischer Grundlage," Franz Deuticke, Vienna, 1925
202. Terzaghi, K., "Shield Tunnels of the Chicago Subway," Journal of the Boston Society of Civil Engineers, Vol. 329, No. 3, July, 1942, pp.67-114
203. Terzaghi, K., "Theoretical Soil Mechanics," John Wiley & Sons, 1943
204. Timoshenko, S. P., J. H. Goodier, "Theory of Elasticity," Third Edition, McGraw Hill, New York, 1970, p.567
205. Tsukada, A., T. Niwa, "Selection of Shield Type for Various Ground Condition," Shield Tunneling Methods and Ground Conditions, Japan Society of Soil Mechanics and Foundation Engineering, 1981, pp.105-123
206. Venturini, W. S., C. Brebbia, "The Boundary Element Method for the Solution of No-Tension Materials," Proceedings, 3rd International Seminar on Boundary Element Methods, Irvine, California, July, 1981, pp.371-395
207. Ward, W. H., M. J. Pender, "Tunneling in Soft Ground - General Report," Vol. 4, Proceedings, 10th International Conference on Soil Mechanics and Foundation Engineering, Stockholm, 1981, pp.261-275
208. Wood, D. M., "True Triaxial Stress-Strain Behavior of Kaolin," Proceedings, Symposium on the Role of Plasticity in Soil Mechanics, Cambridge University, England, 1973, pp.67-93
209. Wroth, C. P., "The Predicted Performance of Soft Clay under a Trial Embankment Loading Based on the Cam-clay Model." Finite Elements in Geomechanics, Edited by G. Gudehus, John Wiley, London, 1975, pp.191-208
210. Yamada, Y., A. S. Wifi, "Large Strain Analysis of Some Geomechanics Problems by the Finite Element Method," International Journal for Numerical and Analytical Methods in Geomechanics, Vol. 1, 1977, pp.299-318
211. Yamamoto, M., H. Kawada, M. Higo, "Shield Tunneling Methods and Ground Conditions: Shield Segments," Tsuchi-to-Kiso, Journal of Japan Society of Soil Mechanics and Foundation Engineering, Vol. 26, No. 1, 1978
212. Yamazaki, H., "Problems of Slurry Shield Method and Their Counter-measures," Presented at Tunneling '76 Symposium of the Japan Tunneling Association, 1976

213. Yoshizawa, K., H. Shimazu, N. Hosoda, "Effects of Instantaneous Backfill Grouting of Liner on Ground Movements in Soft Clay Tunneling," Proceedings, 29th Japan Symposium on Soil Mechanics and Foundation Engineering, Tokyo, Japan, November, 1984
214. Ziegler, H., "A Modification of Prager's Hardening Rule," Quarterly Applied Mathematics, Vol. XVII, No. 1, 1959, pp.55-65
215. Zienkiewicz, O. C., "The Finite Element Method," Third Edition, McGraw Hill, London, 1977

Appendix A

MATHEMATICAL EXPRESSION OF PREVOST MODEL

A.1 Inversion Procedure of Constitutive Equation

Since the strain increment is related to the stress increment in terms of equations 3.33a and 3.33b, an inversion is required to express the stress increment in terms of the strain increment so that the constitutive equation be readily applicable to implementation based on the deformation formulation such as the ordinary finite element method.

Equation 3.33a may be rewritten in a form such that the mean pressure and the deviatoric stress are completely separated.

$$\dot{\epsilon}_v = \left[ \frac{1}{B} + \frac{1}{H'} \frac{9P''Q''}{|Q_{kl}|^2} \right] \dot{p} + \frac{3P''}{H'} \frac{1}{|Q_{kl}|^2} Q'_{mn} \dot{s}_{mn} \quad (A.1)$$

Similarly equation 3.33b is modified after taken a scalar product with  $Q'_{ij}$

$$Q'_{ij} \dot{\epsilon}_{ij} = \left( \frac{1}{2G} + \frac{1}{H'} \frac{|Q'_{pr}|^2}{|Q_{kl}|^2} \right) Q'_{ij} \dot{s}_{ij} + \frac{1}{H'} \frac{|Q'_{pr}|^2}{|Q_{kl}|^2} 3Q'' \dot{p} \quad (A.2)$$

Equations A.1 and A.2 can be solved for  $\dot{p}$  and  $Q'_{ij} \dot{\epsilon}_{ij}$  ;

$$\dot{p} = \frac{B \left[ \left(1 + \frac{2G}{H'}\right) |Q'_{pr}|^2 + 3Q''^2 \right] \dot{\epsilon}_v - \frac{2BG}{H'} 3P''Q'_{mn} \dot{\epsilon}_{mn}}{\left(1 + \frac{2G}{H'}\right) |Q'_{pr}|^2 + 3Q''^2 + 9 \frac{B}{H'} P''Q''} \quad (A.3)$$

$$Q'_{ij} \dot{\epsilon}_{ij} = \frac{\left[ 2G|Q'_{pr}|^2 + 6GQ''^2 + \frac{2GB}{H'} 9P''Q'' \right] Q'_{mn} \dot{\epsilon}_{mn} - \frac{2GB}{H'} |Q'_{pr}|^2 3Q'' \dot{\epsilon}_v}{\left(1 + \frac{2G}{H'}\right) |Q'_{pr}|^2 + 3Q''^2 + 9 \frac{B}{H'} P''Q''} \quad (A.4)$$

The projection of stress increment onto the normal of the yield surface,

$Q'_{ij} e_{ij}$ , can be expressed now in terms of the strain increment if one substitutes equations A.3 and A.4 into an equation below,

$$\frac{Q_{mn} \dot{\sigma}_{mn}}{|Q_{kl}|^2} = \frac{Q'_{mn} \dot{s}_{mn} + 3Q''\dot{p}}{|Q_{kl}|^2} = 2G \cdot X \quad (A.5)$$

in which

$$X = \frac{Q'_{mn} \dot{\epsilon}_{mn} + \left(\frac{B}{2G}\right) 3Q''\dot{\epsilon}_v}{\left(1 + \frac{2G}{H'}\right) |Q'_{pr}|^2 + 3Q''^2 + 9\left(\frac{B}{H'}\right) P''Q''} \quad (A.6)$$

Equations 3.33a and 3.33b are simply modified and combined with the above equations. It leads to

$$\begin{aligned} \dot{p} &= B\dot{\epsilon}_v - \frac{B}{H'} 3P'' \frac{Q_{mn} \dot{\sigma}_{mn}}{|Q_{kl}|^2} \\ &= B\dot{\epsilon}_v - \frac{2GB}{H'} 3P'' X \end{aligned} \quad (A.7)$$

$$\begin{aligned} \dot{s}_{ij} &= 2G\dot{\epsilon}_{ij} - \frac{2G}{H'} Q'_{ij} \frac{Q_{mn} \dot{\sigma}_{mn}}{|Q_{kl}|^2} \\ &= 2G\dot{\epsilon}_{ij} - \frac{4G^2}{H'} Q'_{ij} X \end{aligned} \quad (A.8)$$

which are identical to equations 3.34a and 3.34b.

## A.2 Translation Rule for Nested Yield Surface

The translation of nested yield surface  $f_m$  follows equation 3.45

$$\dot{\xi}_{ij} = \delta \mu \mu_{ij} \quad (A.9)$$

where  $\mu_{ij}$  defines the translation direction and is decomposed into the deviatoric and hystatic parts:

$$\mu_{ij} = \mu'_{ij} + \delta_{ij} \mu'' \quad (A.10)$$

The stress point  $\sigma_{ij}$  stays on  $f_m$ . After a stress increment  $\dot{\sigma}_{ij}$  is applied, new stress point  $\sigma_{ij} + \dot{\sigma}_{ij}$  should be also on the yield surface. This leads to a set of equations, which are the decomposed form:

$$\frac{3}{2} (s_{ij} - \alpha_{ij}) (s_{ij} - \alpha_{ij}) + c^2 (p - \beta)^2 - k^2 = 0 \quad (\text{A.11a})$$

$$\begin{aligned} \frac{3}{2} [ (s_{ij} - \alpha_{ij}) + (\dot{s}_{ij} - \dot{\alpha}_{ij}) ] [ (s_{ij} - \alpha_{ij}) + (\dot{s}_{ij} - \dot{\alpha}_{ij}) ] \\ + c^2 [ (p - \beta) + (\dot{p} - \dot{\beta}) ]^2 - (k + \dot{k})^2 = 0 \end{aligned} \quad (\text{A.11b})$$

Combining equations A.9 to A.11b, we get

$$\begin{aligned} \frac{3}{2} \{ \dot{\alpha}_{ij}^2 - 2\dot{\alpha}_{ij} [ (\dot{s}_{ij} - \alpha_{ij}) + s_{ij} ] + 2 (s_{ij} - \alpha_{ij}) \dot{s}_{ij} + \dot{s}_{ij}^2 \} \\ + c^2 \{ \dot{\beta}^2 - 2\dot{\beta} [ (p - \beta) + \dot{p} ] + 2 (p - \beta) \dot{p} + \dot{p}^2 \} - 2k\dot{k} - \dot{k}^2 = 0 \end{aligned} \quad (\text{A.12})$$

And a change of the position of  $f_m$ ,  $\dot{\xi}_{ij}$  can be determined by means of the Mroz translation rule expressed in a decomposed form:

$$\dot{\alpha}_{ij} = \delta\mu \mu'_{ij} = \delta\mu \frac{k_{m+1}}{k_m} (s_{ij} - \alpha_{ij}^{(m)}) - (s_{ij} - \alpha_{ij}^{(m+1)}) \quad (\text{A.13a})$$

$$\dot{\beta} = \delta\mu \mu'' = \delta\mu \frac{k_{m+1}}{k_m} (p - \beta^{(m)}) - (p - \beta^{(m+1)}) \quad (\text{A.13b})$$

Substitution of equations A.13a and A.13b in equation A.12 yields a quadratic equation with respect to  $\delta\mu$

$$A (\delta\mu)^2 - 2B (\delta\mu) + C = 0 \quad (\text{A.14})$$

where

$$\begin{aligned}
 A = & (k_{m+1}) - \frac{3k_{m+1}}{k_m} (s_{ij} - \alpha_{ij}^{(m)}) (s_{ij} - \alpha_{ij}^{(m+1)}) \\
 & + \frac{3}{2} (s_{ij} - \alpha_{ij}^{(m+1)}) (s_{ij} - \alpha_{ij}^{(m+1)}) - \frac{2k_{m+1}}{k_m} c^2 (p - \beta^{(m)}) (p - \beta^{(m+1)}) \\
 & + c^2 (p - \beta^{(m+1)})^2
 \end{aligned} \tag{A.15}$$

$$\begin{aligned}
 B = & k_m k_{m+1} + \frac{3}{2} \mu'_{ij} \dot{s}_{ij} + c^2 \mu'' \dot{p} \\
 & + (s_{ij} - \alpha_{ij}^{(m)}) (s_{ij} - \alpha_{ij}^{(m+1)}) + c^2 (p - \beta^{(m)}) (p - \beta^{(m+1)})
 \end{aligned} \tag{A.16}$$

$$\begin{aligned}
 C = & \frac{3}{2} [ 2 (s_{ij} - \alpha_{ij}^{(m)}) \dot{s}_{ij} + \dot{s}_{ij} \dot{s}_{ij} ] \\
 & + c^2 [ 2 (p - \beta^{(m)}) \dot{p} + \dot{p}^2 ] - 2 k_m \dot{k}_m - \dot{k}_m^2
 \end{aligned} \tag{A.17}$$

Equation A.14 is solved for  $\delta\mu$

$$\delta\mu_1, \delta\mu_2 = \frac{1}{A} ( B \mp \sqrt{B^2 - AC} ) \tag{A.18}$$

Of the two possible solutions,  $\delta\mu$  is selected in conformity with the following considerations. Since the new stress point  $\sigma_{ij} + \dot{\sigma}_{ij}$  should be within  $f_{m+1}$ , the magnitude of yield surface translation is limited as  $\delta\mu < 1$ . The stress increment is supposedly applied as a loading process, that is  $Q_{ij} \dot{\sigma}_{ij} > 0$ , so translation may occur somewhat in this side. Furthermore in order to assure smooth translation, the projection of stress increment onto the conjugate line,  $\mu_{ij} \dot{\sigma}_{ij}$ , naturally stays in the same direction of the  $f_m$  translation, that is,  $\mu_{ij} \dot{\sigma}_{ij}$  and  $\delta\mu$  possess the same signs. This can be simplified as the selection of a smaller value of  $\delta\mu$  when the direction of loading path

in the stress space is not changed significantly, such as radial loading processes. But this feature will become very important for the stress increment which changes the direction of stress path drastically.

However the quadratic equation A.15 does not provide a solution for  $\delta\mu$  unconditionally.  $\delta\mu$  is affected by the relative configuration of  $f_m$  and  $f_{m+1}$  as well as the direction of the stress increment applied.  $\delta\mu$  will not be found when the direction of stress increment  $\dot{\sigma}_{ij}$  is far from the direction of conjugate points  $\mu_{ij}$  and its magnitude is not small enough relative to the size of the yield surface. In such a situation another trial will be done for the conjugate point on the yield surface  $f_{m+2}$  next to the  $f_{m+1}$ . If such a trial happens to fail to obtain  $\delta\mu$ , for all the surfaces outside of  $f_m$ , then the hardening rule is switched to Phillip's kinematic hardening rule with respect to the stress increment  $\dot{\sigma}_{ij}$ , in which the change in size  $\dot{k}$  of  $f_m$  is taken in consideration.

### A.3 Translation and Expansion Rule for the Bounding Yield Surface

The translation and expansion of the bounding yield surface  $f_p$  must follow the critical state line. From equation 3.61 without subscript or superscript  $p$ ,

$$\xi_{ij} = a_{ij} k \quad (A.19)$$

In an incremental form

$$\dot{\xi}_{ij} = a_{ij} \dot{k} \quad (A.20)$$

Using equations A.19 and A.20, we can eliminate the tensor constant

$$\frac{\dot{\xi}_{ij}}{\xi_{ij}} = \frac{\dot{k}}{k} = \frac{\dot{\alpha}_{ij}}{\alpha_{ij}} = \frac{\dot{\beta}}{\beta} = d \quad (\text{A.21})$$

where  $d$  is a scalar constant. The current stress point  $\sigma_{ij}$  moves to a new position in the stress space after applied stress increment  $\dot{\sigma}_{ij}$ . Both stress points  $\sigma_{ij}$  and  $\sigma_{ij} + \dot{\sigma}_{ij}$  must be on the yield surface  $f_p$ .

$$\frac{3}{2} (s_{ij} - \alpha_{ij}) (s_{ij} - \alpha_{ij}) + c^2 (p - \beta)^2 - k^2 = 0 \quad (\text{A.22})$$

$$\begin{aligned} \frac{3}{2} [ (s_{ij} - \alpha_{ij}) + (\dot{s}_{ij} - \dot{\alpha}_{ij}) ] [ (s_{ij} - \alpha_{ij}) + (\dot{s}_{ij} - \dot{\alpha}_{ij}) ]^2 \\ + c^2 [ (p - \beta) + (\dot{p} - \dot{\beta}) ]^2 - (k + \dot{k})^2 = 0 \end{aligned} \quad (\text{A.23})$$

Using equations A.22 and A.23 and combining with equation A.21, we get a quadratic equation with respect to  $d$  :

$$A d^2 - 2B d + C = 0 \quad (\text{A.24})$$

where

$$A = \frac{3}{2} \alpha_{ij} \alpha_{ij} + c^2 \beta^2 + k^2 \quad (\text{A.25})$$

$$B = \frac{3}{2} [ (s_{ij} - \alpha_{ij}) + \dot{s}_{ij} ] \alpha_{ij} + c^2 [ (p - \beta) + \dot{p} ] \beta + k^2 \quad (\text{A.26})$$

$$C = \frac{3}{2} [ 2 (s_{ij} - \alpha_{ij}) s_{ij} + s_{ij} s_{ij} ] + c^2 [ 2 (p - \beta) \dot{p} + (\dot{p})^2 ] \quad (\text{A.27})$$

Equation A.24 can be easily solved for  $d$  and from equation A.21

$$\dot{k}_{1,2} = \frac{k}{A} (B \mp \sqrt{B^2 - AC}) \quad (\text{A.28})$$

$\dot{k}_1$  and  $\dot{k}_2$  are corresponding to negative and positive signs in the right hand side. Since  $A > 0$ , it is found  $\dot{k}_1 < \dot{k}_2$ .

When the material consolidates for the applied stress increment in which

$$\lambda \dot{\epsilon}_V^P > 0 \quad , \quad (A.29)$$

the yield surface  $f_p$  is supposed to expand, that is  $\dot{k} > 0$ . On the other hand the material is dilating,

$$\lambda \dot{\epsilon}_V^P < 0 \quad (A.30)$$

then  $f_p$  is expected to shrink,  $\dot{k} < 0$ . Therefore  $\dot{k}_1$  or  $\dot{k}_2$  is selected such that

$$\lambda \dot{\epsilon}_V^P \cdot \dot{k} > 0 \quad . \quad (A.31)$$

## Appendix B

### USER'S MANUAL OF PROGRAM PRVCNST

#### B.1 General Description of Program PRVCNST

Program PRVCNST calculates the constitutive relation of the Prevost model, which predicts soil behavior for arbitrarily applied loads. This program was written for easy use in predicting soil response to changing stresses. In spite of the sophistication of the Prevost model, the program is so simple that it can be conveniently used to get acquainted with the Prevost model as well as to enable simulation and follow a given stress path.

The Prevost model is an elasto-plastic constitutive model which takes advantage of the nested yield surface with combining isotropic and kinematic hardening rules. Although several options are available, such as using pressure sensitive or nonsensitive material behavior, isoparametric or kinematic hardening rules, of a combination of both, the pressure-sensitive material behavior with a combination hardening rules is mainly used because of its potential versatility. Theoretical development of the Prevost model has been described in the Chapter 3 and is not described here. Knowledge of the Prevost model, especially of the elasto-plastic formulation, the hardening rule, and the critical state concept, will help in using the program more efficiently and understanding the results that the program provides. It also will help in figuring out the causes of unexpected results which happen occasionally. It is advisable that users of the program be at least familiar with the meaning and the way of prepara-

tion of the Prevost model parameters.

As mentioned before, the program PRVCNST calculates stresses for a given set of strains, or strains in terms of prescribed stresses, or mixed cases of unknown strains and stresses. The constitutive relation is formulated in incremental form for prescribed strains in terms of unknown stresses since such a formulation is adopted to ordinary finite element codes. Therefore, for some stresses with known values, a respective part of the constitutive matrix is inverted to obtain the unknown strains. By selecting appropriate strains and stresses, a wide variety of loading conditions such as undrained, drained or a mixed loading path, can be simulated by means of the program PRVCNST.

Input data to the program PRVCNST consist of three types: control parameters on three cards as heading input data, material parameters which characterize elastic and plastic moduli and yield surface configurations, and loading data which specify incremental loading to be applied on the current stress state. In output listings, incremental and accumulated quantities of stresses and strains are printed. Also output are subaccumulated values which are accumulated stresses/strains for the loading steps after their values are reset to zero. This is useful when multistage loading sequences are to be applied.

In addition to the results of stress-strain calculations, yielding information is optionally available. The yielding information is a sort of check list which covers parameters associated with the yielding and hardening process in Prevost model implementation. Ten different levels

of yielding information can be obtained by calling the respective options.

They are:

1. Yield surface indices
2. Current size and position of yield surfaces
3. Updated elastic moduli
4. Updated plastic moduli associated with nested yield surfaces
5. Translation of currently active yield surface
6. Hardening and consistency condition
7. Loading reversal information
8. Relative position of stress point and yield surface
9. Prevost model constitutive matrix
10. Dynamic storage allocation information

Every level of such information is designed as a separate routine, but dependent on each other, so that additional information at another processing stage of the program can be obtained simply by calling the corresponding subroutine if it is required.

The following things should be recognized by users of this program. As for every computer program, the program PRVCNST might be incomplete in the current version. Continual enhancement seems necessary. When unrealistic behavior is observed, it may be a result of poor implementation of the program or by inadequate model parameters evaluated with uncertainty, which can be responsible for unrealistic behavior of the model. Some problems of this kind may be traced for a certain stress path.

It is noted that controversy exists concerning the parameter evaluation procedure of the model. Model parameters are desired reasonable for accurate prediction of soil behavior and effective for computational

ease in the model implementation. Two special stress paths are free from intricate elaboration of parameter evaluation. One is isotropic consolidation and the other is an undrained triaxial test in which pore pressure develops such that the effective mean pressure always stays on the apexes of the yield surfaces. It is recommended that users who are not familiar with the Prevost model begin with those simple cases.

The size of the program is not large relative to finite element programs. However, it contains about four thousand lines of FORTRAN statements. Compiling costs cannot be ignored. Therefore, the program should not be compiled everytime it is used. Instead, it is highly recommended that a load module be built and store it on the MVS system online disk in order to excute the program without excessive compiling and link/edit job steps. This procedure becomes crucial for a repetitive excution of the program which is very common for numerical simulation.

## B.2 Input Data

### B.2.1 Control Cards

A title card is used to input a descriptive title for the problem. This title is printed in the output listing.

Title ( Card 1 )

Card	Columns	Variable	Format	Explanation
1/1	1 - 80	Title	10A8	Title of the problem to be solved

A control parameter card is used to input and specify characteristics of the problem.

Control parameter ( Card 2 )

Card	Columns	Variable	Format	Explanation
1/1	1 - 5	IOPT	15	Analysis option code ( Generally, IOPT = 3 )
	6 - 10	JHPTYP	15	Prevost model subtype
	11 - 15	ISYMM	15	Constitutive matrix symmetry code. ISYMM = 0 symmetry ISYMM ≠ 0 not symmetry
	16 - 20	NYS	15	Number of yield surfaces
	21 - 25	M1	15	Initial yield surface
	26 - 30	MYOUT1	15	First loading step number and,
	31 - 35	MYOUT2	15	Last loading step number for which yielding informations are output. MYOUT1 is left zero or blank if no yielding information is needed.

Besides three-dimensional stress-strain relation for which IOPT = 3 , the program can deal with a problem under the plane strain or plane stress condition for which IOPT = 1 and 2 , respectively. Since three-dimensional

is capable to treat problems with the plane stress or plane strain condition, an option code of three is the best to be used.

JHPTYP specifies the subtype of the Prevost model. JHPTYP = 1 to 5 are used for pressure nonsensitive materials with different types of the hardening/softening rule. JHPTYP = 6 is for pressure sensitive material, the hardening rule of which is a combination of kinematic and isotropic types. The main objective of the program PRVCNST is to analyze this type of material behavior. For pressure nonsensitive material, associative flow rules are assumed so that the constitutive matrix is symmetric. On the other hand, pressure symmetric material provides a nonsymmetric constitutive matrix because of the application of the nonassociative flow rule.

Yielding information output is specified by Card 1 - 3 to be explained next MYOUT1 is not equal to zero. MYOUT1 is left blank if no information is required.

In addition to the nested yield surfaces, a dummy, nonactive yield surface must be set up outside of the nesting yield surfaces. Its size must be selected such that it is larger than all other yield surfaces. M1 includes a dummy yield surface.

When MYOUT1 has a value other than zero, a card is required to select output levels of yielding information which will be explained in the section for output.

Yielding information ( Card 3 )

Card	Columns	Variable	Format	Explanation
1/1	1 - 5	IZ1	15	When IZ1 = 1, yielding information of level 1 is output. If IZ1 = 0, no listing provided for this level. Ten levels of yielding information are available for which IZ's are specified independently with the value of one.
	6 - 10	IZ2	15	
	...	...	...	
	45 - 50	IZ10	15	

B.2.2 Material Cards

The following five cards are used to specify Prevost model parameters : such as, elastic moduli, initial stresses, size and position of yield surfaces and plastic moduli associated with each yield surface.

Elastic moduli ( Card 4 )

Card	Columns	Variable	Format	Explanation
1/1	1 - 10	FM(ND1,1)	F10.0	Elastic shear modulus G
	11 - 20	FM(ND2,1)	F10.0	Scaled initial elasto-plastic shear modulus h
	21 - 30	FM(ND3,1)	F10.0	Elastic bulk modulus B
	31 - 41	FM(ND4,1)	F10.0	Bulk exponent n

For JHPTYP = 1 to 5 , which are for pressure nonsensitive materials, the elastic moduli are constant. On the other hand for JHPTYP = 6 corresponding to pressure sensitive material, such moduli are the reference

values at initial mean pressure since they are to be changed in conformity with the power rule.  $NDi$ 's in the above are  $ND + i$  where  $ND$  is 6 for  $IOPT = 3$  and 4 for  $IOPT = 1$  and 2.

The elasto-plastic shear moduli are scaled in such a way that  $1/h = 1/h' - 1/2G$ , where  $h$  and  $G$  are elasto-plastic and elastic shear module, respectively, physically defined in the plastic theory.

Initial stresses ( Card 5 )

Card	Columns	Variable	Format	Explanation
1/1	1 - 10	FM(1,1)	F10.0	Component 11 of initial stress $\sigma_{11}$
	11 - 20	FM(2,1)	F10.0	Component 22 of initial stress $\sigma_{22}$
	21 - 30	FM(3,1)	F10.0	Component 33 of initial stress $\sigma_{33}$
	31 - 40	FM(4,1)	F10.0	Component 12 of initial stress $\sigma_{12}$
	41 - 50	FM(5,1)	F10.0	Component 23 of initial stress $\sigma_{23}$
	51 - 60	FM(6,1)	F10.0	Component 31 of initial stress $\sigma_{31}$

Sign conversion of stresses should be consistent with those of strains and other material parameters.

Other parameters ( Card 6 )

Card	Columns	Variable	Format	Explanation
1/1	1 - 10	XLAM(3)	F10.0	Softening parameter $\delta_1$
	11 - 20	XLAM(4)	F10.0	Softening parameter $\delta_{ult}$
	21 - 30	XLAM(5)	F10.0	Yield surface axis ratio C
	31 - 40	XLAM(7)	F10.0	Slope of volumetric strain vs mean pressure curve for normally consolidation phase $\lambda$
	41 - 50	XLAM(8)	F10.0	Bulk modulus of pore fluid $B_f$
	51 - 60	XLAM(9)	F10.0	Initial pore pressure $P_f$

Isotropic softening is dealt with for JHPTYP = 4 and 5 when the stress point reaches the outermost yield surface and follows  $h = \delta_1 G$  until  $k \leq \delta_{ult}$ . Therefore,  $h = 0$  on the outer yield surface and kinematic hardening takes place. Although a use of pore fluid might be helpful to simulate the stress controlled undrained stress path, this should be done with care since such a stress path is known to be different from those obtained in terms of loading with a constant volume.

Yield surface data ( Card 7 )

Card	Columns	Variable	Format	Explanation
1/2	1 - 5	M	I5	Yield surface number, 2 to NYS
	11 - 20	FM(ND1,M)	F10.0	Size of yield surface $k_m$
	21 - 30	FM(ND2,M)	F10.0	Scaled elasto-plastic shear modulus $h_m$
	31 - 40	FM(ND3,M)	F10.0	Plastic bulk modulus $B_m^i$
	41 - 50	FM(ND4,M)	F10.0	Degree of non-associativity $A_m$
2/2	1 - 10	FM(1,M)	F10.0	Initial position of yield surface m Component 11 $\xi_{11}$
	11 - 20	FM(2,M)	F10.0	Component 22 $\xi_{22}$
	21 - 30	FM(3,M)	F10.0	Component 33 $\xi_{33}$
	31 - 40	FM(4,M)	F10.0	Component 12 $\xi_{12}$
	41 - 50	FM(5,M)	F10.0	Component 23 $\xi_{23}$
	51 - 60	FM(6,M)	F10.0	Component 31 $\xi_{31}$

NYS-1 sets of card 7 are required to establish all yield surfaces. The above two cards define one yield surface and so.

### B.2.3 Loading Cards

One loading card establishes a loading step which analyzes for incremental response of the material. For each component either stress or strain should be specified for the stress or strain controlled process desired. For the case commonly used,  $IOPT = 3$ , six components are necessarily defined in terms of the stress/strain selection code.

Loading step ( Card 8 )

Card	Columns	Variable	Format	Explanation
1	1 - 8	CH	A8	'END' terminates the job 'RESET' resets the values of partially accumulated stress/strain according to selection code. A commentary word other than 'END' or 'RESET' can be put here.
	9 - 20	ICONT(I) I = 1, 6	6I2	Stress/strain selection code for each component. Icont = 0 stress controlled Icont = 1 strain controlled
	21 - 80	TEMP(I)	6F10.0	Components of incremental loading values respective to stress/strain selection code.

Six components of stress/strain are placed in order of 11, 22, 33, 12, 23, 31. The sign conversion of stress-strain should be identical to those of material properties.

### B.3 Output Listing

Three types of output listings are provided by program PRVCNST: firstly, tables of input parameters including material properties and yield surface data; secondly output listings of computation results for every loading step; and last, listings of yielding information which are optional but useful when intentionally tracing the yielding and hardening process.

### B.3.1 Model Parameters Used

Three output pages listing input parameters consist of a table of general setup parameters of the problem on the first page, a summary of material property data and the initial status on the second page, and a table of yield surface data on the third page. The input parameters have been fully explained in the input section. An example output can be found at the back of this manual.

### B.3.2 Results

Results of the computation are provided in a simple format as is seen in the example output listing. Unknown stresses/strains according to the selection code of stress/strain control are evaluated by means of the Prevost model soil behavior. Besides incremental and accumulated quantities, partially accumulated stresses/strains are output which are the summation of incremental values for subsequent loading intervals after RESET key word has initialized values of respective stress/strain components.

Volumetric and octahedral strains are calculated for strains and mean pressure and octahedral stresses are output for stresses. Commentary words on the loading cards for each loading step are printed with the loading step number.

### B.3.3 Yielding Information

Ten levels of yield information output listings are available according to the output code IZ. The listings provide useful and basic information with respect to yielding and hardening of the Prevost model material behavior. With this information it is possible to trace translation as well as expansion of yield surfaces in the stress space corresponding to the stress point movement due to the loading increment.

Note that the option to obtain yielding information should be carefully used because a large volume of information is output and boosts the cost of printing and data transference. More than one hundred and fifty lines of printing will be provided for each predictor and corrector phase, which may change with number of yield surfaces and iteration procedure of hardening.

Level 1 lists a trace of yield surface numbers. Information consists of the current yield surface, the yield surface associated with highest stress level previously experienced in the course of the loading/unloading process, and the number of loading reversals.

Level 2 tabulates size and position of yield surface currently held for all the yield surfaces. Such yield surface data are updated and modified in terms of volumetric strain changes.

Level 3 provides elastic moduli of material which is updated according

to the power law. Information listed consists of the elastic shear modulus, the elastic bulk modulus, Lamé's constant  $\lambda$ , the plastic shear modulus associated with the  $f_1$  yield surface and the elastic bulk modulus of pore fluid.

Level 4 tabulates plastic moduli associated with the  $m$ -th yield surface. Plastic shear modulus, plastic bulk modulus, nonassociativity constant and size of the yield surface are listed for each yield surface.

Level 5 provides information on the translation of yield surface in stress space. The information listed consists of the current position of the currently active yield surface, the new position and the movement of the yield surface in the deviatoric stress subspace and along the space diagonal axis.

Level 6 describes hardening information. Three types of hardening rules are applied in the program PRVCNST: the pure kinematic hardening rule; the Mroz hardening rule; and the Cambridge University type hardening rule, which reserves the critical state for a new yielding environment successively. The relative position of the current yield surface  $m$  and a yield surface immediately outside of it,  $m + 1$ , defines a vector of the hardening direction for the first two of the three hardening rules. Two possible translations of the yield surface are listed in terms of a scalar multiplier for the direction of hardening. The vector components associated with the translation are printed in the deviatoric subspace and along the space diagonal.

Level 7 supplies loading reversal information which is useful to confirm the situation associated with a complex loading path. Yielding parameters are so sensitive for a certain stress path that an unexpected stress reduction might occur by reason of the use of the best, but not the exact, evaluation of the model parameters. Loading reversal is defined such that the incremental stress vectors are directed inward on active yield surface. However, the incremental stresses are calculated for applied incremental load in conformity with the constitutive formulation so that the relative direction of incremental stress vector to the tangent of the yield surface is calculated and used to check whether its sign changes or not. This is output with notation of  $X$  in the listing. Numerator of  $X$  is also output as noted  $XNUM$  which depends on incremental strains and is free from hardening parameter. Although perhaps not of primary concern, hardening parameters and the projection of yield function and yield potential onto the hydrostatic axis are also output because they have a role in dilatational behavior.

Level 8 describes the position of the stress point and the center of the active yield surface and their relative position in the stress space as well. They are shown as components of the projection into the deviatoric subspace and onto the hydrostatic axis. This is the basis of the constitutive formulation.

Level 9 tabulates the  $6 \times 6$  constitutive matrix of the Prevost model. When  $I29$  is equal to one, the constitutive relation between deviatoric strains and deviatoric stresses is obtained. This is the main subject of the Prevost

model when IZ9 = 2, an ordinary stress-strain relation is printed.

Level 10 provides addresses of dynamic storage allocations in the program. This information is slightly different from other described above. It will be useful when more information on the yielding process of the Prevost model are necessary to capture the whole process of implementation and/or when expanding modification of the program is intended to improve the model behavior and numerical technique of the program.

#### B.4 Sample Input and Output

In the following a set of sample input data is shown. The model parameters are the ones identified for the Bay Mud for which the  $K_0$  value of the initial stress condition is 0.5 and the undrained strength ratio  $s_u/\sigma'_{v_0}$  is 0.31. Five incremental loading steps are prepared in the sample input for simulating a plane strain compression test. The input data are followed by the printing lists obtained with them.

SAMPLE INPUT OF PROGRAM - PRVCNST

```
//GO EXEC PGM=PRVCNST
//STEP1B DD DSN=AFOOF4.TAKESHI.LOADMOD.VERS02,DISP=OLD
//FT05F001 DD DDNAME=SYSIN
//FT06F001 DD SYSOUT=A
//GO.SYSIN DD *
```

```
SFO BAY MUD UNDRAINED BEHAVIOR, PLANE STRAIN C=1.0 ZLM=10.6 KO=.5
3 6 1 12 1 1 3
0 0
72.90 145.8 194.0 1.0
-0.5000 -1.0000 -0.5000 0.0 0.0
0.0 0.0 1.0 -10.6
2 0.0296 128.8 -63.97 -0.4772
-0.4961 -0.9694 -0.4961 0.0 0.0 0.0
3 0.0456 115.7 -44.86 -0.4478
-0.4940 -0.9528 -0.4940 0.0 0.0 0.0
4 0.0743 95.09 -33.48 -0.4309
-0.4902 -0.9232 -0.4902 0.0 0.0 0.0
5 0.1211 64.17 -27.27 -0.3270
-0.4840 -0.8748 -0.4840 0.0 0.0 0.0
6 0.1843 49.95 -25.75 -0.2301
-0.4757 -0.8095 -0.4757 0.0 0.0 0.0
7 0.2640 22.12 -9.480 -0.1176
-0.4663 -0.7263 -0.4663 0.0 0.0 0.0
8 0.3650 6.99 -9.44 -0.1408
-0.4890 -0.6900 -0.4890 0.0 0.0 0.0
9 0.4620 2.29 -9.68 -0.1474
-0.4817 -0.6057 -0.4817 0.0 0.0 0.0
10 0.4890 0.64 -0.402 -0.0155
-0.4753 -0.5793 -0.4753 0.0 0.0 0.0
11 0.5143 0.0 +1.0 0.0
-0.4714 -0.5572 -0.4714 0.0 0.0 0.0
12 0.5143E03 0.0 0.0 0.0
-0.4714 -0.5572 -0.4714 0.0 0.0 0.0
PL COMP 0 1 1 1 1 0.0 -0.0002 0.0
0 1 1 1 1 0.0 -0.0003 0.0
0.001 0 1 1 1 1 0.0 -0.0005 0.0
0.002 0 1 1 1 1 0.0 -0.0005 0.0
END
/*
//
```

SAMPLE OUTPUT OF PROGRAM-PRVCNST

\*\*\*\*\* SFO BAY MUD UNDRAINED BEHAVIOR, PLANE STRAIN C=1.0 ZLN=10.6 K0=.5 \*\*\*\*\*

```

OPTION CODE OF ANALYSIS          IOPT = 3
PREVOST MODEL SUBTYPE           JHPTYP = 6
SYMMETRY OF CONSTITUTIVE MATRIX ISYMM = 1
NUMBER OF YIELD SURFACE         NYS = 12
INITIAL YIELD SURFACE           MI = 1
NO. OF CASES FOR YIELDING INFORMATION OUTPUT MYOUT = 3
FIRST LOADING STEP FOR Y. I. OUTPUT MYOUT1 = 1
LAST LOADING STEP FOR Y. I. OUTPUT MYOUT2 = 3
LEVEL 1= 0   LEVEL 2= 0   LEVEL 3= 0   LEVEL 4= 0   LEVEL 5= 0
LEVEL 6= 0   LEVEL 7= 0   LEVEL 8= 0   LEVEL 9= 0   LEVEL10= 0
    
```

MATERIAL DATA

```

MATERIAL TYPE ..... (MATYP) = 1
J.H. PREVOST MATERIAL SUB-TYPE ..... (JHPTYP) = 6
NUMBER OF YIELD SURFACES ..... (NYS) = 12
INITIAL LOADING SURFACE ..... (MI) = 1

ELASTIC SHEAR MODULUS          { G } = 7.29000000D+01
INITIAL ELASTO-PLASTIC SHEAR MODULUS { H1 } = 1.45800000D+02
INITIAL EFFECTIVE ELASTIC BULK MODULUS { BE } = 1.94000000D+02
BULK EXPONENT                   { N } = 1.00000000D+00

INITIAL EFFECTIVE STRESSES

COMPONENT 11                   { SIG 11 } = -5.00000000D-01
COMPONENT 22                   { SIG 22 } = -1.00000000D+00
COMPONENT 33                   { SIG 33 } = -5.00000000D-01
COMPONENT 12                   { SIG 12 } = 0.0
COMPONENT 23                   { SIG 23 } = 0.0
COMPONENT 31                   { SIG 31 } = 0.0

SOFTENING PARAMETERS

DELTA 1                         = 0.0
DELTA, ULTIMATE                 = 0.0

YIELD SURFACE AXIS RATIO
INITIAL EFFECTIVE MEAN NORMAL STRESS { SC } = 1.00000000D+00
PORE FLUID ELASTIC BULK MODULUS     { PO } = -6.66666667D-01
SLOPE OF VOLUM. STAIRW VS LN(P) CURVE { BF } = 0.0
INITIAL PORE FLUID PRESSURE         { LAMD } = -1.06000000D+01
INITIAL PORE FLUID PRESSURE         { PFO } = 0.0
    
```

YIELD SURFACE DATA

Y.S. N	INITIAL POSITION OF N-TH YIELD SURFACES IN STRESS SPACE							Y.S. SIZE	P. SHEAR	P. BULK	NONASSOCI.	Y.S. N
	GZY 11	GZY 22	GZY 33	GZY 12	GZY 23	GZY 31	KN	MOD. MM	MOD. BM	AM		
2	-4.96100D-01	-9.69400D-01	-4.96100D-01	0.0	0.0	0.0	2.9600D-02	1.2880D+02	-6.5970D+01	-4.7720D-01	2	
3	-4.9400D-01	-9.5280D-01	-4.9400D-01	0.0	0.0	0.0	4.5600D-02	1.1570D+02	-4.4860D+01	-4.4780D-01	3	
4	-4.9020D-01	-9.2320D-01	-4.9020D-01	0.0	0.0	0.0	7.4300D-02	9.5090D+01	-3.3480D+01	-4.3090D-01	4	
5	-4.8400D-01	-8.7480D-01	-4.8400D-01	0.0	0.0	0.0	1.2110D-01	6.4170D+01	-2.7270D+01	-3.2700D-01	5	
6	-4.7570D-01	-8.0950D-01	-4.7570D-01	0.0	0.0	0.0	1.8430D-01	4.9950D+01	-2.5750D+01	-2.3010D-01	6	
7	-4.6630D-01	-7.2630D-01	-4.6630D-01	0.0	0.0	0.0	2.6400D-01	2.2120D+01	-9.4800D+00	-1.1760D-01	7	
8	-4.8900D-01	-6.9000D-01	-4.8900D-01	0.0	0.0	0.0	3.6500D-01	6.9900D+00	-9.4400D+00	-1.4080D-01	8	
9	-4.8170D-01	-6.0570D-01	-4.8170D-01	0.0	0.0	0.0	4.6200D-01	2.2900D+00	-9.6800D+00	-1.4740D-01	9	
10	-4.7530D-01	-5.7930D-01	-4.7530D-01	0.0	0.0	0.0	4.8900D-01	6.4000D-01	-4.0200D-01	-1.5500D-02	10	
11	-4.7140D-01	-5.5720D-01	-4.7140D-01	0.0	0.0	0.0	5.1430D-01	0.0	1.0000D+00	0.0	11	
12	-4.7140D-01	-5.5720D-01	-4.7140D-01	0.0	0.0	0.0	5.1430D+02	0.0	0.0	0.0	12	

\*\*\*\*\* SFO BAY MUD UNDRAINED BEHAVIOR, PLANE STRAIN C=1.0 ZLM=10.6 KO=.5 \*\*\*\*\*

\*\*\*\* EVALUATION OF STRESSES AND STRAINS FOR SOIL BEHAVIOR BASED ON PREVOST MODEL \*\*\*\*

	INITIAL	COMP 11	COMP 22	COMP 33	COMP 12	COMP 23	COMP 31	MEAN/VOLUM.	OCTHEDRAL
INCREMENTAL STRAINS	0.0	0.0	0.0	0.0	0.0	0.0	0.0	0.0	0.0
ACCUMULATED STRAINS	0.0	0.0	0.0	0.0	0.0	0.0	0.0	0.0	0.0
PARTIALLY ACCUM. STRAINS	0.0	0.0	0.0	0.0	0.0	0.0	0.0	0.0	0.0
INCR. EFFECTIVE STRESSES	0.0	0.0	0.0	0.0	0.0	0.0	0.0	0.0	0.0
ACCUM. EFFECTIVE STRESSES	-5.0000D-01	-1.0000D+00	-5.0000D-01	0.0	0.0	0.0	0.0	-6.6667D-01	5.0000D-01
PARTIALLY ACCUM. STRESSES	0.0	0.0	0.0	0.0	0.0	0.0	0.0	0.0	1.0000D+00

LOADING STEP NO. NLOA (NS) = 1

STRESS/STRAIN	PL COMP CONTROL	COMP 11 (0)	COMP 22 (1)	COMP 33 (1)	COMP 12 (1)	COMP 23 (1)	COMP 31 (1)	MEAN/VOLUM.	OCTHEDRAL
INCREMENTAL STRAINS		9.9863D-05	-2.0000D-04	0.0	0.0	0.0	0.0	-1.0014D-04	2.6447D-04
ACCUMULATED STRAINS		9.9863D-05	-2.0000D-04	0.0	0.0	0.0	0.0	-1.0014D-04	2.6447D-04
PARTIALLY ACCUM. STRAINS		9.9863D-05	-2.0000D-04	0.0	0.0	0.0	0.0	-1.0014D-04	2.6447D-04
INCR. EFFECTIVE STRESSES		0.0	-4.3720D-02	-1.4560D-02	0.0	0.0	0.0	-1.9427D-02	3.8560D-02
ACCUM. EFFECTIVE STRESSES		-5.0000D-01	-1.0437D+00	-5.1456D-01	0.0	0.0	0.0	-6.8609D-01	5.1659D-01
PARTIALLY ACCUM. STRESSES		0.0	-4.3720D-02	-1.4560D-02	0.0	0.0	0.0	-1.9427D-02	3.8560D-02

LOADING STEP NO. NLOA (NS) = 2

STRESS/STRAIN	CONTROL	COMP 11 (0)	COMP 22 (1)	COMP 33 (1)	COMP 12 (1)	COMP 23 (1)	COMP 31 (1)	MEAN/VOLUM.	OCTHEDRAL
INCREMENTAL STRAINS		1.8453D-04	-3.0000D-04	0.0	0.0	0.0	0.0	-1.1547D-04	4.2357D-04
ACCUMULATED STRAINS		2.8440D-04	-5.0000D-04	0.0	0.0	0.0	0.0	-2.1560D-04	6.8781D-04
PARTIALLY ACCUM. STRAINS		2.8440D-04	-5.0000D-04	0.0	0.0	0.0	0.0	-2.1560D-04	6.8781D-04
INCR. EFFECTIVE STRESSES		0.0	-1.5397D-02	-2.1862D-02	0.0	0.0	0.0	-1.2420D-02	1.9453D-02
ACCUM. EFFECTIVE STRESSES		-5.0000D-01	-1.0591D+00	-5.3642D-01	0.0	0.0	0.0	-6.9851D-01	5.4182D-01
PARTIALLY ACCUM. STRESSES		0.0	-5.9117D-02	-3.6422D-02	0.0	0.0	0.0	-3.1846D-02	5.1655D-02

LOADING STEP NO. NLOA (NS) = 3

STRESS/STRAIN	0.001 CONTROL	COMP 11 (0)	COMP 22 (1)	COMP 33 (1)	COMP 12 (1)	COMP 23 (1)	COMP 31 (1)	MEAN/VOLUM.	OCTHEDRAL
INCREMENTAL STRAINS		3.0334D-04	-5.0000D-04	0.0	0.0	0.0	0.0	-1.9666D-04	7.0263D-04
ACCUMULATED STRAINS		5.8774D-04	-1.0000D-03	0.0	0.0	0.0	0.0	-4.1226D-04	1.3904D-03
PARTIALLY ACCUM. STRAINS		5.8774D-04	-1.0000D-03	0.0	0.0	0.0	0.0	-4.1226D-04	1.3904D-03
INCR. EFFECTIVE STRESSES		0.0	-1.2078D-02	-3.0260D-02	0.0	0.0	0.0	-1.4113D-02	2.6383D-02
ACCUM. EFFECTIVE STRESSES		-5.0000D-01	-1.0712D+00	-5.6668D-01	0.0	0.0	0.0	-7.1263D-01	5.4094D-01
PARTIALLY ACCUM. STRESSES		0.0	-7.1195D-02	-6.6682D-02	0.0	0.0	0.0	-4.5959D-02	6.9049D-02

LOADING STEP NO. NLOA (NS) = 4

STRESS/STRAIN	CONTROL	COMP 11 (0)	COMP 22 (1)	COMP 33 (1)	COMP 12 (1)	COMP 23 (1)	COMP 31 (1)	MEAN/VOLUM.	OCTHEDRAL
INCREMENTAL STRAINS		3.0586D-04	-5.0000D-04	0.0	0.0	0.0	0.0	-1.9414D-04	7.0461D-04
ACCUMULATED STRAINS		8.9360D-04	-1.5000D-03	0.0	0.0	0.0	0.0	-6.0640D-04	2.0950D-03
PARTIALLY ACCUM. STRAINS		8.9360D-04	-1.5000D-03	0.0	0.0	0.0	0.0	-6.0640D-04	2.0950D-03
INCR. EFFECTIVE STRESSES		-1.3878D-17	-1.0374D-02	-2.5848D-02	0.0	0.0	0.0	-1.2074D-02	2.2530D-02
ACCUM. EFFECTIVE STRESSES		-5.0000D-01	-1.0816D+00	-5.9253D-01	0.0	0.0	0.0	-7.2470D-01	5.4127D-01
PARTIALLY ACCUM. STRESSES		-1.3878D-17	-8.1569D-02	-9.2531D-02	0.0	0.0	0.0	-5.8033D-02	8.7566D-02

LOADING STEP NO. NLOA (NS) = 5

STRESS/STRAIN	0.002 CONTROL	COMP 11 (0)	COMP 22 (1)	COMP 33 (1)	COMP 12 (1)	COMP 23 (1)	COMP 31 (1)	MEAN/VOLUM.	OCTHEDRAL
INCREMENTAL STRAINS		6.1761D-04	-1.0000D-03	0.0	0.0	0.0	0.0	-3.8239D-04	1.4139D-03
ACCUMULATED STRAINS		1.3112D-03	-2.5000D-03	0.0	0.0	0.0	0.0	-9.8879D-04	3.5088D-03
PARTIALLY ACCUM. STRAINS		1.3112D-03	-2.5000D-03	0.0	0.0	0.0	0.0	-9.8879D-04	3.5088D-03
INCR. EFFECTIVE STRESSES		1.3878D-17	-1.0275D-02	-3.7857D-02	0.0	0.0	0.0	-1.6044D-02	3.3908D-02
ACCUM. EFFECTIVE STRESSES		-5.0000D-01	-1.0918D+00	-6.3039D-01	0.0	0.0	0.0	-7.4074D-01	5.3862D-01
PARTIALLY ACCUM. STRESSES		0.0	-9.1844D-02	-1.3039D-01	0.0	0.0	0.0	-7.4077D-02	1.1602D-01

\*\*\* JOB END \*\*\*

## Appendix C

### USER'S MANUAL OF PROGRAM JFSEST

#### C.1 Introduction

JFSEST is an acronym for Johnston-Finno-Shirasuna Elastic-plastic Soil-Tunnel interaction. The original version of the program was developed at Stanford University by Paul R. Johnston (1981) and later modified by Richard J. Finno (1983). It has been used by the developers and others to analyze conventional and advanced shield tunneling in cohesive soils and other geotechnical problems associated with soil-structure interaction in soft clays. The program was further modified by Takeshi Shirasuna to incorporate the Prevost elasto-plastic soil model. The new program has essentially the same framework for FEM formulation as the previous version. Some large parts of the program, in association with the Prevost soil model formulation, have been necessarily revised. Details pertaining to the theory behind the code are found in Chapter 3 and Chapter 6.

#### C.2 Program Capabilities

The capabilities of this finite element code extend to broad branches. The current version includes the following features:

##### (1) Analysis mode

- Plane strain or axisymmetric analysis
- Partially mixed formulation to couple effective stresses of soil with pore fluid pressure

(2) Material library

- Elastic analysis
- Nonlinear pseudo-elastic analysis using the Duncan-Chang soil model
- Elasto-plastic analysis using the Prevost soil model

(3) Pore fluid behavior

- Fully drained analysis or simplified undrained analysis
- Steady or unsteady fluid flow analysis
- Consolidation analysis

(4) Loading application

- Incremental loading and incremental pore pressure
- Automated surface traction and volume loading
- Automated excavation analysis
- Initial stress generation
- Installation of structural members
- Embankment construction

(5) Algorithm techniques

- Symmetric and nonsymmetric matrix solver
- Load incremental analysis with predictor-corrector type iteration
- Residual stress correction
- Time integration for pore pressure changes
- Small or large deformation formulation
- Restart capabilities using continuation file

(6) Optional element characterization

- Selective Gaussian integration scheme
- Selective stress points where material properties are calculated
- Alternation of material properties of elements
- Mesh generator

- Independent evaluation of volumetric and deviatoric contribution to element stiffness
- Initial stress contribution to element stiffness

#### (7) Storage usage and program control

- Multi-leveled dynamic storage allocation
- Storage restoration function for shortage of working area
- Skyline algorithm for upper, and lower if nonsymmetric, triangle parts of global stiffness matrices
- Expandable element and material libraries
- Output control and print dump function of continuation file
- Selective continuation file preservation for back-up
- Keyword controlled input

Some element types without frequent use in the former version of the program are removed from the library to reduce the program size. Cam Clay soil model and an interface element with pore pressure adjustment done by the Lagrange multiplier, which are available in JFEST, may be used even in this program with the same procedure as before. There has been no chance with the current program, however, to work for them to the present.

### C.3 Program Overview

#### C.3.1 Structure and storage allocation system

The program consists of a main program and more than one hundred subroutines. Some supplementary programs provide convenience when working with JFEST; plotting service (JFESTP), the Prevost model constitutive relation (PRVCNST as described in Appendix B), and parameter identification procedure to obtain the Prevost model parameter (REDUCT).

The program has four phases through execution. Figure C.1 shows this structure with brief explanation of each phase function on the side. Excluding the initial phase, a series of the predictor, corrector and output phases are associated with each incremental loading step. Therefore circulations continue until all the loadings are analyzed.

A region size required for the program execution depends upon the problem to be analyzed. A fixed memory size of 337 KB is occupied by the load module of the program without any overlay structure (Figure C.2). Another area must be available for a working storage noted as blank common A. The required size of A varies with degree of freedom, band width and unsymmetry of global stiffness matrix, Prevost model configuration, etc., as major factors.

When the working storage is not sufficiently large to store FEM information and vectors of skylined global stiffness matrices, the restoration function is called. All the data except Canchy multiplier information, load vector, displacement vector and the skyline indices are unloaded temporarily onto a disk storage and the area so created is used to assemble global stiffness matrices to pass forward to the solver. After the solver gives a solution to the displacement vector, all the information is resumed as it was for following phases of stress recovery and other further processing. This procedure is illustrated in Figure C.2. For example, the tunnel analysis for the homogeneous clay layer with the Prevost soil model, which has been discussed in Chapter 9, required 953 KB region for the program execution. The restoration size for that was 460 KB.

### C.3.2 Element Library

Two element types are to be described: four-noded and eight-noded isoparametric quadrilateral elements which are used with the Prevost soil model, termed Q4 and Q8, respectively. Three other element types are available as were in the former version of the program (Finno 1983), though they are not explained here. Pore pressure degree of freedom is able to be added at the corner nodes of the element, noted as the Q4P4 or Q8P4 element.

The local node numbering for the element connectivity and the local coordinate system are shown in Figure C.3. Shape functions for each element are selected from the Serendipity family (Zienkiewicz 1977) but not shown here since they are very popular. Stress point (SPT) is the point where stresses and other material state parameters are represented. Integration point (I.P.) is the Gauss point used in integration over the element volume to calculate the element stiffness matrix. The sequence of these points is different between elements with the Prevost soil model and other models, as shown in Figure C.3. Stresses and strains are given at those stress points and thus it is important to identify locations of the stress points exactly.

The element stiffness matrix consists of five parts as discussed in Chapter 6. Except for a role of pore fluid bulk modulus in the undrained analysis, other parts corresponding to the volumetric, deviatoric, pore fluid flow, and initial stress contributions are calculated by means of the independently specified integration scheme. Applying different schemes of the Gauss quadrature on particular parts, special advantages could be expected such as less instability of reduced integration for incompressibility or

pore pressure representation coupled with the soil's effective stresses. However, it should be done carefully with sufficient knowledge of the application of such an incompatible mode of element.

### C.3.3 Material Library (MAT)

Materials may be specified as linear elastic, nonlinear pseudo-elastic, or elasto-plastic. The nonlinear pseudo-elastic material response is defined by parameters which approximate the stress-strain curve of the soil as hyperbola. This model was first proposed by Konder (1963) and extended by Duncan-Chang (1970). Clough (1969) incorporated it with one FEM program. The elasto-plastic material response is defined using the Prevost soil model. A procedure specifying this material is to be described in detail. Although the Cam Clay model may also be used, it is not referred to here because Johnston (1981) and Finno (1983) gave it a complete explanation. The material types and their parameters are explained in the following sections. The next table defines the material type number, which specifies the material type to be used.

Table C.1 Material Type Numbers

MTYPE	Material type	
1	Linear elastic	(ELA)
2	Cam Clay	(CAM)
6	Nonlinear elastic interfact	(INT)
7	Spring stiffness	(SPR)
8	Nonlinear pseudo-elastic	(HYP)
9	Prevost elasto-plastic	(PRV)

MAT.1 Linear elastic material for two-dimensional elements, called ELA.

The material parameters are given on Table C.2.

Table C.2 Parameters for Material Type 1, Elastic

Variable	Explanation
PR(1,NMAT)	$i_{gx}$ x-component of the hydrostatic head
PR(2,NMAT)	$i_{gy}$ y-component of the hydrostatic head
PR(3,NMAT)	$i_{gz}$ z-component of the hydrostatic head
PR(4,NMAT)	$\gamma_w$ unit weight of water
PR(5,NMAT)	$k_x$ coefficient of permeability in x-direction
PR(6,NMAT)	$k_y$ coefficient of permeability in y-direction
PR(7,NMAT)	$k_z$ coefficient of permeability in z-direction
PR(8,NMAT)	E Young's modulus
PR(9,NMAT)	$\nu$ Poisson's ratio
PR(10,NMAT)	$B_f$ Bulk modulus of water

The first seven parameters may be set to zero when elements that do not possess pore pressure degrees of freedom are being used. The last parameter is used only for simplified undrained analyses and may be set to zero when this option is not employed.

The input for the first three parameters control the direction of the gravitational field. If the hydrostatic water head increases in the negative y-direction, then  $i_{gx} = 0.0$  ,  $i_{gy} = -1.0$  and  $i_{gz} = 0.0$  .

MAT.2 Cam Clay material (CAM) can be referred to Johnston (1981) and Finno (1983) for thorough description.

MAT.3 Nonlinear elastic interface response (INT) can be referred to Finno (1983).

MAT.4 Linear elastic response for spring elements (SPR). Only one material property is required for this material type, a spring stiffness equal to  $AE/L$ , where:

- A = cross-sectional area
- E = Young's modulus
- L = length of spring element

MAT.5 Nonlinear stress-dependent hyperbolic soil parameters (HYP) for conditions of drained loading only. A stress-dependent, linear response is assumed for unloading and reloading. Isotropic behavior is assumed with the response dependent of the principal stress difference. Eleven material parameters which define the response are presented in Table C.3.

Table C.3 Parameters for Material Type 8, Nonlinear Elastic

Variable	Explanation	
PR(1,NMAT)	GUI	Poisson's ratio before failure
PR(2,NMAT)	GUF	Poisson's ratio at failure
PR(3,NMAT)	R <sub>f</sub>	Correlation factor, ratio of measured strength at failure to ultimate hyperbolic strength
PR(4,NMAT)	PHI	Effective friction angle, degrees
PR(5,NMAT)	COH	Cohesion
PR(6,NMAT)	XXP	Exponent 'n' in the initial tangent and unload-reload moduli expressions
PR(7,NMAT)	HCOEF	Modulus number, K <sub>m</sub>

PR(8,NMAT)	ULCOEF	Unload-reload modulus number, $K_{ur}$
PR(9,NMAT)	ETF	Tangent modulus at failure
PR(10,NMAT)	EIMN	Minimum value of initial tangent modulus
PR(11,NMAT)	$P_a$	Atmospheric pressure

MAT.6 Prevost material (PRV). This material be specified with combination of material parameters and element characterization parameters. Material parameters independent of the Prevost soil model are specified using the material property array (PR) such as those for other material types. These include PR(1,NMAX) to PR(7,NMAX) in Table C.2. Others are in Table C.4. Material parameters which specify the Prevost elasto-plastic behavior are identical to those in Card 4 through Card 7 used in the program PRVCNST. Those are explained in Section B.2.2. This is the main body of the Prevost soil model which is not input in the mesh block but in the initial stress block. Element characterization parameters are integer constants stored in the later part of the PR array.

Table C.4 Common Parameters for Material Type 9, Prevost Elasto-plastic

Variable	Explanation
PR(8,NMAX)	$l_{eg}$ Equivalent length for out-of-plane drainage
PR(9,NMAX)	$Y_{WT}$ y-coordinate of initial ground water table
PR(10,NMAX)	$P_{ext}$ Fractional contribution of seepage force due to externally applied incremental nodal pore pressure, usually set equal to zero
IPR(1,NMAX)	JHPTYP Prevost model subtype

IPR(2,NMAX)	ISYME	Symmetry code of element stiffness matrix, 0 for symmetric, 1 for nonsymmetric
IPR(3,NMAX)	NSTP	Number of stress points
IPR(4,NMAX)	NIEF	Number of I.P. for initial stress part
IPR(5,NMAX)	NIEV	Number of I.P. for volumetric part
IPR(6,NMAX)	NIED	Number of I.P. for deviatoric part
IPR(7,NMAX)	NIEP	Number of I.P. for pore fluid flow part
IPR(8,NMAX)	ILRG	0 = small deformation formulation, 1 = large deformation formulation, 2 = simplified updated-coordinate formulation
IPR(9,NMAX)	NYS	Number of yield surfaces
IPR(10,NMAX)	M5	Size of stress vector
IPR(11,NMAX)	MI	Initial yield surface number

Information on the material state at the stress points of an element is stored in a portion of stress vector SVT for the respective element. The location in the SVT is controlled by the address index vector LSV. Elements with other types than the Prevost model have their stress vector with simple forms. For such elements the stress points coincide with the integration points.

Table C.5 Material State Parameters for Non-Prevost Material

Variable	Explanation
SVT(LSVT)	$\epsilon_x$ Strain in the x-direction
SVT(LSVT+1)	$\epsilon_y$ Strain in the y-direction
SVT(LSVT+2)	$\epsilon_z$ Strain in the z-direction
SVT(LSVT+3)	$\gamma_{xy}$ Shear strain
SVT(LSVT+4)	$\alpha_x'$ Effective stress in the x-direction
SVT(LSVT+5)	$\alpha_y'$ Effective stress in the y-direction
SVT(LSVT+6)	$\alpha_z'$ Effective stress in the z-direction
SVT(LSVT+7)	$\tau_{xy}$ Shear stress
SVT(LSVT+8)	$n$ Pore pressure
SVT(LSVT+9)	$P_c$ Effective preconsolidation pressure (CAM), or $\tau_m$ maximum shear stress experienced during loading (HYP)

SVT(LSVT+10)	p	Effective mean normal stress (CAM), or $E_i$ initial tangent modulus for current stress level (HYP)
SVT(LSVT+11)	q	Octahedral shear stress (CAM), or $E_t$ tangent modulus corresponding to the current stress level (HYP)
SVT(LSVT+12)	e	Current void ratio (CAM) or $\nu$ current Poisson's ratio (HYP)
SVT(LSVT+13)	SL	Current stress level (HYP)

Stress vector SVT for elements with the Prevost model is quite different. It consists of six parts as shown in Figure C.4. For an element  $l$ , the size and position of stress vector is stored in  $IPR(10, NMAT) = M5$  and  $LSV(l) = LSVT$ , respectively. Many parameters must be kept to represent the material state and so a large size of memory are required. An example condition such as 9 stress points within a Q8P4 element whose material type is the pressure dependent Prevost model with 12 yield surfaces should have 1005 words of memory to store all the material parameters for only one element.

With reference to the stress vector, stresses and strains are output for each loading increment. Items to be output may be specified in terms of selection codes (IXPRT). Correlation between the selection code and the physical quantities are indicated in Table C.6.

Table C.6 Output Selection Code IXPRT

IXPRT	Description	IXPRT	Description	IXPRT	Description
1*	$\sigma_x$	13	q/p	25	$\epsilon_1$
2*	$\sigma_y$	14*	u	26	$\epsilon_3$
3	$\sigma_z$	15	$p_c$	27	$(\epsilon_1 + \epsilon_3)/2$
4*	$\tau_{xy}$	16	$\tau_{max}$	28	$(\epsilon_1 - \epsilon_3)/2$
5*	$\sigma_1$	17		29	$\phi_\epsilon$
6*	$\sigma_3$	18		30	$\epsilon_m = \epsilon_{kk}$
7*	$(\sigma_1 + \sigma_3)/2$	19		31	e
8*	$(\sigma_1 - \sigma_3)/2$	20		32	
9*	$\phi_\sigma$	21	$\epsilon_x$	33	
10	$p = \sigma_{kk}/3$	22	$\epsilon_y$	34	
11*	$q = (3/2 S_{ij} S_{ij})^{1/2}$	23	$\epsilon_z = 0$	35	
12	$\theta_{OCT}$	24	$\gamma_{xy}$	36	

\* Default option for output selection

#### C.4 Input Data Assembly

The input for JFSEST is separated into four blocks: control block (CNT), mesh block (MSH), initial stress block (INT) and load block (LOA). They must be assembled in that sequence. Each input block is terminated by an appropriate END card.

Within each block there may be a number of groups of cards. Each group has a descriptive keyword on its first card. The first eight columns are used to identify the keyword while the remaining space on the same card can be used for placing arbitrary commentary words. For example, the first card in the material parameters group has the keyword MATERIAL, and the cards which follow

this card contain the material parameters. Within any given block, the groups of cards may be arranged in any order. Only those groups pertinent to the problem under consideration need be included. For example, if a restart file is not to be used, then the RESTART group need not be used.

#### C.4.1 Control Block (CNT)

This block contains information regarding the type of analysis, the size of the problem, the number of load increments and the type of algorithm desired. The information provided in this block is analyzed by the subroutine RDCONT and to allocate the array space.

##### CNT.1 Title group

This group of cards is used to input a descriptive title for the problem. The group may be repeated if more that one title line is desired.

Card	Columns	Variable	Format	Explanation
CNT.1	Title			
1	1 - 8	WORD	A8	Enter the word TITLE
2	1 - 80	TITLE	10A8	Enter a title for the problem

##### CNT.2 Size group

This group of cards is used for the purpose of internally dimensioning the arrays.

CNT.2 Problem Size

Card	Columns	Variable	Format	Explanation
1	1 - 8	WORD	A8	Enter the word SIZE
2	1 - 5	NN	15	Number of nodes
	6 - 10	NE	15	Number of elements
	11 - 15	NMJT	15	Number of interface elements
	16 - 20	NMSP	15	Number of spring elements
	21 - 25	NJYPEL	15	Number of soil elements with hyperbolic material response
	26 - 30	NM	15	Number of materials
	31 - 35	NBC	15	Number of boundary conditions
	36 - 40	NOUT	15	Number of output segments

CNT.3 Residual load correction

By specifying this option, the out-of-balance forces are calculated at the end of each increment and applied as nodal loads during the next increment. For this effective option, elements must be compatible and integration over their volume must be carried out to be theoretically exact.

CNT.3 Residual Load Correction

Card	Columns	Variable	Format	Explanation
1	1 - 8	WORD	A8	Enter the word RESIDUAL

CNT.4 Print group

This group may be used to suppress output or define the number of load

increments between printings. This group may be placed in any of the four load blocks. For example, if  $IPRT = 3$ , increments that are multiples of 3 will be printed, i.e., 3, 6, 9, 12, etc. If  $IPRT = 1$  for the first 4 increments, then is changed to 3 at the fifth increment, increments 1, 2, 3, 4, 6, 9, 12, etc. are output instead of 1, 2, 3, 4, 7, 10, 13, etc. Thus it is possible to turn the printing on and off as desired. The default printing causes every load increment to be printed; this results in large amounts of output for nonlinear or consolidation problems.

CNT.4		Print		
Card	Columns	Variable	Format	Explanation
1	1 - 8	WORD	A8	Enter the word PRINT
2	1 - 5	IPRT	I5	Results are printed every IPRT increments. IPRT = 1 is the default. Set IPRT = 0 to suppress output.

#### CNT.5 Restart group

This group is used to save the results of a run on a restart file. The option may then be used subsequently to read this file and continue an analysis. If the read option in this group is used, then the mesh block and initial stress block must be omitted, since this information was provided in a previous run and saved on the restart file (the continuation file). This option is particularly useful in consolidation analyses when the time needed for excess pore pressures to dissipate is unknown. It is also useful in

elasto-plastic runs to break up a large run into a number of smaller runs to reduce the chances of wasting money on one bad run. This size of a restart file is fairly large, particularly for an analysis with the Prevost soil model. For this reason an interval of reserving restart file can be widened by using the same keyword in the load block.

CNT.5		Restart			
Card	Columns	Variable	Format	Explanation	
1	1 - 8	WORD	A8	Enter the word RESTART	
2	1 - 5	IRST	I5	Load increment number IRST will be read from the restart file. Set IRST = -1 if this option is not used.	
	5 - 10	IWST	I5	Results will be saved on a restart file beginning at load increment IWST. Set IWST = -1 if this option is not used.	

CNT.6 Number of load increments group

This group must be used if more than one increment is needed or if the predictor-corrector algorithm is desired.

CNT.6		Increments			
Card	Columns	Variable	Format	Explanation	
1	1 - 8	WORD	A8	Enter the word INCREMEN	
2	1 - 5	NFLI	I5	Number of first load increment	
	6 - 10	NLLI	I5	Number of last load increment	

11 - 15	NALPH	15	Number of load increments that ALPHA not equal to 0.
16 - 25	ALPHA	F10.3	Parameter which controls the predictor time instant Use ALPHA = 0.5 for stress-controlled loading Use ALPHA = 0.0 when not using predictor-corrector algorithm

**CNT.7** Pore pressure degree of freedom group

This group must be used to define the time integration parameter when pore pressure degrees of freedom are used for consolidation or fluid flow problems (when Q8P4 elements are used).

**CNT.7** Pore Pressure

Card	Columns	Variable	Format	Explanation
1	1 - 8	WORD	A8	Enter the word PORE PRE
2	1 - 10	BETA	F10.0	Time integration parameter, the recommended value is BETA = 0.5

**CNT.8** Simplified undrained analysis option

This option is used when an undrained analysis is being performed without the use of elements possessing pore pressure degrees of freedom.

CNT.8 Simplified Undrained Analysis

Card	Columns	Variable	Format	Explanation
1	1 - 8	WORD	A8	Enter the word UNDRAINE

CNT.9 Axisymmetric analysis option

Numerical integration is performed over one radian; loads should be calculated accordingly.

CNT.9 Axisymmetric Analysis

Card	Columns	Variable	Format	Explanation
1	1 - 8	WORD	A8	Enter the word AXISYMME

CNT.10 Plane strain analysis option

CNT.10 Plane Strain Analysis

Card	Columns	Variable	Format	Explanation
1	1 - 8	WORD	A8	Enter the word PL STRAI

CNT.11 Type of material group

This group specifies the material types used in the analysis. For detail of the available material types, users should refer to the material library section. The material type numbers are given in Table C.1.

CNT.11 Type of Materials				
Card	Columns	Variable	Format	Explanation
1	1 - 8	WORD	A8	Enter the word TYPE MAT
2	1 - 5	N	15	Number of different material types
	6 - 45	NTYPE(I)	815	List of numbers of types of materials used

CNT.12 Type of elements group

This group specifies the element types used in the analysis. For details of the available element types, users should consult the element library section.

CNT.12 Type of Elements				
Card	Columns	Variable	Format	Explanation
1	1 - 8	WORD	A8	Enter the word TYPE ELE
2	1 - 5	N	15	Number of different element types
	6 - 30	NTYPE(I)	515	List of numbers of types of elements used

CNT.13 Lagrange multiplier group

This group specifies the number of Lagrange multipliers used in the analysis. The Lagrange multipliers add constraints which force specified degrees of freedom at any pair of nodes to be equal. For example, they must be specified when interface elements are used in conjunction with Q8P4 elements in a consolidation analysis to assure continuity of pore pressure across the interface.

CNT.13		Lagrange Multipliers			
Card	Columns	Variable	Format	Explanation	
1	1 - 8	WORD	A8	Enter the word LAGRANGE	
2	1 - 5	NLAM	I5	Number of Lagrange multipliers	

CNT.14 Large displacement option

This card is used if a large displacement analysis is to be performed. When this option is invoked with use of the Prevost soil model, the initial stress stiffness matrix is added, and rotations are considered when updating the stresses. The nodal coordinates are updated to evaluate strains from an Eulerian viewpoint. On the other hand large displacement formulation for other material types than the Prevost is based simply on the updated coordinate method.

CNT.14 Large Displacements

Card	Columns	Variable	Format	Explanation
1	1 - 8	WORD	A8	Enter the word LARGE DI

CNT.15 End of control block card

This card is required to define the end of the control block input.

CNT.15 End of Control Block

Card	Columns	Variable	Format	Explanation
1	1 - 8	WORD	A8	Enter the word END CONT

### C.4.2 Mesh Block (MSH)

This block contains the detailed information describing the mesh geometry, its material parameters and boundary conditions. Information of this block is analyzed by the subroutine RDMESH. This entire block must be omitted if a continuation run is being made using the RESTART option.

#### MSH.1 Nodal coordinate group

The coordinates are input for each node. They may be placed in any order.

MSH.1	Nodes			
Card	Columns	Variable	Format	Explanation
1	1 - 8	WORD	A8	Enter the word NODES
2	1 - 5	N	15	Number of nodes in this group
	6 - 10	NCH	15	Number of space coordinates per node
3	1 - 5	NNOD	15	Nodal point number
	6 - 35	X(1,NNOD)	3F10.0	Nodal coordinates $l = 1,NCN$

Card 3 is repeated N times.

#### MSH.2 Element connectivity group

The connectivity is input for each element. The elements may be placed in any order. The numbering sequence for a given element is found in the element library section. This group must be used more than once if more than one element type or more than one material is used.

MSH.2 Elements

Card	Columns	Variable	Format	Explanation
1	1 - 8	WORD	A8	Enter the word ELEMENTS
2	1 - 5	N	15	Number of elements in this group
	6 - 10	NETY	15	Element type number
	11 - 15	NMAT	15	Material number
3	1 - 5	NELE	15	Element number
	6 - 80	LC(I,NELE)	1515	Element connectivity I = 1,NNE NNE = number of nodes in element

Card 3 is repeated N times.

MSH.3 Material parameters group

The material parameters are input in any order for each material in the mesh. The parameters to be specified for each material type are shown in the material library section. If more than one type of material is used, it is necessary to use this group more than once.

MSH.3 Material Parameters

Card	Columns	Variable	Format	Explanation
1	1 - 8	WORD	A8	Enter the word MATERIAL
2	1 - 5	N	15	Number of materials in this group
	6 - 10	NMTY	15	Material type number

For material types other than the Prevost material type (NMTY#9)

3	1 - 5	NMAT	15	Material number
	6 - 75	PR(I,NMAT)	7F10.0	Material parameters for I=1,7

4 1 - 80 PR(I,NMAT) 8F10.0 Material parameters for I=1,NPRM  
NPRM = number of parameters for  
this material type

For the Prevost material type (NMTY=9)

3 1 - 55 IPR(I,NMAT) 11I5 Element characterization  
parameters for I=1,11  
4 1 - 80 PR(I,NMAT) 8F10.0 Material parameter for I=1,8  
5 1 - 20 PR(I,NMAT) 2F10.0 Material parameter for I=9,10

Cards 3 and 4 (NMTY=9) and/or cards 3 to 5 (NMTY=9) are repeated  
in groups for a total of N times.

#### MSH.4 Boundary conditions group

The boundary conditions are input in this group. The total number of  
constraints must equal the value of NBC specified in the control block.

#### MSH.4 Boundary Conditions

Card	Columns	Variable	Format	Explanation
1	1 - 8	WORD	A8	Enter the word BOUNDARY
2	1 - 5	NSETS	15	Number of sets of constraints
3	1 - 5	N	15	Number of nodes in this set
	6 - 10	NDOF	15	Degree of freedom number being constrained in this set
	11 - 20	ADIS	F10.0	Applied displacement for this set
4	1 - 80	NNBC(I)	16I5	Node number I=1,N

Cards 3 and 4 are repeated in pairs for a total of NSETS times.

#### MSH.5 Mesh generation group

This group may be used to generate both nodal coordinates and element

connectivity for four- and eight- noded quadrilateral elements. The mesh so generated can be either rectangular (MGTY = 1, 3, 4 and 5) or radial (MGTY = 2). The first node has the smallest values of x and y as coordinates. The node numbers increase first along a line of constant y for MGTY = 1, 2 and 5 while along a line of constant x for MGTY = 3, 4. The elements are numbered in clockwise direction for MGTY = 1, 2 and 5 while in counter-clockwise direction for MGTY = 3 and 4.

This group may be used to generate all or part of the mesh, and may be used more than once.

MSH.5	Mesh Generator			
Card	Columns	Variable	Format	Explanation
1	1 - 8	WORD	A8	Enter the word MESH GEN
2	1 - 5	MGTY	I5	Mesh generator type code
	6 - 10	NETY	I5	Element type number
	11 - 15	NMAT	I5	Material number
3	1 - 5	NE1	I5	First node number generated
	6 - 10	NEX	I5	First element number generated
	11 - 15	NEX	I5	Number of elements in the x or r direction
	16 - 20	NEY	I5	Number of elements in the y or $\theta$ direction
4	1 - 80	CX(I)	8F10.0	Corner nodal coordinates in the x or r direction for $l = 1, NEX+1$
5	1 - 80	CY(I)	8F10.0	Corner nodal coordinates in the y or $\theta$ direction for $l = 1, NEY+1$

#### MSH.6 Lagrange multiplier group

The lagrange multipliers are used to introduce supplementary quantitative constraints on nodal freedoms. This group is used when interface

elements are used in conjunction with Q8P4 elements for a consolidation analysis. Pore pressure may be maintained constant at each pair of corner nodes of the interface elements.

**MSH.6 Lagrange Multipliers**

Card	Columns	Variable	Format	Explanation
1	1 - 8	WORD	A8	Enter the word LAGRANGE
2	1 - 5	LMN1(I)	15	First node number of Lagrange pair
	6 - 10	LMD1(I)	15	Constrained degree of freedom for above node
	11 - 15	LMN2(I)	15	Second node number of Lagrange pair
	16 - 20	LMD2(I)	15	Constrained degree of freedom for above node

Card 2 is repeated NLAM times. LMD1(I) and LMD2(I) are set = 3 when constraining the pore pressures at the corner nodes of an interface element.

**MSH.7 Output selection group**

Output is controlled by information on this group. Element numbers and output selection codes of output valuables for those elements are defined. Numbers of elements and selection codes concerned in each of these groups are represented by NEPR and NSPR, respectively. As shown in Figure C.6, the default option of output selection is obtained by specifying NSPR = 0. If NSPR = -1, averaged quantities over stress points of an element are printed for the default output menu. If NSPR = -2, outputs for selected elements are suppressed.

Element number may be specified in arbitrary order. When a series of consecutive elements are concerned, only the first and last element numbers are sufficient for the request, with a hyphen behind the first one.

**MSH.7      Output Selection Group**

Card	Columns	Variable	Format	Explanation
1	1 - 8	WORD	A8	Enter the word OUTPUT
2	1 - 5	NSPR	15	Number of output selection codes
	6 - 10	NEPR	15	Number of elements concerned
3	1 - 80	IEPRT(1)	1615	Output selection code I=1,NSPR
4	1	HPH	A1	Hyphen identifier
	2 - 5	KNPR(1)	14	Element number
	6 - 80			Repeated set of HPH and KNPR for a total of NEPR elements

Card 4 is repeated so as to cover whole NEPR elements.

Card 2 to 4 must be repeated in a set for a total of NOUT times.

**MSH.8      End of mesh block card**

This card is required to define the end of the mesh block input.

**MSH.8      End of Mesh Block**

Card	Columns	Variable	Format	Explanation
1	1 - 8	WORD	A8	Enter the word END MESH

### C.4.3 Initial Stress Block

This block is dealt with by the subroutine RDINIT. It sets up the initial stress conditions in the soil. For elements with the Prevost material type, material parameters representing elasto-plastic properties are specified together with the initial stress establishment in this block. If zero initial stresses are desired, then only the end of initial stress block card is needed. The entire block should be omitted if a continuation run is being made using the RESTART option.

### INT.1 Initial time group

The total and incremental times may be set in this group.

Card	Columns	Variable	Format	Explanation
1	1 - 8	WORD	A8	Enter the word TIME
2	1 - 10	TIMEI	F10.0	Incremental time
	11 - 20	TIMET	F10.0	Total time

### INT.2 Initial stress variable group

Element stress and strain variables may be explicitly set by using this group. The order of the stress input depends on the material type. For elements with material types other than the Prevost model, the order of stresses is the same as that in the stress vector and may be found in the material library section. If Q8P4 element with the same material type

is used, then the initial pore pressure group must be used to set the initial pore pressure at the corner nodal points. The gravity group can be used to input the initial stresses instead of using this group.

For elements with the Prevost material, elasto-plastic moduli and yield surface information are set together with setting initial stresses. The order of input data to be placed in the stress vector is not the order in the stress vector, but it is the same as that used in the input sequence for the program PRVCNST. Material cards (Cards 4 to 7) described in Section B.2.2 are identically used for the input of this group.

#### INT.2 Initial Stresses

Card	Columns	Variable	Format	Explanation
1	1 - 8	WORD	A8	Enter the word STRESS
2	1 - 5	NSETS	I5	Number of initial conditions sets

For elements with material other than the Prevost model type.

3	1 - 5	NE1	I5	First element number
	6 - 10	NE2	I5	Last element number
	11 - 15	NI1	I5	First integration point number
	16 - 20	NI2	I5	Last integration point number
	21 - 25	NSV	I5	Number of stress variables to be set at each integration point
4	1 - 80	SIG(I)	8F10.0	Initial stress values for I=1,NSV

For elements with the Prevost material.

3	1 - 5	NE1	I5	First element number
	6 - 10	NE2	I5	Last element number
	11 - 15	NI1	I5	First stress point number
	16 - 20	NI2	I5	Last stress point number

If NI1 and NI2 are equal to zero, all the stress points are covered.

4	1 - 40	FM(I,1)	4F10.0	Elastic moduli,	Card 4 in B.2.2
5	1 - 60	FM(I,1)	6F10.0	Initial stresses,	Card 5 in B.2.2
6	1 - 60	XLAM(I)	6F10.0	Axis ratio, etc.,	Card 6 in B.2.2
7	1 - 5	M	15	Yield surface (Y.S.) number	
11	- 50	FM(I,M)	4F10.0	Plastic moduli,	Card 7.1 in B.2.2
8	1 - 60	FM(I,M)	6F10.0	Y.S. positions,	Card 7.2 in B.2.2

Cards 3 and 4 in pairs for non-Prevost material and Card 4 to 8 in sets for the Prevost material are repeated together for a total of NSETS times.

### INT.3 Initial pore pressure group

This group is used to set the pore pressure at nodal points. Pore pressures are set at the stress points by using the previous group. If the gravity group is used to set up the initial stresses in the mesh, then this group is not needed.

#### INT.3 Initial Pore Pressures

Card	Columns	Variable	Format	Explanation
1	1 - 8	WORD	A8	Enter the words PORE PRE
2	1 - 5	N	15	Number of nodes in this group
3	1 - 5	NNOD	15	Node number
	6 - 15	U	F10.0	Pore pressure

Card 3 is repeated for a total of N times.

### INT.4 Gravity group

This group is used to simulate gravity turn-on for materials associated with the effective stress analysis. Material types based on the critical

state soil plasticity has no strength at zero initial stress. Hence, it is not possible to use the normal procedure of gravity turn on. The stresses are calculated at each stress point as shown subsequently, where the elevation,  $Y$ , is taken to be the negative of the  $y$ -coordinate at that point. The pore pressure,  $u$ , is given by:

$$u = \gamma_w(YREF - Y) + q_w \quad (C.1)$$

The initial effective stresses are given by:

$$\sigma_y = \gamma_t(YREF - Y) + q_t - u \quad (C.2)$$

$$\sigma_x = \sigma_z = k_0 \sigma_y \quad (C.3)$$

where the constant  $q_w$  and  $q_t$  measured at reference elevation YREF may be used to simulate a linear change of stress with depth for any water table and overburden pressure.

#### INT.4 Gravity

Card	Columns	Variable	Format	Explanation
1	1 - 8	WORD	A8	Enter the word GRAVITY
2	1 - 5	NSETS	I5	Number of sets of elements for which gravity parameters are input
3	1 - 5	NE1	I5	First element number
	6 - 10	NE2	I5	Last element number
	11 - 20	PRG(1)	F10.0	$\gamma_t$ total unit weight of soil
	21 - 30	PRG(2)	F10.0	$\gamma_w$ unit weight of water
	31 - 40	PRG(3)	F10.0	$k_0$ coefficient of earth pressure at rest
	41 - 50	PRG(4)	F10.0	OCR overconsolidation ratio
	51 - 60	PRG(5)	F10.0	$q_t$ overburden pressure

61 - 70	PRG(6)	F10.0	$q_w$ hydrostatic pressure
71 - 80	PRG(7)	F10.0	YREF elevation of reference

Card 3 is repeated NSETS times.

#### INT.5 End of initial stress block card

This card is required to define the end of the initial stress input.

#### INT.5 End of Initial Stress Block

Card	Columns	Variable	Format	Explanation
1	1 - 8	WORD	A8	Enter the word END INIT

#### C.4.4 Load Block (LOA)

This block is used to apply loads and is handled by the subroutine RDLOAD. The entire block may be repeated so that incremental load problems may be solved. The maximum number of load increments applied in one run is controlled by the value of NLLI, which is input in the control block.

The incremental load vector is initially set to zero, but it is not reset to zero between increments. Thus, nodal loads applied in one increment will be applied again in the next increment unless PINC is set to zero in the proportional increment group.

LOA.1 Proportional increment group

This group may be used for two purposes; to scale the existing load vector and to apply repeated load increments without repeating the entire load block. The incremental load vector may be reset to zero at any time in the loading sequence by using this group with PINC = 0.0.

Card	Columns	Variable	Format	Explanation
1	1 - 8	WORD	A8	Enter the word PROPORTI
2	1 - 5	NPINC	I5	The number of load increments for which PINC is to be applied
	6 - 15	PINC	F10.0	The incremental load vector is scaled by this factor

LOA.2 Time increment group

This group is used to control the time increment for problems which have pore pressure degrees of freedom. After each increment, the total time is incremented by adding the incremental time; however, the incremental time is not reset to zero. Thus, if the incremental time is set in the initial stress block and this group is not used, the time increment will remain constant. For most consolidation problems, this is undesirable, since simulating conditions from undrained to fully drained usually requires about a 1000- to 10000-fold increase in time. The following two schemes are provided for altering this time step:

1. The manual method is implemented by explicitly setting the time increment for each step. This is done by setting  $NTINC = 0$  and using this group in each repeated load block.
2. The automatic method is used to specify how many increments are desired to achieve a tenfold increase in time. For example,  $TINC = 0.2$  allows the time to increase by a factor of ten after every 5 increments. The time increments will appear evenly spaced when plotted on a logarithmic scale. The incremental time is computed using the following formula:

$$t_i = t_0 \{10^{TINC} - 1\} \quad (C.4)$$

where  $t_0$  is the total time at the start of the increment.

LOA.2		Time Increment		
Card	Columns	Variable	Format	Explanation
1	1 - 8	WORD	A8	Enter the word TIME INC
2	1 - 5	NTINC	I5	Number of time increments NTINC = 0 for absolute increment
	6 - 15	TINC	F10.0	Logarithmic incremental factor Absolute increments are used when NTINC = 0.

### LOA.3 Nodal load group

This group may be used to apply nodal loads. These incremental loads are added to the existing values in the incremental load vector.

LOA.3 Nodal Loads

Card	Columns	Variable	Format	Explanation
1	1 - 8	WORD	A8	Enter the word NODAL LO
2	1 - 5	N	I5	Number of nodes in this group
	6 - 10	NDFN	I5	Number of DOF to be loaded
3	1 - 5	NNOD	I5	Node number
	6 - 75	A(I)	7F10.0	Nodal loads I = 1,NDFN

LOA.4 Boundary displacement group

This group can be used to apply displacement-controlled loading at a fixed boundary location.

LOA.4 Boundary Displacements

Card	Columns	Variable	Format	Explanation
1	1 - 8	WORD	A8	Enter the word BOUNDARY
2	1 - 5	NUMBV	I5	Number of induced boundary displacements
3	1 - 5	NNOD	I5	Node number of applied displacement
	6 - 10	NDOF	I5	DOF number of applied displacement
	11 - 20	BV	F10.0	Value of applied displacement

Card 3 is repeated NUMBV times.

LOA.5 Change material group

This group is used to change the material parameters of an existing

material. With careful choice of the parameters it may be used in the simulation of construction of an embankment or an excavation.

LOA.5 Change Material				
Card	Columns	Variable	Format	Explanation
1	1 - 8	WORD	A8	Enter the word CHANGE M
2	1 - 5	NMAT	I5	Material number
	6 - 10	NPRM	I5	Number of parameters for this material
3	1 - 80	PR(1,NMAT)	8F10.0	New parameters I = 1,NPRM

#### LOA.6 Excavate group

This group is used to compute and apply equivalent nodal loads to an excavated surface. The stiffness of the excavated material is eliminated or replaced in accordance with new material property selected for the excavated elements. The equivalent nodal forces are computed based on the stresses in the excavated elements adjacent to the excavated surface (IEXOPT = 0, 1), or in the soil elements adjacent to the tunnel periphery (IEXOPT = 3). Liner activation can be simulated with this group.

LOA.6 Excavate group				
Card	Columns	Variable	Format	Explanation
1	1 - 8	WORD	A8	Enter the word EXCAVATE
2	1 - 5	IEXOPT	I5	Excavation option code
	6 - 10	NEXCEL	I5	Number of excavated elements

	11 - 15	NNLOAD	15	Number of exposed nodes to be loaded by excavation forces
	16 - 20	NUMAIR	15	Material number of air
3	1 - 5	IEXCA(1,1)	15	Element number to be excavated
	6 - 10	IEXCA(1,2)	15	New material number for excavated element

Card 3 is repeated NEXCEL times.

4	1 - 80	INLOAD(1)	1615	Number of node loaded by excavation forces, 1 = 1, NNLOAD
5	1 - 5	IMATCH(1)	15	Material number for liner in case of IEXOPT = 1

If IEXOPT = 3, then stresses from excavated elements will not be zeroed out.

#### LOA.7 Distributed load group

This group is used to apply surface pressures and volumetric loads to a side of an element or elements. Uniform or linearly varying pressures (ILOAD = 1), elliptically varying pressures used to simulated heaving caused by advanced shield tunneling (ILOAD = 2) and volumetric loads (ILOAD = 3) can be specified.

#### LOA.7 Distributed Loads

Card	Columns	Variable	Format	Explanation
1	1 - 8	WORD	A8	Enter the word DISTRIBU
2	1 - 5	NSETS	15	Number of sets of loaded elements
3	1 - 5	NFE	15	Number of first loaded element
	6 - 10	NLE	15	Number of last loaded element
	11 - 15	NSIDE	15	Number of loaded side of element
	16 - 20	ILOAD	15	Loading type number (1, 2 or 3)

21 - 30	B0	F10.0	Pressure distribution constant
31 - 40	BX	F10.0	Pressure distribution constant
41 - 50	BY	F10.0	Pressure distribution constant
51 - 60	XCEN	F10.0	X-coordinate of reference
61 - 70	YCEN	F10.0	Y-coordinate of reference

Card 3 is repeated NSETS times.

A series of elements with numbers NFE through NLE count one for the value of NSETS. NSIDE is specified on the basis of the local nodal numbering system of the loaded elements, as shown on Figure C.3. Sequentially numbered loaded elements thus must also have the same local node numbering to be included in the same NSETS number with other loaded elements.

Using the last 5 input parameters different pressure distributions are defined. For ILOAD = 1, the applied pressure at any point on the loaded surface is computed with relative position to the reference point (XCEN, YCEN).

$$p = B0 + BX(x - XCEN) + BY(y - YCEN) \quad (C.5)$$

For ILOAD = 2, the elliptic distribution of pressure is defined as,

$$p = B0 + BX \cos\theta + BY \sin\theta/2 \quad (C.6)$$

where  $\theta$  is measured from a horizontal line which passes the center point (XCEN, YCEN).  $\theta$  is positive in the counterclockwise direction. For ILOAD = 3, body force intensities per unit volume in z-, x- and y- directions are indicated by B0, BX and BY, respectively. The reference coordinates are left blank.

When ILOAD = 1 or 2, the pressure is considered positive when it acts towards the center of the element. When ILOAD = 3, the force/unit volume is considered positive in the direction of the positive axes coordinates.

LOA.8 Restart file saving interval

An interval of saving the restart file (the continuation data file) may be altered by this option. Since the restart file requires a large disk storage, it is desirable to store only a few files which are considered necessary from the viewpoint of the security and convenience for further analysis. Default value of the storing frequency is one so that every load increment establishes its restart file.

LOA. 8 Restart File Storing Interval

Card	Columns	Variable	Format	Explanation
1	1 - 8	WORD	A8	Enter the word RESTART
2	1 - 5	IRST	I5	Restart file frequency

LOA.9 End of load block card

This card is required to define the end of the load block. This block should be repeated if more than one load increment is desired, unless NPINC or NTINC is greater than one.

LOA.9      End of Load Block

Card	Columns	Variable	Format	Explanation
1	1 - 8	WORD	A8	Enter the word END LOAD

### C.5      Restart File and External Memories

As described on restart group (CNT.5) in the section C.4.1, the restart file (the continuation data file) is very useful to break up a large run into a number of smaller runs to reduce the chances of wasting money and time due to unexpected bad results. The restore file is written on a disk. Similarly, the restoration file described in the section C.3.1 also uses an external memory. In this section the program's use of external memories is explained so that JCL cards may easily be prepared. Then a review of the restart file and plotting services are described later.

#### C.5.1      DD Statement in JCL Cards

As the program JFSESF is written in FORTRAN, a set of DD statement are required to define I/O device numbers for every reference of read/write operation. Device unit 5 and 6 are reserved for the system read and write, respectively.

The restart files are written to unit 8 and they are read from unit 9. The expected size of a restart file is recognized in view of Figure C.2. A

restart file saves data in addresses from MBGN to LWRT2 and LWRT3 to LEND. These address information are provided in a print listing.

Three other devices are in use for temporary storages. Unit 15 is used to save arrays for stress recovery for elements with non-Prevost material types. The required space is expected not larger than 72 words times the number of elements with the non-Prevost material types. Unit 16 stores the element stiffness matrix and other element-related information for the Prevost material type elements. At most 435 words of data are saved for one element with this material type. Such a value times the total number of the Prevost model elements becomes the required space for the unit 15. Unit 17 saves the restoration file to provide a memory storage space for assembling the global stiffness matrix. The restoration size is shown in Figure C.2. Its size is equivalent to the addresses from LWRT1 to LWRT2 and is printed in the listing.

All except system I/O's employ unformatted I/O data transfer so that their record format should be a variable spanned block. Sample DD statements are found in the sample input, which follows the section C.6.

#### C.5.2 Print out of Restart File

Restart file may be dumped to the printer by means of a combined use of the RESTART (CNT.5) and INCREMENTS (CNT.6) control keywords of the control block. It is useful to determine whether an inquiring file is one concerned. If load increment numbers IRST, IWST and NFLI are all identical while NLLI equals zero, then all the computing processes are suppressed but print out

of the NFLI increment from the restart file on a disk. The job is terminated consequently. Only control block of input data in a set is required for this purpose, though subsequent blocks of input data are not necessarily removed.

### C.5.3 Plotting functions

Results of the program JFSEST may appear in plotting using restart files. The program JFESTP is an independent program for plotting. Optional plotting functions are nodal point number, element number, original and deformed meshes, and principle stress direction. Specific elements may be omitted intentionally from the plotting. Input for JFESTP must follow this procedure: Plotting option codes, KEY1 to KEY6 have a value of 1 or larger if plotting is requested; zero if no operation for plotting.

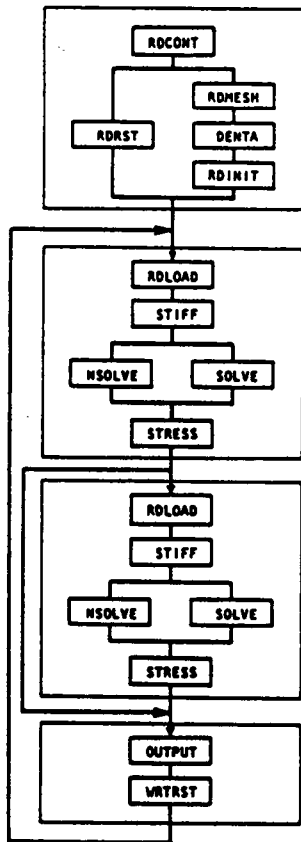
#### PLT.1 Plotting Using the Restart File

Card	Columns	Variable	Format	Explanation
1	1 - 5	15	IRST	Increment number to be plotted
2	1 - 5	15	KEY1	Nodal point number plotting code
	6 - 10	15	KEY2	Element number plotting code
	11 - 15	15	KEY3	Deformed mesh plotting code
	16 - 20	15	KEY4	Value specifies line thickness Displacement vector arrow plotting code
	21 - 25	15	KEY5	Undeformed mesh plotting code
	26 - 30	15	KEY6	Principal stress direction plotting code
	31 - 35	15	NOMIT	Number of element to be omitted
	36 - 40	15	NEE	Number of nodes per element
3	1 - 10	F10.0	X0	X-coord. of the plotting origin
	11 - 20	F10.0	Y0	Y-coord. of the plotting origin
4	1 - 10	F10.0	SCAX	Scale in X-direction for 1 inch
	11 - 20	F10.0	SCAY	Scale in Y-direction for 1 inch

21 - 30	F10.0	FCTX	Magnification factor of X displacements
31 - 40	F10.0	FCTY	Magnification factor of Y displacements
41 - 50	F10.0	OBJXSZ	Maximum plotting size in Y direction
51 - 60	F10.0	ARRO	Average arrow size of principal stresses
61 - 70	F10.0	ARRS	Variation factor of the arrow size
5 1 - 80	1615	INDX(I)	Element number to be omitted, I = 1,NOMIT Card 5 is repeated for a total of NOMIT This card may be suppressed if NOMIT = 0

#### C.6 Sample Input

The input for the N-2 tunnel transverse section analysis described in Chapter 8 is given below. The sample input data consists of five job runs which are independent but related to successive ones with the restart procedure using the continuation data file. Each analysis corresponds to one of the five loading stages of the tunnel construction performance, as illustrated in Figure 8.2.



**Initial Setup**

Input control parameters (RDCONT), mesh scheme information (RDMESH), and initial stress calculation (RDINIT) from external input data or restart files already established on the tape or the disc (RDRST). Skyline scheme of global stiffness matrix is designed (DENTA).

**Predictor Phase**

As a loading step of incremental analyses, load vector and global stiffness matrix are formed (RLOAD, STIFF). Symmetric or nonsymmetric solver (SOLVE, NSOLVE) provides a primary solution which is further treated for stresses and strains. Moduli for subsequent step are prepared (STRESS).

**Corrector Phase**

Similar to the previous phase solution for the incremental load of the step is obtained. Stresses, strains, elastic and plastic moduli and other state dependent properties are replaced by updated values. This phase is bypassed if iteration is not used.

**Output**

Nodal values and stresses at integration points are printed (OUTPUT). Parameters identifying the problem in blank common A are all preserved for future continuation of the analysis (WRTRST).

Figure C.1 Program JFSEST Overview

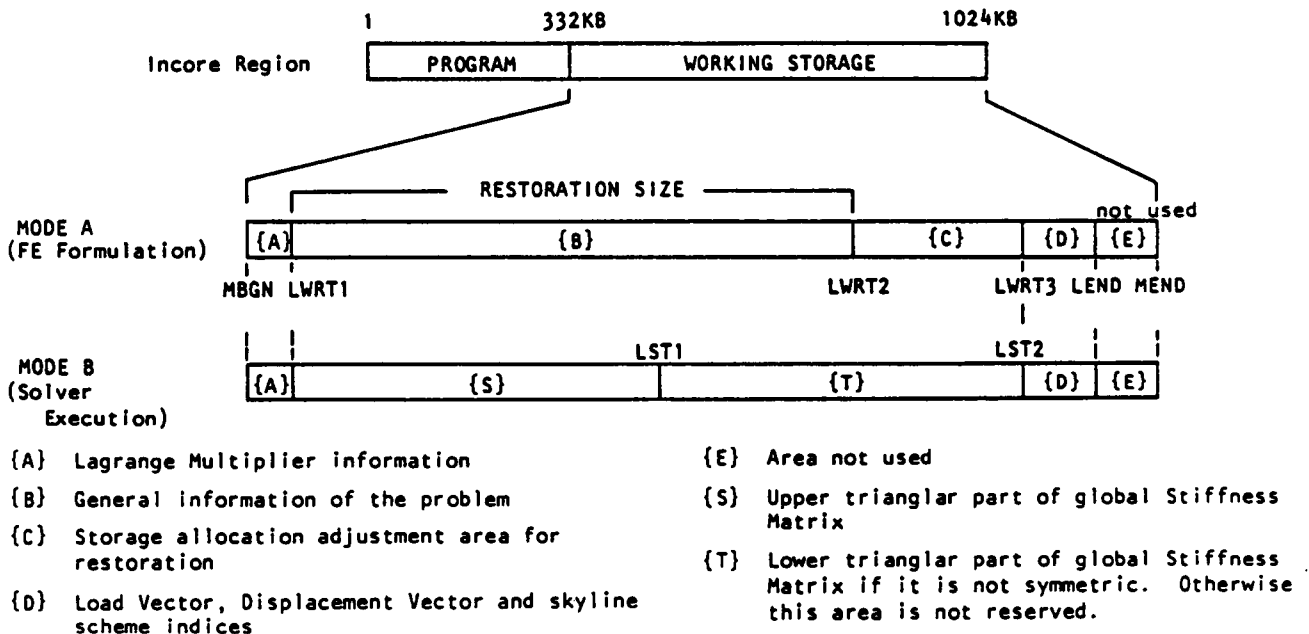
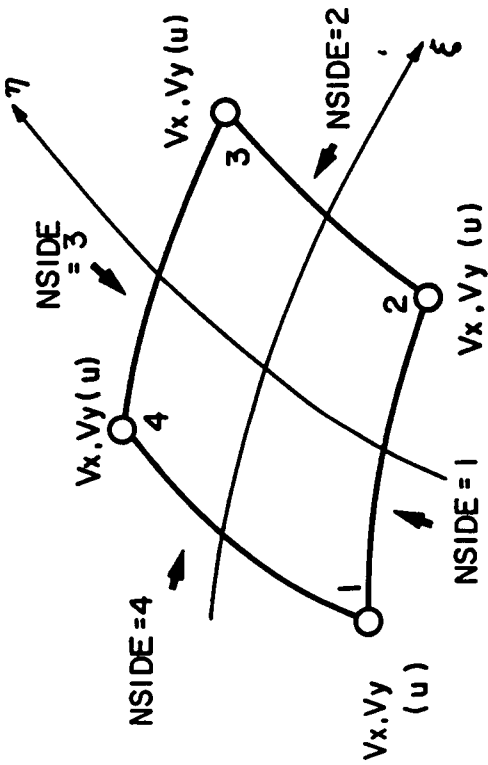
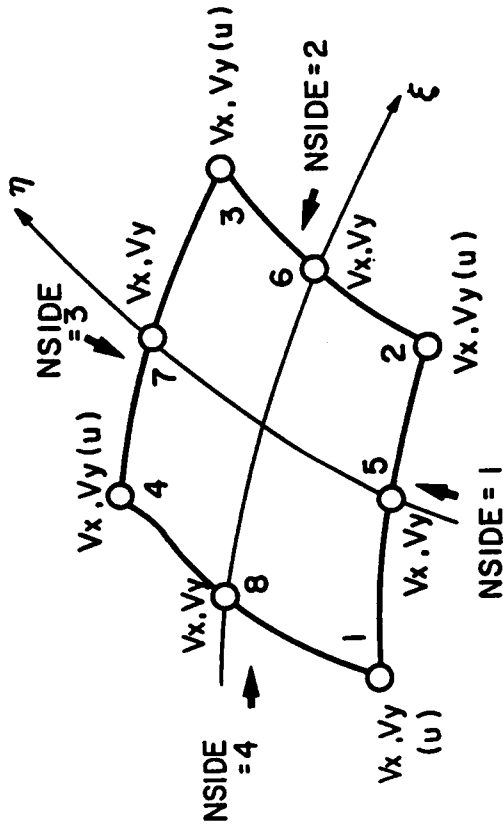


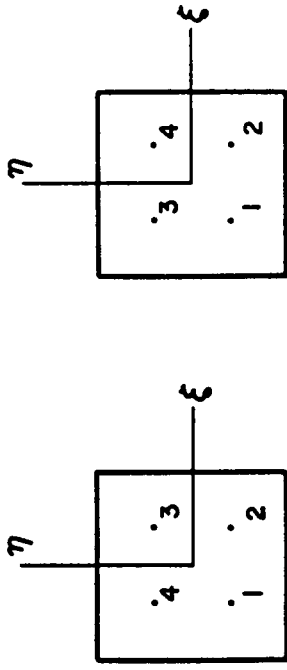
Figure C.2 Memory Utilization Design for Restoration Procedure



(a) Q4 / Q4P4 Element

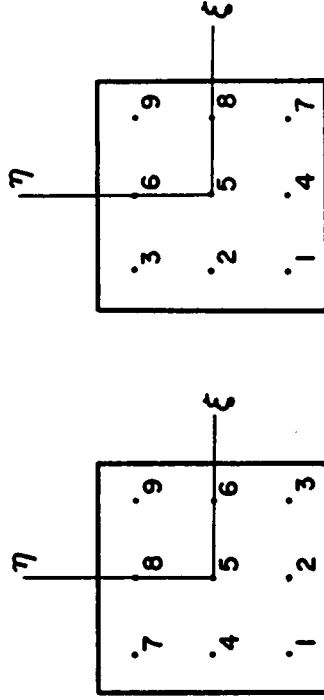


(b) Q8, Q8P4 Element



Prevost Type  
Linear/Nonlinear Elastic,  
Cam Clay Type

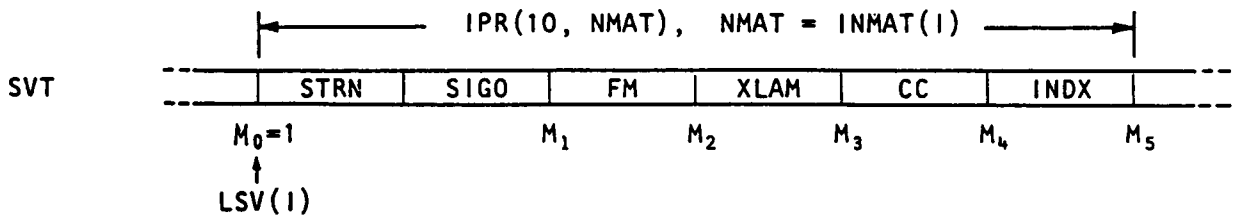
(c) Four Points Integration Scheme



Prevost Type  
Linear/Nonlinear Elastic,  
Cam Clay Type

(d) Nine Points Integration Scheme

Figure C.3 Element Library with Prevost Soil Model



Symbol	Notation	Description	(Vector Size)
STRN	$\epsilon_x, \epsilon_y, \epsilon_z, \gamma_{xy}$	Lagrangian strains	( ND x NSPT )
SIGO	$\sigma_{x0}, \sigma_{y0}, \sigma_{z0}, \tau_{xy0}$	Initial stresses	( ND x NSPT )
FM	$\sigma_{11}, \sigma_{22}, \sigma_{33}, \sigma_{12}$	Current stresses	
	$G, h, B^E$	Elastic moduli and initial plastic moduli	
	$n$	Bulk exponent	
	$\xi_{11}^{(m)}, \xi_{22}^{(m)}, \xi_{33}^{(m)}, \xi_{12}^{(m)}, k_m$	Position and size of yield surface $m$	
	$h_m, B_m, A_m$	Plastic moduli and nonassociativity associated with yield surface $m$ $m = 1, NYS$ ( ND4 x NSPT x NYS )	
XLAM	$\delta \bar{\epsilon}^P, \bar{\epsilon}^P, \delta_1, \delta_{ult}$	Plastic strain intensity and softening parameters	
	SC	Yield surface axis ratio	
	$p$	Effective mean pressure	
	$\lambda$	Slope of $\epsilon_V^P$ vs $p$ curve	
	$u, B_F$	Pore pressure and bulk modulus of fluid	
	$\epsilon_V^P$	Plastic volumetric strain	
	$k_x, k_y, \mu_k$	Permeabilities, nonlinearity exponent of permeability	( 13 x NSPT )
	CC	AL	Volumetric part of elasto-plastic modulus
	$C_{ij}$	Deviatoric part of elasto-plastic modulus matrix	( 1 + NDxND )
INDX	IND1 - IND4	Indices of yield surface configuration and count of loading reversals	(4)

Example of SVT array for an element with Prevost material

Conditions : 9 point scheme, Q8P4 element, JHPTYP = 6, NYS = 12

Size of SVT:  $M_5 = 1005$

Figure C.4 Description of Stress Vector SVT for Prevost Type Material

SAMPLE INPUT OF PROGRAM - JFSEST

```

//GO EXEC PGM=JFSEST01
//STEPLIB DD DSN=AF00F4.TAKESHI,LOADMOD,VER502,DISP=OLD
//T0100 DD DNAME=SYSIN
//T0100 DD SYSDAT=A
//*****
//** M2 TUNNEL LINE-4 SIMULATION BY MEANS OF PROGRAM JFSEST ***
//** HEAVING, UNLOADING, LINER ACTIVATION, AND CONSOLIDATION **
//*****
//GO.FT08F001 DD SPACE=(TRK,(10,5),RLSE),DISP=(NEW,CATLG),
// DCB=(RECFM=VSB,BLKSIZE=6233),VOL=SER=USER05,UNIT=DISH,
// DSN=AF00F4.TAKESHI.TUNNELAS.820T2603
//GO.FT09F001 DD DUMMY
//GO.FT15F001 DD UNIT=DISH,SPACE=(TRK,(10,5)),
// DCB=(RECFM=VSB,BLKSIZE=623)
//GO.FT16F001 DD UNIT=DISH,SPACE=(TRK,(10,5)),
// DCB=(RECFM=VSB,BLKSIZE=623)
//GO.FT17F001 DD UNIT=DISH,SPACE=(TRK,(10,5)),
// DCB=(RECFM=VSB,BLKSIZE=623)
//GO.SYSIN DD *

TITLE
M2 TUNNEL LINE 4, DISTORTED HEAVE Z-DRAIN 24FT 26*60PSF H26V00L00C00
SIZE 309 88 0 0 32 6 93 1
RESTART -1
INCREMENT 20
PORE PRE 1 26 26 0.5
PL STRAI 0.5
LARGE DI
TYPE MAT 1 8 9
TYPE ELE 1 8 9
END CONT 3
MATERIAL 1 1 1.0 0.01
2 2
30000000. 0.3
MATERIAL 2 9 6 1 4 4 4 4 4 4 1 12
0.0 -1.0 0.0 62.4 0.014 0.0028 1.0 24.0
60.0 6 6 1 4 4 4 4 4 4 1 12
0.0 -1.0 0.0 62.4 0.014 0.0028 1.0 24.0
MATERIAL 2 8
4 0.30 10.0 0.49 10.0 0.95 30.0 250.0 0.5 200.0
5 200.0 0.35 10.0 0.49 10.0 0.90 20.0 1000.0 0.4 945.0
945.0 10.0 10.0 10.0 2117.0
PRINT
MESH GEN 0
1 3
2 5
3 5
4 8 2
5 8 1421
6 10.0 16.0 26.0 38.0 50.0 62.0
80.0
0.0 16.0 24.0
MESH GEN 1 3
241 73 4 2
0.0 10.0 16.0 26.0 38.0 50.0 62.0

```

```

80.0 80.0 70.0
50.0 60.0 60.0
MESH GEN 1 4 6
215 49 8 1
80.0 4.1421 10.0 16.0 26.0 38.0 50.0 62.0
44.0 50.0

```

MODES

```

145 0.0000 19.0000000
146 0.9784563 39.0019100
202 1.913418038 1531400
200 1.913418038 1531400
197 2.777842038 1531400
191 3.535533037 5355200
181 4.157347036 7778400
162 4.619397035 9134000
152 4.903925034 9754400
151 5.000000034 0000000
150 4.903925033 0245300
149 4.619397032 0865700
148 4.157347031 2221300
147 3.535533030 4644600
146 2.777842029 8426500
145 1.913418029 3805900
144 0.975456259 0966600
143 0.00000 29.0000000
210 0.00000 39.5000000
192 1.88487037 0813200
193 1.88487037 0813200
165 3.081346034 1647600
142 5.500000034 0000000
141 5.081336031 8952300
140 3.889087030 1109000
139 2.104760028 9186500
138 0.00000 28.5000000
211 0.00000 40.0000000
207 1.170546039 8447000
202 2.296102039 5432700
198 3.33422038 9888100
193 4.282641038 2426300
182 4.988818037 3334100
184 5.53276036 2960900
153 2.884711035 1705300
121 6.000000034 0000000
120 2.58121032 9794500
119 2.98818031 6286000
117 4.242641029 7573600
116 3.33382029 0111600
115 2.296102028 4567100
114 1.170546028 1152800
113 0.00000 28.0000000
212 0.00000 41.0000000
203 2.678786040 4671400
194 4.949748038 9497300
165 6.467156036 6787700
122 7.000000034 0000000
104 6.467156031 3212100
103 4.949748029 0502400
102 2.678786027 5328300
101 0.00000 27.0000000
213 0.00000 42.0000000
208 1.260720041 8628000
199 3.444563040 2192000
198 3.444563039 5648400
183 4.651757038 4445400
166 7.391036037 0616600
154 7.846282035 5607100
123 8.000000034 0000000
105 7.846282032 4392700
86 7.391036030 9385200
85 6.651757029 5554300
84 5.656855028 3431300
83 4.444563027 3468200
82 3.061870026 6089600
81 1.560729026 1537100
80 0.00000 26.0000000
71 3.6011785 25.30448

```





TITLE  
M2 TUNNEL LINE 4 UNLOADING TO CLOSE GAP 208-75PSF H21V43100C00 S43T43D1  
SIZE  
RESTAR 88 0 0 32 6 93  
INCREMEN 43  
22 43 6 0.5  
PORE PRE 0.5  
PL STRAI  
LARGE DI  
TYPE MAT  
TYPE ELE 1 2 8  
END COM 3  
RESTART  
PRINT 1  
DISTRIBU 1  
0 10 1 2 -75.0 25.0 0.0 0.0 34.0  
11 14 4 2 -75.0 25.0 0.0 0.0 34.0  
15 16 3 2 -75.0 25.0 0.0 0.0 34.0  
TIME INC .0031  
PRINT 0  
PROPERTI 4 STEP=22-NO DP=-75 UNLD-50/-100  
19 1.0  
END LOAD  
PRINT  
PROPERTI 1 STEP=41-43 DP=-75 UNLD-50/-100  
4 1.0  
END LOAD  
/°

PROPERTI 0.0  
EXCAVATE 8 17 1  
0 3  
10 3  
11 3  
12 3  
13 3  
14 3  
15 3  
16 3  
113 114 115 116 117 118 119 120 121 153 164 182 193 198 202 207  
211  
DISTRIBU 103 PCF / (0.1333\*6)  
PROPERTI 1 8 0 3 0.0 0.0 -128.8  
ACCOUNTING FOR STRESSES CARRIED BY CEMENT GROUTING BY 20%  
PRINT 1 0.1333  
49  
END LOAD  
PROPERTI 1.0  
END LOAD  
/°

TITLE  
M2 TUNNEL LINE 4, CONSOLIDATION STP50T63 BY 14 TIME STEPS H21V43T49C63  
SIZE  
RESTAR 88 0 0 32 6 93  
INCREMEN 55  
50 63 5 0.5  
PORE PRE 0.5  
PL STRAI  
LARGE DI  
TYPE MAT  
TYPE ELE 1 2 8  
END COM 3 4  
CHANGE M MOBILIZING BENDING STIFFNESS OF LINER  
1 10  
RESTAR 0.3  
PRINT 8  
TIME INC 0.2  
PROPERTI 0.0  
END LOAD  
TIME INC 0.2  
PRINT 2  
TIME INC 0.2  
END LOAD  
/°

TITLE  
M2 TUNNEL LINE 4, LINER ACTIVATE STP44T49 BY 6 SUBSTPS H21V43L49C00  
SIZE  
RESTAR 88 0 0 32 6 93  
INCREMEN 43 49  
44 49 6 0.5  
PORE PRE 0.5  
PL STRAI  
LARGE DI  
TYPE MAT  
TYPE ELE 1 2 8  
END COM 3 4  
RESTART  
PRINT 3  
CHANGE M MOBILIZING COMPRESSIVE STIFFNESS OF LINER  
1 10  
TIME INC 0.3  
TIME INC .00625

11.0E06

118.0E06

**The vita has been removed from  
the scanned document**